UNIVERSITAT DE BARCELONA

Advanced Modelling of Metallic Nanomaterials for Catalysis

Lorena Vega Domínguez

Advanced Modelling of Metallic Nanomaterials for Catalysis

Doctoral Thesis by

Lorena Vega Domínguez

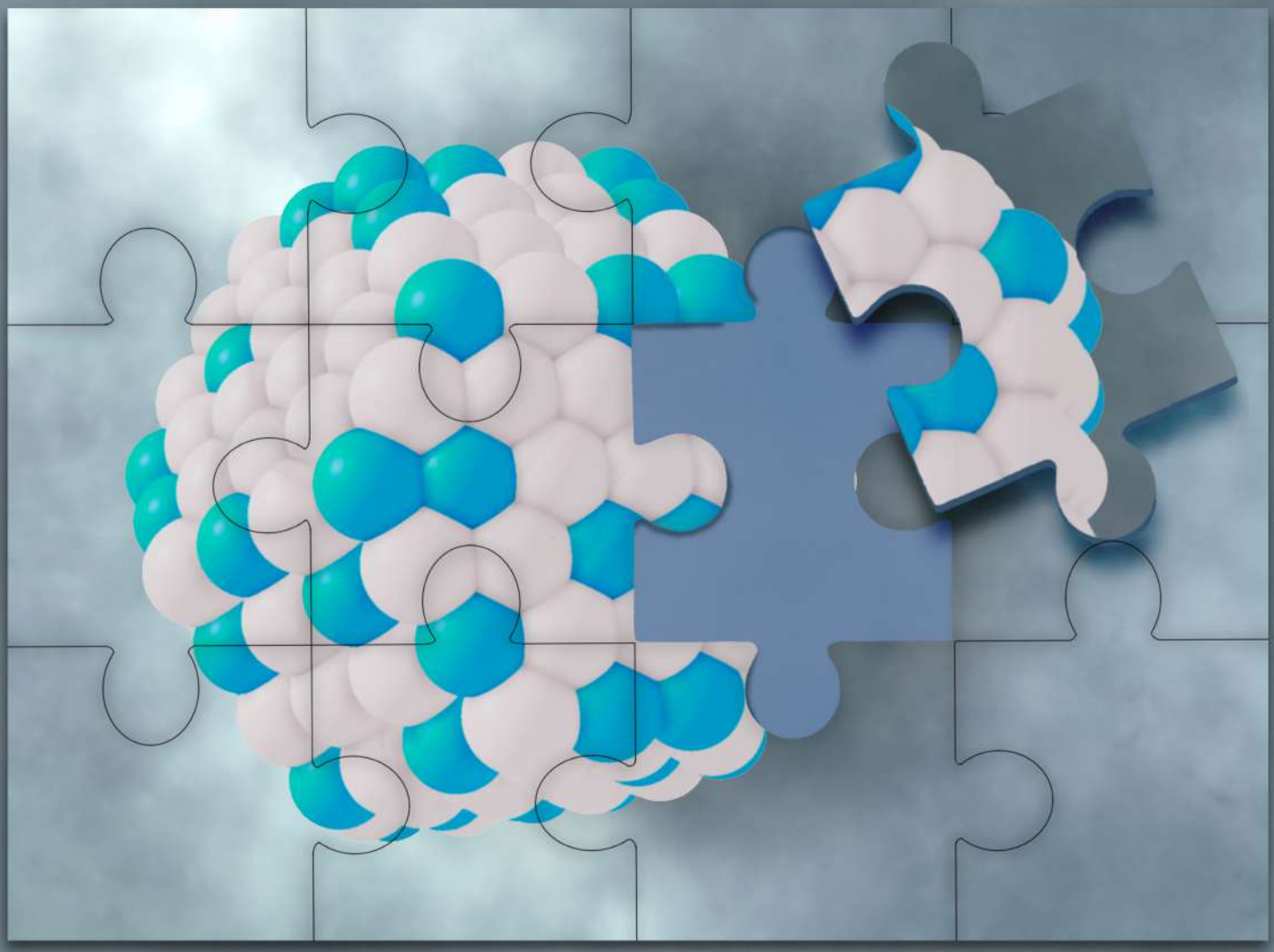

UNIVERSITAT DE BARCELONA

Memòria presentada per

Lorena Vega Domínguez

Per a optar al grau de Doctor per la

Universitat de Barcelona

Programa de doctorat en Química Teòrica i Computacional

Advanced Modelling of Metallic Nanomaterials for Catalysis

Dirigida per:

Prof. Konstantin M. Neyman

Universitat de Barcelona

Institució Catalana de Recerca i Estudis Avançats

Dr. Francesc Viñes

Universitat de Barcelona

Tutor:

Prof. Francesc Illas Riera

Universitat de Barcelona

UNIVERSITAT DE BARCELONA

Barcelona, 2021

ABSTRACT

Nanoparticles are highly relevant for catalysis due to their nanostructure, which increases the fraction of surface atoms, and the size dependent morphology and properties. Catalytic properties of nanoalloys also depend on the composition and chemical ordering. Therefore, it is important to understand how geometrical and topological features of mono- and bimetallic nanoparticles affect their stability and reactivity of the exposed surface sites. This Thesis deals with computational study of monometallic and bimetallic nanoparticles using methods based on Density Functional Theory (DFT). First, the exchange-correlation functional PBE was identified to reproduce experimental bulk and surface properties of Transition Metals overall more accurately than other examined functionals VWN, PBEsol, RPBE and TPSS. The performance was further improved by choosing exchange and correlation parameters between those of PBE and PBEsol functionals or restoring the local spin approximation of PBEsol. The *d*-band centre was found the most robust and transferrable among the studied electronic descriptors for different functionals.

For different monometallic Pd nanoparticles it was shown that their energies can be quantitatively described using linear dependence on the quantity of atoms with different coordination numbers. Whereas employing such morphological features as number of corner sites, length of the edges, particle area and volume allowed only a qualitative energy prediction.

Equilibrium chemical ordering for bare PdRh, PtNi, PtAu, PtAg, and PtCu bimetallic nanoparticles at low temperature was determined employing the so-called Topological Method parameterized on DFT data. Effects of temperature and reactive environment on the chemical ordering were also evaluated. A remarkable experimental finding of our collaborators is that CO molecules can bind stronger on some core@shell Cu@Pt particles than on pure Pt particles. It was rationalised by DFT calculations of specific surface sites, such as single Pt atom surrounded by surface Cu atoms, under-coordinated Pt atom, Pt adatom and vacancies with missing Pt atoms.

ACKNOWLEGMENTS

First of all, I want to thank to my advisors Prof. Konstantin M. Neyman and Dr. Francesc Viñes for their tuition and knowledge during this PhD period. Also, I would like to thank all my collaborators, MsC. Biel Martínez, Prof. Pere Cabot and MsC. Júlia, Dr. Ivan Khalakhan and his group, Dr. Aleksandro Fortunelli, Prof. Mauro Stener and their MsC. Nicola and Sofia that were working with us in HPC stay by 3 months, and Dr. Hristiyan Aleksandrov, Dr. Albert Bruix, and MsC. Riccardo Farris. Specially to Prof. Francesc Illas, who is my PhD tutor, and Dr. Hristiyan Aleksandrov for their support and the extended discussion of the results and the methodology. Last but not least, to Dr. Albert Bruix to be always helpful, provide good advices and scientific discussions.

También me gustaría agradecer a toda la gente y buenas amistades que han formado parte de esta etapa y han hecho que sea llevadera siendo un apoyo esencial no sólo en el trabajo, sino en otros aspectos de mi vida. Primero de todo, a los que han estado en primera línea viéndome cada día trabajando en esta tesis. Cristina, Marc, Genís, Raúl, y Toni muchas gracias por ser los mejores compañeros de despacho, por las risas, muchas risas, discusiones, bromas, pero sobretodo el apoyo mutuo y buen ambiente que se respiraba. Sois todos muy grandes. También, sigo sin olvidar con los que comencé en mi primer despacho y los primeros que conocí del departamento Juanjo, Sergi y Oriol Lamiel, un muy buen trío, con el que me dio lástima no haber compartido más tiempo. De hecho, ocupó mi sitio en ese despacho Martí, con el cuál compartí un máster duro y se forjó un gran vínculo que durante estos años se ha reforzado. Así que, no le puedo guardar rencor por ello. Berta es otra persona que ya conocía de antes del departamento. Coincidimos en la carrera y aunque en su momento no teníamos mucha relación ahora para mi es una amiga terremoto a la que valoro un montón. También me gustaría agradecerles a mis recientes miembros de grupo, Pablo, Riccardo y Jon por todo este último apoyo, ayuda, y por compartir reuniones y charlas muy distendidas durante la comida. Ojalá, haber tenido dicho grupo antes, hubiese sido mucho más fácil todo este camino. A Júlia, la cuál no sólo conozco por

nuestra colaboración, me gustaría agradecer el haber tenido el placer de compartir un gran congreso en Bulgaria y las asperezas y alegrías del doctorado. De dicho congreso, también me llevo otra amistad, Joan, mi compi de “machines bb”, gracias a él este periodo ha sido más ligero y entretenido, y un muy buen apoyo. Aparte de ellos, me llevo también a personas como Roger y Dani, y sus interesantes debates y puntos de vista. Gracias a todos, sois lo que en un futuro más echaré en falta de esta etapa.

Para finalizar, aunque no me extenderé con ellos porque me faltaría papel, quiero agradecer a mi familia y amigos de toda la vida que siempre están ahí. Obviamente, esta etapa no ha sido menos. Gracias por vuestro apoyo, paciencia y amor. Por último y en especial, a Oriol, por entrar en mi vida, quedarse y hacerla mejor de lo que era antes. Gracias por apoyarme en cada uno de los pasos que he dado, bregar de cerca con todas mis inseguridades y ayudarme en el proceso.

TABLE OF CONTENTS

LIST OF ABBREVIATIONS **1**

PART I. INTRODUCTION **3**

CHAPTER 1. OVERVIEW OF THE THESIS **3**

CHAPTER 2. BASIC COMPUTATIONAL METHODOLOGY **5**

2.1 DENSITY FUNCTIONAL THEORY *5*

2.2 BASIS SETS *11*

2.2.1 Plane Waves and Pseudopotentials 11

2.2.2 Numerical Atomic Orbitals 12

2.3 MONTE CARLO APPROACH *13*

2.4 MINIMA ANALYSIS *14*

2.4.1 Work Function 14

2.4.2 Density of States 15

2.4.3 Bader Charge 15

2.4.4 Charge Density Difference 16

CHAPTER 3. MODELLING FROM BULK TO NANOPARTICLES **17**

3.1 PERIODIC BOUNDARY CONDITIONS *17*

3.2 RECIPROCAL LATTICE *19*

3.3 BLOCH'S THEOREM *20*

3.4 MILLER INDICES *21*

3.5 SURFACE AND NANOPARTICLES MODELS *22*

PART II. RESULTS ON MONOMETALLIC SYSTEMS **25**

CHAPTER 4. PERFORMANCE AND IMPROVEMENT OF THE MOST COMMON FUNCTIONALS FOR TRANSITION METALS **25**

4.1 INTRODUCTION *25*

4.2 OBJECTIVES *26*

4.3 ASSESSING THE PERFORMANCE OF BROADLY USED DENSITY FUNCTIONALS ON TRANSITION METAL SURFACE PROPERTIES *27*

4.3.1 Summary 27

4.3.2 Publication 34

4.4 ROBUSTNESS OF SURFACE ACTIVITY ELECTRONIC STRUCTURE-BASED DESCRIPTORS OF TRANSITION METALS *43*

4.4.1 Summary 43

4.4.2 Publication 49

4.5 GENERALIZED GRADIENT APPROXIMATION ADJUSTED TO TRANSITION METALS PROPERTIES: KEY ROLES OF EXCHANGE AND LOCAL SPIN DENSITY *56*
4.5.1 Summary 56
4.5.2 Publication 60
CHAPTER 5. UNRAVELLING MORPHOLOGICAL AND TOPOLOGICAL KEY ASPECTS OF PD NANOPARTICLES **66**
5.1 SUMMARY *66*
5.2 PUBLICATION *75*
PART III. RESULTS ON BIMETALLIC SYSTEMS **83**
CHAPTER 6. CHEMICAL ORDERING OF BIMETALLIC NANOPARTICLES **83**
6.1 INTRODUCTION *83*
6.2 OBJECTIVES *87*
6.3 USING DENSITY FUNCTIONAL CALCULATIONS TO ELUCIDATE ATOMIC ORDERING OF PdRh NANOPARTICLES AT SIZES RELEVANT FOR CATALYTIC APPLICATIONS *88*
6.3.1 Summary 88
6.3.2 Publication 96
6.4 IRREVERSIBLE STRUCTURAL DYNAMICS ON THE SURFACE OF BIMETALLIC PtNi ALLOY CATALYST UNDER ALTERNATING OXIDIZING AND REDUCING ENVIRONMENTS *105*
6.4.1 Summary 105
6.4.2 Publication 110
6.5 ELUCIDATION OF THE STRUCTURE OF PtX (X=Cu, Au, Ag) NANOPARTICLES OF DIFFERENT SIZES BY DENSITY FUNCTIONAL CALCULATIONS *119*
6.5.1 Summary 119
6.5.2 Publication 129
CHAPTER 7. NANOSTRUCTURING DETERMINES POISONING: TAILORING CO ADSORPTION ON PTCU BIMETALLIC NANOPARTICLES **143**
7.1 SUMMARY *143*
7.2 PUBLICATION *149*
PART IV. CONCLUSIONS **173**
LIST OF PUBLICATIONS **177**

APPENDIX..... 179

A. Supplementary Information of Jacob's Ladder as Sketched by Escher: Assessing the Performance of Broadly-Used Density Functionals on Transition Metal Surface Properties 179

B. Supplementary Information of Robustness of Surface Activity Electronic Structure-Based Descriptors of Transition Metals 221

C. Supplementary Information of Generalized Gradient Approximation Adjusted to Transition Metals Properties: Key Roles of Exchange and Local Spin Density 237

D. Supplementary Information of Unravelling Morphological and Topological Key Aspects of Pd Nanoparticles 253

E. Supplementary Information of Irreversible Structural Dynamics on the Surface of Bimetallic PtNi Alloy Catalyst under Alternating Oxidizing and Reducing Environments 267

F. Supplementary Information of Elucidation of the Structure of PtX (X=Cu, Au, Ag) Nanoparticles of Different Sizes by Density Functional Calculations 273

G. Supplementary Information of Nanostructuring Determines Poisoning: Tailoring CO Adsorption on PtCu Bimetallic Nanoparticles 275

H. Inner ordered phase $L1_1$ of PtAg Nanoparticles 279

REFERENCES 281

LIST OF ABBREVIATIONS

γ	Surface Energy
δ	Minimum interatomic distance
δ_{ij}	Minimum interlayer distance
ε_d	d-band centre
ε_d^W	Width corrected d-band centre
ε_u	Highest point of the imaginary part of the Hilbert transform of the d-projected Density of States
ε_{xc}	Exchange and correlation particle energy
$\rho_0(\boldsymbol{r})$	Ground state electronic density
$\rho(\boldsymbol{r})$	Electronic density
ϕ	Work Function
A@B	Core@Shell structures where core atoms are A and shell atoms are B
bcc	Body centre cubic
B_0	Bulk moduli
CDD	Charge Density Difference
CN	Coordination Number
DFT	Density Functional Theory
DOS	Density of States
E_{coh}	Cohesive energy
E_{xc}	Exchange and correlation total energy
fcc	Face centred cubic
FHI-AIMS	Fritz-Haber Institute Ab Initio Molecular Simulations
GGA	Generalized Gradient Approximation
hcp	Hexagonal close packet
$\widehat{H}_e$	Electronic Hamiltonian
HF	Hartree-Fock
LDA	Local Density Approximation
LSD	Local Spin Density

MAE	Mean Absolute Error
MAPE	Mean Absolute Percentage Error
MC	Monte Carlo
NAO	Numeric Atom-centred Orbitals
NP	Nanoparticle
PAW	Projected Augmented Wave
PBC	Periodic Boundary Conditions
PBE	Perdew-Burke-Ernzenhof
$\hat{T}_e$	Electron kinetic energy
TMs	Transition Metals
TOP	Topological
TPSS	Tao-Perdew-Staroverov-Scuseria
VASP	Vienna Ab Initio Simulation Program
$V_{ee}[\rho]$	Potential energy between electrons
$\hat{V}_{NN}$	Potential energy between nuclei
VWN	Vosko-Wilk-Nusair
xc	Exchange and correlation

PART I. INTRODUCTION

Chapter 1. Overview of the Thesis

Nanoparticles (NPs) are clusters of atoms, ions, or molecules, with dimensions *circa* 1-20 nm.[1,2] This size range is quite interesting in science because it fills the gap between small molecules, with discrete energy states, and bulk materials, with continuous energy states. Consequently, one of the main interests is the size-evolution of the geometric and electronic structures of clusters and their physical and chemical properties. Since NPs often have different properties from those of discrete molecules or bulk solids, they can be considered a new type of materials. The Thesis is focused on metallic NPs, specifically those formed by Transition Metals (TMs).[3] Many properties such as ionization energy, electron affinity, or cohesive energy, among others, follow a simple scaling law in large metallic NPs. Meaning that the properties scale linearly with size until the bulk limit.[4] However, small NPs show significant deviations with respect to the agreement of the scaling laws due to quantum confinement and surface effects. Quantum confinement leads to a collapse of the continuous energy bands of a bulk state into discrete energy levels when the dimensions of a material reach the nanoscale. Surface effects are referred to the higher surface-to-volume ratio at this regime. Metallic NPs can be formed of a single metal or more than one metallic element, becoming nanoalloys.[2] Nanoalloys are technologically interesting because their chemical and physical properties can be modified by the choice of composition, their atomic ordering, and, as in monometallic NPs, their shape. In the case of catalysis, different surface sites formed upon combining two metals determine the catalytic activity of these materials.

To calculate the properties of TMs with first principles methods, the most common employed methodology with the best balance between accuracy and computational cost is the Density Functional Theory (DFT). Within the DFT, there are different exchange-correlation (*xc*) functionals due to the exact

one is unknown. Each of them is classified according to different levels of complexity. The best choice of approximation depends on the system and properties one tries to calculate. Therefore, it is relevant to study which one is appropriate to compute the target systems, in our case the TMs.

Then, the main topics of this Thesis are the evaluation and improvement of the DFT functionals for the description of TMs, and the understanding of interplay between the structure and stability of mono- and bimetallic nanoparticles. Because the stability of different sites is intrinsically related with the reactivity, some projects deal with molecular adsorption. Each of the topics mentioned above will be further developed in their corresponding Thesis section. The general objectives of the Thesis are:

- Evaluate the performance of different functionals through bulk and surface properties of TMs.
- Establish the most robust electronic surface descriptor through different functionals.
- Improve the performance of PBE-based functionals as PBE and PBEsol through bulk and surface properties of TMs.
- Unravel Pd NP energy in structural contributions based on the coordination number and geometric features.
- Obtain the chemical orderings of bimetallic NPs under different temperature and reactive conditions using the topological method.
- Analyse the topological method.
- Find adsorption sites on Cu@Pt core@shell NPs where CO binding is stronger than in the pure Pt NPs.

The Thesis is structured as follows: the first part, the introduction, explains the methodology and modelling approaches employed in the present work. The second part, on monometallic systems, reports the results obtained in this work for pure transition metals. The third part, on bimetallic systems, describes the results obtained for alloy NPs formed by two transition metals. Finally, the fourth part concludes with a summary of the results obtained through out the development of the Thesis. These conclusions are in line with the general objectives listed above.

Chapter 2. Basic Computational Methodology

The following sections in this Chapter outline fundaments of the theory, the computational methods and analysis tools used through the Thesis. So, here the theoretical frame is provided, but not the objects of the simulations.

2.1 DENSITY FUNCTIONAL THEORY

The time independent Schrödinger's equation (see equation 2.1) is the main mathematical problem in quantum mechanics that must be solved to obtain the electronic and nuclear structure of a given static system,

$$\widehat{H}\Psi = E\Psi \qquad (2.1).$$

Here, $\widehat{H}$ is the Hamiltonian operator, Ψ is the system's wavefunction, and E the system energy. The Hamiltonian is separated into the kinetic energy operators (one for the electrons, $\hat{T}_e$, and another for the nuclei, $\hat{T}_N$), and the potential energies operators for electron-electron, $\hat{V}_{ee}$, electron-nuclei, $\hat{V}_{eN}$, and nuclei-nuclei, $\hat{V}_{NN}$, interactions

$$\widehat{H} = \hat{T}_e + \hat{T}_N + \hat{V}_{ee} + \hat{V}_{eN} + \hat{V}_{NN} \qquad (2.2).$$

Since the nuclei are more massive than electrons, the latter move much faster and the Hamiltonian can be split into an electronic, $\widehat{H}_e$ (see equation 2.3), and a nuclear part, $\widehat{H}_N$. This is known as the Born-Oppenheimer approximation, which decouples the movement of the electrons and nuclei. Thus, the $\hat{T}_e$ does not depend on the nuclei movements and $\hat{V}_{NN}$ is constant for any given nuclear configuration. Within this approximation, the wavefunction of the system depends directly on the electronic coordinates while the nuclei coordinates are taken as parameters.

$$\widehat{H}_e = \hat{T}_e + \hat{V}_{ee} + \hat{V}_{eN} \qquad (2.3)$$

As mentioned above, the time independent Schrödinger's equation is central problem to solve to many theoretical methods. The most challenging part is the $\widehat{H}_e$ in a multi-electronic system. Different methodologies to solve the Schrödinger's equation are classified as two main groups: wavefunction methods and density functional theory (DFT) methods. The most

representative wavefunction method is the Hartree-Fock (HF)[5,6] approximation, which is also used as starting point for other referred to as post-HF methods. The HF method begins from the simple way to describe the wavefunction of a multi-electronic system, using the product of monoelectronic spin orbitals, known as Hartree product. The problem is that electrons are fermions, but the obtained wavefunction of the Hartree product is not antisymmetric. To solve it a determinant which is a mathematical construct that switches its sign when permuting some of its elements in such a manner, is introduced. The Slater determinant considers the correlation the movement of electrons with the same spin, but not the movement of electron with the opposite spin. Then, the HF approximation is a method without certain amount of electronic correlation and thus implies that the obtained energy from the HF method is an upper bound with respect to the real energy of the system. In order to improve these results, post-HF methods as the Coupled Cluster (CC), Møller-Plesset (MP) Perturbational Theory[7] or Complete Active Space (CAS) introduce electronic correlation effects. Nevertheless, usually the addition of the electronic correlation demands a high computational cost.

In contrast, specifically for metallic systems, the other main methodological group, DFT, represents a good balance between computational effort and obtained accuracy. The basic idea behind this theory is that the ground state energy of a system is defined by its electronic density, making unnecessary to know the wavefunction of the system. DFT principles are two theorems proposed by Hohenberg and Kohn.[7]

The first theorem establishes that the electronic density of the ground state, $\rho_0(\boldsymbol{r})$, can only be derived from a unique external potential, the electron-nuclei potential, V_{eN}. Thus, the non-degenerate ground state energy, E_0, is determined as a functional of $\rho_0(\boldsymbol{r})$ being

$$E_0 = E_0[\rho_0(\boldsymbol{r})] \tag{2.4}$$

The second theorem uses the variational principle to determine the $\rho_0(\boldsymbol{r})$ and the E_0 under the external potential. Then, $\rho_0(\boldsymbol{r})$ can be calculated

from the electronic density that minimizes the non-degenerate ground state energy.

These two important theorems allow replacing the problem of solving a 3N-dimensional wave function by instead solving the electronic density of the system that only depends on 3 spatial variables, see equation below.

$$E[\rho(\boldsymbol{r})] = E_{ext}[\rho] + F[\rho] = \int \rho(\boldsymbol{r}) V_{ext}(\boldsymbol{r}) dr + F[\rho] \qquad (2.5)$$

$F[\rho]$ is a universal density functional that includes the kinetic energy, coulombic interactions, and the exchange and correlation contributions,

$$F[\rho] = T[\rho] + V_{ee}[\rho] \qquad (2.6).$$

Thus, the $T[\rho]$ term is the kinetic energy of the system with electronic density $\rho(\boldsymbol{r})$, and the $V_{ee}[\rho]$ term contains the Coulombic repulsion exchange and correlations contributions for the system with the particular $\rho(\boldsymbol{r})$.

In addition to the Hohenberg-Kohn theorems, an important step in the development of the DFT was the computational formalism proposed by Kohn and Sham to iteratively solve equation 2.5.[8] They suggested that a solution for a polyelectronic system with $\rho(\boldsymbol{r})$ could be obtained by constructing an auxiliary system of non-interacting electrons with the same $\rho(\boldsymbol{r})$. This density of non-interacting system can be described as the sum of squares of N monoelectronic spin-orbitals, called Kohn-Sham orbitals, as

$$\rho_{KS}(\boldsymbol{r}) = \sum_{i=1}^{N} |\psi_i(\boldsymbol{r})|^2 \qquad (2.7).$$

Then, the kinetic energy of the system could be exactly obtained from the Kohn-Sham orbitals as,

$$T_s[\rho(\boldsymbol{r})] = -\frac{1}{2}\sum_{i=1}^{N} \langle \psi_i(\boldsymbol{r}) | \nabla^2 | \psi_i(\boldsymbol{r}) \rangle \qquad (2.8).$$

Assuming the hypothesis of the non-interacting system with the same $\rho(r)$ as the real target system to solve, the system energy expression proposed in the equation 2.5 and including the expansion of equation 2.6, would be expressed as

$$E[\rho(\boldsymbol{r})] = E_{ext}[\rho] + F[\rho] = E_{ext}[\rho] + T_s[\rho] + J[\rho] + E_{xc}[\rho] = \int \rho(\boldsymbol{r}) V_{ext}(\boldsymbol{r}) dr + T_s[\rho(\boldsymbol{r})] + \frac{1}{2}\iint \frac{\rho(\boldsymbol{r})\rho(\boldsymbol{r}')}{|\boldsymbol{r} - \boldsymbol{r}'|} d\boldsymbol{r} d\boldsymbol{r}' + E_{xc}[\rho(\boldsymbol{r})] \quad (2.9).$$

In summary, the equation is constituted by the external potential, E_{ext}, which essentially is the nuclei-electrons interaction, the kinetic energy of the electrons, T_s, the Coulombic repulsion between the electrons, J, and finally the exchange and correlation term, E_{xc}, which is the difference between the kinetic energy of the real system and the non-interacting system and includes the exchange and correlation energies. The exact functional E_{xc} is unknown but can be expressed as

$$E_{xc}[\rho(\boldsymbol{r})] \equiv T[\rho] - T_s[\rho] + V_{ee}[\rho] - J[\rho] \quad (2.10),$$

where the $T[\rho] - T_s[\rho]$ is the kinetic energy from the electronic interaction, the difference in kinetic energy between interacting and non-interacting systems. $V_{ee}[\rho] - J[\rho]$ is the exchange-correlation contribution, so the non-classic part of $V_{ee}[\rho]$. In order to minimize the functional of the expression 2.9 the Lagrange multipliers are useful in consideration with the constraint of the total number of electrons,

$$\int \rho(\boldsymbol{r}) d(\boldsymbol{r}) = N \quad (2.11).$$

Thus, the total energy functional within the Kohn-Sham formalism is obtained from the combination of the equations 2.7 and 2.9, expressing a dependence to a set of electronic states doubly occupied $\{\psi_i\}$ instead of the $\rho(\boldsymbol{r})$. Thus, the $\{\psi_i\}$ could be calculated minimizing the following equation:

$$\left(-\frac{1}{2}\nabla^2 + V_{ext} + \int \frac{\rho(\boldsymbol{r}')}{|\boldsymbol{r} - \boldsymbol{r}'|} d\boldsymbol{r}' + V_{xc}\right)\psi_i(\boldsymbol{r}) = \varepsilon_i \psi_i(\boldsymbol{r}) \quad (2.12),$$

where the first term is the electronic kinetic energy, the second is the external potential, the third is the Coulombic repulsion between electrons, and the last one is the exchange-correlation and kinetic energy potential defined by

$$V_{xc} = \frac{\delta E_{xc}[\rho]}{\delta \rho} \quad (2.13).$$

The last three terms form the known effective potential, and since it depends on the $\rho(\boldsymbol{r})$, the equation must be solved iteratively. With an initial effective potential (an initial electronic density), one can extract the

monoelectronic states from equation 2.12, build with them a new electronic density from equation 2.7, and repeat this until an electronic density convergence.

As explained earlier, from whole this approach the only term that remains unknown is the E_{xc}, and then by default its derivative V_{xc} (see relation in equation 2.13). To solve this problem, several works proposed different approaches to accurately describe the exchange-correlation effects. The different functionals are classified by the balance between computational cost/simplicity and accuracy in the Jacob's Ladder[9] being the last step in the ladder the unknown real form of the exchange and correlation (*xc*) functional.

The first group of *xc* functionals of this ladder and the simplest way to calculate the E_{xc} is the Local Density Approximation (LDA). Its basis of that group is that the particle *xc* energy, ε_{xc}, depends only on the electronic density (see equation 2.14).

$$E_{xc}^{LDA} = \int \rho(\boldsymbol{r})\varepsilon_{xc}(\rho)d\boldsymbol{r} \tag{2.14}$$

The exchange and correlation contributions are treated separately in all the groups of *xc* functionals, being

$$E_{xc} = E_x + E_c \tag{2.15},$$

$$\varepsilon_{xc} = \varepsilon_x + \varepsilon_c \tag{2.16}.$$

In LDA, the electron gas model with a constant and homogeneous $\rho(\boldsymbol{r})$ is used for the exchange part. This part can be exactly derived from the Jellium system. So, the ε_x^{LDA} has the following form,[10]

$$\varepsilon_x^{LDA} = -\frac{3}{4}\left(\frac{3\rho(\boldsymbol{r})}{\pi}\right)^{\frac{1}{3}} \tag{2.17},$$

and the total exchange energy, E_x^{LDA}, is consequently defined by

$$E_x^{LDA} = -\frac{3}{4}\left(\frac{3}{\pi}\right)^{\frac{1}{3}}\int \rho(\boldsymbol{r})^{\frac{4}{3}}d\boldsymbol{r} \tag{2.18}.$$

On the other hand, the correlation energy does not have an explicit formula, but many authors suggested different analytical expressions.[11] The LDA functionals have a quite good performance for metals, as such systems are close to the Jellium model, providing rather accurate lattice parameters

and minimum interatomic distances. However, this approximation misses a lot of accuracy when molecules or clusters (non-homogeneous systems) are treated, or any other strongly correlated system. Also, they overestimate bond energies.[11–14] As examples of LDA functionals, one can find Ceperly and Alder (CA)[15] and Vosko-Wilk-Nusair (VWN)[16] functionals, among others.

In order to improve the LDA functionals, a new group of functionals called Generalized Gradient Approximation (GGA) was developed being the next upper level in the Jacob's Ladder. Here, the ε_{xc} is not only dependent of the $\rho(\boldsymbol{r})$, it also depends on the density gradient, $\nabla\rho$, which allows introducing variations in the density, and making a semilocal approximation,

$$E_{xc}^{GGA} = \int \rho(\boldsymbol{r})\varepsilon_{xc}(\rho(\boldsymbol{r}), \nabla\rho(\boldsymbol{r}))d\boldsymbol{r} \qquad (2.19).$$

There are many GGA *xc* functionals. One of the most common and most used in this Thesis is the Perdew-Burke-Erzenhof (PBE)[17,18], the successor of Perdew-Wang 91 (PW91)[19], developed without any fitting procedure and reducing the number of parameters used at PW91. With respect to the LDA functionals, PBE, and generally the exchange part, has an additional term F_x that depends on the density gradient.

$$E_x = \int \rho(\boldsymbol{r})\varepsilon_x^{LDA}(\rho)F_x(s(\boldsymbol{r}))d\boldsymbol{r} \qquad (2.20),$$

$$F_x = 1 + \kappa - \frac{\kappa}{1 - \frac{\mu s^2}{\kappa}} \qquad (2.21),$$

$$s = \frac{|\nabla\rho(\boldsymbol{r})|}{2(3\pi^2)^{\frac{1}{3}}\rho(\boldsymbol{r})^{\frac{4}{3}}} \qquad (2.22).$$

In the case of PBE, the $\kappa = 0.804$ and $\mu = 0.21951$ that it comes from $\mu = \beta\left(\frac{\pi^2}{3}\right)$ where $\beta = 0.06672$ is a parameter of gradient contribution of the correlation part (E_c). Other variations of PBE differs from this parameters numbers as in the example cases of rPBE[20] where $\kappa = 1.245$ or PBEsol[21] with $\beta = 0.046$. Both cases modify PBE in order to improve properties description by the fitting of the parameters with results of complex methods. Nevertheless, the Lieb-Oxford bound is not satisfied in the rPBE it is not satisfied on spin-polarized densities.[22] Also, there is the RPBE[23] which in order to fix the local Lieb-Oxford bound varies function of F_x proposed at PBE.

About the performance, the GGA functionals, in general, provide better results in bond energies, but they still overestimate bond distances.[14]

So, another step adding complexity to approach the *xc* functional is including the Laplacian of the density too. This group is called the meta-GGA functionals, which normally represent an improvement in thermochemistry estimates of molecules, but they generally do not notably improve accuracy improvement with respect to the GGA when describing extended TM systems.[24] The functional from this group used in the thesis is Tao-Perdew-Staroverov-Scuseria (TPSS) one.[25]

Finally, hybrid functionals include a part of the exchange of non-local HF in the explicit form developed by Kohn-Sham. In general, most of them have been parametrized with molecular properties data. One of the most used functional is the hybrid version of PBE functional, PBE0,[26]

$$E_{xc}^{Hyb} = E_{xc}^{PBE} + a_0(E_X^{HF} - E_X^{PBE}) \quad (2.23),$$

where $a_0 = 0.25$ using arguments from perturbation theory. Since the hybrids usually fail describing delocalised systems as metals,[27,28] and they have the highest computational cost, they were not used in this Thesis.

2.2 BASIS SETS

To describe properly the electron density a suitable basis set is needed to represent the wave functions. Two different types of basis sets explained here are used in the two different codes employed in this Thesis, Vienna Ab Initio Simulation Program (VASP) which uses Plane Waves and Fritz-Haber Institute Ab Initio Molecular Simulations (FHI-AIMS) which employs Numerical Atomic Orbitals. Although, Pseudopotentials are not a basis set, they are introduced here because they are implemented with Plane Waves.

2.2.1 Plane Waves and Pseudopotentials

In calculations of periodic systems, plane wave functions are commonly used as the basis sets,

$$PW_{basis} = e^{ikr} \quad (2.24),$$

where k is the plane wave vector. The use of plane wave functions is computationally advantageous, however, a very large number of them is needed to describe all the electrons accurately. The solution to this problem is to reduce the number electrons to be represented by the plane wave functions without losing the accuracy but decreasing the computational cost. Accordingly, since core electrons are normally not involved in the bond making/breaking processes, they can be simulated with an effective core potential, commonly known as pseudopotential. Thus, during the calculation the core electrons are frozen and the interaction between them and the valence electrons is introduced by a potential.

There are different types of pseudopotentials, but the usual ones employed with plane waves on periodic models are ultrasoft potentials,[29] norm-conserving pseudopotentials[30] and the projected augmented wave (PAW) potentials.[31] PAW is a method that allows to approximate the all-electron wave-function by considering a set of fixed basis functions to describe the core-electrons. Particularly in this Thesis, PAW method is used because it restores the pseudo wavefunction which arise from the construction of pseudopotential to the all-electron wavefunction. Consequently, it has the advantages of the all-electron basis. The core electrons are modelled by the difference between the exact wave function and the pseudo-wave function.

2.2.2 Numerical Atomic Orbitals

For non-periodic systems, the common basis sets are usually composed by localised atomic orbitals, and these, in turn, are a linear combination of basis functions (*e.g.* Gaussian or Slater functions) centred in the atomic nuclei. However, they can also be used for periodic systems where crystalline orbitals are treated as linear combinations of Bloch functions, which is a function that obeys Bloch's Theorem, introduced in the next Chapter.[32] Specifically, Numerical Atomic Orbitals (NAO) were implemented to satisfy general goals of accurate all-electron wavefunction, a similar efficiency to the fastest existing plane waves pseudopotential schemes and, a good scalability of the calculation of larger systems.[33] NAO basis function has the following form,

$$\varphi_i(\boldsymbol{r}) = \frac{u_i(r)}{r} Y_{lm}(\Omega) \qquad (2.25),$$

where $u_i(r)$ is the numerically tabulated radial function, $Y_{lm}(\Omega)$ denotes the real part $(m = 0, \dots, l)$ and imaginary parts $(m = -l, \dots, -1)$ of complex spherical harmonics, being l an implicit function of ith radial function.

2.3 MONTE CARLO APPROACH

In many cases analytical solutions of some equations are too complicated, and one can only get numerical solutions by running simulations.[34] Monte Carlo (MC) approaches are a group of simulation methods. The aim of them is to compute equilibrium properties of classical many-body systems.[35] In particular, here it is used a Markov Chain approximation. This approach is a stochastic method that describes the evolution of a given system by carrying out sequential steps with a probability that depends only on the current state of the system. Specifically, a random walk is constructed in such a way that the probability of visiting a particular point r^N, the coordinates of all N particles are proportional to the Boltzmann factor $e^{-\frac{\Delta E}{k_B T}}$, being ΔE the difference in energy between the current (r'^N) and previous (r^N) configurations, k_B is the Boltzmann constant and T is an arbitrary temperature with no physical meaning. There are many ways to construct such a random walk. In the approximation shown by Metropolis *et al.*,[36] the following scheme is proposed:

1. Select a random structure to start and calculate its energy $E(r^N)$.
2. Modify the current structure randomly and calculate its new energy $E(r'^N)$.
3. Accept the move from r^N to r'^N with probability

$$P(r^N \to r'^N) \begin{cases} = 1 & E(r'^N) < E(r^N) \\ = e^{-\frac{\Delta E}{k_B T}} & E(r'^N) > E(r^N) \end{cases} \qquad (2.26).$$

To start the simulation, initial positions should be assigned to all the system particles (r^N). All reasonable initial conditions are in principle acceptable as the equilibrium properties of the system do not, or should not, depend on them. When the simulation is for the solid state of a particular

model system, the crystal structure of the system of interest is the most logical choice to initialise the procedure. Then, once the modification of the initial structure is accepted, the cycle will be repeated from the step 2 being now the current structures the one modified. This procedure will be repeated until reaching the number of MC steps specified for the simulation.

2.4 MINIMA ANALYSIS

Once the minimum energy geometry of a system under scrutiny is determined, one can apply several types of analyses to characterize its electronic structure depending on the information needed. The following kinds of analyses are employed through the different studies of this Thesis:

2.4.1 Work Function

The work function, ϕ, is the energy required to take an electron from the last(highest) occupied level, as known as Fermi level, and place it in the vacuum,

$$\phi = V - E_F \qquad (2.27),$$

where V is the electrostatic potential energy of the electron in vacuum and E_F is the energy of the Fermi level. The meaning of the work function is related to the ability of a surface to donate charge. A low work function value implies that the metal surface is a good electron donor, and a high work function value implies that it is a good electron acceptor. To compute the work function, the Fermi level is obtained by the occupation of the electronic states, and the average electrostatic potential energy is calculated in each point of the unit cell following the surface direction. Inside the surface, the potential energy oscillates due to the atomic positions, and in vacuum it increases to a constant maximum value, V.

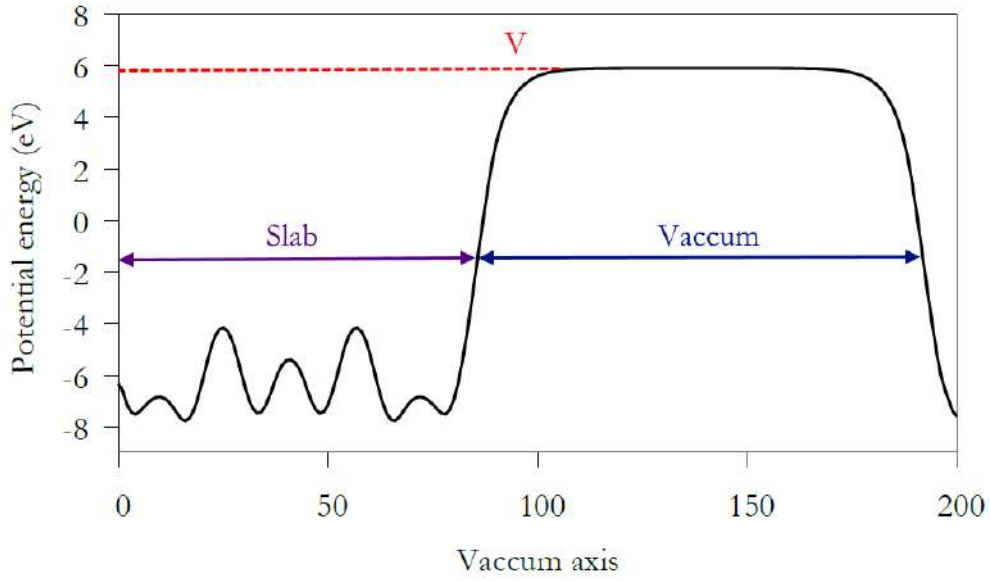

Figure 2.1 Variation of the electrostatic potential energy for a 6-layered slab of the Mo surface (001) with the length of the vacuum axis.

2.4.2 Density of States

The density of states (DOS) of a system is the description of the number of states that lie at each energy. In the case of periodic boundary conditions, as the orbitals or bands do not have a discrete energy, a projection into spherical harmonics is used to the DOS from given atoms or orbitals. Thus, the values may belong to each atom and have a specific radius that depends on the element and the embedding of every atom, called Wigner-Seitz radius. For solids, two bands can be differentiated: the valence band and the conduction band, which for metals are shown as a continuum. In the first one, the orbitals occupied are below the Fermi level, E_F, and in the second one the states are not occupied, above the Fermi level.

2.4.3 Bader Charge

The analysis of atoms in molecules by Richard Bader is a useful tool to assign charge density to different atoms in a molecule.[37] The definition of an atom that he provides is based purely on the electronic charge density. In particular, the charge density forms a surface of minimum density between atoms, which defines a surface that contains the atomic volume in molecular

systems. Thus, the Bader's scheme is used in charge analysis to examine the accumulation or depletion of electrons of the atoms in different environments. One obtains the atomic charge by calculating the difference between the electronic charge within the atom volume and the number of electrons of the neutral, isolated atom.

2.4.4 Charge Density Difference

A common analysis of the electronic density is done by Charge Density Difference (CDD) maps. They are very useful to see how the interaction between two or more different components in a system affects the electronic density. For that, one subtracts from the electronic density of a complete system the electronic density of two different isolated forming parts, obtaining the areas of charge transfer or rearrangement (accumulation or depletion of charge density). An example can be an adsorbed system to study the charge transfer between the adsorbate and the substrate. Then, from the total electronic density of the adsorbed system, the electronic density of the isolated adsorbate and the substrate is subtracted.

Chapter 3. Modelling from Bulk to Nanoparticles

In this Chapter objects of the simulations will be treated, that is, the solid state, in particular bulk, surface, and nanoparticle systems. The following sections deal with the choice of models and how these, either periodic or cluster models, are applied to properly describe the solid materials.

3.1 PERIODIC BOUNDARY CONDITIONS

Periodic models are used to simulate infinite crystalline solids with an ordered structure with one-, two- or three-dimensional extensions by translational symmetry. Periodic models are based on the periodic boundary conditions (PBC) where a defined unit cell is replicated in all directions (see Figure 3.1). PBC are a powerful tool to simulate infinite solids because of the impossibility to solve the Schrödinger equation for all the system atoms.

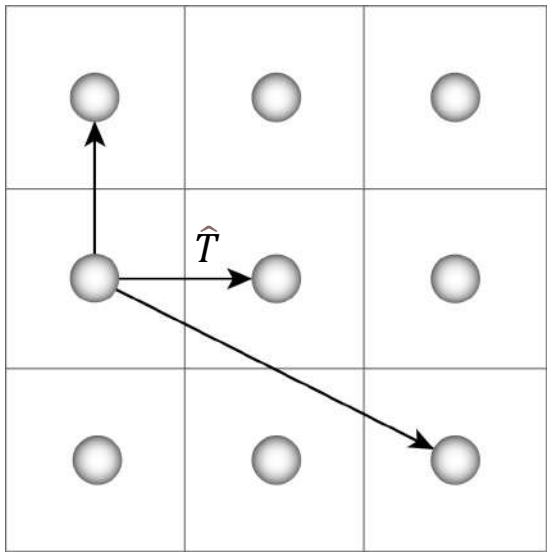

Figure 3.1 Translation operations of a centred atom of a unit cell under PBC.

The Schrödinger equation only must be solved for the atoms defined in the unit cell because applying the translational operator, $\hat{T}$ (see equation 3.1), the wave function does not change.

$$\hat{T} = n_1\boldsymbol{a} + n_2\boldsymbol{b} + n_3\boldsymbol{c} \qquad (3.1).$$

In the above equation, n_i are integer numbers that multiply the cell vectors $\boldsymbol{a}$, $\boldsymbol{b}$, and $\boldsymbol{c}$. Unit cells can be classified as primitive and non-primitive. The primitive one is the irreducible form of the atomic solid pattern and provides a one-to-one correspondence between it and the discrete lattice points, being the equation 3.1 limited

$$\hat{T} = n_1\boldsymbol{a} + n_2\boldsymbol{b} + n_3\boldsymbol{c} \qquad \text{where } 0 \leq n_i < 1 \qquad (3.2).$$

The primitive unit cells of a concrete systems have always the same volume independently of their shape. The non-primitive unit cell volume will be an integer multiple of the primitive unit cell volume.

The discrete translation operations generate an infinite array of atomic positions in 3D space known as Bravais lattice. A typical example of Bravais lattice is Simple Cubic one depicted in Figure 3.2.

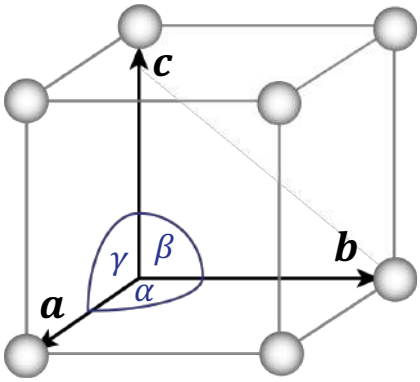

Figure 3.2 Simple Cubic Bravais lattice with $\boldsymbol{a} = \boldsymbol{b} = \boldsymbol{c}$, $\alpha = \beta = \gamma = 90°$ and one atom in the origin.

The following most common unit cells for metallic crystalline structures (see Figure 3.3) are studied in the thesis:

- Body centred cubic (*bcc*)
- Face centred cubic (*fcc*)
- Hexagonal closed packet (*hcp*)

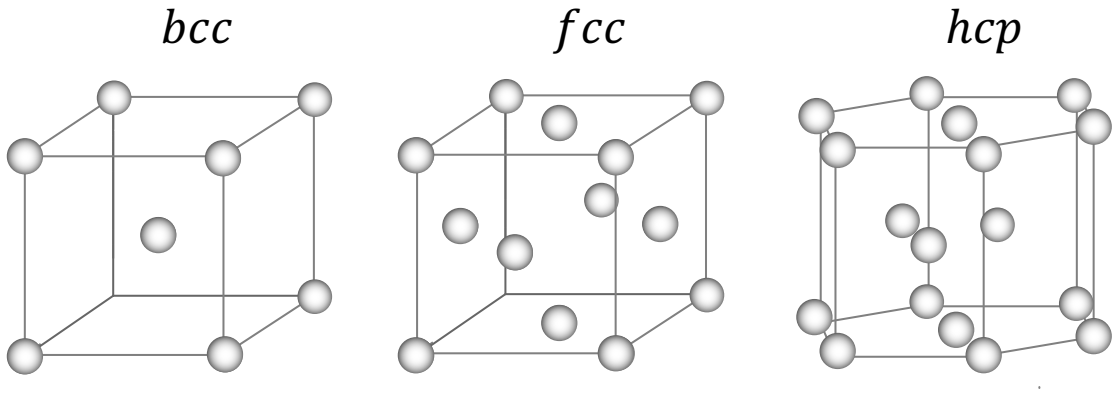

Figure 3.3 Common crystalline structures.

The *fcc* and *hcp* structures have the highest atomic packing factor (APF) 0.74, *bcc* one has an APF of 0.68 and the simple cubic structure of 0.52.

3.2 RECIPROCAL LATTICE

To use the periodic models, one needs to work in the reciprocal space. Reciprocal space is a mathematical construction associated with the real space described by the lattice. In the real space the lattice is defined by the unit cell vectors $\boldsymbol{a}, \boldsymbol{b}, \boldsymbol{c}$. In the reciprocal space they have their translated version $\boldsymbol{a}', \boldsymbol{b}', \boldsymbol{c}'$, and the relation between them is given by

$$\boldsymbol{a}' = 2\pi \frac{\boldsymbol{b} \times \boldsymbol{c}}{\boldsymbol{a} \cdot (\boldsymbol{b} \times \boldsymbol{c})};\ \boldsymbol{b}' = 2\pi \frac{\boldsymbol{a} \times \boldsymbol{c}}{\boldsymbol{b} \cdot (\boldsymbol{a} \times \boldsymbol{c})};\ \boldsymbol{c}' = 2\pi \frac{\boldsymbol{a} \times \boldsymbol{b}}{\boldsymbol{c} \cdot (\boldsymbol{a} \times \boldsymbol{b})} \qquad (3.3).$$

Therefore, in analogy with the real space, any vector of the reciprocal space would be defined as

$$\boldsymbol{G} = m_1\boldsymbol{a}' + m_2\boldsymbol{b}' + m_3\boldsymbol{c}' \qquad (3.4),$$

where m_i are integers numbers. Therefore, the description of the direct unit cell could be done through the description of the corresponding reciprocal unit cell, known as Brillouin zone or Wigner Seitz cell (see Figure 3.4 for a one-dimensional lattice example, with a being the lattice spacing). In addition, it is important to note that a small volume of the reciprocal cell implies a large volume of the real unit cell. This affects the number of k points employed to describe properly the unit cells, small unit cell needs more k points than a big unit cell which only needs one (Γ point).

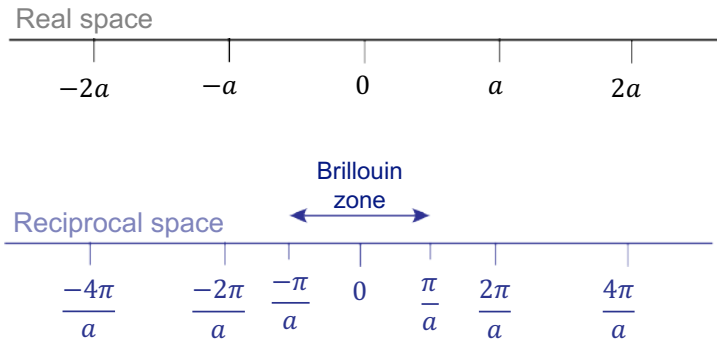

Figure 3.4 One-dimensional lattice in real space and reciprocal space.

3.3 BLOCH'S THEOREM

The potential, V, in a specific position of the unit cell, $\boldsymbol{r}$, is the same as the potential in an equivalent position in the replicated cell, $\boldsymbol{r}+\boldsymbol{R}$, obtained by the translational operator, $\hat{T}$.

$$V(\boldsymbol{r}) = V(\boldsymbol{r}+\boldsymbol{R}) \tag{3.5}$$

Then, the invariance of the potential in the homologous points in the replicated cells brings the periodic character determining the electronic density not only in the unit cell, but also in the complete crystalline structure. From this statement, the wave functions need to describe the electrons of a solid are reduced due to the translational symmetry and could be defined as

$$\Psi_i(\boldsymbol{r}) = e^{i\boldsymbol{k}\boldsymbol{r}}\nu_i(\boldsymbol{r}) \tag{3.6}$$

where $e^{i\boldsymbol{k}\boldsymbol{r}}$ is a plane wave with a wave vector $\boldsymbol{k}$ and ν_i is a periodic function that can be expressed by a linear combination of plane waves,

$$\nu_i(\boldsymbol{r}) = \sum_{\boldsymbol{G}} C_{i,\boldsymbol{G}} e^{i\boldsymbol{G}\boldsymbol{r}} \tag{3.7}$$

In combination with the previous equation, they will lead to

$$\Psi_i(\boldsymbol{r}) = \sum_{\boldsymbol{G}} C_{i,\boldsymbol{k}+\boldsymbol{G}} e^{i(\boldsymbol{k}+\boldsymbol{G})\boldsymbol{r}} \tag{3.8}$$

with $\boldsymbol{G}$ being the reciprocal vector (see equation 3.4). Each plane wave of the linear combination is characterized by a kinetic energy, $\frac{|\boldsymbol{k}+\boldsymbol{G}|^2 h}{2m}$. Consequently, depending on the kinetic energy value the number of plane waves will vary and, with it, the description of the observables of the system, such as the energy.

Therefore, the problem of the infinite number of the system electrons is transformed to express the wave function in an infinite number of reciprocal space vectors, $\boldsymbol{k}$, in the first Brillouin zone. In order to simplify this using the symmetry, only a part of the first Brillouin zone is studied. Furthermore, the eigenvalues of the close $\boldsymbol{k}$ vectors are essentially the same so the number of $\boldsymbol{k}$ vectors needed is considerably reduced to only a discrete ones, called k-points.

3.4 MILLER INDICES

The Miller indices are a notation of the planes in the Bravais lattice. The intersection between a plane and the real space axis $(\boldsymbol{a}, \boldsymbol{b}, \boldsymbol{c})$ is formed by three points, $x, y,$ and z. From that, Miller indices (hkl) are defined as the reciprocal shortest perpendicular vector to the plane, by

$$h = \frac{1}{x}; k = \frac{1}{y}; l = \frac{1}{z} \tag{3.9}.$$

For example, for $x = 2, y = 1, z = 2$, the Miller indices are (121), calculated using the least common multiple. There are some considerations to take into account as for example, when the plane does not intersect with the axis then the Miller index is 0. Also, in the case that the intersection point is negative then the Miller index is notated with a slash on the top of the value, *e.g.* $\bar{1}$. From the cubic Bravais lattice the most common set of equivalent planes studied is {100}, {110}, and {111}, see Figure 3.5 for one representative plane of each set. Note that the notation changes to braces when a set of equivalent planes is represented.

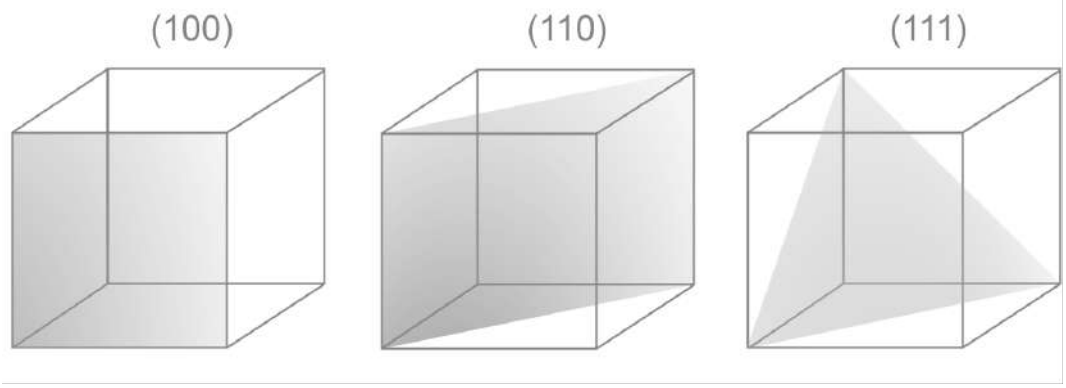

Figure 3.5 Representation of three common Miller indices planes of the Cubic Bravais lattice.

3.5 SURFACE AND NANOPARTICLES MODELS

To simulate surfaces, the periodicity of the unit cell is only needed in 2 dimensions, *e.g.* x and y axis. To model a surface within PBC, one normally applies a large vacuum region (≥ 10 Å) along the z axis to avoid interactions between the so-called slabs. The slabs are referred to as the unit cell of the surface to model. Consequently, they contain a considerable number of atomic layers to accurately describe surface and bulk properties (see Figure 3.6). The slab notation used is (n×m), where n and m are the number of times the primitive cell is replicated in the two distinct surface cell vectors, respectively. Furthermore, there are different ways to treat such slabs:

- All atomic layers of the slab are relaxed in terms of allowed local displacements of atoms. This option is used mostly for no-adsorption simulations and when using many.
- Both upper and bottom layers of the slab are relaxed, while the internal layers are fixed, simulating the bulk (symmetric slab).
- One or more outer layers on one side of the slab are relaxed, whereas its other layers are fixed (antisymmetric slab).

The last two approaches are used when the surface is used to adsorb an atom or a molecule. The disadvantage of the symmetric slab is that it needs to contain the double number of layers than the antisymmetric one to simulate properly the bulk, so it will be more computationally expensive. Nevertheless, it can be useful to quantify possible interactions between two species adsorbed on different surfaces of the slab.

Nanoparticles can be also studied under periodic conditions employing the same trick than for surfaces but, adding vacuum in all directions avoiding possible interactions between species in adjacent cells (see Figure 3.7). This is the same treatment as used for modelling isolated atoms or molecules. For surfaces and nanoparticles of TMs, spin-polarization was only considered when highly magnetic Fe, Co and Ni atoms were involved. Test calculations of other mono- and bi- metallic nanoparticles were carried out considering spin-polarization. Their results showed that the unrestricted calculations converged essentially to the restricted solutions. Therefore, all models not

containing Fe, Co or Ni atoms were calculated without considering spin-polarization as it does not incur in significant structural or energetical changes.

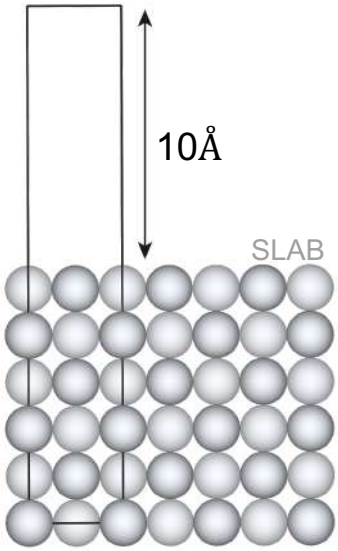

Figure 3.6 Side view of a six-layer slab with 10 Å of vacuum modelling the surface (001) of a *fcc* structure.

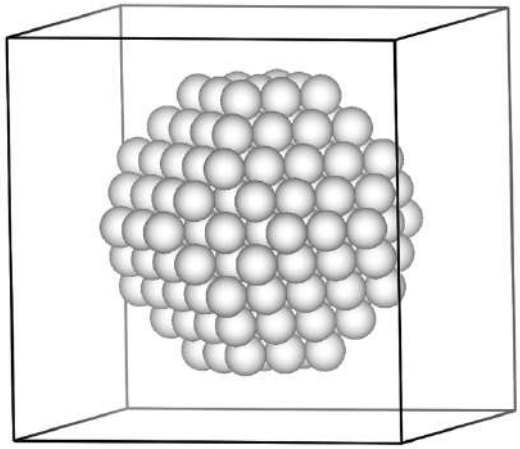

Figure 3.7 Nanoparticle of 201 atoms in a cell with ~10 Å of vacuum in each direction.

PART II. RESULTS ON MONOMETALLIC SYSTEMS

Chapter 4. Performance and Improvement of the Most Common Functionals for Transition Metals

4.1 INTRODUCTION

In this Chapter, the studies dealing with benchmarks and improvements of diverse *xc* functionals with respect to description of different properties of the TMs are compiled.

A good choice of the employed *xc* functional for a specific system needs to be substantiated by a balance between accuracy and computational cost. As already mentioned in the Chapter 2, *xc* functionals could be classified depending on its theory level, and indirectly by the computational effort, by the so-called Jacob's Ladder. Thus, benchmark studies with a proper quantity of cases are needed to duly select, and even to improve, a *xc* functional for a particular system and/or property. Aside, from the results of the cases calculated directly one can extrapolate the overall performance of the functional. Then, the first aim is to address this lack of testing and make a direct comparison between the commonly used functionals (such as VWN,[16] PBE,[17,18] PBEsol,[21] RPBE,[23] and TPSS[25]) when describing structural, energetic, and electronic properties of the TMs (see Figure 4.1). The present study considers bulk environments, more extensively used to test the functionals because of their low computational cost, and also three the most common surfaces of each type of TM structures (see Figure 4.2). Moreover, we explored the performance and transferability of electronic structure-based descriptors of such functionals. Finally, we proposed a PBE-based functional that improves description of the TM properties.

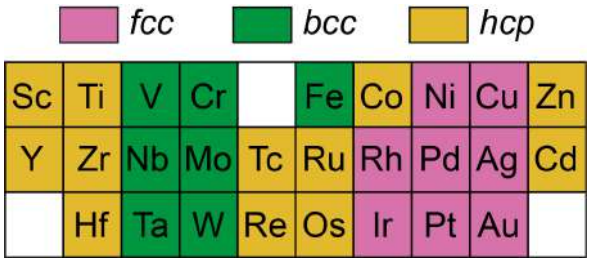

Figure 4.1 Studied transition metals classified by the different crystallographic structures.

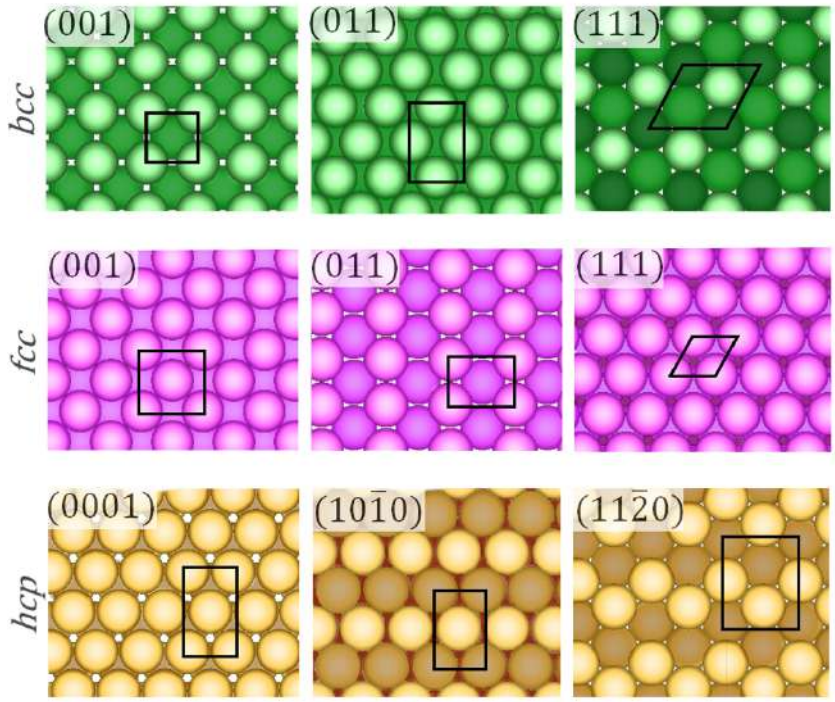

Figure 4.2 Studied surfaces for each type of structure and its employed unit cell.

4.2 OBJECTIVES

The objectives we want to reach in the present Chapter are:

- To assess the best *xc* functional among the ones aforementioned when describing bulk and surface properties of the TMs (Section 4.3).
- To establish the most robust electronic descriptor among the surface *d*-band centre, width corrected *d*-band centre, and the highest peak of the Hilbert transform of the *d*-band for the VWN, PBE, and TPSS functionals (Section 4.4).
- To formulate a new *xc* functional (PBE-based), which decreases the errors of the calculated results for the TMs under scrutiny. (Section 4.5).

4.3 ASSESSING THE PERFORMANCE OF BROADLY USED DENSITY FUNCTIONALS ON TRANSITION METAL SURFACE PROPERTIES

4.3.1 Summary

Introduction It is important to choose an appropriate *xc* functional for each kind of systems under study. An example, and the seed of the following results, are the studies by Janthon *et al.*,[38,39] where various bulk properties of 27 TMs were tested with more than 10 functionals through different levels of theory. The properties selected were the minimum interatomic distance (δ), the cohesive energy (E_{coh}) and the bulk modulus (B_0), each of them describing a different aspect of the system: the structure, the energy, and the interplay of energy and structure, respectively. The *xc* functional PBE[17,18] and PW91,[19] closely followed by TPSS[25] from meta-GGA group, were found as the overall best functionals describing the above-mentioned properties of the TMs bulk systems. Although bulk systems are essential for the solid state, surfaces are indispensable, for instance, in catalytic applications and thus are in the focus of this Thesis work. Therefore, to continue the line of the previous studies, the next step was testing some functionals for the TMs surfaces. This provided a general view allowing to establish the best functional for TMs taking into account both the bulk and the surface properties. The surfaces studied were the (001), (011), and (111) for *bcc* and *fcc* structures, and (0001), (10$\bar{1}$0) and (11$\bar{2}$0) for *hcp* structures, as in general the most stable and common surfaces featuring the lowest Miller indices.

Since the computational cost to model such surfaces is higher than their bulks, and the total amount of surfaces is 81, the list of functionals to test was smaller than that for the bulk studies.[38,39] The functionals chosen were VWN[16] from the LDA type, PBE, PBEsol[21] and RPBE[23] from the GGA type, and a meta-GGA TPSS functional. The selection of three GGA functionals is due to the fact that PBE was one of the most common functionals employed to model solid state and exhibited best results for TMs

bulks. PBEsol and RPBE functionals were included as modifications of PBE functional aiming to improve the results of the latter for solid state. Hybrid functionals were not included because they provided quite high errors for TMs (except for HSE06 performing well for bulk properties) tending to localize electrons,[40] and due a high cost required for plane-wave calculations using hybrid functionals. The chosen properties to evaluate the TM surfaces were the interlayer distance (δ_{ij}) as a structural aspect, surface energy (γ) as the energetic one, and the work function (ϕ) to describe the electronic structure. The calculations of these properties are detailed in the Publication below.

Experimentally, the γ is measured by the liquid surface tension and the solid-liquid interfacial energy of the metal. Then, the solid surface energy is estimated on the melted metal, and under isotropic approximations it is extrapolated to 0 K.[41] Consequently, it is impossible to measure the γ of a specific surface and the measurement is on a mix of different surfaces. Since the calculated γ is on a specific surface, a weighted average of the values obtained is computed using the Wulff constructions[42] in order to compare it with the experimental data. The Wulff constructions are the equilibrium shape of a crystal minimizing the surface free energy (see Figure 5.11). There, the free energy difference is calculated by,

$$\Delta G_i = \sum_j \gamma_j A_j \qquad (4.1),$$

where the A is the area of each surface j. To compute which surfaces are exposed, the length of the normal vector to each surface plane is proportional to a constant λ,

$$h_j = \lambda \gamma_j \qquad (4.2).$$

Once the exposed surfaces are computed, the percentage of exposure of each surface is calculated with the sum of the areas of the equivalent planes divided by the total area of the Wulff construction.[43]

The contribution of the Thesis author in this publication was i) to create the models of bulks and surfaces of *bcc* and *hcp* metals, and of the (111) surfaces of *fcc* metals; ii) to optimize all the bulk and surface models for all the xc functionals, except the bulk, and (001) and (011) surfaces of *fcc* metals

by PBE; iii) to calculate all the surface properties and to compute the error bars. The author used the bulk properties computed and tabulated for each *xc* functional by Janthon *et al.* [38,39]

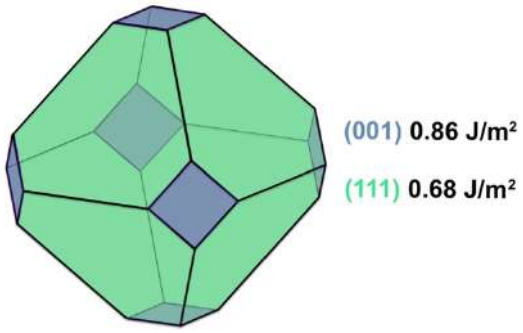

Figure 4.3 Wulff construction of gold with PBE obtained by using three surfaces (001) 0.86 J/m², (011) 0.86 J/m², and (111) 0.68 J/m². The [011] is not expressed because the normal vector of [111] planes is shorter than the normal vector of [011].

Results The main results of the project —further discussion of them and extended data can be found in the appended publication and Appendix A— are presented divided on the three surface properties studied and an overall functional assessment. As we mentioned in the summary introduction, the experimental surface energy measures are taken nearby the melting point of the metal, so not exposing a particular surface. For this reason, two ways were proposed to compare the experimental data with the calculated surface energy of each TM surface: either taking the calculated values of the most stable surface of the TM (γ^{calc}) or employing the Wulff constructions to make a weighted average with the γ of all the three surfaces of the TM (γ^{calc}_{Wulff}). As shown in Figure 4.4, the values of the most stable surface follow the experimental trend, especially the surface energies calculated with VWN and PBEsol functionals. The latter two cases are characterized by a high linear regression coefficient R=0.90 and the slopes closest to 1, a=0.98 and 0.97 for VWN and PBEsol respectively, as well as the intercepts (units in J/m²) closest to 0, b=-0.01 and b=-0.12. PBE and RPBE functionals with R=0.88 and a=0.89, b=-0.23 for PBE and, a=0.85, b=-0.34 for RPBE provide a worse agreement than to VWN and PBEsol data. Finally, TPSS shows the worst agreement with the coefficients R=0.52, a=0.81, and b=0.27. A fitting of the Wulff averaged surface energies resulted in slightly better R, a, and b values. In the RPBE case R drops from 0.88 to 0.56 although the slope and intercept

reveal a better agreement than the RPBE using Wulff averaged surfaces with the experimental data. This high dispersion of the points could imply that RPBE functional describes poorly not only the most stable surfaces, but also the other considered surfaces. Analysing the Mean Absolute Percentage Error (MAPE) for each functional, the MAPE of γ_{Wulff}^{calc} is lower than that of γ^{calc}, except for RPBE. VWN is the functional showing a lower MAPE in the surface energy calculation in both cases, 12.24% in the case of γ_{Wulff}^{calc} and 13.48% in the case of γ^{calc}.

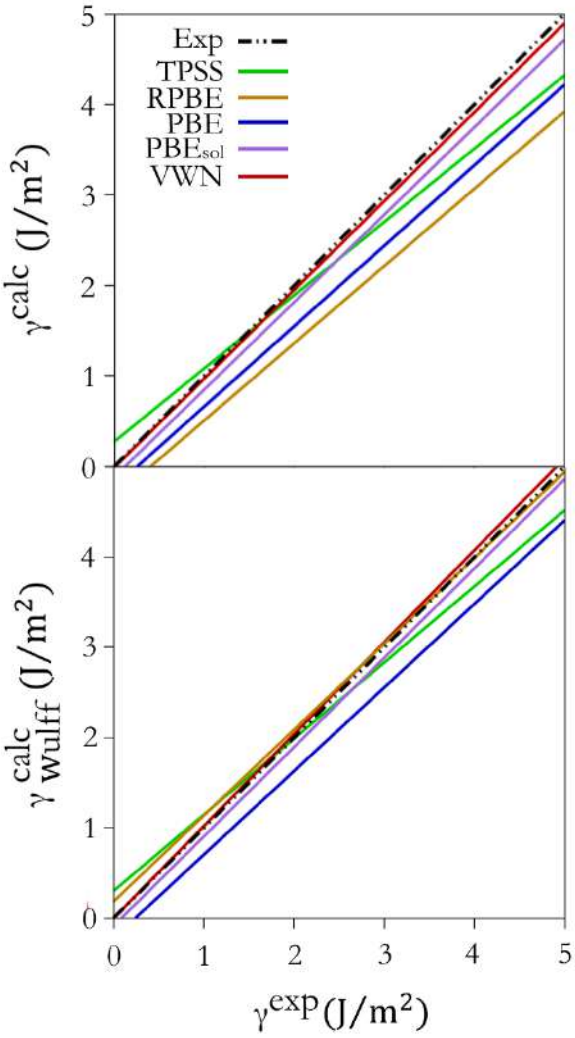

Figure 4.4 Comparison of the linear fitting between calculated (calc) and experimental (exp) surface energies for the different explored xc functionals. The top panel considers only the most stable surface, γ^{calc} whereas in the bottom panel Wulff shape averaged values, γ_{Wulff}^{calc} , are compared.

There are experimentally measured work function data for polycrystalline samples and specific surfaces. Therefore, as before, the Wulff averaged work function values (ϕ_{Wulff}^{calc}) are compared to the polycrystalline experimental data. But in this case the calculated values for particular surfaces (ϕ_{Single}^{calc}) are also compared directly with experimental single-crystal

data for these surfaces (see Figure 4.5). PBE functional provides the best MAPE results, with 20.77% for ϕ_{Single}^{calc} and 19.37% for ϕ_{Wulff}^{calc}. The performance decreases as PBE > PBEsol > RPBE > TPSS > VWN for analysis of the single-crystal surfaces. This trend is almost maintained for the polycrystalline data, where only PBEsol and RPBE values swap the positions. A better correlation not unexpectedly found using the direct comparison with the single-crystal surface energies than with the polycrystalline data justifies relying in our forthcoming analysis solely on the single-crystal data.

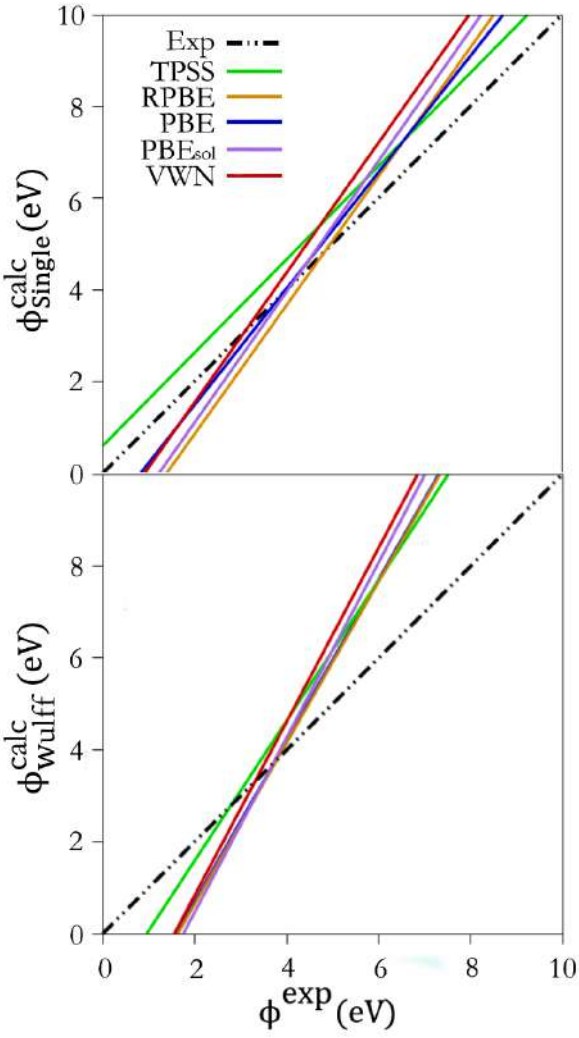

Figure 4.5 Comparison of the linear fitting between calculated (calc) and experimental (exp) work functions for the different explored xc functionals. The top panel considers only single crystal data, ϕ_{Single}^{calc}, whereas in the bottom panel Wulff shape averaged values, ϕ_{Wulff}^{calc}, are compared. All values are given in eV.

Finally, we obtained the interlayer distance δ_{ij}^{exp} by the application of the experimental interlayer percentage relaxations of interlayer distances extrapolated to 0 K. Thus, obtained experimental values are compared with the computed interlayer distances (δ_{ij}) for each xc functional. In general, the

interlayer distances for different functionals nicely fit the experimental results. So, all the regressions show slopes ~0.8, intercepts below 0.4 Å, and R^2 ~0.8. However, PBE performs slightly better as one can see from Figure 4.6 and the statistical analysis according to which PBE has the smallest MAPE (10.11%).

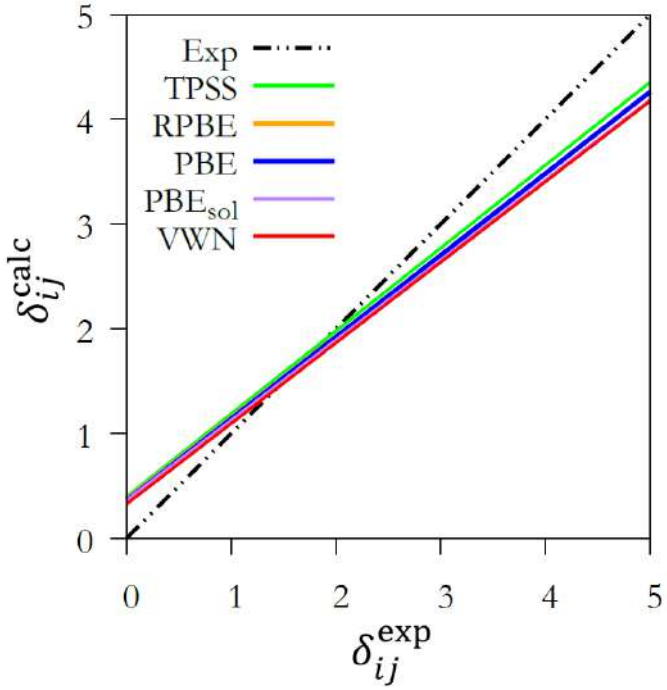

Figure 4.6 Comparison of δ_{ij} MAPE to experimental data, δ_{ij}^{exp}, as calculated and adjusted to linear regression for each functional.

Adding the MAPE obtained for the three surfaces properties, surface energy (based on γ_{Wulff}^{calc}), work function (based on ϕ_{Single}^{calc}) and the interlayer distance, PBEsol appears to be the most balanced functional, even if it is not the best one in any of these specific properties. Combining the present results with those previously obtained for the TMs bulk properties (cohesive energies, bulk moduli, and nearest-neighbour interatomic distances),[31,32] the most accurate *xc* functional of the overall surface and bulk properties of transition metals is PBE, closely followed by PBEsol one (see Figure 4.7).

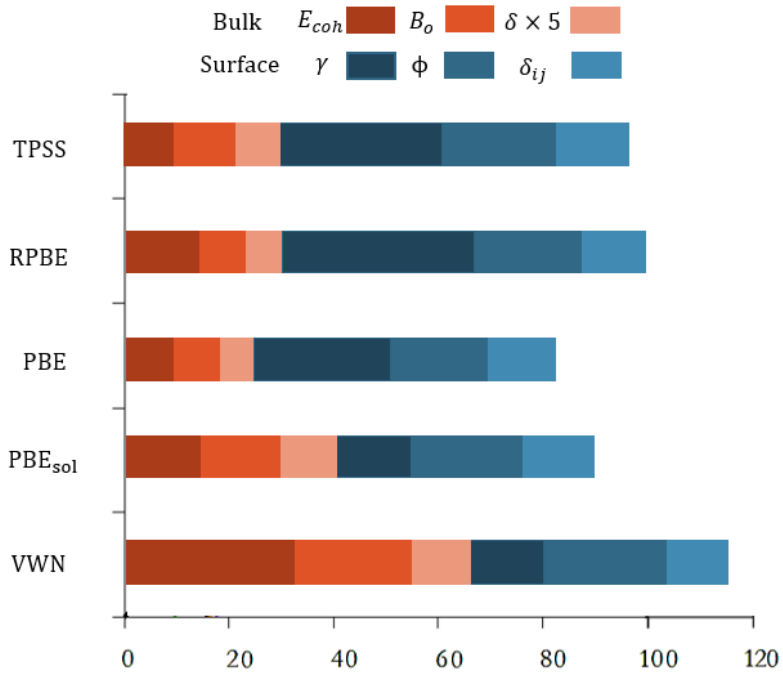

Figure 4.7 Summary of xc functional accuracy in describing bulk and surface related properties, according to the added MAPE values. Accuracies of distance related properties have been arbitrarily enlarged 5 times to help in clearly differentiating the performance of the different xc functionals on them.

Conclusions The following conclusions are drawn from the results presented in this Section 4.3:

- There is not a unique *xc* functional which describes better all studied here three surface properties. Also, for each TM, the best functional among the different studied surface properties varies.
- In general, the best functionals for each surface property are: VWN for γ and PBE for δ_{ij} and ϕ.
- The functional which provides the lowest balanced error of all surfaces properties is PBEsol.
- Taking into account surface and bulk properties calculated in previous studies, the best overall functional is PBE.

JCTC Journal of Chemical Theory and Computation

Article

Cite This: J. Chem. Theory Comput. 2018, 14, 395−403

pubs.acs.org/JCTC

Jacob's Ladder as Sketched by Escher: Assessing the Performance of Broadly Used Density Functionals on Transition Metal Surface Properties

Lorena Vega, Judit Ruvireta, Francesc Viñes,* and Francesc Illas

Departament de Ciència de Materials i Química Física and Institut de Química Teòrica i Computacional (IQTCUB), Universitat de Barcelona, c/Martí i Franquès 1, Barcelona 08028, Spain

Supporting Information

ABSTRACT: The present work surveys the performance of various widely used density functional theory exchange−correlation (xc) functionals in describing observable surface properties of a total of 27 transition metals with face-centered cubic (fcc), body-centered cubic (bcc), or hexagonal close-packed (hcp) crystallographic structures. A total of 81 low Miller index surfaces were considered employing slab models. Exemplary xc functionals within the three first rungs of Jacob's ladder were considered, including the Vosko−Wilk−Nusair xc functional within the local density approximation, the Perdew−Burke−Ernzerhof (PBE) functional within the generalized gradient approximation (GGA), and the Tao−Perdew−Staroverov−Scuseria functional as a meta-GGA functional. Hybrids were excluded in the survey because they are known to fail in properly describing metallic systems. In addition, two variants of PBE were considered, PBE adapted for solids (PBEsol) and revised PBE (RPBE), aimed at improving adsorption energies. Interlayer atomic distances, surface energies, and surface work functions were chosen as the scrutinized properties. A comparison with available experimental data, including single-crystal and polycrystalline values, shows that no xc functional is best at describing all of the surface properties. However, in statistical mean terms the PBEsol xc functional is advised, while PBE is recommended when considering both bulk and surface properties. On the basis of the present results, a discussion of adapting GGA functionals to the treatment of metallic surfaces in an alternative way to meta-GGA or hybrids is provided.

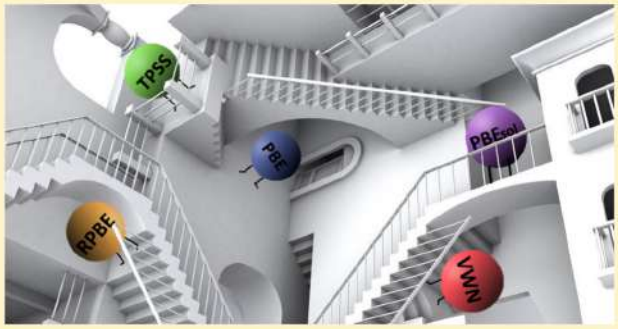

INTRODUCTION

Nowadays, density functional theory (DFT)[1] has become the workhorse in the theoretical and computational study of chemical processes, encompassing a rich and varied range of scientific fields, including quantum chemistry, solid-state physics, materials science, and heterogeneous catalysis, to name a few. This success arises mainly from the ability of DFT methods to provide relatively accurate results at an affordable computational cost. However, a general exchange−correlation (xc) functional that permits the exact calculation of the ground-state energy of a given system is still missing. Over the last decades a handful of different approximations with increasing complexity and alleged accuracy have arisen trying to solve this issue. This is often conceptualized in terms of the so-called Jacob's ladder of xc systematic improvement, a.k.a. Perdew's dream.[2] To a large extent, such a systematic improvement very much relies on validation against experiments through appropriate atomic and molecular data sets. It has recently been found that many basic physicochemical properties are highly dependent on the employed xc functional,[3] and for materials science some functionals are better-suited for particular materials families and/or properties; e.g., hybrid xc functionals are advised when dealing with light-atom molecular systems[4,5] or when treating semiconductor or insulator band structures,[6−8] even if energy-related properties of the latter can already be satisfactorily described within the generalized gradient approximation (GGA).[9,10]

Here we focus on the series of transition metals (TMs), as these are present in many fields of chemistry, physics, and materials science, such as in nanotechnology,[11] sensors,[12] homogeneous[13] and heterogeneous catalysis,[14,15] and H_2 generation in green chemistry,[16] to cite some. In many of these applications, such as in heterogeneous catalysis, TMs are typically employed in the shape of nanoparticles supported on an appropriate substrate.[17] Improvements related to the higher rungs of Jacob's ladder, which imply hybrid functionals, do not necessarily work for transition metals. Indeed, the optimal percentage of Hartree−Fock (HF) exchange in a hybrid xc functional required to make it suitable for bulk transition metals is close to zero.[18] Therefore, apparently the inclusion of HF exchange is detrimental for the accuracy of xc functionals on transition metals. This has been confirmed in recent studies exploring the ability of 15 different xc functionals to describe

Received: October 16, 2017
Published: November 28, 2017

DOI: 10.1021/acs.jctc.7b01047
J. Chem. Theory Comput. 2018, 14, 395−403

energetic, structural, and compressive parameter properties of bulk TMs.[19,20] These studies showed that for bulk TMs, hybrid functionals perform worse than local density approximation (LDA), GGA, and meta-GGA functionals. The presence of HF exchange in the xc functional leads to unphysically localized TM bands, disrupting the proper description of transition metal properties.[21] Furthermore, a very recent study showed that it is possible to describe the thermochemistry of 3d TMs without having to rely on hybrid approaches.[22]

The above-mentioned previous studies pointed to xc functionals within the GGA as the best choice for describing TM bulk properties. In particular, on average, the Perdew–Burke–Ernzerhof (PBE)[23] xc functional was found to be the most accurate one, while the Tao–Perdew–Staroverov–Scuseria (TPSS)[24] would be the next-best-suited and broadly used functional from another Jacob's ladder rung, often considered necessary when dealing with main-group-element molecular systems, as in the case of adsorbates on surfaces.[25] We note in passing that there have been recent improvements in semilocal meta-GGAs,[26] including the intermediate-range description of dispersive forces, which in principle can lead to a significant description upgrade on a diversity of chemical systems.[27] Finally, the Vosko–Wilk–Nusair parametrization of the LDA would be the best-adapted in that rung.[28] It should be noticed, however, that this analysis was carried out solely for *bulk* transition metals, where surface peculiarities were disregarded. At this point one may wonder up to which point functionals that are well-suited for describing bulk TMs perform equally well in describing surfaces and related properties. This is a pertinent question since xc functionals are mostly validated against bulk crystallographic structures. Answering this question can shed light on the adequacy of xc functionals in the treatment of surface states and related properties, an important issue in computational heterogeneous catalysis.

To clarify this issue, we selected a wide database involving 27 TMs displaying either a hexagonal close-packed (hcp) crystallographic structure (Sc, Y, Ti, Zr, Hf, Tc, Re, Ru, Os, Co, Zn, and Cd), a face-centered cubic (fcc) structure (Rh, Ir, Ni, Pd, Pt, Cu, Ag, and Au), or a body-centered one (bcc) crystal packing (V, Nb, Ta, Cr, Mo, W, and Fe). For these 27 TMs, different low Miller index surfaces with a maximum index order of 1 were considered, thus featuring in principle the most stable surface termination according to their crystal structure. Specifically, these are the (001), (011), and (111) surfaces for fcc and bcc structures and the (0001), (10$\bar{1}$0), and (11$\bar{2}$0) surfaces for hcp structures. Miller–Bravais indexes are used in the case of hcp TMs (Figure 1).

Following the strategy used in previous studies on the bulk of TMs,[19,20] three surface properties were investigated. One structural property was chosen, the interlayer distance relaxation, as e.g. obtained in metal single crystal low-energy electron diffraction (LEED) experiments, including, when possible, relaxation of inner layers. The main energetic property, the surface energy γ, was also evaluated, as it defines the surface stability and, allegedly, the surface chemical activity.[29] It should be noted that surface energies are available from a compendium of 0 K extrapolated values obtained by a collection of measurements of TM surface tensions at/near their melting temperatures.[30] Finally, the surface work function, ϕ, was considered here as a main electronic structure property, as inherently defined by the position of the Fermi level (E_F) with respect to the vacuum energy level, often measured by, e.g., scanning Kelvin probe force microscopy (SKPFM).[31]

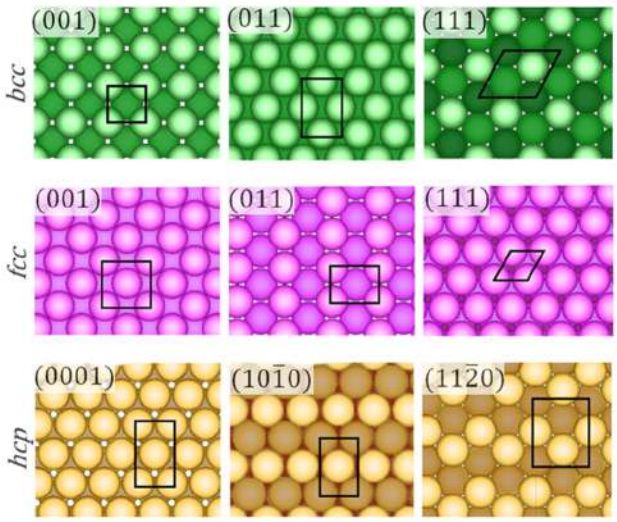

Figure 1. Schematic representation of the studied (001), (011), and (111) surfaces for fcc and bcc TMs and the (0001), (10$\bar{1}$0), and (11$\bar{2}$0) surfaces for hcp TMs, with zenithal perspective views. The employed (1 × 1) surface unit cells are shown in solid black lines. Atomic positions are denoted by colored spheres, which turn darker when going subsurface. The particular cases presented are Nb (bcc), Pt (fcc), and Ru (hcp), all optimized using PBE.

Surface energies and work functions are two fundamental physicochemical parameters that are important to understand surface processes, including charge transfer, activity issues pivotal in surface-catalyzed reactions, adsorptive processes, surface segregation and corrosion, growth rates, and the formation of grain boundaries, to name a few. These two properties are typically experimentally determined on mixed or polycrystalline samples exposing typically multiple facets, and those situations therefore should be better assessed considering the equilibrium shape of crystals. Consequently, here the different crystal orientations were weighted using the Wulff representation of crystal equilibrium shapes,[32,33] although in the case of work functions, some single-crystal surface-specific values are available.

■ COMPUTATIONAL DETAILS

DFT-based calculations were performed using the Vienna Ab Initio Simulation Package (VASP) code,[34] employing periodic boundary conditions and using the above-mentioned VWN within the LDA, PBE within the GGA, and TPSS as an example of a meta-GGA xc functional. Furthermore, other GGA xc functionals a priori adapted for bulk solids and surfaces were closely inspected, including PBE adapted for solids (PBEsol)[35] and revised PBE (RPBE),[36] alleged to better describe adsorption energies.

All of the TM surfaces were modeled as six-layer slabs using (1 × 1) surface unit cells with a minimum 10 Å vacuum space, which is known to be enough to isolate slabs from their periodically repeated replicas, although in selected systems, such as in magnetic metals, a larger vacuum up to 30 Å was used to avoid magnetic coupling. Slab surfaces were constructed from bulk optimized structures obtained using the very same xc functionals and the same computational

DOI: 10.1021/acs.jctc.7b01047
J. Chem. Theory Comput. 2018, 14, 395–403

setup.[19,20] During structural optimization, the slab cells were kept fixed, whereas all atomic positions were fully relaxed.

The valence electron density was expanded in a plane-wave basis set with a 415 eV cutoff for the kinetic energy, while the effect of the atomic cores on the valence electron density was described using the projector augmented wave (PAW) method.[37] A tetrahedron smearing method with a width of 0.2 eV was used to speed up the electronic convergence,[38] yet final energy values were corrected to 0 K. An electronic convergence criterion of 10^{-6} eV was used, and ionic relaxation was considered converged when the forces acting on atoms were smaller than 0.01 eV/Å. The electronic structure calculations were by default non-spin-polarized, except for magnetic Fe, Co, and Ni bulks and surfaces. An optimal Monkhorst–Pack[39] 7 × 7 × 7 k-points grid was found to be sufficient for accurate bulk total energy calculations in the most stringent metals[19,20] and was therefore used in all cases. In the case of slab calculations, a 7 × 7 × 1 k-points grid was used.

The surface energies, γ, were calculated following eq 1,

$$\gamma = \frac{E_{\text{slab}} - (N \cdot E_{\text{bulk}})}{2 \cdot A} \tag{1}$$

where E_{slab} is the energy of the optimized slab, E_{bulk} is the energy of a metal atom in its bulk environment, N is the number of atoms in the employed slab model, and A is the exposed surface area in each of the two exposed facets of the slab model.

The work function, ϕ, is defined as the minimum energy needed to remove an electron from a solid, i.e., to move the electron from the Fermi level (E_F) and place it in the vacuum energy level (V):

$$\phi = V - E_F \tag{2}$$

In order to acquire V, the electron electrostatic potential energy was averaged for each surface along the normal to the surface direction until a constant value was found in the vacuum region (see Figure 2). E_F was obtained from the total density of states (DOS) sampled by ca. 10 000 points, ensuring a numerical precision of 0.001 eV.

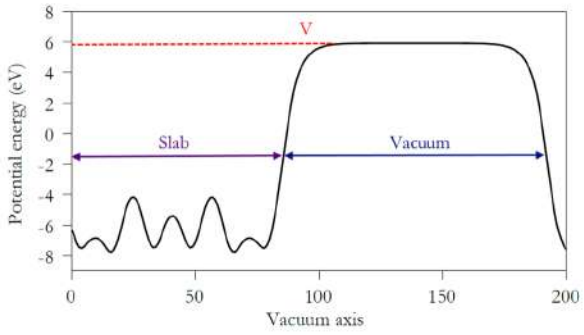

Figure 2. Electrostatic potential energy for a prototypical six-layer slab—Mo(001) surface, TPSS functional—as a function of vacuum axis length.

Finally, the surface relaxation was evaluated as the layer contraction/expansion percentage, Δ_{ij}, given with respect to the bulk environment. For the studied TMs, the interlayer spacing between two vicinal layers i and j is constant for a given crystallographic direction in the bulk, so Δ_{ij} is given as

$$\Delta_{ij} = \frac{\delta_{ij} - \delta_{ij}^{\text{bulk}}}{\delta_{ij}^{\text{bulk}}} \cdot 100 \tag{3}$$

where $\delta_{ij}^{\text{bulk}}$ is the bulk interlayer distance along the direction perpendicular to the surface and δ_{ij} is the equivalent interlayer distance in the slab model. In the bulk, the ij index is a constant, whereas in the slab it refers to a pair of consecutive atomic layers. Hence, $i = 1$ corresponds to the surface layer and $j = 2$ to the first subsurface layer. Thus, δ_{12} would refer to the interlayer distance between the surface and the first subsurface layer in the slab model. Within this definition, negative values of Δ_{ij} imply an interlayer distance shortening, whereas positive values refer to interlayer distance lengthening.

RESULTS AND DISCUSSION

For convenience, results concerning surface energies are presented first, followed by a discussion of the results for surface work functions. The analysis of the structural relaxation is then reported at the end of this section, followed by an overall discusison.

1. Surface Energies. In order to determine the best-suited xc functional for this property, we first compare the computed surface energies with the 0 K extrapolated experimental data. Such extrapolations are typically done from polycrystalline samples near the melting temperatures and likely correspond to admixtures of different exposed surfaces.[30] However, it is unclear whether the 0 K extrapolated data would belong to the most stable surface or still to an admixture of competing surfaces. For that purpose we used Wulff constructions such as those described in Figure 3. For each transition metal, the Wulff constructions were obtained from the calculated surface energies obtained for each xc functional. For fcc and bcc structures these were built using the Visualization for Electronic and Structural Analysis (VESTA) package,[40] whereas the WinXMorph suite was used for the hcp ones.[41] There, for each TM and each xc functional, the constructed Wulff shapes provide the percentage of area exposed by each exposed surface. The specific computed surface energies, γ^{calc}, for each particular surface and each employed xc are found in Table S1 in the Supporting Information, alongside the experimental surface energies, γ^{exp}. The obtained 0 K Wulff contributions are listed in Table S2.

The performance of the different xc functionals in describing surface energies is analyzed in Figure 4 by comparing the computed estimates to experimental values. Two comparisons are made here, using either γ^{calc} values for the most stable surfaces, consistently evaluated for each TM surface and xc functional, or Wulff-shape-averaged values, $\gamma_{\text{Wulff}}^{\text{calc}}$, thus considering contribution fractions of all surfaces of a given TM at a given xc level. The latter provide a better comparison since, as mentioned above, a large number of experimental values correspond to averages over exposed surfaces. For clarity, only linear fits are plotted, although dispersion is evaluated by the linear regression factor R (see Table S3) and the error analysis listed in Table 1. Here quantitative analysis of the accuracy is based on mean errors (MEs), mean absolute errors (MAEs), and mean absolute percentage errors (MAPEs).

A close inspection of Figure 4 shows that the approximation of comparing calculated to measured surface energies assuming that experiments correspond to the most stable facets—the γ^{calc} case—can be justified since the experimental trends are duly followed, especially when considering the VWN and PBEsol

DOI: 10.1021/acs.jctc.7b01047
J. Chem. Theory Comput. 2018, 14, 395−403

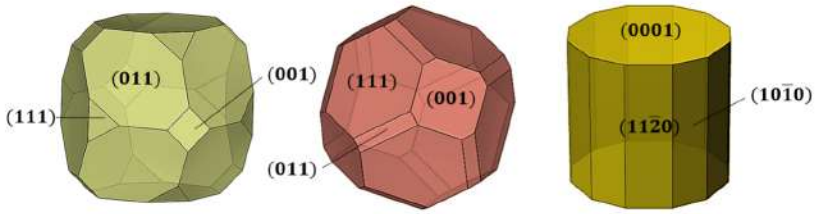

Figure 3. Exemplary Wulff shape representations of different TMs predicted using different xc functionals. The green shape belongs to bcc W obtained with the VWN xc functional, the pink shape to fcc Ni obtained with PBEsol, and the yellow one to hcp Zr obtained with TPSS. Tags for the different surfaces are located near the exposed facets.

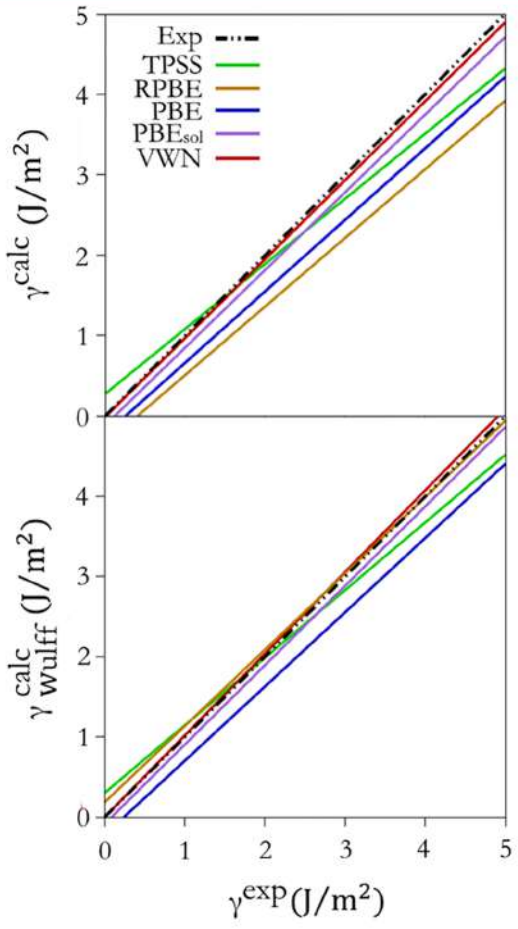

Figure 4. Comparison of the linear fits between calculated (calc) and experimental (exp) surface energies for the different explored xc functionals. The top panel considers only the most stable surface, γ^{calc}, whereas the bottom panel compares Wulff-shape-averaged values, γ^{calc}_{Wulff}.

functionals, which display linear regression with R coefficients over 0.90, slopes near unity, and intercepts of only −0.01 J/m^2 (VWN) and −0.12 J/m^2 (PBEsol). The performance of PBE and RPBE in this point can be considered as quite good, whereas the meta-GGA TPSS functional displays poor adjustment, with an R value of only 0.51 (see Table S2).

Considering an admixture of surfaces, here simulated by Wulff-averaged surface energy values—the γ^{calc}_{Wulff} case—one realizes that a better fit is obtained (see Figure 4). This is accompanied by slightly better R coefficients, slopes, and intercepts (see Table S2). The only exception to this fact is RPBE: the Wulff-averaged calculated value leads to a slope

Table 1. Mean Errors (MEs), Mean Absolute Errors (MAEs), and Mean Absolute Percentage Errors (MAPEs) of Calculated Most Stable Surface Energies, γ^{calc}, and of Wulff-Construction-Weighted Values, γ^{calc}_{Wulff}, with Respect to Experiments as Obtained at the VWN, PBEsol, PBE, RPBE, and TPSS xc Levels[a]

error type	VWN	PBEsol	PBE	RPBE	TPSS
		γ^{calc}			
ME	−0.05	−0.20	−0.49	−0.69	−0.17
MAE	0.28	0.34	0.57	0.73	0.72
MAPE	13.48	16.58	27.11	34.84	31.42
		γ^{calc}_{Wulff}			
ME	0.04	−0.11	−0.40	0.07	−0.06
MAE	0.27	0.29	0.49	0.96	0.68
MAPE	12.24	14.02	23.25	48.49	29.04

[a]All values are given in J/m^2, except for MAPE values, which are given in %.

increase from 0.85 to 0.95, and the intercept changes from −0.34 to 0.18 J/m^2. This apparent better fit is indeed not better, as R drops from 0.88 to 0.56. As a matter of fact, the poor description of surface energies by RPBE applies not only to the most stable surfaces but also to others, which scales to the admixture of all contemplated surfaces (see Table S1). This unrealistic treatment of surfaces on an equal footing upraises the Wulff overall surface energies in a quite unbalanced fashion, leading to a higher dispersion. Therefore, the apparently better fit is an artifact stemming from the poor performance of RPBE in describing surface energies rather than a proper description based on a realistic physical description.

A quantitative analysis based on the statistical errors is shown in Table S1. It should be noted that the ME and MAE values for γ^{calc} differ, meaning that the different xc functionals do not exhibit an absolute systematic error, i.e., having constant over- and underestimations. Nevertheless, a general underestimation is noticeable, and actually, the surface energies tend to follow the bonding strengths. The gradation of bonding strengths on TM bulks has been established previously from the cohesive energy, E_{coh}, as VWN > PBEsol > PBE > RPBE.[19] According to the bond-cutting model, surface energies are directly proportional to E_{coh},[42] and therefore, the surface energies follow the very same trend, yet are always underestimated. As shown in Table S4, a crystallographic decomposed quantitative analysis yields differences among structures, which can be quite mild for xc functionals such as VWN, with MAPE variations below 6% using γ^{calc}, and quite severe for others, such as TPSS, with MAPE variations above 30%. For γ^{calc}_{Wulff} the differences became more acute, such as below 9% (VWN) and above 49% (TPSS). Clearly, the trends are not uniform, and the only particularly better crystallographic description deviation is noted for bcc

DOI: 10.1021/acs.jctc.7b01047
J. Chem. Theory Comput. 2018, 14, 395−403

TMs, where PBEsol seems to be better-suited than VWN, with a MAPE slightly above 15%, whereas TPSS provides a clearly worse description (MAPE above 57%), and an improvement of RPBE (MAPE around 20%).

In any case, the average performance is acceptable, with VWN being the best-suited xc functional in describing surface energies, with a deviation of ca. 12%. The present results excellently agree within 4% with previous results on a subset of fcc (111) surfaces obtained at the LDA and GGA levels.[19] Concerning comparison with experiments, it should be noticed on one hand that the average precision of the surface tension experiments is ±2%, a point that partially amends the disagreement with the present estimates. Further than that, in the present study we neglected the contributions to the surface energy from other defects, including nanoparticle edges and corners, terrace steps and kinks, and other facets with higher-order Miller or Miller–Bravais indices, which, taken into account, could overall slightly increase the agreement between the calculated and experimental surface energy values.

2. Work Functions. Next, we discuss the performance of the different functionals in predicting surface work functions. The complete set of calculated values is reported in Table S5. Following the same procedure as in the previous section, we rely on the Wulff constructions to obtain an averaged value of ϕ to be compared with the experimental values obtained from polycrystalline samples.[31] However, for this observable there are also a significant number of surface-specific measurements obtained from TM single crystals cut in the desired studied directions. Therefore, for this subset of data, a direct comparison is possible and the list of experimental values is reported in Table S5. It should be noted that 26 polycrystalline values are accessible—all TMs except synthetic Tc. Concerning well-defined surfaces, 50 experimental values are available, corresponding to ∼62% of the studied cases. Concerning temperature effects, we here compare 0 K estimated values of ϕ to experimental values normally obtained at or near room temperature. However, there is experimental evidence that the transition metal work functions change with temperature by between 10^{-4} to 10^{-6} eV/K.[43,44] Therefore, the disagreement due to thermal effects under standard conditions cannot exceed 0.04 eV. Consequently, this small deviation is neglected in the oncoming analysis and discussion.

Two sets of values are used for comparison to polycrystalline values: Wulff-averaged values, ϕ^{calc}_{Wulff}, and single-crystal data for well-defined surfaces, ϕ^{calc}_{Single}. The trends from linear fits are reported in Figure 5, whereas the corresponding statistical analysis is summarized in Table 2. As one can see, a better correlation is obtained from the one-to-one comparison to single-crystal surfaces, as expected. It should be noted that for this property, and at variance with the surface energies, VWN does not show a good fit, and actually, the calculated set that seems to better meet the experimental trend is PBE for both single-crystal and polycrystalline samples. Slight quantitative differences are found depending on the utilization of single-crystal or polycrystalline values (see Table 2), although the performance decreases as PBE > PBEsol > RPBE > TPSS > VWN for the single-crystal analysis. This trend is almost maintained in the comparison to the polycrystalline data, where only PBEsol and RPBE swap positions. In Figure 5, at variance to surface energies, the trends for work functions appear to show an overestimation of large ϕ values and an underestimation of small ϕ ones, with transient points located at ∼4 and ∼3 eV for the single-crystal and polycrystalline cases, respectively. For the oncoming analysis, we decided that it would be better to rely on the single-crystal data, as slab models provide a realistic representation of these systems. Thus, we neglect other higher-order Miller index surfaces and other low-coordinated sites on the nanoparticle approximation, which can

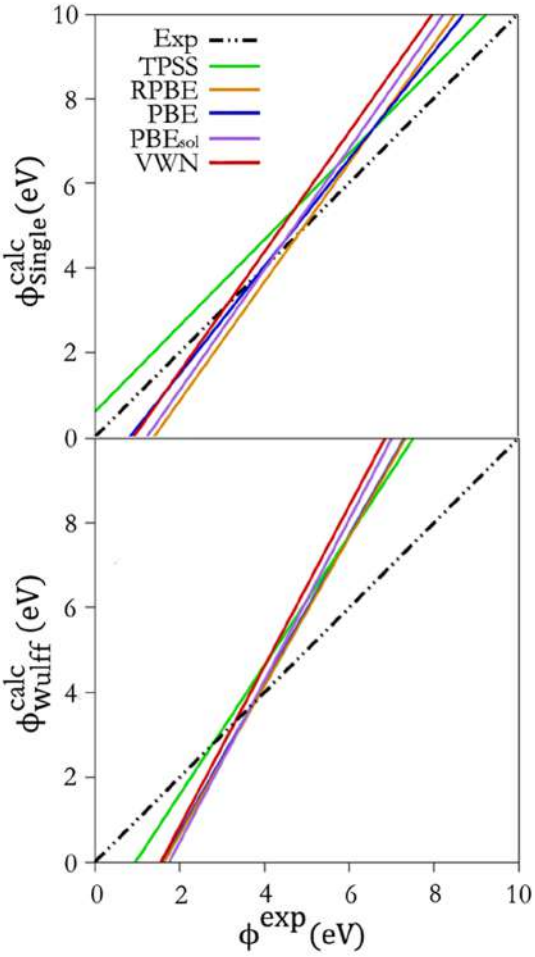

Figure 5. Comparison of the linear fits between calculated (calc) and experimental (exp) work functions for the different explored xc functionals. The top panel considers only single-crystal data, ϕ^{calc}_{Single}, whereas the bottom panel compares Wulff-shape-averaged values, ϕ^{calc}_{Wulff}. All values are given in eV.

Table 2. Statistical Analysis Based on MEs, MAEs, and MAPEs of Calculated Work Functions with Respect to Experiments (Single-Crystal Surfaces, ϕ^{calc}_{Single}, and Polycrystalline Values, ϕ^{calc}_{Wulff}) as Obtained at the VWN, PBEsol, PBE, RPBE, and TPSS Levels[a]

error type	VWN	PBEsol	PBE	RPBE	TPSS
		ϕ^{calc}_{Single}			
ME	0.79	0.38	0.30	0.07	0.69
MAE	1.13	1.06	1.02	1.08	1.10
MAPE	22.85	21.42	20.77	22.04	22.41
		ϕ^{calc}_{Wulff}			
ME	1.10	0.77	0.61	0.57	0.97
MAE	1.25	0.99	0.91	0.94	1.18
MAPE	26.49	20.91	19.39	20.15	25.36

[a]All values are given in eV, except for MAPE values, which are given in %.

DOI: 10.1021/acs.jctc.7b01047
J. Chem. Theory Comput. 2018, 14, 395−403

affect the simulated values. From this analysis, PBE appears to be the best-performing xc functional.

For the linear fits, some caveats ought to be mentioned. The slopes (a), intercepts (b), and R values of the linear fits in Figure 5 are reported in Table S6. These generally show a clear deviation with respect the expected linear trend for the ϕ^{calc}_{Wulff} case, with slopes overestimated well above 1.5 and intercepts far from zero by a few eV. Moreover, the data dispersion is reflected by exceedingly small R values, below 0.8. For the ϕ^{calc}_{Single} data, the slopes are reduced to 1.45 or below, and the intercepts significantly approach the ideal value of zero by 0.8–1.5 eV. The TPSS ϕ^{calc}_{Single} case is to be highlighted, as it displays a and b of 1.05 and 0.46 eV, respectively, although this improvement in the linear fit is gained at the expense of a poorer dispersion of the data with a reduced regression coefficient, a common denominator in fitting to single-crystal data. This said, a further close inspection of the crystallographic itemized statistics, shown in Table S7, indicates a general pattern in the sense that the work functions of fcc metal surfaces are better described than those of hcp and bcc ones, and for this situation, TPSS performs better. However, bcc surfaces are described better when comparing to polycrystalline data, although there the best description comes from the PBE functional. At variance with the above-discussed case of surface energies, the work function experimental accuracy (below ±0.3%) barely helps in concealing estimates and measurements.

3. Interlayer Distances. Finally, as far as surface relaxation is concerned, a limited amount of experimental data is available, most focused on the interlayer distance between the surface and first subsurface layers, δ_{12}. In addition, the experimental reference data for the full set of surfaces and TMs is incomplete and exhibits a sensible heterogeneity of values with different accuracies and experimental precisions, sometimes contradictory for a particular TM surface. Because of this, we selected as reference data those that display (i) higher precision, (ii) a larger amount of interlayer distances, and (iii) for (i) and (ii) being on an equal footing, those obtained most recently. The full set of data and concomitant references are reported in Table S8, with the used values highlighted in bold.

The calculated data at all of the explored xc levels, including the three different interlayer relaxation values (Δ_{12}, Δ_{23}, and Δ_{34}) are contained in Table S9. However, the relaxation percentage as usually provided in the experiments is of little use in evaluating xc performance because it is already a referenced datum. Because of this, it seems more justified to directly compare the computed interlayer distances δ_{ij} to the experimental values derived from the experimentally available interlayer relaxations. To obtain δ^{exp}_{ij}, the experimental interlayer percentage relaxations were applied to the 0 K extrapolated interlayer distances.[20] The computed values are reported in Table S10. The performance of the different methods in predicting δ_{ij} was analyzed statistically, and the results are reported in Table 3. Graphically, the calculated values nicely fit the experimental set of values, as can be seen in Figure 6, with very small deviations of typically around 0.15–0.22 Å (Table 3) with little variations among the different considered xc functionals. This is also reflected in the data from the linear fits shown in Table S11, with slopes near ∼0.8, intercepts below 0.4 Å, and R values of ca. 0.8. This is in agreement with the rather good description of geometrical structure by LDA, GGA, and meta-GGA xc functionals in general, and on bulk TMs in particular.[19,20] Despite this, Figure 6 shows that PBE performs slightly better, with comparison to experiments, than the other explored xc functionals. This is aligned with PBE having the smallest MAPE value in Table 3. However, this result varies with the crystallographic structure, as shown in Table S12, with bcc being the most accurate for this property. In addition, it is important to remark that experiments show a wide range of precision, ±1.5% on average, which actually closes the gap of any DFT calculation, and the differences among functionals seem to be not so acute as those previously found for γ and ϕ.

Table 3. Statistical Analysis Based on MEs, MAEs, and MAPEs of Calculated Interlayer Distances, δ_{ij}, Compared to Experimental Ones, δ^{exp}_{ij}, as Obtained at the VWN, PBEsol, PBE, RPBE, and TPSS Levels[a]

error type	VWN	PBEsol	PBE	RPBE	TPSS
ME	−0.08	−0.07	−0.03	−0.01	0.03
MAE	0.18	0.17	0.15	0.16	0.22
MAPE	11.51	10.87	10.11	10.36	13.76

[a]All values are given in pm, except for MAPE values, which are given in %.

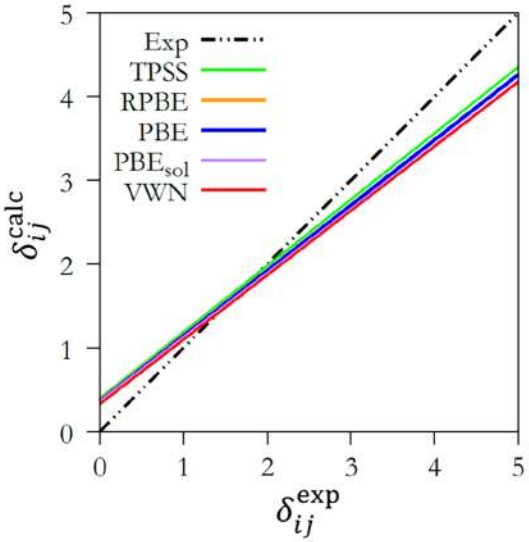

Figure 6. Comparison of δ_{ij} MAPE to experimental data, δ^{exp}_{ij}, as calculated and adjusted to linear regression for each functional.

4. Overall Functional Assessment. To summarize, a general view of the performance, in terms of MAPE, of the different explored functionals in predicting surface relaxations, surface energies, and surface work functions is provided. It should be noticed that concerning the assessment of the different functionals, the results evidence heterogeneity on the properties under study—even crystallographic groups and specific TMs (see Figure S1). Even so, an overall better performance for specific cases is observed for VWN concerning γ, and for RPBE for ϕ, yet for the latter property the mean best performance is again for PBE. On average, VWN is best-adapted to surface energies and PBE to work functions and interlayer distances. However, for a general assessment of surface properties, one can add up the obtained MAPEs for each xc functional under study, as shown in Figure 7. A close inspection reveals that according to this criterion, the most balanced surface properties are provided by PBEsol, despite the fact that this functional does not provide better fits between calculations and experiment for the properties under inspection.

DOI: 10.1021/acs.jctc.7b01047
J. Chem. Theory Comput. 2018, 14, 395−403

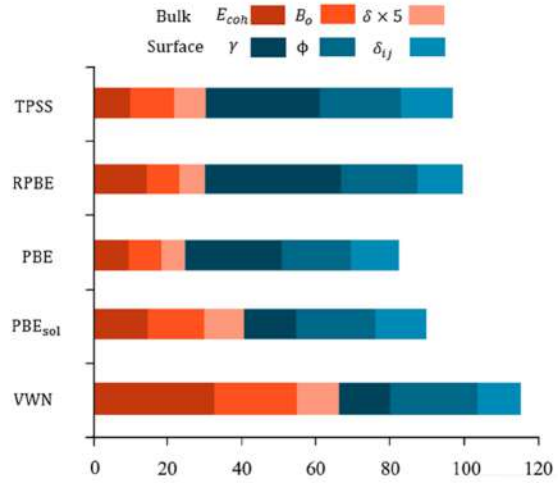

Figure 7. Summary of xc functional accuracy in describing bulk and surface related properties according to the sum of MAPE values. The accuracies of distance related properties have been arbitrarily enlarged 5 times to help in clearly differentiating the performance of the different xc functionals on them.

Further than that, when the present analysis is combined with that of TM bulk properties—cohesive energies, E_{coh}, bulk moduli, B_0, and shortest interatomic distances δ—obtained earlier with the same procedure as applied here,[19,20] the most accurate xc functional is PBE, closely followed by PBEsol and TPSS.

In this sense, one would not advise the use of VWN and RPBE to compute TM bulk or surface properties, although VWN is particularly suited when estimating surface energies. All that said, RPBE has been claimed to represent an improvement regarding the adsorption of main-group molecules on TM surfaces,[36] a point out of the scope of the present study, although the TPSS meta-GGA functional also represents an improvement in the description of the thermochemistry of main-group systems, fact that, coupled to its present good performance, can place TPSS in a best-compromise situation for studying the interactions of atoms and/or molecules on TM surfaces.[20,24] Moreover, the present study further reveals that at least for TM extended systems, the development of new xc functionals needs to consider a broad number of properties, much in the same spirit of the G2 and related data sets used in molecular quantum chemistry.[45] This has been exemplified here by assessing the performance of a series of functionals on predicting surface (and bulk) properties, which hopefully will serve as a spur and guidance for future DFT xc functional improvements.

Along this line, functional research targeting the description of transition metal properties should address as well the possible effect of dispersive forces in any of the explored metals, properties, and functionals, a point not contemplated here. A recent study by Patra et al.[46] showed that the strongly constrained appropriately normed (SCAN) semilocal meta-GGA functional[47]—including an intermediate-range van der Waals (vdW) description—and the addition of Vydrov–Voorhis vdW to SCAN (SCAN+rVV10)[48]—including as well long-range vdW interactions—affected the surface energies and work functions for a subset of seven fcc TMs, increasing the surface energies by ∼10% and work functions by ∼3%. More importantly, SCAN+rVV10 showed the best description regardless of the property, although such a statement remains to be confirmed by considering a broader set of TMs as was done in the present work.

CONCLUSIONS

A survey of the performance of various widely used DFT xc functionals in describing surface observables of all transition metals with fcc, bcc, or hcp crystallographic structures has been presented. The properties under scrutiny included structural (interlayer distances), energetic (surface energies), and electron transfer (work functions) properties. These were estimated on appropriate models of low Miller index (Miller–Bravais for hcp) surfaces and obtained with broadly used xc functionals within the three first rungs of Jacob's ladder, including VWN within the LDA; PBE, PBEsol, and RPBE within the GGA; and TPSS as a meta-GGA representative. A comparison to a large set of available experimental data, including single-crystal when available, is provided. A comparative to polycrystalline values is also carried out with the help of Wulff constructions for the equilibrium shapes of nanoparticles. This strategy allowed the estimation of surface properties averaged according to the proportion of exhibited facets in polycrystalline samples.

The results show that no xc functional is best at simultaneously describing all surface properties, with slight variations depending on the property, transition metal, and even the crystallographic arrangement. Despite this, the present results show that, on average terms, VWN is best-suited for predicting surface energies, whereas PBE provides the best description for interlayer atomic distances and work functions. However, the use of the PBEsol xc functional is advised in order to obtain a mean, balanced description of surface properties, while PBE is recommended when simultaneously considering both bulk and surface properties. The present results highlight the importance of fitting xc functionals to a diverse range of properties and transition metal extended systems for improved performance.

ASSOCIATED CONTENT

Supporting Information

The Supporting Information is available free of charge on the ACS Publications website at DOI: 10.1021/acs.jctc.7b01047.

Computed surface energies for each TM, functional, and surface as well as the experimental values (Table S1); percentage of expression of each surface for each TM as self-consistently obtained at each DFT level using the Wulff constructions (Table S2); linear adjustment parameters corresponding to Figures 4, 5, and 6 (Tables S3, S6, and S11, respectively); statistical analysis of Tables 1–3 but decomposed according to fcc, bcc, and hcp crystallographic structure families (Tables S4, S7, and S12, respectively); computed work functions for each TM, functional, and surface as well as experimental polycrystalline and single-crystal data (Table S5); experimental interlayer distances found in the literature, highlighting those used as reference data (Table S8); computed interlayer relaxations and distances (Tables S9 and S10); best functional for each bulk and surface TM property (Figure S1) (PDF)

AUTHOR INFORMATION

Corresponding Author

*E-mail: francesc.vines@ub.edu.

DOI: 10.1021/acs.jctc.7b01047
J. Chem. Theory Comput. 2018, 14, 395–403

ORCID

Francesc Viñes: 0000-0001-9987-8654

Francesc Illas: 0000-0003-2104-6123

Funding

This work was supported by Spanish MINECO/FEDER Grant CTQ2015-64618-R and in part by Generalitat de Catalunya Grants 2014SGR97 and XRQTC and the NOMAD Center of Excellence Project; the latter project received funding from the European Union Horizon 2020 Research and Innovation Programme under Grant Agreement 676580. F.V. thanks the Spanish MINECO for postdoctoral contracts under the Ramón y Cajal Program (RYC-2012-10129), and F.I. acknowledges additional support through the ICREA Academia Award for Excellence in Research.

Notes

The authors declare no competing financial interest.

REFERENCES

(1) Parr, R. G.; Yang, W. *Density Functional Theory of Atoms and Molecules*; Oxford University Press: Oxford, U.K., 1989.

(2) Perdew, J. P.; Schmidt, K. Jacob's Ladder of Density Functional Approximations for the Exchange−Correlation Energy. *AIP Conf. Proc.* **2000**, *577*, 1.

(3) Medvedev, M. G.; Bushmarinov, I. S.; Sun, J.; Perdew, J. P.; Lyssenko, K. A. Density Functional Theory is Straying from the Path Toward the Exact Functional. *Science* **2017**, *355*, 49−52.

(4) Sousa, S. F.; Fernandes, P. A.; Ramos, M. J. General Performance of Density Functionals. *J. Phys. Chem. A* **2007**, *111*, 10439−10452.

(5) Peverati, R.; Truhlar, D. G. An Improved and Broadly Accurate Local Approximation to the Exchange−Correlation Density Functional: The MN12-L Functional for Electronic Structure Calculations in Chemistry and Physics. *Phys. Chem. Chem. Phys.* **2012**, *14*, 13171−13174.

(6) Tomić, S.; Montanari, B.; Harrison, N. M. The Group III−V's Semiconductor Energy Gaps Predicted Using the B3LYP Hybrid Functional. *Phys. E* **2008**, *40*, 2125−2127.

(7) Viñes, F.; Lamiel-Garcia, O.; Ko, K. C.; Lee, J. Y.; Illas, F. Systematic Study of the Effect of HSE Functional Internal Parameters on the Electronic Structure and Band Gap of a Representative Set of Metal Oxides. *J. Comput. Chem.* **2017**, *38*, 781−789.

(8) Peverati, R.; Truhlar, D. G. Performance of the M11-L Density Functional for Bandgaps and Lattice Constants of Unary and Binary Semiconductors. *J. Chem. Phys.* **2012**, *136*, 134704.

(9) Viñes, F.; Lamiel-Garcia, O.; Bromley, S. T.; Illas, F. Size Dependent Structural and Polymorphic Transitions in ZnO: from Nanocluster to Bulk. *Nanoscale* **2017**, *9*, 10067−10074.

(10) Lamiel-Garcia, O.; Ko, K. C.; Lee, J. Y.; Bromley, S. T.; Illas, F. When Anatase Nanoparticles Become Bulklike: Properties of Realistic TiO_2 Nanoparticles in the 1−6 nm Size Range from All Electron Relativistic Density Functional Theory Based Calculations. *J. Chem. Theory Comput.* **2017**, *13*, 1785−1793.

(11) Viñes, F.; Görling, A. Template-Assisted Formation of Fullerenes from Short-Chain Hydrocarbons by Supported Platinum Nanoparticles. *Angew. Chem., Int. Ed.* **2011**, *50*, 4611−4614.

(12) Yang, M. H.; Yang, Y. H.; Liu, Y. L.; Shen, G. L.; Yu, R. Q. Platinum Nanoparticles-Doped Sol-Gel/Carbon Nanotubes Composite Electrochemical Sensors and Biosensors. *Biosens. Bioelectron.* **2006**, *21*, 1125−1131.

(13) Frenking, G. *Theoretical Aspects of Transition Metal Catalysis*; Springer: Berlin, 2005.

(14) Thomas, J. M.; Thomas, W. J. *Principles and Practice of Heterogeneous Catalysis*, 2nd ed.; Wiley-VCH: Weinheim, Germany, 2015.

(15) Anderson, J. A.; Fernández-García, M. *Supported Metals in Catalysis*; Imperial College Press: London, 2011.

(16) Wu, J.; Yang, H. Platinum-Based Oxygen Reduction Electrocatalysts. *Acc. Chem. Res.* **2013**, *46*, 1848−1857.

(17) Van Santen, R. A.; Neurock, M. *Molecular Heterogeneous Catalysis*; Wiley-VCH: Weinheim, Germany, 2006.

(18) Perdew, J. P.; Ernzerhof, M.; Burke, K. Rationale for Mixing Exact Exchange with Density Functional Approximations. *J. Chem. Phys.* **1996**, *105*, 9982.

(19) Janthon, P.; Kozlov, S. M.; Viñes, F.; Limtrakul, J.; Illas, F. Establishing the Accuracy of Broadly Used Density Functionals in Describing Bulk Properties of Transition Metals. *J. Chem. Theory Comput.* **2013**, *9*, 1631−1640.

(20) Janthon, P.; Luo, S.; Kozlov, S. M.; Viñes, F.; Limtrakul, J.; Truhlar, D. G.; Illas, F. Bulk Properties of Transition Metals: A Challenge for the Design of Universal Density Functionals. *J. Chem. Theory Comput.* **2014**, *10*, 3832−3839.

(21) Notario-Estévez, A.; Kozlov, S. M.; Viñes, F.; Illas, F. Electronic-structure-based material descriptors: (in)dependence on self-interaction and Hartree−Fock exchange. *Chem. Commun.* **2015**, *51*, 5602−5605.

(22) Determan, J. J.; Poole, K.; Scalmani, G.; Frisch, M. J.; Janesko, B. G.; Wilson, A. K. Comparative Study of Nonhybrid Density Functional Approximations for the Prediction of 3*d* Transition Metal Thermochemistry. *J. Chem. Theory Comput.* **2017**, *13*, 4907−4913.

(23) Perdew, J. P.; Burke, K.; Ernzerhof, M. Generalized Gradient Approximation Made Simple. *Phys. Rev. Lett.* **1996**, *77*, 3865−3868.

(24) Tao, J.; Perdew, J. P.; Staroverov, V. N.; Scuseria, G. E. Climbing the Density Functional Ladder: Nonempirical Meta-Generalized Gradient Approximation Designed for Molecules and Solids. *Phys. Rev. Lett.* **2003**, *91*, 146401.

(25) Fajín, J. L.; Viñes, F.; Cordeiro, N. D. S.; Illas, F.; Gomes, J. R. B. Effect of the Exchange-Correlation Potential on the Transferability of Brønsted-Evans-Polanyi Relationships in Heterogeneous Catalysis. *J. Chem. Theory Comput.* **2016**, *12*, 2121−2126.

(26) Sun, J.; Xiao, B.; Fang, Y.; Haunschild, R.; Hao, P.; Ruzsinszky, A.; Csonka, G. I.; Scuseria, G. E.; Perdew, J. P. Density Functionals that Recognize Covalent, Metallic, and Weak Bonds. *Phys. Rev. Lett.* **2013**, *111*, 106401.

(27) Sun, J.; Remsing, R. C.; Zhang, Y.; Sun, Z.; Ruzsinszky, A.; Peng, H.; Yang, Z.; Paul, A.; Waghmare, U.; Wu, X.; Klein, M. L.; Perdew, J. P. Accurate First-Principles Structures and Energies of Diversely Bonded Systems from an Efficient Density Functional. *Nat. Chem.* **2016**, *8*, 831−836.

(28) Vosko, S. H.; Wilk, L.; Nusair, M. Accurate Spin-Dependent Electron Liquid Correlation Energies for Local Spin Density Calculations: A Critical Analysis. *Can. J. Phys.* **1980**, *58*, 1200.

(29) Zhuang, H.; Tkalych, A. J.; Carter, E. Surface Energy as a Descriptor of Catalytic Activity. *J. Phys. Chem. C* **2016**, *120*, 23698.

(30) Mills, K. C.; Su, Y. C. Review of Surface Tension Data for Metallic Elements and Alloys: Part 1 − Pure Metals. *Int. Mater. Rev.* **2006**, *51*, 329.

(31) Michaelson, H. B. The Work Function of the Elements and its Periodicity. *J. Appl. Phys.* **1977**, *48*, 4729.

(32) Wulff, G. Zur Frage der Geschwindigkeit des Wachstums und der Auflösung von Krystallflächen. *Z. Kristallogr. - Cryst. Mater.* **1901**, *34*, 449.

(33) Viñes, F.; Gomes, J. R. B.; Illas, F. Understanding the Reactivity of Metallic Nanoparticles: Beyond the Extended Surface Model for Catalysis. *Chem. Soc. Rev.* **2014**, *43*, 4922−4939.

(34) Kresse, G.; Furthmüller, J. Efficiency of Ab-Initio Total Energy Calculations for Metals and Semiconductors Using a Plane-Wave Basis Set. *Comput. Mater. Sci.* **1996**, *6*, 15.

(35) Perdew, J. P.; Ruzsinszky, A.; Csonka, G. I.; Vydrov, O. A.; Scuseria, G. E.; Constantin, L. A.; Zhou, X.; Burke, K. Restoring the Density-Gradient Expansion for Exchange in Solids and Surfaces. *Phys. Rev. Lett.* **2008**, *100*, 136406.

(36) Hammer, B.; Hansen, L. B.; Nørskov, J. K. Improved Adsorption Energetics within Density-Functional Theory Using Revised Perdew-Burke-Ernzerhof Functionals. *Phys. Rev. B: Condens. Matter Mater. Phys.* **1999**, *59*, 7413.

(37) Blöchl, P. E. Projector Augmented-Wave Method. *Phys. Rev. B: Condens. Matter Mater. Phys.* **1994**, *50*, 17953.

DOI: 10.1021/acs.jctc.7b01047
J. Chem. Theory Comput. 2018, 14, 395−403

(38) Blöchl, P. E.; Jepsen, O.; Andersen, O. K. Improved Tetrahedron Method for Brillouin-Zone Integrations. *Phys. Rev. B: Condens. Matter Mater. Phys.* **1994**, *49*, 16223.
(39) Monkhorst, H. J.; Pack, J. D. Special Points for Brillouin-Zone Integrations. *Phys. Rev. B* **1976**, *13*, 5188.
(40) Momma, K.; Izumi, F. VESTA 3 for Three-dimensional Visualization of Crystal, Volumetric and Morphology Data. *J. Appl. Crystallogr.* **2011**, *44*, 1272.
(41) Kaminsky, W. From CIF to Virtual Morphology Using the WinXMorph Program. *J. Appl. Crystallogr.* **2007**, *40*, 382.
(42) Ruvireta, J.; Vega, L.; Viñes, F. Cohesion and Coordination Effects on Transition Metal Surface Energies. *Surf. Sci.* **2017**, *664*, 45−49.
(43) Comsa, G.; Gelberg, A.; Iosifescu, B. Temperature Dependence of the Work Function of Metals (Mo,Ni). *Phys. Rev.* **1961**, *122*, 1091.
(44) Kiejna, A.; Wojciechowski, K. F.; Zebrowksi, J. The Temperature Dependence of Metal Work Functions. *J. Phys. F: Met. Phys.* **1979**, *9*, 1361−1366.
(45) Curtiss, L. A.; Raghavachari, K.; Trucks, G. W.; Pople, J. A. Gaussian-2 Theory for Molecular Energies of First- and Second-row Compound. *J. Chem. Phys.* **1991**, *94*, 7221.
(46) Patra, A.; Bates, J. E.; Sun, J.; Perdew, J. P. Properties of Real Metallic Surfaces: Effects of Density Functional Semilocality and van der Waals Nonlocality. *Proc. Natl. Acad. Sci. U. S. A.* **2017**, *114*, E9188−E9196.
(47) Sun, J.; Ruzsinszky, A.; Perdew, J. P. Strongly Constrained and Appropriately Normed Semilocal Density Functional. *Phys. Rev. Lett.* **2015**, *115*, 036402.
(48) Peng, H.; Yang, Z. H.; Perdew, J. P.; Sun, J. Versatile van der Waals Density Functional Based on a Meta-Generalized Gradient Approximation. *Phys. Rev. X* **2016**, *6*, 041005.

DOI: 10.1021/acs.jctc.7b01047
J. Chem. Theory Comput. 2018, 14, 395−403

4.4 ROBUSTNESS OF SURFACE ACTIVITY ELECTRONIC STRUCTURE-BASED DESCRIPTORS OF TRANSITION METALS

4.4.1 Summary

Introduction Electronic structure-based descriptors play a key role in material design for many scientific fields. Descriptors are useful to predict material properties, once the relation between them are known, In the most recent studies descriptors are widely used to nurture machine learning algorithms in machine learning tools to predict materials properties. Thus, one way or other descriptors may allow a simple scanning over different materials avoiding the property measure.[44] In our study of TM surfaces outlined in the following, the specific electronic descriptors are the *d*-band centre (ε_d), the width corrected *d*-band centre (ε_d^W) and the highest point of the imaginary part of the Hilbert transform (ε_u) of the *d*-projected DOS (*d*-PDOS), and the materials are the TM surfaces (see Figure 4.8). However, our goal is not to calculate the descriptors and correlate them with a property, but to evaluate how dependent are these descriptors on *xc* functionals. The considered functionals are, as in the previous chapter, the VWN, PBE, PBEsol, RPBE, and TPSS. In addition, the optimized surfaces from our work presented in the previous section are reemployed as the systems under study. Earlier, the author's group performed a similar study, where the TM bulks where analysed by four functionals VWN, TPSS, Heyd-Scuseria-Ernzerhof (HSE06) and PBE as reference.[40] They observed a very good transferability of all the electronic structure-based descriptors for the TMs bulk through the functionals under scrutiny, except for hybrid functional by HSE06 for ε_d and ε_u descriptors showing somewhat larger deviations.

The contribution of the author in this study is the calculation of all the electronic descriptors for the different surfaces and functionals. Also, all the analysis of the obtained results was performed by the author. The python

program used to calculate the descriptors was developed by the MSc. Biel Martínez.

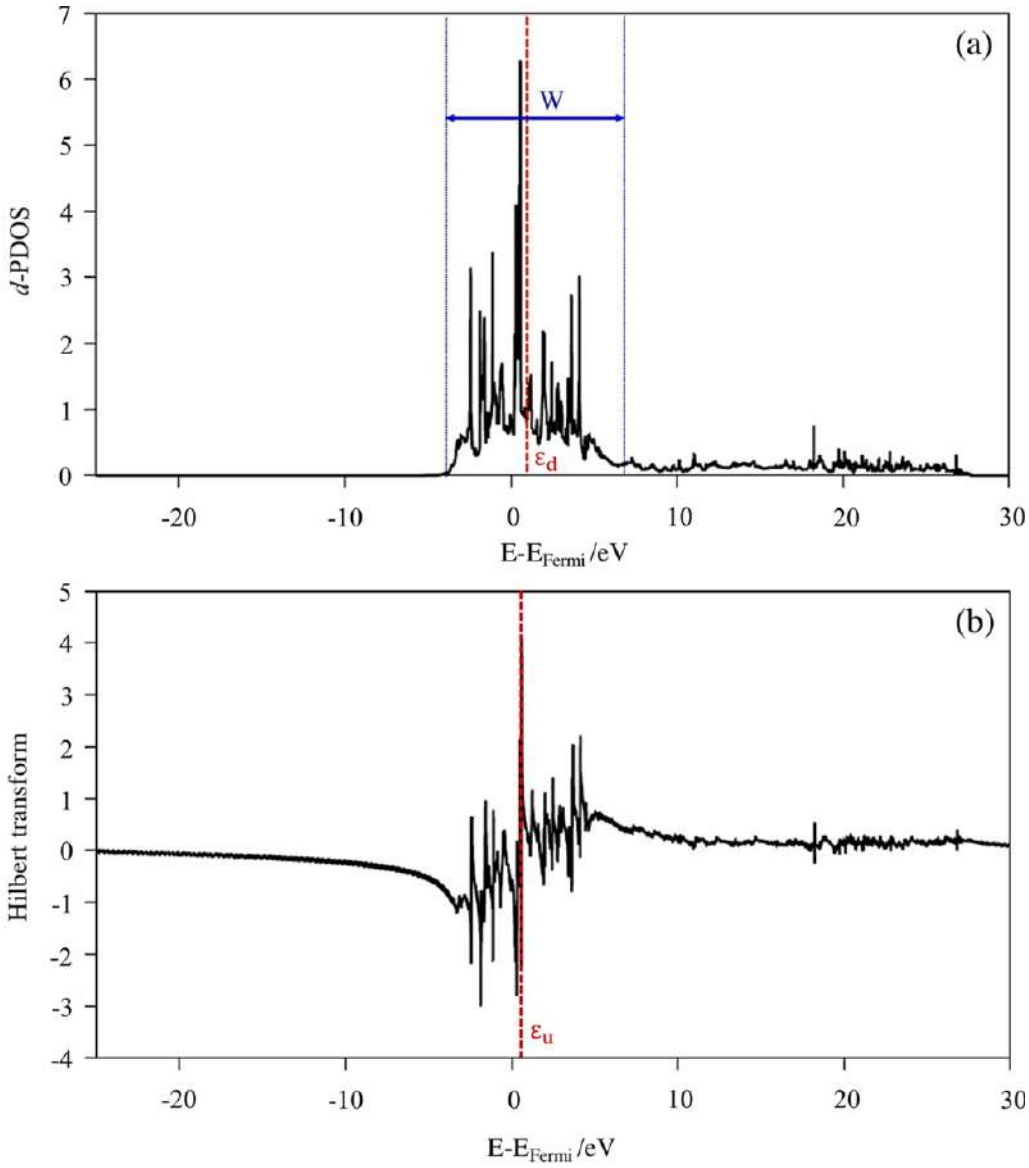

Figure 4.8 (a) Representation of *d*-PDOS, with the band width, W, in blue, and the d-band centre, ε_d, in red. (b) Representation of the imaginary part of Hilbert transform of the previous *d*-PDOS with the highest peak, ε_u, marked in red. The shown case corresponds to Nb (001) surface as calculated using PBE functional.

Results The ε_X descriptors calculated for the TMs surfaces are not observables. For this reason, the transferability of values among the functionals is analysed using a set of reference values. In this case, the reference set is that obtained by PBE functional, as it was found previously to be in general the most accurate for describing TM surface and bulk properties. The main results (further details and data are given in the publication shown at the end and Appendix B) are that for ε_d there is an excellent agreement between the different functionals, for the ε_d^W still a very good agreement is found but with slightly larger intercepts and TPSS functional showing quite large deviation. The largest deviations were found between the different functionals studied for the ε_u descriptor, see Figure 4.9 left panel.

Another aspect to investigate was, to what extent the descriptor transferability is affected by the structure relaxation using each functional. To evaluate this, the PBE optimized structures were employed to calculate the reference electronic descriptors values for all the functionals. It is shown that subtle differences in the surface relaxation explain part of the ε_d and ε_d^W dependence on the *xc* functional. For the ε_u the use of the fixed PBE optimized structures only the R coefficient and intercept improved slightly in some cases (see Figure 4.9 right panel). Overall, the descriptors transferability through the *xc* functionals remains [40] as $\varepsilon_d > \varepsilon_d^W \gg \varepsilon_u$.

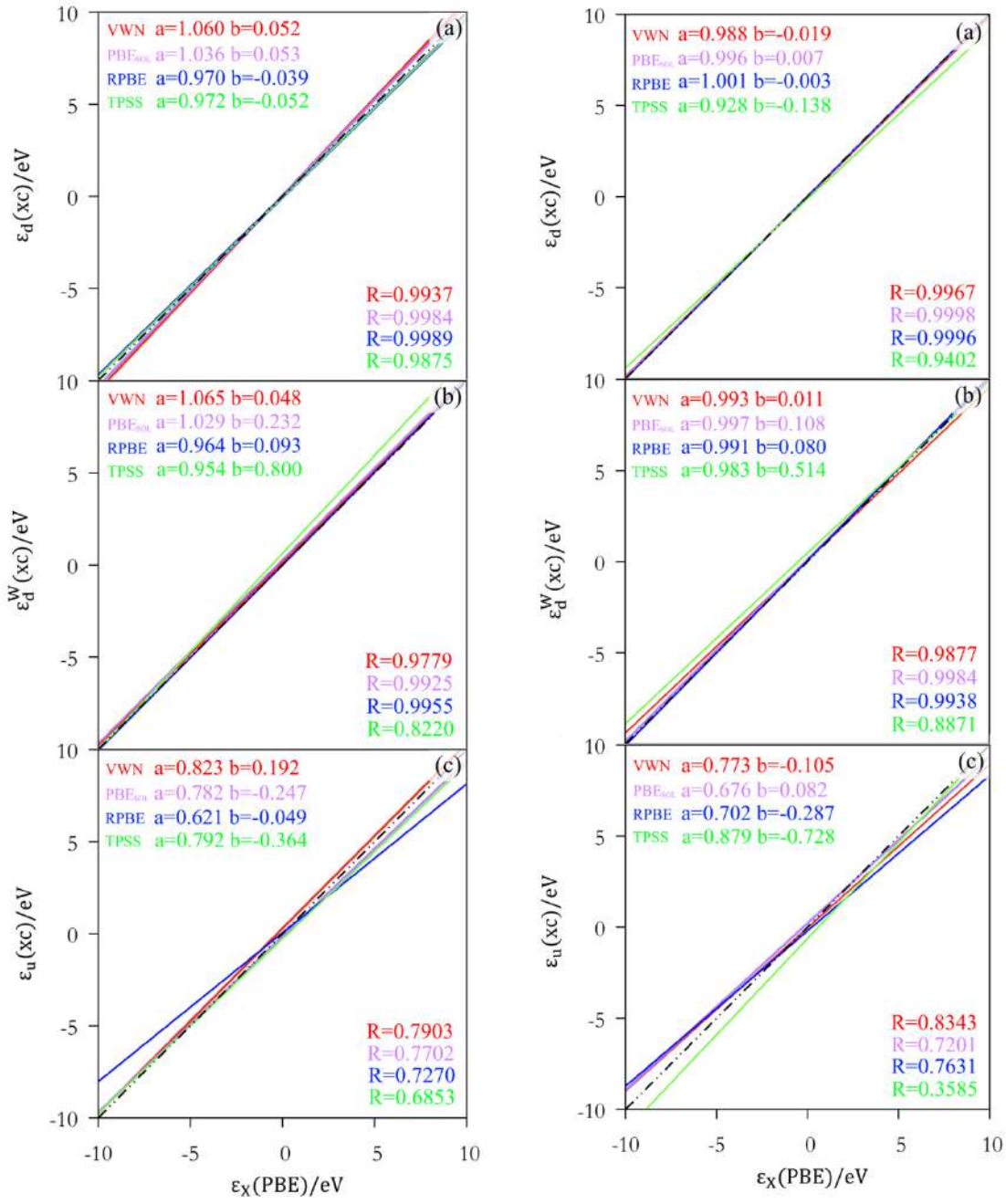

Figure 4.9 Variation of the (a) *d*-band centre, ε_d, (b) width-corrected *d*-band centre, ε_d^W , and (c) highest Hilbert transform peak, ε_u, energy values, all given in eV, calculated using different xc functionals with respect to those obtained at the PBE level (on the left panel) and those obtained at the PBE level with the structure obtained with PBE (on right panel). Dashed black line represents ideal matching with respect to PBE values. The linear regression applied follows the equation ε_X, =a $\cdot\varepsilon_d^{PBE}$+b, where ε_X can be ε_d, ε_d^W, or ε_u, and R is the regression coefficient.

Finally, the relation between the electronic descriptors and such structural descriptor as the surface Coordination Number (CN) was studied. The hypothesis was that a more compact surface, e.g., with a CN of atoms closer to the bulk CN, would have more similar ε_d than other surfaces less compact surfaces with lower CN of atoms. This was confirmed for TMs with *hcp* and *bcc* structures, although the (001) and (111) *bcc* surfaces with CN=4 provide quite different trends. But for *fcc* structure, the surface (011) with CN=7 is characterized by ε_d values more similar to that of the bulk than the surfaces (001) CN=8 and (111) CN=9. To rationalize this unexpected behaviour, we studied the emergence of surface states. For that the absolute difference between bulk and surface *d*-PDOS was integrated (see Figure 4.10). From it we observed that 27.8% of the *hcp* cases exhibit intense surface states, whereas they are majority states (61.9%) for *bcc* and (83.3%) for *fcc* TM surfaces. This can explain the disagreement of the CN of the surfaces and the bulk-similarity of the ε_d regressions for *bcc* and *fcc* metals.

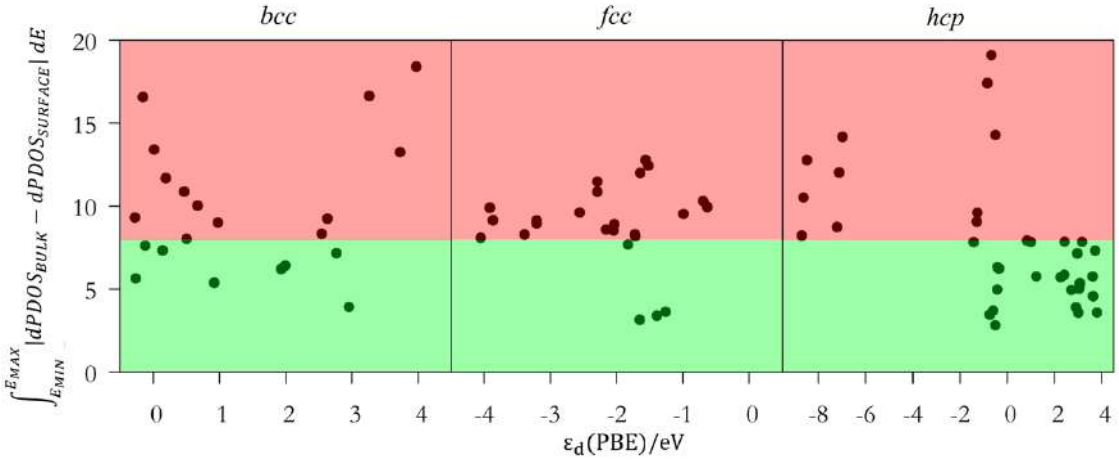

Figure 4.10 Representation of the integral values of the absolute difference between the bulk and surface *d*-PDOS in front of the ε_d, all data obtained at PBE level. The considered highest integral cases are in the red part and the rest in the green part.

Conclusions The following conclusions are drawn from the results presented in this section:

- The transferability of the surface TM descriptors through the studied *xc* functionals is worse than that for the bulk descriptors.
- The surface descriptors transferability decreases from being excellent for $\varepsilon_d$as follows: $\varepsilon_d > \varepsilon_d^W \gg \varepsilon_u$.
- The different surface relaxation plays a minor role in the variability of the descriptors values of each *xc* functional.
- There is a relation between the CN of TM surface atoms and the ε_d. Surfaces with the CN close to that of the bulk exhibit ε_d values similar to the bulk ones, unless the surface states play an important role, as found for *fcc* structures.

PCCP

PAPER

View Article Online
View Journal | View Issue

Cite this: *Phys. Chem. Chem. Phys.*, 2018, **20**, 20548

Robustness of surface activity electronic structure-based descriptors of transition metals†

Lorena Vega, Biel Martínez, Francesc Viñes * and Francesc Illas

Efficient yet simple electronic structure-based descriptors of transition metal surfaces are key in material design for many scientific fields in research and technology. Density functional theory-based methods provide the framework to systematically explore the performance and transferability of such descriptors. Using appropriate surface models and the Vosko–Wilk–Nussair (VWN), Perdew–Burke–Ernzerhof (PBE), PBE adapted for solids (PBE_{sol}), revised PBE (RPBE), and Tao–Perdew–Staroverov–Scuseria (TPSS) exchange–correlation functionals, we study the transferability of three descriptors: the d-band centre, the width-corrected d-band centre, and the Hilbert transform highest peak, among the low-index Miller surfaces for the metals of transition elements. We show that the d-band centre and the width-corrected d-band centre descriptors are almost independent of the functional used whereas a dependency is seen in the Hilbert transform highest peak. Moreover, it is seen that the differences between the surface descriptor values and predictions from the bulk ones are affected by the presence of surface states. Interestingly, a direct relation between the surface coordination number and the d-band centre electronic descriptor is found when surface states are absent.

Received 26th May 2018,
Accepted 20th July 2018

DOI: 10.1039/c8cp03356k

rsc.li/pccp

Introduction

The metals of transition elements, hereafter named transition metals (TMs), are intensively used in many fields of applied chemistry and materials science, *e.g.* nanotechnology,[1] gas sensing,[2] green chemistry,[3] and heterogeneous catalysis,[4] to name a few. These materials are used either as pure metals, alloys,[5] or also bimetallic nanoparticles.[6] The performance of the TMs in different applications is closely correlated to their surface chemistry and often interlinked with electronic structure-based descriptors. These descriptors have arisen as a powerful tool to predict material properties. Knowing the relation between these descriptors and targeted material properties allows for rapid quantitative screening over a large set of materials based on such validated descriptors saving the effort of actually measuring the desired property, *e.g.* the adsorption energy of a molecule on the family of TMs can be screened easily without actually carrying out calorimetric experiments. Thus, from an economical point of view, the prediction will be less expensive than either testing or simulating the systems themselves.

For TM systems, useful and broadly used descriptors such 'as the d-band centre, ε_d,[7] obtained from the d-contribution of a surface atom to the projected density of states (this is, the surface first-layer atom d-projected density of states, d-PDOS), have been successfully employed in understanding the surface chemistry, physics, and related processes of these TMs,[8] and also in the computational design of novel solid catalysts.[9] The d-band centre is simply defined as the d-band DOS gravimetric centre of a surface atom, as in eqn (1),

$$\varepsilon_d = \frac{\int_{E_i}^{E_f} (E - E_{Fermi}) \cdot \mathrm{dPDOS}}{\int_{E_i}^{E_f} \mathrm{dPDOS}} \quad (1)$$

where the E_i limit is the d-band onset and E_f is considered to be the energy point where the d-PDOS integral would belong to a d^{10} electronic configuration. Other improved d-band based descriptors have been proposed in recent times, such as the width corrected d-band centre, ε_d^W,[10] calculated as in eqn (2) by adding half of the band width, W, taken as $E_f - E_i$ (see Fig. 1) to the value obtained from eqn (1).

$$\varepsilon_d^W = \varepsilon_d + \frac{W}{2} \quad (2)$$

Finally, the highest point of the Hilbert transform applied to the d-PDOS, ε_u,[11] has been proposed as a novel and, in principle, more accurate electronic structure-based descriptor, especially when compared to ε_d. These descriptors are not physical observables although they are easily reachable by means of first principles calculations, those based on density functional theory (DFT) being the common choice. The practical easiness of DFT, as well as the agreement of its trends with

Departament de Ciència de Materials i Química Física, Institut de Química Teórica i Computacional (IQTCUB), Universitat de Barcelona, c/Martí i Franquès 1, 08028 Barcelona, Spain. E-mail: francesc.vines@ub.edu

† Electronic supplementary information (ESI) available. See DOI: 10.1039/c8cp03356k

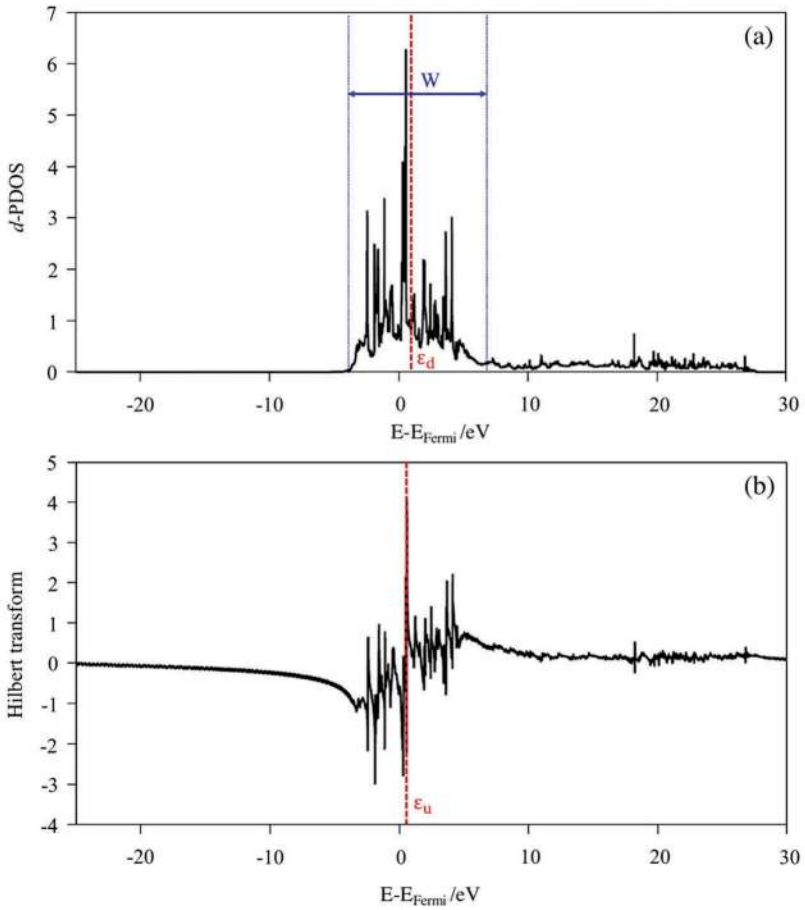

Fig. 1 Textbook (a) representation of d-PDOS, with the band width, W, in blue, and the d-band centre, ε_d, in red. (b) Representation of the imaginary part of the Hilbert transform of the previous d-PDOS with the highest peak, ε_u, marked in red. The shown case belongs to the Nb(001) surface as calculated at the PBE level.

physicochemical properties,[7–11] make the above commented parameters suited to be considered chemical descriptors. A recent study[12] across the 3d, 4d, and 5d bulk TMs thoroughly evaluated whether the value of such descriptors, hereafter globally renamed ε_X (*i.e.* ε_d, ε_d^W, and ε_u), depends on the choice of the DFT method, revealing that the numerical value of the descriptor was generally rather independent. Note, however, that this conclusion holds for functionals belonging to the so-called Local Density Approximation (LDA), Generalized Gradient Aproximation (GGA), or meta-GGA families of functionals, in increasing order of both complexity and accuracy (see below). Hybrid functionals usually provide better results for the thermochemistry of gas phase molecules of main group elements. However, they were here excluded since in a previous study it was found that they fail in describing the electronic delocalization of metallic systems, causing concomitant wrong deviations in the electronic structure. Nevertheless, in spite of the apparent reported transferability of DFT based descriptors for bulk models, the unavoidable emerging question mark is whether this excellent transferability holds true when applied to TM surfaces. To answer this question, we evaluate here by DFT means the transferability of various commonly used exchange and correlation (xc) functionals on a set of 81 TM surfaces. Such a thorough study will determine whether the prediction of trends of TM physicochemical properties by means of electronic structure-based descriptors is a solid matter or is biased by the employed DFT functional, or even by the selected electronic descriptor.

Computational details

27 TMs are here studied (hexagonal close-packed (hcp) Sc, Y, Ti, Zr, Hf, Tc, Re, Ru, Os, Co, Zn, and Cd; face-centred cubic (fcc) Rh, Ir, Ni, Pd, Pt, Cu, Ag, and Au; and finally V, Nb, Ta, Cr, Mo, W, and Fe, being body-centred cubic (bcc) TMs). For these metals, different low-index Miller surfaces, thus featuring in principle their most stable surfaces, have been considered. Specifically, these are the (001), (011), and (111) surfaces for fcc and bcc structures, and (0001), (10$\bar{1}$0), and (11$\bar{2}$0) ones for hcp structures, following Miller-Bravais indices in the latter case. A total of 81 distinct TM surfaces have been studied.

DFT based periodic calculations employing the Vienna ab initio simulation package (VASP)[13] have been carried out for six-atomic layer slab models. A cutoff energy of the plane-wave basis set of 415 eV is used in a periodic cell containing

10 Å of vacuum along the surface direction. The reciprocal space has been sampled using a *k*-point Monkhorst–Pack[14] mesh of 7×7×1 dimensions for surfaces. The projector augmented wave[15] method is used to describe the interaction of core electrons with valence density. Surface structures previously optimized with each of the considered DFT xc functionals are employed, with further details of these described in the literature. Thus, these structures are used to obtain the required DOS for the calculation of the descriptors.[16]

The ε_X descriptors have been obtained for five different xc functionals, chosen in concordance with previous systematic studies for the bulk and surfaces of the considered TMs.[16–18] Explicitly, within the local density approximation (LDA) we used Vosko–Wilk–Nussair xc (VWN);[19] from the generalized gradient approximation (GGA) Perdew–Burke–Ernzerhof (PBE) was chosen,[20] and last but not least, from the meta-GGA family, Tao–Perdew–Staroverov–Scuseria (TPSS) was selected.[21] PBE is considered one of the most accurate functionals for the description of bulk TMs and TM surfaces in general average terms.[16–18] Nevertheless, revised PBE (RPBE),[22] claimed to better describe adsorption energies, and PBE adapted for solids (PBE_{sol}),[23] posed as a better functional for bulk materials, were contemplated as well. Note that the usage of periodic boundary condition constraints, as happens here, tends to imply integration and projection of the DOS on given defined atomic radii, and, therefore, may not fully sample all the system band space. However, as we deal here with differences of d-PDOS and trends, such inaccuracies must cancel each other, and can be disregarded in the forthcoming discussion.

Results and discussion

As already commented, for the density functionals mentioned above the numerical values of the ε_X descriptors extracted from bulk models were found to be almost independent of the choice of the DFT method in a previous study,[12] given the close values they obtained of linear regression slopes and intercepts for VWN and TPSS xc with respect the PBE values for all ε_X. The exception to this rule was found for the Heyd–Scuseria–Ernzerhof (HSE06) hybrid functional,[24] which presented a larger deviation of slopes and intercepts for ε_d and ε_u (see Table 1). Here, this issue was addressed for the same ε_X descriptors but for values derived from the surface models, in this case (001), (011) and (111) surfaces for bcc and fcc TMs, and (0001), $(10\bar{1}0)$, and $(11\bar{2}0)$ surfaces for hcp structures. This is an important remaining question since one may wish to combine surface (electronic) descriptors as obtained using different DFT methods for practical applications. Then, the robustness of these methods for calculating the surface electronic descriptors is relevant in order to correctly describe the surface TM trends in chemical or catalytic activities and other related properties, independently of the employed functional. Since the ε_X descriptors are not observables, the comparison necessarily involves calculated values to be contrasted with one of the set taken as a reference. Here, the assessment of the descriptors as predicted by different DFT xc methods is carried out taking the PBE values as a reference. This is justified since, among the DFT functionals explored, PBE was found to be one of the most accurate in describing experimental observables for the whole set of TMs including bulk and surface properties.[16,18] It was indicated as the most accurate by adding all the mean absolute error percentages obtained for each property under inspection, including bulk interatomic distances, bulk moduli, and cohesive energies for bulk properties, and surfaces energies, work functions, and interlayer distances for surface properties.

Table 1 Linear regression parameters of the ε_X descriptors for the bulk values obtained in ref. 12 by VWN, TPSS and HSE06, a hybrid xc functional. The slope is *a*, the intercept *b*, and *R* the linear regression coefficient

ε_X	xc	*a*	*b*	*R*
ε_d	VWN	1.10	0.03	0.9994
	TPSS	1.03	−0.03	0.9977
	HSE06	1.11	−0.43	0.9921
ε_d^W	VWN	1.02	−0.06	0.9977
	TPSS	1.01	−0.04	0.9932
	HSE06	1.01	0.07	0.9792
ε_u	VWN	0.99	−0.01	0.9998
	TPSS	1.03	0.00	0.9994
	HSE06	1.22	−0.02	0.9934

Fig. 2 reports the plots of ε_X values obtained with each functional, contained in Tables S1–S3 of the ESI,† against the reference, PBE ones. It evidences that there is excellent agreement between the different xc functionals for ε_d, following the previously observed trends for this descriptor in bulk models (see Table 1). Slopes are close to unity, and intercepts below 0.06 eV, with regression coefficient values larger than 0.98. Consequently, all the inspected functionals provide very similar d-band centre descriptors, and, therefore, they describe the very same electronic structure situation, as evaluated through the d-PDOS. For the ε_d^W descriptor, in concordance, excellent agreement is found as well, with slopes again near unity, although with slightly larger intercepts, yet all below 0.23 eV, and a faint reduction of *R* values being still above 0.97. A larger deviation is found for TPSS, with an intercept value of 0.80 eV and a regression coefficient below 0.83. Here, these results differ from the bulk ones, see Table 1, where the obtained intercepts are lower than 0.08, see *e.g.* the bulk TPSS case where the intercept is −0.04, close to 0, whereas for surfaces the intercept increases to near 1. Clearly, despite the fact that the d-band centre is equally described by the different functionals, the d-band width is slightly more sensitive to the DFT method employed, providing then these larger differences in regression slope and intercept values. In the case of ε_u there are significant deviations of the obtained descriptor values when studied using different functionals, although there is maybe fortuitous good agreement between PBE_{sol} and TPSS. Notice that, despite that intercepts can be very small, 0.05 eV for RPBE, with both the slope and *R* below 0.73, apparently, the Hilbert transform based descriptor largely depends on the particular d-PDOS gradients. Consequently, subtle changes originated by a given

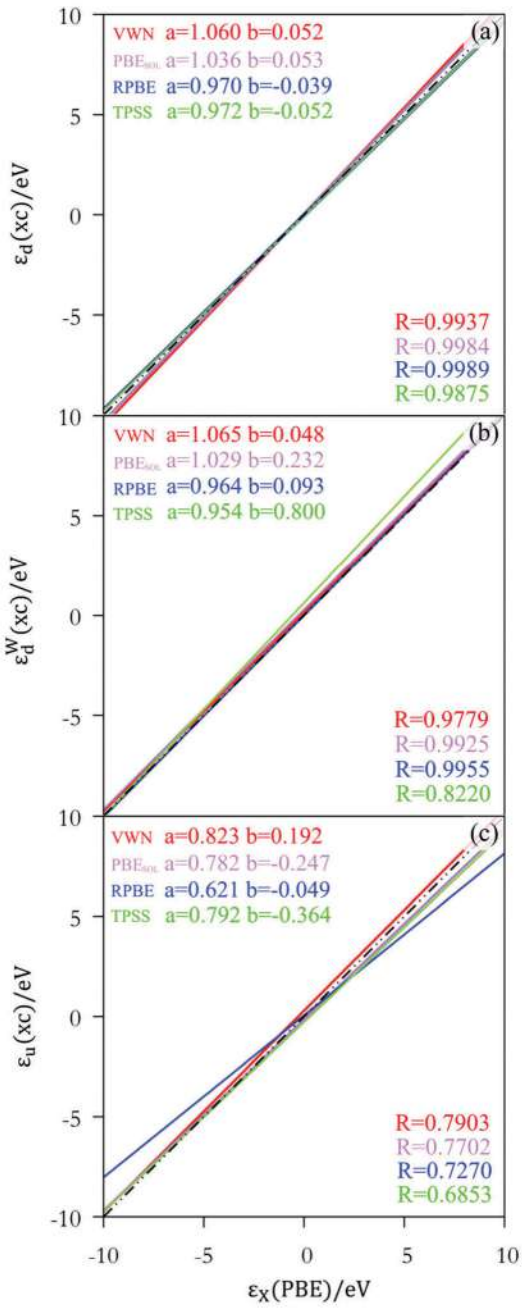

Fig. 2 Variation of the (a) d-band centre, ε_d, (b) width-corrected d-band centre, ε_d^W, and (c) highest Hilbert transform peak, ε_u, energy values, all given in eV, calculated using different xc functionals with respect to those obtained at the PBE level. The dashed black line represents ideal matching with respect to PBE values. Coloured solid lines belong to regressions of xc values, whose slopes *a*, intercepts *b*, and regression coefficients, *R*, are displayed. The linear regression applied follows the equation $\varepsilon_X = a{\cdot}\varepsilon_X^{PBE} + b$, where ε_X can be ε_d, ε_d^W, or ε_u.

functional, that do not affect the d-band gravimetric centre, do affect the ε_u descriptor. Again, comparing with the ε_u bulk results, see Table 1, the linear regression coefficients on surface models get worse, but not only due to larger intercepts as happened in ε_d^W, but also because the slopes are far from unity and the *R* values range between 0.68 and 0.79. In light of these results, the transferability among descriptors obtained using the above commented xc functionals decreases as $\varepsilon_d > \varepsilon_d^W \gg \varepsilon_u$, ε_d being the safest one to use when mixing results obtained at different DFT levels for TM surfaces.

Another point to inspect is whether the descriptor transferability is biased by a variation in the structural relaxation predicted by the different functionals. A different computed slab relaxation could affect the electronic structure of a surface atom whose d-PDOS is under scrutiny, thus modifying the derived ε_X values. To evaluate this possibility the PBE optimized structures were taken as fixed and the electronic part calculated with the different functionals. The list of values is encompassed in Tables S4–S6 of the ESI.† The comparison with respect to self-consistent PBE ε_X values is shown in Fig. 3. Except for the TPSS ε_d case, all ε_d and ε_d^W values are closer to the PBE reference, with slopes nearer to unity, intercepts closer to zero, and regression coefficients slightly increased. The results show that subtle differences in the surface relaxation for each xc functional are behind the ε_d and ε_d^W dependence with the DFT xc functional. However, ε_u did improve only in some cases. The VWN ε_u regression features a worse slope but a better intercept and *R*, and PBE_{sol} regression improves only its intercept, while TPSS regression improves the slope. In the case of RPBE regression, there is a slight improvement in *R* and in the slope, although the intercept deviates significantly from zero. Then, also here, the transferability among descriptors using PBE optimized geometries remains as $\varepsilon_d > \varepsilon_d^W \gg \varepsilon_u$.

A further aspect of interest, beyond the variation of the surface electronic structure descriptor calculations caused by structure relaxations, is the relation between electronic descriptors like the here studied and structural descriptors such as the coordination number (CN, here understood as the number of nearest neighbours to the atom of interest within the solid-state structure of the metal). Apart from previous relationships which show that electronic and structural types of descriptors seem to be inseparable factors of the TM surface chemical activity,[25] one would expect that an atom at the surface with a CN closer to the bulk CN than other contemplated surfaces would display a more similar ε_d. Here ε_d is taken as the representative electronic descriptor due to the independency found of its values with respect to the functionals under scrutiny. This hypothesis is confirmed for TMs with hcp and bcc structures in Fig. 4 with the plot of ε_d with respect to CN, where CN values were taken from the literature.[26] For these TM surfaces, the intercepts are close to zero and slopes are closer to the bulk regression slopes as the bulk CN is closer to the CN of the surface. However, for the (001) and (111) surfaces of bcc metals, their regressions differ despite that they have the same CN. For fcc, the (011) surface, with CN = 7, ε_d results are more similar to the bulk (CN = 12) than to (001) and (111), with CN = 8 and CN = 9, respectively.

This different behaviour can be due to variations between the electronic band structure of the bulk and surfaces caused by the emergence of surface states. The effect of different

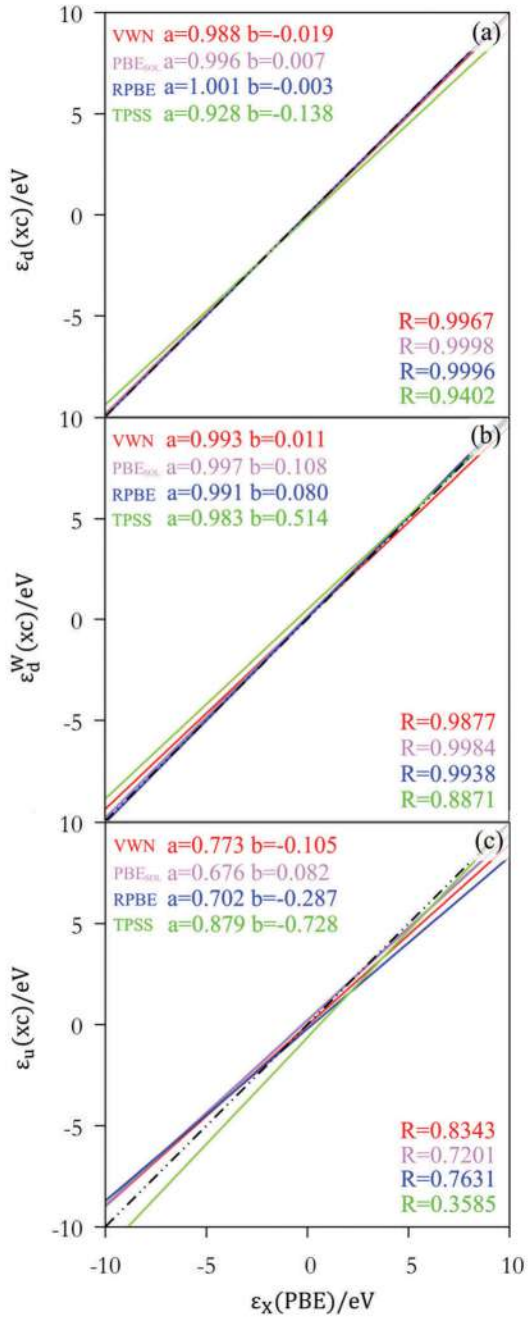

Fig. 3 Variation of the (a) d-band centre, ε_d, (b) width-corrected d-band centre, ε_d^W, and (c) highest Hilbert transform peak, ε_u, energy values, all given in eV, calculated using different xc functionals with respect to those obtained at the PBE level with the structure obtained with PBE. The dashed black line represents ideal matching with respect to PBE values. Coloured solid lines belong to regressions of xc values, whose slopes a, intercepts b, and regression coefficients, R, are displayed. The linear regression applied follows the equation $\varepsilon_X = a \cdot \varepsilon_X^{PBE} + b$, where ε_X can be ε_d, ε_d^W, or ε_u.

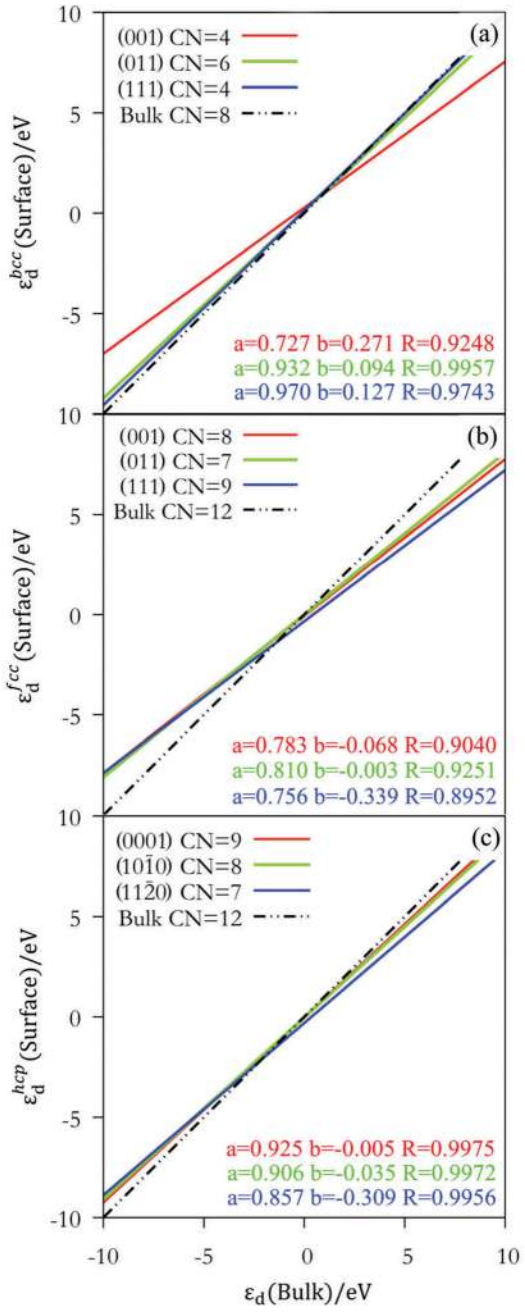

Fig. 4 Comparison between the PBE d-band centre, ε_d, obtained for the bulk and the different surfaces for each structure (a) bcc, (b) fcc and (c) hcp. The linear regression applied follows the equation ε_d(surface) = $a \cdot \varepsilon_d$(bulk) + b.

structural optimization is discarded since calculations for bulk truncated frozen surfaces display the same trends. So, here, comparing bulk and surface results, the trend seems to be induced by a difference between the electronic structures of the systems. In order to quantify the effect of surface states, the absolute difference between the bulk and surface d-PDOS was integrated, see Fig. 5. With this one finds that only 27.8% of the hcp cases exhibit intense surface states above 8 eV^{-1}, whereas this becomes the majority (61.9%) for bcc and (83.3%) for fcc TM surfaces. Clearly, the presence of surface states dominates the d-PDOS of fcc metals and explains the above commented disagreement between the CN of the surfaces and the bulk-similarity of the ε_d regressions for bcc and fcc cases.

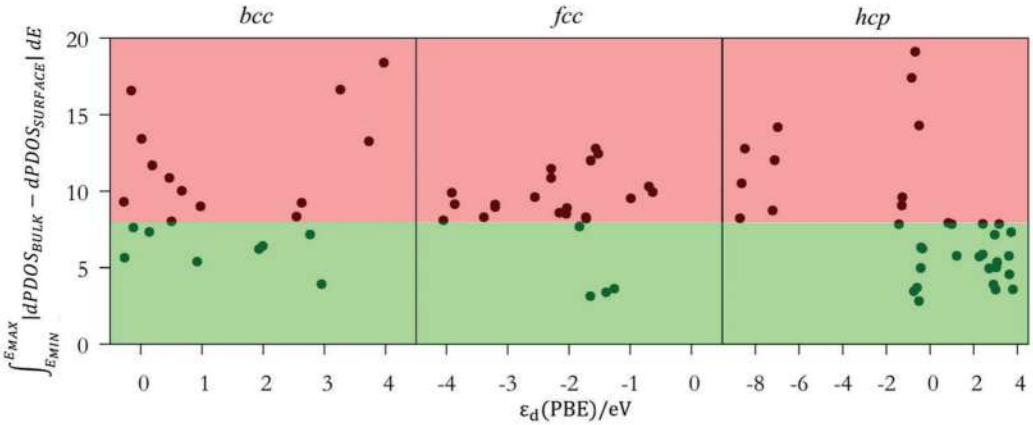

Fig. 5 Representation of the integral values of the absolute difference between the bulk and surface d-PDOS against ε_d, all data obtained at the PBE level. The considered highest integral cases are in the red part and the rest in the green part.

Conclusions

To conclude, we have found that the influence of the exchange–correlation functional used to estimate electronic descriptors of TM surfaces differs from that observed for descriptors extracted from bulk models.[12] The transferability of surface derived descriptors is worse for all functionals explored and, in addition, the transferability decreases among the descriptors as $\varepsilon_d > \varepsilon_d^W \gg \varepsilon_u$. Differences are found regarding what was reported for bulk derived descriptors, where good transferability was always observed. Even so, transferability in the surface structures remains excellent for ε_d. Whereas the differences in the descriptor values for each xc functional have a contribution from the different description of the geometry, the different behaviour of each surface and bulk derived descriptor stems mostly from the electronic part, and the different surface relaxation predicted by different DFT methods plays a minor role. The present results also highlight the relationship between electronic descriptors such as ε_d and structural descriptors such as the CN. Structures with similar CN have similar ε_d values and those with the CN closer to the bulk display also closer to bulk ε_d values, unless when surface states play an important role, as does happen for fcc TM surfaces.

Conflicts of interest

There are no conflicts to declare.

Acknowledgements

This work was supported by Spanish MINECO/FEDER Grant CTQ2015-64618-R and in part by Generalitat de Catalunya Grants 2014SGR97 and XRQTC and by the NOMAD Center of Excellence Project receiving funding from the European Union Horizon 2020 Research and Innovation Programme, Grant Agreement 676580. F. V. thanks the Spanish MINECO for a Ramoń y Cajal research contract (RYC-2012-10129), F. I. acknowledges additional support through the ICREA Academia Award for Excellence in Research and L. V. thanks Generalitat de Catalunya for a predoctoral grant (B_00384).

Notes and references

1 B. Nikoobakht and M. A. El-Sayed, *Chem. Mater.*, 2003, **15**, 1957.
2 Z. Liu and P. C. Searson, *J. Phys. Chem. B*, 2006, **110**, 4381.
3 M. Favaro, H. Xiao, T. Cheng, W. A. Goddard III, J. Yano and E. J. Crumlin, *Proc. Natl. Acad. Sci. U. S. A.*, 2017, **114**, 6706.
4 J. Greeley, J. K. Nørskov and M. Mavrikakis, *Annu. Rev. Phys. Chem.*, 2002, **53**, 319.
5 P. Mani, R. Srivastava and P. Strasser, *J. Phys. Chem. C*, 2008, **112**, 2770.
6 M. Turner, V. B. Golovko, O. P. H. Vaughan, P. Abdulkin, A. Berenguer-Murcia, M. S. Tikhov, B. F. G. Johnson and R. M. Lambert, *Nature*, 2008, **454**, 981.
7 B. Hammer and J. K. Nørskov, *Surf. Sci.*, 1995, **343**, 211.
8 J. K. Nørskov, T. Bligaard, J. Rossmeisl and C. H. Christensen, *Nat. Chem.*, 2009, **1**, 37.
9 V. R. Stamenkovic, B. S. Mun, M. Arenz, K. J. J. Mayrhofer, C. A. Lucas, G. F. Wang, P. N. Ross and N. M. Markovic, *Nat. Mater.*, 2007, **6**, 241.
10 A. Vojvodic, J. K. Nørskov and F. Abild-Pedersen, *Top. Catal.*, 2014, **57**, 25.
11 H. Xin, A. Vojvodic, J. Voss, J. K. Nørskov and F. Abild-Pedersen, *Phys. Rev. B: Condens. Matter Mater. Phys.*, 2014, **89**, 115114.
12 A. Notario-Estévez, S. M. Kozlov, F. Viñes and F. Illas, *Chem. Commun.*, 2015, **51**, 5602.
13 G. Kresse and J. Furthmüller, *Comput. Mater. Sci.*, 1996, **6**, 15.
14 H. J. Monkhorst and J. D. Pack, *Phys. Rev. B: Solid State*, 1976, **13**, 5188.
15 P. E. Blöchl, *Phys. Rev. B: Condens. Matter Mater. Phys.*, 1994, **50**, 17953.
16 L. Vega, J. Ruvireta, F. Viñes and F. Illas, *J. Chem. Theory Comput.*, 2018, **14**, 395.
17 P. Janthon, S. Lao, S. M. Kozlov, F. Viñes, J. Limtrakul and F. Illas, *J. Chem. Theory Comput.*, 2013, **9**, 1631.
18 P. Janthon, S. Lao, S. M. Kozlov, F. Viñes, J. Limtrakul, D. G. Truhlar and F. Illas, *J. Chem. Theory Comput.*, 2014, **10**, 3832.

19 S. H. Vosko, L. Wilk and M. Nussair, *Can. J. Phys.*, 1980, **58**, 1200.
20 J. P. Perdew, K. Burke and M. Ernzerhof, *Phys. Rev. Lett.*, 1996, **77**, 3865.
21 J. Tao, J. P. Perdew, V. N. Statoverov and G. E. Scuseria, *Phys. Rev. Lett.*, 2003, **91**, 146401.
22 B. Hammer, L. B. Hansen and J. K. Nørskov, *Phys. Rev. B: Condens. Matter Mater. Phys.*, 1999, **59**, 7413.
23 J. P. Perdew, A. Ruzsinszky, G. I. Csonka, O. Vydrov, G. E. Scuseria, L. A. Constantin, X. Zhou and K. Burke, *Phys. Rev. Lett.*, 2008, **100**, 136406.
24 A. V. Krukau, O. A. Vydrov, A. F. Izmaylov and G. E. Scuseria, *J. Chem. Phys.*, 2006, **125**, 224106.
25 F. Calle-Vallejo, J. I. Martínez, J. M. García-Lastra, P. Sautet and D. Loffreda, *Angew. Chem., Int. Ed.*, 2014, **53**, 8316.
26 J. Ruvireta, L. Vega and F. Viñes, *Surf. Sci.*, 2017, **664**, 45.

4.5 GENERALIZED GRADIENT APPROXIMATION ADJUSTED TO TRANSITION METALS PROPERTIES: KEY ROLES OF EXCHANGE AND LOCAL SPIN DENSITY

4.5.1 Summary

Introduction According to the section 4.3 the *xc* functionals PBE and PBEsol show the best overall performance for describing bulk and surface properties of TMs. The difference between these functionals is in the exchange μ and the correlation β parameters. The PBE functional has $\mu = 0.2195$ and $\beta = 0.0667$ and the PBEsol has $\mu = 0.1235$ and $\beta = 0.046$. In the case of PBEsol, the Local Spin Density (LSD) approximation is not preserved because the relation between μ and β does not follow the condition $\mu = \frac{2\pi^2\beta}{3}$. The reason of not choosing the corresponding value of β is to satisfy a fitting of Jellium surface energy TPSS values. Analysis of these data suggests two ways to improve a functional for TMs: to identify the minimum by scanning the 2-dimensional surface error between the PBE and PBEsol μ and β values (hereafter called VV) or to restore the LSD approximation in the PBEsol case (called VVsol). The bulk and surface properties under evaluation are the same as explored in the section 4.3. In the first case, the scanning is done for the bulk properties studied before (δ, E_{coh}, and B_0) and the overall error minimum point is extrapolated to the surface properties to be evaluated, γ, ϕ, and δ_{ij} again. A previous study[45] also attempted to restore the LSD approximation for PBEsol but the tested materials or properties were notably more limited. Furthermore, there are other similar studies of exploring the surface error but modifying the μ and κ (a parameter inside the enhancement factor used to calculate the exchange contribution) parameters and fixing the value of β.

The author contribution was to modify the VASP program to be able of modifying the μ and β values of the PBE-based functionals, to calculate different bulk and surfaces properties for the different functionals and metals, to evaluate the errors comparing with experimental values of the properties, and to analyse the obtained results.

Results For the three different bulk properties (δ, E_{coh}, and B_0), a scan of the MAPE between calculated properties and the available experimental data was done in a mesh of 11×11 points between the μ/ß values of PBE (μ= 0.2195, ß = 0.0667) and PBEsol (μ = 0.1235, ß = 0.046). Each property, obtained by MAPE average of all the 27 TMs studied, has its own different minima point and even each TM has its own minimizing point (in this case the result being the addition of the obtained MAPE of the three properties). Since the employment of different μ/ß values for each particular case is non practical, we obtained the TM MAPE at each point of the mesh from each bulk property across the 27 TMs and then, the property MAPEs added up in order to obtain a general minimum, named VV, which is at (μ = 0.2099, ß = 0.0667) with a total MAPE of 18.77%, slightly less than PBE (20.18%) but moved away from PBEsol (30.40%), see Figure 4.11. With a strict convergence criterion, from 0.02 eV/Å to 0.007 eV/ Å, almost identical MAPE surfaces are obtained concluding than the convergence criterion in this range does not affect the results shown before. From the Figure 4.11, it is seen that the exchange parameter has more influence on the MAPE dispersion than the correlation parameter. This could imply that a correct treatment of the exchange is a key in the development of new *xc* functionals. We note that this statement can be

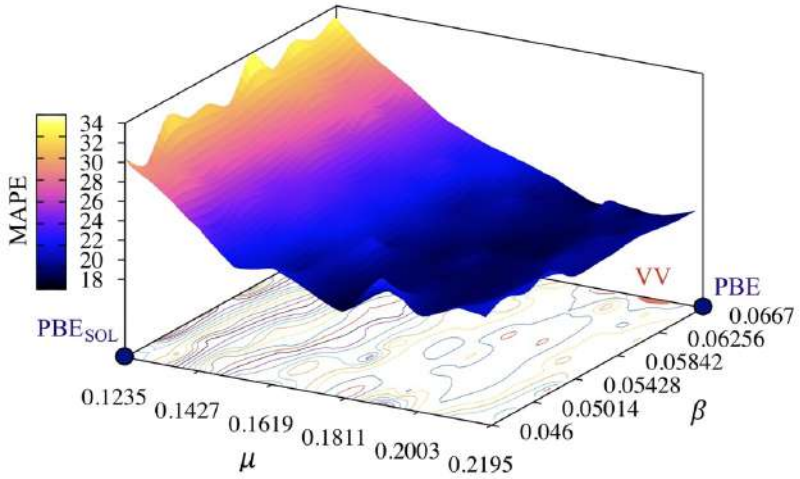

Figure 4.11 Surface variation of the MAPE sum of bulk properties of 27 TMs over the μ/ß space between PBE and PBEsol parameters, plus the orographic projection in the basis. Obtained with a force's criterion on atoms below 0.02 eV/Å.

only ensured for the calculated space of μ/ß. Finally, the PBEsol *xc* functional with restored LSD approximation, named VVsol, has a 3–4.5% of error for bulk properties higher than PBE and VV. However, it obtained less percentage of error for bulk properties than PBEsol.

In the case of the surface properties (γ, ϕ, and δ_{ij}), to reduce the computational cost, instead of a scanning on the μ/ß mesh we took the VV point expecting that it will improve also surface results. Then, we obtained for surface that VV shows a slightly higher error than that using PBEsol, but still lower than PBE by ~3.51%. VVsol shows the lowest error for the surface properties, *circa* 2.34% lower than PBEsol. So, considering bulk and surface properties, the VVsol global MAPE is decreased by 6–10% compared with PBE and PBEsol functionals, see Figure 4.12. The VV global MAPE is slight worse than VVsol, but still improving the PBE and PBEsol accuracies by 5–8%. Although, these percentage differences might appear insignificant, they are the double and more in comparison with the improvement of PBE over PBEsol (~3%). An extended discussion of the results is the included in the publication at the end of the summary. The Supporting Information for the manuscript is found Appendix C.

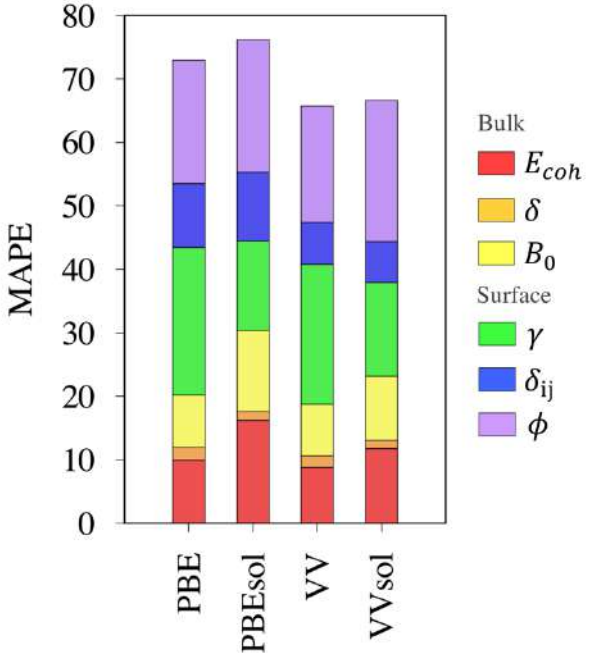

Figure 4.12 Property MAPE histogram, in %, for each studied *xc* functional.

Conclusions The following conclusions are drawn from the results presented in this section:

- The minimum point of the two-dimensional μ/β variables between the *xc* functionals PBE and PBEsol (VV) that analyse the error of TM bulk properties is found near of PBE values with $\mu = 0.2099$ and $\beta = 0.0667$.
- VV and the restored LSD approximation of PBEsol, called VVsol, represents a 5-8% and a 6-10% of improvement with respect to PBE and PBEsol functionals in TM bulk and surface properties, respectively; more than the improvement that PBEsol represented with respect to PBE.
- The results show a strong sensitivity to the μ parameter.
- The recovering of LSD response causes a better performance of PBEsol on the TMs.

Received: 26 July 2020 | Revised: 18 August 2020 | Accepted: 18 August 2020

DOI: 10.1002/jcc.26415

FULL PAPER

Journal of COMPUTATIONAL CHEMISTRY WILEY

Generalized gradient approximation adjusted to transition metals properties: Key roles of exchange and local spin density

Lorena Vega | Francesc Viñes

Departament de Ciència de Materials i Química Física & Institut de Química Teòrica i Computacional (IQTCUB), Universitat de Barcelona, Barcelona, Spain

Correspondence
Francesc Viñes, Departament de Ciència de Materials i Química Física & Institut de Química Teòrica i Computacional (IQTCUB), Universitat de Barcelona, Barcelona, Spain.
Email: francesc.vines@ub.edu

Funding information
Generalitat de Catalunya, Grant/Award Numbers: 2014SGR97, 2017SGR13, 2018FI-B-00384, XRQTC; Ministerio de Ciencia e Innovación, Grant/Award Numbers: MDM-2017- 0767, RTI2018-095460-B-I00; Ministerio de Economía y Competitividad, Grant/Award Numbers: CTQ2015-64618-R, RYC-2012-10129

Abstract

Perdew-Burke-Ernzerhof (PBE) and PBE adapted for solids (PBEsol) are exchange-correlation (xc) functionals widely used in density functional theory simulations. Their differences are the exchange, μ, and correlation, β, coefficients, causing PBEsol to lose the Local Spin Density (LSD) response. Here, the μ/β two-dimensional (2D) accuracy landscape is analyzed between PBE and PBEsol xc functional limits for 27 transition metal (TM) bulks, as well as for 81 TM surfaces. Several properties are analyzed, including the shortest interatomic distances, cohesive energies, and bulk moduli for TM bulks, and surface relaxation degree, surface energies, and work functions for TM surfaces. The exploration, comparing the accuracy degree with respect experimental values, reveals that the found xc minimum, called VV, being a PBE variant, represents an improvement of 5% in mean absolute percentage error terms, whereas this improvement reaches ~11% for VVsol, a xc resulting from the restoration of LSD response in PBEsol, and so regarded as its variant.

KEYWORDS

DFT, exchange and correlation, functional, PBE, PBEsol, transition metals

1 | INTRODUCTION

In the last decades, ground-state Kohn-Sham density functional theory (DFT)[1–3] has been extensively employed for the electronic structure calculations of molecular and solid-state systems and their physicochemical properties estimations. Therein, the key aspect to get an accurate system description is the exchange-correlation (xc) energy, which is approximated as a functional of electron spin densities, $n(\mathbf{r})$, for which there have been continuous scientific endeavors explicitly aimed at improving their accuracy performance. In a first stage, DFT grounded on local spin density (LSD) approximation, appropriate for slow variations of the electronic density, defined as

$$E_{xc}^{LSD}[n] = \int d^3r n(\mathbf{r}) \epsilon_{xc}(n(\mathbf{r})), \quad (1)$$

where ϵ_{xc} is ϵ_{xc}^{unif}; here, the xc potential of a uniform (*unif*) electron gas per particle. Later, the generalized gradient approximation (GGA) was developed, adding the density gradient contribution, $\nabla n(\mathbf{r})$, to the xc *ansatz*, so to improve the calculated energetic and structural results;

$$E_{xc}^{GGA}[n] = \int d^3r \epsilon_{xc}(n(\mathbf{r}), \nabla n(\mathbf{r})). \quad (2)$$

Finally, following an increasing order of complexity on the electronic density, the meta-GGA rung of the so-known Jacob's ladder of xc functional development added the kinetic energy density dependence for the occupied Kohn-Sham orbitals, $\tau(\mathbf{r})$, as,

$$E_{xc}^{meta-GGA}[n] = \int d^3r \epsilon_{xc}(n(\mathbf{r}), \nabla n(\mathbf{r}), \tau(\mathbf{r})). \quad (3)$$

The GGA rung xc functionals are hitherto widely used to study diverse systems, ranging from molecules,[4,5] to organometallic complexes,[6,7] and solid-state systems,[8–11] to name a few. However, GGA xc functionals excelled in the description of systems with metallicity, including not only metals,[12,13] but also transition metals

carbides and nitrides,[14–16] even carbon-based structures,[17,18] being a very good compromise in between accuracy and computational cost. Through the different functionals developed so far, one of the most frequently used is the Perdew-Burke-Ernzerhof (PBE).[19] The PBE xc triggered the derivation of a less common functional, specialized toward the description of solid-state systems, called PBEsol.[20]

The PBEsol initial accuracy was tested on a set of few materials of each type; including semiconductors, simple metals, ionic solids, and transitions metals (TMs), comparing the errors obtained for PBE and PBEsol optimized lattice constants with respect experimental values. The basic difference between PBE and PBEsol was the restoration in the latter of the gradient expansion (GE) using $\mu_{GE} = 0.1235$, basic for the correct accounting of the exchange energy in solids, considering them as slow varying electron gases systems, instead of using $2\mu_{GE} = 0.2195$ as in PBE, which would be accurate then for exchange energies of free neutral atoms. The μ is relevant to the enhancement factor of the given GGA, $F_x(s)$, that, when recovering the uniform gas limit, appears as,

$$F_x(s) = 1 + \mu s^2 + \ldots (s \to 0). \tag{4}$$

In turn, the F_x is part of the exchange energy contribution,

$$E_x^{GGA} = \int d^3 r \epsilon_x^{unif}(n(\boldsymbol{r}) F_x(s(\boldsymbol{r}))), \tag{5}$$

where $= \frac{|\nabla n|}{2k_F n}$, with $k_F = \left(3\pi^2 n\right)^{\frac{1}{3}}$, is the dimensionless density gradient.

Nevertheless, this was not the only difference between PBE and PBEsol. An important PBE feature is that it retains the LSD approximation response, thus satisfying,

$$\mu = \frac{\pi^2 \beta}{3}, \tag{6}$$

with $\beta = \beta_{GE} = 0.0667$.[21] On the contrary, PBEsol follows another constraint, which was a better fit to Jellium surface energy results obtained using the Tao-Perdew-Staroverov-Scuseria (TPSS) xc meta-GGA functional.[22] Consequently, PBEsol violates Equation (6), which should have $\beta = 0.0375$ according the value of μ_{GE}, by using $\beta = 0.046$ in the final PBEsol framework. While in the case of μ this affected the exchange contribution, the β affects the correlation contribution,

$$E_c^{GGA} = \int d^3 r n(\boldsymbol{r}) \left\{ \epsilon_c^{unif}(n(\boldsymbol{r}) + \beta t^2(\boldsymbol{r}) + \ldots \right\}. \tag{7}$$

Here, t is the appropriate dimensionless density gradient for the correlation, where $t = \frac{|\nabla n|}{\{2k_{TF} n\}}$ using the Thomas-Fermi screening wave vector $k_{TF} = \sqrt{\frac{4k_F}{\pi}}$ instead of k_F.

At this stage one could wonder whether neglecting the LSD response on the PBEsol genesis was detrimental for its accuracy, even whether that was the case in the adjustment of PBE μ/β values to the lattice constants of selected systems of different types of materials, or even to the meta-GGA TPSS Jellium surface energy estimates. Recent systematic studies evaluating the accuracy of a number of xc functionals across Jacob's ladder on a variety of TM bulk and surface properties highlighted the average best accuracy of PBE, closely followed by PBEsol, which actually impoverished the broad description on such properties by ~3% in mean absolute percentage terms.[12,13] Motivated by this, the aim here is to explore the two-dimensional (2D) accuracy landscape in between PBE and PBEsol functionals by tuning the μ and β coefficients, minimizing the xc error compared with a rather wide set of experimental values, focusing on bulk and surface properties for a family of 27 TMs; the functional corresponding to the minimum of xc error landscape, hereafter called VV, is to be regarded as a variant between PBE and PBEsol. This approach very much inspires in a previous 2D PBE scan, where the μ/κ space was explored on a variety and diversity of systems, which only included Ag and Au TMs, though.[23] There, the k factor was taken from the Padé-polynomial enhancement factor,[24] where

$$F_x(s) = 1 + k + \frac{k}{1 + \frac{\mu s^2}{k}}. \tag{5}$$

Here, however, k is maintained to 0.804, the maximum value allowed by the Lieb-Oxford bound for the exchange energy,[25] as done in PBE. In other works,[26] this value differs and enforces a tighter Lieb-Oxford bound. Apart from the μ/β space scan in between PBE and PBEsol, the latter rejected PBEsol version of $\mu = \mu_{GE} = 0.1235$ and $\beta = 0.0375$, satisfying the LSD response, is explored as well for the same group of properties and TMs, being this PBEsol derived xc functional named VVsol in the following.

Specifically, the 2D landscape is here fully evaluated only for bulk properties, and the minimum bulk point is used to seize the surface properties of 81 low-index Miller surfaces with maximum index order of one.[12] The chosen properties to evaluate the accuracy are, on one hand, the shortest interatomic distance (δ), the cohesive energy (E_{coh}), and the bulk modulus (B_0) for bulk TMs. On the other hand, the surface energy (γ), the work function (ϕ), and the interlayer distance (δ_{ij}) are contemplated for the TM surfaces. In such a way the accuracy is assessed from a broader and diverse point where structural, energetic, elastic, and electronic properties for the TM bulks and surfaces are accounted for, at variance to previous PBE and PBEsol accuracy assessments and adjustments, which were carried out on a single property, and on a narrow set of metallic systems.[19,20] The present broader approach further allows comparing with an earlier accuracy study in which the LSD Vosko-Wilk-Nussair (VWN)[27] functional and the meta-GGA TPSS accuracies were scrutinized likewise.[12]

2 | COMPUTATIONAL DETAILS

The Vienna Ab Initio Package (VASP) code[28] was used to carry out the DFT calculations within periodic boundary conditions, using a 11×11 mesh of functionals comprised between the μ and β values of

PBE and PBEsol. All calculations used, for the valence electron density, a plane-wave basis set with a 415 eV cutoff for the kinetic energy, while the effect of the atomic cores electrons was described using the projector augmented wave (PAW) method. [29] A convergence criterion threshold of 10^{-6} eV was used for the electronic convergence, and optimizations were considered finalized when forces acting on atoms were below 0.02 eV/Å. A tetrahedron smearing method with a width of 0.2 eV[30] was employed to speed up the convergence, yet the final total energies were considered extrapolated to 0 K.

By default, the calculations were non-spin-polarized, except for magnetic Fe, Co, and Ni TMs. The TM bulk crystal structures templates have been taken from Janthon *et al.*,[13] and freely optimized considering cell parameters and atomic positions. The surfaces were modeled as six-layer slabs using *p*(1×1) or *c*(1×1) surface unit cells constructed from the bulk as-optimized structures, and adding 10 Å of vacuum to avoid interaction between repeated slab. Monkhorst-Pack grids[31] of 7×7×7 and 7×7×1 **k**-points grid were used for bulk and surface models, respectively. Further bulk calculation details, including the estimated properties, δ, E_{coh}, and B_0, have been obtained as described in a previous study, and we refer to our previous work concerning the details of surface calculations, and the estimates of γ, ϕ, and δ_{ij} properties.[12]

3 | RESULTS AND DISCUSSION

The μ/β 2D landscape scan in between PBE (μ = 0.2195, β = 0.0667) and PBEsol (μ = 0.1235, β = 0.046) extensively samples a 11×11 mesh of points, being PBE derived xc functional variants. The mean absolute percentage error (MAPE) will be used to seize the reached accuracy between calculated properties and the available experimental data. By this, MAPE estimations are independent of the scale magnitudes of analyzed properties, and so MAPE values can be added to gain a general, total MAPE value of a given functional. Furthermore, the same MAPE analysis was carried out in previous works[12,13] allowing for a direct comparison.

The MAPE results reveal that different minima of μ/β are found for the three different bulk properties (δ, E_{coh}, and B_0) normally implying a stony valley of minima, in a similar fashion to the aforementioned μ/κ mapping.[23] For instance, for E_{coh} an average minimum is obtained at (μ = 0.1811, β = 0.046) with a MAPE of 8.58%, whereas for B_0 the minimum is found at (μ = 0.2003, β = 0.0667) with a value of 7.70%. Note that these are averaged minima, and, actually, each TM has its own point minimizing a given property MAPE. For instance, V and Zr display different minima for B_0, at (μ = 0.2099, β = 0.0667) and (μ = 0.2195, β = 0.04807), respectively. As dealing with different minima for each property and TM—even TM surface—is nonpractical, the TM MAPE is obtained at each point of the mesh from each bulk property across the 27 TMs and then, the property MAPEs added up in order to obtain a general minimum, called VV, found to be at (μ = 0.2099, β = 0.0667) with a total MAPE of 18.77%, see Figure 1.

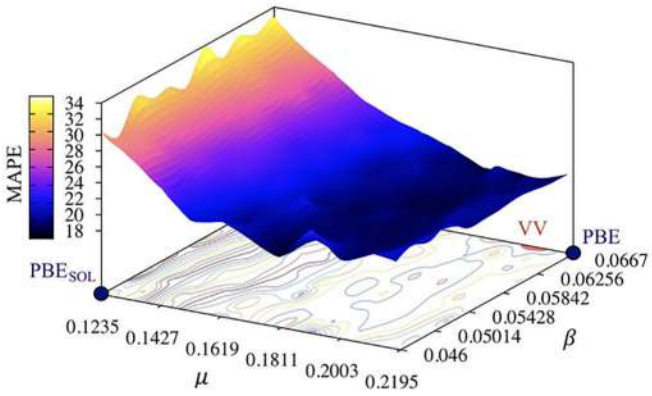

FIGURE 1 MAPE surface, in percentage, for the sum of bulk properties of the 27 studied TMs at each set of employed μ and β values, plus the orographic projection on the basis [Color figure can be viewed at wileyonlinelibrary.com]

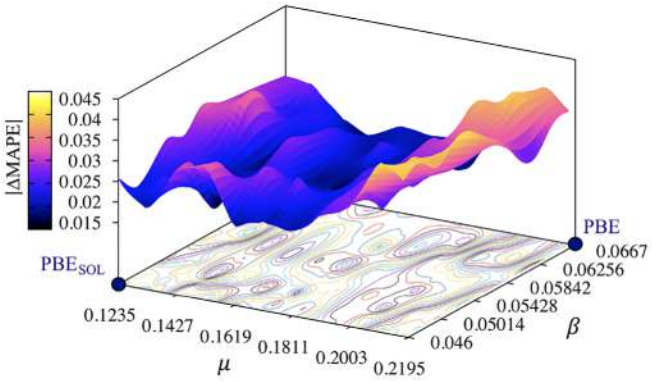

FIGURE 2 Surface variation of MAPE, ΔMAPE, in percentage, of δ for the 27 studied TMs, obtained with forces criteria on atoms below 0.02 and 0.007 eV/Å [Color figure can be viewed at wileyonlinelibrary.com]

Since one could argue that a somewhat poor convergence criterion might affect the MAPE surface, causing the observed fluctuations across the stony valley, results from a stricter convergence criterion of 0.007 eV/Å were compared with the 0.02 eV/Å ones, revealing an almost identical MAPE surface shape, see for example, the test case for δ values in Figure 2, with variations of MAPE, |ΔMAPE|, of at most 0.045%. Thus, the irregularities in the valley bed are a result of the mixing of systems rather than to the optimizations numerical noise.

Comparing the VV results to PBE and PBEsol ones, the bulk VV MAPE of 18.77% is slightly less than PBE (20.18%), but moved away from PBEsol (30.40%), see itemized values of bulk properties in Table 1, which also allow a general evaluation of the explored xc functional based on certain properties, or discrimination in between bulk and surface types. The overall VV assessment comes natural as it is actually located close to PBE in the μ/β space. Another interesting aspect is that μ generates more MAPE dispersion than β, circa 16% for the former, and below 4% for the latter. From this analysis one can deduce that the correct treatment of exchange in such TM delocalized

TABLE 1 MAPEs, in percentage, for bulk and surface TM properties, and the global MAPE for each explored functional

	Bulk				Surface				
Functional	E_{coh}	δ	B_0	Total	γ	δ_{ij}	ϕ	Total	Global
PBE	9.94	1.96	8.28	20.18	23.25	10.11	19.39	52.75	72.93
PBEsol	16.22	1.34	12.84	30.40	14.02	10.87	20.91	45.80	76.20
VV	8.77	1.84	8.16	18.77	22.01	6.57	20.66	49.24	68.01
VVsol	11.75	1.33	10.07	23.15	14.76	6.43	22.27	43.46	66.61

electronic structures seems to be key in the development of new or improved xc functionals, although the validity of this statement in an outer region from the explored map has to be taken with a grain of salt. Finally, when inspecting the neglected VVsol, in other words, the PBEsol xc with restored LSD approximation response, it displays a higher MAPE for bulk properties compared with PBE and VV, by 3–4.5% respectively, but lower than PBEsol. Notice, however, that VVsol is cut out of the scanned region, although it would be naturally found along the course of the minima valley. This explains why its performance is smaller than PBEsol, even though is in relatively close proximity within the μ/β space.

Nevertheless, not only bulk properties are relevant for TM systems, but also does the description of surface properties (γ, ϕ, and δ_{ij}). Thus, the VV functional gained from bulk properties has been tested for such surface properties, avoiding a complete highly computationally expensive scan analysis so as to have a wide spectrum for which TMs description, and, by that, expecting that the VV minimum could decrease as well surface and global MAPEs. Taking into account all the casuistry of the explored 81 TM surfaces, VV displays a slightly higher error than that gained for PBEsol, but still lower than PBE by ~3.51%, while VVsol shows the lowest error for the surface properties, *circa* 2.34% lower than PBEsol. Adding the pieces together, the VVsol global MAPE, encompassing bulk and surface properties, is decreased by 6–10% compared with previous PBE and PBEsol functionals. Following the previous procedure, the VV global MAPE is very similar to VVsol, improving the PBE and PBEsol accuracies by 5–8%. Even though such improvements may appear mild, one can place them in a better significant context when comparing to the achieved improvement of PBE over PBEsol, of ~3%.

In summary, PBE has been long considered among the best choices in describing TM bulk and surface systems, closely followed by PBEsol, see added MAPE values in Figure 3. Despite their similarity, their μ and β coefficients differ, emphasizing the correlation or exchange roles of the GGA xc functional. In the case of PBEsol, the employed β implies losing the LSD approximation response. Opening the μ/β space in between PBE (μ = 0.2195, β =0 .0667) and PBEsol (μ = 0.1235, β = 0.046), and even considering recovering the LSD approximation response in PBEsol (μ = 0.1235, β = 0.0375) add other levels of xc accuracy tuning, as exemplified here in the evaluation of a wide diversity of TM bulk and surface properties, and, by that, underscoring the lack of necessity of matching meta-GGA TPSS Jellium surface energies. The 2D scan obtained minimum; VV (μ = 0.2099, β = 0.0667) and the LSD response recovered PBEsol; VVsol (μ = 0.1235, β = 0.0375) allow finding μ and β tailored xc functionals able to

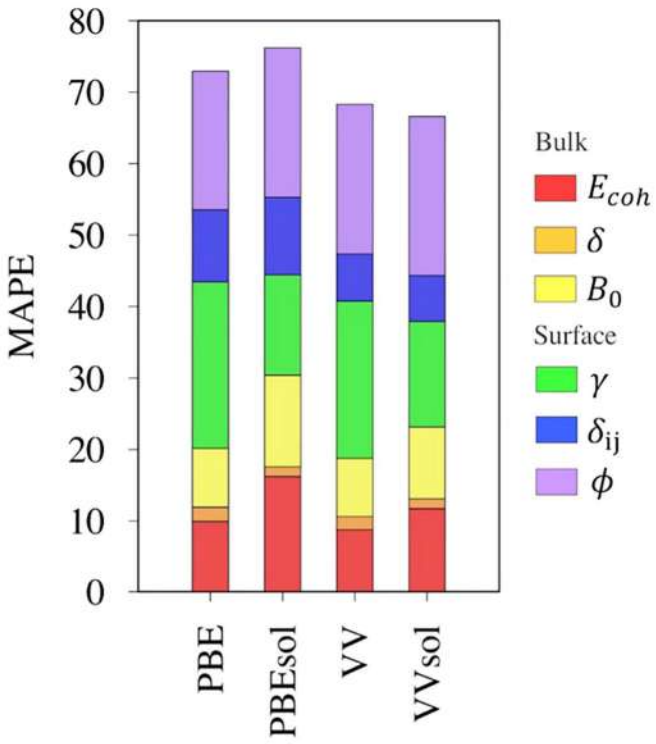

FIGURE 3 Property MAPE histogram, in percentage, for each studied xc functional [Color figure can be viewed at wileyonlinelibrary.com]

significantly further improve the properties description accuracy by reducing the added up MAPEs by 6–10% compared with standardized PBE and PBEsol functionals, see Figure 3, and at least doubling the achieved accuracy of ~3% as achieved by PBE compared with PBEsol.

The complete list of VV and VVsol computed properties estimates, including experimental reference values, is found in Tables S1–S4 of the Supporting Information (SI), and Tables S6–S8, whereas Table S5 contains the Wulff construction surface percentages, to better correlate presently computed surface energies to the experimental ones.[12,32] Notice, that the use of VV or VVsol in treating TM systems is thus encouraged, although should be taken cautiously, as none of them is yet a panacea to the DFT exchange-correlation accuracy issues; actually, they are, in average terms, a better choice, but, specifically, they represent a clear better choice only for given TMs and properties, as graphically displayed in Figure S1 of the SI, where the

most accurate xc functional is highlighted for each explored TM and property, adjoining current VV and VVsol results to a previous analysis carried out on other 15 functionals,[12,13] revealing the spread impact of the latter across particular systems and properties.

Beyond this practical utility on TM systems, the present study highlights (a) the sensitivity of the exchange μ parameter on the overall xc performance, (b) the questioning of neglecting theoretical thresholds, as shown here in the recovery of the LSD response, (c) the requirement to broaden the adjustment to a wider set of properties with experimentally available and reliable data, and (d) the necessity of adjusting them to families of similar compounds, for example, delocalized electronic structure materials, as exemplified here on TMs family.

The philosophy of adjusting an xc functional to a type of materials, with a broad and diverse set of properties, is contrary to the, perhaps futile, attempt to mix properties of different types of molecular and solid-state systems, with inherently different electronic structure, difficult to be sheltered under the same theoretical umbrella, or even to focus on a given particular property, since, as shown here, the improvement on one property is not necessarily followed by others, or the improvement in bulk properties is not necessarily followed by the surface ones, illustrating, in a nutshell, the necessity to tailor different xc functionals for chemical systems different in nature.[33,34]

4 | CONCLUSIONS

The present study addresses the exchange/correlation-related μ/β 2D landscape in between PBE (μ = 0.2195, β = 0.0667) and PBEsol (μ = 0.1235, β = 0.046), being both landmarks in the description of delocalized electronic structure materials, as exemplified, for example, in TM bulk and surface properties. The study extensively samples a 11×11 mesh of points in between PBE and PBEsol varying μ and β, being thus PBE xc functional variants, exploring a collection of bulk properties, including δ, E_{coh}, and B_0 of 27 TMs, displaying bcc, fcc, or hcp crystal structures. The estimates, compared with experimental measurements of such observables, generate a MAPE with the shape of a stony valley, where its minimum, called VV (μ = 0.2099, β = 0.0667), is found close to PBE. Aside, the PBEsol xc functional with recovered LSD response, named VVsol (μ = 0.1235, β = 0.0375) is also explored. The further evaluation of PBE, PBEsol, VV, and VVsol on 81 TM surface properties, including γ, ϕ, and δ_{ij} observables, compared with experimental estimations reveal that the usage of VV or VVsol would represent an accuracy of improvement of 5–8% and 6–10% MAPE, respectively, in TM bulk and surface properties description.

The study reveals that such a description is quite sensitive to the μ exchange-related parameterization, at least for the bulk materials family of TMs and the explored region, and so this should be regarded in the future developing or adjustment of new xc functionals in their description. The gained minimum over the explored μ/β 2D landscape, called VV, represents a 5–8% improvement with respect PBE and PBEsol, and this sheds light in the necessity of adjusting xc functionals to a broad set of similar materials while regarding a collection of diverse properties altogether. Finally, the good performance PBEsol when recovering the LSD response, called VVsol, implies an improvement of ~10% MAPE, unfolding the detriment of neglecting certain xc constrains. Altogether, the VV or VVsol xc functionals at least double the accuracy as, for example, achieved by PBE over PBEsol of solely ~3%, pointing for their general use.

ACKNOWLEDGMENTS

This work was supported by Spanish MINECO/FEDER grant CTQ2015-64618-R, Spanish MICIUN RTI2018-095460-B-I00 and the Spanish Structures of Excellence *María de Maeztu* program through grant MDM-2017- 0767, and in part by *Generalitat de Catalunya* grants 2014SGR97, 2017SGR13, and XRQTC. L. V. thanks funding to *Generalitat de Catalunya* via a pre-doctoral grant 2018FI-B-00384. F. V. thanks the Spanish MINECO for postdoctoral contracts under the *Ramón y Cajal* Program (RYC-2012-10129).

ORCID

Francesc Viñes https://orcid.org/0000-0001-9987-8654

REFERENCES

[1] W. Kohn, L. J. Sham, *Phys. Rev. A* **2010**, *140*, A1133.
[2] R. M. Dreizler, E. K. U. Gross, *Density Functional Theory*, Springer-Verlag, Berlin-New York **1990**.
[3] R. G. Parr, W. Yang, *Density functional theory of atoms and molecules*, Oxford University Press, New York **1989**.
[4] E. D. Murray, K. Lee, D. C. Langreth, *J. Chem. Theory Comput.* **2009**, *5*, 2754.
[5] Y. Zhang, W. Yang, *Phys. Rev. Lett.* **1998**, *80*, 890.
[6] K. Boussof, R. Boulmene, M. Prakash, N. Komiha, M. Taleb, M. M. Al-Mogren, M. Hochlaf, *Phys. Chem. Chem. Phys.* **2015**, *17*, 14417.
[7] N. E. Schultz, Y. Zhao, D. G. Truhlar, *J. Phys. Chem. A* **2005**, *109*, 11127.
[8] P. Haas, F. Tran, P. Blaha, K. Schwarz, R. Laskowski, *Phys. Rev. B* **2009**, *80*, 195109.
[9] G. I. Csonka, J. P. Perdew, A. Ruzsinszky, P. H. T. Philipsen, S. Lebègue, J. Paier, O. A. Vydro, J. G. Ángyán, *Phys. Rev. B* **2009**, *79*, 115107.
[10] A. Jain, G. Hautier, C. J. Moore, S. P. Ong, C. C. Fischer, T. Mueller, K. A. Persson, G. Ceder, *Comput. Mater. Sci.* **2011**, *50*, 2295.
[11] K. Lejaeghere, V. Van Speybroeck, G. Van Oost, S. Cottenier, *Crit. Rev. Solid State Mater. Sci.* **2014**, *39*, 1.
[12] L. Vega, J. Ruvireta, F. Viñes, F. Illas, *J. Chem. Theory Comput.* **2018**, *14*, 395.
[13] P. Janthon, S. Luo, S. M. Kozlov, F. Viñes, J. Limtrakul, D. G. Truhlar, F. Illas, *J. Chem. Theory Comput.* **2014**, *10*, 3832.
[14] M. G. Quesne, A. Roldán, N. H. De Leeuw, C. R. A. Catlow, *Phys. Chem. Chem. Phys.* **2018**, *20*, 6905.
[15] M. Marlo, V. Milman, *Phys. Rev. B* **2000**, *62*, 2899.
[16] J. R. d. S. Politi, F. Viñes, J. A. Rodriguez, F. Illas, *Phys. Chem. Chem. Phys.* **2013**, *15*, 12617.
[17] B. Dong, H. Guo, Z. Liu, Y. Yang, P. Tao, S. Tang, R. Saito, Z. Zhang, *Carbon* **2018**, *131*, 223.
[18] D. Malko, C. Neiss, F. Viñes, A. Görling, *Phys. Rev. Lett.* **2012**, *108*, 086804.
[19] J. P. Perdew, K. Burke, M. Ernzerhof, *Phys. Rev. Lett.* **1996**, *77*, 3865.
[20] J. P. Perdew, A. Ruzsinsky, G. I. Csonka, O. A. Vydrov, G. E. Scuseria, L. A. Constantin, X. Zhou, K. Burke, *Phys. Rev. Lett.* **2008**, *100*, 136406.

[21] S.-K. Ma, K. A. Brueckner, *Phys. Rev.* **1968**, *165*, 18.
[22] J. Tao, J. P. Perdew, V. N. Staroverov, G. E. Scuseria, *Phys. Rev. Lett.* **2003**, *91*, 146401.
[23] E. Fabiano, L. A. Constantin, F. Della Sala, *J. Chem. Theory Comput.* **2011**, *7*, 3548.
[24] A. D. Becke, *J. Chem. Phys.* **1986**, *84*, 4524.
[25] M. Levy, *Int. J. Quantum Chem.* **1989**, *36*, 617.
[26] Y. Zhao, D. G. Truhlar, *J. Chem. Phys.* **2008**, *128*, 184109.
[27] S. H. Vosko, L. Wilk, M. Nusair, *Can. J. Phys.* **1980**, *58*, 1200.
[28] G. Kresse, J. Furthmüller, *Comput. Mater. Sci.* **1996**, *6*, 15.
[29] P. E. Blöchl, *Phys. Rev. B: Condens. Matter Mater. Phys.* **1999**, *50*, 17953.
[30] P. E. Blöchl, O. Jepsen, O. K. Andersen, *Phys. Rev. B: Condens. Matter Mater. Phys.* **1994**, *49*, 16223.
[31] H. J. Monkhorst, J. D. Pack, *Phys. Rev. B* **1976**, *13*, 5188.
[32] F. Viñes, J. R. B. Gomes, F. Illas, *Chem. Soc. Rev.* **2014**, *43*, 4922.
[33] X. Xu, W. A. Goddard, *J. Chem. Phys.* **2004**, *121*, 4068.
[34] L. S. Pedroza, A. J. R. Da Silva, K. Capelle, *Phys. Rev. B* **2009**, *79*, 201106.

SUPPORTING INFORMATION

Additional supporting information may be found online in the Supporting Information section at the end of this article.

How to cite this article: Vega L, Viñes F. Generalized gradient approximation adjusted to transition metals properties: Key roles of exchange and local spin density. *J Comput Chem*. 2020;41:2598–2603. https://doi.org/10.1002/jcc.26415

Chapter 5. Unravelling Morphological and Topological Key Aspects of Pd Nanoparticles

5.1 SUMMARY

Introduction Nanostructuring, i.e. the use of metallic nanoparticles (NPs) has become an extended way of improving the catalyst activity while reducing the amount of precious and expensive transition metals (TMs). From the atomic-level point of view, the better catalytic properties of NPs arise from the special sites exposed involving low-coordinated atoms at corners, edges or facets of the NP. For instance, low-coordinated atoms are key for the molecular hydrogen dissociation on gold.[46] In addition, particle shape varies often with particle size[47] and it can affect the number of low-coordinated sites available. Thus, particle properties are size dependent, which makes the material tunable.[48–52] For this reason, unravelling the morphology and topology of metallic nanoparticles is critical. Particularly, in this work we focus our attention on Pd_n NPs with n ranging from 10 to 1504 atoms. We extend our analysis further from the Wulff construction, Truncated Octahedron (To), considering different shapes such as Cube (C), Truncated Cube (Tc), Octahedron (Oh), Cuboctahedron (Ch), Icosahedron (Ih), Sphere (S), Tetrahedron (Th) and Decahedron (Dh), see Figure 5.1 for a depiction of the different shapes.

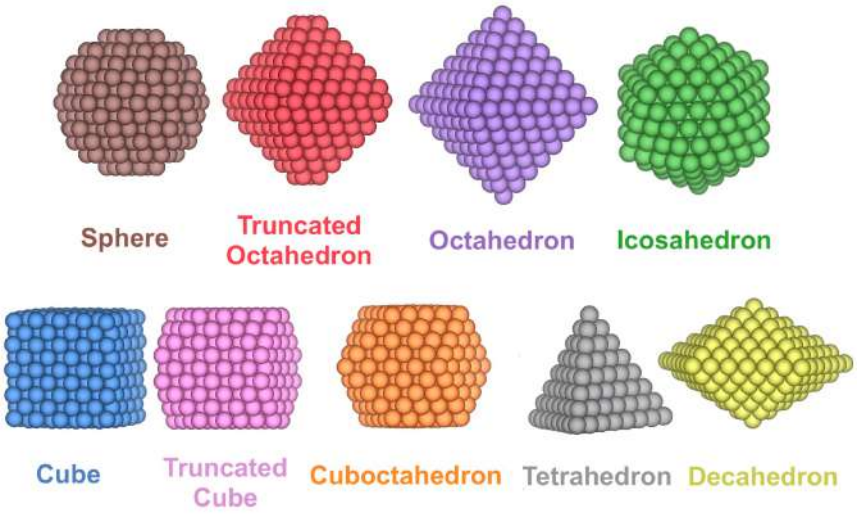

Figure 5.1 Schematic representation of the different shapes contemplated for Pd_n NPs.

Pd is broadly used as a catalyst with a variety of applications. For instance, ultradispersed supported Pd clusters (up to 2 nm) act as highly active catalysts in hydrogenation processes.[53] Here, interatomic distance (δ) and cohesive energy (E_{coh}) are analysed in front of $n^{-1/3}$, being n the total number of NP atoms, in order to examine the size-dependent evolution of NP properties and structure towards the bulk limit. [54–60] Furthermore, the data is also used to unfold how the amount of atomic sites with each different CN, such as corner, edge, facet, or bulk-like sites, are affecting the energetic stability, allowing for a breakdown of the energy by topological contributions.[36,55] A last analysis, where instead of using CN, we considered geometrical contributions as: i) the number of corner sites, ii) the addition of all edge site lengths, iii) the total exposed area of the NP, and iv) the total NP volume to analyse the energetic stability of the NP. Both analyses allow to predict the energy of any NP independently of its size or shape. An extended discussion of the results is the included in the manuscript at the end of the summary. Further supporting data is found Appendix D.

The author contribution to the project was to carry out part of the optimizations, concretely the ones with bigger sizes and shapes as Tetrahedrons, Spheres, Truncated Cubes and Decahedrons. Furthermore, the author also performed all the analysis here exposed, the redaction, and the image assembling.

Results The first property that is evaluated with the NP size is the δ(Pd-Pd), see Figure 5.2. For all the studied shapes, the distance increases with size, from small sizes to the bulk limit, reaching an approximated value of the δ_{Bulk}(Pd-Pd). Similar shapes as Cuboctahedron, Octahedron, Truncated Octahedron, Truncated Cube and Sphere show a similar behaviour. Icosahedron is the one featuring the longest distance, which can be caused by the distortion on the *fcc* structure. On the other hand, Cube, Tetrahedron and Decahedron are the ones with the shortest distance, which can be caused by their superior surface strain.

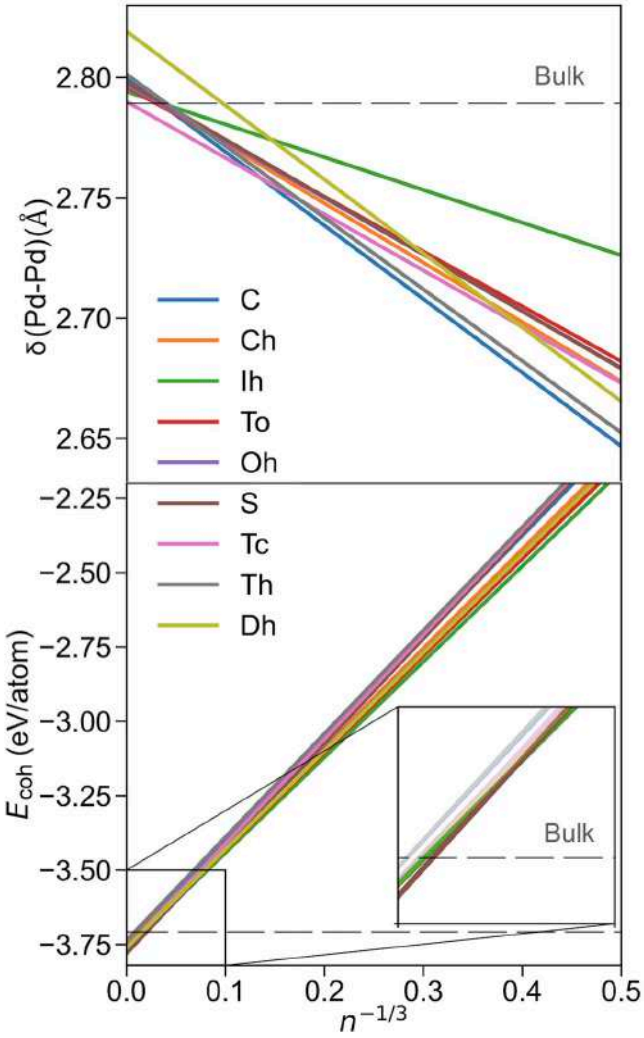

Figure 5.2 (Top panel) Evolution of the minimum interatomic distance of Pd-Pd, δ(Pd-Pd), in Å with the size, where n is the number of atoms of the NP. (Bottom panel) Evolution of the cohesive energy, E_{coh}, in eV/atom with the size. Each line corresponds to the regression of each shape following the color legend.

The second property evaluated is the cohesive energy in front of NP size. From the bottom panel of Figure 5.2, one can see that icosahedron is the most stable shape for smaller NPs. All exposed surfaces in icosahedron are (111)-like, which is the most stable surface of Pd and other *fcc* TMs. In addition, previous studies[61,62] reported the icosahedron as the most stable shape in smaller NPs. Concretely, Rapps *et al.* [61] found the icosahedron as the most stable shape for smaller NPs of Pd. However, at larger NPs regime, from $n^{-1/3}$=0.053 ca. n=6530, the stable shape is the sphere. This is different from the result derived from Wulff construction, Truncated Octahedron. Possible reasons could be that Wulff construction does not account for the effect of Corners and Edges on the energetic stability. Another reason could be that smaller spherical NPs have a similar shape to truncated octahedrons due to the way they were modelled. The Sphere was modelled cutting off Pd atoms out of a radius from the centre of the *fcc* Pd bulk. Anyway, inside the

truncated octahedrons group, it is possible to differentiate subgroups by the exposition proportion of the {001} and {111} surfaces. Differentiating them and comparing with the most stable shapes revealed in the bottom panel of Figure 5.2, Figure 5.3 shows that in the large NPs region the most stable shape, from $n^{-1/3}$ = 0.08, *i.e. ca.* n = 1500, is a subgroup of the truncated octahedrons. Concretely, the subgroup is the one with more exposition of the {001} surface, contrary to the expected by Wulff. But this result has to be taken with caution, since the number of points used on the regression was limited.

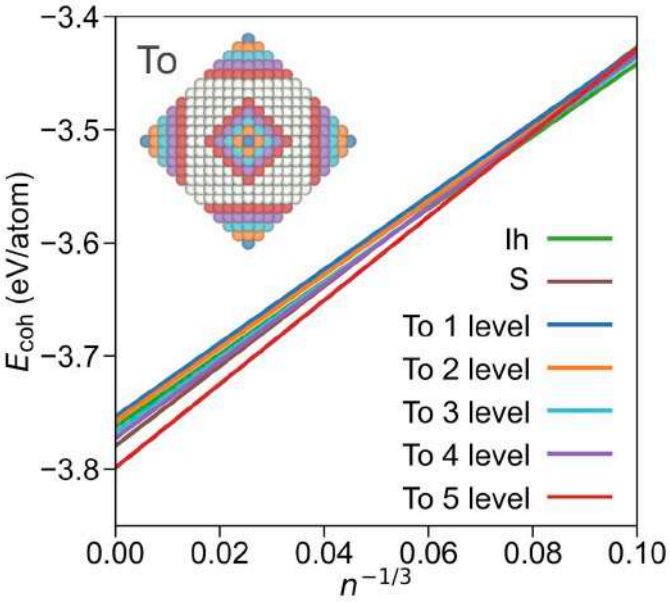

Figure 5.3 Comparison of the most stable Icosahedron and Sphere shapes and the Truncated Octahedron (To), split by each level of {001} cuts departing from Octahedron shapes. Inset NP image illustrates the removed atoms from each level from an Octahedron NP. Sphere and Icosahedron colour coding as in the signalled linear adjustments.

Apart from the size-dependent study of the Pd-Pd distance and shape stability of Pd NPs, a model can be obtained using the dataset employed to predict the energy of unexplored larger or different-shape Pd NPs. The models are based on the CN and the geometrical features as number of corners, edge length, area and volume of the NP. For both cases, a multilinear regression is employed, since understandable conclusions can be drawn from it. The amount of data is not enough to split the data into training and a test set without biasing our model depending on the selection of data in each set. Therefore, a cross-validation (CV)[63] of the regression is carried out by a

Shuffle Split. This means that the data is split randomly *m* times in a training and test set, subsequently fitting and evaluating the model for each pair of training and test sets. In our case, we used m = 100 and the total data is randomly divided each time in a 75% and 25% of training and test set, respectively. Since there are 100 different fittings, the discussed regression coefficients and errors are an average of all of them.

Then, the first proposed model is to disaggregate the NP energy using the cohesive energy of the NP, E_{coh}, in front of the proportion of atoms of each CN, χ_i (see equation 5.1). E.M. Dietze et al.[64] showed a similar analysis for more metals but less shapes. The χ_{12} is not included because the correlation between the other variables due to the direct relation of $n = \sum_{i=3}^{12} n_i$. Further than that, the Icosahedron shape has not been initially regarded since, at variance with the rest of shapes, it features a distorted core *fcc* structure. Within such treatment, the coefficients are the destabilization energy respect the intercept term which represents the *fcc* Pd bulk cohesive energy.

$$\chi_i = \frac{n_i}{n} \quad ; \quad i = [3-11] \tag{5.1}$$

The mean coefficients obtained are:

$$\begin{aligned} E_{coh} = -3.72 &+ 1.95\chi_3 + 1.88\chi_4 + 1.47\chi_5 + 1.29\chi_6 \\ &+ 1.01\chi_7 + 0.66\chi_8 + 0.52\chi_9 \\ &+ 0.14\chi_{10} + 0.04\chi_{11} \end{aligned} \tag{5.2}.$$

As one can notice, the coefficients stabilize in energy when the CN increases. The measured mean test errors show a good agreement between the calculated and the predicted energies, with R^2=0.995 and Mean Absolute Error (MAE) of 0.011 eV/atom. These errors are depicted on Figure 5.4, where the top panel shows the excellent R^2 between the predicted and the calculated E_{coh} and bottom panel shows the averaged MAE learning curve. This learning curve represents the averaged MAE evolution of the CV training and test set with the number of training set points, while keeping the test points ratio. From it, one can observe that with ca. 40 training samples a similar MAE can be obtained. The regression coefficients do not vary much when Icosahedrons are included:

$$E_{coh} = -3.73 + 1.89\chi_3 + 1.83\chi_4 + 1.50\chi_5 + 1.33\chi_6 + 1.03\chi_7 + 0.75\chi_8 + 0.56\chi_9 + 0.18\chi_{10} + 0.03\chi_{11} \quad (5.3)$$

However, the errors are slightly higher with values of R^2=0.972 and a MAE of 0.022 eV/atom.

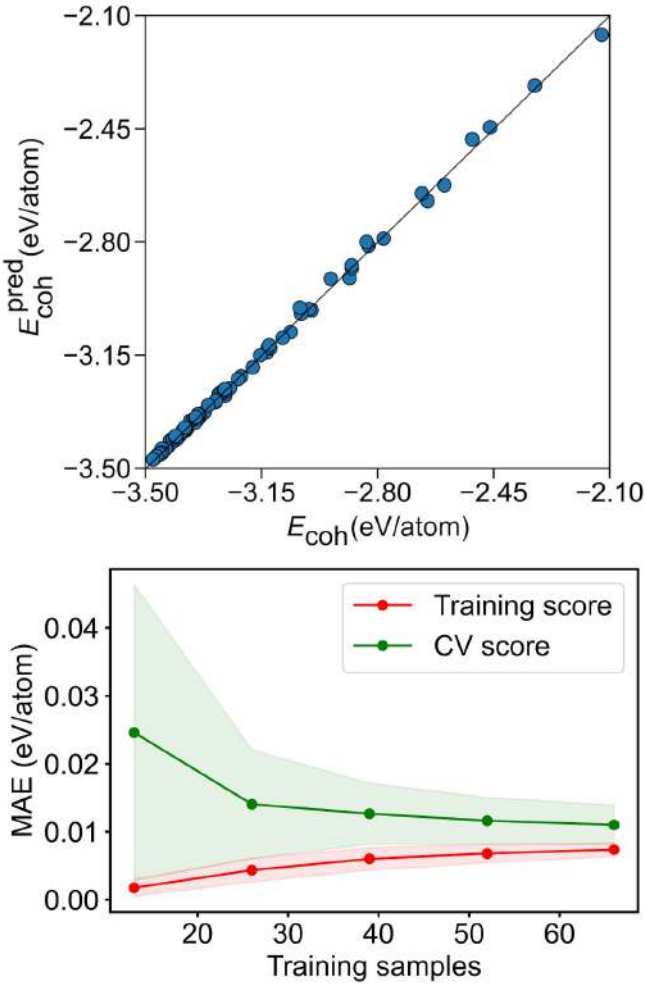

Figure 5.4 Top panel: comparison of calculated E_{coh} *versus* the predicted E_{coh}, E_{coh}^{pred}, for the CN breakdown. Bottom panel: MAE learning curve for the training and CV scores. The coloured areas represent the standard variation limits as a result of the 100 different fittings.

In turn of the geometric analysis, the cohesive energy is fitted without using intercept in front of the features as the number of corners (C), total longitude of edges (L), total exposed area (A) and NP volume (V) divided per n. For this case, only regular shapes are employed, so spheres and truncated shapes are out of the analysis. Consequently, the number of cases in our dataset is reduced to 40. Applying the same CV explained before, with the

same m and the same percentages of training and test sets, the obtained mean coefficients are:

$$E_{coh} = 0.54\frac{C}{n} - 0.09\frac{L}{n} - 0.29\frac{A}{n} - 0.23\frac{V}{n} \quad (5.4).$$

The obtained coefficients show that corners destabilize the energy, the longitude subtly stabilizes it, and area and volume have the greatest contribution on the stabilization. Curiously, volume substantially contributes to the stabilization, by -0.23 eV, but less than area. This is simply because particularly for large NPs the NP volume is extensively larger than its exposed surfaces. The mean errors for the test set are R^2=0.763 and MAE=0.11 eV/atom. In the learning curve (see Figure 5.5), it is shown that at around 15 training data points, the MAE of training and test set converge at 0.11 eV/atom.

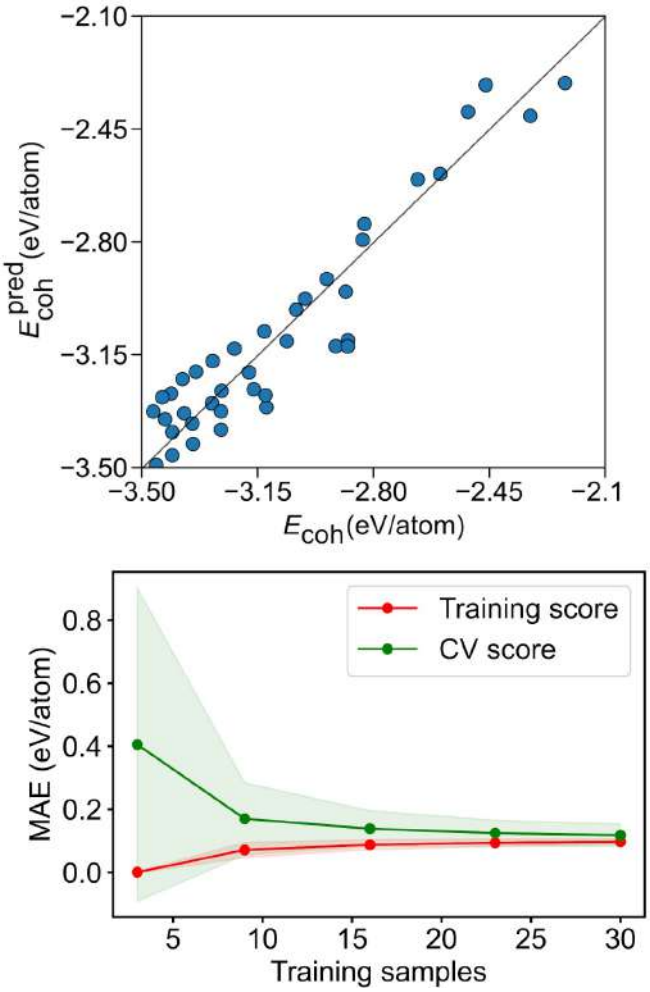

Figure 5.5 Top panel: comparison of calculated E_{coh} *versus* the predicted E_{coh}, E_{coh}^{pred}, for the geometry breakdown. Bottom panel: MAE learning curve for the training and CV scores. The coloured areas represent the standard variation limits as a result of the 100 different fittings.

A possible problem of the previous model is that different types of corners, edges and surfaces are considered the same. For example, surface (111) and (001) are not differentiated. To assess this effect, we calculated the energy only provided by surface elements for the Cube and Octahedron shapes, following a procedure earlier employed to obtain step and row energies.[65,66] According to it, energies can be decomposed as

$$E = n\varepsilon_{bulk} + \gamma A + \beta L + \xi C \qquad (5.5),$$

where ε_{bulk} is the energy of a single Pd atom in the bulk Pd *fcc* structure, and γ, β, and ξ are surface, edge, and corner energies, respectively. Notice than Cube and Octahedron have different surfaces, (001) surfaces in the Cube case and (111) surfaces in the Octahedron shape. This implies that edges and corners are different according its facet neighbours. The most relevant result is that from surfaces values, A, (001) and (111) facets energies are 0.09 and 0.08 eV·Å^2, this is, values of 1.41 and 1.24 J·m^{-2}. These values are different from the obtained for extended surfaces, 1.5 and 1.14 J·m^{-2}, respectively, meaning that on Pd NPs, the (001) surfaces are 0.09 J·m^{-2} more stable and (111) surfaces 0.10 J·m^{-2} less stable. This difference may be because of the reduction of the δ(Pd-Pd) distance in the NP and the stabilization or destabilization of the Pd atoms found near the edges. Thus, these results could explain why the Truncated Octahedron was more stable within the increase of (001) exposure on Figure 5.3.

Conclusions To conclude this chapter:

- Icosahedral shape is the most stable shape of Pd NPs until 1500 atoms approximately. Contrary to what is derived from Wulff constructions, Truncated octahedron with higher (001) surface exposure is found as the most stable one beyond 1500 atoms. This is caused because on Pd NPs the (001) surface is found to be more stable than on extended surfaces.
- About the models to unravel Pd NP energies, cohesive energies in front of the proportion of atoms of each CN, provides quite good test errors of R^2=0.995 and MAE=0.011 eV/atom without including icosahedrons in the

fitting. Including them, the errors increase slightly with values of R^2=0.972 and MAE=0.022 eV/atom. The coefficients have a physical meaning, this being the proportional energy that an atom with a specific CN destabilizes the bulk cohesive energy (intercept). Cohesive energies in front of the corners, edges, areas and volumes divided by the number of atoms provides higher test errors with an R^2=0.763 and MAE=0.110 eV/atom only providing a qualitative assessment.

PAPER

Unravelling Morphological and Topological Energy Contributions of Metal Nanoparticles

Received 00th October 2021,
Accepted 00th January 2021

DOI: 10.1039/x0xx00000x

Lorena Vega,[a,b] Francesc Viñes*[a,b] and Konstantin M. Neyman [a,b,c]

Metal nanoparticles (NPs) are ubiquitious in many fields, from nanotechnology to heterogeneous catalysis, with properties differing from those of single-crystal surfaces and bulks. A key interesting aspect is the size-dependent evolution of NP properties towards the bulk limit, including the adoption of differnet NP shapes, which may bias the NP stability along the NP size. Herein, the stability of different Pd_n NPs (n=10-1504 atoms) considering a myriad of shapes is investigated by first-principles energy optimization, allowing determining that Icosahedron shapes are the most stable up to a size of *ca.* 4 nm. From that size on, Truncated Octahedron shapes become more stable, yet a presence of larger {001} facets than the Wulff construction is forecasted due to their increased stability compared to (001) single-crystal surfaces, and the lower stability of {111} facets compared to (111) single-crystal surfaces. The NP cohesive energy breakdown in terms of coordination numbers is found to be an excellent quantiative tool of the stability assesment, with mean absolute errors of solely 0.01 eV·atom^{-1}, while a geometry breakdown allows only for a qualitative stability screening.

Introduction

Over the last decades nanomaterials have become ubiquitous in various industrial and/or technological applications, including, *e.g.* energy storage,[1] antimicrobial agents,[2] selective release of drugs,[3] and heterogeneous catalysts,[4] to name a few. In the latter field, nanostructuring, *i.e.* the use of metallic nanoparticles (NPs), has become an ubiquitous way of improving efficiency of a catalyst while reducing the employed amount of it, a key point when using precious and expensive late transition metals, regular active phases in a large number of catalytic processes.[5] Paramount examples are, *e.g.* the renowned increased catalytic activity of Au NPs in the oxidation of CO when the NPs were supported on TiO_2,[6] or the increase in selectivity towards pyrrolidine compared to n-butylamine when reducing the size of the employed Pt NPs in the catalysis of pyrrole hydrogenation.[7]

From the atomic-level point of view, the catalytic activity of a given metal NP is the result of exposing special sites involving low-coordinated atoms, such those located at NP corners, edges, or facets, and their peculiar electronic structure.[4,5] For instance, low-coordinated gold atoms have been identified as key sites in the catalytic dissociation of H_2 molecules.[8] In addition, particle shape often varies with particle size,[9] which can in turn affect the number of exposed low-coordinated sites, ultimately biasing the overall NP catalytic activity. Consequently, size and shape dependent properties of metal NPs make their catalytic properties tunable.[10-13]

Is for that reason that unravelling the morphology and topology of metal NPs becomes crucial. Experimentally, different studies tackled this issue using metallic NPs deposited on a variety of supports.[14-17] Given the technical difficulties in experimentally controlling size and shape, usually obtaining a distribution of them, plus the inherent averaged experimental analysis, many studies relied on computational simulations to gain the necessary atomistic insight, allowing even for the NP analysis in the absence of support, and so, weighting its effect[18-22] compared to models accounting for the support.[23,24] However, such computational studies are note exempt of difficulties; for instance, when dealing with NP models of transition metals within the so-called scalable regime, a size limit of ~100 atoms from which the metal NPs properties scale linearly with size,[4] their first-principles computational simulation is at the frontier of the computational power of modern computing cluster architectures and the capabilities of standard codes.

However, the nowadays rise of high-performance parallel supercomputers coupled to massively parallelized modern quantum computing codes allows a leap forward in the explicit treatment of NPs containing from a few hundreds to a few thousands of atoms. This has been already successfully demonstrated for oxide semiconductors (TiO_2 and ZnO), unfolding a rich diversity of structures in the nanoregion.[25,26] Such calculations were done employing density functional theory (DFT), the regular working horse when studying metal NPs, yielding accurate results at a reasonable computing time. For transition metals (TMs), generalized gradient approximation (GGA) exchange-correlation functionals such as the Perdew-Burke-Ernzerhof (PBE)[27] have been found to be among the best describing TMs bulk and surface properties.[28,29] However, as long as NP modelling is concerned, even if periodic surface models are extremely useful,[28] a duly simulation requires the employment of well-shaped isolated NPs.

[a] Departament de Ciència de Materials i Química Física, Universitat de Barcelona, c/ Martí i Franquès 1-11, 08028 Barcelona, Spain
[b] Institut de Química Teòrica i Computacional (IQTCUB), Universitat de Barcelona, c/ Martí i Franquès 1-11, 08028 Barcelona, Spain
[c] ICREA (Institució Catalana de Recerca i Estudis Avançats), Pg. Lluís Companys 23, 08010 Barcelona, Spain
* Corresponding author: Francesc Viñes (francesc.vines@ub.edu)
Electronic Supplementary Information (ESI) available: See DOI: 10.1039/x0xx00000x

This was shown in the seminal work of Yudanov *et al.* exemplified on Pd NPs,[30] exploiting the NPs point group symmetries, and later exploited on Pd and other late TMs using a periodic code and employing plane-waves as basis set.[31,32] This allowed the growingly use of such models to study heterogeneous catalysts and nanotechnological devices, profiting from the aforementioned description scalable towards the bulk limit or converged with size,[4,33] and the wise combination of NP with periodic slab models to present a rather complete description of larger NPs.[34,35]

Here we step forward to exploit high-performance parallel supercomputing facilities combined with a highly parallelized computational code using numeric atom-centred orbitals (NAOs) to push the limit of metal NPs description, allowing for a full shape analysis as a matter of size and permitting breakdown of the NPs energies either in terms of atomic contributions related to their coordination number (CN), or as NP geometric factors, both analyses allowing predicting the energy of any NPs independently of its size or shape. To this end Pd NPs are inspected, a common playground of previous analyses[30,31] and a nanomaterial of catalytic interest, *e.g.* nano-engineered Pd NPs are used in nitrite reduction,[36] or as catalysts for Suzuki cross-coupling reactions.[37]

Computational Details

Pd_n NPs with n ranging from 10 to 1504 atoms, this is, from the sub-nm size up to a size of ~4 nm, have been modelled for a wide variety of shapes. Specifically, besides the Truncated Octahedron (To) Wulff construction shape for Pd_n minimizing the overall NP surface tension,[38] other experimentally reported[39-42] shapes were considered that retain the bulk Pd face-centred cubic (*fcc*) arrangement such as Cube (C), Truncated Cube (Tc), Octahedron (Oh), Cuboctahedron (Ch), Spheres (S), Tetrahedron (Th), and Decahedron (Dh) shapes, plus Icosahedrons (Ih), with a distorted bulk Pd structure, see Fig. 1. All the shapes have been cut from *fcc* Pd bulk, except for Icosahedron shapes, and Spheres, the latter built from *fcc* Pd bulk, but defining a NP sphere radius to cut off outer Pd atoms.

Two main properties of the NPs were analysed: one geometrical, this is, the average interatomic distance between neighbouring Pd atoms, δ(Pd-Pd), and one energetic, in this case, the mean atomic cohesive energy, E_{coh}. Such features can be analysed depending on the NPs size, accounted either by $n^{-1/3}$, this is, following the spherical cluster approximation,[43] or by the average coordination number, CN_{av}, to examine the size-dependent evolution of NPs properties towards the bulk limit,[4,31,32,44,45] reached at $n^{-1/3} = 0$ and $CN_{av} = 12$ of bulk *fcc* Pd. This way, 94 NPs with different shapes were modelled, see the list of shapes in Table S1 of the Electronic Supplementary Information (ESI). These NPs account for a large diversity of sites with different CNs, allowing for breakdown of the energy based on either topological contributions,[44] or geometry components, as done earlier to isolate energies of steps on CeO_2 islands,[46] and energies of a row on Cu surfaces.[47]

The total energies of the locally optimized NPs were computed using non spin-polarized DFT calculations employing the PBE exchange-correlation functional,[27] as implemented within the all-electron full-potential Fritz-Haber Institute *ab initio* molecular simulations (FHI-aims) package.[48] There, Kohn-Sham orbitals were expanded using NAOs,[49,50] hierarchically constructed by adding functions to a minimal basis set to yield an accuracy of the total energy at the meV level. The calculations were performed employing the first light-tier basis set, which includes all most important basis functions. Relativistic effects were considered though the scaled zeroth order regular approximation (ZORA).[50,51]

To achieve the self-consistency of the electron density optimization, two criteria were imposed: The differences between consecutive steps of the total energy and atomic forces set to $1{\cdot}10^{-6}$ eV and $1{\cdot}10^{-4}$ eV·Å^{-1}, respectively. Furthermore, a Gaussian smearing parameter of 0.3 eV was used to speed up convergence. Geometrical optimizations were performed using the Broyden-Fletcher-Goldfarb-Shanno (BFGS) algorithm,[52,53] and equilibrium geometries were found once all atomic forces were smaller than $1{\cdot}10^{-2}$ eV·Å^{-1}.

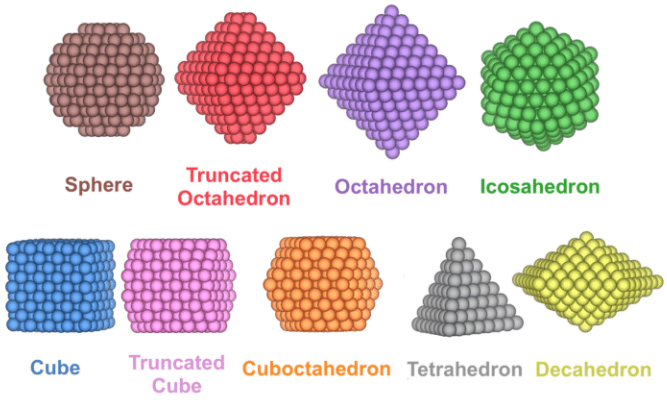

Fig. 1. Examples of the different shapes studied for Pd_n NPs.

Results and discussion

Once the Pd_n NPs of different shapes were optimized, see Fig. 1, the size-dependent evolution of the NPs properties towards the bulk limit was tackled. Note that the different shapes provide different surface features, *i.e.* different types of exposed facets, edges, and corners, that are later used to break down the NPs energies. Following previous studies, the first evaluated is δ(Pd-Pd) *versus* $n^{-1/3}$, see Fig. 2. The average minimum interatomic distances δ(Pd-Pd) calculated for each NP are listed in Table S2 of the ESI. A linear regression for each shape family was obtained, with intercepts, slopes, and regression coefficients listed in Table S3 of the ESI. The linear trends reveal structural information, as in all cases, δ(Pd-Pd) increases with NP size approaching the bulk limit here estimated to be 2.79 Å, succinctly implying NPs get more shrunk when reducing their size. The only outliers of this trend are Decahedron NPs, which feature a slightly larger extrapolated bulk limit of 2.82 Å, although this extrapolation could be biased by the reduced number of NPs used in the linear regression.

Notably, similar Cuboctahedron, Octahedron, Truncated Octahedron, and Truncated Cube shapes evolve similarly with size, also found for Spherical NPs, see Fig. 2. Icosahedron is the shape which features the longest distances, which becomes particularly evident for smaller NPs. Still, the maximum elongation of 0.03 Å is found for Ih Pd_{55} compared to To Pd_{55}, as a result of distorting the inner core NP *fcc* crystal structure at Icosahedron shapes. Conversely, Cube, Tetrahedron, and Decahedron shapes are the ones with the shortest δ(Pd-Pd) distances, again especially for small NPs, due to the surface strain of their peculiar edges.

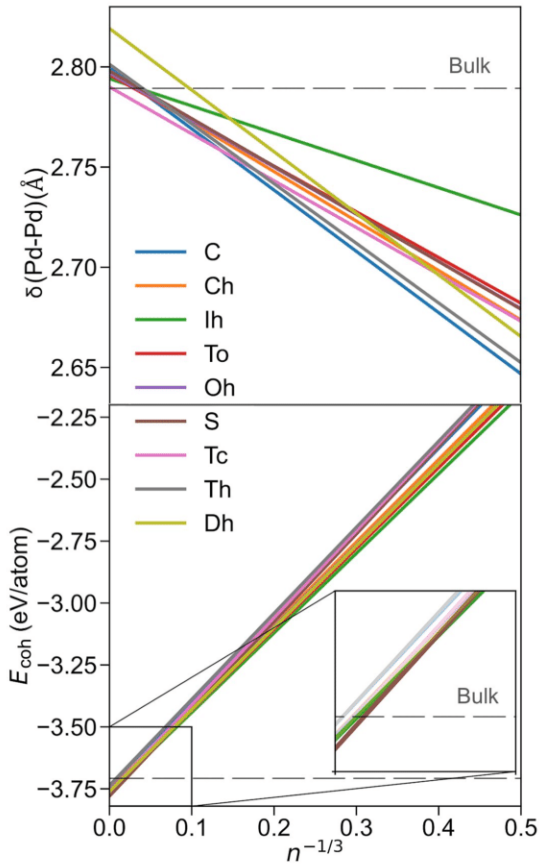

Fig. 2. Top panel: Evolution of δ(Pd-Pd) with size, here estimated by $n^{-1/3}$, where n is the number of Pd atoms of the NP. For a better readability of trends, only linear regressions are shown. Bottom panel: Evolution of the cohesive energy, E_{coh}, with $n^{-1/3}$. Colour coding as in Fig. 1.

In order to assess stability of the shape at different NP sizes, a linear regression for each shape was performed, see Fig. 2, where the E_{coh} values of each NP, listed in Table S4 of the ESI, are fitted respective to $n^{-1/3}$, (see regression parameters in Table S5 of the ESI). As one can readily notice, Icosahedron is the most stable shape for the smaller NPs, understandable as all the exposed surfaces are (111)-like, which is the most stable surface for Pd and other *fcc* TMs in general. Indeed, Icosahedron shape can be the most stable as long as the reduction of surface tension energy compensates the inner core deformation. Present results are in line with data of previous studies reporting Icosahedron shapes as the most stable for small NPs.[54,55]

However, Icosahedron shape ceases to be the preferred one at larger NPs sizes; from $n^{-1/3}$ = 0.053, *i.e. ca.* n = 6530, and NPs with a diameter Ø ~ 7 nm, the most stable shape is the Sphere, surprisingly different from the expected Truncated Octahedron shape derived from the Wulff construction,[38] and thus behaving different from other similar TMs, such as Pt.[56] Possible reasons for such a peculiar behaviour is that Wulff construction, in its mathematical shaping *ansatz*, accounts for neither edge nor corner energies. Aside, as aforementioned, Spherical NPs were shaped cutting off Pd atoms beyond a defined radius measured from the centre of an *fcc* bulk; this procedure actually yields for very small spherical NPs a truncated octahedron-like shape.

Furthermore, within the truncated octahedrons family it is possible to differentiate subgroups, depending on the degree of exposition {001} and {111} facets. Plotting subfamilies, the crossing points and stabilities vary (see linear regression coefficients in Table S6 of the ESI). As shown in Fig. 3, the Icosahedron shape is most stable up to $n^{-1/3}$ = 0.08, *i.e. ca.* n = 1500, and NPs with a diameter Ø ~ 4 nm. At larger sizes the Truncated Octahedron shape with a large exposure of {001} facets is preferred; indeed, close to a Cuboctahedral shape, but still quite more stable than the latter and the Octahedron shape, (see Figure S2 of the ESI). From the analysis of different Truncated Octahedron subfamilies it seems clear that the stability is reached upon exposing larger {001} facets. Still, one has to be cautious with such adjustments as, for some cases, the number of points in the linear regression is limited. Nevertheless, the present assessment indicates that the Wulff shape is an appropriate educated guess for large NPs, but this simplification misrepresents, as the present explicit calculations reveal, a larger {001} facet exposure than that resulting from the Wulff approach.[28,38]

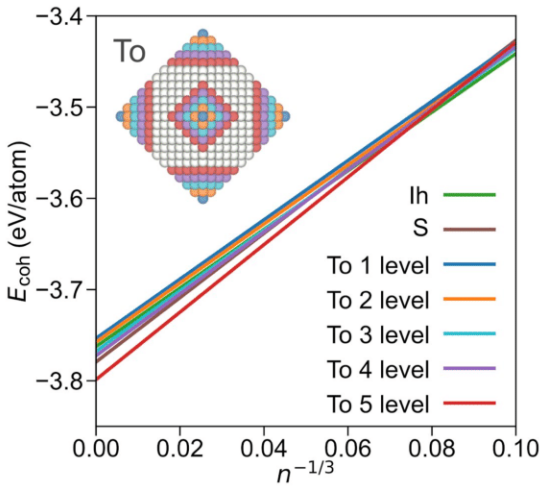

Fig. 3. Comparison of most stable Icosahedron and Sphere shapes and the Truncated Octahedron (To) shapes, split by each level of {001} cuts departing from Octahedron shapes. Inset NP image illustrates the removed atoms from each level from an Octahedron NP. Sphere and Icosahedron colour coding as in the signalled linear adjustments.

Small energy difference for different shapes, of *ca.* 0.02 eV/atom in the nm size region, implies that Pd NPs are malleable, and so, could easily adopt different shapes, as found experimentally.[39-42] Such shape modification can also be facilitated by the medium, in the sense that the released energy due to the adsorption of certain species on Pd NPs may compensate the energy cost required to change the shape.

Going beyond the mere size-dependency of δ(Pd-Pd) and E_{coh} of Pd NPs, the obtained data for a wide variety of NPs and shapes representing altogether 94 independent cases allows for an energy breakdown in terms of geometrical parameters as well as atomic coordination environment, which could ultimately enable predicting the energy of unexplored larger or different shape Pd NPs. This is tackled in the following focusing on either the atomic CN or geometrical features such as the number of vertexes, length of edges, surface areas, and NP volume.

For both approaches a multilinear regression is applied, a simple breakdown process, based on which understandable conclusions can be drawn. More than just the description, creating predictive tools is envisaged. Thus, following machine learning protocols, one would ideally split the data into training

and test sets. However, since the number of data is limited, that could bias the model depending on the selection of data for each set. Therefore, the regression is cross-validated by a shuffle split.[57] Briefly, the full set of data is randomly split *m* times in training and test sets, and each split is fitted and evaluated. Here, *m* = 100 and for each random split ¾ of the data has been assigned to training, and ¼ to testing, see Figure S1 in the ESI. The henceforth discussed regression coefficients and errors are thus averaged over 100 fittings.

The first proposed model is to decompose the NP energy, employing the atomic E_{coh}, as a function of the number of atoms and the CN of each type.[44] Thus,

$$\boldsymbol{E_{coh} = \sum_{i=1}^{CN} \varepsilon_i \chi_i + C} \quad (1),$$

where $\boldsymbol{\varepsilon_i}$ is the energy contribution to the E_{coh} of the atoms with a given *i* CN, and $\boldsymbol{\chi_i}$ is the fraction of Pd atoms with the *i* CN with respect the total number *n* of Pd atoms, see Table S7 of the ESI. Notice that an independent term is regarded, whereas the $\boldsymbol{\varepsilon_{12}}$ and $\boldsymbol{\chi_{12}}$ terms are not considered in the multilinear regression, since $\boldsymbol{\chi_{12}}$ is already correlated to the other atomic fractions. Further than that, CN = 1 and 2 terms are not featured in any of the studied NPs, and consequently disregarded as well. Moreover, Icosahedron shapes have not been initially regarded since, at variance with the other studied shapes, it features a distorted core *fcc* structure. Within such a treatment, the independent $\boldsymbol{C}$ term is the *fcc* Pd bulk cohesive energy, and the $\boldsymbol{\varepsilon_i}$ coefficients describe an energy destabilization contribution with respect to the Pd *fcc* bulk environment. Following this procedure, the obtained mean $\boldsymbol{\varepsilon_i}$ coefficients are:

$$\boldsymbol{E_{coh} = -3.72 + 1.95\chi_3 + 1.88\chi_4 + 1.47\chi_5 + 1.29\chi_6 + 1.01\chi_7 + 0.66\chi_8 + 0.52\chi_9 + 0.14\chi_{10} + 0.04\chi_{11}} \quad (2).$$

As one can notice, all the coefficients destabilize the atomic cohesive energy, and indeed, the more the lower is the CN. Fig. 4 evidences a clear linearity of coefficient destabilization with respect to CN, a finding to be expected for similar TMs. Note that very similar coefficients and a similar evolution of them with changing CN is achieved when accounting for the Icosahedron shape, see Equation S1 and Figure S3 of the ESI.

Going beyond the just mentioned basic adjustment, the mean test errors of the gained equation show an excellent agreement to the created model, with a regression coefficient of R^2 = 0.995, and, consequently an excellent associated mean absolute error (MAE) of solely 0.011 eV/atom. When accounting for Icosahedron shapes, the R^2 gets just slightly reduced, to R^2 = 0.972, and a twice larger MAE of 0.022 eV/atom is found. These results suggest that such an energy breakdown is suited for a quantitative analysis even when mixing different bulk crystal structures. Although the adjustment is visually quite accurate for *fcc* based NPs, see Figure 5, it clearly shows Icosahedron shapes as outliers, see Figure S4 of the ESI.

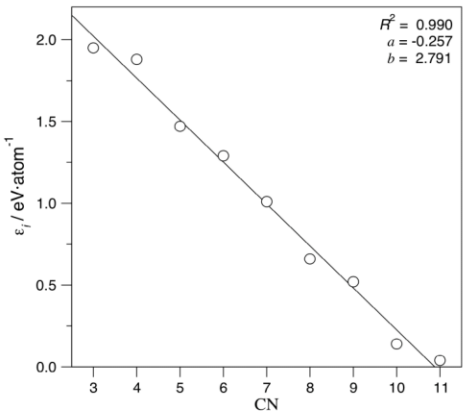

Fig. 4. Linear adjustment coefficients $\boldsymbol{\varepsilon_i}$ *vs.* CN. Regression coefficient, R^2, slope, *a*, and intercept, *b*, are also specified.

To assess the prediction capacity of the CN breakdown, a learning curve of the cross-validation (CV) analysis for training and test sets is shown in Figs. 5 and S5 of the ESI, increasing number of training set points while keeping the test points ratio. As expected, a small MAE below 0.02 eV/atom is achieved already for very small samples in the training set. On the CV, a MAE ~0.01 eV/atom is achievable using a reasonably small number of *ca.* 40 training samples, but fewer samples yields larger errors, given the low quantity of fitting data compared to the nine $\boldsymbol{\chi_i}$ variables, where at least the same number of data as variables is needed to solve the system equations. Thus, underfitting appears to be at the origin of the larger errors.

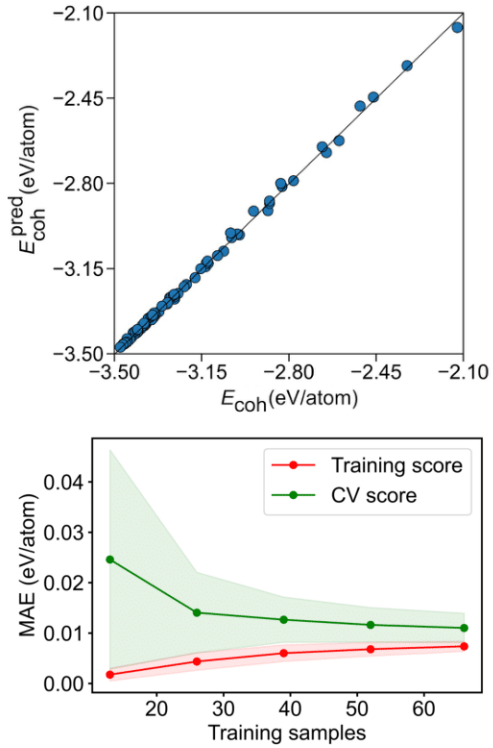

Fig. 5. Top panel: comparison of calculated E_{coh} *versus* the predicted E_{coh}, E_{coh}^{pred}, for the CN breakdown. Bottom panel: MAE learning curve for the training and CV scores. The coloured areas represent the standard variation limits as a result of the 100 different fittings.

As far as the geometric analysis is concerned, E_{coh} is fitted without defining any intercept for the topological features including the number of corners (C), the total longitude of edges (L), the total exposed area (A), and the NP volume (V), normalized by the number of Pd atoms, *n*, to have comparative values across sizes. Thus;

$$\boldsymbol{E_{coh} = \varepsilon_C \frac{C}{n} + \varepsilon_L \frac{L}{n} + \varepsilon_A \frac{A}{n} + \varepsilon_V \frac{V}{n}} \quad (3),$$

where $\boldsymbol{\varepsilon_C}$, $\boldsymbol{\varepsilon_L}$, $\boldsymbol{\varepsilon_A}$, and $\boldsymbol{\varepsilon_V}$ are the contributions to the atomic cohesive energy of the NP corners, edges, surfaces, and volume, respectively. In this case only regular shapes were considered, excluding the Sphere, Truncated Octahedron, and Truncated Cube shapes from the analysis. Thus, the extentof the dataset was reduced to 40 cases for only four fitting parameters, instead of the nine parameters used for the CN-based energy breakdown. Applying the same CV as explained before for the E_{coh} breakdown as a function of the atomic CN, and considering the same *m* = 100, and percentages of training (75%) and test (25%) sets, the obtained mean coefficients are:

$$\boldsymbol{E_{coh} = 0.54 \frac{C}{n} - 0.08 \frac{L}{n} - 0.29 \frac{A}{n} - 0.23 \frac{V}{n}} \quad (4).$$

These results clearly reveal that corners are the only topologic points detrimental to the atomic cohesive energy by 0.54 eV, due to their very low coordination. In this sense, NP edges slightly contribute in stabilizing the shape by -0.08 eV, and even more the surfaces, with the contribution of -0.29 eV, thus going along the increased coordination. Volume substantially contributes to the stabilization, by -0.23 eV, but curiously, less than surface. Such a result has to be taken with a grain of salt, since the NP volume is the topological feature actually contributing more to the NP cohesion, due to its highest coordination. This is because the NP volume is extensively larger than its exposed surface, particularly true for large NPs, see number of atoms with CN 12 in Table S7 and topological data in Table S8 of the ESI.

The calculated and predicted model E_{coh} values are compared in Fig. 6. It can be clearly seen that the geometry breakdown delivers a looser description compared to the CN breakdown, with the data rather dispersed. This is translated into a poorer regression coefficient of R^2 = 0.763 and a significantly higher MAE of 0.110 eV/atom. Even if the learning curve in Figure 6 reveals that the training set can reach rather accurate levels with a reduced number of samples, the CV score needs at least 15 points for the MAE to converge to 0.11 eV/atom. This refrains from quantitative using this energy breakdown method, although it seems useful for rapid, qualitative assessments.

Surely the accuracy of this method is biased by the small number of variables, which often mix different situations. For instance, all exposed surfaces are treated equally, *e.g.* considering (001) and (111) types of facets the same, even if their surface energy is different.[28] The same occurs for edges, as there are different types, depending on via which side facets connects, this is, it is expectable that edges separating (001) and (111) facets have different energy than those between (111) facets. Finally, different kinds of corners are present, with different CNs and spatial positions of the neighbouring atoms.

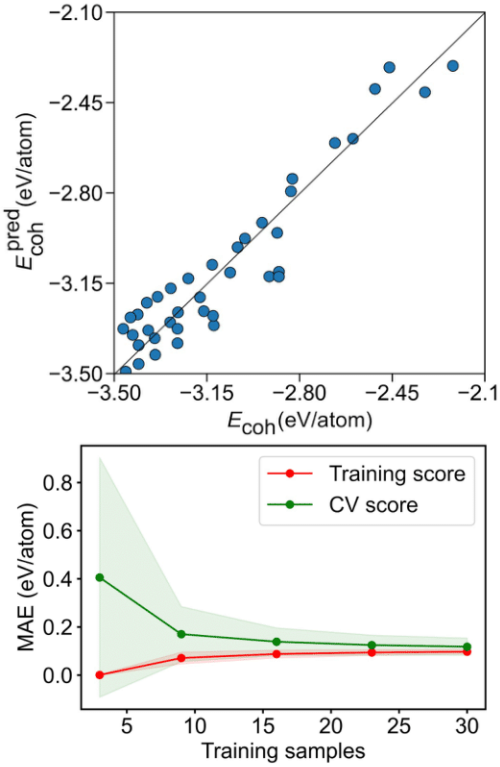

Fig. 6. Top panel: comparison of calculated E_{coh} *versus* the predicted E_{coh}, E_{coh}^{pred}, for the geometry breakdown. Bottom panel: MAE learning curve for the training and CV scores. The coloured areas represent the standard variation limits as a result of the 100 different fittings.

To assess this effect we decomposed, for the Cube, and Octahedron families, the total energy of the samples as a function of bulk *fcc* Pd energies, plus the contributions to the energy corresponding to surface, edge, and corner energies, following a procedure earlier employed to obtain step and row energies.[46,47] According to it, the cubic and octahedron NPs energies can be decomposed as

$$\boldsymbol{E = n\varepsilon_{bulk} + \gamma A + \beta L + \xi C} \quad (5),$$

where $\boldsymbol{\varepsilon_{bulk}}$ is the energy of a single Pd atom in the bulk Pd *fcc* structure, and $\boldsymbol{\gamma}$, $\boldsymbol{\beta}$, and $\boldsymbol{\xi}$ are surface, edge, and point energies, respectively. Notice that for cubic NPs, the whole exposed area *A* belongs to (001) type of surfaces, and so $\boldsymbol{\gamma}$ corresponds to the (001) surface energy, while *L* longitudes belong to edges between (001) facets, and so define the edge energy, β. Finally, the corner energies, $\boldsymbol{\xi}$, are for corners having vicinal (001) facets. Likewise one can decompose the energy of Octahedron NPs, but relating to the (111) facets only.

The obtained surface, edge, and corner energies are displayed in Table 1. From Cubes and Octahedrons one gains (001) and (111) facets energies of 0.09 and 0.08 eV·Å^2, this is, values of 1.41 and 1.24 J·m^{-2}, respectively. These values somewhat differ from the extended surfaces estimations using slab models of 1.5 and 1.14 J·m^{-2}. Thus, on such Pd NPs, (001) surfaces become somewhat more stable, by 0.09 J·m^{-2}, while (111) surfaces become less stable by 0.10 J·m^{-2}. This difference has its origin at the reduction of δ(Pd-Pd) distance, and how this affects the particular energy of such facets, and also at the stabilization or destabilization of the Pd atoms located at the

facets boundary regions. Regardless of this, these data already explains the Truncated Octahedron preferential shape shown in Fig. 3, as the (001) surfaces are to be largely exposed.

Table 1 Surface, γ, edge, β, and point ξ energies, given in eV·Å^{-2}, eV·Å^{-1}, and eV, respectively, estimated for Cubic and Octahedral Pd NPs using Eq. 5.

NPs	$\gamma_{(001)}$	$\gamma_{(111)}$	$\beta_{(001)}$	$\beta_{(111)}$	ξ
C	0.09	—	0.27	—	0.07
Oh	—	0.08	—	0.27	-0.50

Interestingly, this change of shape does not compromise edge energy, being the same, 0.27 eV·Å^{-1}, for edges connecting either (001) facets or (111) facets. The point energy of corners differs substantially, from 0.07 eV for Cubes, to -0.50 eV for Oh; however, these contributions barely affect the overall surface tension as their number are quite small compared to the exposed facets area and edges lengths, particularly true for large NPs, see Table S8 of the ESI.

Conclusions

The present study addresses explicitly optimized by DFT Pd$_n$ clusters and NPs including a vast myriad of shapes, and reaching unprecedented sizes of $n \sim 1500$ atoms and diameter $\emptyset \sim 4$ nm. The size evolution of the mean neighbouring Pd-Pd distances, δ(Pd-Pd), and the atomic cohesive energy, E_{coh}, towards the bulk limit are shown to be linear with respect to $n^{-1/3}$ for all considered NP shapes. From the analysis of NP shape dependence on their size, the Icosahedral shape with the bulk structure distorted *vs. fcc* resulted as the most stable for NPs with up to 1500 Pd atoms. From this size on, the Truncated Octahedron shape with a large exposure of (001) facets appears to become the most stable. The Wulff construction model is partially followed, but with a presence of larger (001) facets. The latter is shown here to be due to stronger stabilization of (001) facets and a similar destabilization for (111) facets.

The large number of studied structures, 94, and the variety of shapes, nine different families, allowed decomposing E_{coh} in terms of atomic contributions grouped by CN, as well as geometric contributions accounting for number of corners, edges lengths, facets areas, and NP volumes. The energy breakdown based on CNs is found to be quantitative, with a MAE of solely 0.01 eV·atom^{-1}, for NPs with *fcc* arrangement of Pd bulk. Including Icosahedrons with a different arrangement of inner Pd atoms only slightly rises the MAE to 0.02 eV·atom^{-1}. The breakdown reveals the smaller the CN, the larger the destabilization from the bulk cohesive energy is.

The breakdown employing geometric terms, performed on a subset of 40 NPs with a clearly defined geometry, featured a poorer accuracy with a MAE of 0.11 eV·atom^{-1}. Yet, this is sufficient for a qualitative assessment, for instance, revealing that corner points are the only destabilizing geometric feature. The reduced accuracy of this model is related to accounting for all exposed facets, edges, and corners with the same energetic contributions, although the present DFT data analysis reveals that they may significantly differ from each other.

Conflicts of interest

There are no conflicts to declare.

Acknowledgements

This work was supported by Spanish MINECO/FEDER grant CTQ2015-64618-R, Spanish MICIUN-FEDER RTI2018-095460-B-I00 and PGC2018-093863-B-C22 grants and the Spanish Structures of Excellence *María de Maeztu* program through grant MDM-2017-0767, and in part by *Generalitat de Catalunya* grants 2017SGR13 and XRQTC. L. V. thanks funding to *Generalitat de Catalunya via* a pre-doctoral grant 2018FI-B-00384. F. V. thanks the Spanish MINECO for his research contract under the *Ramón y Cajal* Program (RYC-2012-10129).

Notes and references

1 E. Pomerantseva, F. Bonaccorso, X. Feng, Y. Cui and Y. Gogotsi, *Science*, 2019, **366**, eaan8285.
2 A. Raghunath and E. Perumal, *Int. J. Antimicrob. Agents*, 2017, **49**, 137–152.
3 M. Kumar and K. Raza, *Pharm. Nanotechnol.*, 2017, **5**, 169–179.
4 F. Viñes, J. R. B. Gomes and F. Illas, *Chem. Soc. Rev.*, 2014, **43**, 4922–4939.
5 A. J. Medford, A. Vojvodic, J. S. Hummelshøj, J. Voss, F. Abild-Pedersen, F. Studt, T. Bligaard, A. Nilsson and J. K. Nørskov, *J. Catal.*, 2015, **328**, 36–42.
6 M. Haruta, N. Yamada, T. Kobayashi and S. Iijima, *J. Catal.*, 1989, **115**, 301–309.
7 J. N. Kuhn, W. Huang, C. Tsung, Y. Zhang and G. A. Somorjai, *J. Am. Chem. Soc.*, 2008, **130**, 14026–14027.
8 A. Corma, M. Boronat, S. González and F. Illas, *Chem. Commun.*, 2007, 3371–3373.
9 F. Baletto, R. Ferrando, A. Fortunelli, F. Montalenti and C. Mottet, *J. Chem. Phys.*, 2002, **116**, 3856–3863.
10 S. Krüger, S. Vent and N. Rösch, *Ber. Bunsen Phys. Chem.*, 1997, **101**, 1640–1643.
11 C. M. Sánchez-Sánchez, J. Solla-Gullón, F. J. Vidal-Iglesias, A. Aldaz, V. Montiel and E. Herrero,. *J. Am. Chem. Soc.*, 2010, **132**, 5622–5624
12 S. Mitchell, R. Qin, N. Zheng, J. Pérez-Ramírez, *Nat. Nanotechnol.*, 2021, **16**, 129–139.
13 A. S. Barnard and L.A. Curtiss, *ChemPhysChem* 2006, **7**, 1544–1553.
14 Y. Maeda, M. Okumura, S. Tsubota, M. Kohyama and M. Haruta, *Appl. Surf. Sci.*, 2004, **222**, 409–414.
15 O. H. Pakarinen, C. Barth, A. S. Foster, R .M. Nieminen and C. R. Henry, *Phys. Rev. B*, 2006, **73**, 235428.
16 T. Akita, M. Okumura, K. Tanaka, M. Kohyama and M. Haruta, *J. Mater. Sci.*, 2005, **40**, 3101–3106.
17 U. Heiz, A. Sanchez, S. Abbet and W.-D. Schneider, *J. Amer. Chem. Soc.,* 1999, **121**, 3214–3217.
18 E. Aprà, R. Ferrando and A. Fortunelli, *Phys. Rev. B,* 2006, **73**, 205414.
19 X. Yang, W. Cai and X. Shao, *J. Phys. Chem. A*, 2007, **111**, 5048–5056.
20 K. P. McKenna, P. V. Sushko and A. L. Shluger, *J. Chem. Phys.*, 2007, **126**, 154704.
21 D. Ricci, A. Bongiorno, G. Pacchioni and U. Landman, *Phys. Rev. Lett.,* 2006, **97**, 36106.
22 N. T. Wilson and R. L. Johnston, *J. Mater. Chem.*, 2002, **12**, 2913–2922.
23 S. M. Kozlov, H. A. Aleksandrov, J. Goniakowski and K. M. Neyman, *J. Chem. Phys.*, 2013, **139**, 084701.
24 H. Prats, R. A. Gutiérrez, J. J. Piñero, F. Viñes, S. T. Bromley, P. J. Ramírez, J. A. Rodriguez and F. Illas, *J. Am. Chem. Soc.*, 2019, **141**, 5303–5313.

25 K. C. Ko, S. T. Bromley, J. Y. Lee and F. Illas, *J. Phys. Chem. Lett.,* 2017, **8**, 5593–5598.
26 F. Viñes, O. Lamiel-Garcia, F. Illas and S. T. Bromley, *Nanoscale,* 2017, **9**, 10067–10074.
27 J. P. Perdew, K. Burke and M. Ernzerhof, *Phys. Rev. Lett.*, 1996, **77**, 3865–3868.
28 L. Vega, J. Ruvireta, F. Viñes and F.Illas, *J. Chem. Theory Comput.*, 2018, **14**, 295–403.
29 L. Vega and F. Viñes, *J. Comput. Chem.*, 2020, 41, 2598–2603.
30 I.V. Yudanov, R. Sahnoun, K .M. Neyman and N. Rösch, *J. Chem. Phys.,* 2002, **117**, 9887–9896.
31 F. Viñes, F. Illas and K. M. Neyman, *J. Phys. Chem. A,* 2008, **112**, 8911–8915.
32 A. Roldán, F. Viñes, F. Illas, J. M. Ricart and K. M. Neyman, *Theor. Chem. Acc.,* 2008, **120**, 565–573.
33 S. M. Kozlov and K.M Neyman, *Top. Catal.,* 2013, **56**, 867–873.
34 F. Viñes, Y. Lykhach, T. Staudt, M. P. A. Lorenz, C. Papp, H.-P. Steinrück, J. Libuda, K. M. Neyman and A. Görling, *Chem. Eur. J.,* 2010, **16**, 6530–6539.
35 S. M. Kozlov and K. M. Neyman, *J. Catal.*, 2016, **337**, 111-121.
36 Z. Zhang, J. Lu, B. Zhang, W. Shi, Y. Guo, F. Cui, *Environ. Sci.: Nano*, 2020, **7**, 2117–2129.
37 M. Pérez-Lorenzo, *J. Phys. Chem. Lett.*, 2012, **3**, 167–174.
38 J. Ruvireta, L. Vega and F. Viñes, *Surf. Sci.*, 2017, **664**, 45-49.
39 S. Yang, C. Shen, Y. Tian, X. Zhang and H.-J. Gao, *Nanoscale*, 2014, **6**, 13154–13162.
40 N. Fujie, M. Yugo, M. Kohsuke, M. Tomoo, E. Kohki and K. Kiyotomi, *Chem. Lett.*, 2006, **35**, 276–277.
41 H. Zhao, W. Qi, W. Ji, T. Wang, H. Peng, Q. Wang, Y. Jia and J. He, *J. Nanopart. Res.*, 2017, **19**, 162.
42 Q. Zhang, J. Xie, J. Yang and J. Y. Lee, *ACS Nano*, 2009, **3**, 139–148.
43 R. Johnston, Masters Series in Physics and Astronomy, in *Atomic and Molecular Clusters*, Taylor and Francis, London, 2002.
44 E. M. Dietze, P. N. Plessow and F. Studt, *J. Phys. Chem. C,* 2019, **123**, 25464–25469.
45 B. Farkaš and N. H. Leeuw, *Nanotechnology,* 2020, **31**, 195711.
46 S. M. Kozlov, F. Viñes, N. Nilius, S. Shaikhutdinov and K. M. Neyman, *J. Phys. Chem. Lett.*, 2012, **3**, 1956–1961.
47 L. Álvarez-Falcón, F. Viñes, A. Notario-Estévez and F. Illas, *Surf. Sci.*, 2016, **646**, 221–229.
48 V. Blum, R. Gehrke F. Hanke, P. Havu, V. Havu, X. Ren, K. Reuter and M. Scheffler, *Compu. Phys. Commun.*, 2009, **180**, 2175–2196.
49 V. Havu, V. Blum, P. Havu and M. Scheffler, *J. Comput. Phys.,* 2009, **228**, 8367–8379.
50 E. van Lenthe, E. J. Baerends and J. G. Snijders, *J. Chem. Phys.*, 1994, **101**, 9783-9792.
51 C. Chang, M. Pelissier and P. Durand, *Phys. Scr.*, 1986, **34**, 394–404.
52 W. H. Press, S. A. Teukolsky, W. T. Vetterling and B.P. Flannery, *Numerical recipes: the art of scientific computing*. (Cambridge University Press, 2007).
53 J. Nocedal and S. Wright, *Numerical Optimization*. (Springer New York, 2006).
54 T. Rapps, R. Ahlrichs, E. Waldt, M.M. Kappes and D. Schooss, *Angewandte Chemie International Edition*, 2013, **52**, 6102-6105.
55 M. J. Piotrowski et al., *J. Phys. Chem. C,* 2016, **120**, 28844–28856.
56 F. Viñes and A. Görling, *Chem. Eur. J.*, 2020, **26**, 11478–11491.
57 M. Stone, *J. R. Stat. Soc. Series B Stat. Methodol.*, 1974, **36**, 111–147.

PART III. RESULTS OF BIMETALLIC SYSTEMS

Chapter 6. Chemical Ordering of Bimetallic Nanoparticles

6.1 INTRODUCTION

Bi- or multicomponent metallic particles are known as nanoalloys. Among the peculiarities of these systems are the complexity of their geometrical structures and the dependence of their properties not only on the size, like in the monometallic particles, but also on the composition. The notably increased complexity makes studies of the nanoalloys challenging both from the experimental and theoretical points of view. The presence of the second metal makes necessary determining the composition and the chemical (or atomic) ordering. The chemical ordering is the pattern in which atoms of different metals are spatially arranged with respect to each other within the crystalline positions of the NP under scrutiny. One can differentiate between the mixing and the non-mixing patterns. Among the mixing patterns, ordered phases and completely mixed solutions exist depending on the component miscibility in the bulk (see Figure 6.1).

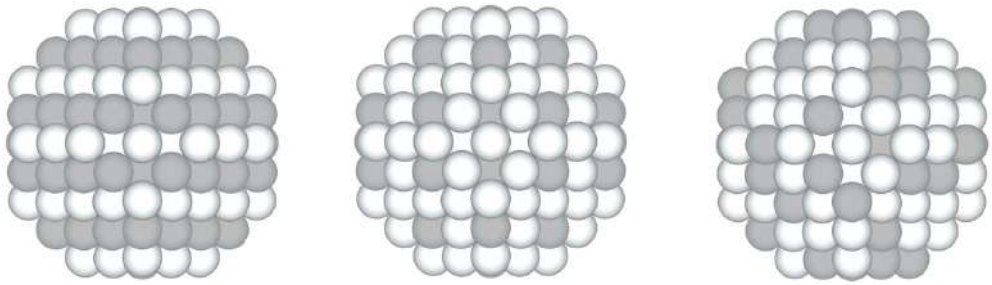

Figure 6.1 Representation of different mixing patterns from the ordered phases, left panels, and the completely random mixing, right panel.

The non-mixing chemical ordering patterns are characterized by phase separation. Common structures of this group are of core@shell types, meaning that A-type atoms form a compact inner aggrupation, and all B-type atoms are located at the outer shell. The notation specifying the atoms A of the core and B of the shell is A@B core@shell. At variance, the location of A and B atoms on the opposite sides of the NP results in the so-called Janus structure (see Figure 6.2). There are also other intermediate types of the chemical ordering patterns besides these most significant ones to be addressed in the following. Among the factors favoring the segregation of A and B atoms are their weak miscibility in the bulk, different surface energies of the two metals and a mismatch of atomic size triggering the larger atoms to be located on the surface to reduce the atomic stress.[67]

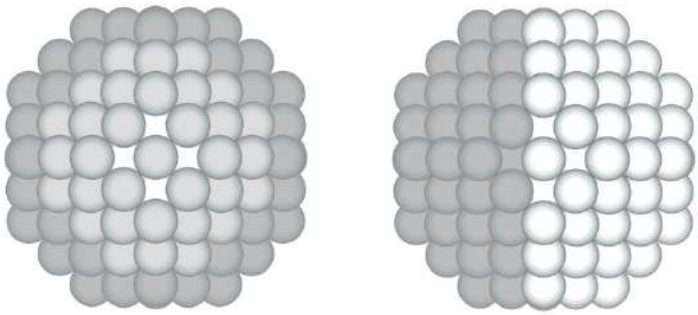

Figure 6.2 Representation of most relevant non-mixing patterns the core@shell structure on the left and the Janus structure on the right. Atoms A – grey spheres, atoms B – white spheres. The notation of the core-shell structure is A@B.

All possible chemical orderings of atoms in a NP with a given shape, size, and composition are called *homotops*. The latter are defined as the structures which differ only by permutations of atoms of different elements.[68] Simulating the chemical ordering is a highly challenging combinatorial problem of considering a huge number of homotops N_{hom} estimated for a NP comprising N_A atoms A and N_B atoms B, $N = N_A + N_B$, to be

$$N_{hom} \approx \frac{N!}{N_A!\,N_B!} \qquad (6.1).$$

Complexity of this problem grows very rapidly with the size increase of NPs. For instance, already a ~2 nm large bimetallic crystallite of 200 atoms

can feature a colossal number of up to 10^{50} homotops,[69] direct consideration of all of them is excessive for any computational method. To overcome this hurdle, our present studies employ a lattice-model approach recently developed in the research group of Prof. Neyman. The so-called topological (TOP) method allows to efficiently determine the lowest-energy chemical ordering of a bimetallic NP by parameterizing the energies of some homotops calculated by DFT.[37] In this methodology, the DFT energy of a NP, E_{DFT}, is approximated by the topological energy, E_{TOP}, defined as,

$$E_{TOP} = \varepsilon_{BOND}^{A-B} N_{BOND}^{A-B} + \varepsilon_{CORNER}^{A} N_{CORNER}^{A} + \varepsilon_{EDGE}^{A} N_{EDGE}^{A} + \varepsilon_{FACET}^{A} N_{FACET}^{A} + E_0 \quad (6.2),$$

where N_{BOND}^{A-B} is the number of heteroatomic bonds (nearest-neighbour A-B contacts), the N_{CORNER}^{A}, N_{EDGE}^{A}, and N_{FACET}^{A} are the numbers of A atoms on corners, edges and facets sites, respectively (see Figure 6.3).

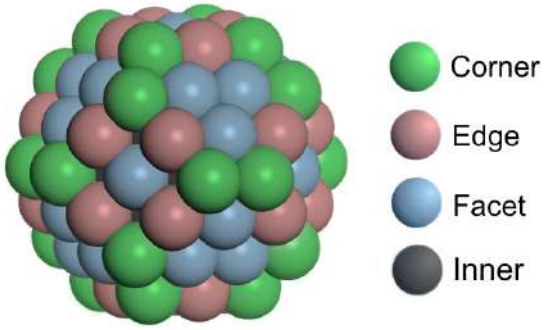

Figure 6.3 Different surface atomic positions in a truncated-octahedral *fcc* metal NP of 116 atoms.

Other variables, such as N_{BOND}^{A-A}, N_{BOND}^{B-B}, N_{CORNER}^{B}, N_{EDGE}^{B} and N_{FACET}^{B} or N_{INNER}^{A}, and N_{INNER}^{B} are not considered, mainly to avoid the linear dependence with the employed variables for a given NP size and composition. E_0 is the practically unimportant fitting intercept, a constant shift between the DFT and TOP energies, disappearing in the equation for the energy difference between two homotops, ΔE_{TOP},

$$\Delta E_{TOP} = \varepsilon_{BOND}^{A-B} \Delta N_{BOND}^{A-B} + \varepsilon_{CORNER}^{A} \Delta N_{CORNER}^{A} + \varepsilon_{EDGE}^{A} \Delta N_{EDGE}^{A} + \varepsilon_{FACET}^{A} \Delta N_{FACET}^{A} \quad (6.3),$$

ε_i are the energetic parameters associated with the corresponding N_i, as known as descriptors; not to be confused with the chemical descriptors

exposed in Chapter 4. Each topological descriptor has a specific physical meaning. For instance, ε_{BOND}^{A-B} characterizes the gain or loss of energy upon creating one heteroatomic bond.

The descriptors are obtained following an iterative procedure depicted on Figure 6.4. First, a set of descriptors is used as a first guess to the TOP equation. They are employed to generate new homotops through a MC simulation. The lowest energy homotops generated are then optimized within the DFT approach. The obtained DFT energies will then be compared with the corresponding TOP energies. In case of poor agreement, the descriptors will be fitted using the obtained DFT energies of the generated and previous homotops, if any. This procedure will be repeated until a good agreement between DFT and TOP energies is obtained. The double residual standard deviation (δ) (see equation 6.4) and the difference between the minimum E_{TOP} value and the E_{TOP} value corresponding to the minimum DFT energy homotop are used to evaluate the agreement between DFT and TOP energies.

$$\delta = 2\sqrt{\frac{\sum(E_{DFT} - E_{TOP})^2 - \frac{(\sum(E_{DFT} - E_{TOP}))^2}{N_{TEST}}}{N_{TEST} - 1}} \qquad (6.4).$$

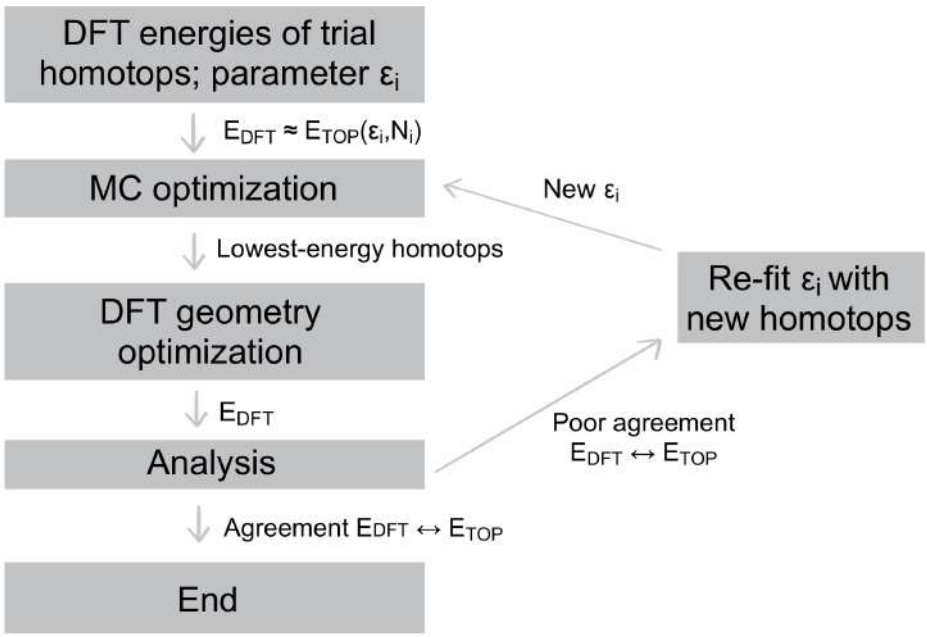

Figure 6.4 Iterative procedure diagram followed by E_{TOP} to obtain the final set of topological descriptors.

The present MC simulations were performed as described in Ref. [36].The TOP method addresses the chemical orderings of NPs in vacuum without explicitly considering effects of reactive environments or interactions with supports on which bimetallic NPs under scrutiny are deposited in experiments and applications. The environment and support effects on the nanoalloys are important because they could change not only the chemical ordering, but also the shape of the particles. Therefore, the effects of reactive environment on the NPs are evaluated in this Thesis employing the data provided by the TOP method.

6.2 OBJECTIVES

Objectives of the studies presented in this Chapter are to computationally predict and analyse chemical orderings in the bimetallic NPs PdRh (Section 6.3), PtNi (Section 6.4), PtCu, PtAg and PtAu (Section 6.5) with *fcc* crystallinity and different contents of two metals. The modelling procedure consisted of DFT calculations of the NPs in the routinely accessible particle size ranges of up to *ca.* 200 atoms, using the DFT ordering/energy relations data to parameterize the TOP equations enabling efficient Monte Carlo pre-screening of the lowest-energy orderings with subsequent validation of the latter (and of the TOP equations) by DFT energy minimization. The resulting TOP equations have been applied to determine by Monte Carlo calculations the lowest-energy chemical orderings in the NPs of the same metal combinations with more than a thousand atoms, which are too large for DFT treatment. Using this simplified computational procedure, temperature effects on the surface segregation and related rearrangements of the chemical orderings have been studied and estimates of the surface sites changes by typical adsorbates and reactants from the gas-phase environment have been performed.

6.3 USING DENSITY FUNCTIONAL CALCULATIONS TO ELUCIDATE ATOMIC ORDERING OF PdRh NANOPARTICLES AT SIZES RELEVANT FOR CATALYTIC APPLICATIONS

6.3.1 Summary

Introduction The first studied bimetallic nanosystem is PdRh. Its NPs form a promising nanomaterial catalysing a variety of reactions, including CO oxidation,[70] three-way converters in the exhaust pipes of gasoline-powered engines,[71,72] glucose oxidation,[73] Suzuki cross-coupling,[74] and many hydrogenation reactions,[75] among other processes.[76,77]For this reason, we selected PdRh to deeper investigate chemical ordering in its bare NPs with different contents of the constituting metals and then to predict the surface restructuring elevated temperature and in the presence of reactive environment. Also, a previous research on the modelling of the atomic ordering of cuboctahedral 55-atomic PdRh NPs that combined DFT calculations with cluster expansion approach[78] provided a reference for comparing bare and oxygen-covered NPs of different compositions.[79] These results revealed a simple alloying behaviour and a strong tendency of forming Rh@Pd core@shell structures for bare NPs. The presence of adsorbed atomic O causes surface segregation of Rh up to a reverse pattern Pd@Rh is formed at higher O coverage. The presently studied NPs are bigger, to belong to the scalable-with-size regime, thus making the ordering patterns representative of those in much larger PdRh NPs of technologically relevant size range. So, we modelled Pd-Rh NPs of different Pd:Rh ratios comprising from 140 to 3630 atoms (1.4 to 5.4 nm, respectively) using for determining the equilibrium atomic ordering of large bimetallic NPs the methodology introduced above, and based on 6.5 of the type of equation 6.3.[36,80]

$$\Delta E_{TOP} = \varepsilon_{BOND}^{Pd-Rh}\Delta N_{BOND}^{Pd-Rh} + \varepsilon_{CORNER}^{Pd}\Delta N_{CORNER}^{Pd} + \varepsilon_{EDGE}^{Pd}\Delta N_{EDGE}^{Pd} + \varepsilon_{FACET}^{Pd}\Delta N_{FACET}^{Pd} \quad (6.5).$$

The data of Wang *et al.* for 55-atom particles served as a reference [74] not expected to be dramatically changed for the chemical ordering pattern of

larger NPs driven by the lower surface energy of Rh compared to Pd and the absent miscibility of Pd and Rh atoms in the bulk of PdRh alloys.

Among the aims of the study outlined in the present Section are *i)* to determine using DFT calculations the most stable atomic orderings and segregation effects in PdRh NPs containing up to 201 atoms at different Pd:Rh ratios; *ii)* to employ the developed Topological models to predict preferred atomic orderings in inaccessible by DFT larger PdRh NPs with sizes 4-5 nm common for catalytic metal particles; and *iii)* to evaluate surface segregation effects induced by adsorbates on the arrangement of surface sites exposed by Pd-Rh nanoalloy catalysts.

The author of the Thesis contributed to this work by performing DFT calculations of the model NPs $Pd_{51}Rh_{150}$, $Pd_{101}Rh_{100}$, and $Pd_{151}Rh_{50}$, generating the TOP equations from these data, analysing the temperature effects on the chemical ordering in larger NPs, studying the adsorption-induced resurfacing of Rh atoms, preparing images, tables, Supporting Information and other material for publication as well as writing a part of the description of results and discussion of the published article. The published article is shown at the end of present summary.

Results The main result for the atomic ordering obtained for the PdRh NPs is a clear preference of Pd atoms vs. Rh atoms to occupy under-coordinated surface positions and the formation of non-mixed patterns. Particularly, 73% of the surface of $Pd_{70}Rh_{70}$ is occupied by Pd atoms, including all corner and edge positions and a part of terrace positions. Rh atoms form a complete core and expose compact nano-islands on terraces (see Figure 6.5).

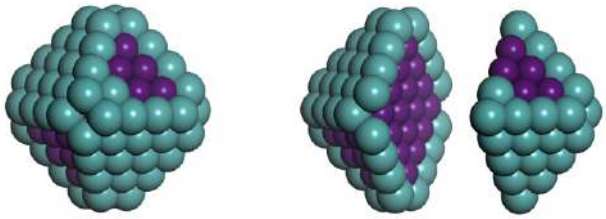

Figure 6.5 Atomic ordering in the lowest-energy homotops of $Pd_{70}Rh_{70}$ particle. As shown in the split image of the particle in the right panel, its inner region consists of Rh atoms only. Color coding: Pd – turquoise, Rh – purple.

Also, in a larger 201-atomic $Pd_{101}Rh_{100}$ NP of the same 1:1 composition Pd atoms are notably stabilized on the surface (see Figure 6.6), with the least-coordinated surface sites of corners being preferred ones and the most-coordinated surface sites on {111} terrace stabilized less than others. Here, at variance with $Pd_{70}Rh_{70}$ particle, Pd atoms do not form a complete shell, because it is not enough atoms to form it. Changing the Pd:Rh composition at the same size and shape of the NPs, at lower Pd content of $Pd_{50}Rh_{151}$ NP the relative sites stability dependence on the CN varies slightly making the 7-coordinated site (edge) the most energetically preferable instead of the 6-coordinated site (corner). In this case all 50 Pd atoms are located on the surface, where 72 Rh atoms are also present. Contrary, due to a higher content of Pd, there is enough Pd atoms in $Pd_{151}Rh_{50}$ NP to complete the outer shell by 122 atoms and remaining 29 Pd atoms are located in the inner positions.

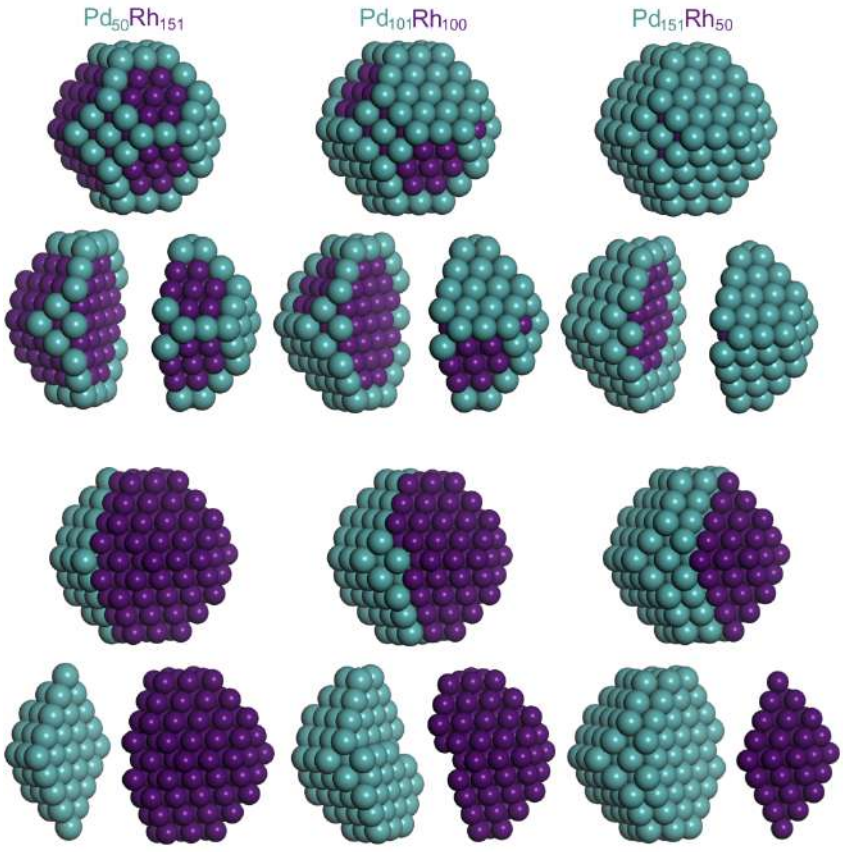

Figure 6.6 Atomic ordering in the lowest-energy (upper two rows) and Janus-type (lower two rows) homotops 201-atomic NPs with $Pd_{50}Rh_{151}$, $Pd_{101}Rh_{100}$ and $Pd_{151}Rh_{50}$. Colour coding as in Figure 6.5.

To quantify the miscibility of two metal components in PdRh NPs, one can compare the lowest-energy homotops with those featuring the most separated components in the so-called Janus-type atomic ordering (bottom panel of Figure 6.6). The latter structures possess around a half of the (slightly) destabilizing PdRh bonds compared to the corresponding found lowest-energy homotops, 96 *vs.* 197 for $Pd_{50}Rh_{151}$, 128 *vs.* 270 for $Pd_{101}Rh_{100}$, and 96 *vs.* 208 for $Pd_{151}Rh_{50}$. However, both DFT and TOP energies of the Janus-type homotops are notably higher than energies of the respective lowest-energy homotops. The cause of such a difference is a strong propensity of Pd atoms to be on the surface over Rh atom. Another measure of the miscibility of metal components at the nanoscale is the so-called excess energy (E_{exc}), which for the 201-atomic PdRh NPs under discussion reads

$$E_{exc}(Pd_{201-n}Rh_n) = \frac{E(Pd_{201-n}Rh_n) - \left(\frac{201-n}{201}\right)E(Pd_{201}) - \left(\frac{n}{201}\right)E(Rh_{201})}{201} \qquad (6.6).$$

There, from the energy of the PdRh system, $E(Pd_{201-n}Rh_n)$, one subtracts the proportional fraction of energy of the pure monometallic NPs of each component, $E(Pd_{201})$ and $E(Rh_{201})$, of the same size and geometry as the evaluated nanoalloy particle. The calculated negative E_{exc} values (see Figure 6.7) indicate miscibility of Pd and Rh components in terms of the preference of partially separated core@shell Rh@Pd structures over the Janus-type structures with completely separated Pd and Rh components.

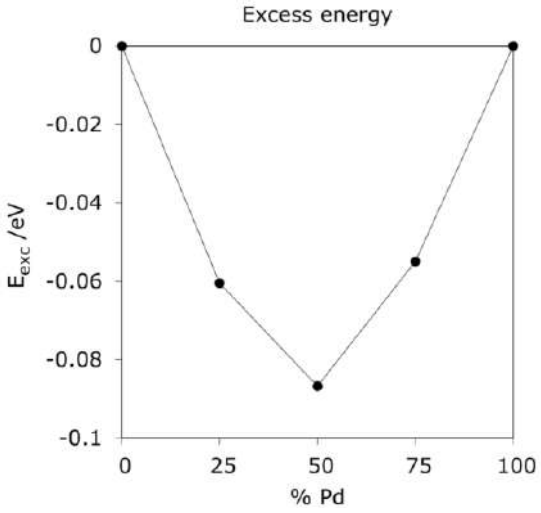

Figure 6.7 DFT excess energies E_{exc} per atom of $Pd_{201-n}Rh_n$ (n = 50, 100, 151) NPs.

Employing the energetic parameters from the TOP equations for 140 and 201 atomic NPs (Table 1), the equilibrium atomic orderings were calculated in truncated octahedral and cuboctahedral PdRh NPs of 1463 and 3630 atoms (see Figure 6.8 and Figure 6.9).

Table 6.1 Descriptors ε_i [a] in the topological energy expressions ΔE_{TOP}[b] for Pd-Rh nanoparticles of 1:3 ($Pd_{50}Rh_{151}$), 1:1 ($Pd_{70}Rh_{70}$, $Pd_{101}Rh_{100}$,), and 3:1 ($Pd_{151}Rh_{50}$) compositions. All energies are given in meV.

	$Pd_{50}Rh_{151}$	$Pd_{101}Rh_{100}$ $Pd_{70}Rh_{70}$	$Pd_{151}Rh_{50}$
$\varepsilon_{BOND}^{Pd-Rh}$	18_{-21}^{+14}	24_{-6}^{+6} 21_{-2}^{+2}	32_{-7}^{+6}
$\varepsilon_{CORNER}^{Pd}$	-603_{-87}^{+60}	-755_{-83}^{+101} -814_{-23}^{+34}	-691_{-95}^{+91}
ε_{EDGE}^{Pd}	-631_{-152}^{+107}	-536_{-47}^{+40} -588_{-37}^{+26}	-597_{-46}^{+39}
$\varepsilon_{TERRACE}^{Pd}$	-544_{-75}^{+87}	-356_{-40}^{+41} -456_{-46}^{+30}	-362_{-14}^{+16}

[a] 95% confidence intervals of ε_i are also given, *e.g.* 32_{-7}^{+6} denotes the interval 25 – 38.

Validity of calculating the chemical orderings in much larger NPs using the TOP parameters determined for moderately large NPs calculated by DFT was justified in previous studies[36,80–82] by the evidence that the TOP parameters of smaller NPs commonly vary only very slightly for larger NPs with the same relative contents of the two metals. This is also the case for Pd-Rh NPs, where the TOP descriptors calculated for $Pd_{70}Rh_{70}$ and $Pd_{101}Rh_{100}$ NPs are essentially the same. In addition, we found that a very similar chemical ordering is obtained in larger NP by using the descriptors for same and different compositions of PdRh. In the Figure 6.8 and Figure 6.9, the upper images are the arrangements obtained by the descriptors of the 201 atomic NPs of the corresponding compositions and the lower panels are the arrangements obtained using the $Pd_{101}Rh_{100}$ descriptors for 1:3 and 3:1 compositions of larger NPs, and $Pd_{70}Rh_{70}$ descriptors for their 1:1 composition. Close similarities in the chemical orderings of both obtained

structures for $Pd_{366}Rh_{1097}$, $Pd_{1097}Rh_{36}$, $Pd_{908}Rh_{2722}$, and $Pd_{2722}Rh_{908}$ NPs are evident.

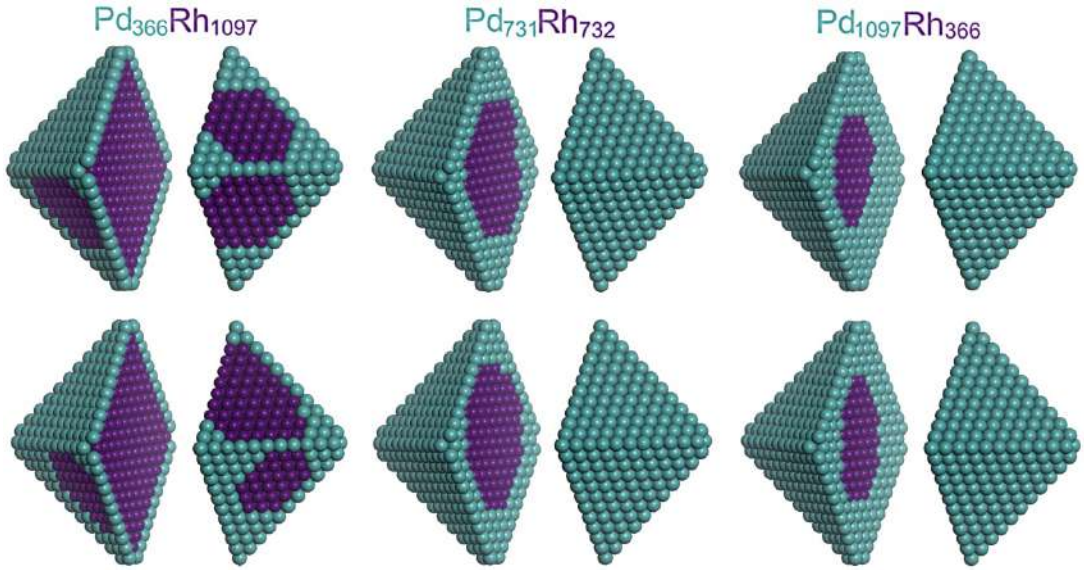

Figure 6.8 Atomic ordering in the lowest-energy homotops of *ca.* 4.4 nm large truncated octahedral 1463-atomic NPs with varying Pd:Rh composition: 1:3 – $Pd_{366}Rh_{1097}$, 1:1 – $Pd_{731}Rh_{732}$, and 3:1 – $Pd_{1097}Rh_{366}$. Upper panels (from left to right) display homotops calculated using the TOP equations. of $Pd_{50}Rh_{151}$, $Pd_{101}Rh_{100}$, and $Pd151Rh_{50}$, respectively. Images in the corresponding lower panels are obtained using the equations $Pd_{101}Rh_{100}$, $Pd_{70}Rh_{70}$, and $Pd_{101}Rh_{100}$. Color coding is the same as in Figure 6.5.

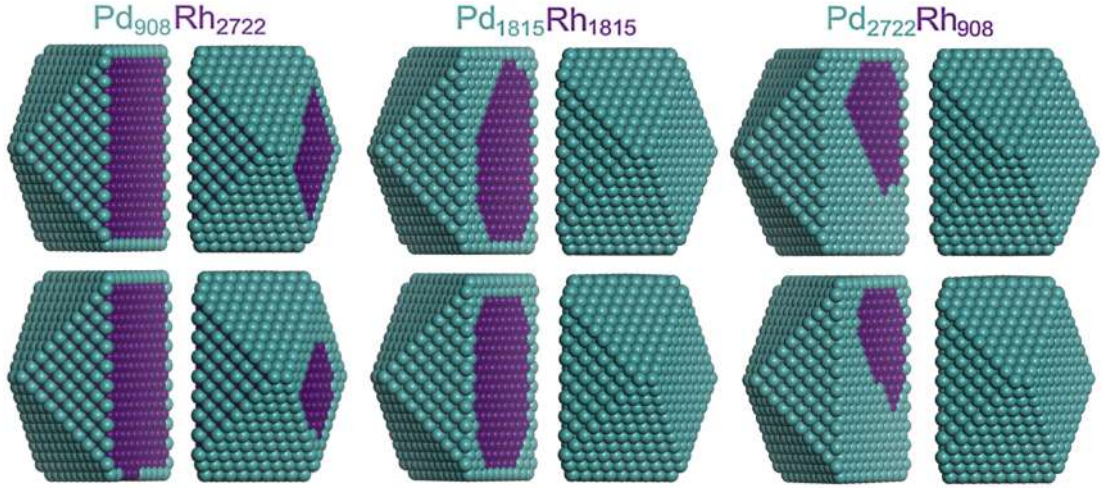

Figure 6.9 Atomic ordering in the lowest-energy homotops of *ca.* 5.4 nm large cube-octahedral 3630-atomic NPs with varying Pd:Rh composition: 1:3 – $Pd_{908}Rh_{2722}$, 1:1 – $Pd_{1815}Rh_{1815}$ and 3:1 – $Pd_{2722}Rh_{908}$. Upper panels (from left to right) display homotops calculated using the TOP equations of $Pd_{50}Rh_{151}$, $Pd_{101}Rh_{100}$, and $Pd151Rh_{50}$, respectively. Images in the corresponding lower panels are obtained using the equations $Pd_{101}Rh_{100}$, $Pd_{70}Rh_{70}$, and $Pd_{101}Rh_{100}$. Color coding is the same as in Figure 6.5.

All results discussed so far in the Section were computed at 0 K. However, the MC simulation allow estimate the chemical ordering at higher temperatures as an average structure according to the Boltzmann population. $Pd_{366}Rh_{1097}$ and $Pd_{731}Rh_{732}$ NPs were used to explore the temperature effects on the chemical orderings, see Figure 6.10. Temperature increase makes Rh surface islands in $Pd_{366}Rh_{1097}$ NP first less regular (at 600 K) and then completely disappearing and revealing a disordered pattern (at 1000 K). In the second case, the equilibrium chemical ordering of $Pd_{731}Rh_{732}$ NP is a perfect core@shell Rh@Pd at 0 K. Although the core@shell structure remains at 600 K, the compact Rh core becomes visibly less regular than at 0 K. Finally, at 1000 K some Rh atoms appear in the surface shell and the even less regular Rh core is expanded to the subsurface layer. The immiscibility of Pd-Rh and quite strong preference of Pd atoms to occupy surface positions causes the weak influence of temperature on the atomic ordering of PdRh NPs compared, for instance, to PdAu NPs.[80]

Finally, from the energetic TOP descriptors and the adsorption energy of molecules of interest one can estimate how the ordering pattern of bimetallic NPs could be modified by a reactive environmental media. For our

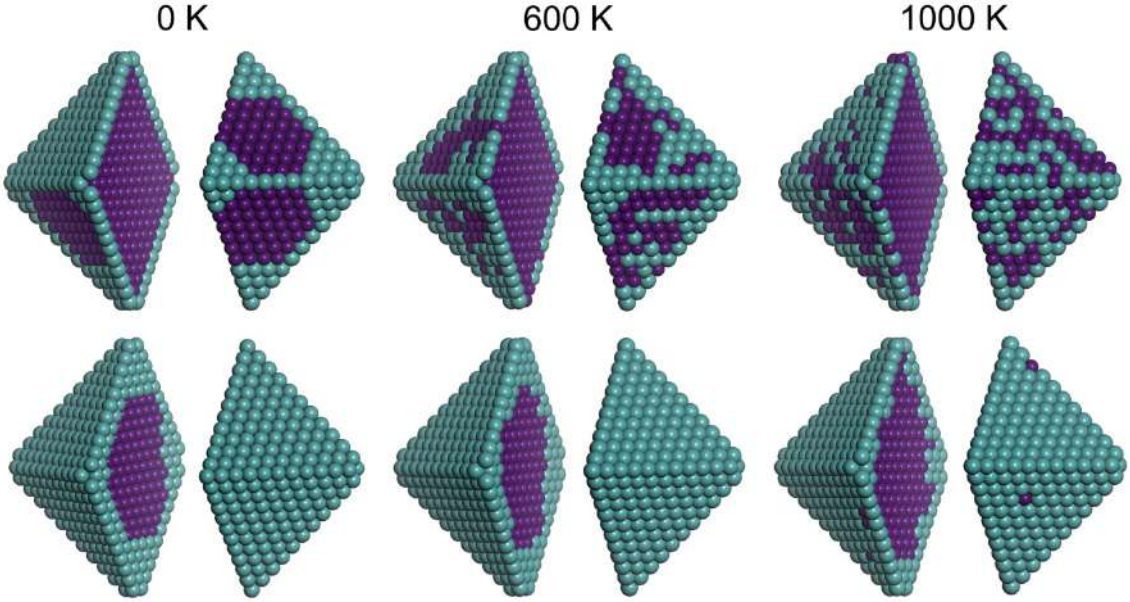

Figure 6.10 Temperature effects on the atomic ordering in the representative homotops of truncated octahedral 1463-atomic Pd-Rh NPs at 0, 600, and 1000 K. Upper panels – $Pd_{366}Rh_{1097}$, bottom panels – $Pd_{731}Rh_{732}$

PdRh NPs under scrutiny we have chosen as test adsorbates atomic O and CO and NO molecules. Their adsorption energies calculated using the same GGA functionals on extended Pd (111) and Rh (111) surfaces, respectively, are (in eV): O – 4.64 and 5.22, CO – 2.16 and 1.99, NO – 2.37 and 2.49. Then, using the facet energy descriptor from Table and knowing the number of Pd atoms comprising {111} terraces of the modeled 1463 atomic NPs one can estimate the coverage of the adsorbates needed to a complete surface segregation of Rh atoms.

Conclusions The study outlined in the present section can be summarized as follows:

- DFT calculations in combination with the Topological method were used to quantify the chemical ordering in PdRh NPs with ≤201 atoms and Pd:Rh compositions 1:3, 1:1, and 3:1. At all compositions Pd atoms show energetic preference over Rh atoms to be located at the surface, at less coordinated positions. The complete Pd surface shell is predicted to form in $Pd_{151}Rh_{50}$ NP when the number of Pd atoms becomes sufficient for that. Despite that the Pd-Rh bonds are found to be unfavourable with respect to the homometallic bonds, the strong preference of Pd atoms to stay on the surface causes the formation of Pd@Rh core@shell ordering instead of a Janus-type ordering with complete separation of Pd and Rh components.
- The lowest-energy atomic orderings were predicted for 1:3, 1:1, and 3:1 Pd:Rh compositions of 1463 and 3630 atomic PdRh NPs. The core@shell Rh@Pd NPs are formed with 1:1 and 3:1 compositions.
- A simple approach of calculating the adsorption energy of different molecules on Pd and Rh (111) surface and knowing relative energies of different atomic ordering of the NP from the Topological description allows predicting the surface re-segregation induced by interactions with adsorbates and reactants from the environment. Here, the effects of adsorbed O, CO, and NO species has been studied.

Chinese Journal of Catalysis 40 (2019) 1749–1757

available at www.sciencedirect.com

ScienceDirect

journal homepage: www.elsevier.com/locate/chnjc

Article (Special Issue on Celebrating the 70th Anniversary of Dalian Institute of Chemical Physics, CAS)

Using density functional calculations to elucidate atomic ordering of Pd-Rh nanoparticles at sizes relevant for catalytic applications

Lorena Vega [a], Hristiyan A. Aleksandrov [b,*], Konstantin M. Neyman [a,c,#]

[a] *Departament de Ciència dels Materials i Química Física & Institut de Química Teòrica i Computacional, Universitat de Barcelona, 08028 Barcelona, Spain*
[b] *Faculty of Chemistry and Pharmacy, University of Sofia, 1126 Sofia, Bulgaria*
[c] *Institució Catalana de Recerca i Estudis Avançats (ICREA), 08010 Barcelona, Spain*

ARTICLE INFO

Article history:
Received 2 March 2019
Accepted 6 April 2019
Published 5 November 2019

Keywords:
Density functional calculations
Atomic ordering
Pd-Rh nanoparticles
Size relevant

ABSTRACT

Pd-Rh nanoparticles are known to easily undergo surface restructuring in reactive environment. This study quantifies, with the help of density functional (DFT) calculations and a novel topological approach, atomic ordering and surface segregation effects in Pd-Rh particles with compositions 1:3, 1:1 and 3:1 containing up to 201 atoms (ca. 1.7 nm). The obtained data are used to reliably optimise energetically preferred atomic orderings in inaccessible by DFT Pd-Rh particles containing thousands of atoms and exhibiting sizes exceeding 5 nm, which are typical for catalytic metal particles. It is outlined, how segregation effects on the surface arrangement of Pd-Rh nanoalloy catalysts induced by adsorbates can be evaluated in a simple way within the present modelling setup.

1. Introduction

A combination of Pd and Rh metals is present in the active component of modern automotive three-way catalysts [1,2]. Moreover, bimetallic Pd-Rh nanoparticles (NPs) are known to efficiently catalyse, beyond purification of car exhaust gases [3], reactions of CO_2 methanation [4], methanol oxidation [5] and ethanol steam reforming [6], just to mention a few processes. Pd-Rh NPs reveal remarkably easy surface restructuring under reaction conditions due to interactions with oxidizing and reducing environments [7–9] as well as with oxide supports [10]. Notably, Pd and Rh immiscible at low temperatures in bulk [11–13] can mix in NPs [3–10,14].

Atomic-level understanding various peculiarities of catalytic Pd-Rh NPs requires reliable information on their thermodynamically stable surface arrangements in the absence of perturbations by reactants and/or supports. Obtaining such reference data experimentally is complicated by high sensitivity of the surface atomic ordering of Pd-Rh NPs to environment. This sensitivity resulted in a variety of surface arrangements [3–10] different from the ordering Pd-shell/Rh-core expected in vacuum for strongly surface segregated Pd on the basis of its lower surface energy compared to Rh [15] and in line with the surface segregation propensity of Pd impurity in Rh metal [16]. Hence, the knowledge about the detailed structure of such versatile entities as Pd-Rh NPs is crucial for tuning their properties in order to extend and make more efficient their catalytic applications.

Computational modelling of bimetallic nanoparticles using density functional theory (DFT) methods can provide valuable information on the structure-properties relations, complementary to experimental data. DFT calculations of bimetallic nanoparticles containing over hundred atoms (~1.5 nm large) became feasible more than a decade ago [17]. Yet, the dramati-

* Corresponding author. E-mail: haa@chem.uni-sofia.bg
# Corresponding author. E-mail: konstantin.neyman@icrea.cat
DOI: S1872-2067(19)63362-0 | http://www.sciencedirect.com/science/journal/18722067 | Chin. J. Catal., Vol. 40, No. 11, November 2019

cally increased complexity of alloy NPs due to the presence of two types of metal atoms hinders their extensive computational studies. Two more degrees of freedom characterise a bimetallic particle A_mB_n of a specified geometry (shape) and number of atoms m + n compared to the corresponding monometallic particles A_{m+n} and B_{m+n}: (1) the composition – $m : n$ ratio and (2) the atomic ordering – pattern of positions that atoms A and B occupy in this particle geometry. Structures different only by positions of atoms A and B in a given particle geometry, denoted as homotops [18], rapidly increase in number with particle size. For instance, already for ~1 nm large $A_{40}B_{40}$ particle of just 80 atoms the number of homotops (including symmetry-equivalent ones) reaches an astronomical value of 10^{23}. This limits comprehensive exploration of the homotop landscape to much smaller particles than those consisting of many hundred to several thousand atoms common in catalytic applications.

State-of-the-art modelling atomic ordering of alloy particles combines DFT calculations [19] with cluster expansion method [20]. Extension of this sophisticated approach to treat bimetallic particles with adsorbates allowed Wang et al. [21] to comparatively study bare and oxygen-covered cuboctahedral 55-atomic Pd-Rh particles at various Pd : Rh compositions. Bare NPs were shown to exhibit a simple alloying behavior and strong Rh-core/Pd-shell preference. Gradual increase of oxygen coverage caused Rh atoms to emerge on the surface, up to a total reversal to Pd-core/Rh-shell. Yet, the studied 55-atomic Pd-Rh particles with very high ratio of surface to inner atoms may not be in the scalable-with-size regime [22–24] required to represent in sufficient details surface structures and segregation of atoms in Pd-Rh NPs of much larger sizes typical for technical catalysts. In order to address this issue, we modelled in the present work Pd-Rh NPs of different Pd : Rh ratios formed of 140 to 3630 atoms (1.4 to 5.4 nm, respectively) using a novel efficient tool for optimising atomic ordering of large bimetallic NPs [25,26].

Among the main goals of our study are: (1) to quantify using DFT calculations atomic ordering and segregation effects in Pd-Rh NPs containing up to 201 atoms at varying Pd : Rh compositions; (2) using these data to describe with DFT accuracy energetically preferred atomic orderings in inaccessible by DFT larger Pd-Rh NPs with sizes 4-5 nm common for catalytic metal particles; (3) to illustrate how one can evaluate induced by adsorbates expected segregation effects on the surface arrangement of Pd-Rh nanoalloy catalysts.

2. Computational details

DFT calculations were performed with the help of a plane-wave code VASP [27,28]. A gradient-corrected Perdew-Becke-Ernzerhof (PBE) exchange-correlation functional [29] was employed in combination with the projector augmented wave representation of core electrons [30,31]. Only Γ-point was used for the Brillouin zone sampling. Cutoff energy for the wave functions was 250.925 eV. One-electron levels were smeared by 0.1 eV and the converged energies were finally extrapolated to the zero smearing. All atoms were locally relaxed without any restrictions until forces on each atom became less than 0.02 eV.

Our common DFT models of Pd-Rh nanoalloy particles with varying Pd : Rh composition comprised 201 atoms. These truncated octahedral NPs with *fcc* structure were located in 2.5×2.5×2.5 nm large periodically repeated cells with the ≥0.9 nm separation between adjacent particles. Interactions of metal NPs at such distances are shown to be negligible [32].

We determined contributions governing the atomic arrangement (atomic or chemical ordering) in Pd-Rh nanoalloys employing our recent method [25] for the global optimization of the ordering in a NP of a given shape, size and composition. As described in details elsewhere [25,26], this method, hereafter denoted TOP, is based on simple energy expressions defined by locations of atoms of two metals in crystalline positions of the NP, i.e. solely by the topology of the latter. The TOP method is widely applicable to bimetallic nanocrystallites composed of different metals. Deviation from the crystallinity, e.g. in small, sub-nanometer particles or in combinations of metals with large mismatch of the atomic sizes, is one of few factors limiting the applicability. The method involves the use of ε_i parameters (descriptors) associated either with the surface segregation energy of Pd atoms or the interaction energy of Pd-Rh pairs of the nearest atoms (denoted hereafter Pd-Rh bond energy, which can also be destabilising). The values of ε_i were obtained via fitting to DFT energies of several dozens of NP structures with different chemical orderings. The resulting TOP expressions were employed in efficient Monte-Carlo (MC) simulations to find globally optimised atomic orderings in Pd-Rh NPs with the accuracy of DFT calculations.

3. Results and discussion

3.1. Atomic ordering in $Pd_{70}Rh_{70}$, $Pd_{50}Rh_{151}$, $Pd_{101}Rh_{100}$ and $Pd_{151}Rh_{50}$ nanoparticles from DFT calculations

Our DFT results calculated for two types of truncated octahedral model Pd-Rh NPs with different Pd : Rh compositions, $Pd_{50}Rh_{151}$ (1:3), $Pd_{101}Rh_{100}$ and $Pd_{70}Rh_{70}$ (1 : 1) and $Pd_{151}Rh_{50}$ (3 : 1), are presented in Figs. 1 and 2 in the form of structural sketches corresponding to the lowest-energy optimised atomic ordering for each kind of the NPs. Pre-screening of various atomic orderings for finding putative lowest-energy homotops was performed by MC simulations [25] using the TOP energy descriptors ε_i listed in Table 1. The descriptors define TOP expressions for energy difference ΔE_{TOP} between any two homotops of a given Pd-Rh NP.

$$\Delta E_{\mathrm{TOP}} = \varepsilon_{BOND}^{Pd-Rh}\Delta N_{BOND}^{Pd-Rh} + \varepsilon_{CORNER}^{Pd}\Delta N_{CORNER}^{Pd} + \varepsilon_{EDGE}^{Pd}\Delta N_{EDGE}^{Pd} + \varepsilon_{TERRACE}^{Pd}\Delta N_{TERRACE}^{Pd} \quad (1)$$

which depends on the number of Pd-Rh bonds (N_{BOND}^{Pd-Rh}) and the numbers of corner (N_{CORNER}^{Pd}), edge (N_{EDGE}^{Pd}) and terrace ($N_{TERRACE}^{Pd}$) surface Pd atoms in each homotop.

The following individual TOP expressions (in eV) correspond to four kinds of the calculated by DFT Pd-Rh NPs with 140 and 201 atoms:

$$\Delta E_{\mathrm{TOP}}(Pd_{70}Rh_{70}) = 0.021\Delta N_{BOND}^{Pd-Rh} - 0.814\Delta N_{CORNER}^{Pd} - 0.588\Delta N_{EDGE}^{Pd} - 0.456\Delta N_{TERRACE}^{Pd} \quad (2)$$

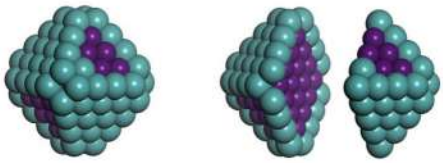

Fig. 1. Atomic ordering in the lowest-energy homotop of 1.4 nm large truncated octahedral $Pd_{70}Rh_{70}$ particle. As shown in the split image of the particle in the right panel, its inner region consists of Rh atoms only. Color coding: Pd – turquoise, Rh – purple.

$$\Delta E_{TOP}(Pd_{50}Rh_{151}) = 0.018\,\Delta N_{BOND}^{Pd-Rh} - 0.603\,\Delta N_{CORNER}^{Pd} - 0.631\,\Delta N_{EDGE}^{Pd} - 0.544\,\Delta N_{TERRACE}^{Pd} \quad (3)$$

$$\Delta E_{TOP}(Pd_{101}Rh_{100}) = 0.024\,\Delta N_{BOND}^{Pd-Rh} - 0.755\,\Delta N_{CORNER}^{Pd} - 0.536\,\Delta N_{EDGE}^{Pd} - 0.356\,\Delta N_{TERRACE}^{Pd} \quad (4)$$

$$\Delta E_{TOP}(Pd_{151}Rh_{50}) = 0.032\,\Delta N_{BOND}^{Pd-Rh} - 0.691\,\Delta N_{CORNER}^{Pd} - 0.597\,\Delta N_{EDGE}^{Pd} - 0.362\,\Delta N_{TERRACE}^{Pd} \quad (5)$$

3.1.1. $Pd_{70}Rh_{70}$ nanoparticle

Fig. 1 displays the lowest-energy homotop of the $Pd_{70}Rh_{70}$ NP. Pd forms there a part of the 96-atomic monolayer thick shell, in which all 70 Pd atoms are located. They occupy all 48 available corner and edge positions along with 22 of 48 available positions on the {111} terraces. The remaining 26 surface terrace sites of the NP are occupied by compact nano-islands of Rh atoms. The inner part (core) of the NP completely consists of 44 Rh atoms. These results illustrate propensity of Pd atoms to be strongly energetically stabilised in low-coordinated surface sites of Pd-Rh particles. Indeed, the TOP descriptor values (Table 1) estimate the energy gain to be 814 meV for each Pd atom emerging from the NP core in a 6-coordinated corner position, assuming unchanged total number of nearest-neighbor Pd-Rh contacts (bonds). The corresponding energy gains are 588 and 456 meV for the appearance of a core Pd atom in 7-coordinated edge and 9-coordinated {111} terrace positions, respectively. This revealed by our DFT calculations behavior of Pd to surface segregation in nanoalloys with Rh (atoms of which are only 3 pm smaller than Pd ones) is fully consistent with the already mentioned for extended systems lower surface energy of Pd compared with Rh [15] and a clear preference of Pd (Rh) atom impurities in Rh (Pd) slabs to surface (inner) locations [16].

Data in Table 1 for the $Pd_{70}Rh_{70}$ NP point to destabilising interaction between the nearest Pd and Rh atoms (Pd-Rh bond) vs. a half of the sum of two monometallic Pd-Pd and Rh-Rh bonds, by 21 meV on average. Hence, the immiscibility of Pd and Rh in the bulk (*vide supra*) still noticeably affects alloying propensity of these metals in 1.5 nm large 1 : 1 Pd:Rh NPs.

Next we explore how the findings for the $Pd_{70}Rh_{70}$ NP depend on the size and composition based on our DFT data for larger 201-atomic Pd-Rh NPs with varying Pd : Rh contents.

3.1.2. 201 atomic Pd-Rh nanoparticles with 1 : 3, 1 : 1 and 3 : 1 compositions

$Pd_{101}Rh_{100}$ nanoparticle. Results for larger 1 : 1 Pd-Rh NP $Pd_{101}Rh_{100}$ (Table 1 and Fig. 2) are similar to those for $Pd_{70}Rh_{70}$ NP. Again, Pd atoms are notably stabilised on the surface with the stabilisation magnitude correlating with the coordination numbers of the surface sites. The stabilisation ranges from 755 meV in corner sites with the lowest coordination to 356 meV in {111} terrace sites with the highest surface coordination. Notably, these descriptors characterising surface segregation energy of Pd atoms in the $Pd_{101}Rh_{100}$ NP practically coincide (with the statistical accuracy) with the corresponding descriptors for the $Pd_{70}Rh_{70}$ NP and the Pd-Rh bond energy descriptors are also statistically indistinguishable for the both NPs with the same 1 : 1 Pd : Rh composition. Hence, it is not surprising that the atomic ordering in the $Pd_{101}Rh_{100}$ NP (Fig. 2) essentially does not alter with the particle size increase from $Pd_{70}Rh_{70}$. As in the latter, Pd atoms form a monatomic shell in the $Pd_{101}Rh_{100}$ NP, which is not complete solely because of the insufficient number of 101 Pd atoms to occupy all exposed surface sites. These observations indicate that the general structural and related features of quite small $Pd_{70}Rh_{70}$ and $Pd_{101}Rh_{100}$ NPs should be representative of the corresponding features of notably larger Pd-Rh NPs with the same composition, in line with results for other bimetallic NPs of similar sizes [25,26,33,34]. But what about atomic ordering in Pd-Rh NPs with other compositions different from 1 : 1?

$Pd_{50}Rh_{151}$ nanoparticle. The surface segregation propensity of Pd atoms in 201-atomic Pd-Rh NP at smaller Pd content remains substantial. Yet, the noticed for 1 : 1 Pd-Rh NPs clear dependence of the segregation energy on the coordination numbers of particular surface sites becomes less expressed in the $Pd_{50}Rh_{151}$ NP (Table 1). There, the segregation of Pd to 6-coordinated corner sites is not the most energetically preferable anymore and 7-coordinated edge sites turn out to be similarly stabilising for Pd atoms. The lowest-energy atomic

Table 1
Descriptors ε_i[a] in the topological energy expressions ΔE_{TOP}[b] for Pd-Rh nanoparticles of 1:3 ($Pd_{50}Rh_{151}$), 1:1 ($Pd_{70}Rh_{70}$, $Pd_{101}Rh_{100}$,) and 3:1 ($Pd_{151}Rh_{50}$) compositions along with their precision δ and accuracy ΔE, also showing number of DFT-optimised structures N_{FIT} used for defining the TOP expressions. All energies are in meV.

	$Pd_{50}Rh_{151}$	$Pd_{101}Rh_{100}$ $Pd_{70}Rh_{70}$	$Pd_{151}Rh_{50}$
$\varepsilon_{BOND}^{Pd-Rh}$	18^{+14}_{-21}	24^{+6}_{-6} 21^{+2}_{-2}	32^{+6}_{-7}
$\varepsilon_{CORNER}^{Pd}$	-603^{+60}_{-87}	-755^{+101}_{-83} -814^{+34}_{-23}	-691^{+91}_{-95}
ε_{EDGE}^{Pd}	-631^{+107}_{-152}	-536^{+40}_{-47} -588^{+26}_{-37}	-597^{+39}_{-46}
$\varepsilon_{TERRACE}^{Pd}$	-544^{+87}_{-75}	-356^{+41}_{-40} -456^{+30}_{-46}	-362^{+16}_{-14}
N_{FIT}	30	31 44	29
precision, $\delta(E_{DFT} - E_{TOP})$	131	348 519	127
accuracy, ΔE	0	123 125	0

[a] 95% confidence intervals of ε_i are also given, e.g. 32^{+6}_{-7} denotes the interval 25 – 38.
[b] See Eq. (1) and Ref. [25].

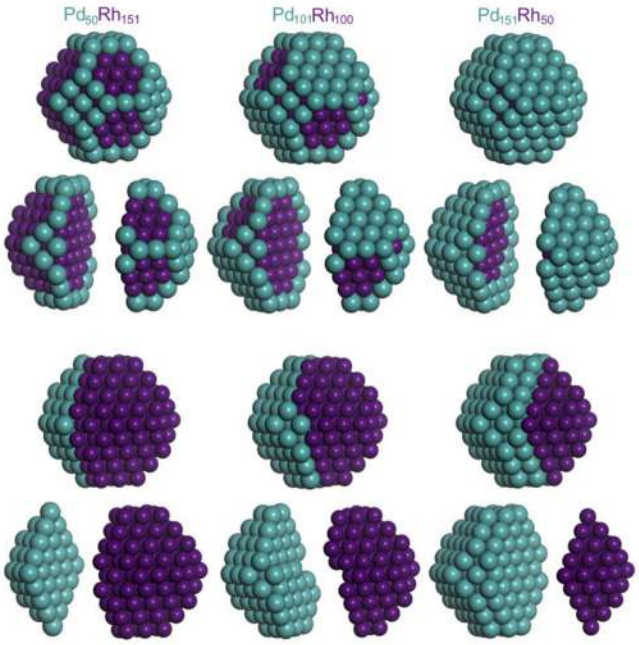

Fig. 2. Atomic ordering in the lowest-energy (upper two rows) and Janus-type (lower two rows) homotops of 1.7 nm large truncated octahedral 201-atomic NPs with varying Pd : Rh composition: 1:3 – $Pd_{50}Rh_{151}$, 1:1 – $Pd_{101}Rh_{100}$ and 3:1 – $Pd_{151}Rh_{50}$. Color coding as in Fig. 1.

ordering $Pd_{50}Rh_{151}$ homotop (Fig. 2) exhibits all 50 Pd atoms located solely in the corner (19), edge (27) and {100} terrace (4) sites, with the shell completed by 72 Rh atoms. The core is formed of only Rh atoms, Rh_{79}. No statistically significant alteration of the energetics of pair Pd-Rh interactions is observed.

$Pd_{151}Rh_{50}$ nanoparticle. No important differences in segregation and bonding properties of Pd and Rh atoms are calculated for 3 : 1 Pd-Rh NP $Pd_{151}Rh_{50}$ (Table 1, Fig. 2). Due to higher Pd content, there are sufficient atoms to form a purely Pd shell in it. A 79-atomic core of $Pd_{151}Rh_{50}$ consists of 50 Rh and 29 Pd atoms. The clear trend of more stabilised Pd atoms in less coordinated surface positions is the same as for the 1 : 1 Pd-Rh NPs addressed above. Pd-Rh interactions are calculated slightly more destabilising than for the other compositions under scrutiny. Notably, core-shell atomic ordering of Pd and Rh components remains characteristic for the studied 201-atomic Pd-Rh NPs at all compositions. This deserves a closer look in view of the known immiscibility of Pd and Rh in bulk [11–14].

3.1.3. On the mixing of Pd and Rh components

One way to analyse and quantify miscibility of Pd and Rh at the nanoscale is to compare stability of the lowest-energy Rh-core/Pd-shell homotops (Fig. 2, upper panels) with stability of the homotops featuring as much as possible separated components of these two metals. As such models of most separated components of the 201-atomic Pd-Rh NPs we have chosen homotops with the so-called Janus-type atomic ordering (Fig. 2, lower panels). Number of the nearest-neighbour Pd-Rh pairs, which destabilise mixing of these two metals according to the positive Pd-Rh bond energy descriptors $\varepsilon_{BOND}^{Pd-Rh}$ (Table 1), is in the Janus-type structures only a half of that in the corresponding core-shell structures: 96 vs. 197 for $Pd_{50}Rh_{151}$, 128 vs. 270 for $Pd_{101}Rh_{100}$, and 96 vs. 208 for $Pd_{151}Rh_{50}$. Nevertheless, DFT (TOP) energies of the Janus structures are higher than those of the respective optimised lowest-energy structures by as much as (in eV): 9.68 (7.56) – $Pd_{50}Rh_{151}$, 18.21 (18.79) – $Pd_{101}Rh_{100}$ and 14.47 (14.32) – $Pd_{151}Rh_{50}$. Such overcoming of the destabilising effect of the Pd-Rh contacts in the bimetallic particles is related to a very substantial energy gain due to strong propensity of Pd atoms to segregate on the surface forming a shell around a core of Rh. We note here in passing that the good agreement of the DFT and TOP relative energies of the NPs with Janus and core-shell orderings corroborates applicability of the TOP expressions to estimate (almost with DFT accuracy) stabilities of various homotops, both low-lying and quite high in energy.

One can also evaluate miscibility of Pd and Rh at the nanoscale by calculating so-called excess energy of Pd-Rn NPs versus monometallic Pd and Rh NPs with the same numbers of atoms and structure. For the studied $Pd_{201-n}Rh_n$ NPs the excess energy per atom [35,36] is:

$$E_{exc}(Pd_{201-n}Rh_n) = \{E(Pd_{201-n}Rh_n) - [(201-n)/201]E(Pd_{201}) - (n/201)E(Rh_{201})\}/201 \quad (6)$$

The negative E_{exc} values (Fig. 3) indicate miscibility, in full agreement with our observation of the preference of Rh-core/Pd-shell atomic orderings over Janus-type ones with more separate Pd and Rh components. Interestingly, the E_{exc} values of 0.06 – 0.09 eV per atom corresponding to the Pd : Rh ratios 1:3, 1:1 and 3:1 are close to the values calculated for nanoalloys with such well miscible atoms as Pd-Au [11–14].

3.2. Atomic ordering in bare Pd-Rh nanoparticles containing thousands atoms

Using TOP descriptors from Table 1 determined for 140- and 201-atomic Pd-Rh NPs and defined by them TOP Eqs. (2) – (5) we performed a MC search for the lowest-energy homotops of truncated octahedral and cuboctahedral Pd-Rh NPs formed of 1463 and 3630 atoms, respectively. The sizes of these NPs, ca. 4.4 and 5.4 nm, relevant for catalytic applications are well

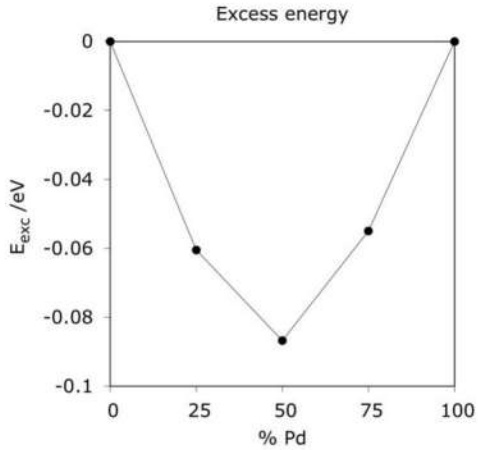

Fig. 3. DFT excess energies E_{exc} per atom of $Pd_{201-n}Rh_n$ (n = 50, 100, 151) NPs.

beyond sizes accessible by ordinary DFT calculations. The Pd : Rh compositions 1 : 3, 1 : 1 and 3 : 1 have been studied for both 1463- (Fig. 4) and 3630-atomic (Fig. 5) NPs.

In all cases the lowest-energy homotops of these NPs exhibit core-shell structures with the shells consisting of Pd atoms and the cores formed of Rh atoms. Hence, the atomic ordering patterns of quite large NPs with somewhat different shapes are qualitatively very similar to the patterns of the NPs smaller than 2 nm. The main effect causing some differences in the surface compositions of the smaller and larger NPs at a given Pd : Rh content is the ratio of surface (corner + edge + terrace) to inner atoms, which rapidly decreases with increasing particle size. This ratio (24+36+62) : 79 = 1.54 for the 201-atomic NPs drops to (24+108+440) : 891 = 0.64 for the 1463-atomic NPs and to just (24+192+744) : 2670 = 0.36 for the 3630-atomic NPs.

What justifies application of the TOP descriptors and expressions determined for the 140- and 201-atomic NPs to model realistically enough atomic ordering in much larger NPs? The evidence for that discussed in the TOP studies of other bimetallic NPs [25,26,33,34] is that TOP descriptors calculated for ca. 100-atomic particles change only insignificantly for still accessible by DFT larger NPs having the same proportion of two metals. This is also the case for the Pd-Rh NPs under scrutiny, as revealed (*vide supra*) by very close resemblance of the TOP descriptors for 1 : 1 NPs of two sizes, $Pd_{70}Rh_{70}$ and $Pd_{101}Rh_{100}$ (Table 1). This resemblance is evidenced by images in the central columns of Fig. 4 (for $Pd_{731}Rh_{732}$) and of Fig. 5 (for $Pd_{1815}Rh_{1815}$). The upper images sketch atomic ordering of the lowest-energy homotops optimised using the TOP descriptors obtained for the larger $Pd_{101}Rh_{100}$ NP, whereas the lower images with very similar orderings correspond to the lowest-energy homotops optimised using the TOP descriptors for $Pd_{70}Rh_{70}$. The TOP energy differences between these differently optimised pairs of $Pd_{731}Rh_{732}$ and $Pd_{1815}Rh_{1815}$ homotops are negligibly small, only 0.14 eV ($\Delta N_{BOND}^{Pd-Rh} = 6$) and 0.29 eV ($\Delta N_{BOND}^{Pd-Rh} = 12$), respectively. Applicability of the TOP descriptors to notably larger Pd-Rh NPs is also supported by another important finding, which was not made previously for

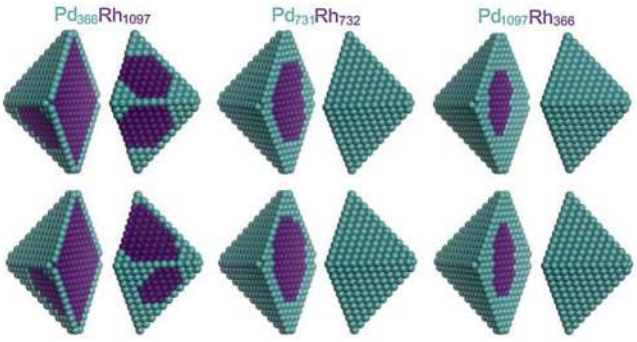

Fig. 4. Atomic ordering in the lowest-energy homotops of ca. 4.4 nm large truncated octahedral 1463-atomic NPs with varying Pd : Rh composition: 1:3 – $Pd_{366}Rh_{1097}$, 1:1 – $Pd_{731}Rh_{732}$ and 3:1 – $Pd_{1097}Rh_{366}$. Upper panels (from left to right) display homotops calculated using the TOP Eqs. (3), (4) and (5), respectively. Images in the corresponding lower panels are obtained using the equations 4, 2 and 4. Color coding is the same as in Fig. 1.

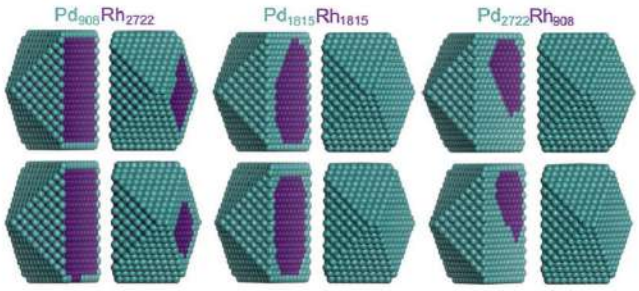

Fig. 5. Atomic ordering in the lowest-energy homotops of ca. 5.4 nm large cube-octahedral 3630-atomic NPs with varying Pd : Rh composition: 1:3 – $Pd_{908}Rh_{2722}$, 1:1 – $Pd_{1815}Rh_{1815}$ and 3:1 – $Pd_{2722}Rh_{908}$. Upper panels (from left to right) display homotops calculated using the TOP Eqs. (3), (4) and (5), respectively. Images in the corresponding lower panels are obtained using the Eqs. (4), (2) and (4). Color coding is the same as in Fig. 1.

bimetallic NPs [25,26,33,34]. Namely, that very similar ordering patterns of the lowest-energy homotops result from the application of the TOP descriptors for both the same and different Pd : Rh ratios. One can see, for instance, qualitatively very similar orderings in the upper and lower images of 1 : 3 $Pd_{366}Rh_{1097}$ NP in Fig. 4 optimised using TOP descriptors for NPs with the same ratio 1 : 3 ($Pd_{50}Rh_{151}$) and with different ratio 1 : 1 ($Pd_{101}Rh_{100}$), respectively. The same conclusion could be drawn for the other pairs of homotops $Pd_{1097}Rh_{366}$, $Pd_{908}Rh_{2722}$ and $Pd_{2722}Rh_{908}$ shown in Figs. 4 and 5.

DFT and TOP data presented so far correspond to 0 K. The TOP method allows estimating properties associated with the Boltzmann population of different homotops of a particular NP at a given temperature by accounting for entropy contributions related with atomic ordering, not considering atomic vibrations [26]. We applied this protocol to calculate probabilities of occupying each site by either Pd or Rh atoms and to estimate average atomic orderings in the 1463-atomic NPs with Pd : Rh ratios 1 : 3 and 1 : 1 at 600 K and 1000 K (Fig. 6 and Table 2).

Temperature increase mainly acts on $Pd_{366}Rh_{1097}$ NP to exchange Pd atoms, all of which are on the surface, with surface Rh atoms. It transforms compact surface Rh islands present at 0 K into smaller and less regular ones at 600 K and causes complete disappearance of the islands of Rh at 1000 K. This enhanced mixing is manifested by substantially increased

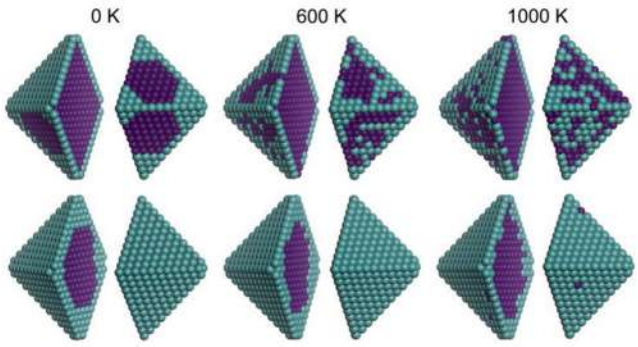

Fig. 6. Temperature effects on the atomic ordering in the representative homotops of truncated octahedral 1463-atomic Pd-Rh NPs at 0 K, 600 K and 1000 K. Upper panels – $Pd_{366}Rh_{1097}$, bottom panels – $Pd_{731}Rh_{732}$. Color coding is the same as in Fig. 1.

Table 2
Temperature dependence of the TOP atomic ordering in the representative homotops of truncated octahedral $Pd_{366}Rh_{1097}$ and $Pd_{731}Rh_{732}$ nanoparticles shown in Fig. 6.

System	Temperature, K		
	0	600	1000
$Pd_{366}Rh_{1097}$			
N_{BOND}^{Pd-Rh}	1060	1419	1555
N_{CORNER}^{Pd}	24	23	20
N_{EDGE}^{Pd}	108	103	93
$N_{TERRACE}^{Pd}$	234	240	252
$Pd_{731}Rh_{732}$			
N_{BOND}^{Pd-Rh}	1238	1331	1766
N_{CORNER}^{Pd}	24	24	24
N_{EDGE}^{Pd}	108	108	107
$N_{TERRACE}^{Pd}$	440	440	435

N_{BOND}^{Pd-Rh} – number of Pd-Rh bonds (nearest neighbours);
N_{CORNER}^{Pd}, N_{EDGE}^{Pd} and $N_{TERRACE}^{Pd}$ – numbers of Pd surface atoms in the corner, edge and terrace positions, respectively.

number of Pd-Rh pairs of atoms and more terrace Pd atoms formed by displacements from corner and edge sites (Table 2). Interestingly, the propensity of Pd atoms to remain on the surface in Pd-Rh nanoalloys revealed by the TOP descriptors (Table 1) is so strong that almost no temperature-induced exchange of surface Pd atoms with inner Rh atoms has been calculated. Even at 1000 K the representative homotop of the $Pd_{366}Rh_{1097}$ NP is predicted to exhibit just one inner Pd atom (Table 2). $Pd_{731}Rh_{732}$ NP featuring at 0 K a compact Rh core covered by a Pd shell thicker than one atomic layer exhibits even weaker temperature effects (see bottom images in Fig. 6 and Table 2) than $Pd_{366}Rh_{1097}$ NP. Only at 1000 K emergence of few single Rh atoms on the surface of $Pd_{731}Rh_{732}$ NPs becomes energetically feasible. Such small influence of temperature on the atomic ordering of Pd-Rh NPs compared, for instance with that of Pd-Au NPs [26], is related with both the immiscibility of Pd and Rh atoms and quite strong preference of Pd atoms to stay on the surface. Notably, the simple TOP descriptors allow rationalising and predicting atomic ordering differences in the surface segregation of different nanoalloys and their temperature dependence.

3.3. On the reactive media effects on the surface arrangement of catalytic nanoparticles

As mentioned in the Introduction, atomic orderings of Pd-Rh NPs under experimental conditions can be very different from the Pd-shell/Rh-core arrangement predicted by our modelling as energetically the most stable in vacuum. Provided that experimentally prepared catalytic Pd-Rh NPs were annealed long enough at sufficiently high temperature to minimise the internal energy, the major effects triggering their atomic ordering to deviate from Pd-shell/Rh-core are usually interactions of the NPs with adsorbates and supports [7,10].

There are several levels of the computational modelling approaches to address surface restructuring of bimetallic NPs caused by interactions with adsorbates present in reactive environments. A rigorous approach, albeit too computationally intensive for routine applications to particles larger than 1 nm, is an extension of the cluster expansion method to DFT treatment of bimetallic particles with adsorbates [21]. The TOP approach used in the present work was also employed to evaluate surface segregation effects induced by adsorbates in quite large bimetallic NPs [34,37]. The latter predictions of the surface ordering relied on a simple concept that an adsorbate more strongly interacting with surface sites formed by atoms of metal one than by atoms of metal two energetically stabilises surface atoms of the metal one and the degree of such stabilisation is defined by the adsorption energy difference for the most strongly binding sites of these metals forming the studied nanoalloy. In this way, DFT calculations of CH_X adsorbates on Cu and Ni sites of Cu-Ni NPs in combination with the TOP descriptors defining surface segregation in the bare NPs quantified coverages of the CH_X adsorbates required to cover under reaction conditions Cu-Ni NPs by active Ni atoms instead of inert Cu ones, as was desired for improving the catalytic function [34]. Similarly, employment of TOP descriptors together with DFT adsorption energies of CO molecules on Pd and Au sites of Pd-Au NPs enabled predicting CO coverages, at which experimentally observed significant CO-induced surface segregation of Pd takes place [37].

In case of well-ordered metal NPs with abundant sites at extended terraces that bind adsorbates similarly strong as the corresponding single-crystal surfaces [22] one can greatly reduce computational expenditures employing adsorption preference energy defined as a difference of binding energies of a given adsorbate on surfaces of two metals forming bimetallic NPs under study [38]. If less quantitative predictions of the adsorbate-induced surface segregation are sufficient, one can merely use published adsorption energies of the most relevant reactants and intermediates on single-crystal monometallic surfaces and thus to completely avoid expensive DFT calculations of NPs with adsorbates.

To shed light on induced by adsorbates changes of the surface atomic ordering in Pd-Rh NPs we calculated adsorption energies of O atom as well as CO and NO molecules on 6-layers thick Pd(111) and Rh (111) slabs with 3×3 surface cells. The following DFT (PBE) adsorption energies (in eV) are obtained on Pd(111) and Rh (111), respectively: O – 4.64 and 5.22, CO – 2.16 and 1.99, NO – 2.37 and 2.49. From these data the adsorption preference of O to the Rh surface *vs.* Pd one is 0.58 eV and that of NO is 0.12 eV. Negative CO adsorption preference, -0.17 eV, indicates stronger adsorption on Pd(111) than on Rh(111). Combining these data with TOP descriptors from Table 1 defining surface segregation energy of Pd and Rh atoms on {111} nanofacets, $\varepsilon_{TERRACE}^{Pd} = -\varepsilon_{TERRACE}^{Rh}$, being respectively ca. –0.54 and –0.36 eV for 1 : 3 and 1 : 1 201-atomic Pd-Rh NPs, one can rationalise surface atomic ordering of various Pd-Rh NPs in the presence of the chosen adsorbates and predict variation of the ordering with the coverage of the adsorbates. Of course, this simple approach cannot account for surface reconstruction effects expected in case of strong adsorbate-metal interactions.

For instance, surface segregation of Rh atoms on the {111}

terraces of $Pd_{366}Rh_{1097}$ NP to substitute all 234 Pd atoms located there at 0 K (Table 2) will destabilise the NP by the amount equivalent to the energy gained by adsorption on Rh terrace sites of 218 O atoms, each stabilising the system by 0.58 eV. Thus, ca. 0.5 monolayer (ML) O coverage of in total 440 {111} terrace sites exposed on the $Pd_{366}Rh_{1097}$ NP is estimated to be energetically sufficient to make all these metal atomic positions occupied by Rh atoms. For $Pd_{731}Rh_{732}$ and $Pd_{1097}Rh_{366}$ NPs, which feature complete Pd shells (Fig. 4), the estimated O coverage required to stabilise the orderings with Rh atoms segregated on all available 440 {111} terrace sites is ~0.6 ML (or 273 O atoms). This small coverage increase is due to lower terrace segregation propensity of Pd atoms in case of higher Pd contents.

The outlined above evidences of triggered by adsorbed oxygen Rh surface segregation in Pd-Rh NPs featuring Pd shell arrangement without adsorbates strongly suggests that the experimentally found arrangements of the as-synthesised large Pd-Rh NPs with Rh-rich shells [7] correspond to surface oxidised situations. According to the present calculations, NO shows preference to be adsorbed on Rh rather than Pd sites of Pd-Rh surfaces (although expressed 5 times weaker than that for O), whereas CO adsorption is preferred on Pd sites vs. Rh ones. These calculated data are in qualitative agreement with the Rh-rich shell structure observed in the presence of NO (or O_2) adsorbates and substantially increased Pd concentration in the shells in the presence of adsorbed CO [7]. However, the latter experiments have been performed under too complicated conditions, including catalytic ones, to be described in more details by the simplified computational approaches applied in the present study.

4. Conclusions

This theoretical modelling study addressed atomic ordering in bimetallic Pd-Rh nanoparticles of different compositions formed of up to more than 3600 atoms. Pd-Rh nanoalloy materials are widely used for applications in catalysis. One of their peculiarities is that the surface composition is very easily adjustable to interactions with adsorbates present in reactive environment. Therefore, the work was focused on detail analysis of the surface composition of bare Pd-Rh nanoparticles and its dependence on the particle size and Pd : Rh stoichiometry.

First, DFT calculations were employed in combination with a novel topological (TOP) approach to quantify atomic ordering and segregation effects in Pd-Rh nanoparticles of ≤201 atoms and Pd : Rh compositions 1 : 3, 1 : 1 and 3 : 1. In all these nanoparticles Pd atoms were notably stabilised in surface positions forming a Pd shell, whereas Rh atoms preferred to occupy inner positions forming a Rh core. Due to high surface to volume ratio in such particles it was enough Pd atoms to form a complete Pd-shell/Rh-core lowest-energy structure only in the particle $Pd_{151}Rh_{50}$ with the highest Pd content. TOP analysis of the DFT data provided quantitative estimates of the energy gained (lost) by appearance of an inner Pd (Rh) atoms in particular surface positions of the studied nanoparticles. This analysis also revealed that the nearest-neighbour Pd-Rh contacts (bonds) do not stabilise mixing of these two metal components, in line with experimental observations for bulk materials. Nevertheless, as follows from both DFT and TOP data, at the nanoscale the strong propensity to form the Pd-shell/Rh-core ordering triggers mixing of Pd and Rh atoms with respect to the Janus-type ordering with the most separated compact Pd and Rh regions.

Next, the knowledge on the atomic arrangements and the energetics obtained from the DFT and TOP modelling of smaller nanoparticles was used to describe (with DFT accuracy) energetically preferred atomic orderings in the so far inaccessible by DFT 4–5 nm large Pd-Rh particles approaching the size common for catalytic metal particles. The lowest-energy atomic orderings were determined for 1 : 3, 1 : 1 and 3 : 1 Pd-Rh fcc crystallites consisting of 1463 and 3630 atoms. The latter, similarly to the aforementioned smaller particles, were found to be energetically the most stable as core-shell structures with the shells consisting of Pd atoms and the cores built of Rh atoms. Variation of Pd : Rh compositions affected the preferred atomic ordering mainly due to the shortage of Pd atoms to form complete Pd shells for the 1 : 3 stoichiometry, resulting in the appearance on the surface terraces of $Pd_{366}Rh_{1097}$ and $Pd_{908}Rh_{2722}$ particles of Rh patches affecting surface reactivity. The 1463- and 3630-atomic 1 : 1 and 3 : 1 Pd-Rh particles are predicted to expose perfect Pd shells.

Finally, it was outlined, how the information on atomic ordering in bare bimetallic nanoparticles, in particular, the TOP data, can be used for predicting effects of reacting media on the surface composition and arrangement of the nanoparticles under experimental conditions. For such predictions one usually needs additional data from (often quite intense) calculations of adsorption systems. Employing the TOP analysis makes it possible to estimate surface re-segregation and the resulting surface composition of a nanoalloy in the presence of given amount of adsorbed reactants or intermediates without additional expensive DFT calculations, only using readily available adsorption energies on extended monometallic surfaces. This approach was illustrated for considering surface re-segregation of Rh in Pd-shell/Rh-core nanoparticles in the presence of adsorbed oxygen, CO and NO reactants. Such simple predictions are expected to be widely applicable to various catalytically important bimetallic particles and to help bridging the gap between idealised surface models and surfaces of technical catalysts.

Acknowledgments

Work of LV was financed by the Generalitat de Catalunya via a pre-doctoral grant 2018FI-B-00384. HAA is grateful to the Operational program "Science and Education for Smart Growth", project BG05M2OP001-2.009-0028 for funding his research stay in the University of Barcelona and for financial support by the Bulgarian Ministry of Education and Science under the National Research Programme "Low-carbon Energy for the Transport and Domestic Use (EPLUS)" approved by DCM # 577/17.08.2018" (contract DO1-214/28.11.2018). KMN acknowledges a support by the Spanish grants

Graphical Abstract

Chin. J. Catal., 2019, 40: 1749–1757 doi: S1872-2067(19)63362-0

Using density functional calculations to elucidate atomic ordering of Pd-Rh nanoparticles at sizes relevant for catalytic applications

Lorena Vega, Hristiyan A. Aleksandrov *, Konstantin M. Neyman *
University of Barcelona, Spain; University of Sofia, Bulgaria; Catalan Institution for Research and Advanced Studies (ICREA), Spain

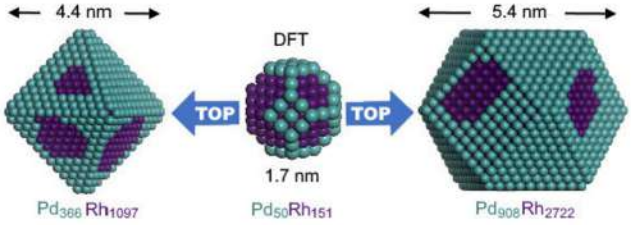

Catalytically active Pd-Rh nanoparticles adapt their surface to chemical environment. Density functional modelling identifies surface composition of Pd-Rh particles containing thousands atoms and paves the way for evaluating surface segregation caused by adsorbed reactants.

PGC2018-093863-B-C22, CTQ2015-64618-R and MDM-2017-0767 as well as by the grant 2017SGR13 of the Generalitat de Catalunya. LV and KMN thank the Red Española de Supercomputación for providing computer resources and technical support.

Conflicts of interest

There are no conflicts to declare.

References

[1] J. Kaspar, P. Fornasiero, N. Hickley, *Catal. Today*, **2003**, 77, 419–449.
[2] H. Goto, K. Komata, S. Minami, *SAE Technical Paper 2014-01-1503*, **2014**, 1–5.
[3] A. A. Vedyagin, M. S. Gavrilov, A. M. Volodin, V. O. Stoyanovskii, E. M. Slavinskaya, I. V. Mishakov, Yu. V. Shubin, *Top. Catal.*, **2013**, 56, 1008–1014.
[4] Y.-T. Pan, H. Yang, *ChemNanoMat*, **2017**, 3, 639–645.
[5] C.-T. Hsieh, P.-Y. Yu, D.-Y. Tzou, J.-P. Hsu, Y.-R. Chiu, *J. Electroanal. Chem.*, **2016**, 761, 28–36.
[6] H. Idriss, M. Scott, J. Llorca, S. C. Chan, W. Chiu, P.-Y. Sheng, A. Yee, M. Blackford, S. Pas, A. J. Hill, F. M. Alamgir, R. Rettew, C. Petersburg, S. D. Senanayake, M. A. Barteau, *ChemSusChem*, **2008**, 1, 905–910.
[7] F. Tao, M. E. Grass, Y. Zhang, D. R. Butcher, J. R. Renzas, Z. Liu, J. Y. Chung, B. S. Mun, M. Salmeron, G. A. Somorjai, *Science*, **2008**, 322, 932–934.
[8] F. Bernardi, M. E. Grass, Y. P. Hong, R. Chang, N. Jabeen, C. Zhang, B. W. Eichhorn, B. Seo, S. Alayoglu, Z. Hussain, S. H. Joo, Z. Liu, *Catal. Today*, **2016**, 260, 95–99.
[9] P. Müller, U. Hejral, U. Rütt, A. Stierle, *Phys. Chem. Chem. Phys.*, **2014**, 16, 13866–13874.
[10] N. J. Divins, I. Angurell, C. Escudero, V. Pérez-Dieste, J. Llorca, *Science*, **2014**, 346, 620–623.
[11] K. M. Myles, *Trans. Met. Soc. AIME*, **1968**, 242, 1523–1526.
[12] L. H. Bennett, R. E. Watson, *CALPHAD*, **1981**, 5, 19–23.
[13] Y. Oumellal, J.-M. Joubert, C. M. Ghimbeu, J.-M. Le Meins, J. Bourgon, C. Zlotea, *Nano-Struct. Nano-Obj.*, **2016**, 7, 92–100.
[14] Yu. V. Shubin, P. E. Plyusnin, S. V. Korenev, *J. Alloys Compd.*, **2015**, 622, 1055–1060.
[15] F. Mittendorfer, N. Seriani, O. Dubay, G. Kresse, *Phys. Rev. B*, **2007**, 76, 233413/1–233413/4.
[16] A. V. Ruban, H. L. Skriver, J. K. Nørskov, *Phys. Rev. B*, **1999**, 59, 15990–16000.
[17] K. M. Neyman, R. Sahnoun, C. Inntam, S. Hengrasmee, N. Rösch, *J. Phys. Chem. B*, **2004**, 108, 5424–5430.
[18] R. Ferrando, J. Jellinek, R. L. Johnston, *Chem. Rev.*, **2008**, 108, 845–910.
[19] L. Cao, C. Li, T. Mueller, *J. Chem. Inf. Model.*, **2018**, 58, 2401–2413.
[20] J. M. Sanchez, F. Ducastelle, D. Gratias, *Phys. A*, **1984**, 128, 334–350.
[21] L.-L. Wang, T. L. Tan, D. D. Johnson, *Nano Lett.*, **2014**, 14, 7077–7084.
[22] I. V. Yudanov, R. Sahnoun, K. M. Neyman, N. Rösch, *J. Chem. Phys.*, **2002**, 117, 9887–9896.
[23] A. Roldán, F. Viñes, F. Illas, J. M. Ricart, K. M. Neyman, *Theor. Chem. Acc.*, **2008**, 120, 565–573.
[24] S. M. Kozlov, K. M. Neyman, *Top. Catal.*, **2013**, 56, 867–873.
[25] S. M. Kozlov, G. Kovács, R. Ferrando, K. M. Neyman, *Chem. Sci.*, **2015**, 6, 3868–3880.
[26] G. Kovács, S. M. Kozlov, K. M. Neyman, *J. Phys. Chem. C*, **2017**, 121, 10803–10808.
[27] G. Kresse, J. Furthmüller, *Phys. Rev. B*, **1996**, 54, 11169–11186.
[28] G. Kresse, J. Hafner, *Phys. Rev. B*, **1994**, 49, 14251–14269.
[29] J. P. Perdew, K. Burke, M. Ernzerhof, *Phys. Rev. Lett.*, **1996**, 77, 3865–3868; *Phys. Rev. Lett.*, **1997**, 78, 1396–1396.
[30] P. E. Blöchl, *Phys. Rev. B*, **1994**, 50, 17953–17979.
[31] G. Kresse, D. Joubert, *Phys. Rev. B*, **1999**, 59, 1758–1775.
[32] F. Viñes, F. Illas, K. M. Neyman, *Angew. Chem. Int. Ed.*, **2007**, 46, 7094–7097.
[33] G. Kovács, S. M. Kozlov, I. Matolínová, M. Vorokhta, V. Matolín, K. M. Neyman, *Phys. Chem. Chem. Phys.*, **2015**, 17, 28298–28310.
[34] A. Wolfbeisser, G. Kovács, S. M. Kozlov, K. Föttinger, J. Bernardi, B.

Klötzer, K. M. Neyman, G. Rupprechter, *Catal. Today*, **2017**, 283, 134–143.
[35] R. Ferrando, A. Fortunelli, G. Rossi, *Phys. Rev. B*, **2005**, 72, 085449/1–085449/9.
[36] I. V. Yudanov, K. M. Neyman, *Phys. Chem. Chem. Phys.*, **2010**, 12, 5094–5100.
[37] M. Mamatkulov, I. V. Yudanov, A. V. Bukhtiyarov, I. P. Prosvirin, V. I. Bukhtiyarov, K. M. Neyman, *J. Phys. Chem. C*, **2019**, 123, 8037–8046.
[38] S. Liu, Z.-J. Zhao, C. Yang, S. Zha, K. M. Neyman, F. Studt, J. Gong, *ACS Catal.*, **2019**, 9, 5011–5018.

利用密度泛函计算阐明Pd-Rh纳米颗粒在与催化应用相关尺寸下的原子排序

Lorena Vega [a], Hristiyan A. Aleksandrov [b,*] , Konstantin M. Neyman [a,c,#]
[a]巴塞罗那大学材料科学与化学物理系, 理论化学计算研究所, 巴塞罗那, 西班牙
[b]索非亚大学化学与药学系,索非亚, 保加利亚
[c]加泰罗尼亚自治大学, 巴塞罗那, 西班牙

摘要: 从所周知, Pd-Rh纳米颗粒在反应环境中容易发生表面再构. 本文借助密度泛函(DFT)计算和一种新的拓扑方法, 对组成分别为1:3、1:1和3:1的(多达201个原子, 约1.7 nm)的Pd-Rh粒子中的原子排序和表面偏析效应进行了定量研究. 所得数据用于可靠优化用DFT无法研究的、含有数千个原子且尺寸超过5nm的Pd-Rh粒子能量优先原子排序, 这是典型的催化金属粒子. 概述了在现有的模拟装置中, 如何通过简单的方法评估偏析效应对吸附质诱导的Pd-Rh纳米合金催化剂表面排列的影响.

关键词: 密度函数计算; 原子序; Pd-Rh纳米粒子; 尺寸相关

收稿日期: 2019-03-02. 接受日期: 2019-04-06. 出版日期: 2019-11-05.
*通讯联系人. 电子信箱: haa@chem.uni-sofia.bg
#通讯联系人. 电子信箱: konstantin.neyman@icrea.cat
本文的电子版全文由Elsevier出版社在ScienceDirect上出版(http://www.sciencedirect.com/science/journal/18722067).

For Author Index:

VEGA Lorena, ALEKSANDROV Hristiyan A., NEYMAN Konstantin M.

6.4 IRREVERSIBLE STRUCTURAL DYNAMICS ON THE SURFACE OF BIMETALLIC PtNi ALLOY CATALYST UNDER ALTERNATING OXIDIZING AND REDUCING ENVIRONMENTS

6.4.1 Summary

Introduction In this section, application of the TOP method to PtNi system is outlined accompanied with experiments performed by collaboration partners validating the obtained computational results. The bimetallic structure does not always remain intact under experimental conditions, when elevated temperature and presence of reactive gases at different pressures can modify the structure affecting the properties of the alloy. In particular, the PtNi alloy is interesting as a cathode catalyst in proton exchange membrane fuel cells (PEMFCs). To obtain new insights into the restructuring that occurs during oxidation and reduction cycles, the structure changes in PtNi NPs are investigated by our experimental collaborators at the alternating oxidation (O_2) and reduction (H_2) gaseous atmospheres using X-ray photoelectron spectroscopy (XPS) and synchrotron radiation photoelectron spectroscopy (SRPES) techniques. XPS can characterize the material composition and chemical states by high X-ray energy. SRPES, in turn, is a technique allowing to tune the excitation energy of photons (E_p) so that the kinetic energy of escaping photoelectrons for both metals constituting the alloy under scrutiny can be set the same ensuring consistent measurement of the contribution of individual metals. In addition, E_p can be set to obtain the desired surface sensitivity, enabling that SRPES detects just a few top atomic layers.

The experimental evidences provided by the group of Dr. Khalakhan (Charles University Prague) for PtNi nanoalloys were substantiated by the computational modelling. The author of the Thesis carried out all calculations described in the theoretical part of the corresponding article published in the journal *Appl. Catal. B*, designed computational models, analysed the

calculated data and prepared them to publication, wrote the theoretical part of the article and contributed to revising its other parts.

Results The experimental data by Khalakhan and co-workers outlined in the following allow putting the theoretical results in the context. As in other Chapters of the Thesis, the complete description of the results is provided in the published article in the end of this Section. Further data is available on Appendix F. Experimentally, the PtNi system was exposed to alternating gaseous atmospheres of O_2 (oxidation) and H_2 (reduction) at different temperatures aiming to simulate working behaviour of the cathode in the PEMFCs. SRPES technique was used to determine the stoichiometry of the outer layers of the PtNi alloy from the integrations of the area of the Ni 3*p* and Pt 4*f* spectra. The first oxidation cycle revealed notable dependence of atomic concentrations in the upper PtNi layers on the treatment temperature and significantly different concentrations compared to the as-deposited (AD) sample not exposed yet to a reactive environment, see Table 6.2. This shows that interaction with oxygen induces surface segregation of Ni, possibly due to stronger Ni-O bonding compared to Pt-O, and that this effect is noticeably temperature-dependent.

Table 6.2 Relative atomic compositions of Pt and Ni in the outer layers of the as-deposited (AD) PtNi sample after the first oxidation cycle performed at different temperatures.

	Pt (at.%)	**Ni (at.%)**
AD	55	45
Ox1 298 K	43	57
Ox1 373 K	38	62
Ox1 523 K	8	92

Using the same methodology, the concentration of Pt and Ni was determined after the first reduction step carried out at each working temperature after the previous oxidation cycle, see Table 6.3. The presence of hydrogen causes a diffusion of surface Ni atoms into inner part of the alloy. However, gradual enrichment of Ni concentration in the upper layers of the

alloy takes place during subsequent oxidation-reduction cycles and finally becomes irreversible after 5 such cycles at the highest temperature 523 K. These results could be rationalised in terms of the bond strength preferences of oxygen with Ni and Pt metals versus supposed to be smaller for weaker-bound hydrogen.

Table 6.3 Relative atomic composition of Pt and Ni in the outer layers after the first reduction at different temperatures.

	Pt (at.%)	**Ni (at.%)**
Red1 298 K	51	49
Red1 373 K	45	55
Red1 523 K	30	70

The theoretical modelling predicted the equilibrium chemical ordering in *ca.* 4.4 nm large PtNi NPs with 1:1 Pt:Ni composition, of similar size and composition as in the experimental samples, and estimated effects of the experimental working temperature on the chemical ordering. For that several homotops of $Pt_{101}Ni_{100}$ and $Pt_{157}Ni_{157}$ NPs were calculated to obtain the following topological equations (in eV):

$$\Delta E_{TOP}(Pt_{101}Ni_{100}) = -0.048N_{BOND}^{Pt-Ni} - 0.581N_{CORNER}^{Pt} - 0.513N_{EDGE}^{Pt} - 0.399N_{TERRACE}^{Pt} \quad (6.7),$$

$$\Delta E_{TOP}(Pt_{157}Ni_{157}) = -0.033N_{BOND}^{Pt-Ni} - 0.465N_{CORNER}^{Pt} - 0.490N_{EDGE}^{Pt} - 0.324N_{TERRACE}^{Pt} \quad (6.8).$$

Application of these equations results in the equilibrium chemical orderings of the larger $Pt_{731}Ni_{732}$ NPs at 0 K shown in Figure 6.11. There, the A column shows images corresponding to equation 6.7, and the B column to equation 6.8. The TOP method allows simulations of the ordering patterns at different temperatures by the Boltzmann population of different homotops at a given temperature. Results of such simulations are also presented in Figure 6.11. Irrespective of the TOP equations applied to calculate the chemical orderings of the $Pt_{731}Ni_{732}$ NPs at elevated temperatures Pt is preferentially placed in surface positions, where the presence of Ni slightly increases with

the temperature. This finding is in line with the experimental observations that Ni atoms tend to segregate to the surface when the temperature increases. Finally, to model effects of the adsorption of oxygen and hydrogen on the chemical ordering pattern, the adsorption energies of atomic O and H on the surface of Pt and Ni were calculated. Knowing the adsorption energy of O and H species on both surfaces, the energy required to segregate one atom of Ni to the NP terrace provided by the corresponding energy parameter of the TOP equation, and the number of Pt terrace atoms, one can estimate the number of O and H needed to revert the equilibrium ordering pattern at 0 K (neglecting edge and corner positions), see bottom row of Figure 6.11.

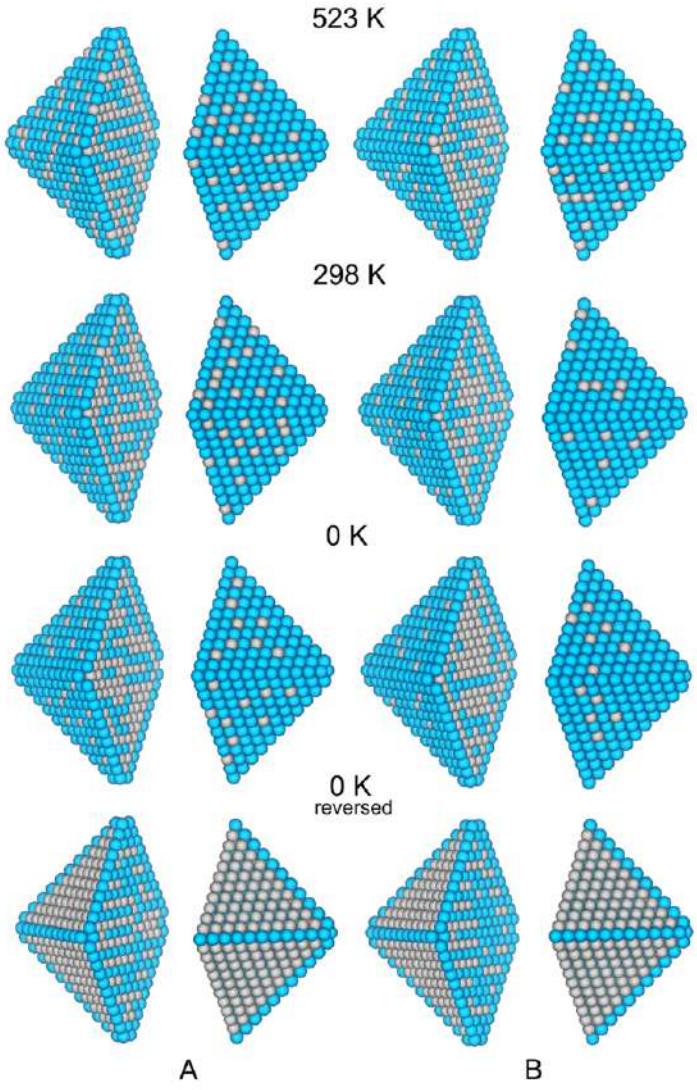

Figure 6.11. Atomic ordering in the lowest-energy homotops of truncated octahedral $Pt_{731}Ni_{732}$ NP at varying temperature. Columns A and B display homotops calculated using the TOP eqs. 6.7 and 6.8 respectively. Here the Pt is represented in blue and Ni in grey.

The estimation in the oxidation case is that oxygen coverage of 0.3 monolayer is enough to revert the pattern of all the facets of the NP to make them composed solely of Ni atoms. However, in the reduction case it is impossible to revert the pattern even with a maximum coverage of H. This is also in line with the experimental data that after the first reduction at 523 K *ca.* 30% of surface atoms are Pt although after the first oxidation at same temperature only an 8% of surface atoms are Pt. Most important here is that the experimental difference in the percentage of surface Ni and Pt atoms at the oxidation and reduction condition situations is in qualitative agreement with the coverage estimation from the simulations. Note that in the simulations only the monatomic outermost layer is considered as the surface, whereas experimentally the surface is considered as a range of outer layers.

Conclusions The study outlined in the present Section can be summarized as follows:

- Under oxidation environment PtNi alloy is oxidized on the surface mainly through the formation of Ni oxides, which forces Ni atoms to segregate to the surface. Under reduction environment the oxides are reduced, and Ni diffuses back into the alloy. During the first several oxidation/reduction cycles the surface changes were reversible, with slight enrichment of the average composition by Ni at elevated cycling temperatures. The deviations from the perfect reversibility are consistent with stronger Ni-O binding compared to Ni-H binding.
- The modelling data corroborate the experimentally observed effect of slightly increased Ni surface proportion at temperature increase. Strong propensity of Pt to surface segregation in the absence of the oxidizing media is predicted. It is estimated that 0.3 monolayer of adsorbed oxygen is sufficient to revert the surface ordering pattern with terraces of the PtNi NPs completely formed of Pt atoms to those completely consisting of Ni atoms.

Applied Catalysis B: Environmental 264 (2020) 118476

Contents lists available at ScienceDirect

Applied Catalysis B: Environmental

journal homepage: www.elsevier.com/locate/apcatb

Irreversible structural dynamics on the surface of bimetallic PtNi alloy catalyst under alternating oxidizing and reducing environments

Ivan Khalakhan[a,*], Lorena Vega[b], Mykhailo Vorokhta[a], Tomáš Skála[a], Francesc Viñes[b], Yurii V. Yakovlev[a], Konstantin M. Neyman[b,c,**], Iva Matolínová[a]

[a] Department of Surface and Plasma Science, Faculty of Mathematics and Physics, Charles University, V Holešovičkách 2, 18000 Prague, Czech Republic
[b] Departament de Ciència de Materials i Química Física & Institut de Química Teòrica i Computacional de la Universitat de Barcelona (IQTCUB), c/ Martí i Franquès 1-11, 08028 Barcelona, Spain
[c] ICREA (Institució Catalana de Recerca i Estudis Avançats), 08010 Barcelona, Spain

ARTICLE INFO

Keywords:
Fuel cells
Bimetallic alloy catalyst
Oxidation
Reduction
Surface reconstruction

ABSTRACT

In this work changes in surface chemistry and morphology of PtNi alloy induced by redox environments were investigated by photoelectron spectroscopy, atomic force microscopy and substantiated by theoretical calculations. PtNi was exposed to alternating oxidation (O_2) and reduction (H_2) gaseous atmospheres at different temperatures (298, 373, 523 K) to simulate its behavior as a cathode catalyst in proton exchange membrane fuel cells.

Results showed that the PtNi alloy undergoes surface nickel enrichment under switched reactive environments. The most significant effects occurred at 523 K, when the Ni/Pt surface atomic ratio increased from 0.8 to 6.7 after five redox cycles, while the bulk Ni/Pt value reached 2.3. Along with compositional changes catalyst coarsening was observed.

The revealed behavior of the PtNi alloy allows a better understanding of the structural dynamics of a bimetallic catalyst during its interaction with reactive environments that is a prerequisite for development of efficient fuel cell catalyst.

1. Introduction

In many catalytic reactions, bimetallic nanoalloys exhibit higher activity than their monometallic counterparts [1–3]. Such activity enhancement has been attributed to a structural modification of catalyst and also to changes in its electronic structure, which is more favorable for the interaction with the reaction intermediates. That is why engineering the structure and composition of the bimetallic catalyst allows tuning its catalytic activity toward selected reaction for emerging nanotechnologies [3–8]. Among bimetallic catalytic systems, one of the most vivid examples is alloying platinum with low-cost 3d transition metals for the cathode catalyst in proton exchange membrane fuel cells (PEMFCs) [7,9–11]. Such alloying was found to optimize the surface properties of Pt to enhance a sluggish oxygen reduction reaction (ORR).

On the other hand, bimetallic catalysts are very complex systems, which often do not maintain their surface structure and chemical integrity under specific reaction conditions [12–15]. The reactive gases, temperature, as well as pressure conditions of catalytic reactions could initiate interdiffusion of constituent elements and significantly affect valuable properties of alloy materials [4,13,16–18]. Such behavior is a complex phenomenon driven by the interplay of multiple parameters, such as bonding of each metallic component with a given adsorbate, their surface energies, diffusion barriers, etc. The behavior of bimetallic catalysts under specific reaction conditions is becoming a major focus of researchers in order to advance the understanding of the alloy restructuring for the further optimization of such systems.

X-ray photoelectron spectroscopy (XPS) is one of the most widely used techniques able to provide a profound understanding of the chemical restructuring processes on the surface of bimetallic alloys because it can characterize both the material composition and chemical states of the constituent elements [19]. Yet, conventional XPS instruments work with fixed and relatively high X-ray energy (*e.g.*, 1486.6 eV for Al Kα excitation). Thus, they are unable to resolve small changes in the elements contributions in the outer layer of the alloy because of the

* Corresponding author.
** Corresponding author at: Departament de Ciència de Materials i Química Física & Institut de Química Teòrica i Computacional de la Universitat de Barcelona (IQTCUB), c/ Martí i Franquès 1-11, 08028 Barcelona, Spain.
E-mail addresses: khalakhan@gmail.com (I. Khalakhan), konstantin.neyman@icrea.cat (K.M. Neyman).

https://doi.org/10.1016/j.apcatb.2019.118476
Received 1 September 2019; Received in revised form 25 November 2019; Accepted 26 November 2019
Available online 27 November 2019
0926-3373/

relatively high inelastic mean free paths of detected photoelectrons [20]. Moreover, different inelastic mean free paths of photoelectrons for different elements can impede precise characterization of bimetallic alloys. Synchrotron radiation photoelectron spectroscopy (SRPES), in turn, allows tuning the excitation energy of photons (E_p), so that the kinetic energy of escaping photoelectrons for both studied metals can be set to the same value ensuring precise measurements of the constituent elements distribution. Furthermore, photon energies can be adjusted to obtain different surface sensitivity including the highest one, which typically detects just a few top atomic layers. This allows a depth-weighted analysis of the bimetallic alloy.

In this work, we report a fundamental study on the phenomena that occur on the surface of cathode bimetallic catalyst during PEMFCs operation. In addition to the overall complexity of PEMFCs operation the severity in operating conditions is further escalated by their transient and cyclic nature. For example, during high load operation of the fuel cell (0.6-0.8 V) the catalyst is in its metallic state. Contrary, during shut-down or start-up conditions (potential is $0.95-1$ V and up to 1.5 V, respectively) the cathode catalyst is oxidized. The so-called accelerated stress tests (ASTs) were thus developed to accurately simulate catalyst degradation in the fuel cells in the much shorter time frame [21–23]. During AST the oxidation and reduction of the catalyst are realized by potential cycling from low to high potentials in an acidic electrolyte. In order to gain advanced insights on the processes that occur during oxidation and reduction cycles, we investigate the temperature-dependent surface restructuring of a PtNi thin film catalyst in response to a series of alternating oxidation (O_2) and reduction (H_2) gaseous atmospheres using SRPES and XPS techniques. The experimental results are substantiated by theoretical calculations of model PtNi nanoalloys. The focus is given to the surface chemistry aspects in PtNi alloy top layers induced by reducing and oxidizing media which simulates catalyst behavior in a real fuel cell device.

2. Experimental

2.1. Sample preparation

PtNi films were deposited on glassy carbon (GC) substrates (Alfa Aesar) using simultaneous magnetron sputtering from two targets: 2" Pt (99.99 % Safina) and 2" Ni (99.99 % Lesker). Circular TORUS magnetrons (Lesker) were placed both under the angle of 45° to the substrate. The target-to-substrate distance was 120 mm. Prior to the deposition, the chamber was evacuated to 7×10^{-6} mbar. The sputtering was carried out in 5×10^{-3} mbar of Ar atmosphere in DC mode by applying 20 W and 28 W for the Pt and Ni targets, respectively. The total sputtering time was 3.5 min, which at above-listed parameters forms a 10 ± 0.4 nm PtNi film with a composition of approximately 50 at.% Pt and 50 at.% Ni.

2.2. Sample characterization

The high-resolution SRPES measurements were performed at the Materials Science Beamline at the Elettra synchrotron light source in Trieste, Italy. The beamline uses a plane grating monochromator, providing narrow band synchrotron light in the energy range of 21–1000 eV. The end-station consists of a main ultra-high vacuum (UHV) chamber (base pressure 2×10^{-10} mbar) equipped with a Specs Phoibos 150 electron energy analyzer and additionally with a dual Mg/Al X-ray source for conventional XPS measurements. The sample oxidation and reduction were performed in the preparation chamber (connected to the analysis chamber) in O_2 and H_2 atmospheres, respectively; in both cases at 5 mbar for 1 h. Three different temperatures were used: room temperature (298 K), 100 °C (373 K), and 250 °C (523 K). After each oxidation and reduction step, the sample was transferred back to the analysis chamber without exposure to air. During all SRPES measurements the Pt 4f, Ni 3p, Ni 2p, and O 1s core level spectra were recorded at different photon energies (180 eV for Pt 4f and Ni 3p, 650 eV for O 1s, 980 eV for Ni 2p). XPS spectra were acquired at 1486.6 eV (Al Kα radiation) photon energy. The data processing was done using the KolXPD software [24].

The initial surface cleaning was performed in two steps. First, the sample was exposed to hydrogen atmosphere (5 mbar, room temperature) to reduce a surface oxide layer and remove adsorbates from the catalysts. Afterward, it was subjected to mild Ar^+ ion bombardment (1000 eV for 5 min).

Energy-dispersive X-ray spectroscopy (EDX) was performed using a Bruker XFlash detector attached to a Tescan Mira III scanning electron microscope (SEM) operated at 20 kV electron energy.

Atomic Force Microscopy (AFM) measurements were taken on a MultiMode 8 AFM (Bruker) in tapping mode under ambient conditions. SCANASYST-AIR probes (Bruker) were used with a nominal tip radius of 2 nm. Image processing was carried out using the NanoScope 1.5 software.

2.3. Computational details

Density functional theory (DFT) calculations were carried out using the plane-wave basis set code Vienna *ab initio* simulation package (VASP) [25,26]. The generalized gradient approximation (GGA) Perdew-Burke-Ernzerhof (PBE) exchange-correlation functional [27] was employed in combination with the projector augmented wave representation of core electron density [28,29]. The PBE functional has been proven to be among the most accurate choices in describing transition metal bulk and surface properties [30,31]. Only the **Γ**-point of the reciprocal space Brillouin zone was sampled for the numerical integrations, given that the nanoparticle models are isolated in large cubic periodic boxes, *vide infra*. The cutoff energy for the plane-wave functions was set to ~230 eV, which has been found sufficient for bimetallic systems [32]. One-electron Kohn-Sham levels were smeared by 0.1 eV yet final energies were extrapolated to a zero smearing situation. All atoms were locally relaxed without any restrictions until forces acting on each atom became less than 0.02 eV·Å^{-1}.

The studied by DFT atomic models are 1:1 Pt:Ni nanoalloy particles formed of 201 or 314 atoms. The data for these nanoparticles (NPs) were used to calculate the chemical ordering in bigger nanoparticles of 1463 atoms. These truncated octahedral NPs maintain the parent Pt or Ni face centered cubic (*fcc*) crystallographic structure, featuring (001) and (111) types of facets according to the Wulff constructions minimizing the NP surface tension [33]. The 201 and 314 atoms NPs are in the size regime, where properties are either scalable to bulk or basically converged with size [34], allowing their use to simulate larger NPs or low-coordinated sites. Such NPs were isolated in $2.5 \times 2.5 \times 2.5$ nm and $2.7 \times 2.7 \times 2.7$ nm large periodically repeated cells, respectively, always ensuring more than 0.8 nm between adjacent replicated NPs particles, thus interacting negligibly weak with each other [35].

The contributions governing the atomic arrangement (atomic or chemical ordering) in Pt-Ni nanoalloys were determined employing our method for global optimization of the ordering in a NP of a given shape, size, and composition. This method [32,36], hereafter denoted TOP, is based on simple energy expressions defined by locations of metal atoms in crystalline positions of the NP, *i.e.* solely by the topology of the latter. The TOP method has been successfully applied to such different bimetallic nanocrystallites as Pd–Au [32,36,37], Pd–Ag [32], Pd–Cu [32], Pd–Zn [32], Pd–Rh [38], Pt-Ag [39], Pt–Co [40,41], Pt–Sn [42], and Ni–Cu [43]. Deviation from the crystallinity, *e.g.* in sub-nanometer particles or in combinations of metal atoms with large size mismatch, is one of few factors limiting the applicability of the TOP method. The method provides ε_i parameters (descriptors) associated either with the surface segregation energy of one given element, here Pt, or with the interaction energy of the nearest-neighbor Pt–Ni pairs of atoms (termed hereafter Pt–Ni bond energy). The values of ε_i were obtained *via* fitting to DFT energies of several dozens of NP structures with different

chemical orderings. The corresponding TOP expressions were employed in efficient Monte-Carlo (MC) simulations to predict globally optimized atomic orderings in PtNi NPs subsequently confirmed by DFT calculations, and also used to get energetic estimates of much larger PtNi NPs, see below. The adsorbate entropy contribution was not taken into account, because it only marginally affects the overall system energy, mainly governed by the adsorption energy [44].

3. Results and discussion

The simultaneous magnetron co-sputtering of Pt and Ni leads to the formation of very homogeneous alloy films as can be seen on the elemental maps acquired using EDX in Fig. S1a. The PtNi elemental bulk composition of as-received samples estimated from EDX spectrum (Fig. S1b) was $Pt_{0.53}Ni_{0.47}$.

The as-received bimetallic catalyst was further investigated using SRPES. Due to the sample transferring from the deposition chamber to the analysis chamber through air, it is partially oxidized on the surface (see upper SRPES spectra in Fig. S2 of the Supporting Information). The Pt 4f + Ni 3p, Ni $2p_{3/2}$ and the O 1s SRPES spectra of the cleaned sample in Fig. S2 (bottom spectra) indicate that both elements are in fully metallic states. Pt 4f shows single doublet at the binding energy (BE) of 71.1–74.4 eV which corresponds to metallic platinum [14,16,45]. The Ni $2p_{3/2}$ spectrum consists of one peak at 852.6 eV and its satellite characteristic for metallic nickel. Metallic character is also substantiated by the absence of the O 1s peak after the cleaning procedure. We will refer to the cleaned sample as the as-deposited (AD). The elemental composition of as-deposited PtNi alloy obtained from fitted SRPES spectra is $Pt_{0.54}Ni_{0.46}$ which is in good agreement with the composition measured by EDX indicating that cleaning procedure resulted in the exposure of bulk material with the desired atomic ratio.

Our samples were then subjected to series of altering O_2 (5 mbar) and H_2 (5 mbar) gas environments at 298, 373, and 523 K. Note that different photon energies were chosen for measuring Pt 4f (180 eV) and Ni 2p (980 eV) core levels in order to equalize kinetic energies of escaping electrons (providing very close photoelectron inelastic mean free paths) for Pt and Ni. Thus, comparable probing depth (~1 nm or ~3 monolayers) has been achieved for both elements. Results of the first oxidation step (Ox1) are presented in Fig. 1, where high-resolution SRPES spectra of Pt 4f together with Ni 3p and Ni $2p_{3/2}$ core levels acquired at different substrate temperatures are illustrated. Ni $2p_{3/2}$ spectra were used for determination of the chemical state of nickel. In turn, the Ni 3p spectra were used to calculate Pt_xNi_y stoichiometry because they were acquired at the same parameters (photon flux, transmission function, surface sensitivity) as the Pt 4f spectra. Since Ni 3p partially overlaps the Pf 4f spectrum, for the proper Pt 4f fitting, we first measured the Ni 3p spectrum of pure Ni oxide film. The fitted Ni 3p spectrum in Fig. S3 consists of three doublets corresponding to metallic nickel, nickel oxide, and nickel hydroxide [46,47]. The same fitting procedure as for the Ni 3p spectra was then applied for all samples when fitting the Pt 4f + Ni 3p spectra. We also remark that for Ni 2p the spin-orbit splitting of the $2p_{3/2}$ and $2p_{1/2}$ is sufficient to consider only the more intense $2p_{3/2}$ signal [48].

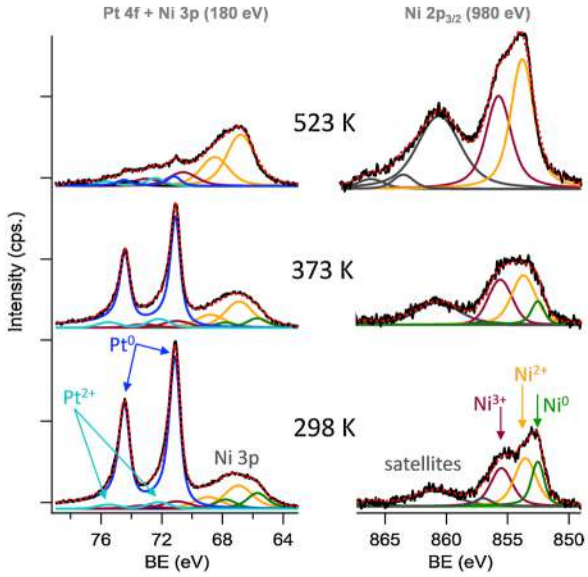

Fig. 1. SRPES spectra of Pt 4f together with Ni 3p (180 eV photon energy) and the Ni $2p_{3/2}$ (980 eV photon energy) core level regions of the PtNi catalyst acquired after its oxidation in 5 mbar of O_2 (Ox1) at different substrate temperatures.

The bottom Ni $2p_{3/2}$ spectrum in Fig. 1 corresponds to the sample oxidized at 298 K. It is deconvoluted into multiple contributions. In addition to the peak of metallic nickel at 852.6 eV and its satellite [14,48,49], the oxidation at room temperature is characterized by the appearance of two peaks at 854.0 and 855.7 eV and their satellites. The first peak can be assigned to Ni^{2+} (NiO) and second, due to the multiplet splitting of Ni $2p_{3/2}$ for NiO, to both Ni^{2+} (NiO) and Ni^{3+} (Ni_2O_3/$Ni(OH)_2$) [48–50]. In turn, platinum remains predominantly in the metallic state with a doublet at 71.1–74.4 eV (bottom spectrum in Fig. 1) [14,16,45]. Yet a very minor fraction of Pt^{2+} can be distinguished at 72.2–75.5 eV, which can be attributed to platinum–nickel mixed oxide phase [16,45]. After oxidation at 373 K, the spectra of Ni become evidently dominated by oxidic species with respect to the previous case. However, a significant fraction of Ni^0 can be still observed evidencing the presence of metallic nickel probably at the subsurface regions of PtNi alloy. Pt is insignificantly affected by oxidation at 373 K since no drastic changes can be observed in the Pt 4f spectra in comparison to the case of oxidation at 298 K. The O_2 treatment at 523 K results in high oxidation of both metals. The Ni $2p_{3/2}$ spectrum shows complete disappearance of the Ni^0 signal at the outermost layers of the PtNi alloy. Beyond that, a significant decrease of the Pt 4f signal together with additional oxidation of platinum is observed. The results point to the formation of relatively thick bulk mixed oxides on the surface of the alloy. The evolution of oxidic species on the surface of PtNi alloy can be also seen in the O 1s spectra shown in Fig. S4.

The observed chemical transformations induce significant composition changes on the surface of the alloy catalyst. Table 1 contains relative elemental compositions of the PtNi alloy estimated from the integrated areas of the fitted Pt 4f and Ni 3p spectra after taking into account sensitivity factors (2.276 for Pt 4f and 0.8804 for Ni 3p). The results show that under O_2 treatment the formation of surface nickel oxide species is accompanied by nickel enrichment on the surface. With increasing temperature nickel diffusion to the surface increases and becomes particularly strong at 523 K where only 10 % of Pt remains in the outermost layers of the alloy. Such interdiffusion behavior is consistent with previously published reports [17,18,49,51–53]. Contrarily to the behavior of PtNi annealed in vacuum, the stronger bonding of O to Ni as compared to Pt is the main driving force making Ni segregation to the surface of an alloy a dominating mechanism in an oxidizing media. The results also show a temperature driven Ni segregation behavior. The amount of Ni segregated to the surface at 298 K is much lower than at 523 K.

Table 1
Relative atomic concentration of Pt and Ni in outer layers calculated from the fitted Pt 4f and Ni 3p spectra acquired at 180 eV photon energy after oxidation (Ox1) at different temperatures.

	Pt (at.%)	Ni (at.%)
AD	55	45
Ox1 298 K	43	57
Ox1 373 K	38	62
Ox1 523 K	8	92

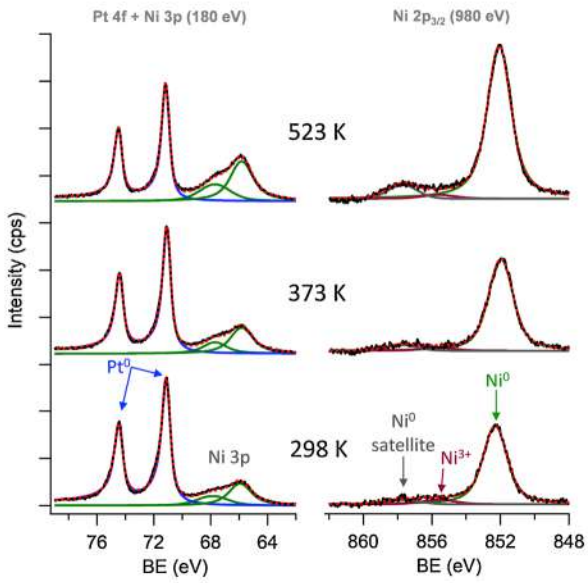

Fig. 2. SRPES spectra of Pt 4f together with Ni 3p (180 eV photon energy) and Ni $2p_{3/2}$ (980 eV photon energy) core level regions of the PtNi catalyst acquired after reduction in 5 mbar of H_2 (Red1) at different substrate temperatures.

Subsequent exposure of our samples to 5 mbar of H_2 for 1 h (denoted as Red1) causes the reduction of oxide species, formed on the surface during oxidation, back to metallic state as can be seen in Fig. 2. Ni $2p_{3/2}$ spectra show that independently of the temperature all peaks corresponding to nickel oxides and its satellites almost vanished. The dominant peak at 852.6 eV and its satellite correspond to metallic nickel. Yet, a very minor fraction of Ni hydroxide leftovers can be distinguished at 855.6 eV. The presence of Ni hydroxide species on the surface after reduction is confirmed by the O 1s spectra in Fig. S4. The Pt 4f spectra consist of only one doublet of metallic platinum at 71.1–74.4 eV.

The reduction, in turn, causes back diffusion of Ni atoms inside the host alloy. Table 2 summarizes relative elemental compositions of PtNi alloy estimated from the integrated areas of the fitted spectra shown in Fig. 2 taking into account the sensitivity factors. Notably, the composition of PtNi after reduction differs from the original one before oxidation evidencing not completely reversible compositional changes. Apparently, the driving force for Ni diffusion back into the alloy (or Pt segregation to the surface) in H_2 is much weaker than that for the discussed above Ni segregation in O_2 leading to Ni enrichment in the surface layers of the alloy after one oxidation/reduction cycle [17].

More detailed insights into the behavior of the PtNi films during altered oxidizing and reducing environments can be derived from Fig. 3, where evolution of the Pt 4f + Ni 3p and the Ni 2p spectra during five consecutive oxidation/reduction cycles at different temperatures is shown. At each cycle, the spectra obtained during oxidation are imposed with the spectra acquired during subsequent reduction to facilitate the comparison. In turn, Fig. 4a displays the evolution of the Ni/Pt atomic ratios during all five oxidation/reduction cycles estimated from the integrated areas of all fitted Pt 4f and Ni 3p spectra depicted in Fig. 3 divided by the corresponding photoionization cross sections.

Table 2
The relative atomic concentration of Pt and Ni in outer layers calculated from the fitted Pt 4f and Ni 3p spectra acquired at 180 eV photon energy after reduction (Red1) at different temperatures.

	Pt (at.%)	Ni (at.%)
Red1 298 K	51	49
Red1 373 K	45	55
Red1 523 K	30	70

Independently of the temperature, an oscillatory behavior can be observed consisting of surface segregation of Ni in the oxidizing environment and its subsequent back diffusion in the reducing environment. Nearly reversible changes can be observed at 298 K only. However, the small difference in alloy composition after 5 cycles can be distinguished even at room temperature. At 373 K surface changes in response to reactive environments become more pronounced: in fact, the Ni/Pt atomic ratio changes from 0.8 to 1.9 during the entire cycling procedure. At 523 K PtNi alloy undergoes significant surface reconstruction during switching between oxidizing and reducing conditions in terms of relative surface nickel enrichment. The Ni/Pt atomic ratio increases from 0.8 to 6.7. It is noteworthy that oscillations of the surface composition are stabilized after two cycles and become more or less reversible.

In order to dig more into the bulk of PtNi alloy XPS measurements were carried out. The photoelectron energy of 1486.6 eV allows probing ~5 nm of the material. This time we are only focusing on Pt 4f and Ni 3p spectra to achieve comparable kinetic energies of photoelectrons (probing depth) for both elements. Fig. 5 displays the evolution of the Pt 4f and the Ni 3p spectra during five consecutive oxidation/reduction cycles at different temperatures. It is evident that changes are much smaller than those in Fig. 3, which is attributed to smaller deviation in the alloy composition in the bulk.

The evolution of the relative atomic ratio of Ni during all five oxidation/reduction cycles estimated from the integrated areas of all fitted Pt 4f and Ni 3p XPS spectra divided by the corresponding photoionization cross sections is depicted in Fig. 4b. The oscillatory behavior at 298 K and 373 K is more subtle, but nevertheless detectable. The composition of PtNi remains practically reversible during five redox cycles. At 523 K PtNi alloy undergoes irreversible changes upon cycling. The Ni/Pt atomic ratio changes from 1 to 2.6 during the entire cycling procedure. However, it should be noted that about 60 % of total XPS signal comes from the first 1.7 nm of the alloy. As a result, our bulk measurements are still influenced by the relatively high surface changes described above.

The interdiffusion of Pt and Ni and corresponding structural switching between the surface NiO and the Pt-skin surface during alternating oxidation and reduction environments have been reported previously [16,18,54,55]. The observed changes in alloy composition, however, were much smaller than the presently identified changes and in some works were even reported as completely reversible. We attribute this to the fact that conventional XPS was used giving higher probing depth and additionally different mean free paths for Pt 4f and Ni photoelectrons. In our case, where only 2–3 outermost monolayers are probed with the similar mean free paths for both Pt and Ni photoelectrons, changes in the Ni/Pt ratio can be followed more precisely. As mentioned above, the driving force for Ni reabsorption (or Pt segregation to the surface) in H_2 should be weaker than the Ni segregation in O_2. This causes gradual Ni enrichment in the surface layers of the alloy during oxidation/reduction cycle as was observed by aberration-corrected environmental TEM for PtCo alloy [17]. Even though the evaporation of Pt in the form of PtO_2 in oxidizing atmosphere at higher temperature [16,56] cannot be excluded completely, our results rather point to the Pt inward segregation scenario. This is also substantiated by EDX bulk measurements after the entire cycling procedure at 523 K (not shown herein) which shows no substantial changes in the atomic ratio compared to that measured before cycling.

Along with the compositional variation, oxidation/reduction cycling causes morphological changes of the PtNi catalyst. Fig. 6 displays *ex situ* AFM images of PtNi alloy. Image (a) corresponds to the cleaned sample before interaction with reactive atmospheres. Images (b) and (c) were acquired after five oxidation/reduction cycles at 298 K and 523 K, respectively.

It should be noted that when measured by AFM grain size differs from the absolute value because of the effect of convolution between

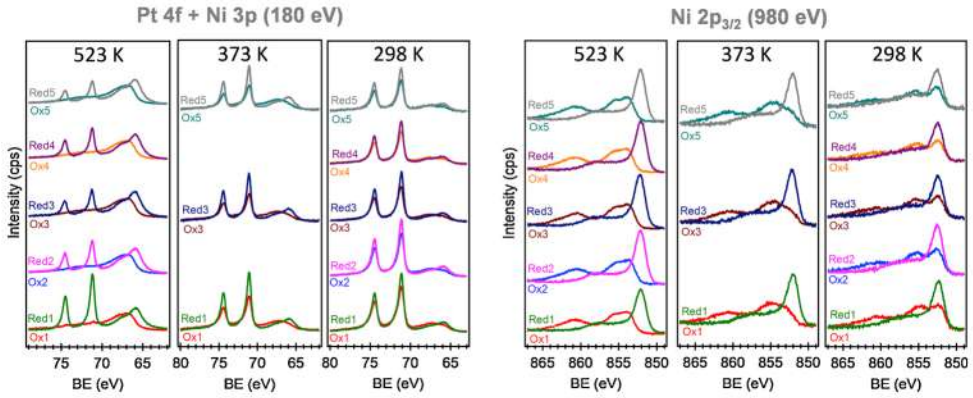

Fig. 3. The set of SRPES Pt 4f + Ni 3p acquired at 180 eV photon energy and the Ni $2p_{3/2}$ spectra acquired at 980 eV photon energy during five oxidation/reduction cycles of PtNi alloy.

catalyst grains and the AFM tip. A statistical analysis of AFM images can help to quantitatively inspect the characteristics of the surface morphology. This was achieved by analyzing the height-height correlation functions (HHCFs) computed from the corresponding AFM images [57]. The root mean square roughness (R_q) representing a vertical deviation of the surface morphology and correlation length (ξ) which, in turn, represents a lateral roughness (related to the grain size) were calculated from HHCF [58,59] and summarized in Table 3. The results show a modest change of the surface morphology after 5 oxidation/reduction cycles at 298 K. At 523 K more prominent catalyst coarsening occurs, which can be explained by enhanced atomic (Ostwald ripening) and grains (coalescence) mobility at elevated temperatures [16,55]. Such behaviour is in line with electrochemical studies where oxidation and reduction of PtNi alloy is realized by cyclic voltammetry [14,60–62].

In a real fuel cell device, due to corrosive condition at cathode side, surface Ni atoms would dissolve to electrolyte [14,63]. In our previous studies on PtNi and PtCo catalysts investigated under potentiodynamic cycling in acidic electrolyte we observed continuous Ni(Co) leaching with increasing of cycle number [14,64]. We showed that structural changes during cycling were responsible for the continuous dissolution of 3d-metal, even that buried under protective platinum layers. Moreover, we suggested that during electrochemical cycling the surface oxidation at each cycle may additionally contribute to Ni segregation and its dissolution. The results described in this paper corroborate this suggestion. Indeed, with increasing the number of redox cycle in gaseous atmosphere continuous Ni enrichment on the surface of the alloy was detected. The continuous leaching of Ni from the surface of the alloy during fuel cell operation will result in increasing of the thickness of pure Pt overlayers and catalyst will eventually lose its remarkable properties given by the presence of Ni. Moreover, irretrievable Ni dissolution in real fuel cells can cause membrane and catalyst poisoning

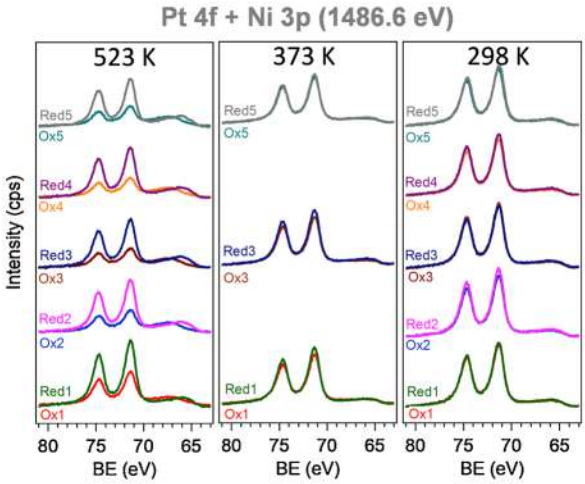

Fig. 5. The set of SRPES Pt 4f + Ni 3p spectra acquired at 1486.6 eV photon energy during five oxidation/reduction cycles of PtNi alloy.

[65].

In order to deepen the understanding of the structure of our catalyst, we carried out theoretical calculations for model PtNi NPs. DFT calculations of bimetallic particles containing over hundred atoms became feasible more than a decade ago [66]. Yet, the great complexity of alloy NPs due to the presence of two types of metal atoms hindered their extensive computational studies. Two more degrees of freedom characterize a bimetallic particle A_mB_n of a specified geometry (shape) and number of atoms m + n compared to the corresponding monometallic particles A_{m+n} and B_{m+n}: (*i*) the composition - this is, the m:n ratio -

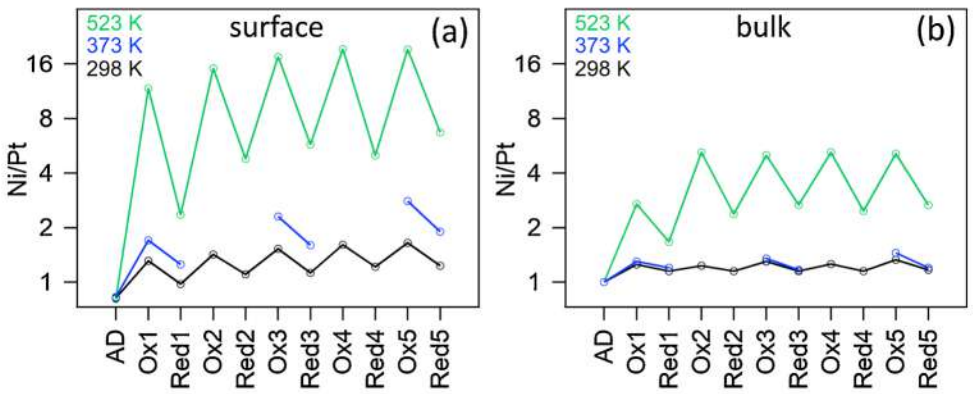

Fig. 4. The evolution of Ni/Pt atomic ratio on the surface (a) and the bulk (b) of PtNi alloy during five oxidation/reduction cycles extracted from the integrated areas of the Pt 4f and Ni 3p spectra divided by the corresponding photoionization cross sections.

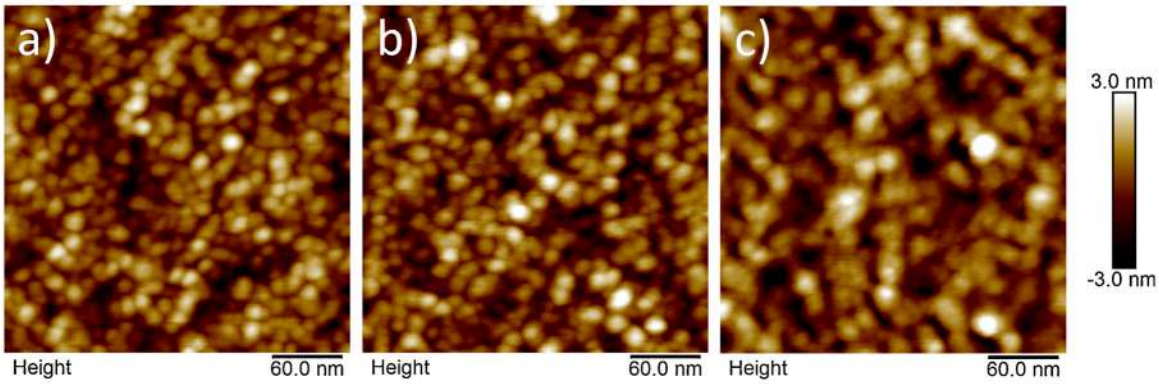

Fig. 6. *Ex situ* AFM images of PtNi alloy: (a) as-deposited; (b) after five oxidation/reduction cycles at 298 K; (c) after five oxidation/reduction cycles at 523 K.

Table 3
Values of the root mean square roughness (R_q) and correlation length (ξ) calculated from the HHCFs for the as-deposited sample and samples processed 5 oxidation/reduction cycles at different temperatures.

	R_q (nm)	ξ (nm)
AD	1.05	10
5 cycles at 298 K	1.15	11
5 cycles at 523 K	1.30	14

and (*ii*) the atomic ordering — the pattern of positions that A and B atoms occupy in the given particle geometry. The number of structures different only by A and B atomic positions in a given particle geometry, denoted as homotops [67], exponentially increases with particle size. This limits detail exploration of the homotop landscape to much smaller particles than those of thousand and more atoms common in catalytic applications. In order to address this issue, we model in the present work PtNi NPs of 1:1 composition formed of 201–1463 atoms (1.5–4.4 nm, respectively) using a novel efficient tool for optimizing atomic ordering of large bimetallic NPs evaluating their stability based on the TOP energetic descriptors [32,36].

Structures with the lowest-energy atomic orderings of truncated octahedral model NPs $Pt_{101}Ni_{100}$ and $Pt_{157}Ni_{157}$ optimized by DFT calculations are shown in Fig. S5. Pre-screening of atomic orderings for finding putative lowest-energy homotops was performed by MC simulations [32] using the ε_i energy descriptors. These descriptors define the TOP energy differences ΔE_{TOP} between any two homotops of a given Pt_nNi_m NP as

$$\Delta E_{TOP}(Pt_nNi_m) = \varepsilon^{Pt-Ni}_{BOND}\cdot\Delta N^{Pt-Ni}_{BOND} + \varepsilon^{Pt}_{CORNER}\cdot\Delta N^{Pt}_{CORNER} + \varepsilon^{Pt}_{EDGE}\cdot\Delta N^{Pt}_{EDGE} + \varepsilon^{Pt}_{TERRACE}\cdot\Delta N^{Pt}_{TERRACE} \quad (1)$$

depending on the difference (ΔN) in the number of Pt–Ni bonds (N^{Pt-Ni}_{BOND}) and the numbers of corner (N^{Pt}_{CORNER}), edge (N^{Pt}_{EDGE}) and terrace ($N^{Pt}_{TERRACE}$) surface Pt atoms in each homotop.

The following TOP expressions (in eV) correspond to two kinds of the studied PtNi NPs with 201 and 314 atoms:

$$\Delta E_{TOP}(Pt_{101}Ni_{100}) = -0.048\cdot N^{Pt-Ni}_{BOND} - 0.581\cdot N^{Pt}_{CORNER} - 0.513\cdot N^{Pt}_{EDGE} - 0.399\cdot N^{Pt}_{TERRACE} \quad (2)$$

$$\Delta E_{TOP}(Pt_{157}Ni_{157}) = -0.033\cdot N^{Pt-Ni}_{BOND} - 0.465\cdot N^{Pt}_{CORNER} - 0.490\cdot N^{Pt}_{EDGE} - 0.324\cdot N^{Pt}_{TERRACE} \quad (3)$$

More information about $Pt_{101}Ni_{100}$ and $Pt_{157}Ni_{157}$ NPs is given in the Supplementary Information.

We then applied TOP Eqs. (2) and (3) determined by descriptors for 201- and 314-atomic 1:1 PtNi NPs to perform a MC search for the lowest-energy homotop of truncated octahedral 1463-atomic PtNi NP exposing extended {111} facets (see Fig. 7). This NP has a size of *ca.* 4.4 nm, which is well beyond the sizes practically accessible by DFT calculations and comparable with NP sizes in catalytic experiments. The lowest-energy homotops of this NP exhibit core@shell structures with the outer shell formed of Pt atoms and Ni atoms tending to be located inside the NP. Hence, the atomic ordering patterns of this large NP are similar to the patterns of the NPs smaller than 2 nm (see Fig. S5 in SI).

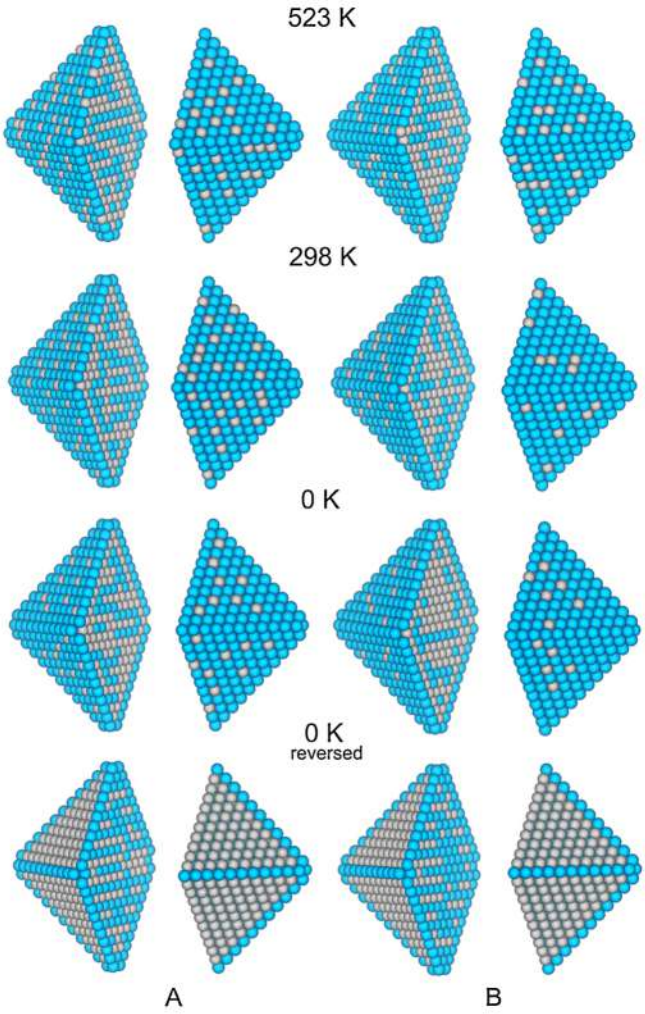

Fig. 7. Atomic ordering in the lowest-energy homotops of *ca.* 4.4 nm large truncated octahedral 1463-atomic NP $Pt_{731}Ni_{732}$ at varying temperature. Columns A and B display homotops calculated using the TOP Eqs. (2) and (3), respectively. Color coding: Pt – blue, Ni – grey. (For interpretation of the references to colour in this figure legend, the reader is referred to the web version of this article).

The main cause for some differences in the surface compositions of the smaller and larger 1:1 NPs is the ratio of surface (corner + edge + terrace) to inner atoms, which rapidly decreases with increasing particle size. This ratio (24 + 36 + 62):79 = 1.54 for the 201-atomic NP decreases to (24 + 48 + 102):140 = 1.24 for the 314-atomic NP and drops to just (24 + 108 + 440):891 = 0.64 for the 1463-atomic NP.

The applicability of the TOP Eqs. (2) and (3), determined for the 201- and 314-atomic NPs, respectively, to model atomic ordering in much larger NPs is corroborated by the findings that the TOP descriptors for particles starting from just *ca.* 100 atoms commonly change only insignificantly for accessible by DFT larger NPs with the same content of two metals. This resemblance of the TOP descriptors for the NPs of two sizes, $Pt_{101}Ni_{100}$ and $Pt_{157}Ni_{157}$, is also the case for the PtNi NPs under scrutiny (*vide supra*). This is illustrated for the lowest-energy homotops of $Pt_{731}Ni_{732}$ NP in Fig. 7, where the images in columns A and B depict the atomic ordering patterns of the homotops optimized using the TOP Eq. (2) for the smaller $Pt_{101}Ni_{100}$ NP and Eq. (3) for the larger $Pt_{157}Ni_{157}$ NP, respectively. The TOP energy difference for this differently optimized pair of $Pt_{731}Ni_{732}$ homotops is very small, only 0.6 eV or just 0.4 meV/atom (Eq. (3)) and 1.8 eV or 1.2 meV/atoms (Eq. (2)).

The DFT and TOP data presented so far correspond to 0 K. The TOP method allows estimating properties associated with the Boltzmann population of different homotops of a NP at a given temperature by accounting for entropy contributions related to atomic ordering, not considering, however, the atomic vibrations [36]. We applied this protocol to calculate probabilities of occupying each site by either Pt or Ni atoms and to estimate average atomic orderings in the 1463-atomic NPs $Pt_{731}Ni_{732}$ at 298 K and 523 K (see Fig. 7 and Table S1). The temperature increase does not substantially change the atomic ordering pattern. It mainly acts to slightly decrease the number of surface terrace and (to lesser extent) edge Pt atoms by relocating them inside the NP with a concomitant increase of the number of Pt-Ni bonds, thus enhancing the mixing of two metal components. Overall, these data support experimental results on Pt surface segregation in the AD sample, as determined by SRPES, and also the Ni increase on the surface by annealing.

To shed light on changes induced by adsorbates in the surface composition of well-ordered metal NPs with extended terraces that bind adsorbates essentially as strong as the corresponding single-crystal surfaces [68], one can use adsorption preference energies defined as the difference of binding energies of a given adsorbate on surfaces of two metals forming the bimetallic NPs under study [69]. Along this line, we calculated adsorption energies of a single O atom on {111} facets of the corresponding monometallic Pt_{201} and Ni_{201} NPs. Atomic oxygen adsorption is more relevant to the present experiments than the molecular adsorption due to facile O_2 dissociation on both Pt and Ni surface sites, with the corresponding DFT O_2 dissociation activation barriers 0.3-0.45 eV [70] and 0.2 eV [71]. DFT (PBE) adsorption energies of atomic O on three-fold hollow *fcc* sites of Pt(111) and Ni(111) surfaces are 3.12 and 4.26 eV, respectively. From these data the adsorption preference of O to the Ni(111) surface *vs.* Pt(111) one is 1.14 eV. Combining this value with the TOP descriptor values from Eqs. (2) and (3), defining surface segregation energy of Pt and Ni atoms on {111} nanofacets, $\varepsilon^{Pt}_{TERRACE} = -\varepsilon^{Ni}_{TERRACE}$, *ca.* 0.40 and 0.32 eV, respectively, one can estimate surface atomic ordering of PtNi NPs in the presence of adsorbed O and predict, neglecting surface reconstruction effects, variation of the ordering with the adsorbate coverage. Thus, the adsorption of one O atom on a NP with a Ni@Pt core@shell like structure provides a stabilization energetically sufficient for surface re-segregation of three to four Ni atoms. For instance, the surface segregation of Ni atoms on the {111} terraces of the $Pt_{731}Ni_{732}$ NP, optimized using Eq. (2), to substitute all 367 Pt atoms located there at 0 K (see Table S1) would destabilize the NP by 146.4 eV, an equivalent amount to the energy gained by adsorption on Ni terrace sites of 128 O atoms, each stabilizing the system by *ca.* 1.14 eV. The corresponding data for the $Pt_{731}Ni_{732}$ NP, optimized using Eq. (3), are 403 Pt atoms on the {111} terraces, whose replacement by Ni is destabilizing by 130.6 eV, to be compensated by adsorption of 115 terrace O atoms. This estimation implies that already *ca.* 0.30 monolayer (ML) O coverage of in total 440 {111} terrace sites exposed on the $Pt_{731}Ni_{732}$ NP is energetically sufficient to make all {111} terrace atomic positions occupied by Ni atoms, defined as *reversed* homotops in Fig. 7 and abbreviated as *rev* in Table S1. Explicit TOP energy differences between the lowest-energy homotops at 0 K $Pt_{731}Ni_{732}$ with all {111} terrace Pt atoms and the so-called reversed homotops taking into account also different numbers of the Pt–Ni bonds are 138.3 eV (Eq. (2)) and 114.4 eV (Eq. (3)). This slightly decreases the estimated O coverage required to substitute all Pt atoms on {111} facets of $Pt_{731}Ni_{732}$ by Ni atoms to 0.23–0.28 ML.

A similar analysis has also been performed employing DFT adsorption energies of atomic H on the three-fold hollow *fcc* sites of Pt and Ni (111) surfaces, 1.43 and 1.52 eV, respectively. The adsorption energy preference for H, 0.09 eV, is thus an order of magnitude smaller than that for O. Consequently, the complete surface segregation of Ni atoms on the {111} terraces of the $Pt_{731}Ni_{732}$ NP evaluated using Eq. (2) destabilized by 146.4 eV would require the energy gained by adsorption of many more H atoms than of O atoms, namely 1627 H atoms on Ni terrace sites. The corresponding destabilization of $Pt_{731}Ni_{732}$ NP evaluated using Eq. 3, 130.6 eV, could be counteracted by the adsorption of 1451 H atoms on Ni terrace sites. These estimated numbers of the adsorbed H atoms required for the complete surface re-segregation of Ni to terrace sites by far exceed the total number of terrace atoms, 440 in the $Pt_{731}Ni_{732}$ NP. This implies that even a full coverage of H would not be enough energetically to reverse the pattern of the NPs whose spectroscopic fingerprints are shown in the bottom part of Fig. 2. This result is in line with the experimental data that 30 % of surface atoms after reduction at 523 K are Pt ones (Table 2), whereas after oxidation at the same high temperature only 8 % of the spectroscopically probed surface atoms remain Pt (Table 1).

The fundamental study described in this paper point to a great importance of precise control of the catalyst surface composition before it is used in a real fuel cell and engineer it accordingly. Catalyst surface composition can be, in principle, different already after fuel cell setup. For example, the same catalyst can be employed at both electrodes of a fuel cell and its surface composition will be rather different because of two different environments. Moreover, as we have shown the composition can further change upon fuel cell operation, especially at critical conditions like start up/shut down cycling. The PtNi alloy thus should be protected by a Pt overlayer. However, the thickness of this overlayer should be higher than one monolayer as we have shown that Ni can overcome this protection and segregate to the surface under oxidation conditions. One has to ensure appropriate thickness of Pt overlayer as the catalyst should maintain its exceptional properties given by the presence of Ni. The thicker overlayer, for example, three monolayers of Pt, could help to mitigate or at least slow down the compositional changes on the surface of PtNi alloy. At the same time, it is thin enough to maintain the benefit from the strain and/or electronic-induced activity given by the Ni atoms underneath. Nevertheless, full understanding of phenomena that occur on the surface of bimetallic alloys under reaction condition requires further investigations. Particularly, the use of ambient/near ambient pressure SRPES would provide an advance understanding by pinpointing the active surface *in situ*, under H_2 or O_2 atmospheres.

4. Conclusions

We investigated the temperature-dependent surface restructuring of the PtNi thin film catalyst in response to series of alternating oxidation (O_2) and reduction (H_2) atmospheres using well-defined conditions, surface sensitive SRPES technique, bulk sensitive XPS technique and theoretical calculations. The results revealed that under oxidation environment PtNi alloy is oxidized on the surface mainly through the

formation of Ni oxides, which forces Ni atoms to segregate to the surface. Under reducing atmosphere oxides are reduced and Ni diffuses back into the alloy. The series of five oxidation/reduction cycles led to an oscillatory behavior of the surface composition. The changes were qualitatively reversible; quantitatively, however, the average composition was slightly shifting towards nickel enrichment at elevated cycling temperatures. During switching between oxidizing and reducing conditions the bimetallic catalyst did not maintain its chemical integrity and underwent surface reconstruction in terms of relative surface nickel enrichment. Moreover, we observed significant catalyst coarsening after five oxidation/reduction cycles at 523 K assigned to enhanced atomic (Ostwald ripening) and grains (coalescence) mobility at elevated temperatures in gaseous atmospheres.

This work provides valuable insights into the PtNi alloy surface chemistry under switched reactive environments that help to gain advanced understanding of their catalytic activity in real conditions. The described behavior of PtNi nanoalloy plays a significant role in its longtime performance as a catalyst in fuel cell devices. The enrichment of Ni species on the surface after an interaction with the reactive environments suppresses PtNi alloy on the surface which is critical for its high electrocatalytic performance. Furthermore, our results propose a general strategy towards adjustment of PtNi catalyst surfaces. The redox pre-treatment of the surface structure of bimetallic catalysts may open an effective way to engineer highly efficient catalysts for many catalytic processes.

Author contributions

Y.Y. prepared the samples. I.K., M.V. and T.S performed the SRPES and XPS measurements and analysed the data. L.V., F.V and K.N. performed theoretical calculations and analysed their results. I.K performed EDX and AFM measurements and analysed the data. I.K., K.N. and I.M. supervised the work. I.K. and K.N. prepared the manuscript with the help of all other co-authors.

Declaration of Competing Interest

None.

Acknowledgements

The work was financially supported by the structural fund project No. CZ.02.1.01/0.0/0.0/16_025/0007414 and the Czech Science Foundation grant No. 18-06989Y. The authors further acknowledge the CERIC-ERIC Consortium for access to experimental facilities and financial support. Work of L. V. was financed by the *Generalitat de Catalunya*via a pre-doctoral grant 2018FI-B-00384. F. V. is thankful to MEC for his RYC-2012-10129 *Ramón y Cajal* research contract. L. V., F. V., and K. M. N. acknowledge support by the Spanish/FEDER grants PGC2018-093863-B-C22, RTI2018-095460-B-I00, CTQ2015-64618-R, and MDM-2017-0767 as well as by the grant 2017SGR13 of the *Generalitat de Catalunya* and its support to XRQTC. L. V., F. V., and K. M. N. are thankful to the *Red Española de Supercomputación* for providing computer resources and technical support (QCM-2019-1-0032 and QS-2019-2-0022).

Appendix A. Supplementary data

Supplementary material related to this article can be found, in the online version, at doi:https://doi.org/10.1016/j.apcatb.2019.118476.

References

[1] M. Sankar, N. Dimitratos, P.J. Miedziak, P.P. Wells, C.J. Kiely, G.J. Hutchings, Designing bimetallic catalysts for a green and sustainable future, Chem. Soc. Rev. 41 (2012) 8099–8139.
[2] V. Dal Santo, A. Gallo, A. Naldoni, M. Guidotti, R. Psaro, Bimetallic heterogeneous catalysts for hydrogen production, Catal. Today 197 (2012) 190–205.
[3] J.H. Sinfelt, Catalysis by alloys and bimetallic clusters, Acc. Chem. Res. 10 (1977) 15–20.
[4] A. Lu, Z.P. Wu, B. Chen, D.L. Peng, S. Yan, S. Shan, Z. Skeete, F. Chang, Y. Chen, H. Zheng, D. Zeng, L. Yang, A. Sharma, J. Luo, L. Wang, V. Petkov, C.J. Zhong, From a Au-rich core/PtNi-rich shell to a Ni-rich core/PtAu-rich shell: an effective thermochemical pathway to nanoengineering catalysts for fuel cells, J. Mater. Chem. A 6 (2018) 5143–5155.
[5] S. Shan, V. Petkov, B. Prasai, J. Wu, P. Joseph, Z. Skeete, E. Kim, D. Mott, O. Malis, J. Luo, C.J. Zhong, Catalytic activity of bimetallic catalysts highly sensitive to the atomic composition and phase structure at the nanoscale, Nanoscale 7 (2015) 18936–18948.
[6] H. Yang, Y.-T. Frank Pan, J. Wu, P. Li, X. Yin, S. Warren, Surface lattice-engineered bimetallic nanoparticles and their catalytic properties, Chem. Soc. Rev. 41 (2012) 8066.
[7] V. Stamenkovic, B.S. Mun, K.J.J. Mayrhofer, P.N. Ross, N.M. Markovic, J. Rossmeisl, J. Greeley, J.K. Nørskov, Changing the activity of electrocatalysts for oxygen reduction by tuning the surface electronic structure, Angew. Chemie Int. Ed. 45 (2006) 2897–2901.
[8] I.E.L. Stephens, A.S. Bondarenko, F.J. Perez-Alonso, F. Calle-Vallejo, L. Bech, T.P. Johansson, A.K. Jepsen, R. Frydendal, B.P. Knudsen, J. Rossmeisl, I. Chorkendorff, Tuning the activity of Pt(111) for oxygen electroreduction by subsurface alloying, J. Am. Chem. Soc. 133 (2011) 5485–5491.
[9] J. Greeley, I.E.L. Stephens, A.S. Bondarenko, T.P. Johansson, H.A. Hansen, T.F. Jaramillo, J. Rossmeisl, I. Chorkendorff, J.K. Nørskov, Alloys of platinum and early transition metals as oxygen reduction electrocatalysts, Nat. Chem. 1 (2009) 552–556.
[10] V.R. Stamenkovic, B.S. Mun, M. Arenz, K.J.J. Mayrhofer, C.A. Lucas, G. Wang, P.N. Ross, N.M. Markovic, Trends in electrocatalysis on extended and nanoscale Pt-bimetallic alloy surfaces, Nat. Mater. 6 (2007) 241–247.
[11] I. Matanović, F.H. Garzon, N.J. Henson, Theoretical study of electrochemical processes on Pt–Ni alloys, J. Phys. Chem. C 115 (2011) 10640–10650.
[12] F. Tao, S. Zhang, N. Luan, X. Zhang, Action of bimetallic nanocatalysts under reaction conditions and during catalysis: evolution of chemistry from high vacuum conditions to reaction conditions, Chem. Soc. Rev. 41 (2012) 7980–7993.
[13] F. Tao, M.E. Grass, Y. Zhang, D.R. Butcher, J.R. Renzas, Z. Liu, J.Y. Chung, B.S. Mun, M. Salmeron, G.A. Somorjai, Reaction-driven restructuring of Rh-Pd and Pt-Pd core-shell nanoparticles, Science 322 (2008) 932–934.
[14] I. Khalakhan, M. Vorokhta, P. Kúš, M. Dopita, M. Václavů, R. Fiala, N. Tsud, T. Skála, V. Matolín, In situ probing of magnetron sputtered Pt-Ni alloy fuel cell catalysts during accelerated durability test using EC-AFM, Electrochim. Acta 245 (2017) 760–769.
[15] I. Khalakhan, F. Waidhas, O. Brummel, M. Vorokhta, P. Kúš, Y.V. Yakovlev, M. Bertram, M. Dopita, I. Matolínová, J. Libuda, V. Matolín, Nanoscale morphological and structural transformations of PtCu alloy electrocatalysts during potentiodynamic cycling, J. Phys. Chem. C 122 (2018) 21974–21982.
[16] M. Ahmadi, F. Behafarid, C. Cui, P. Strasser, B.R. Cuenya, Long-range segregation phenomena in shape-selected bimetallic nanoparticles: chemical state effects, ACS Nano 7 (2013) 9195–9204.
[17] L.-W. Wang, M. Salmeron, S. Alayoglu, H. Zheng, E.A. Stach, G.A. Somorjai, C.-M. Wang, L. Kovarik, H.L. Xin, A. Genc, R. Tao, Revealing the atomic restructuring of Pt–Co nanoparticles, Nano Lett. 14 (2014) 3203–3207.
[18] R. Mu, Q. Fu, H. Liu, D. Tan, R. Zhai, X. Bao, Reversible surface structural changes in Pt-based bimetallic nanoparticles during oxidation and reduction cycles, Appl. Surf. Sci. 255 (2009) 7296–7301.
[19] H. Liao, A. Fisher, Z.J. Xu, Surface segregation in bimetallic nanoparticles: a critical issue in electrocatalyst engineering, Small 11 (2015) 3221–3246.
[20] S. Tanuma, C.J. Powell, D.R. Penn, Calculations of electron inelastic mean free paths. IX. Data for 41 elemental solids over the 50 eV to 30 keV range, Surf. Interface Anal. 43 (2011) 689–713.
[21] J. Wu, X.Z. Yuan, J.J. Martin, H. Wang, J. Zhang, J. Shen, S. Wu, W. Merida, A review of PEM fuel cell durability: degradation mechanisms and mitigation strategies, J. Power Sources 184 (2008) 104–119.
[22] R. Sharma, S.M. Andersen, An opinion on catalyst degradation mechanisms during catalyst support focused accelerated stress test (AST) for proton exchange membrane fuel cells (PEMFCs), Appl. Catal. B Environ. 239 (2018) 636–643.
[23] U.S.D. Fuel, C. Tech, FCTT AST And Polarization Curve Protocols for PEMFCs - U.S. DRIVE Fuel Cell Tech Team Cell Component Accelerated Stress Test and Polarization Curve Protocols for PEM Fuel Cells, U.S. DRIVE Fuel Cell Tech Team, (2013) http://energy.gov/sites/prod/files/2015/08/f25/fcto_dwg_usdrive_fctt_accelerated_stress_tests_jan2013.pdf.
[24] J. Libra, KolXPD: Software for Spectroscopy Data Measurement and Processing, (2019) http://www.kolibrik.net/science/kolxpd/.
[25] G. Kresse, J. Furthmüller, Efficient iterative schemes for ab initio total-energy calculations using a plane-wave basis set, Phys. Rev. B Condens. Matter Mater. Phys. 54 (1996) 11169–11186.
[26] G. Kresse, J. Hafner, Ab initio molecular-dynamics simulation of the liquid-metal–amorphous-semiconductor transition in germanium, Phys. Rev. B 49 (1994) 14251–14269.
[27] J.P. Perdew, K. Burke, M. Ernzerhof, Generalized gradient approximation made simple, Phys. Rev. Lett. 77 (1996) 1758–1775.
[28] P.E. Blöchl, Projector augmented-wave method, Probl. Solid State Phys. Solut. 50 (1994) 17953–17979.
[29] G. Kresse, D. Joubert, From ultrasoft pseudopotentials to the projector augmented-wave method, Phys. Rev. B 59 (1999) 1758–1775.

[30] L. Vega, J. Ruvireta, F. Viñes, F. Illas, Jacob's ladder as sketched by Escher: assessing the performance of broadly used density functionals on transition metal surface properties, J. Chem. Theory Comput. 14 (2018) 395–403.
[31] P. Janthon, S. Luo, S.M. Kozlov, F. Viñes, J. Limtrakul, D.G. Truhlar, F. Illas, Bulk properties of transition metals: a challenge for the design of universal density functionals, J. Chem. Theory Comput. 10 (2014) 3832–3839.
[32] S.M. Kozlov, G. Kovács, R. Ferrando, K.M. Neyman, How to determine accurate chemical ordering in several nanometer large bimetallic crystallites from electronic structure calculations, Chem. Sci. 6 (2015) 3868–3880.
[33] J. Ruvireta, L. Vega, F. Viñes, Cohesion and coordination effects on transition metal surface energies, Surf. Sci. 664 (2017) 45–49.
[34] F. Viñes, J.R.B. Gomes, F. Illas, Understanding the reactivity of metallic nanoparticles: beyond the extended surface model for catalysis, Chem. Soc. Rev. 43 (2014) 4922–4939.
[35] F. Viñes, F. Illas, K.M. Neyman, On the mechanism of formation of metal nanowires by self-assembly, Angew. Chemie Int. Ed. 46 (2007) 7094–7097.
[36] G. Kovács, S.M. Kozlov, K.M. Neyman, Versatile optimization of chemical ordering in bimetallic nanoparticles, J. Phys. Chem. C 121 (2017) 10803–10808.
[37] M. Mamatkulov, I.V. Yudanov, A.V. Bukhtiyarov, I.P. Prosvirin, V.I. Bukhtiyarov, K.M. Neyman, Pd segregation on the surface of bimetallic PdAu nanoparticles induced by low coverage of adsorbed CO, J. Phys. Chem. C 123 (2019) 8037–8046.
[38] L. Vega, H.A. Aleksandrov, K.M. Neyman, Using density functional calculations to elucidate atomic ordering of Pd-Rh nanoparticles at sizes relevant for catalytic applications, Chin. J. Catal. 40 (2019) 1749–1757.
[39] S. Olobardi, L. Vega, A. Fortunelli, M. Stener, F. Vines, K.M. Neyman, Optical properties and chemical ordering of Ag-Pt nanoalloys: a computational study, J. Phys. Chem. C. 123 (2019) 25482–25491.
[40] G. Kovács, S.M. Kozlov, I. Matolínová, M. Vorokhta, V. Matolín, K.M. Neyman, Revealing chemical ordering in Pt-Co nanoparticles using electronic structure calculations and X-ray photoelectron spectroscopy, Phys. Chem. Chem. Phys. 17 (2015) 28298–28310.
[41] M. Vorokhta, I. Khalakhan, M. Václavů, G. Kovács, S.M. Kozlov, P. Kúš, T. Skála, N. Tsud, J. Lavková, V. Potin, I. Matolínová, K.M. Neyman, V. Matolín, Surface composition of magnetron sputtered Pt-Co thin film catalyst for proton exchange membrane fuel cells, Appl. Surf. Sci. 365 (2016) 245–251.
[42] A. Neitzel, G. Kovács, Y. Lykhach, S.M. Kozlov, N. Tsud, T. Skála, M. Vorokhta, V. Matolín, K.M. Neyman, J. Libuda, Atomic ordering and Sn segregation in Pt–Sn nanoalloys supported on CeO_2 thin films, Top. Catal. 60 (2017) 522–532.
[43] A. Wolfbeisser, G. Kovács, S.M. Kozlov, K. Föttinger, J. Bernardi, B. Klötzer, K.M. Neyman, G. Rupprechter, Surface composition changes of CuNi-ZrO_2 during methane decomposition: an operando NAP-XPS and density functional study, Catal. Today 283 (2017) 134–143.
[44] J. Rogal, K. Reuter, Ab initio atomistic thermodynamics for surfaces: a primer, Experiment, Modeling and Simulation of Gas- Surface Interactions for Reactive Flows in Hypersonic Flights, Educ. Notes RTO-EN-AVT-142, Pap. 2 (2007) 2–1 – 2–18.
[45] R. Mom, L. Frevel, J.-J. Velasco-Vélez, M. Plodinec, A. Knop-Gericke, R. Schlögl, The oxidation of platinum under wet conditions observed by electrochemical X-ray photoelectron spectroscopy, J. Am. Chem. Soc. 141 (2019) 6537–6544.
[46] L. Qiao, X. Bi, Direct observation of Ni^{3+} and Ni^{2+} in correlated LaNiO3-δ films, Epl 93 (2011) 57002.
[47] B. Zhao, B. Yan, Z. Jiang, S. Yao, Z. Liu, Q. Wu, R. Ran, S.D. Senanayake, D. Weng, J.G. Chen, High selectivity of CO2 hydrogenation to CO by controlling the valence state of nickel using perovskite, Chem. Commun. 54 (2018) 7354–7357.
[48] M.C. Biesinger, B.P. Payne, L.W.M. Lau, A. Gerson, R.S.C. Smart, X-ray photoelectron spectroscopic chemical state quantification of mixed nickel metal, oxide and hydroxide systems, Surf. Interface Anal. 41 (2009) 324–332.
[49] L. Pielsticker, I. Zegkinoglou, N.J. Divins, H. Mistry, Y.T. Chen, A. Kostka, J.A. Boscoboinik, B.R. Cuenya, Segregation phenomena in size-selected bimetallic CuNi nanoparticle catalysts, J. Phys. Chem. B 122 (2018) 919–926.
[50] A.P. Grosvenor, M.C. Biesinger, R.S.C. Smart, N.S. McIntyre, New interpretations of XPS spectra of nickel metal and oxides, Surf. Sci. 600 (2006) 1771–1779.
[51] S. Aloni, M. Salmeron, C.-K. Tsung, J.R. Renzas, Z. Zhu, F. Aksoy, D.R. Butcher, V. Altoe, Z. Liu, M.E. Grass, F. Tao, G.A. Somorjai, Y. Zhang, S. Alayoglu, Evolution of structure and chemistry of bimetallic nanoparticle catalysts under reaction conditions, J. Am. Chem. Soc. 132 (2010) 8697–8703.
[52] C.A. Menning, H.H. Hwu, J.G. Chen, Experimental and theoretical investigation of the stability of Pt-3d-Pt(111) bimetallic surfaces under oxygen environment, J. Phys. Chem. B 110 (2006) 15471–15477.
[53] S. Zafeiratos, S. Piccinin, D. Teschner, Alloys in catalysis: phase separation and surface segregation phenomena in response to the reactive environment, Catal. Sci. Technol. 2 (2012) 1787–1801.
[54] R. Mu, X. Guo, Q. Fu, X. Bao, Oscillation of surface structure and reactivity of PtNi bimetallic catalysts with redox treatments at variable temperatures, J. Phys. Chem. C 115 (2011) 20590–20595.
[55] M. Ahmadi, C. Cui, H. Mistry, P. Strasser, B. Roldan Cuenya, Carbon monoxide-induced stability and atomic segregation phenomena in shape-selected octahedral PtNi nanoparticles, ACS Nano 9 (2015) 10686–10694.
[56] K. Leistner, C. Gonzalez Braga, A. Kumar, K. Kamasamudram, L. Olsson, Volatilisation and subsequent deposition of platinum oxides from diesel oxidation catalysts, Appl. Catal. B Environ. 241 (2019) 338–350.
[57] Y. Zhao, G.-C. Wang, T.-M. Lu, Characterization of Amorphous and Crystalline Rough Surface: Principles and Applications, Academic Press, San Diego, 2001.
[58] I. Khalakhan, A. Choukourov, M. Vorokhta, P. Kúš, I. Matolínová, V. Matolín, In situ electrochemical AFM monitoring of the potential-dependent deterioration of platinum catalyst during potentiodynamic cycling, Ultramicroscopy 187 (2018) 64–70.
[59] A. Choukourov, O. Kylián, M. Petr, M. Vaidulych, D. Nikitin, J. Hanuš, A. Artemenko, A. Shelemin, I. Gordeev, Z. Kolská, P. Solař, I. Khalakhan, A. Ryabov, J. Májek, D. Slavínská, H. Biederman, RMS roughness-independent tuning of surface wettability by tailoring silver nanoparticles with a fluorocarbon plasma polymer, Nanoscale 9 (2017) 2616–2625.
[60] X. Tuaev, S. Rudi, V. Petkov, A. Hoell, P. Strasser, In situ study of atomic structure transformations of Pt-Ni nanoparticle catalysts during electrochemical potential cycling, ACS Nano 7 (2013) 5666–5674.
[61] C. Cui, L. Gan, M. Heggen, S. Rudi, P. Strasser, Compositional segregation in shaped Pt alloy nanoparticles and their structural behaviour during electrocatalysis, Nat. Mater. 12 (2013) 765–771.
[62] N. Hodnik, M. Zorko, M. Bele, S. Hočevar, M. Gaberšček, Identical location scanning electron microscopy: a case study of electrochemical degradation of PtNi nanoparticles using a new nondestructive method, J. Phys. Chem. C 116 (2012) 21326–21333.
[63] M. Pourbaix, Atlas of electrochemical equilibria in aqueous solutions, (2nd English Ed.), Natl. Assoc. Corros. Eng. (1974) 551 pages.
[64] I. Khalakhan, M. Vorokhta, M. Václavů, B. Šmíd, J. Lavková, I. Matolínová, R. Fiala, N. Tsud, T. Skála, V. Matolín, In-situ electrochemical atomic force microscopy study of aging of magnetron sputtered Pt-Co nanoalloy thin films during accelerated degradation test, Electrochim. Acta 211 (2016) 52–58.
[65] J. Durst, M. Chatenet, F. Maillard, Impact of metal cations on the electrocatalytic properties of Pt/C nanoparticles at multiple phase interfaces, Phys. Chem. Chem. Phys. 14 (2012) 13000–13009.
[66] K.M. Neyman, R. Sahnoun, C. Inntam, S. Hengrasmee, N. Rösch, Computational study of model Pd – Zn nanoclusters and their adsorption complexes with CO molecules, J. Phys. Chem. B 108 (2004) 5424–5430.
[67] R. Ferrando, J. Jellinek, R.L. Johnston, Nanoalloys: from theory to applications of alloy clusters and nanoparticles, Chem. Rev. 108 (2008) 845–910.
[68] I.V. Yudanov, R. Sahnoun, K.M. Neyman, N. Rösch, Metal nanoparticles as models of single crystal surfaces and supported catalysts: density functional study of size effects for CO/Pd(1 1 1), J. Chem. Phys. 117 (2002) 9887–9896.
[69] S. Liu, Z.J. Zhao, C. Yang, S. Zha, K.M. Neyman, F. Studt, J. Gong, Adsorption preference determines segregation direction: a shortcut to more realistic surface models of alloy catalysts, ACS Catal. 9 (2019) 5011–5018.
[70] P.C. Jennings, H.A. Aleksandrov, K.M. Neyman, R.L. Johnston, A DFT study of oxygen dissociation on platinum based nanoparticles, Nanoscale 6 (2014) 1153–1165.
[71] F. Mittendorfer, A. Eichler, J. Hafner, Molecular precursors in the dissociative adsorption of O on Ni (111), Surf. Sci. 435 (1999) 756–760.

6.5 ELUCIDATION OF THE STRUCTURE OF PtX (X=Cu, Au, Ag) NANOPARTICLES OF DIFFERENT SIZES BY DENSITY FUNCTIONAL CALCULATIONS

6.5.1 Summary

Introduction Our chemical ordering study of PtX bimetallic NPs of Pt with quite inert coinage metals X = Cu, Au, Ag is overviewed in the following. Large quantities of atoms of NP catalysts are essentially wasted since only atoms at the surface take part in catalytic reactions. For such expensive metals in catalyst as Pd and Pt this price aspect is a significant concern.[83] Thus, for systems involving catalytically active precious metals, A@B core@shell structures of nanocatalysts are beneficial, where A is a relatively cheap metal (*e.g.*, Co, Ni, Cu) and B is a more expensive metal, often more catalytically active. Furthermore, the addition of a metal A may also result in synergistic effects on the catalytic properties of both metals. Combinations of Pt with coinage metals are actively studied as single-atom alloy catalysts, a rapidly developing field in catalysis[84–86] where individual Pt atoms surrounded by coinage atoms can act as very selective catalytic centres.

As in the previous Sections, in this Section the insights into the chemical ordering obtained from DFT calculations of NPs with ≤201 atoms are extended to NPs of larger sizes, closer to the sizes in common catalysts, and temperature effects on the orderings of such larger NPs are considered. Furthermore, since a previous study of our group dealt with similar PdX NPs, X=Cu, Au, Ag, a comparative analysis of the chemical orderings of the Pt- and Pd-based NPs calculated by the same methodology is performed. A notable difference with the previous studies is that in this work the TOP methodology is analysed in depth, highlighting its weaknesses and strengths.

To summarize, the aims of the present study are: *i)* to quantify by DFT calculations the chemical orderings and surface segregation in up to ~2 nm large PtAu, PtAg, and PtCu NPs at different concentrations of the metals employing the TOP method; *ii)* to compare the structure, bonding and charge distributions in these NPs with the analogous Pd-containing NPs studied

earlier; *iii)* to deepen the knowledge of the accuracy and applicability of the TOP approach; *iv)* to identify equilibrium chemical orderings in PtAu, PtAg, and PtCu particles at common for catalysis sizes over 4 nm, also at elevated temperatures.

The author contribution to this project was to provide all DFT data for PtCu NPs, to calculate chemical orderings in bigger PtAu, PtAg and PtCu NPs, to perform Bader charge analysis for all studied systems, to evaluate performance of the TOP method. Also, the author decisively contributed to the preparation of the manuscript to publication by writing several parts of it, drawing images and graphs and creatively discussing all the results. As in other Chapters of the Thesis, the complete description of the results is provided in the published article in the end of this Section. Further supporting data is found at Appendix G.

Results

i) Regarding the quantification by DFT calculations of the chemical ordering:

The obtained energy terms in the TOP equations are listed in Table 6.4. Pt and Au atoms in the Pt-Au NPs are found slightly immiscible independent of the NP size. Quite similar positive values $\varepsilon_{\mathrm{BOND}}^{\mathrm{Pt-Au}}$ for $Pt_{70}Au_{70}$ and $Pt_{101}Au_{100}$ NPs support this finding. Au atoms tend to occupy low-coordinated positions, see and Figure 6.13.

These features are maintained for different Pt:Au compositions 1:3, 1:1, and 3:1 in 201-atomic NPs. According to the Bader charge analysis, the charge redistribution between Pt and Au atoms is minor, see Table 6.5. Similar to the results for PtAu NPs, the slightly positive $\varepsilon_{\mathrm{BOND}}^{\mathrm{Pt-Ag}}$ terms point to the unfavorable formation of heterometallic PtAg bonds, triggering immiscibility of Pt and Ag atoms. The substantial surface segregation propensity of Ag atoms in PtAg NPs decreases from the corner, to the edge and the facet positions. Important difference of PtAg systems with respect to Pt-Au ones is revealed by the Bader charge analysis, according to which notable electron density transfer occurs from Ag atoms to more electronegative Pt atoms in

PtAg NPs, see Table 6.5. Surface Pt atoms in Pt-Ag NPs are negatively charged and surface Ag atoms bear positive charges up to 0.15 *e*. These modified charge states of the atoms suggest their noticeably different reactivity compared to the corresponding sites of bare Pt and Ag NPs.

Table 6.4 Energy terms, ε, in the topological expressions for energy differences $\Delta E_{ij}^{\mathrm{TOP}}$ of homotops i and j of Pt_nX_m (X = Au, Ag, Cu; m+n = 140, 201) particles $\Delta E_{ij}^{\mathrm{TOP}}=\varepsilon_{\mathrm{BOND}}^{\mathrm{Pt-X}} \cdot \Delta N_{ij,\mathrm{BOND}}^{\mathrm{Pt-X}} + \varepsilon_{\mathrm{CORNER}}^{\mathrm{X}} \cdot \Delta N_{ij,\mathrm{CORNER}}^{\mathrm{X}} + \varepsilon_{EDGE}^{X} \cdot \Delta N_{ij,EDGE}^{X} + \varepsilon_{FACET}^{X} \cdot \Delta N_{ij,FACET}^{X}$ are numbers of heterometallic bonds Pt-X (nearest-neighbour pairs of Pt-X atoms) and atoms X in the corner (vertex), edge and facet positions of the particle, respectively. All energies are in meV. Data for analogous $Pd_{70}Au_{70}$, $Pd_{70}Ag_{70}$, and $Pd_{70}Cu_{70}$ particles from Ref.[81] are also shown.

Nanoparticle	$\boldsymbol{\varepsilon_{\mathrm{BOND}}^{\mathrm{Pt-X}}}$	$\boldsymbol{\varepsilon_{\mathrm{CORNER}}^{\mathrm{X}}}$	$\boldsymbol{\varepsilon_{\mathrm{EDGE}}^{\mathrm{X}}}$	$\boldsymbol{\varepsilon_{\mathrm{FACET}}^{\mathrm{X}}}$
$Pt_{70}Au_{70}$	19^{+4}_{-2}	-619^{+62}_{-48}	-377^{+44}_{-44}	-256^{+88}_{-69}
$Pd_{70}Au_{70}$	-13^{+4}_{-6}	-404^{+76}_{-72}	-301^{+52}_{-77}	-200^{+52}_{-64}
$Pt_{70}Ag_{70}$	11^{+10}_{-13}	-625^{+122}_{-185}	-336^{+72}_{-185}	-195^{+75}_{-58}
$Pd_{70}Ag_{70}$	-1^{+2}_{-2}	-361^{+50}_{-68}	-289^{+78}_{-129}	-163^{+43}_{-64}
$Pt_{70}Cu_{70}$	-35^{+4}_{-4}	-27^{+47}_{-44}	182^{+56}_{-54}	344^{+43}_{-36}
$Pd_{70}Cu_{70}$	-26^{+5}_{-5}	95^{+36}_{-33}	147^{+46}_{-45}	183^{+42}_{-40}
$Pt_{151}Au_{50}$	21^{+1}_{-1}	-507^{+51}_{-62}	-543^{+16}_{-18}	-431^{+30}_{-43}
$Pt_{101}Au_{100}$	21^{+7}_{-6}	-530^{+136}_{-107}	-492^{+59}_{-56}	-335^{+83}_{-95}
$Pt_{51}Au_{150}$	15^{+14}_{-15}	-558^{+49}_{-34}	-547^{+53}_{-84}	-259^{+47}_{-92}
$Pt_{151}Ag_{50}$	32^{+11}_{-12}	-396^{+108}_{-135}	-380^{+95}_{-90}	-237^{+103}_{-95}
$Pt_{101}Ag_{100}$	16^{+9}_{-10}	-499^{+95}_{-112}	-466^{+87}_{-83}	-308^{+77}_{-91}
$Pt_{51}Ag_{150}$	7^{+5}_{-5}	-408^{+118}_{-158}	-511^{+79}_{-68}	-240^{+49}_{-65}
$Pt_{151}Cu_{50}$	-25^{+9}_{-13}	267^{+30}_{-22}	342^{+14}_{-14}	372^{+42}_{-44}
$Pt_{101}Cu_{100}$	-43^{+6}_{-5}	15^{+60}_{-72}	208^{+55}_{-68}	325^{+34}_{-41}
$Pt_{51}Cu_{150}$	-54^{+14}_{-15}	134^{+73}_{-78}	184^{+151}_{-93}	259^{+65}_{-59}

[a] 95% confidence interval of ε given as, *e.g.* 19^{+4}_{-2} denotes a range from 17 meV to 23 meV.

Similar to the results for PtAu NPs, the slightly positive $\varepsilon_{\mathrm{BOND}}^{\mathrm{Pt-Ag}}$ terms point to unfavourable formation of heterometallic Pt-Ag bonds, triggering immiscibility of Pt and Ag atoms. The substantial surface segregation propensity of Ag atoms in PtAg NPs decreases from the corner, to the edge and the facet positions. Important difference of PtAg systems with respect to

Table 6.5 Average Bader charges, in *e*, on atoms with coordination numbers 6, 7, 8, 9, 12 in $Pt_{70}X_{70}$, $Pt_{151}X_{50}$, $Pt_{101}X_{100}$, and $Pt_{51}X_{150}$ (X = Au, Ag, Cu) NPs with the lowest E^{TOP} energy. The charges in the monometallic Pt_{201} and X_{201} NPs are also shown for comparison.

Particle	Pt					X				
	6	7	8	9	12	6	7	8	9	12
$Pt_{70}Au_{70}$	-	-	-	-0.02	0.05	-0.05	-0.02		0.02	-
$Pt_{151}Au_{50}$	-0.09	-0.07	-0.08	-0.02	0.02	-0.05	-0.03	-	-	-
$Pt_{101}Au_{100}$	-	-	-0.09	-0.04	0.03	-0.05	-0.03	0.01	0.02	-
$Pt_{51}Au_{150}$	-	-	-	-	0.01	-0.06	-0.03	-0.01	0.01	0.06
$Pt_{70}Ag_{70}$				-0.17	-0.04	0.05	0.10		0.10	-
$Pt_{151}Ag_{50}$	-0.13	-0.13	-0.24	-0.11	0.02	0.12	0.15	-	-	-
$Pt_{101}Ag_{100}$	-	-	-0.30	-0.16	-0.05	0.05	0.08	0.13	0.09	-
$Pt_{51}Ag_{150}$	-	-	-	-	-0.11	-0.02	0.01	0.04	0.04	0.12
$Pt_{70}Cu_{70}$	-	-0.25		-0.23	-0.33	0.18	0.27		-	0.30
$Pt_{151}Cu_{50}$	-0.14	-0.11	-0.08	-0.07	-0.23	-	-	-	-	0.37
$Pt_{101}Cu_{100}$	-	-0.29	-0.12	-0.27	-0.39	0.27	0.22	-	0.32	0.31
$Pt_{51}Cu_{150}$	-	-	-0.57	-0.46	-0.60	0.11	0.15	-	0.19	0.19
Pt_{201}	-0.09	-0.06	-0.03	-0.01	0.07					
Au_{201}						-0.07	-0.04	-0.02	-0.01	0.04
Ag_{201}						-0.04	-0.03	0.01	-0.01	0.03
Cu_{201}						-0.05	-0.02	0.02	-0.01	0.03

PtAu ones is revealed by the Bader charge analysis, according to which notable electron density transfer occurs from Ag atoms to more electronegative Pt atoms in PtAg NPs, see Table 6.5. Surface Pt atoms in Pt-Ag NPs are negatively charged and surface Ag atoms bear positive charges up to 0.15 *e*. These modified charge states of the atoms suggest their noticeably different reactivity compared to the corresponding sites of bare Pt and Ag NPs.

Equilibrium chemical orderings and electronic properties of PtCu NPs are quite different from those of the aforementioned PtAu and PtAg NPs. Firstly, the TOP equation term show that Cu atoms are less stable in all

surface positions than Pt atoms. Although the surface energy of Cu (0.77 eV/atom) is smaller than that of Pt (1.03 eV/atom), the notably smaller size of Cu atoms leads to reverting their surface segregation expected from the surface energies to decrease the structural stress. Particularly, surface Cu atoms in 201-atomic NPs of different Pt:Cu compositions are more destabilized in facet positions, followed by edge and corner positions. In fact, the corner position becomes favourable by 27 meV in the smaller $Pt_{70}Cu_{70}$ NPs. One more notable difference of the Pt-Cu system with respect to PtAu and PtAg ones is that the heterometallic Pt-Cu bonds are characterized by negative energy terms in the TOP equations reflecting favourable mixing of Pt and Cu atoms. Regarding the charge distribution, PtCu NPs feature the highest electron density accumulated on Pt atoms, up to *ca.* -0.6 *e* per Pt atom depending on the NP size and Pt content. The notable negative charges on Pt atoms bound to Cu atoms acquiring positive charges up to 0.3 *e* are expected to significantly change the reactivity of both Pt and Cu surface sites.

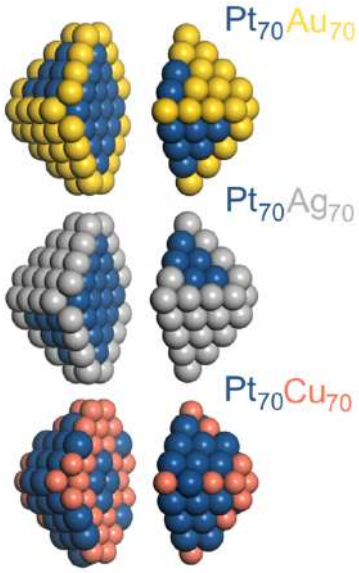

Figure 6.12 Chemical orderings of *ca.* 1.4 nm large 140-atomic truncated-octahedral fcc nanoparticles $Pt_{70}Au_{70}$, $Pt_{70}Ag_{70}$, and $Pt_{70}Cu_{70}$ with the lowest DFT energies. Particles images are split in two parts for better visualization. Pt – blue, Au – yellow, Ag – gray, Cu – red-brown.

Besides the indicator $\varepsilon_{BOND}^{Pt-X}$, the miscibility of Pt and X atoms has been characterized by the excess energies E_{exc}, see Figure 6.14. The energies for PtAu NPs range from -38 to -65 meV and for PtAg NPs from -58 to -90 meV depending on the concentration. For PtCu NPs the excess energies are notably more negative, from -127 to -163 meV, in line with the observed miscibility of the Pt and Cu components in the bulk and the propensity of the

formation of heteroatomic bonds indicated by the corresponding energy term in the TOP equations. For all 201-atomic PtX NPs the excess energy curve reaches minimum close to the 1:1 compositions, with the values very similar to those of the corresponding smaller $Pt_{70}X_{70}$ NPs.

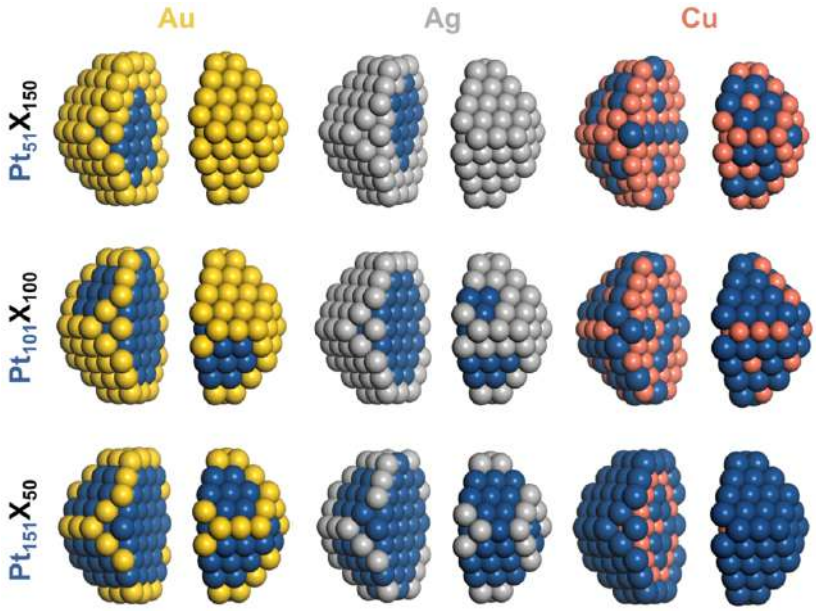

Figure 6.13 Chemical orderings of 1.7–1.8 nm large 201-atomic truncated-octahedral *fcc* nanoparticles of the compositions Pt:X (X = Au, Ag, Cu): 1:3 – $Pt_{51}X_{150}$, 1:1 – $Pt_{101}X_{100}$, 3:1 – $Pt_{151}X_{50}$ with the lowest DFT energies. Particles images are split in two parts for better visualization. Colors of atoms as in Figure 6.2.

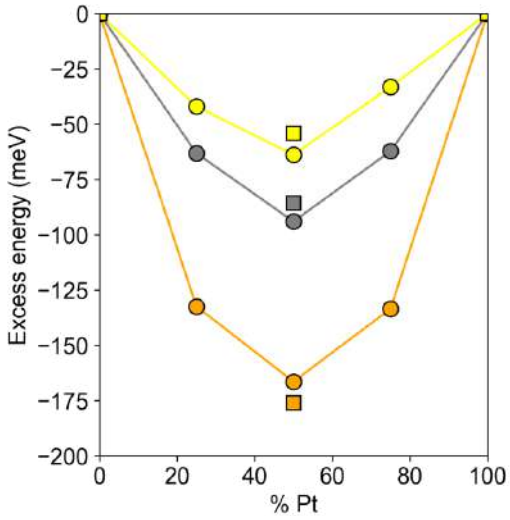

Figure 6.14 DFT excess energies E_{exc} per atom (see Eq. 2) circles – of $Pt_{201-n}X_n$ (X = Au, Ag, Cu; n = 50, 100, 150) nanoparticles and squares – of $Pt_{70}X_{70}$ nanoparticles. PtAu – yellow, PtAg – gray, PtCu – orange.

ii) Regarding the comparison between Pd-X and Pt-X systems:

In the case of X = Au and Ag the main difference from Pt is that Pd becomes slightly miscible with X. The preference of Au and Ag to be located on the surface of nanoalloys with Pd follows the same trend with the coordination number; stabilization of the surface site increases with decreasing its coordination number. For both PtCu and PdCu NPs the formation of heterometallic bonds is favorable. Also, the surface occupation propensity follows the same order for both systems, Cu is more destabilized in the surface positions with larger coordination numbers.

iii) Regarding the performance of the TOP method:

The employed method for pre-screening different homotops and their DFT energies relies on a simple equation based on the topology to reach the lowest-energy chemical ordering. The strength of this method is its simplicity sufficient to describe the topology trends and clear physical meaning of its parameters. The price for that are simplifications such as: accounting only for interactions between the nearest-neighbour pairs of atoms and assuming all bond types to be equal; describing positions of atoms in the NP lattice solely by the coordination numbers, distinguishing between surface atoms with different coordination numbers but treating all inner atoms of each metal type as equivalent; grouping homotops in so-called *topologies* of the same $N_{\mathrm{BOND}}^{\mathrm{Pt-X}}.N_{\mathrm{CORNER}}^{\mathrm{X}}.N_{\mathrm{EDGE}}^{\mathrm{X}}.N_{\mathrm{FACET}}^{\mathrm{X}}$ numbers in TOP equation, and assuming that an arbitrarily chosen homotop of a given topology represents reasonably well the DFT energy and the chemical ordering of all other homotops of the same topology.

To evaluate some of these simplifications ≥10 random homotops of Pt-Au and PtCu systems with the same $N_{\mathrm{BOND}}^{\mathrm{Pt-X}}.N_{\mathrm{CORNER}}^{\mathrm{X}}.N_{\mathrm{EDGE}}^{\mathrm{X}}.N_{\mathrm{FACET}}^{\mathrm{X}}$ numbers were generated and optimized with DFT. The spread in DFT energy is the magnitude of error of assuming that two homotops with same N parameters have the same energy by TOP method. The biggest spread for both systems was 1568 meV found for the lowest-energy $Pt_{70}Cu_{70}$ homotop, similar to that calculated for $Pt_{70}Au_{70}$. Analysing these spreads, we observed that not all

atoms of one type (Pt-Pt, Pt-X, or X-X bonds) are equivalent, *i.e.* that the energy of bonds formed by Pt or X atoms to each of their first neighbours is partially dependent on the identity (and quantity) of the rest of first neighbours. In fact, certain structural motifs (such as {111} facets solely composed of Au) seem to become stable for some compositions due to elusive long-range interactions. But these long-range interactions are neglected in the present topological description. In a nutshell, irrespective of possible inaccuracies of the used TOP approach based on the DFT structure optimization, the equilibrium chemical orderings in bimetallic nanoalloys provided by this approach approximate reasonably well the orderings obtained with the employed DFT exchange-correlation functional. An important point is that the calculated atomic-level data are much more detailed than those currently accessible experimentally and are very useful for rationalizing surface reactivity of bimetallic catalysts and related applications.

iv) Chemical ordering of larger Pt-X NPs and temperature effects:

The energy terms of the TOP equations for 140 and 201 atomic NPs are used to determine the chemical ordering of 1463 atomic NPs. In the case of $Pt_{732}Au_{731}$ and $Pt_{732}Ag_{731}$ similar core@shell Pt@Ag and Pt@Au orderings are obtained independently of the energy terms set employed, see Figure 6.15. For $Pt_{732}Cu_{731}$, the number of surface Cu atoms obtained when using the energy terms for 201 atomic NPs is more than twice larger than the obtained with the energy terms for 140 atomic NPs.

By increasing the temperature, several Pt atoms appeared at the surface of $Pt_{732}Au_{731}$ and $Pt_{732}Ag_{731}$ NPs and some Au and Ag atoms migrated to the core. In addition, the number of both Pt-Au and Pt-Ag bonds increased at higher temperature. In $Pt_{732}Cu_{731}$ NP, Cu atoms migrate upon the temperature increase from corner and edge positions most populated at 0 K primarily to surface terrace positions. In this case, the number of Pt-Cu bonds slightly decreased at higher temperatures, from 58% at 0 K to 54% at 1000 K.

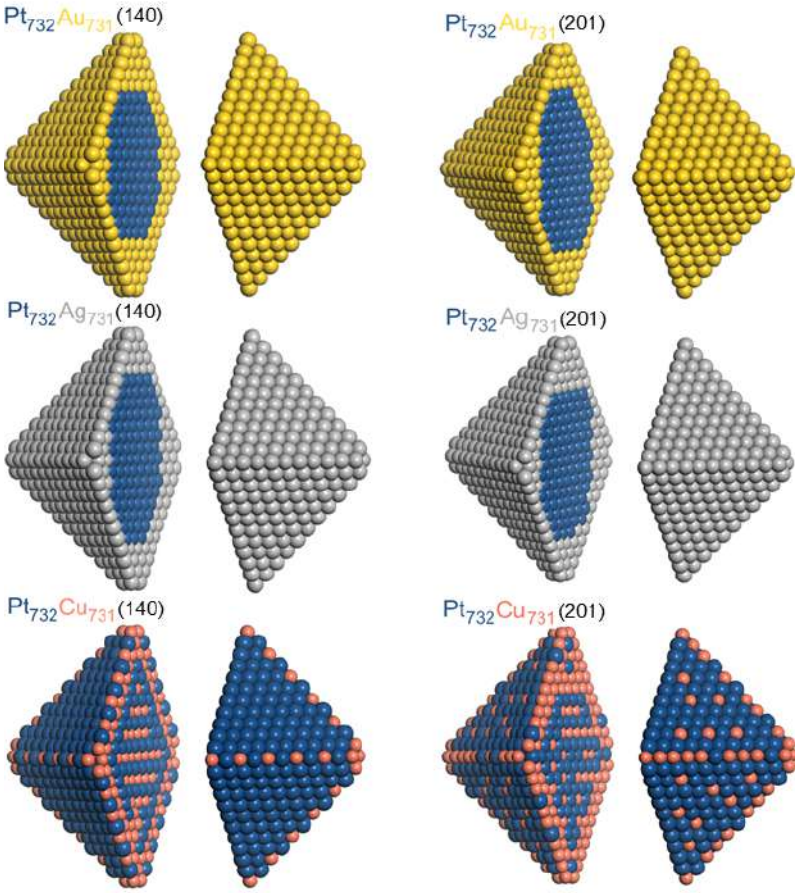

Figure 6.15 Equilibrium chemical orderings of *ca.* 4.4 nm large truncated-octahedral fcc $Pt_{732}Au_{731}$, $Pt_{732}Ag_{731}$, and $Pt_{732}Cu_{731}$ nanoparticles at 0K with the lowest TOP energies calculated using TOP equation for $Pt_{70}X_{70}$ particles ($Pt_{732}X_{731}^{(140)}$, left column) and $Pt_{101}X_{100}$ (particles $Pt_{732}X_{731}^{(201)}$, right column). Colors of atoms are as in Figure 6.12.

Conclusions The study outlined in this Section can be summarized as follows:

- The energy terms in the TOP equations for $Pt_{70}X_{70}$ and $Pt_{101}X_{100}$ NPs are very similar justifying that the equations are applicable for determining the chemical ordering of much larger bimetallic PtX particles.
- Au and Ag atoms in Pt-Au and Pt-Ag NPs are strongly energetically favored to be exposed on the surface, whereas Pt atoms preferentially occupy inner positions. This results in the core@shell chemical orderings Pt@Au and Pt@Ag. Charge distribution in PtAu NPs shows essentially neutral character of atoms. Pt and Ag atoms in PtAg

nanoparticles are moderately charged negatively and positively, respectively, suggesting noticeably different reactivity of surface Pt sites on PtAg NPs compared to purely Pt NPs.

- PtCu NPs exhibit the preference of Pt atoms at surface sites with higher coordination number, with terrace {111} positions being the most stable. In this case, the formation of heterometallic bonds is favorable. Surface Pt atoms in PtCu NPs withdraw very significant electron density, up to -0.5 *e* in terms of the Bader atomic charge, from less electronegative nearby Cu atoms.
- Pd-based nanoalloys with Au and Ag differ from the Pt-based ones by forming slightly destabilizing heterometallic bonds favoring mixing. PtCu and PdCu NPs exhibit similar lowest-energy chemical orderings, reflecting that their stability is driven by the stabilizing heterometallic bonds.
- Independently of the terms of the topological energy equation employed, for 140- or 201-atom NPs, a similar chemical ordering is predicted in $Pt_{732}Au_{731}$ and $Pt_{732}Ag_{731}$ NPs. However, Pt and Cu atoms in $Pt_{732}Cu_{731}$ NP are arranged somewhat differently in the lowest-energy $Pt_{732}Cu_{731}^{(140)}$ and $Pt_{732}Cu_{731}^{(201)}$ homotops. All studied bimetallic NPs show more disorder upon temperature increase. Notably, heating leads to appearance of (mainly) single-atom surface Pt sites on facets of $Pt_{732}Au_{731}$ and $Pt_{732}Ag_{731}$ NPs and enriches concentration of surface Cu atoms on facets of $Pt_{732}Cu_{731}$ particle.

Materials Advances

ROYAL SOCIETY OF CHEMISTRY

PAPER

Cite this: *Mater. Adv.*, 2021, 2, 6589

Chemical ordering in Pt–Au, Pt–Ag and Pt–Cu nanoparticles from density functional calculations using a topological approach†

Lorena Vega,[a] Hristiyan A. Aleksandrov, *[b] Riccardo Farris,[a] Albert Bruix, [a] Francesc Viñes [a] and Konstantin M. Neyman *[ac]

Bimetallic alloys are actively investigated as promising new materials for catalytic and other energy-related applications. However, the stable arrangements of the two metals in prevailing nanostructured systems, which define their structure and surface reactivity, are seldom addressed. The equilibrium chemical orderings of bimetallic nanoparticles are usually different from those in the corresponding bulk phases and hard to control experimentally, which hampers assessment of the relations between composition, structure, and reactivity. Herewith, we study mixtures of platinum—an essential metal in catalysis—alloyed with coinage metals gold, silver, and copper. These systems are interesting, for instance, for reducing the costly Pt content and designing improved multifunctional catalysts, but the chemical orderings in such mixtures at the nanoscale are still debated. We therefore explore chemical orderings and properties of Pt-containing nanoalloys by means of a topological method based on density functional calculations. We determine the lowest-energy chemical orderings in 1.4 to 4.4 nm large Pt–Au, Pt–Ag and Pt–Cu particles with different contents of metals. Chemical ordering, bonding, and charge distribution in the nanoparticles are analyzed, identifying how peculiar structural motifs relevant for catalysis and sensing applications, such as monometallic skins and surface single-atom sites, emerge. We compare these results with previous data for the corresponding Pd-based particles, identifying trends in chemical ordering, deepening understanding of the behaviour of catalytically relevant bimetallic compositions, and establishing appropriate models for studying the bimetallic nanoalloys.

Received 17th June 2021,
Accepted 4th August 2021

DOI: 10.1039/d1ma00529d

rsc.li/materials-advances

1. Introduction

Studies of materials containing bimetallic nanoparticles (NPs), often referred to as nanoalloys, is a dynamically developing research area. The latter is interrelated to diverse applications of nanoalloy particles ranging from optics and magnetism to medicine and catalysis.[1,2] Properties of a bimetallic NP are defined, besides its geometric structure and size, by the relative amount (composition) of the two constituting metals. Tuning the composition extends the design variables of materials containing bimetallic NPs tailor-made for the desired applications to function better, often at reduced cost.

The size, shape, and composition of bimetallic NPs can be quite well controlled by the preparation conditions. At variance, such elusive degree of complexity as chemical (or atomic) ordering, *i.e.* a distribution pattern of metal atoms of two types among lattice positions of an alloy NP, is hard to precisely control experimentally. The reactivity of metal NPs is directly related to their surface arrangement. The chemical ordering defines what types and how many surface sites are exposed by a bimetallic NP of a given size, shape, and composition. This is key information for catalysis, sensing, and many other applications. Yet, it remains barely accessible experimentally at the atom-by-atom level even for the most modern structure characterization techniques.

Computational modeling using Density Functional Theory (DFT) can provide detailed information about the structure and properties of bimetallic NPs, complementing experimental data. DFT calculations of bimetallic NPs with over a hundred atoms and sizes of ~1.5 nm, which are required to realistically

[a] *Departament de Ciència de Materials i Química Física & Institut de Química Teòrica i Computacional (IQTCUB), Universitat de Barcelona, 08028 Barcelona, Spain*

[b] *Faculty of Chemistry and Pharmacy, University of Sofia, 1126 Sofia, Bulgaria. E-mail: haa@chem.uni-sofia.bg*

[c] *ICREA (Institució Catalana de Recerca i Estudis Avançats), 08010 Barcelona, Spain. E-mail: konstantin.neyman@icrea.cat*

† Electronic supplementary information (ESI) available: Structural and energy data calculated by DFT of the discussed in the article Pt–Au, Pt–Ag and Pt–Cu nanoparticles (PDF). See DOI: 10.1039/d1ma00529d

represent larger particles dealt with in catalysis,[3–5] are feasible since two decades.[6] However, the presence of more than one type of atoms in nanoalloys severely hinders their comprehensive DFT simulation, often restricting it to quite small particles and considering only several chemical orderings (homotops).[7–12] In fact, a direct search for the equilibrium chemical ordering in a ~2 nm large bimetallic crystallite comprising ~200 atoms requires calculating energies of a colossal number of 10^{50} homotops (including symmetry-equivalent ones),[13] which is excessive for any computational method.

This challenge can be dealt with by a Topological (TOP) approach,[14,15] which enables determining equilibrium chemical orderings in bimetallic nanocrystallites containing 10^2–10^4 atoms of different metals across the Periodic Table from a small number of DFT calculations. Briefly, the TOP method divides all homotops of a bimetallic nanocrystallite with a given stoichiometry and shape into groups with the same topologies. Definition of the latter depends on how atomically detailed the resulting ordering needs to be. For instance, for studying the catalytic activity of a bimetallic M'_mM_n NP comprising $m + n$ atoms it is essential to know how many active surface sites of each type the NP exposes. These data are related to the propensity of M′ and M atoms to segregate on the surface and define which atoms occupy surface positions of the NP with different coordination numbers, *e.g.* in corner, edge, and terrace sites. Since all homotops of the NP under scrutiny share the same crystal lattice and composition, it suffices to specify atomic positions for just one of the two metals. The types of the exposed surface sites and their abundance are also affected by the propensity of the metals M′ and M to mix, which is reflected by the number of heterometallic bonds (nearest-neighbor atom pairs) M′–M formed. For surface reactivity studies it is often sufficient to specify ordering patterns in bimetallic nanoalloys by the topology defined solely by the number of M′–M bonds $\left(N_{\mathrm{BOND}}^{\mathrm{M'-M}}\right)$ and surface M atoms in the corner/vertex ($N_{\mathrm{CORNER}}^{\mathrm{M}}$), edge ($N_{\mathrm{EDGE}}^{\mathrm{M}}$), and facet/terrace ($N_{\mathrm{FACET}}^{\mathrm{M}}$) positions. Hereafter, topologies of M'_mM_n NPs are designated as $M'_mM_n\text{–}N_{\mathrm{BOND}}^{\mathrm{M'-M}} \cdot N_{\mathrm{CORNER}}^{\mathrm{M}} \cdot N_{\mathrm{EDGE}}^{\mathrm{M}} \cdot N_{\mathrm{FACET}}^{\mathrm{M}}$; to specify a particular homotop of the considered topology, its E^{DFT} value in eV is added to the above designation, resulting in the designation $M'_mM_n\text{–}N_{\mathrm{BOND}}^{\mathrm{M'-M}} \cdot N_{\mathrm{CORNER}}^{\mathrm{M}} \cdot N_{\mathrm{EDGE}}^{\mathrm{M}} \cdot N_{\mathrm{FACET}}^{\mathrm{M}} E^{\mathrm{DFT}}$. Energies of all homotops with a given topology are represented in the TOP method by the energy of just one of the homotops, chosen arbitrarily.[14]

Energy difference, $\Delta E_{ij}^{\mathrm{TOP}}$, between any two homotops i and j of a bimetallic NP reads:[14,16]

$$\begin{aligned}\Delta E_{ij}^{\mathrm{TOP}} &= E_j^{\mathrm{TOP}}\left(N_{j,\mathrm{BOND}}^{\mathrm{M'-M}}, N_{j,\mathrm{CORNER}}^{\mathrm{M}}, N_{j,\mathrm{EDGE}}^{\mathrm{M}}, N_{j,\mathrm{FACET}}^{\mathrm{M}}\right) \\ &\quad - E_i^{\mathrm{TOP}}\left(N_{i,\mathrm{BOND}}^{\mathrm{M'-M}}, N_{i,\mathrm{CORNER}}^{\mathrm{M}}, N_{i,\mathrm{EDGE}}^{\mathrm{M}}, N_{i,\mathrm{FACET}}^{\mathrm{M}}\right) \\ &= \varepsilon_{\mathrm{BOND}}^{\mathrm{M'-M}} \cdot \Delta N_{ij,\mathrm{BOND}}^{\mathrm{M'-M}} + \varepsilon_{\mathrm{CORNER}}^{\mathrm{M}} \cdot \Delta N_{ij,\mathrm{CORNER}}^{\mathrm{M}} \\ &\quad + \varepsilon_{\mathrm{EDGE}}^{\mathrm{M}} \cdot \Delta N_{ij,\mathrm{EDGE}}^{\mathrm{M}} + \varepsilon_{\mathrm{FACET}}^{\mathrm{M}} \cdot \Delta N_{ij,\mathrm{FACET}}^{\mathrm{M}}\end{aligned} \quad (1)$$

with $\Delta N_{ij} = N_j - N_i$.

Here, the energies ε are contributions of either a M′–M bond or an M atom located in a certain outer position of the NP to its topological energy E^{TOP}. The terms ε quantify either the surface segregation energy of metal atoms M′ and M or the energy gained or lost upon metals mixing to form a pair M′–M of the nearest-neighbor atoms. These terms are calculated by fitting eqn (1) to DFT energies E^{DFT} of a series of homotops of a bimetallic NP with diverse topologies. Using thus obtained TOP expressions a comprehensive ordering screening is performed by means of Monte Carlo (MC) simulations to find the topology—a set of the N values—of the most energetically stable homotops of the NP along with topologies of less stable homotops. Then, atomic positions in the selected low-energy homotops are optimized by DFT. This allows examining accuracy of the energies ε and eqn (1) overall. The resulting latter expressions can be used to simulate the chemical orderings in bimetallic NPs containing thousands atoms, not accessible for DFT calculations.

Successfully determined chemical orderings in NPs of various metal combinations, such as Pd–Au,[13–17] Pd–Ag,[14] Pd–Cu,[14] Pd–Zn,[14] Pd–Rh,[16] Pt–Ag,[18] Pt–Co,[19,20] Pt–Ni,[21] Pt–Sn,[22] and Ni–Cu,[23] revealed efficiency and broad applicability of the TOP method. This study deals with bimetallic nanoalloys of essential for catalysis metal Pt with quite inert coinage metals Au, Ag, and Cu. These combinations of metals are actively studied in the rapidly developing field of single-atom catalysis[24,25] as single-atom alloy catalysts,[26] where individual Pt atoms surrounded by coinage atoms can act as very selective catalytic centers.

Among the aims of the present study are:(i) quantifying by DFT calculations the chemical orderings and surface segregation in up to ~2 nm large Pt–Au, Pt–Ag and Pt–Cu crystallites at different concentrations of the metals; (ii) analyzing the structure, bonding, and atomic charges in these nanoparticles compared to the analogous Pd-containing nanoalloys studied earlier; (iii) deepening the knowledge of the accuracy and applicability of the Topological approach; (iv) identifying equilibrium chemical orderings in Pt–Au, Pt–Ag and Pt–Cu particles at sizes over 4 nm commonly found in catalysts, also at elevated temperatures.

2. Computational methods

All DFT calculations were performed using the plane-wave code VASP.[27,28] A gradient-corrected Perdew–Burke–Ernzerhof (PBE) exchange–correlation functional[29] was employed as one of the most reliable functionals for transition metals bulks and surfaces[30–32] in combination with the projector augmented wave (PAW) representation of core electrons.[33,34] Insignificant spin-polarization effects for the non-magnetic platinum and coinage metals were neglected. To moderate the computational cost, cutoff energies for the plane-wave functions were defined by the values of the PBE core-electrons PAW potentials:Cu – 273.2 eV, Ag – 249.85 eV, Au – 229.95 eV and Pt – 230.28 eV. According to our benchmarks, the total energy differences between distinct chemical orderings of a given NP computed using these cutoff energies are essentially as accurate as when

using the cutoff energy 415 eV (typically used for describing adsorbate–metal interactions). The Brillouin zone was sampled only at the Γ-point. One-electron Kohn–Sham levels were smeared by 0.1 eV and the converged energies were finally extrapolated to zero smearing. All atoms were locally relaxed without any restrictions until forces acting on each atom decreased to 0.2 eV nm^{-1}.

In line with our DFT calculations of other nanoalloy particles,[13,14,16,21] here the Pt–X (X = Au, Ag, Cu) NPs were also represented by truncated octahedrons with the fcc lattice. *Ca.* 1.4 nm large 140-atomic $Pt_{70}Au_{70}$, $Pt_{70}Ag_{70}$, and $Pt_{70}Cu_{70}$ NPs, see Fig. 1, were considered for comparison with the results for Pd-based $Pd_{70}Au_{70}$, $Pd_{70}Ag_{70}$, and $Pd_{70}Cu_{70}$ analogs.[14] 1.7–1.8 nm large 201-atomic NPs Pt–Au, Pt–Ag and Pt–Cu with Pt : X 1 : 3, 1 : 1, and 3 : 1 compositions, see Fig. 2, were modelled to study the size, shape, and composition effects. Placing these 140- and 201-atom NPs in periodically repeated cubic cells of $2.3 \times 2.3 \times 2.3$ and $2.5 \times 2.5 \times 2.5$ nm^3 allowed separation >0.7 nm between them. At such distances interaction of metal particles with their periodic images is negligible for the purpose of this work.[35,36]

3. Results and discussion

In the following we present and discuss results for model Pt–X (X = Au, Ag, Cu) NPs $Pt_{51}X_{150}$ (1 : 3), $Pt_{101}X_{100}$ (1 : 1), $Pt_{151}X_{50}$ (3 : 1), and $Pt_{70}X_{70}$ (1 : 1). These fcc crystallites expose surface atoms with the coordination numbers (CN) 6 (corner/vertex), 7 (edge), and 9 ({111} facets). Besides, the 201-atomic particles contain one atom with CN = 8 in each of their six {100} facets. Table 1 shows the calculated energy terms ε in the topological expressions (eqn (1)). Details of the lowest-energy chemical orderings resulting from DFT calculations (E^{DFT}) and from MC calculations using eqn (1) (E^{TOP}) are specified in Table 2. These two kinds of chemical orderings are quite similar for each studied model NP. Thus, unless stated otherwise, herein we consider the chemical orderings corresponding to the E^{TOP} values.

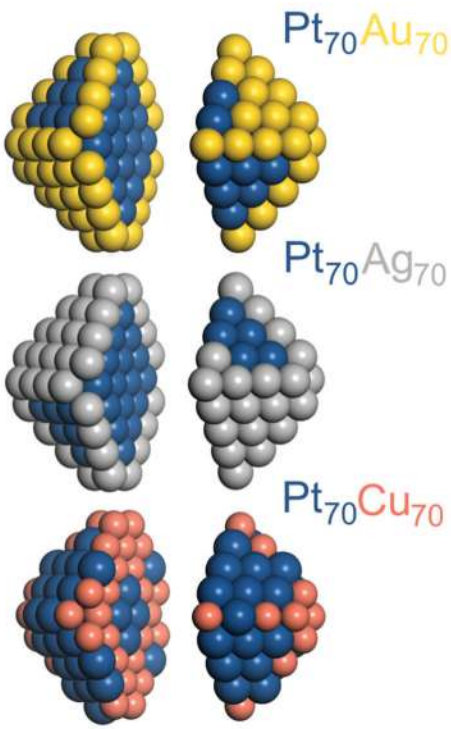

Fig. 1 Chemical orderings of *ca.* 1.4 nm large 140-atomic truncated-octahedral fcc nanoparticles $Pt_{70}Au_{70}$, $Pt_{70}Ag_{70}$, and $Pt_{70}Cu_{70}$ with the lowest DFT energies. Particles images are split in two parts for better visualization. Pt – blue, Au – yellow, Ag – gray, Cu – red-brown.

The following literature data are relevant for the present study of the Pt–X nanoalloys:(i) the surface energies calculated for close-packed surfaces of the pure metals are 1.03 (Pt), 0.72 (Au), 0.58 (Ag), and 0.77 eV per atom (Cu);[37] (ii) calculated solutes/hosts surface segregation energies of monoatomic impurities (solutes) in fcc(111) metal hosts are −0.36 (Au/Pt), 0.34 (Pt/Au), −0.27 (Ag/Pt), 0.34 (Pt/Ag), 0.32 (Cu/Pt), and −0.04 eV (Pt/Cu), where the negative sign indicates stabilizing surface segregation of the solute;[37] (iii) Pt atoms in the bulk alloys are immiscible with Au[38–41] and Ag[40] atoms, but miscible with Cu[40,42–44] atoms; and (iv) relative sizes of metal atoms,[45] 139 (Pt), 144 (Au), 144 (Ag), and 128 pm (Cu), affect the propensity of smaller atoms to surface segregate in compressively strained bimetallic particles[40,46–48] so that the surface segregation of Cu is suppressed in Pt–Cu nanoalloys despite Cu has a lower surface energy than Pt (see above).

3.1. DFT data for chemical orderings of Pt–Au nanoparticles

$Pt_{51}Au_{150}$, $Pt_{101}Au_{100}$, and $Pt_{151}Au_{50}$ nanoparticles. Calculated data for 201-atomic Pt–Au NPs with the Pt : Au compositions 1 : 3, 1 : 1, and 3 : 1, see Tables 1, 2 and Fig. 2, reveal that their chemical orderings are controlled, in agreement with the data for Pt–Au bulk, surface, and nanoalloys,[37–40] by the following effects:first, the positive energies $\varepsilon_{BOND}^{Pt\text{-}Au}$ = 15–21 meV (Table 1) indicate that the formation of Pt–Au bonds in the alloys is disfavored with respect to Pt–Pt and Au–Au bonds, suppressing mixing of Pt and Au atoms. Second, quite large in magnitude negative terms $\varepsilon_{CORNER}^{Au}$ = −507 to −558 meV, ε_{EDGE}^{Au} = −492 to −547 meV and ε_{FACET}^{Au} = −259 to −431 meV show that Au atoms are notably more stable on the surface of the NPs than inside them and thus segregate on the surface. More open corner and edge Au atoms are more stable than higher-coordinated facet Au atoms. Increase of ε_{FACET}^{Au} in magnitude with increasing Pt : Au content from 1 : 3 to 1 : 1, and to 3 : 1 suggests that the location of Pt atoms in facets of Pt–Au NPs is less energetically penalized at lower Pt concentrations than at higher ones. The surface segregation of Au atoms in the 201-atomic Pt–Au NPs with the lowest-energy orderings is illustrated in Fig. 2 and additionally detailed in Table 2 by numbers of atoms in various sites. Au atoms of $Pt_{51}Au_{150}$ occupy all 24 corner, 36 edge, and 62 facet sites forming a complete monolayer Au skin. The remaining 28 Au atoms are located inside, tending to minimize the number of unfavorable Pt–Au nearest-neighbor contacts. $Pt_{101}Au_{100}$ NP has insufficient Au atoms to complete the Au skin. There, 100 Au atoms occupy

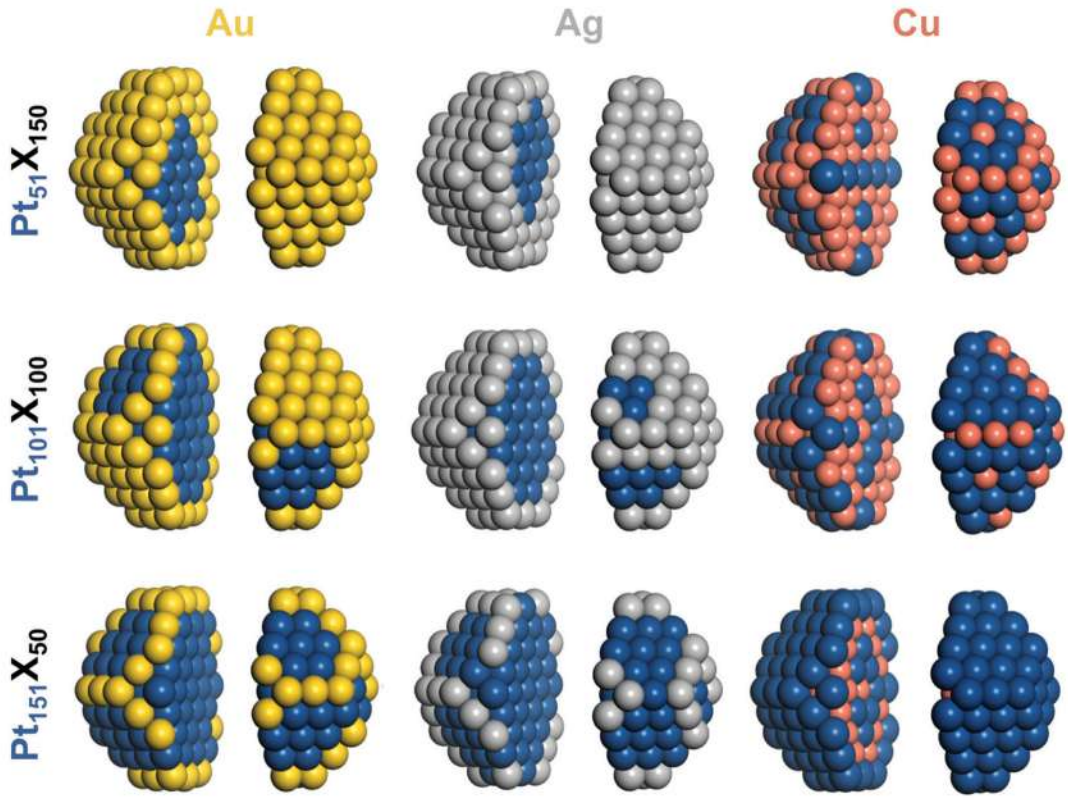

Fig. 2 Chemical orderings of 1.7–1.8 nm large 201-atomic truncated-octahedral fcc nanoparticles of the compositions Pt:X (X = Au, Ag, Cu):1: 3 – $Pt_{51}X_{150}$, 1:1 – $Pt_{101}X_{100}$, 3:1 – $Pt_{151}X_{50}$ with the lowest DFT energies. Particles images are split in two parts for better visualization. Colors of atoms as in Fig. 1.

all 24 corner and 36 edge surface sites plus 40 of 62 facet sites. Even fewer Au atoms in $Pt_{151}Au_{50}$ NP results in their competition to partly occupy only corner and edge sites.

The usefulness of the TOP approach and the meaning of terms in eqn (1) can be illustrated by comparing the TOP and DFT segregation energies. A homotop of $Pt_{51}Au_{150}$ with almost lowest TOP energy, $Pt_{51}Au_{150}$_212.24.36.62–729.864 (see ESI†), is characterized by $N_{\mathrm{BOND}}^{\mathrm{Pt\text{-}Au}} = 212$, $N_{\mathrm{CORNER}}^{\mathrm{Au}} = 24$, $N_{\mathrm{EDGE}}^{\mathrm{Au}} = 36$ and $N_{\mathrm{FACET}}^{\mathrm{Au}} = 62$ and $E^{\mathrm{DFT}} = -729.864$ eV (homotops are labeled in this way throughout the present article). Exchange of an atom Au from center of a {111} facet with a near-neighbor subsurface atom Pt (each of the exchanged atoms Au number 39 and Pt number 198 formed 3 Pt–Au bonds) results in the homotop $Pt_{51}Au_{150}$_223.24.36.61–729.507 (see ESI†), where, the surface Pt atom forms 7 Pt–Au bonds and the Au atom moved to the subsurface forms 10 Pt–Au bonds. Its energy increase with respect to the pristine homotop is $\Delta E^{\mathrm{TOP}} = \varepsilon_{\mathrm{BOND}}^{\mathrm{Pt-Au}}\Delta N_{\mathrm{BOND}}^{\mathrm{Pt-Au}} + \varepsilon_{\mathrm{FACET}}^{\mathrm{Au}}\Delta N_{\mathrm{FACET}}^{\mathrm{Au}} = 11 \times 15\ \mathrm{meV} + 259\ \mathrm{meV} = 424\ \mathrm{meV}$, using eqn (1) and energies ε in Table 1. The DFT energy increase 357 meV is close to the ΔE^{TOP} value in terms of the precision $\delta(E^{\mathrm{DFT}} - E^{\mathrm{TOP}}) = 279$ meV (Table 1). $\delta(E^{\mathrm{DFT}} - E^{\mathrm{TOP}})$ is twice the residual standard deviation between E^{DFT} and E^{TOP} energies for homotops of $\geq$10 test low-energy topologies, according to which the respective ΔE^{TOP} and ΔE^{DFT} values differ by less than δ with the probability $\geq$95%.[14] Exchange of an edge atom Au with a nearby subsurface atom Pt in the pristine homotop models even less favorable surface segregation of inner atoms Pt to edge sites. $N_{\mathrm{BOND}}^{\mathrm{Pt\text{-}Au}}$ after this exchange of atom Au number 132 with atom Pt number 176 (see ESI†) increases in the resulting homotop $Pt_{51}Au_{150}$_219.24.35.62–729.345 for the atom Au from 1 to 6 and for the atom Pt from 5 to 7. The energy increase *vs.* the pristine homotop, $\Delta E^{\mathrm{TOP}} = \varepsilon_{\mathrm{BOND}}^{\mathrm{Pt-Au}}\Delta N_{\mathrm{BOND}}^{\mathrm{Pt-Au}} + \varepsilon_{\mathrm{EDGE}}^{\mathrm{Au}}\Delta N_{\mathrm{EDGE}}^{\mathrm{Au}} = 7 \times 15\ \mathrm{meV} + 547\ \mathrm{meV} = 652\ \mathrm{meV}$, is indeed larger than for the displacement of the inner atom Pt to a {111} facet and reasonably well agrees with $\Delta E^{\mathrm{DFT}} = 519$ meV.

These two examples demonstrate that the TOP method, beyond providing adequate relative energies of different chemical orderings of a bimetallic NP, also allows rationalizing the energy differences in such important terms as propensities of their two types of metal atoms to form heterometallic bonds and to occupy differently coordinated surface sites.

$Pt_{70}Au_{70}$ nanoparticle. The size-sensitivity of the interactions governing equilibrium orderings in Pt–Au NPs at a given Pt:Au composition can be explored by comparing the ordering of the $Pt_{101}Au_{100}$ particle with that of the smaller $Pt_{70}Au_{70}$ particle sketched in Fig. 1. One can see from Table 1 that $\varepsilon_{\mathrm{BOND}}^{\mathrm{Pt\text{-}Au}} = 19$ meV for $Pt_{70}Au_{70}$ remains within the error bar of the same quantity for $Pt_{101}Au_{100}$, indicating that quite low immiscibility of Pt and Au atoms is almost independent of the particle size in this size range. Surface segregation of Au atoms is strongly energetically preferred also in the $Pt_{70}Au_{70}$ particle. There, the energy gain by displacement of an inner atom Au to a corner without changing the number of Pt–Au bonds (*i.e.* $\varepsilon_{\mathrm{CORNER}}^{\mathrm{Au}}$) is 619 meV, exceeding that for $Pt_{101}Au_{100}$ particle, 530 meV. At

Table 1 Energy terms,[a] ε, in the topological expressions[14,15] (eqn (1)) for energy differences ΔE_{ij}^{TOP} of homotops i and j of Pt_nX_m (X = Au, Ag, Cu; $m + n = 140$, 201) particles $\Delta E_{ij}^{TOP} = \varepsilon_{BOND}^{Pt\text{-}X}\cdot\Delta N_{ij,BOND}^{Pt\text{-}X} + \varepsilon_{CORNER}^{X}\cdot\Delta N_{ij,CORNER}^{X} + \varepsilon_{FACET}^{X}\cdot\Delta N_{ij,FACET}^{X}$. Here, $\Delta N_{ij} = N_j - N_i$, $N_{BOND}^{Pt\text{-}X}$, N_{CORNER}^{X}, N_{EDGE}^{X}, N_{FACET}^{X}, are numbers of heterometallic bonds Pt–X (nearest-neighbor pairs of Pt–X atoms) and atoms X in the corner (vertex), edge and facet positions of the particle, respectively. The $\delta(E^{DFT} - E^{TOP})^b$ and ΔE (calculated using E^{TOP}) are precision and accuracy values, respectively.[14] All energies are in meV. N_{FIT} is the number of homotops calculated by DFT for each NP used to fit the TOP expressions. Data for analogous $Pd_{70}Au_{70}$, $Pd_{70}Ag_{70}$, and $Pd_{70}Cu_{70}$ particles from ref. 14 are also shown

Nanoparticle	$\varepsilon_{BOND}^{Pt\text{-}X}$	ε_{CORNER}^{X}	ε_{EDGE}^{X}	ε_{FACET}^{X}	δ	ΔE	N_{FIT}
$Pt_{70}Au_{70}$	19^{+4}_{-2}	-619^{+62}_{-48}	-377^{+44}_{-44}	-256^{+88}_{-69}	470	0	35
$Pd_{70}Au_{70}$	-13^{+4}_{-6}	-404^{+76}_{-72}	-301^{+52}_{-77}	-200^{+52}_{-64}	115	26	32
$Pt_{70}Ag_{70}$	11^{+10}_{-13}	-625^{+122}_{-185}	-336^{+72}_{-185}	-195^{+75}_{-58}	358	0	45
$Pd_{70}Ag_{70}$	-1^{+2}_{-2}	-361^{+50}_{-68}	-289^{+78}_{-129}	-163^{+43}_{-64}	150	29	53
$Pt_{70}Cu_{70}$	-35^{+4}_{-4}	-27^{+47}_{-44}	182^{+56}_{-54}	344^{+43}_{-36}	879	415	65
$Pd_{70}Cu_{70}$	-26^{+5}_{-5}	95^{+36}_{-33}	147^{+46}_{-45}	183^{+42}_{-40}	360	171	127
$Pt_{151}Au_{50}$	21^{+1}_{-1}	-507^{+51}_{-62}	-543^{+16}_{-18}	-431^{+30}_{-43}	114	354	101
$Pt_{101}Au_{100}$	21^{+7}_{-6}	-530^{+136}_{-107}	-492^{+59}_{-56}	-335^{+83}_{-95}	456	0	68
$Pt_{51}Au_{150}$	15^{+14}_{-15}	-558^{+49}_{-34}	-547^{+53}_{-84}	-259^{+47}_{-92}	279	198	44
$Pt_{151}Ag_{50}$	32^{+11}_{-12}	-396^{+108}_{-135}	-380^{+95}_{-90}	-237^{+103}_{-95}	461	176	90
$Pt_{101}Ag_{100}$	16^{+9}_{-10}	-499^{+95}_{-112}	-466^{+87}_{-83}	-308^{+77}_{-91}	493	65	68
$Pt_{51}Ag_{150}$	7^{+5}_{-5}	-408^{+118}_{-158}	-511^{+79}_{-68}	-240^{+49}_{-65}	169	43	99
$Pt_{151}Cu_{50}$	-25^{+9}_{-13}	267^{+30}_{-22}	342^{+14}_{-14}	372^{+42}_{-44}	784	204	165
$Pt_{101}Cu_{100}$	-43^{+6}_{-5}	15^{+60}_{-72}	208^{+55}_{-68}	325^{+34}_{-41}	576	284	87
$Pt_{51}Cu_{150}$	-54^{+14}_{-15}	134^{+73}_{-78}	184^{+151}_{-93}	259^{+65}_{-59}	239	0	40

[a] 95% confidence interval of ε given as, *e.g.* 19^{+4}_{-2} denotes a range from 17 meV to 23 meV. [b] When several homotops were optimized by DFT for one of the selected ≥10 low-energy topologies, see Section 3.6, all these E^{DFT} values were also used in the calculations of δ.

variance, the energy gained by the relocation of an inner Au atom to edges and terraces (*i.e.* ε_{EDGE}^{Au} and ε_{FACET}^{Au}) is 377 and 256 meV, respectively, smaller than for $Pt_{101}Au_{100}$ particle, 492 and 335 meV. These findings indicate that Au atoms are better distributed between low-coordinated (corner, edge) positions and higher-coordinated terrace positions in larger 1:1 Pt–Au particles than in smaller ones, where Au clearly prefers corners. The lowest-energy topology of the $Pt_{70}Au_{70}$ particle, see Table 2, corresponds to complete occupation of all 24 corner and 24 edge sites by Au atoms and location of all remaining 22 Au atoms on the facets. The percentage of 196 Pt–Au bonds in $Pt_{70}Au_{70}$, 31% of all metal–metal bonds, is comparable to 28% of 267 Pt–Au bonds in $Pt_{101}Au_{100}$. Some $Pt_{70}Au_{70}$ results will be further discussed in the sections dealing with the comparison of Pt–X NPs with their Pd–X analogs as well as with predicting chemical orderings in larger Pt–X NPs, where DFT calculations are unfeasible.

Charge distribution. Only a minor charge redistribution occurs between Pt and Au atoms in Pt–Au NPs. According to the Bader charge analysis, see Table 3, for most of surface Pt and Au atoms in Pt–Au nanoalloys the average charges are within 0.03 $|e|$ of the charges calculated in the corresponding surface positions of the monometallic Pt_{201} and Au_{201} particles. (Note that in the monometallic particles Bader charges of surface atoms are slightly negative and grow in magnitude with decreasing coordination numbers.) These data suggest a close similarity of the adsorption and reactivity properties of pure Pt and Au surface sites in Pt–Au NPs with the corresponding surface sites in monometallic Pt and Au NPs.

3.2. DFT data for chemical orderings of Pt–Ag nanoparticles

$Pt_{51}Ag_{150}$, $Pt_{101}Ag_{100}$, and $Pt_{151}Ag_{50}$ nanoparticles. Data defining orderings in Pt–Ag NPs, see Tables 1, 2 and Fig. 2, resemble the data for the Pt–Au NPs. In particular, slightly positive energies $\varepsilon_{BOND}^{Pt\text{-}Ag}$ (Table 1) reveal disfavoured mixing of Pt and Ag atoms with the formation of the Pt–Ag bonds, similar to the Pt–Au bonds. This propensity of Pt and Ag components to stay separate is counteracted in NPs by 380–510 meV strong stabilization of Ag atoms in low-coordinated surface corner and edge positions. The stabilization of Ag atoms in surface terrace (facet) positions is somewhat weaker, but still significant, 240–310 meV.

Ordering of the lowest-energy homotops of $Pt_{101}Ag_{100}$ NP is very similar to those of $Pt_{101}Au_{100}$ NP, see Fig. 2 and Table 2. All Ag atoms are located on the surface occupying all 24 corner and 36 edge sites and 40 of 62 terrace sites. Pt atoms occupy the remaining terrace sites and all 79 inner sites. This ordering exhibits incomplete Ag outer shell and monometallic Pt core. Qualitatively the same values of energies ε guiding the orderings in 201-atom NPs with other Pt:Ag ratios, $Pt_{51}Ag_{150}$, and

Table 2 Numbers of Pt–X bonds and atoms X = Au, Ag, Cu in various positions with the coordination numbers 6 – corner/vertex, 7 – edge, 8 + 9 – {100} + {111} facets, and 8 – {100} facets in the lowest-energy homotops of the $Pt_{70}X_{70}$, $Pt_{151}X_{50}$, $Pt_{101}X_{100}$, and $Pt_{51}X_{150}$ particles optimized at DFT/TOP levels along with DFT energies of these homotops, E_{DFTmin}^{DFT} and E_{TOPmin}^{DFT}, respectively[a]

Particle	$N_{BOND}^{Pt\text{-}X}$	N_{CORNER}^{X}	N_{EDGE}^{X}	N_{FACET}^{X}	N_{100}^{X}	E_{DFTmin}^{DFT} (eV)	E_{TOPmin}^{DFT} (eV)
$Pt_{70}Au_{70}$	196/196	24/24	24/24	22/22		−588.108	−588.108
$Pt_{70}Ag_{70}$	196/196	24/24	24/24	22/22		−561.294	−561.294
$Pt_{70}Cu_{70}$	308/340	23/24	8/12	0/0		−626.920	−626.610
$Pt_{151}Au_{50}$	215/214	23/20	25/30	2/0	2/0	−978.389	−978.283
$Pt_{151}Ag_{50}$	222/215	24/21	26/29	0/0	0/0	−962.454	−961.772
$Pt_{151}Cu_{50}$	404/412	0/0	0/0	0/0	0/0	−1015.683	−1015.214
$Pt_{101}Au_{100}$	267/267	24/24	36/36	40/40	5/5	−859.505	−859.505
$Pt_{101}Ag_{100}$	274/270	24/24	36/36	40/40	6/4	−822.032	−821.660
$Pt_{101}Cu_{100}$	525/560	24/24	10/8	3/8	0/0	−914.377	−913.767
$Pt_{51}Au_{150}$	224/210	24/24	36/36	62/62	6/6	−730.046	−729.869
$Pt_{51}Ag_{150}$	220/214	24/24	36/36	62/62	6/6	−669.026	−668.827
$Pt_{51}Cu_{150}$	418/418	24/24	36/36	18/18	0/0	−799.627	−799.627

[a] The overall topological numbers N_{BOND}, N_{CORNER}, N_{EDGE}, N_{FACET}, and N_{INSIDE} are 636, 24, 24, 48, 44 ($Pt_{70}X_{70}$), and 948, 24, 36, 62, 79 ($Pt_{201-n}X_n$), respectively.

Table 3 Average Bader charges, in |e|, on atoms with coordination numbers 6, 7, 8, 9, 12 in $Pt_{70}X_{70}$, $Pt_{151}X_{50}$, $Pt_{101}X_{100}$, and $Pt_{51}X_{150}$ (X = Au, Ag, Cu) NPs with the lowest E^{TOP} energy. The charges in the monometallic Pt_{201} and X_{201} NPs are also shown for comparison

	Pt					X				
Particle	6	7	8	9	12	6	7	8	9	12
$Pt_{70}Au_{70}$	—	—	—	−0.02	0.05	−0.05	−0.02		0.02	—
$Pt_{151}Au_{50}$	−0.09	−0.07	−0.08	−0.02	0.02	−0.05	−0.03	—	—	—
$Pt_{101}Au_{100}$	—	—	−0.09	−0.04	0.03	−0.05	−0.03	0.01	0.02	—
$Pt_{51}Au_{150}$	—	—	—	—	0.01	−0.06	−0.03	−0.01	0.01	0.06
$Pt_{70}Ag_{70}$				−0.17	−0.04	0.05	0.10		0.10	—
$Pt_{151}Ag_{50}$	−0.13	−0.13	−0.24	−0.11	0.02	0.12	0.15	—	—	—
$Pt_{101}Ag_{100}$	—	—	−0.30	−0.16	−0.05	0.05	0.08	0.13	0.09	—
$Pt_{51}Ag_{150}$	—	—	—	—	−0.11	−0.02	0.01	0.04	0.04	0.12
$Pt_{70}Cu_{70}$	—	−0.25		−0.23	−0.33	0.18	0.27		—	0.30
$Pt_{151}Cu_{50}$	−0.14	−0.11	−0.08	−0.07	−0.23	—	—	—	—	0.37
$Pt_{101}Cu_{100}$	—	−0.29	−0.12	−0.27	−0.39	0.27	0.22	—	0.32	0.31
$Pt_{51}Cu_{150}$	—	—	−0.57	−0.46	−0.60	0.11	0.15	—	0.19	0.19
Pt_{201}	−0.09	−0.06	−0.03	−0.01	0.07					
Au_{201}						−0.07	−0.04	−0.02	−0.01	0.04
Ag_{201}						−0.04	−0.03	0.01	−0.01	0.03
Cu_{201}						−0.05	−0.02	0.02	−0.01	0.03

$Pt_{151}Ag_{50}$, as in the $Pt_{101}Ag_{100}$ NP, result in completing the Ag skin in the former case and depleting the skin (mainly by the facet atoms) in the latter case. Comparing equilibrium chemical orderings of the 201-atomic Pt–Ag NPs with their Pt–Au analogs, see Table 2, one notices very close similarities, especially at low Pt concentrations. Indeed, topologies of most corresponding Pt–Ag and Pt–Au pairs of NPs differ at most by just small amount of heterometallic bonds contributing up to a fraction of an eV to the NP energy. It is worth mentioning that a peculiar layered chemical ordering $L1_1$ was experimentally identified inside monolayer Ag skins of some relatively small Pt–Ag NPs.[49] Small energetic preference calculated by DFT of such layering in Pt–Ag NPs[18] becomes even smaller in the analogous Pd–Ag NPs and disappears in Pt–Au and Pd–Au NPs that feature monolayer Au skins.[50] Thus, the elusive phenomenon of Pt and Pd layering inside the coinage metal skins appears to be uncommon.

$Pt_{70}Ag_{70}$ nanoparticle. Data in Tables 1 and 2 show that the size decrease of Pt–Ag NPs from 201 to 140 atoms does not change the chemical ordering pattern. In particular, the term $\varepsilon_{BOND}^{Pt\text{-}Ag} = 11^{+10}_{-13}$ meV for $Pt_{70}Ag_{70}$ NP remains within the error bar the same as for $Pt_{101}Ag_{100}$ NP, 16^{+9}_{-10} meV. Furthermore, similarly to 201-atom Pt–Ag particles, Ag atoms in $Pt_{70}Ag_{70}$ NP feature a strong stabilization in surface sites that decreases with increasing their coordination numbers, from 625 meV in the 6-coordinated corner site, to 336 meV in the 7-coordinated edge site and to 195 meV in the 9-coordinated facet (terrace) site, see Table 1. The equilibrium ordering in $Pt_{70}Ag_{70}$ NP, see Fig. 1 and Table 2, reflects these individual topological energy contributions, which lead all Ag atoms on the surface of the NP where they form a part of its monolayer skin. Ag atoms occupy all 24 edge and 24 corner positions and 22 of 48 surface terrace sites, preferring compact locations to completely occupy some of the terraces to minimize the number of Pt–Ag bonds. All 44 positions in the particle core are occupied by Pt atoms. Interestingly, the equilibrium topology of the $Pt_{70}Ag_{70}$ NP is exactly the same as that of the $Pt_{70}Au_{70}$ NP, reflecting a very similar alloying of Ag and Au atoms with Pt atoms.

Charge distribution. At variance with Pt–Au NPs, where Pt and Au atoms are basically neutral according to their Bader charges (see Section 3.1), notable electron density transfer occurs from Ag atoms to more electronegative Pt atoms in Pt–Ag NPs, see Table 3. There, surface Pt atoms acquire a negative charge reaching *ca.* −0.2 |*e*| for atoms with CN = 9 and −0.3 |*e*| for more open CN = 8 atoms. Concomitantly, surface Ag atoms bear positive charges up to 0.15 |*e*|. These data suggest noticeably different reactivity of surface Pt sites on Pt–Ag NPs compared to the corresponding sites on pure Pt NPs. Reactivity of the positively charged Ag surface sites on Pt–Ag NPs should also differ from reactivity of these sites on Ag NPs.

3.3. DFT data for chemical orderings of Pt–Cu nanoparticles

$Pt_{51}Cu_{150}$, $Pt_{101}Cu_{100}$, and $Pt_{151}Cu_{50}$ nanoparticles. Structural and electronic properties of Pt–Cu NPs are substantially different from those of the addressed above Pt–Au and Pt–Ag NPs. The energy terms ε in Table 1 reveal that Cu atoms being smaller than Pt ones (and Au and Ag atoms) are destabilized in the surface positions of Pt–Cu NPs. This occurs despite the smaller surface energy of Cu metal (0.77 eV per atom) than that of Pt metal (1.03 eV per atom).[37] Thus, relative size of the constituting atoms can reverse direction of their surface segregation in structurally stressed bimetallic nanoalloys with respect to the direction defined by the surface energies.[51] Consequently, Pt–Cu NPs at equilibrium tend to expose monolayer skins formed of Pt atoms, unlike Pt–Au and Pt–Ag NPs, which feature coinage-atom skins and Pt atoms inside the particles, see Sections 3.1 and 3.2. More specifically, based on the energies ε, 201-atom Pt–Cu NPs at different Pt:Cu compositions are more destabilized by Cu atoms in terrace positions, followed by edge and corner Cu atoms. The equilibrium orderings of $Pt_{101}Cu_{100}$ and $Pt_{51}Cu_{150}$ NPs containing surface Cu atoms first feature them in corner sites and then, at growing Cu content, in edge sites, see Table 2. An important difference of Pt–Cu NPs from Pt–Au and Pt–Ag ones is that Pt and Cu atoms favourably mix forming Pt–Cu bonds, as shown by the negative

terms $\varepsilon_{BOND}^{Pt\text{-}Cu}$, see Table 1. The mixing notably decreases the propensity to separate of two metal components in the Pt–Cu systems compared to the Pt–Au and Pt–Ag analogues, see Table 2 and Fig. 1, 2.

At the lowest studied Cu content (3 : 1 Pt : Cu), all 50 Cu atoms of $Pt_{151}Cu_{50}$ NP are energetically driven to be located inside the monolayer Pt skin and to form 412 bonds with inner and surface Pt atoms, see Table 2 and Fig. 2. At the 1 : 1 Cu : Pt content, 60 out of the 100 Cu atoms of $Pt_{101}Cu_{100}$ NP stay in the core, 24 Cu atoms occupy all corner positions and the remaining 16 Cu atoms are distributed over edge (8 atoms) and facet (8 atoms) positions. The number of Pt–Cu bonds increases to 560. At the lower 1 : 3 Pt : Cu content, all corner and edge positions of $Pt_{51}Cu_{150}$ NP are occupied by Cu atoms. Cu atoms are also located in 18 of 62 facet positions and form most of the 79-atom core. Interestingly, see Fig. 2, most of surface Pt atoms are directly neighboring other Pt atoms instead of being completely surrounded by Cu atoms, which would enable maximizing the number of Pt–Cu bonds. This implies that low Pt contents are required to form stable single Pt atoms on the surface of Pt–Cu NPs.

$Pt_{70}Cu_{70}$ nanoparticle. Similar to that atomic immiscibility of two metals in 1 : 1 201-atom Pt–Au and Pt–Ag NPs only slightly changed *vs* that in 140-atom NPs, one notices essentially the same mixing propensity of Pt and Cu atoms in $Pt_{101}Cu_{100}$ and $Pt_{70}Cu_{70}$ NPs, with $\varepsilon_{BOND}^{Pt\text{-}Cu}$ equals to −31 and −39 meV, respectively. However, the unfavorable by 15 meV corner position for Cu atom in $Pt_{101}Cu_{100}$ NP becomes favorable by 27 meV in the smaller $Pt_{70}Cu_{70}$ NP, see Table 1. The destabilizing contributions of the edge and facet positions occupied by Cu atoms remain almost the same in the 201- and 140-atomic Pt–Cu NPs. The terms ε rationalize that 100% of the corner positions and 50% of the edge positions in the lowest-energy homotop of $Pt_{70}Cu_{70}$ NP are occupied by Cu, whereas no Cu atoms are located in terrace positions and 77% of the core sites are occupied by Cu. Importantly, more than a half of all metal–metal bonds in $Pt_{70}Cu_{70}$ NP are stabilizing heterometallic Pt–Cu bonds, in comparison with only less than one-third of Pt–Au and Pt–Ag bonds in the corresponding equilibrium structures of $Pt_{70}Au_{70}$ and $Pt_{70}Ag_{70}$ NPs.

Charge distribution. Of all studied Pt nanoalloys with coinage metal, the combination Pt–Cu exhibits the highest electron density accumulated on Pt atoms, see Bader charges in Table 3, reaching up to *ca.* −0.6 $|e|$ per Pt atom depending on the NP size and Pt content. The reactivity of such strongly negatively charged surface Pt atoms is expected to significantly differ from that of Pt atoms bound to more electronegative Au, Ag, and Pt atoms. For instance, according to our calculations on-top adsorption of CO molecule on terrace Pt atoms of 201-atomic Pt–Cu NPs is *ca.* 0.2 eV weaker than of the Pt_{201} NP, in line with the propensity of more negatively charged Pt atoms in particles to bind CO adsorbate weaker.[52,53] Weakening the adsorption by merely 0.2 eV was shown to be enough for reducing CO poisoning of metal catalysts so much that their CO oxidation activity increased dramatically.[54] The reactivity of surface Cu atoms positively charged by 0.2–0.3 $|e|$ should also be singular compared with the reactivity of metallic Cu atoms, with a decreased propensity to form bonds with electrophilic species such as O. Notably, large negative charges on Pt atoms and positive charges on Cu atoms acquired upon alloying increase the size mismatch between larger Pt atoms and smaller Cu atoms. As a consequence, atoms become more displaced from their regular lattice positions in Pt–Cu NPs further affecting the reactivity of their surface sites.

3.4. Miscibility of Pt atoms with Au, Ag, and Cu atoms at the nanoscale

As already mentioned, Pt atoms in bulk alloys are immiscible at common conditions with Au and Ag atoms, but they mix with Cu atoms. These miscibility relations in the bulk are properly reflected in the terms $\varepsilon_{BOND}^{Pt\text{-}X}$ of the studied Pt–X NPs, see Table 1, manifesting relative energies of heterometallic bonds Pt–X. The energies $\varepsilon_{BOND}^{Pt\text{-}X}$ are positive for Pt–Au and Pt–Ag NPs (unfavorable formation of the heterometallic bonds) and negative for Pt–Cu NPs (favorable formation of the Pt–Cu bonds). At the nanoscale, the bulk immiscibility of bimetallic alloys can be counterbalanced by significant propensity of one metal component to segregate on the surface. That is why the equilibrium chemical orderings of Pt–Au and Pt–Ag NPs do not feature separate, as compact as possible domains of the two metals, *e.g.* Janus-type ones,[1,16] but feature core–shell arrangements with full or partially incomplete Au and Ag skins, see Fig. 1 and 2.

The miscibility of metals M and M′ in a bimetallic $M_mM'_n$ NP can be also evaluated by its excess energy *vs* the energies of the corresponding monometallic M_{n+m} and M'_{n+m} particles of the same size and structure.[7,55] The excess energy (also known as mixing energy) per atom for a Pt_mX_n particle is calculated as:

$$E_{exc}(Pt_mX_n) = \{E(Pt_mX_n) - [m/(m+n)]E(Pt_{m+n}) - [n/(m+n)]E(X_{m+n})\}/(m+n), \quad (2)$$

where a negative sign of E_{exc} indicates favorable mixing of Pt and X atoms in the particle.

The DFT excess energies of 201-atom Pt–X NPs are plotted in Fig. 3. The energies for Pt–Au and Pt–Ag NPs with Pt and X atoms that are immiscible in the bulk are spread depending on the concentrations of atoms X from −38 to −65 meV and from −58 to −90 meV, respectively. The corresponding energies for Pt–Cu NPs ranging from −127 to −163 meV are notably more negative, as expected for the miscible Pt and Cu atoms. For all these 201-atomic Pt–X NPs the miscibility in terms of the excess energies reaches maximum close to the 1 : 1 compositions. This mixing indicator remains nearly the same for the 1 : 1 140-atomic NPs, see Fig. 3: −54, −80, and −165 meV for $Pt_{70}Au_{70}$, $Pt_{70}Ag_{70}$, and $Pt_{70}Cu_{70}$, respectively.

3.5. Comparison of Pt–X and Pd–X nanoparticles (X = Au, Ag, Cu)

To better understand differences and similarities in the catalytic behavior of Pt- and Pd-based nanomaterials we compare the chemical ordering and related properties of the $Pt_{70}X_{70}$ NPs with the previously calculated data for the $Pd_{70}X_{70}$ NPs.[14]

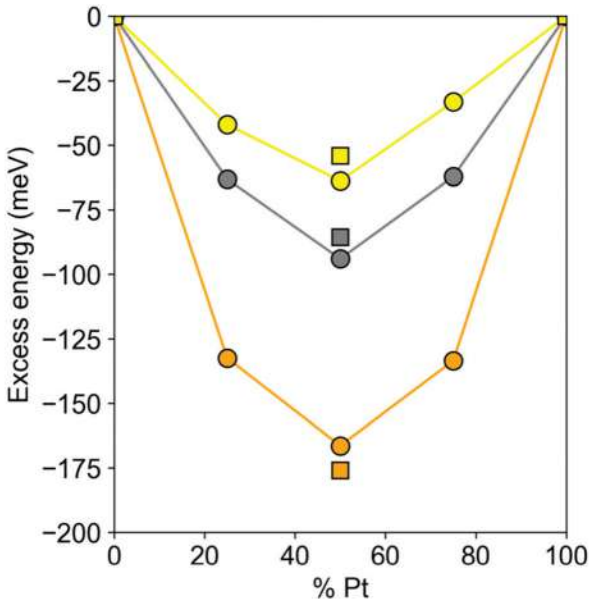

Fig. 3 DFT excess energies E_{exc} per atom (see eqn (2)) circles – of $Pt_{201-n}X_n$ (X = Au, Ag, Cu; n = 50, 100, 150) nanoparticles and squares – of $Pt_{70}X_{70}$ nanoparticles. Pt–Au – yellow, Pt–Ag – gray, Pt–Cu – orange.

The main qualitative difference of changing Pt to Pd in the nanoalloys with Au and Ag, see Table 1, is that, at variance with Pt, Pd becomes slightly miscible with these coinage metals, by −13 and −1 meV per Pd–X bond, respectively. On the other hand, the notable preference of Au and Ag atoms to occupy surface positions remains present in the Pd-based NPs, although the corresponding energies ε for them are significantly smaller than for the analogous Pt-based NPs. The stabilizing effect of the location of Au and Ag atoms in surface positions decreases in both Pt- and Pd-based NPs with increasing coordination number of the surface position. The most favorable are 6-coordinated corner sites, then 7-coordinated edge sites, and finally 9-coordinated sites in the {111} facets. Similarities of the energies ε for the corresponding $Pt_{70}X_{70}$ and $Pd_{70}X_{70}$ (X = Ag, Au) NPs result in similar orderings of their lowest-energy homotops. In all four NPs X atoms occupy all 48 corner plus edge sites, while the remaining 22 X atoms are located in the {111} facet sites. Pt and Pd atoms occupy the remaining 26 surface sites of the facets and all 44 positions in the interior of the NPs. The main difference in the orderings comes from the number of heterometallic bonds. The equilibrium $Pt_{70}X_{70}$ structures feature 196 Pt–X bonds, 31% of overall 636 bonds in the 140-atomic NP, to be compared with significantly larger number of heterometallic bonds in the $Pd_{70}X_{70}$ structures, 234–262 (37–41%). A consequence of the different numbers of the heterometallic bonds is that most of the {111} facets in the $Pt_{70}X_{70}$ structures are formed by either only X or only Pt atoms, whereas the individual facets in the $Pd_{70}X_{70}$ structures contain a mixture of X and Pd atoms, increasing the number of Pd–X bonds.

Miscibility of the coinage and platinum-group metal atoms is favorable in both $Pt_{70}Cu_{70}$ and $Pd_{70}Cu_{70}$ NPs, see Table 1. Each heterometallic bond stabilizes the former particle by 9 meV more than the latter. The occupation of surface positions by Cu destabilizes these two NPs, with one exception. Namely, the occupation of corner position of $Pt_{70}Cu_{70}$ NP by atom Cu instead of atom Pt has a slight stabilizing effect, by −27 meV. The destabilization due to the presence of surface Cu atoms increases with increasing their coordination numbers, though the destabilization values (energy differences between the most stable and the least stable surface positions) are quite different, 371 meV for $Pt_{70}Cu_{70}$ and 88 meV for $Pd_{70}Cu_{70}$. It is least favorable for Cu atoms to occupy terrace sites of $Pt_{70}Cu_{70}$ and $Pd_{70}Cu_{70}$ NPs. Cu atoms are differently distributed on the surface of $Pt_{70}Cu_{70}$ and $Pd_{70}Cu_{70}$ homotops with the lowest E^{TOP} energy. In the $Pt_{70}Cu_{70}$ NP, 36 surface Cu atoms occupy all 24 corner positions and a half of 24 edge positions, leaving all 48 terrace positions to be occupied by Pt atoms, see Table 2. 32 surface Cu atoms of the $Pd_{70}Cu_{70}$ NP are quite evenly spread over three types of sites: corner – 12, edge – 14, and terrace – 8[14] as a result of relatively small energy difference of Cu in these sites. To maximize the number of stabilizing heterometallic bonds the equilibrium $Pt_{70}Cu_{70}$ and $Pd_{70}Cu_{70}$ structures are of quite common onion-like type,[1,2,56,57] with Pt/Pd-rich core, Cu-rich subsurface shell and monatomic skin shared by Pt/Pd and Cu atoms. These chemical orderings allow formation of 340 Pt–Cu and 382 Pd–Cu bonds.

The present topological approach has been recently employed to analyze in detail the formation of single-atom Pd sites in Pd–Au NPs appealing for catalysis as a function of Pd concentration inside the particles.[17] It was shown that no surface Pd atoms emerge at low Pd concentrations in the Au skin at equilibrium chemical orderings. Single-atom surface Pd sites become stable in 201-atom Pd–Au particles when Pd content inside the skin reaches *ca.* 60% (corresponding to 153 Au and 48 Pd atoms) and further increase of Pd content results in more surface Pd, first mostly as single atoms. Such emergence of surface Pd atoms is triggered by stabilizing Pd–Au bonds reflected in negative $\varepsilon_{BOND}^{Pd\text{-}Au}$ energies for Pd–Au NPs.[13–15,17] According to $\varepsilon_{BOND}^{Pt\text{-}X}$ (Table 1), heterometallic bonds of Pt are stabilizing neither in Pt–Au, nor in Pt–Ag NPs. Thus, the location of Pt atoms is not favored on the surface of Pt–Au and Pt–Ag NPs at the equilibrium orderings, unless the number of Au and Ag atoms in these particles is smaller than the 122 required to form complete coinage-metal skins. However, single-atom Pt sites can be easily created on the surface of Pt–Au and Pt–Ag NPs in the course of catalytic reactions already at low Pt concentration due to energetically preferable interactions of Pt centers with reactants and intermediates compared to Au and Ag centers. This adsorbate-induced surface segregation phenomenon is well known for nanoalloy catalysts.[13,16,21,23,25,26,51] In the cases of Pd–Cu and Pt–Cu NPs Pd and Pt atoms show a strong preference to be located in the surface skin and to form stabilizing heterometallic bonds, see Tables 1 and 2. Thus, the presence of Pd and Pt on the surface of these nanoalloys as unique single-atom catalytic sites is conceivable only at very low concentration of the platinum-group metals.

3.6. Performance of the topological method to describe chemical orderings

The present TOP method[14,15] focuses on patterns of the equilibrium chemical orderings of bimetallic NPs, which determine the surface reactivity. The method employs a very simple topological equation (*i.e.* in the form of eqn (1)) to pre-screen a huge number of the chemical orderings (homotops) of a NP to find several best candidates in terms of their lowest E^{TOP} energies for subsequent electronic-structure (DFT) calculations with locally relaxed positions of atoms. Among the method simplifications are: (i) accounting only for interactions between nearest-neighbor pairs of atoms and assuming all bond of the same type (*e.g.* all Pt–Pt bonds) to be equal; (ii) describing positions of atoms in the NP lattice solely by the coordination numbers, distinguishing between surface atoms with different coordination numbers but treating all atoms of each metal type inside the NP as equivalent; (iii) grouping homotops in so-called topologies of the same $N_{BOND}^{Pt-X} \cdot N_{CORNER}^{X} \cdot N_{EDGE}^{X} \cdot N_{FACET}^{X}$ numbers in eqn (1), and assuming that an arbitrarily chosen homotop of a given topology represents reasonably well the DFT energy and the chemical ordering of all other numerous homotops of the same topology.

To evaluate the correctness of some of these assumptions we randomly generated $\geq$10 different homotops for several selected topologies of Pt–Au and Pt–Cu NPs and locally optimized those by DFT; see results in Table S1 (ESI†). The DFT energy splits for the homotops belonging to each of the considered low-energy topologies of 201-atomic Pt–Au NPs are very small, up to *ca.* 1 meV per atom. The splits slightly increase with growing content of Au atoms (preferably located on the surface), ranging from only 25 meV for the topology $Pt_{151}Au_{50}$_214.20.30.0 to 286 meV for the topology $Pt_{51}Au_{150}$_210.24.36.62. DFT energy splits for low-lying topologies of Pt–Cu NPs noticeably increased compared to the corresponding Pt–Au NPs. Noteworthy, the Pt–Cu energy splits also increase with growing content of Pt on the surface, from 153 meV for the topology $Pt_{51}Cu_{150}$_418.24.36.18 to 930 meV for the topology $Pt_{151}Cu_{50}$_412.0.0.0, the latter with solely Pt atoms on the surface. We note that the prediction error of E^{TOP} *vs.* E^{DFT} energies for such low-energy orderings range from 1.1 to 6.8 meV per atom (see Table S1, ESI†), although the errors for high-energy structures are significantly larger. For many practical applications, the up to *ca.* 7 meV per atom uncertainty in total energy of the $Pt_{151}Cu_{50}$_412.0.0.0 homotops provided by the present computational setup may be sufficient. If not, DFT calculations can be performed, as just discussed, for additional homotops of the putative lowest-energy topologies, to more precisely approach equilibrium DFT chemical orderings.

A similar procedure could be applied to go beyond the topology approach, when a more precise energetic representation of chemical orderings is required for assessing notably higher-lying homotops. One can see from Table S1 (ESI†) a substantial energy split in one of the higher-lying topologies of 201-atomic NPs, namely by 1501 meV in $Pt_{101}Au_{100}$_594.24.0.54, but this seems to be not very often the case.

Interestingly, the energy splitting for 10 random homotops with putative lowest-energy topologies $Pt_{70}Au_{70}$_196.24.24.22 and $Pt_{70}Cu_{70}$_340.24.12.0, 1027 and 1568 meV, respectively, see structures of the homotops with minimum and maximum DFT energies of these topologies in Fig. S1 (ESI†), are notably larger than those for the 201-atom Pt–Au and Pt–Cu NPs. Again, the Pt–Cu homotops split more than the Pt–Au homotops. Our detailed analysis of this splitting reveals that not all atoms of one type (Pt–Pt, Pt–X, or X–X bonds) are equivalent, *i.e.* that the energy of bonds formed by Pt or X atoms to each of their first neighbours is partially dependent on the identity (and quantity) of the rest of first neighbours. This challenges the convenient assumption that all bonds between a given pair of atoms are equally strong. In addition, certain structural motifs (such as {111} facets solely composed of Au) seem to become stable for some compositions due to elusive long-range interactions neglected by the employed topological description.

Although the δ values in Table 1 may seem large, they correspond to average prediction errors 1 to 6 meV per atom. The large size of the studied particles obviously increases the errors in total energies, but changes in energy caused by permuting atoms are, on average, rather well approximated. This means that irrespective of possible inaccuracies of the present TOP approach based on the DFT structure optimization, the equilibrium chemical orderings in bimetallic nanoalloys provided by this approach approximate reasonably well those obtained with the employed DFT exchange–correlation functional. The calculated atomic-level data, which are notably more detailed than those currently accessible experimentally, are very useful for rationalizing surface reactivity of bimetallic catalysts and related applications.

3.7. Larger Pt-based nanoparticles and temperature effects on the chemical ordering

Chemical orderings with the lowest-energy topology were also determined for *ca.* 4.4 nm large fcc truncated octahedral $Pt_{732}X_{731}$ NPs using the energies ε obtained for 140-atomic $Pt_{70}X_{70}$ and for 201-atomic $Pt_{101}X_{100}$ NPs, see Table 1. Orderings of these homotops at 0 K, denoted as $Pt_{732}X_{731}^{(140)}$ and $Pt_{732}X_{731}^{(201)}$, respectively, are shown in Fig. 4 and occupations of various atomic positions in them are quantified in Table 4. As the 1463-atomic particles are too large for DFT calculations, results for them were obtained only using the Monte Carlo simulation part of the Topological description approach,[14,15] *vide supra*.

Usage of both the (140) and (201) sets of energies ε results in the same topologies of the lowest-energy orderings of $Pt_{732}Au_{731}$ and $Pt_{732}Ag_{731}$ NPs. These are core–shell orderings with Au and Ag atoms occupying all surface and a part of subsurface positions, while Pt atoms form compact cores inside the monolayer skins of coinage metals. Since Au and Ag atoms tend to surface segregate and Pt–Au and Pt–Ag bonds are destabilizing with respect to forming homometallic bonds, by 11–21 meV each, these 1238 bonds comprise only 16% of all 7776 bonds in the 1463-atom NPs, see Table 4.

The equilibrium ordering in $Pt_{732}Cu_{731}$ NP is more complex, reflecting that Pt–Cu bonds are stabilizing with respect to the corresponding homometallic bonds, and that smaller Cu atoms

alloyed with Pt are less disfavored when located inside the particles compared to Au and Ag atoms. In $Pt_{732}Cu_{731}^{(140)}$ all 24 corner positions are occupied by Cu atoms, each of them stabilizing the system by −27 meV with respect to having Pt in the same positions. Occupation of almost a half of edge positions by Cu atoms alternating with Pt atoms to increase the number of favorable Pt–Cu bonds partially counterbalanced the preference, by 181 meV, of each edge Pt atom compared to having an edge Cu atom. A layered arrangement of inner Pt and Cu atoms seems to be also result from an increased number of favorable Pt–Cu bonds. No Cu atoms occupy terrace sites in line with the largest destabilization by 344 meV per terrace Cu atom with respect to having a Pt atom in those positions. Interestingly, the number of surface Cu atoms in the $Pt_{732}Cu_{731}^{(201)}$ NP, 167, is more than twice larger than in the $Pt_{732}Cu_{731}^{(140)}$ NP, 72. This finding seems counterintuitive based on the energies ε, which indicate stronger destabilization of surface Cu atoms in $Pt_{101}Cu_{100}$ NP than in $Pt_{70}Cu_{70}$ NP. It can be explained by the fact that Cu atoms in the $Pt_{732}Cu_{731}^{(201)}$ NP are scattered and mostly surrounded by Pt atoms forming more favorable Pt–Cu contacts. Indeed, there are more Pt–Cu bonds in the structure $Pt_{732}Cu_{731}^{(201)}$, 4543 (58%), than in $Pt_{732}Cu_{731}^{(140)}$, 3868 (50%), since the $\varepsilon_{BOND}^{Pt\text{-}Cu}$ values for the 201- and 140-atomic NPs are −43 and −35 meV, respectively. The energy gain due to an increased number of Pt–Cu contacts in $Pt_{732}Cu_{731}^{(201)}$ NP, −29.025 eV according to the energies ε, see Table 1, overcompensates the energy penalty caused by the presence of more surface Cu atoms, 26.429 eV. Thus, the equilibrium ordering $Pt_{732}Cu_{731}^{(201)}$ is estimated to be *ca.* 2.6 eV more stable than $Pt_{732}Cu_{731}^{(140)}$ one, which for such large particles translates in a difference of 1.8 meV per atom. Note that many adsorbates from the reacting media interact with Pt surface sites at least

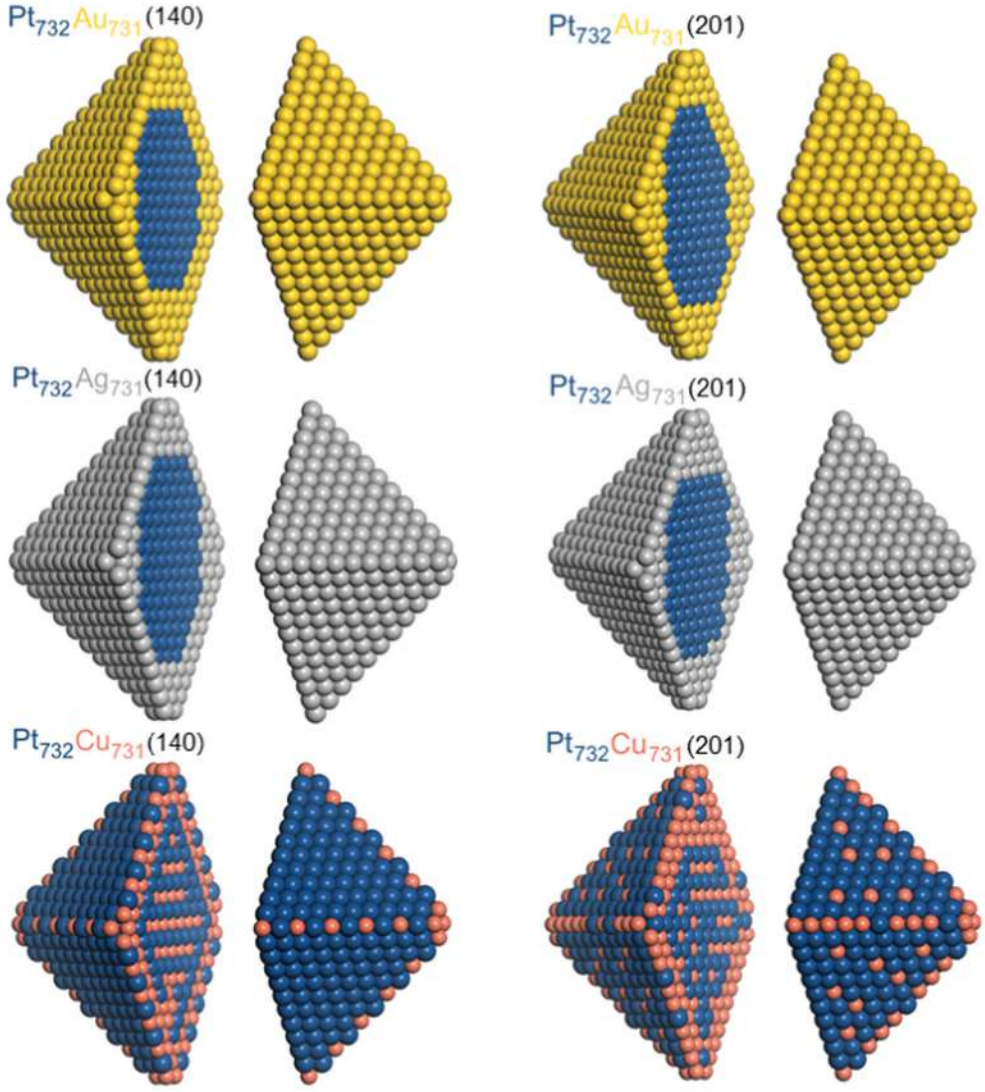

Fig. 4 Equilibrium chemical orderings of *ca.* 4.4 nm large truncated-octahedral fcc $Pt_{732}Au_{731}$, $Pt_{732}Ag_{731}$, and $Pt_{732}Cu_{731}$ nanoparticles at 0 K with the lowest TOP energies calculated using eqn (1) for $Pt_{70}X_{70}$ particles ($Pt_{732}X_{731}^{(140)}$, left column) and $Pt_{101}X_{100}$ (particles $Pt_{732}X_{731}^{(201)}$, right column). Colors of atoms are as in Fig. 1.

Table 4 Chemical ordering in the representative lowest-energy $Pt_{732}X_{731}^{(140)}$ and $Pt_{732}X_{731}^{(201)}$ homotops at different temperature calculated using the TOP equations (see Table 1) for the $Pt_{70}X_{70}$ and $Pt_{101}X_{100}$ NPs, respectively. In parentheses are the fractions (in %) of the total numbers of the metal–metal bonds or atoms X in various lattice positions of $Pt_{732}X_{731}$ NPs

Nanoparticle	T, K	$N_{BOND}^{Pt\text{-}X}$	N_{CORNER}^{X}	N_{EDGE}^{X}	N_{FACET}^{X}	N_{INSIDE}^{X}
$Pt_{732}Au_{731}^{(140)}$	0	1238 (16)	24 (100)	108 (100)	440 (100)	159 (18)
$Pt_{732}Au_{731}^{(201)}$	0	1238 (16)	24 (100)	108 (100)	440 (100)	159 (18)
	300	1309 (17)	24 (100)	108 (100)	439 (100)	160 (18)
	600	1502 (19)	24 (100)	107 (99)	439 (100)	161 (18)
	1000	1885 (24)	23 (96)	108 (100)	433 (98)	167 (19)
$Pt_{732}Ag_{731}^{(140)}$	0	1238 (16)	24 (100)	108 (100)	440 (100)	159 (18)
$Pt_{732}Ag_{731}^{(201)}$	0	1238 (16)	24 (100)	108 (100)	440 (100)	159 (18)
	300	1354 (17)	24 (100)	108 (100)	440 (100)	159 (18)
	600	1671 (21)	24 (100)	107 (99)	440 (100)	160 (18)
	1000	2129 (27)	24 (100)	108 (100)	429 (98)	170 (19)
$Pt_{732}Cu_{731}^{(140)}$	0	3868 (50)	24 (100)	48 (44)	0 (0)	659 (74)
$Pt_{732}Cu_{731}^{(201)}$	0	4543 (58)	24 (100)	86 (80)	57 (13)	564 (63)
	300	4343 (56)	23 (96)	63 (58)	58 (13)	587 (66)
	600	4244 (55)	21 (88)	61 (56)	73 (17)	576 (65)
	1000	4183 (54)	19 (79)	55 (51)	98 (22)	559 (63)

The total topological numbers for the $Pt_{732}X_{731}$ particles are: N_{BOND} = 7776, N_{CORNER} = 24, N_{EDGE} = 108, N_{FACET} = 440, N_{INSIDE} = 891.

1 eV stronger than with the corresponding Cu sites. Therefore, similar changes of the ordering patterns as those simulated for the structures $Pt_{732}Cu_{731}^{(201)}$ and $Pt_{732}Cu_{731}^{(140)}$, see Fig. 4, can be easily caused at experimental conditions in Pt–Cu NPs by adsorbing even a few reacting species from the environment.

The calculated results presented so far have corresponded to equilibrium structurers at temperature 0 K. Since the TOP method allows to approximately account for entropy effects associated with the chemical orderings (neglecting vibrational contributions), we employed a computational setup introduced elsewhere[15] for estimating properties associated with Boltzmann population of different homotops. Specifically, we calculated the average topology in the $Pt_{732}X_{731}$ (X = Au, Ag, Cu) NPs in the temperature range 0–1000 K by means of the Metropolis Monte Carlo algorithm. In particular, the averaging was done over accepted configurations obtained during an MC run at a given temperature, which results in the probability of occupying of each site by either Pt or X atoms. The homotop with the most similar topology to the calculated average is then chosen as the representative model for each run. As expected, temperature increase noticeably increased the disorder in all modeled particles, see Table 4 and Fig. 5 for the results corresponding to 300, 600, and 1000 K.

For instance, several Pt atoms appeared at 600 and 1000 K on the surface of $Pt_{732}Au_{731}$ and $Pt_{732}Ag_{731}$ NPs that exhibited complete surface shells of Au and Ag atoms at 0 and 300 K. Concomitantly, single Au and Ag atoms migrated in the compact Pt cores. Also, the number of both Pt–Au and Pt–Ag bonds

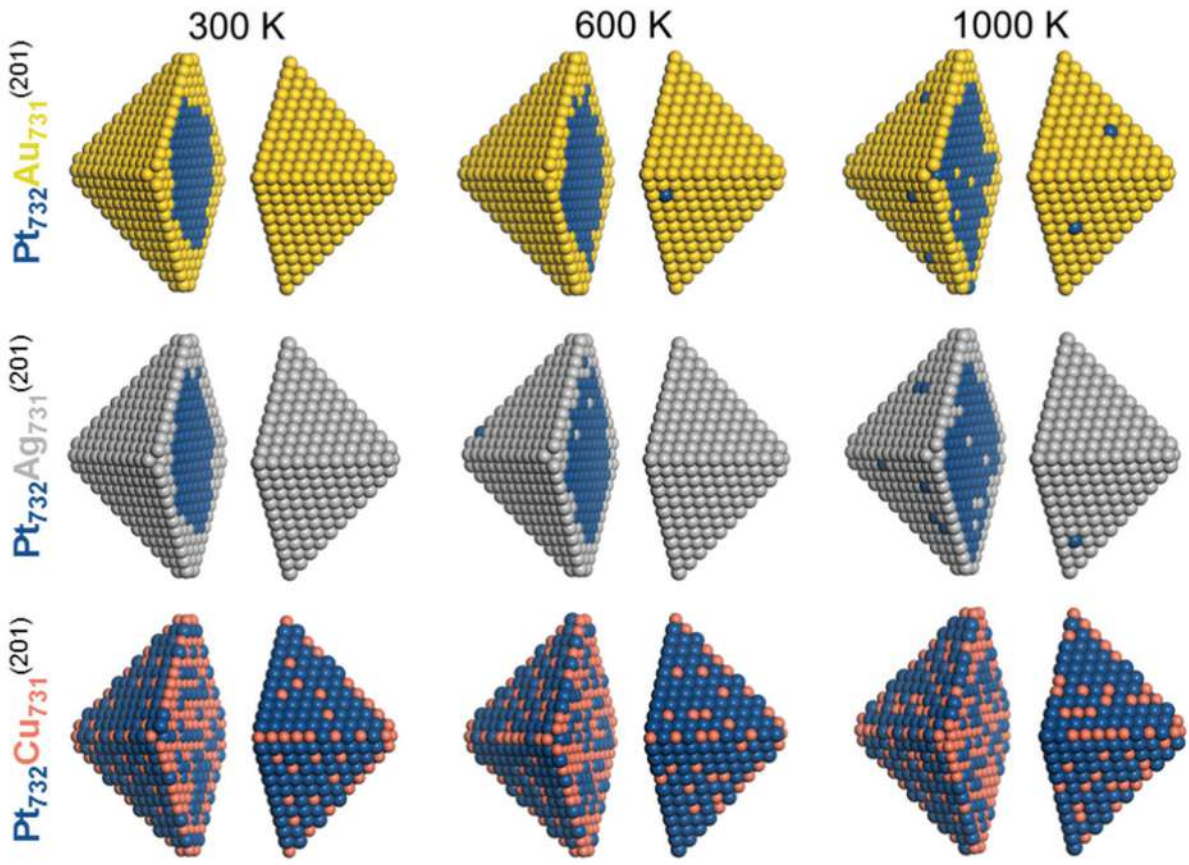

Fig. 5 Equilibrium chemical orderings of $Pt_{732}Au_{731}$, $Pt_{732}Ag_{731}$, and $Pt_{732}Cu_{731}$ nanoparticles at temperatures 300 K, 600 K and 1000 K calculated using eqn (1) for the corresponding $Pt_{101}Au_{100}$, $Pt_{101}Ag_{100}$, and $Pt_{101}Cu_{100}$ particles. Colors of atoms are as in Fig. 1.

increased with the temperature increase. The fraction of Pt–Au bonds in $Pt_{732}Au_{731}$ NP increased from 16% (0 K) to 17% (300 K), 19% (600 K), and 24% (1000 K). The corresponding number of bonds in $Pt_{732}Ag_{731}$ NP increases somewhat more steep at elevated temperature, in line with less destabilizing character of Pt–Ag bonds compared with Pt–Au bonds.

In $Pt_{732}Cu_{731}$ NP the number of stabilizing Pt–Cu bonds slightly decreased at higher temperatures, from 58% at 0 K to 54% at 1000 K. Cu atoms migrate upon the temperature increase from corner and edge positions most populated at 0 K primarily to surface terrace positions.

4. Summary and conclusions

We determined equilibrium chemical orderings in truncated-octahedral Pt–Au, Pt–Ag, and Pt–Cu nanoparticles containing 140 and 201 atoms at metals concentrations 3 : 1, 1 : 1, and 1 : 3 by means of DFT calculations combined with the Topological approach.[14,15]

The equilibrium chemical orderings in the Pt–Au and Pt–Ag particles with $\leq$201 atoms closely resemble each other: Au and Ag atoms are strongly energetically driven to be on the surface, whereas Pt atoms preferentially occupy inner positions. The immiscibility of Au and Ag atoms with Pt atoms prevents the appearance of Pt atoms on the surface of these nanoalloys as single-atom catalytic sites until the coinage metal content becomes low. Atoms in Pt–Au nanoparticles are essentially neutral, whereas in Pt–Ag nanoparticles Pt and Ag atoms are moderately charged negatively and positively, respectively. This suggests noticeably different reactivity of surface Pt sites on Pt–Ag than on single-metal Pt particles.

In Pt–Cu nanoparticles, Pt atoms are driven to the surface and most stabilized in the 9- and 8-coordinated positions of the {111} and {100} nanofacets. Pt–Cu bonds formed upon the favorable mixing of Pt and Cu atoms induce a strong Cu to Pt charge transfer. The up to half of an electron transferred to surface Pt atoms from nearby Cu atoms is expected to substantially affect the surface reactivity of both Pt and Cu sites.

Ordering trends in Pt–X nanoalloys are quite similar to the trends in previously characterized Pd–X nanoalloys, *i.e.* with the coinage metal atoms at the surface for X = Au or Ag, and rather well mixed orderings for X = Cu. The main difference is that heterometallic bonds slightly destabilize (with respect to homometallic bonds) Pt–Ag and Pt–Au particles, but stabilize Pd–Ag and Pd–Au ones, leading to more mixed terraces in the later two.

The most stable orderings in *ca.* 4.4 nm $Pt_{732}Au_{731}$ and $Pt_{732}Ag_{731}$ particles are of the Pt–core/Au(Ag)–shell type. The lowest-energy chemical ordering pattern of $Pt_{732}Cu_{731}$ particle is characterized by surface Cu atoms scattered over Pt atoms in the facets and quite randomly distributed inner atoms of both metals. Modelling the evolution of the orderings upon temperature increase revealed that heating leads to the appearance of single-atom or diatomic surface Pt sites on facets of $Pt_{732}Au_{731}$ and $Pt_{732}Ag_{731}$ particles and increases the disorder and number of surface Cu atoms on facets of $Pt_{732}Cu_{731}$ particle. New surface sites with correspondingly different chemical properties are formed upon heating.

The results presented in this work are relevant for studies in which structure and surface properties of a large number of bimetallic compositions are simulated using machine-learning and/or high-throughput approaches. Such studies often relied on models produced by directly cutting bulk structures,[58,59] without considering that due to the stability of particular chemical orderings inherently different sites can be exposed on the surface.

Author contributions

L. Vega: calculations, conceptualization, data curation, formal analysis, investigation, methodology, validation, visualization, writing – original draft, review & editing; H. A. Aleksandrov: calculations, conceptualization, investigation, methodology, writing – original draft, review & editing; F. Viñes: investigation, supervision, validation, writing – review & editing; R. Farris: calculations, validation; A. Bruix: investigation, methodology, validation, writing – review & editing; K. M. Neyman: conceptualization, methodology, project administration, supervision, validation, writing – original draft, review & editing.

Conflicts of interest

There are no conflicts to declare.

Acknowledgements

Authors acknowledge support by the grants PGC2018-093863-B-C22, RTI2018-095460-B-I00, and MDM-2017-0767 of the Spanish Ministerio de Ciencia y Universitades as well as by the grant 2017SGR13 of the Generalitat de Catalunya. HAA is grateful to the Operational Program "Science and Education for Smart Growth" under contract UNITe No. BG05M2OP001-1.001-0004-C01 (2018–2023). The Generalitat de Catalunya financed the work of LV (*via* pre-doctoral grant 2018FI-B-00384) and AB (*via* grant 2018BP00190). Research contribution of RF has been supported by a visiting grant HPC17YE51L of the HPC-Europa3 program. The study was also supported by Bulgarian Ministry of Education and Science *via* the contract D01-76/2021 and by European COST Action CA18234. Computer resources have been partly provided by the Red Española de Supercomputación (projects QS-2020-2-0020, QS-2019-3-0023, QSM-2018-1-0029).

References

1 R. Ferrando, J. Jellinek and R. L. Johnston, Nanoalloys: From Theory to Applications of Alloy Clusters and Nanoparticles, *Chem. Rev.*, 2008, **108**, 845–910.
2 F. Calvo, *Nanoalloys from Fundamentals to Emergent Applications*, Elsevier, Amsterdam, 2013.

3 I. V. Yudanov, R. Sahnoun, K. M. Neyman and N. Rösch, Carbon Monoxide Adsorption on Palladium Nanoparticles: A Relativistic Density Functional Study, *J. Chem. Phys.*, 2002, **117**, 9887–9896.

4 I. V. Yudanov, R. Sahnoun, K. M. Neyman, N. Rösch, J. Hoffmann, S. Schauermann, V. Johánek, H. Unterhalt, G. Rupprechter, J. Libuda and H.-J. Freund, CO Adsorption on Pd Nanoparticles: Density Functional and Vibrational Spectroscopy Studies, *J. Phys. Chem. B*, 2003, **107**, 255–264.

5 A. Roldán, F. Viñes, F. Illas, J. M. Ricart and K. M. Neyman, Density Functional Studies of Coinage Metal Nanoparticles: Scalability of Their Properties to Bulk, *Theor. Chem. Acc.*, 2008, **120**, 565–573.

6 K. M. Neyman, R. Sahnoun, C. Inntam, S. Hengrasmee and N. Rösch, Computational Study of Model Pd–Zn Nanoclusters and Their Adsorption Complexes with CO Molecules, *J. Phys. Chem. B*, 2004, **108**, 5424–5430.

7 I. V. Yudanov and K. M. Neyman, Stabilization of Au at Edges of Bimetallic PdAu Nanocrystallites, *Phys. Chem. Chem. Phys.*, 2010, **12**, 5094–5100.

8 J. Ryosuke, K. K. T. Suzuki and Y. Morimoto, DFT Calculations on Electro-Oxidations And Dissolutions of Pt and Pt–Au Nanoparticles, *Catal. Today*, 2016, **262**, 100–109.

9 L. Piccolo, Z. Y. Li, I. Demiroglu, F. Moyon, Z. Konuspayeva, G. Berhault, P. Afanasiev, W. Lefebvre, J. Yuan and R. L. Johnston, Understanding And Controlling The Structure And Segregation Behaviour of AuRh Nanocatalysts, *Sci. Rep.*, 2016, **6**, 35226.

10 M. Hu, D. P. Linder, M. B. Nardelli and A. Striolo, Hydrogen Adsorption on Platinum–Gold Bimetallic Nanoparticles: A Density Functional Theory Study, *J. Phys. Chem. C*, 2013, **117**, 15050–15060.

11 X. Lei, H. Mu, S. Li, G. Liu, B. Xu and C. Ouyang, The Structural and Electronic Properties of Pt–Cu Alloy Clusters: Embedding Atom Method Combined with Density Functional Theory Study, *J. Alloys Compd.*, 2018, **741**, 604–609.

12 L.-L. Wang and D. D. Johnson, Predicted Trends of Core-Shell Preferences for 132 Late Transition-Metal Binary-Alloy Nanoparticles, *J. Am. Chem. Soc.*, 2009, **131**, 14023–14029.

13 M. Mamatkulov, I. V. Yudanov, A. V. Bukhtiyarov, I. P. Prosvirin, V. I. Bukhtiyarov and K. M. Neyman, Pd Segregation on the Surface of Bimetallic PdAu Nanoparticles Induced by Low Coverage of Adsorbed CO, *J. Phys. Chem. C*, 2019, **123**, 8037–8046.

14 S. M. Kozlov, G. Kovács, R. Ferrando and K. M. Neyman, How to Determine Accurate Chemical Ordering in Several Nanometer Large Bimetallic Crystallites from Electronic Structure Calculations, *Chem. Sci.*, 2015, **6**, 3868–3880.

15 G. Kovács, S. M. Kozlov and K. M. Neyman, Versatile Optimization of Chemical Ordering in Bimetallic Nanoparticles, *J. Phys. Chem. C*, 2017, **121**, 10803–10808.

16 L. Vega, H. A. Aleksandrov and K. M. Neyman, Using Density Functional Calculations to Elucidate Atomic Ordering of Pd-Rh Nanoparticles at Sizes Relevant for Catalytic Applications, *Chin. J. Catal.*, 2019, **40**, 1749–1757.

17 M. Mamatkulov, I. V. Yudanov, A. V. Bukhtiyarov and K. M. Neyman, Pd Single-atom Sites on the Surface of PdAu Nanoparticles: A DFT-based Topological Search for Suitable Compositions, *Nanomaterials*, 2021, **11**, 122.

18 S. Olobardi, L. Vega, A. Fortunelli, M. Stener, F. Viñes and K. M. Neyman, Optical Properties and Chemical Ordering of Ag–Pt Nanoalloys: A Computational Study, *J. Phys. Chem. C*, 2019, **123**, 25482–25491.

19 G. Kovács, S. M. Kozlov, I. Matolínová, M. Vorokhta, V. Matolín and K. M. Neyman, Revealing Chemical Ordering in Pt–Co Nanoparticles Using Electronic Structure Calculations and X-ray Photoelectron Spectroscopy, *Phys. Chem. Chem. Phys.*, 2015, **17**, 28298–28310.

20 M. Vorokhta, I. Khalakhan, M. Václavů, G. Kovács, S. M. Kozlov, P. Kúš, T. Skála, N. Tsud, J. Lavková, V. Potin, I. Matolínová, K. M. Neyman and V. Matolín, Surface Composition of Magnetron Sputtered Pt–Co Thin Film Catalyst for Proton Exchange Membrane Fuel Cells, *Appl. Surf. Sci.*, 2016, **365**, 245–251.

21 I. Khalakhan, L. Vega, M. Vorokhta, T. Skála, F. Viñes, Y. V. Yakovlev, K. M. Neyman and I. Matolínová, Irreversible Structural Dynamics on the Surface of Bimetallic PtNi Alloy Catalyst under Alternating Oxidizing And Reducing Environments, *Appl. Catal., B*, 2020, **264**, 118476.

22 A. Neitzel, G. Kovács, Y. Lykhach, S. M. Kozlov, N. Tsud, T. Skála, M. Vorokhta, V. Matolín, K. M. Neyman and J. Libuda, Atomic Ordering and Sn Segregation in Pt–Sn Nanoalloys Supported on CeO_2 Thin Films, *Top. Catal.*, 2017, **60**, 522–532.

23 A. Wolfbeisser, G. Kovács, S. M. Kozlov, K. Föttinger, J. Bernardi, B. Klötzer, K. M. Neyman and G. Rupprechter, Surface Composition Changes of CuNi-ZrO_2 During Methane Decomposition: An Operando NAP-XPS and Density Functional Study, *Catal. Today*, 2017, **283**, 134–143.

24 L. Liu and A. Corma, Metal Catalysts for Heterogeneous Catalysis: From Single Atoms to Nanoclusters and Nanoparticles, *Chem. Rev.*, 2018, **118**, 4981–5079.

25 L. Li, X. Chang, X. Lin, Z.-J. Zhao and J. Gong, Theoretical Insights into Single-Atom Catalysts, *Chem. Soc. Rev.*, 2020, **49**, 8156–8178.

26 R. T. Hannagan, G. Giannakakis, M. Flytzani-Stephanopoulos and E. C. H. Sykes, Single-Atom Alloy Catalysis, *Chem. Rev.*, 2020, **120**, 12044–12088.

27 G. Kresse and J. Furthmüller, Efficient Iterative Schemes for *Ab Initio* Total-Energy Calculations Using a Plane-Wave Basis Set, *Phys. Rev. B: Condens. Matter Mater. Phys.*, 1996, **54**, 11169–11186.

28 G. Kresse and J. Hafner, *Ab Initio* Molecular-Dynamics Simulation of the Liquid-Metal–Amorphous-Semiconductor Transition in Germanium, *Phys. Rev. B: Condens. Matter Mater. Phys.*, 1994, **49**, 14251–14269.

29 J. P. Perdew, K. Burke and M. Ernzerhof, Generalized Gradient Approximation Made Simple, *Phys. Rev. Lett.*, 1996, **77**, 3865–3868; J. P. Perdew, K. Burke and M. Ernzerhof, *Phys. Rev. Lett.*, 1997, **78**, 1396.

30 P. Janthon, S. M. Kozlov, F. Viñes, J. Limtrakul and F. Illas, Establishing the Accuracy of Broadly Used Density

Functionals in Describing Bulk Properties of Transition Metals, *J. Chem. Theory Comput.*, 2013, **9**, 1631–1640.
31 P. Janthon, S. Luo, S. M. Kozlov, F. Viñes, J. Limtrakul, D. G. Truhlar and F. Illas, Bulk Properties of Transition Metals: A Challenge for the Design of Universal Density Functionals, *J. Chem. Theory Comput.*, 2014, **10**, 3832–3839.
32 L. Vega, J. Ruvireta, F. Viñes and F. Illas, Jacob's Ladder as Sketched by Escher: Assessing the Performance of Broadly Used Density Functionals on Transition Metal Surface Properties, *J. Chem. Theory Comput.*, 2018, **14**, 395–403.
33 P. E. Blöchl, Projector Augmented-Wave Method, *Phys. Rev. B: Condens. Matter Mater. Phys.*, 1994, **50**, 17953–17979.
34 G. Kresse and D. Joubert, From Ultrasoft Pseudopotentials to the Projector Augmented-Wave Method, *Phys. Rev. B: Condens. Matter Mater. Phys.*, 1999, **59**, 1758–1775.
35 F. Viñes, F. Illas and K. M. Neyman, On the Mechanism of Formation of Metal Nanowires by Self-Assembly, *Angew. Chem., Int. Ed.*, 2007, **46**, 7094–7097.
36 S. M. Kozlov, H. A. Aleksandrov, J. Goniakowski and K. M. Neyman, Effect of MgO(100) Support on Structure and Properties of Pd and Pt Nanoparticles with 49–155 Atoms, *J. Chem. Phys.*, 2013, **139**, 084701.
37 A. Ruban, H. L. Skriver and J. K. Nørskov, Surface Segregation Energies in Transition-Metal Alloys, *Phys. Rev. B: Condens. Matter Mater. Phys.*, 1999, **59**, 15990–16000.
38 V. Grolier and R. Schmid-Fetzer, Experimental Study of Au–Pt–Sn Phase Equilibria and Thermodynamic Assessment of the Au–Pt and Au–Pt–Sn Systems, *J. Electron. Mater.*, 2008, **37**, 264–278.
39 L. Deng, W. Hu, H. Deng and S. Xiao, Surface Segregation and Structural Features of Bimetallic Au–Pt Nanoparticles, *J. Phys. Chem. C*, 2010, **114**, 11026–11032.
40 S. Takizawa, K. Terakura and T. Mohri, Electronic Theory for Phase Stability of Nine AB Binary Alloys, with A = Ni, Pd, or Pt and B = Cu, Ag, or Au, *Phys. Rev. B: Condens. Matter Mater. Phys.*, 1989, **39**, 5792–5797.
41 O. Kubaschewski, C. B. Alcock and P. J. Spencer, *Materials Thermochemistry*, Oxford, Pergamon, 6th edn, 1993.
42 J. Tang, L. Deng, S. Xiao, H. Deng, X. Zhang and W. Hu, Chemical Ordering and Surface Segregation in Cu–Pt Nanoalloys: The Synergetic Roles in the Formation of Multishell Structures, *J. Phys. Chem. C*, 2015, **119**, 21515–21527.
43 T. Abe, B. Sundman and H. Onodera, Thermodynamic Assessment of the Cu–Pt System, *J. Phase Equilibria Diffus.*, 2006, **27**, 5–13.
44 Z. W. Lu, S.-H. Wei, A. Zunger, S. Frota-Pessoa and L. G. Ferreira, First-Principles Statistical Mechanics of Structural Stability of Intermetallic Compounds, *Phys. Rev. B: Condens. Matter Mater. Phys.*, 1991, **44**, 512–544.
45 A. F. Wells, *Structural Inorganic Chemistry*, Clarendon Press, Oxford, 5th edn, 1984.
46 J. Tang, L. Deng, H. Deng, S. Xiao, X. Zhang and W. Hu, Surface Segregation and Chemical Ordering Patterns of Ag–Pd Nanoalloys: Energetic Factors, Nanoscale Effects, and Catalytic Implication, *J. Phys. Chem. C*, 2014, **118**, 27850–27860.
47 J. M. Rahm and P. Erhart, Understanding Chemical Ordering in Bimetallic Nanoparticles from Atomic-Scale Simulations: The Competition between Bulk, Surface, and Strain, *J. Phys. Chem. C*, 2018, **122**, 28439–28445.
48 L. Deng, X. Liu, X. Zhang, L. Wang, W. Wei Li, M. Song, J. Tang, H. Deng, S. Xiao and W. Hu, Intrinsic Strain-Induced Segregation in Multiply Twinned Cu–Pt Icosahedra, *Phys. Chem. Chem. Phys.*, 2019, **21**, 4802–4809.
49 J. Pirart, A. Front, D. Rapetti, C. Andreazza-Vignolle, P. Andreazza, C. Mottet and R. Ferrando, Reversed size-dependent stabilization of ordered nanophases, *Nat. Commun.*, 2019, **10**, 1982.
50 N. Danielis, L. Vega, G. Fronzoni, M. Stener, A. Bruix and K. M. Neyman, AgPd, AuPd, and AuPt Nanoalloys with Ag- or Au-rich Compositions: Modeling Chemical Ordering and Optical Properties, *J. Phys. Chem. C*, 2021, **125**, DOI: 10.1021/acs.jpcc.1c04222.
51 S. Liu, Z.-J. Zhao, C. Yang, S. Zha, K. M. Neyman, F. Studt and J. Gong, Adsorption Preference Determines Segregation Direction: A Shortcut to More Realistic Surface Models of Alloy Catalysts, *ACS Catal.*, 2019, **9**, 5011–5018.
52 Y. Lykhach, S. M. Kozlov, T. Skála, A. Tovt, V. Stetsovych, N. Tsud, F. Dvořák, V. Johánek, A. Neitzel, J. Mysliveček, S. Fabris, V. Matolín, K. M. Neyman and J. Libuda, Counting Electrons on Supported Nanoparticles, *Nat. Mater.*, 2016, **15**, 284–288.
53 F. Viñes and A. Görling, Explaining Cu@Pt Bimetallic Nanoparticles Activity Based on NO Adsorption, *Chem. – Eur. J.*, 2020, **26**, 11478–11491.
54 Y. Suchorski, S. M. Kozlov, I. Bespalov, M. Datler, D. Vogel, Z. Budinska, K. M. Neyman and G. Rupprechter, The Role of Metal/Oxide Interfaces for Long-Range Metal Particle Activation during CO Oxidation, *Nat. Mater.*, 2018, **17**, 519–522.
55 R. Ferrando, A. Fortunelli and G. Rossi, Quantum Effects on The Structure of Pure and Binary Metallic Nanoclusters, *Phys. Rev. B: Condens. Matter Mater. Phys.*, 2005, **72**, 085449.
56 D. Cheng, W. Wang and S. Huang, The Onion-Ring Structure for Pd–Pt Bimetallic Clusters, *J. Phys. Chem. B*, 2006, **110**, 16193–16196.
57 D. Cheng, W. Wang, S. Huang and D. Cao, Atomistic Modeling of Multishell Onion-Ring Bimetallic Nanowires and Clusters, *J. Phys. Chem. C*, 2008, **112**, 4855–4860.
58 C. D. Feldt, R. Moreira, E. Meyer, P. Clawin, W. Riedel, T. Risse, L. Moskaleva, W. Dononelli and T. Klüner, CO Adsorption on Au(332):Combined Infrared Spectroscopy and Density Functional Theory Study, *J. Phys. Chem. C*, 2019, **123**, 8187–8197.
59 K. Tran and Z. W. Ulissi, Active Learning across Intermetallics to Guide Discovery of Electrocatalysts for CO_2 Reduction and H_2 Evolution, *Nat. Catal.*, 2018, **1**, 696–703.

Chapter 7. Nanostructuring Determines Poisoning: Tailoring CO Adsorption on PtCu Bimetallic Nanoparticles

7.1 SUMMARY

Introduction In the last project of Bimetallic Results, the focus is not the chemical ordering of the bimetallic NPs itself, but the chemical activity of different NP sites, in particular for the CO molecule on the PtCu system. Fuel cells are an efficient way to transform chemical energy to electricity with low pollutant emissions.[87] During the last decades, polymer electrolyte membrane (PEM) fuel cells have been one of the most promising fuel cells technologies because of their sustainable zero carbon emission, their high energy conversion, and acceptable durability. Nevertheless, they are expensive and some improvements to reduce their cost are needed. Pt is the most suitable catalyst for PEM fuel cells due to its role in rapid oxidation and reduction reactions, stability, and its high activity towards H_2 dissociation. However, the main problem is that Pt is quite expensive given its scarcity. Moreover, the trace CO found in H_2 gas binds strongly onto Pt surfaces, diminishing H_2 dissociation activity. This phenomenon is known as CO poisoning.

Thus, a possible solution for such limitations is the use of core@shell M@Pt nanoparticles, in which Pt is located at the surface and M at the core. M is a sacrificial cheaper metal which maximizes the surface area to mass ratio when creating small nanoparticles. This solution implies that the electronic properties will be modified by the presence of the M metal.[88] Since the electronic properties change depending on which M is used, the H_2 dissociation activity and CO poisoning of the catalyst can be modified, looking for a perfect case with weaker CO binding and similar or higher H_2 dissociation activity. There are some previous studies using different sacrificial and cheaper transition metal cores.[89–100] For example, Kristian *et al.*[92] synthetized Co@Pt core@shell NPs from Co NPs. The surface atoms of

Co were oxidized and replaced by Pt atoms by the reduction of $PtCl_4^{2-}$. They found that pH had a key role in the activity and morphology of the NPs.

From all, still, one of the most promising metals is Cu, being the most common metal for many industrial applications. Its electrodeposition is quite well known, usually using carbon supports. Cu@Pt core@shell NPs can be obtained from Cu NPs by galvanic exchange with Pt, using the same synthesis method described before for Co@Pt. Adzic and co-workers made this method popular for the synthesis of a Pt-monolayer catalyst for the oxygen reduction reaction.[101–103] Apart from that, the electronic effect caused by the presence of a Cu core induces a reduction of CO poisoning. Recently, single atom alloys (SAA) have been introduced as very good selective catalysts and a more economical way to reduce typical active metals like Pt, Pd, and Rh, since only a few single atoms of the active metal are alloyed in the surface of a more inert host metal. In the case of SAA PtCu catalyst, it has been shown that it is more tolerant to CO poisoning.[104]

For all the previous reasons, Cu@Pt core@shell NPs supported on carbon (Cu@Pt/C) were synthetized by the electrochemical deposition of Cu and galvanic exchange of Pt, to be compared with commercial Cu@Pt/C and Pt nanoparticles also supported on carbon (Pt/C). Note that three different Cu deposition methodologies were used to obtain three different samples of Cu@Pt core@shell NPs. Surprisingly, for one of the Cu@Pt NPs, CO binding is stronger than in the pure Pt NPs. A deep examination of CO adsorption is carried out through the performance of DFT optimizations on proper models. We found out that different defects present in Cu@Pt core@shell NPs feature stronger CO binding than the equivalent situations in Pt NPs. Concretely, those defects are *i)* a Pt adatom at the surface, *ii)* a single atom of Pt surrounded by surface Cu and subsurface Pt, and *iii)* a three-Pt-atom vacancy at the (111) facet. The average diameter of the synthetized NPs is of around 1.5 nm, being a smaller NP size than the ones featured in previous studies. Consequently, we think that the synthesis procedure of the Cu@Pt core@shell NPs could have a critical role on CO poisoning.

The author carried out all the computational part of the project, the adsorptions at different sites, the chemical ordering analysis, and the charge analysis. Furthermore, the author participated actively in the redaction of the manuscript and presentation of the results. The manuscript is included end of this summary. Further supporting data is found Appendix F.

Results Experimentally, the most important result is that one of three synthetized samples of NPs of 1.5 nm and a ratio of Pt:Cu of 60:40 with a core@shell structure of Cu@Pt, featured a peak of potential shifted by ~50 mV to more positive potentials for the CO oxidation peak compared to Pt/C. Thus, implying a stronger CO adsorption with respect to Pt. This result shows a different CO resistance behaviour than the one found for the other synthetized Cu@Pt samples and the one reported by previous studies.[105–109]

To gain a deeper understanding of this unexpected result, we carried out a systematic DFT study of CO adsorptions on realistic NP models. 201-atomic NPs, ~1.5 nm size comparable with the experimental samples, are modelled with a truncated octahedron shape following the Wulff construction. Pt_{201} (model 1) is employed as a reference to compare the results. Different models were created to understand the experiments. The ones where we focus the following discussion are: *i)* Cu@Pt core@shell NP, $Cu_{79}@Pt_{122}$ (model 3), ii) NPs with single surface Pt atoms surrounded by surface Cu neighbours (model 6), *iii)* NPs with single surface Pt atoms surrounded by surface and subsurface Cu neighbours (model 7), *iv)* models derived from the latter by removal of the surface Cu atoms and subsequent local optimization of the structure (model 8). For completeness, other models with surface defects, adatoms and vacancies, created on the immaculate $Cu_{79}@Pt_{122}$ model are studied and compared with the equivalent defects on Pt_{201}. These other NP models are included at the Supporting Information, see Appendix F.

CO adsorption was studied on different possible sites of the NP models (see Appendix F). To evaluate the CO binding strength the adsorption energy was calculated using,

$$E_{ads} = E_{CO/NP} - E_{NP} - E_{CO} \quad (7.1)$$

where E_{CO} is the energy of the optimized CO, E_{NP} the energy of the optimized bare NP and the $E_{CO/NP}$ the energy of the optimized NP with the CO adsorbed.

The relevant models to compare with model 1, are model 3, as the ideal modelling of the experimental samples, and model 6, 7 and 8, because some sites show stronger CO binding, see Figure 7.1. One can observe that model 3 features weaker CO adsorption than model 1 on all the studied sites by 0.35-0.91 eV. This is in agreement with two prepared experimental samples and the literature, where the Cu→Pt charge transfer and lowering of the *d*-band centre may cause weaker CO adsorption.[110,111] Furthermore, isolated Pt atoms (surrounded by Cu) can lead to stronger CO binding than pure Pt NP. Indeed, model 6 still features weaker CO adsorption energies than model 1 but they are 0.21 eV stronger with respect to model 3. However, in the (001) terrace, CO adsorption is stronger than at the equivalent site of model 1. This effect is aggravated by the presence of subsurface Pt. Model 7 shows stronger CO adsorption energies than those of model 1 for all the different studied sites, in the site C case up to 0.44 eV. Besides this, when surface Cu atoms are removed because of Cu oxidation and dissolution after several cycles of CO stripping, model 8 is obtained. The resulting relaxed structure of model 8 becomes distorted featuring highly undercoordinated Pt atoms. The undercoordinated Pt atoms feature similar adsorption energies to model 1. However, at some of the studied sites, it features a strengthened CO adsorption, for example at site C and D, and in other sites a weakened CO adsorption as in site F.

Since defects, such as the vacancies of surface Cu, can lead to a stronger CO poisoning effect, we explored CO adsorption on a Pt adatom and Pt vacancies on (001) and (111) facets, see on Table 7.1. The same sites are modelled on a pure Pt NP for comparison. The cases of a Pt adatom on (111) facets and vacancies of one and three missing Pt atoms in (111) facets, strengthen CO adsorption by 0.28, 1.01 and 1.23 eV, respectively. The last case leads to a surface reconstruction that generates more active (111) facets

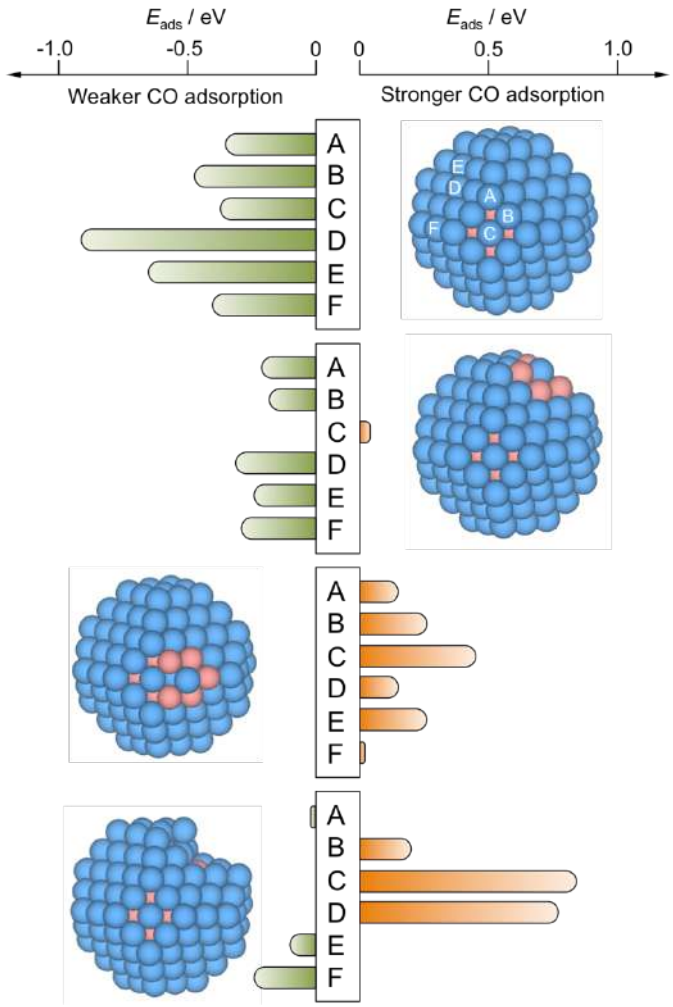

Figure 7.1 Differences in CO adsorption energies, ΔE_{ads}, on PtCu NPs with respect to reference Pt_{201} NP, calculated for all topologically different top sites, see Section S2 of the Appendix F. From top to bottom, perfect Cu@Pt core@shell NP —model **3**, see Section S1 Appendix F— with a surface Pt atom fully coordinated to Cu atoms —model **6**—, with a surface Pt atom coordinated to surface Cu atoms —model **7**— and model **8** resulting from removal of five surface Cu atoms from model **7** and subsequent optimization. For a comprehension of the model notation, we refer to SI of the Manuscript, appended at the end of the Thesis.

and sites. Indeed, CO adsorption on two sites of the Cu@Pt NP —the Pt adatom and the three-Pt atom (Pt_3) vacancy on the (111) facet— is stronger than on the most stable regular site of the Pt_{201} NP.

To have a better understanding of those cases than feature stronger CO adsorption, Bader charge analysis and charge density difference (CDD) plots were analysed. Briefly, the stronger CO bonding is mainly due to the more negative charge of the surface Pt atoms when it is superficially Cu-

surrounded compared to a pure Pt NP case. Such accentuated negatively charged site favours the attraction to it from the $C^{\delta+}$ CO atom. Apart from the Bader analysis, CDD plots reveal a donation/back-donation mechanism. The aforementioned excess charge is back-donated from Pt 5*d* states to the $2\pi^*$ CO orbital, contributing to a stronger binding. This electronic rearrangement is a common feature observed on Pt_3 vacancies and Pt adatoms attaching CO stronger to PtCu NPs than to the pure Pt one.

Table 7.1 CO adsorption energies, E_{ads}, calculated on a Pt adatom or Pt_n vacancies defects in core@shell $Cu_{79}@Pt_{12}$, as well as on reference Pt_{201} model NPs. Values are given in eV.

Facet	Site	$Cu_{79}@Pt_{122}$	Pt_{201}
(001)	Pt adatom	-1.96	-1.95
	Pt vacancy	-1.88	-2.02
(111)	Pt adatom	-2.53	-2.25
	Pt_1 vacancy	-1.70	-0.69
	Pt_3 vacancy	-2.43	-1.21
	Pt_7 vacancy	-0.73	-1.69

Conclusions To conclude this section, the main ideas are:

- That the synthesis method of PtCu NPs defines the NP size and structure, while modifying the CO adsorption strength. Well-shaped particles larger than 2 nm with low Cu content are more resilient towards CO poisoning.
- Single Pt atoms surrounded by surface Cu ones or under-coordinated Pt atoms, Pt adatoms, and few-atom Pt vacancies in Cu@Pt NPs, may even strengthen the CO binding, implying more CO poisoning. This particular cases could be more frequent for core@shell Cu@Pt NPs of *ca.* 1.5 nm with a relatively low Pt:Cu content of ~60:40, where the presence of such defects may become more visible, i.e. less hidden by the presence of other more regular sites.

Nanostructuring Determines Poisoning: Tailoring CO Adsorption on PtCu Bimetallic Nanoparticles

Lorena Vega[a,b,†], Julia Garcia-Cardona[a,†], Francesc Viñes,[a,b*] Pere L. Cabot[a,*], Konstantin M. Neyman[a,b,c]

[a]*Departament de Ciència de Materials i Química Física, Universitat de Barcelona, c/ Martí i Franquès 1-11, 08028 Barcelona, Spain*

[b]*Institut de Química Teòrica i Computacional (IQTCUB), Universitat de Barcelona, c/ Martí i Franquès 1-11, 08028 Barcelona, Spain*

[c]*ICREA (Institució Catalana de Recerca i Estudis Avançats), Pg. Lluís Companys 23, 08010 Barcelona, Spain*

[*] Corresponding authors: Pere L. Cabot (p.cabot@ub.edu), Francesc Viñes (francesc.vines@ub.edu)

Keywords: core@shell nanoparticles; CO stripping voltammograms; PtCu bimetallics; defects; density functional calculations

Abstract

Here we show, through CO stripping voltammograms on different PtCu nanoparticle (NP) low-temperature fuel cells electrocatalysts and density functional calculations, that surface chemical ordering and presence of certain defects explain the CO tolerance *vs.* poisoning of such systems. The CO withdrawal for these duelling *CO-slingers* depends on whether they are well-shaped core@shell Cu@Pt NPs, more CO-tolerant, or having Cu-surrounded surface Pt atoms or adatoms/vacancies surface defects, less CO-tolerant. The latter sites are critical on nm-sized PtCu NPs, displaying stronger CO adsorption compared to pure Pt NPs. Avoiding such sites is key when designing less expensive and CO-poisoned Cu@Pt NP-based electrocatalysts.

[†] L. V. and J. G.-C. equally contributed.

1. Introduction

Fuel cells are regarded as a forefront, efficient way to transform chemical energy into electricity involving low pollutant emissions [1], highly appealing, *e.g.*, to provide power for small residential areas, even when remote. Aside, fuel cells are attractive to the automotive sector and portable electronic devices, to mention a few applications of technological interest [2,3]. In this context, proton exchange membrane fuel cells (PEMFCs) have arisen as one of the most promising technologies contributing to meet the growing global energy demands while keeping sustainable zero carbon emissions, particularly thanks to their high energy density and efficiency, with demonstrated durability [4].

Platinum is the main electrocatalyst for PEMFCs, long regarded as the best material to carry out the hydrogen oxidation reaction (HOR) and the oxygen reduction reaction (ORR). However, Pt scarcity translates into prohibitive costs, plus it gets readily poisoned when the industrial grade hydrogen (H_2) source contains carbon monoxide (CO) impurities [5], given the strong bond of CO to Pt surfaces [6]. The CO tolerance can be improved, *e.g.*, using PtRu alloy electrocatalysts, but at the expense of decreasing the fuel cell efficiency and yet introducing another expensive metal [7].

An appealing way of decreasing the costs is to employ core@shell M@Pt nanoparticles (NPs), in which a more abundant and cheaper metal constitutes the NP core not directly participating in the catalytic process. In addition, the NP shaping aids at increasing the surface-to-mass ratio. Note that such solutions may imply a modulation of the Pt shell electronic structure by the core M metal [8], affecting the catalytic power, the CO affinity, and even the core@shell NP stability [9]. Thus, the core@shell NPs composition, size, and shape are envisaged as controllable features to maximize the H_2 activation while reducing the CO poisoning.

Along this line, diverse experiments have been performed with a plethora of cheaper sacrificial metal cores, M = Co, Ni, Fe, Sn, Mn, Zn, or Pb [10-16]. Among them, the Cu@Pt formulation has attracted great attention [10,17,18] given the availability of Cu, a common catalyst, *e.g.* for the reverse water gas shift reaction [19], and as an electrocatalyst for the carbon dioxide reduction reaction [20]. There exists a number of methodologies to prepare Cu@Pt NPs, including direct current [21], electroless Cu deposition using sodium borohydride ($NaBH_4$) [22], or $NaBH_4$ and

ascorbic acid mixtures with formaldehyde, or water-ethylene glycol mixtures [23,24], all followed by Cu galvanic exchange with Pt often supported on porous carbon [25].

It is known that Cu@Pt NPs are excellent catalysts for NO_x reduction [26]. Their thermodynamic stability, rationalized by density functional theory (DFT) simulations on NP models [27], revealed a significant cohesion of Cu and Pt phases. The improved catalytic activity was assigned to a Cu→Pt electron transfer and a lowering of the Pt *d*-band centre. This mechanism was invoked as well to explain the weaker CO binding on Cu@Pt systems using slab-model DFT simulations of Pt monolayers on Cu support [28]. Note that on extended systems the effect is maintained, although less expressed, even in case of a surface Pt single atom alloy (SAA) as follows from the observations of improved CO poisoning tolerance of PtCu SAA [29].

However, *not all that glitters is gold*, and the manufacturing of Cu@Pt NPs is not exempt of adverse effects in terms of CO poisoning, which may be enhanced by particular NP size, shape, or synthesis procedures. We show this here by decreasing the size limits to *circa* 1.5 nm for Cu@Pt particles obtained by galvanic exchange and Cu selective oxidation, thus prompting the possibility of having a diversity of abundant defects at the NP surface. The CO stripping voltammograms on a series of synthesized and commercially available Cu@Pt NPs with different particle sizes and Pt:Cu ratios reveal that the CO adsorption is, in general terms, weakened compared to pure Pt NPs, but, in the smallest size limit, it may be remarkably strengthened. An atomistic insight gained by DFT simulations on Cu@Pt NP models reveals that certain surface defects, including Cu-surrounded Pt atoms, Pt adatoms, and Pt vacancies, may decrease the tolerance towards CO poisoning.

2. Experimental details

2.1. PtCu bimetallic nanoparticles synthesis

The PtCu catalysts studied in this work were synthesized by different procedures. They all consisted in a two-step synthesis where carbon-supported Cu NPs (Cu/C) were firstly obtained by different deposition methods. Later, once the Cu/C was formed, a partial galvanic replacement took place when the powder was suspended in a 5 mM H_2PtCl_6 + 0.1 M $HClO_4$ solution with vigorous stirring for 45 min, proceeded according to the following reaction:

$$2\ Cu + PtCl_6^{2-} \rightarrow 2\ Cu^{2+} + Pt + 6\ Cl^- \qquad (1)$$

The resulting carbon-supported Cu@Pt core@shell NPs were separated, cleaned, and dried. Carbon XC72 from Cabot Corp. was used as the support in all cases. All the solutions were prepared from Milli-Q water (Merck) and the analytical-grade reagents from Merck GmbH ($NaBH_4$, H_2PtCl_6, Na_2-EDTA, *n*-heptane, Brij-30, acetone, ethanol) and Panreac Applichem GmbH ($CuSO_4 \cdot 5H_2O$, formaldehyde, NaOH, polyvinylpyrrolidone).

The electroless deposition to obtain Cu NPs was performed in basic aqueous media, using formaldehyde or $NaBH_4$ as reducing agents, and in water in oil microemulsion, using $NaBH_4$. Synthesis 1, **S1**, consists in the preparation of the Cu/C catalyst precursor following the work of Georgieva *et al*. [23]. The carbon powder was dispersed in 100 mL of a solution containing 10 mM $CuSO_4 \cdot 5H_2O$ as the Cu precursor, 30 mL/L CH_2O as the reducing agent, 50 mM Na_2-EDTA as the complexing agent, and 0.0005 mM polyvinylpyrrolidone (PVP) as the surfactant. The pH was raised up to 12.5-13.0 with NaOH and then the suspension was kept at 45 ºC in a water bath under stirring for 30 min. The suspended solid was centrifuged at 9500 rpm for 15 min and then re-suspended in ultrapure ethanol and centrifuged again several times to remove the surfactant. The Cu/C NPs were left to dry under vacuum overnight. Synthesis 2, **S2**, was performed from a sonicated suspension containing given amounts of $CuSO_4 \cdot 5H_2O$ and the carbon support in 1.0 M NaOH. Then, $NaBH_4$ was slowly added during 15 min for the copper deposition, the sonication continued for 30 min more and then, the suspension was filtered [25]. In Synthesis 3, **S3**, the catalysts were prepared by a water-in-oil method, which consists in a microemulsion containing *n*-heptane, Brij-30 as the surfactant, and an aqueous solution of $CuSO_4$, with a water-to-surfactant molar ratio of 7 [30]. An excess of $NaBH_4$ was added to form Cu NPs, further sonicating the microemulsion for 2 h. Finally, 21 mg of the carbon support were added to the microemulsion, which was further kept stirred for 1 h and then, the phase separation was produced by acetone addition. Once the organic phase was separated from aqueous phase and cleaned, the resulting powder was filtered.

2.2. CO stripping experiments

The electrochemical experiments were done in a three-electrode electrochemical cell using an $Ag|AgCl|KCl_{sat}$ reference electrode, a Pt stick auxiliary electrode, and a 5 mm-diameter glassy carbon electrode (GCE) as the working one (all from Metrohm). The GCE was polished to mirror finish as described elsewhere [25]. The electrolyte was 0.5

M H_2SO_4 (Merck, analytical grade) and the experiments were performed using an Ecochemie Autolab PGSTAT100 commanded by the Autolab Nova 2.1.4 software. The GCE was coated with 20 μL of the catalyst ink, prepared by sonicating 1 mg of the catalyst powder dispersed in 0.5 cm^3 of a water:isopropanol (analytical grade, Panreac) mixture (1:1 in volume), and left to dry at room temperature. Prior to the CO stripping experiments, the ink-modified electrode was cleaned by repetitive cycling between -0.2 and 0.8 V at 100, 50 and 20 mV s^{-1} up to a steady profile. To obtain the CO stripping curves, CO gas (99.9% Linde) was bubbled through the 0.5 M H_2SO_4 solution for 15 min keeping the electrode potential at -0.1 V. Dissolved CO was removed by N_2 bubbling (99.9995% Linde) through the solution for 30 min and then, the monolayer of CO adsorbed on the surface was oxidized by cyclic voltammetry (CV) between -0.2 and 1.0 V at 20 mV s^{-1} without stirring. The experimental results were compared with those obtained using commercial 20 wt.% Pt/C and 20 wt.% PtCu/C (1:1 at. ratio), both from Premetek, after preparing the corresponding working electrodes in the same way as indicated above.

2.3. X-ray diffraction samples characterization

The X-ray diffraction (XRD) patterns of the synthesized catalysts are shown in Figure 1, where they are compared to commercial Pt/C and PtCu/C samples. The focus on the 35 to 55º region allows one comparing the peaks to the expected signals for Pt and Cu (111) and (200) surfaces, and thus confirming the Pt phase of Pt/C reference, as well as Pt-like and Cu-like phases of different composition on commercial PtCu/C and samples **S1** to **S3**. Table 1 summarizes the XRD results, *i.e.* the average NP size (from Scherrer's equation) and the Pt:Cu ratios (Vegard's law). Note that commercial PtCu/C and Pt/C samples have mean NP sizes of 3.4 and 2.6 nm, the former with a Pt:Cu at.% ratio of 57:43. Samples **S1** to **S3** featured increasing size, from 1.5 to 3.5 nm, and decreasing of the Cu content, from Pt:Cu 64:36 in **S1** to 91:9 for **S3**, in line with a Cu@Pt core@shell structure, since the surface Cu atoms were removed and replaced by Pt atoms during the galvanic exchange [25]. Aside, the lattice parameters, *a*, determined from the XRD diffractograms go along with the Cu content, *i.e.* the larger the Cu content, the smaller is *a*, thus resulting in a concomitant lattice strain increase while reducing the NP size [27].

3. Methods and models

3.1. Computational details

The present DFT calculations were carried out using the plane-wave based Vienna *ab initio* simulation package (VASP) code [31,32]. The Perdew-Burke-Ernzerhof (PBE) [33] exchange-correlation functional was used in the description of the valence electrons, combined with the projector augmented wave (PAW) representation of core electrons [34,35]. Given the strong adsorption of CO on Pt, the inclusion of dispersive forces just slightly increases the adsorption strength, as shown on Pt(111), by ~0.3 eV [36]. Thus, the poisoning by CO due to its strong chemical bonding to Pt, is reasonably well accounted at the PBE level. Metal NPs were modelled within a 2.5×2.5×2.5 nm large periodically repeated cells with at least 0.75 nm separation between adjacent particles, with negligibly weak interactions of metal NPs at such distances [37]. Only the **Γ** Brillouin zone **k**-point was sampled for the single NPs. The kinetic energy cut-off for the plane-waves basis set was set to 415 eV, a value large enough to acquire adsorption energies converged within chemical accuracy, *i.e.* below ~0.04 eV. For the electron density calculation, a cut-off value of 450 eV provided properly converged Bader charges. One-electron levels were smeared by 0.2 eV through a Gaussian function, yet finally the converged energies were extrapolated to zero smearing. All atoms were locally fully relaxed accomplishing a maximum forces criterion of 0.02 $eV \cdot Å^{-1}$. Charges were evaluated through a Bader atoms-in-molecules analysis, and charge density difference (CDD) plots acquired as the difference of the electron density of the system containing the NP with the adsorbed CO, and the electron densities of the isolated NP and CO at fixed geometry of the adsorption system [38].

3.2. Employed nanoparticle models

NP models of the PtCu nanoalloys were constructed following the experimental 60% at. Pt and 40% at. Cu composition, using as a template 201-atomic truncated octahedrons, following the Wulff construction shape minimizing the NP overall surface tension [39], which resulted in an average NPs diameter of ~1.5 nm, thus matching sizes of NPs in the experimental samples. NPs of such a size are well within the so-called scalable regime and can be used as models of larger NPs. The model NPs already feature a metallic band structure, at variance with the discrete energy levels featured by smaller metal clusters [27]. The models created to simulate the experiments were as follows: *i)*

an immaculate (regular) Cu@Pt core@shell NP, $Cu_{79}@Pt_{122}$ —model **3**— which obeys to the topological stability preference [40]; *ii)* a $Cu_{78}Pt@Pt_{121}Cu$ model derived from the latter by exchanging one surface Pt atom with one core Cu atom —model **5**—; *iii)* NPs with single surface Pt atoms surrounded by surface and subsurface Cu neighbours —model **7**—; *iv)* NPs with single surface Pt atoms surrounded by surface Cu neighbours —model **6**—, *v)* models derived from the latter by removal of the surface Cu atoms and subsequent local optimization of the structure —model **8**—; and *vi)* models with surface defects created on the immaculate $Cu_{79}@Pt_{122}$ model —adatom and vacancy models—. Except for the $Cu_{79}@Pt_{122}$ NP, different models had to be built to duly represent the variety of surface defects. Apart from the just mentioned PtCu model NPs, the following reference systems were also calculated: Pristine Pt_{201} —model **1**— and Cu_{201} NPs —model **2**—, inverse $Pt_{79}@Cu_{122}$ —model **4**—, and pure Pt_{201} NPs with generated surface defects, see Figure 2.

3.3. CO adsorption assessment

CO molecule adsorption was systematically studied on these NP models. Numerous positions were considered, see Figure S1 of the Supplementary Material (SM), including top, bridge, and face-centred cubic (*fcc*) hollows, regarded to be more stable than hexagonal close packed (*hcp*) hollows [27]. In addition, CO adsorption was investigated on the surface vacancy defected models with one, three or seven atoms missing on the (001) and (111) facets. CO adsorption energy, E_{ads}, was calculated from the energies of the optimized, CO molecule, E_{CO}, clean NP, E_{NP}, CO adsorbed on the NP model, $E_{CO/NP}$, as follows:

$$E_{ads} = E_{CO/NP} - E_{NP} - E_{CO} \quad (2).$$

Within this definition, the more negative the E_{ads} is, the stronger is the CO adsorption. Aside from testing *hcp* from *fcc* sites, our calculations revealed a clear trend towards the perpendicular CO adsorption *via* its C atom, starting from a parallel CO adsorption mode one with both C and O atoms interact with the NP. Aside, a very weak O-connected CO perpendicular adsorption is characterised at most by E_{ads} of -0.05 eV, see Table S1 of the SM. Thus, the latter adsorption mode has been discarded from the discussion, considering only much stronger C-connected CO perpendicular adsorption, see Table 2.

4. Results and discussion

4.1. CO stripping voltammograms on reference Pt and PtCu bimetallic nanoparticles

The CO stripping studies have been carried out for three PtCu bimetallic NP systems synthesized on a carbonaceous support, named **S1**, **S2**, and **S3**, and compared with Pt/C and PtCu/C commercial catalysts, see Figure 3. The general shape of these curves is typical for Pt [41]. The main peak appears in these curves during the anodic sweep, in the potential range 0.5–0.8 V, which corresponds to the oxidation of adsorbed CO. This peak is preceded by a mere capacitive current due to CO blocking of the active sites. After the CO stripping, Pt is oxidized to surface PtO, which is reduced again to Pt in the cathodic sweep, leading to the peak located at about 0.6 V. Afterwards, the hydrogen adsorption profile, also typical for Pt, appears in the potential range from 0.1 to -0.2 V. Note that the currents have been referred to the CO stripping charge of each specimen, since the stripping charges are proportional to the number of active centres, thus allowing for a better comparison of the catalyst activities. Importantly, no Cu oxidation is perceived in the CV curves of Figure 3. In the case that some free Cu remained on the surface, it should be oxidized at 0.0–0.2 V potentials [42] and no peaks can be observed in this potential region. In the case of the **S1**, **S2**, and **S3** samples, this can happen because *i*) during the galvanic replacement, Pt atoms remove the surface Cu atoms of the previously deposited Cu NPs and *ii*) after the repetitive cycling to reach the steady profile, the possible remaining surface Cu atoms are removed. NPs of the commercial PtCu/C catalyst should also undergo a surface Pt enrichment according to the point *ii*). This agrees with X-ray photoelectron spectroscopy analyses of PtCu NPs deposited on different carbon supports by galvanic exchange showing such a Pt surface enrichment [25]. Thus, the NPs can be described as having core@shell structures with a PtCu alloy core and a shell mainly composed of Pt atoms.

The profiles of the cyclic voltammograms in Figure 3 are then the same as that of Pt/C, although with different potential shifts of the CO stripping peaks. The onset potential of these peaks indicates the strength of CO adsorption, being smaller as the onset potential is shifted in the negative direction. According to literature, many PtCu samples feature more negative onset potential for CO oxidation than pure Pt, seen *e.g.* in Cu@Pt core@shell NPs produced by electrochemical reduction of Cu followed by a partial galvanic replacement with Pt [21], NPs with a Cu-core to Pt-shell gradient structure [43], Pt NPs with a small content of dissolved Cu [44], even PtCu alloy NPs

prepared using a reducing agent in basic media followed by a partial galvanic replacement with Pt [25]. This is indeed observed in the CO stripping plots in Figure 3 for commercial PtCu, PtCu_**S2**, and PtCu_**S3** samples, revealing a weaker CO adsorption when compared to commercial Pt/C. The adsorbed OH necessary to generate CO_2 (and water) during the oxidation process appears to play a minor role, a point quantified by DFT calculations. The calculated hydroxyl adsorption energy below -0.5 eV on pure Pt NPs [44] suggests its easy displacement by CO molecules adsorbed at least 1 eV stronger; *vide infra*. Regarding the deviations with respect to pure Pt, commercial PtCu/C is the closest to Pt/C, with a peak potential shift of merely -10 mV, even when a Pt:Cu ratio is close to 60:40, see Table 1. The PtCu_**S3** shows a peak shift of *ca.* -50 mV; its similar size to commercial PtCu/C implies that the extra shift comes from the Pt:Cu composition of *ca.* 90:10, indicating that some effect is achieved at small contents of Cu, as observed for PtCu NPs with decreasing Cu content [45], even in solid solution limits containing just *ca.* 1% at. Cu [44]. The PtCu_**S2** sample has a particle size close to that of Pt/C, but with a ~70:30 Pt:Cu ratio, also revealing a weaker CO adsorption. Note that in this latter sample, a broad band appears in which one can discern two features at 0.54 and 0.58 V, which could be well related to well-faceted (111) and (100) Pt domains reported in the literature [46].

The most striking feature is that PtCu_**S1** sample with Pt:Cu ratio 60:40 and 1.5 nm large particles features a CO oxidation peak shifted by ~50 mV to more positive potentials compared to Pt/C sample, indicating a stronger CO poisoning of the fomer PtCu_**S1**. To the best of our knowledge, this is the first observation of CO poisoning enhancement for nanostructured PtCu samples. This is in strong contrast with the results obtained for commercial PtCu/C sample featuring not very different Pt:Cu composition, but significantly different NP size (3.4 nm). Note, however, that the negative onset potential shift for CO oxidation for commercial PtCu/C is smaller than those for PtCu_**S2** and PtCu_**S3** samples, suggesting that decreasing the amount of Cu in the PtCu alloy can facilitate the CO removal. However, probably there is not only a mere size effect. The synthesized NPs are the result of a galvanic exchange of Cu by Pt. If the initially deposited Cu NPs have significantly different sizes and surface structures in the applied preparation protocols the galvanic exchange may lead to PtCu NPs varying both sizes and surface defectiveness.

4.2. Computational CO adsorptive landscapes on Pt and PtCu nanoparticles

In order to explain the aforementioned experimental findings, a systematic DFT study of the CO adsorption on realistic NP models has been carried out. Truncated octahedron shapes have been considered, in line to the equilibrium Wulff shape minimizing the NP surface tension [39]. The basic NPs contain 201 atoms, corresponding to ~1.5 nm size, comparable to the particles size in the PtCu_**S1** sample. Pure Pt_{201} was used as a reference, and an immaculate $Cu_{79}@Pt_{122}$ core@shell NP with ~40% at. Cu and ~60% at. Pt has been studied, modeling the experimentally synthesized PtCu_**S1** NPs. Other references, such as pure Cu_{201} and an inverse $Pt_{79}@Cu_{122}$ NP, have been studied as well, *vide supra*. Pt adatoms on Pt_{201} and $Cu_{79}@Pt_{122}$ template NPs were inspected, as an ultimate expression of Pt low-coordination. Also, surface Pt vacancies were generated, mimicking situations in which surface Cu atoms have been selectively oxidized (removed). Furthermore, partially surface oxidized models, still containing Cu surface atoms, were investigated, *e.g.* exchanging core Cu and surface Pt exchange positions — $Cu_{78}Pt@Pt_{121}Cu$—, in line with previous studies suggesting that such surface Cu atoms could be beneficial for the CO oxidation, serving as vicinal OH adsorbing centres [44]. Finally, we explored models with a surface Pt atom surrounded by Cu neighbours, see Figure 2, since such structures have been appointed to bind CO stronger than Pt(111) surfaces, where the CO adsorption may favour the surface segregation of the subsurface Cu and increase the stability of surface alloys [47].

A thorough DFT study on all the plethora of adsorption sites and CO connection ways was carried out employing the above-mentioned NP models. Notice that the goal here is to find particular surface sites or structures that, because of their nature, favour or disfavour the CO bond strength, which is regarded as the key factor determining the CO bias in the experimental CO stripping curves. However, one should refrain from direct comparing the adsorption energies changes with the observed peak shifts, as the latter are also affected by factors other than the specific NP surface structure, *e.g.* coverage, solvation, and presence of electrolytes, to name a few [48].

With that in mind, let us focus on the calculated adsorption energies. Not unexpectedly, the DFT results show stable M-CO adsorption through C atom. The top positions are found to be the most preferred, and even though bridge and hollow positions feature CO adsorption minima, CO molecule tends to displace from many of them upon relaxation, decreasing its coordination, *i.e.* hollow→bridge and bridge→top,

see Tables S2 and S3 of the SM. Thus, for a systematic comparison, only the top adsorption sites are discussed in the following, see Table 2, as they are present on all of the employed PtCu NP models and the Cu_{201} and Pt_{201} references.

Overall results on pure Cu and Pt@Cu NPs, as well as on isolated surface Cu atoms —$Cu_{78}Pt@Pt_{121}Cu$ NP model— reveal weaker CO adsorption compared to Pt_{201}, with the adsorption energy E_{ads} ranging from -0.35 eV —on $Cu_{78}Pt@Pt_{121}Cu$— to -1.25 eV —on Pt@Cu NP—, in line with data for $Pt_{146}Cu$ NP models [44], and clearly smaller in magnitude than on the corresponding sites of Pt_{201} NP, from -1.52 to -2.09 eV. As far as Cu@Pt NPs are concerned, the presence of surface Cu atoms would not prevent CO occupying exposed more strongly adsorbing surface Pt sites. So, surface Cu atoms would only lower the number of available Pt surface active sites per NP. Thus, only weaker CO bonding would be observed on pure Cu or Pt@Cu NPs. However, the Cu phase is not a viable substitute to the Pt phase in PEMFCs, plus the Pt@Cu NPs feature instability issues [26,27]. If any, as aforementioned, such surface Cu atoms could be beneficial for a somewhat stronger OH adsorption, which could tune the CO oxidation performance towards CO_2 [44].

Focusing on the CO adsorption on surface Pt atoms, a comparison is made between reference Pt_{201} NP, pristine $Cu_{79}@Pt_{122}$, and other Cu@Pt models where a Pt surface atom is fully surrounded by Cu atoms —having both surface and subsurface Cu neighbours— or superficially surrounded —having only surface Cu neighbours—. In the latter case, models were relaxed and analysed, in which the surface Cu atoms were removed, mimicking the aforementioned Cu selective oxidation used to prepare the PtCu **S1**-**S3** samples [25]. Figure 4 shows the difference of CO adsorption energy, ΔE_{ads}, for these four models with respect to the Pt_{201} NP reference, and reveals that the perfect Cu@Pt NP consistently features CO adsorption by 0.35 to 0.91 eV weaker, in line with the potential reductions shown in Figure 2, and as a result of Cu→Pt charge transfer and lowering of the *d*-band centre [27].

4.3. Effect of surface Cu

However, the exposure of surface Cu may disrupt this better performance, *e.g.* as a result of a partial selective Cu oxidation, a preference of Cu atoms to be located around surface corner sites at 50:50 Cu:Pt compositions [40], or due to the formation of a surface alloy [47]. Indeed, the NP model exposing surface Pt atoms fully surrounded by Cu atoms features still negative, yet more moderate ΔE_{ads} values, with E_{ads} reduced by

0.21 eV. The presence of Cu atoms around single Pt atoms may even lead to sites with a slightly stronger CO E_{ads} when compared to Pt_{201} NP, as calculated on terrace (001) sites; see Figure 4 and Table 2. Such a CO bond strengthening is aggravated when the surface Pt atom is just superficially surrounded by Cu atoms; thus, the presence of subsurface Pt atoms makes the exposed surface Pt atom a highly active site, strengthening the CO adsorption by up to 0.44 eV, in line with findings for PtCu surface alloy surfaces [47]. This clearly shows that the Pt surface isolation by Cu atoms is detrimental for resistance of PtCu nanoalloys to CO poisoning, and is a plausible explanation for the larger potential observed on PtCu_**S1** sample.

However, the above results have to be taken with caution, as such surface Cu may well be oxidized and dissolved in the course of several cycles of the CO stripping as that shown in Fig. 3. Still, the CO affinity can as well be counteracted or accentuated by this selective oxidation of the surface Cu, see Figure 4. Whenever surface Cu atoms surrounding the surface Pt active centre are removed, the resulting relaxed structure becomes distorted, featuring highly undercoordinated Pt atoms. The adsorption on such sites is quite similar to that on the Pt_{201} reference NP, although with some cases with a strengthened CO adsorption —Pt atom at **C**, see Section S2 of the SI— or a weakened CO adsorption —Pt atom at **F**.

4.4. Effect of surface undercoordinated Pt atoms and vacancies

Indeed, undercoordinated Pt atoms after the surface Cu removal display E_{ads} values larger in magnitude than the most stable **A** site on Pt_{201} model with E_{ads} = -2.07 eV; particularly, E_{ads} for the (001) and (111) facets on model **8** are -2.61 and -2.29 eV respectively, see Table 2. Other types of sites featuring stronger CO adsorption are Pt atoms of the model **7** surrounded by surface Cu atoms, yet having subsurface Pt neighbours, displaying E_{ads} of -2.22, -2.24, and -2.27 eV for **C**, **A**, and **B** sites, respectively. Clearly, Pt isolation, either Cu-surrounded, or as adatoms after Cu oxidation, seems to be a key factor in the CO bond strengthening explaining the peculiarity of the observed CO stripping curve of PtCu_**S1** sample with its peak at larger bias than for pure Pt. Note, that such sites with a stronger CO binding may well be present in other PtCu samples, however, their effect might be hidden for larger NPs exposing a majority of sites binding CO in a weaker fashion. Thus, the effect of the stronger binding sites may be relevant and observable for their statistically sound amount, as appears to be the case for smaller PtCu NPs.

To further substantiate this finding, we examined CO adsorption propensity of a Pt adatom on (001) and (111) facets of Pt_{201} *vs.* the Cu@Pt NP, and of Pt vacancies on the same facet for the same models, see Table 3. In particular, Pt adatom on (111) facets of the Cu@Pt model stabilizes the CO attachment by 0.28 eV. The vacancies of one and three missing Pt atoms strengthen the CO adsorption by 1.01 and 1.23 eV, respectively, due to a surface reconstruction leading to a distorted, and so, *a priori*, more active (111) facet. Indeed, CO adsorption on two sites of the Cu@Pt NP —the Pt adatom and the three-Pt atom (Pt_3) vacancy on the (111) facet— is stronger than on the most stable regular site of the Pt_{201} NP.

4.5. Electronic structure assessment of CO adsorption

The seemingly counterintuitive CO adsorption strengthening can be understood though a Bader charge analysis and charge density difference (CDD) plots, see Figure 5. Briefly, the stronger CO bonding is mainly due to the more negative charge of the surface Pt atom when it is Cu-surrounded compared to a pure Pt NP case. Such accentuated negatively charge site favours attraction to it of the $C^{\delta+}$ CO atom, see Bader charges in Tables S3 and S4 of the SM, and their corresponding discussion. Aside, CDD plots in Figure 5 reveal a donation/back-donation mechanism, where the aforementioned excess charge is back-donated from Pt 5*d* states to the $2\pi^*$ CO orbital, contributing to a stronger binding. This electron transfer is a common feature observed on Pt_3 vacancies and Pt adatoms attaching CO stronger to PtCu NPs than to pure Pt one.

4. Conclusions

To conclude, the CO stripping studies of differently synthesized and commercial PtCu NPs compared to pure Pt NPs reveal notably different CO adsorption behaviour. The latter depends on the synthesis method, which defines the size and structure of PtCu NPs indicating that well-shaped particles larger than 2 nm with low Cu content are more resilient towards CO poisoning. However, this CO resistance is compromised for core@shell PtCu NPs of *ca.* 1.5 nm with a relatively low Pt:Cu content of ~60:40. Rationalising these observations, the present DFT simulations on diverse PtCu models show, as expected, weakening of the CO adsorption on regular sites exposed by the Cu@Pt NPs. Interestingly, this effect is calculated to disappear on such sites as single Pt atoms surrounded by surface Cu ones or under-coordinated Pt atoms resulted *e.g.* from selective oxidation of surface Cu atoms. Indeed, Pt adatoms and few-atom Pt vacancies

in Cu@Pt NPs may even strengthen the CO binding, implying easier poisoning. The effect of these surface defects may get hidden in the presence of a majority of the regular sites, explaining the peak shifts and broadenings detected in the CO stripping voltammograms for differently prepared Cu@Pt NPs. Nevertheless, the effect can become critical for relatively small NPs, highlighting the importance of synthesis procedures in which the appearance of such defects is minimized and setting a size threshold for the employment of PtCu samples as electrocatalysts in PEMFCs. Aside, in order to avoid such CO poisoning enhancement by the surface presence of Cu, or the formation of Pt defects, the PtCu NP synthesis should be driven towards forming a complete and uniform Pt shell, probably favoured by a slow cationic exchange and working temperatures enabling the atomic rearrangement within the NPs.

Acknowledgements

The work has been supported by the *Ministerio de Ciencia y Universidades* (MICIUN) RTI2018-095460-B-I00, PGC2018-093863-B-C22, and CTQ2016-78616-R research grants, and by the Spanish Structures of Excellence *María de Maeztu* program through grant MDM-2017-0767. The research was also funded by the *Agencia Estatal de Investigación* (AEI, Spain) under project number PID2019-109291RB-I00 and the Generalitat de Catalunya (AGAUR, Spain) through the FI-SDUR PhD scholarship received by J.G.C. (2020 FISDU 00005). The authors are grateful to the CCiT-UB (Scientific and Technological Centers of the Universitat de Barcelona) for their support with the XRD analyses. The authors are also grateful to *Generalitat de Catalunya* for the pre-doctoral grant 2018FI-B-00384 for L.V. and partial support through grants 2017SGR13 and XRQTC. F.V. is thankful to *Ministerio de Economía y Competitividad* (MEC) for his *Ramón y Cajal* (RYC-2012-10129) research contract. The authors are thankful to *Red Española de Supercomputación* (RES) for the granted computing time (QS-2020-1-0002 and QS-2020-2-0006).

Appendix A. Supplementary Material

The following supplementary information related to this article can be found, in the online version, at DOI:

Sampled adsorption sites; adsorptive results on different NP models for bridge and hollow sites; electronic analysis of Bader charges, and computed Bader charges.

Fig. 1. XRD patterns of the studied Pt and PtCu catalysts. a) Extended XRD diffractograms and b) magnification of the peaks with higher intensity. The diffraction angles of pure Pt and Cu crystallites have been marked for comparison.

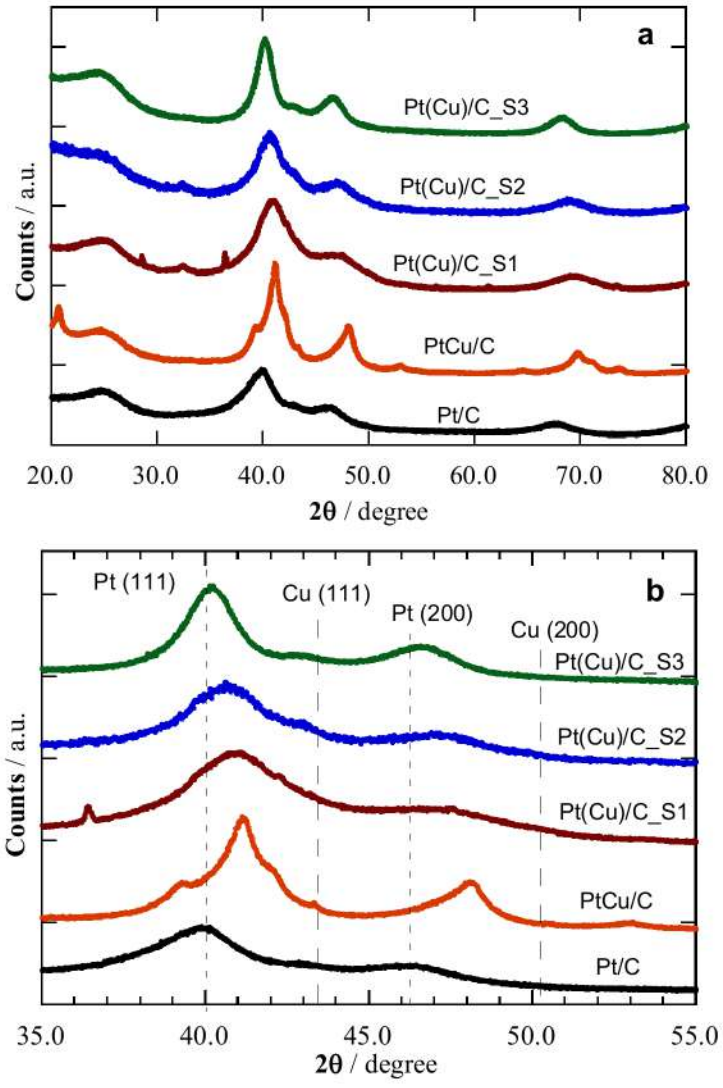

Fig. 2. Eagle-eye views of the different employed NP models: **1:** pure Pt_{201}; **2:** pure Cu_{201}; **3:** $Cu_{79}@Pt_{122}$ – perfect Cu-core@Pt-shell; **4:** $Pt_{79}@Cu_{122}$ – perfect Pt-core@Cu-shell; **5:** $Cu_{78}Pt@Pt_{121}Cu$ – an example of exchanging a core Cu atom with a surface Pt atom (a corner site in the example); **6:** $Cu_{79}@Pt_{117}Cu_5$ – with a surface Pt atom (a corner site in the example) surrounded by surface Cu atoms; **7:** $Cu_{76}Pt_3@Pt_{117}Cu_5$ – as in **6**, but with the Pt atom surrounded by 5 surface Cu atoms and 3 subsurface Pt atoms; **8:** $Cu_{76}Pt_3@Pt_{117}$ – resulted from **7** by removing 5 surface Cu atoms and subsequent geometry optimization. Pt and Cu atoms are shown as blue and brown spheres.

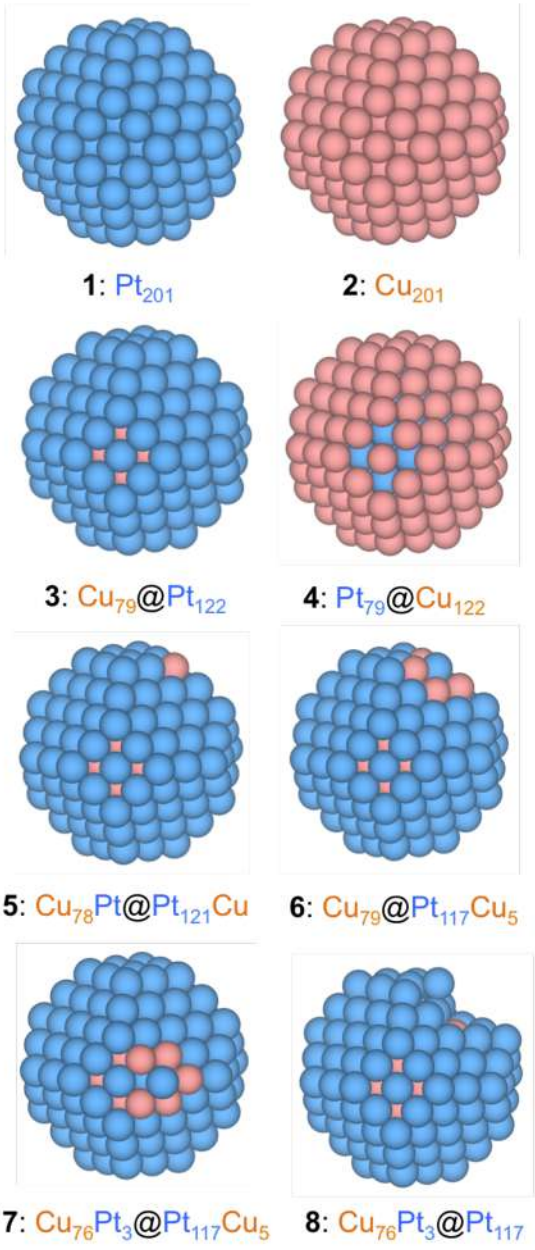

Fig. 3. (a) CO stripping curves of PtCu and reference Pt samples in deaerated 0.5 mol·dm^{-3} H_2SO_4 at a scan rate of 20 mV·s^{-1}. (b) Magnification of the curves to better visualise the onset potential for CO oxidation.

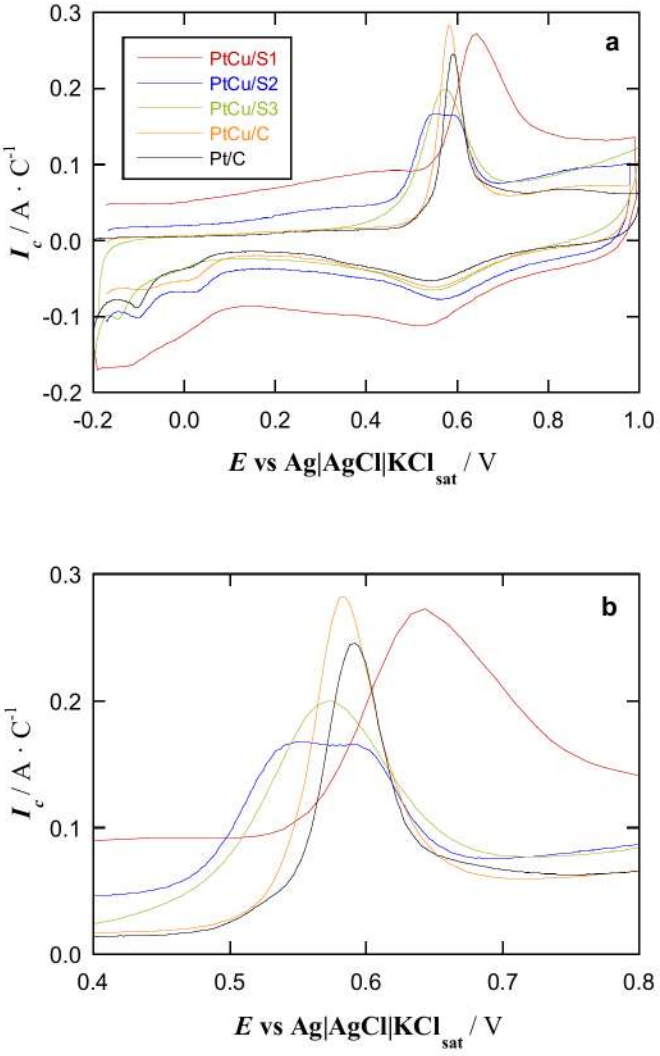

Fig. 4. Differences in CO adsorption energies, ΔE_{ads}, on PtCu NPs with respect to reference Pt_{201} NP, calculated for all topologically different top sites, see Figure S1 of the SI. From top to bottom, perfect Cu@Pt core@shell NP —model **3**, see Figure 3— with a surface Pt atom fully coordinated to Cu atoms —model **6**—, with a surface Pt atom coordinated to surface Cu atoms —model **7**—, and model **8** resulting from removal of five surface Cu atoms from model **7** and subsequent optimization. Sites **A**-**D** are shown in model **1**, but are the same for the rest of models **6**-**8**.

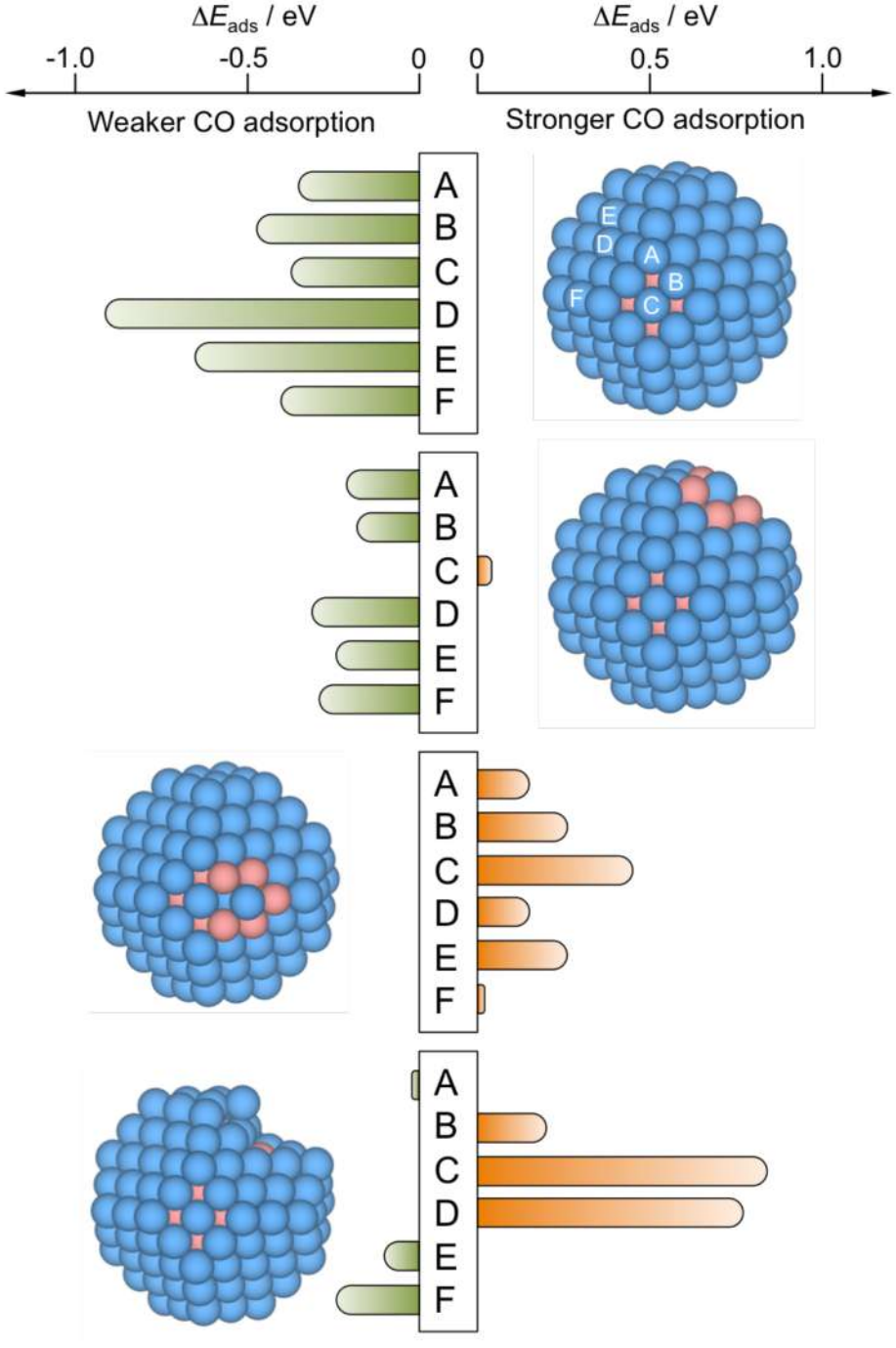

Fig. 5. CDD plots of PtCu NPs (right images) with stronger CO adsorption than on the corresponding sites of purely Pt NPs (left images): a) **A** site on Pt_{201} *vs.* it superficially Cu-surrounded, and having subsurface Pt neighbours; b) CO Adsorption on the centre of 3 Pt atom terrace (111) vacancy of Pt_{201} and on 3 Pt atom terrace (111) vacancy restructured surface of core@shell Cu_{79}@Pt_{122}; c) CO Adsorption on terrace (111) Pt adatom of Pt_{201} and core@shell Cu_{79}@Pt_{122}. Cyan and yellow contours denote electron density depletion and accumulation regions, displayed for values of ±0.001 e·Bohr^3.

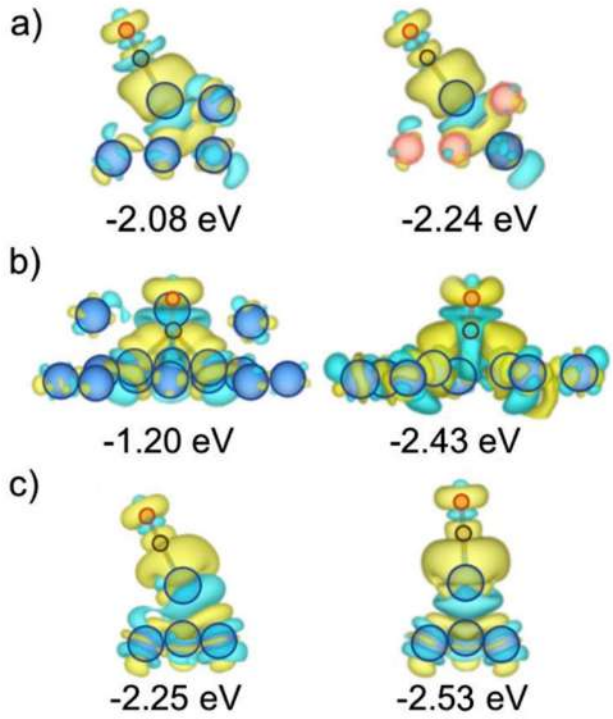

Table 1. Structural data of the catalysts obtained from the XRD analyses. The mean crystallite sizes have been determined by Scherrer's equation and the Pt:Cu at.% ratios have been obtained from Vegard's law.

Catalyst	Crystallite size / nm	Pt:Cu ratio / at.%	Lattice parameter (*a*) / nm
PtCu/C_S1	1.5	64:36	0.3814
PtCu/C_S2	2.0	73:27	0.3838
PtCu/C_S3	3.5	91:9	0.3885
PtCu/C	3.4	57:43	0.3805
Pt/C	2.6	100:0	0.3911

Table 2. Adsorption energies, E_{ads}, in eV, for CO adsorbed in different top positions, see Fig. 2 for different models, and sites in Figure S1 of the SM.

Model / Site	A	B	C	D	E	F
1	-2.08	-2.01	-1.77	-1.52	-1.68	-2.05
2	-0.98	-0.90	-0.79	-0.60	-0.62	-0.86
3	-1.74	-1.54	-1.40	-0.61	-1.03	-1.65
4	-1.25	-1.15	-1.09	-0.97	-0.97	-1.13
5	-0.95	-0.82	-0.60	-0.35	-0.45	-0.88
6	-1.88	-1.83	-1.81	-1.21	-1.44	-1.76
7	-2.24	-2.27	-2.22	-1.67	-1.94	-2.07
8	-2.07	-2.21	-2.61	-2.29	-1.58	-1.81

Table 3. CO adsorption energies, E_{ads}, calculated on a Pt adatom or Pt_n vacancies defects in core@shell $Cu_{79}@Pt_{12}$, as well as on reference Pt_{201} model NPs. Values are given in eV.

Facet	Site	$Cu_{79}@Pt_{122}$	Pt_{201}
(001)	Pt adatom	-1.96	-1.95
	Pt vacancy	-1.88	-2.02
(111)	Pt adatom	-2.53	-2.25
	Pt_1 vacancy	-1.70	-0.69
	Pt_3 vacancy	-2.43	-1.21
	Pt_7 vacancy	-0.73	-1.69

References

[1] D. Thompsett, D. *Pt* Alloys as Oxygen Reduction Catalysts. Handbook of Fuel Cells. Fundamentals, Technology and Applications, John Wiley & Sons, New York, 2003.

[2] M.K. Mahapatra, P. Singh, Fuel Cells: Energy Conversion Technology, Future Energy: Improved, Sustainable and Clean Options for our Planet, Elsevier, London, 2014.

[3] M.K. Debe, Nature 486 (2012) 43–51.

[4] S. Sui, X. Wang, X. Zhou, Y. Su, S. Riffat, C.-J. Liu, J. Mater. Chem. A 5 (2017) 1808–1825.

[5] K. Ruth, M. Vogt, R. Zuber, Development of CO-Tolerant Catalysts on Pt/Ru Catalysts, John Wiley & Sons, New York, 2010.

[6] P. Janthon, F. Viñes, J. Sirijaraensre, J. Limtrakul, F. Illas, J. Phys. Chem. C 121 (2017) 3970–3977.

[7] A. Velázquez-Palenzuela, E. Brillas, C. Arias, F. Centellas, J.A. Garrido, R.M. Rodríguez, P.L. Cabot, J. Catal. 298 (2013) 112–121.

[8] V.R. Stamenkovic, B.S. Mun, M. Arenz, K.J.J. Mayrhoffer, C.A. Lucas, G. Wang, P.N. Ross, N.M. Markovic, Nat. Mater. 6 (2007) 241–247.

[9] Y. Shao, G. Yin, Y. Gao, J. Power Sources 171 (2007) 558–566.

[10] M. Gatalo, M. Bele, F. Ruiz-Zepeda, E. Šest, M. Šala, A.R. Kamšek, N. Maselj, T. Galun, P. Jovanovič, N. Hodnik, M. Gaberšček, Angew. Chem. Int. Ed. 58 (2019) 13266–13270.

[11] N. Kristian, Y. Yu, J.-M. Lee, X. Liu, X. Wang, Electrochim. Acta 56 (2010) 1000–1007.

[12] V.V. Pham, V.-T. Ta, C. Sunglae, Int. J. Hydrogen Energy 42 (2017) 13192–13197.

[13] B.B. Bokhonov, D.V. Dudina, J. Alloys Compd. 707 (2017) 233–237.

[14] M.M.S. Pupo, F.E. López-Suárez, A. Bueno-López, C.T. Menses, K.I.B. Eguiluz, G.R. Salazar-Banda, J. Appl. Electrochem. 45 (2015) 139–150.

[15] K.M. El-Khatib, R.M. Abdel Hameed, R.S. Amin, A.E. Fetochi, Microchem. J. 145 (2019) 566–577.

[16] S. Wojtysiak, M. Kamiński, J. Krajczewski, P. Dłużewski, A. Kudelski, Vib. Spectrosc. 75 (2014) 11–18.

[17] A. Sarkar, A. Manthiram, J. Phys. Chem. C 114 (2010) 4725–4732.

[18] S. Baek, K.H. Kim, M.J. Kim, J.J. Kim, Appl. Catal. B: Environ. 217 (2017) 313–321.

[19] A.A. Gokhale, J.A. Dumesic, M. Mavrikakis, J. Am. Chem. Soc. 130 (2008) 1402–1414.

[20] Y. Hori, A. Murata, R. Takahashi, S. Suzuki, J. Am. Chem. Soc. 109 (1987) 5022–5023.

[21] G. Caballero-Manrique, A. Velázquez-Palenzuela, E. Brillas, F. Centellas, J.A. Garrido, R.M. Rodríguez, P.L. Cabot, Int. J. Hydrogen Energy 39 (2014) 12859–12869.

[22] I. Mintsouli, J. Georgieva, S. Armyanov, E. Valova, G. Avdeev, A. Hubin, O. Steenhaut, J. Dille, D. Tsiplakides, S. Balomenou, S. Sotiropoulos, Appl. Catal. B – Environ. 136-137 (2013) 160–167.

[23] J. Georgieva, E. Valova, I. Mintsouli, S. Sotiropoulos, S. Armyanov, A. Kakaroglou, A. Hubin, O. Steenhaut, J. Dille, J. Appl. Electrochem. 44 (2014) 215–224.

[24] V.V. Pryadchenko, V.V. Srabionyan, A.A. Kurzin, N.V. Bulat, D.B. Shemet, L.A. Avakyan, S.V. Belenov, V.A. Volochaev, I. Zizak, V.E. Guterman, L.A. Bugaev, Appl. Catal. A - Gen. 525 (2016) 226–236.

[25] J. Garcia-Cardona, I. Sirés, F. Alcaide, E. Brillas, F. Centellas, P.L. Cabot, Int. J. Hydrogen Energy 45 (2020) 20582–20593.

[26] S. Zhou, B. Varughese, B. Eichhorn, G. Jackson, K. McIlwrath, Angew. Chem. Int. Ed. 44 (2005) 4539–4543.

[27] F. Viñes, A. Görling, Chem. Eur. J. 26 (2020) 11478–11491.

[28] Z.-J. Zhao, R. Mu, X. Wang, J. Gong, Langmuir 33 (2017) 8700–8706.

[29] G. Giannakakis, M. Flytzani-Stephanopoulos, E.C.H. Sykes, Acc. Chem. Res. 52 (2019) 237–247.

[30] J. Solla-Gullón, V. Montiel, A. Aldaz, J. Clavilier, J. Electrochem. Soc. 150 (2003) E104–E109.

[31] G. Kresse, J. Furthmüller, Phys. Rev. B 54 (1996) 11169–11186.

[32] G. Kresse, J. Hafner, Phys. Rev. B 49 (1994) 14251–14269.

[33] J.P. Perdew, K. Burke, M. Ernzerhof, Phys. Rev. Lett. 77 (1996) 3865–3868.

[34] P.E. Blöchl, Phys. Rev. B 50 (1994) 17953–17979.

[35] G. Kresse, D. Joubert, Phys. Rev. B 59 (1999) 1758–1775.

[36] P. Janthon, F. Viñes, J. Sirijaraensre, J. Limtrakul, F. Illas, J. Phys. Chem. C 121 (2017) 3970–3977.

[37] F. Viñes, F. Illas, K.M. Neyman, Angew. Chem. Int. Ed. 46 (2007) 7094–7097.

[38] M. Happel, N. Luckas, F. Viñes, M. Sobota, M. Laurin, A. Görling, J. Libuda, J. Phys. Chem. C 15 (2011) 479–491.

[39] J. Ruvireta, L. Vega, F. Viñes, Surf. Sci. 664 (2017) 45–49.

[40] L. Vega, H.A. Aleksandrov, R. Farris, A. Bruix, F. Viñes, K.M. Neyman, Mater. Adv. 2 (2021) 6457-6734.

[41] H.A. Gasteiger, N.M. Markovic, P.N. Ross Jr., J. Phys. Chem. 99 (1995) 8290–8298.

[42] G. Caballero-Manrique, E. Brillas, F. Centellas, J.A. Garrido, R.M. Rodríguez, P.L. Cabot, Catalysts 5 (2015) 815–837.

[43] A.A. Alekseenko, V.E. Guterman, S.V. Belenov, V.S. Menshikov, N.Y. Tabachkova, O.I. Safronenko, E.A. Moguchikh, Int. J. Hydrogen Energy 43 (2018) 3676–3687.

[44] L. Luo, L. Zhang, Z. Duan, A.S. Lapp, G. Henkelman, R.M. Crooks, ACS Nano 10 (2016) 8760-8769.

[45] R.M. Castagna, J.M. Sieben, A.E. Alvarez, M.M.E. Duarte, Int. J. Hydrogen Energy 44 (2019) 5970–5982.

[46] M.R. Zamanzad Ghavidel, A.H.A. Monteverde Videla, S. Specchia, E. Bradley Easton, Electrochim. Acta 230 (2017) 58–72.

[47] K.J. Andersson, I. Chorkendorff, Surf. Sci. 604 (2010) 1733–1736.

[48] E.V. Carino, H.Y. Kim, G. Henkelman, R.M. Crooks, J. Am. Chem. Soc. 134 (2012) 4153–4162.

PART IV. CONCLUSIONS

Partial conclusions resulting from each study have been already provided in the end of the corresponding Chapters. These are the general conclusions related to the objectives formulated in the Chapter 1 Overview of the Thesis:

- Performance assessment of LDA, GGA and meta-GGA *xc* functionals VWN, PBE, PBEsol, RPBE and TPSS, to describe surface properties of transition metals such as the surface energy, work function and interlayer distance revealed that PBEsol is the most accurate functional. Considering also the previously examined bulk properties[38,39] such as cohesive energy, bulk modulus, and minimum interatomic distance, PBE functional resulted to be the best overall *xc* functional under scrutiny in describing general properties of transition metals.
- Evaluation for VWN, PBE and TPSS functionals showed that the *d*-band centre is a more robust surface electronic descriptor than other descriptors such as the width-corrected *d*-band centre and the maximum peak of the imaginary part of Hilbert transformation of the *d*-projected DOS. Although this is consistent with the previous finding for bulk electronic descriptors,[40] the transferability between different functionals of bulk descriptors is better than surface ones.
- Analysis of the performance of PBE and PBEsol functionals opened a possibility of improving functionals by modifying their exchange (μ) and correlation (β) parameters. Scanning the 2-dimensional μ/β error surface between PBE and PBEsol resulted in the functional called VV with $\mu = 0.2099$ and $\beta = 0.0667$. Restoring the LSD approximation not fulfilled in the PBEsol functional resulted in the functional called VVsol. The new functionals allowed improving the description of bulk and surface properties of transition metals by 5-8% and 6-10%, respectively, over PBE and PBEsol functionals, which exceeds the improvement for surface properties exhibited by PBEsol functional compared to PBE one.

- For monometallic bare Pd nanoparticles icosahedral shape is found to be more stable than other shapes of Pd nanoparticles up to *ca.* 4 nm size and *ca.* 1500 atoms. Truncated octahedron shape becomes the most stable at larger sizes of Pd nanoparticles, but with exposure of {001} facets which are larger than expected from the Wulff construction approach. The cohesive energy of Pd nanoparticles of different sizes and shapes is found to be quantitatively described employing the proportion of atoms with different coordination numbers. However, considering such geometric features as number of corners, length of edges, area of facets and volume of the nanoparticles allows only for a qualitative estimate of the cohesive energy.
- Chemical orderings of bimetallic nanoparticles containing combinations of different metals PdRh, PtNi, PtAg, PtAu and PtCu were determined using a combination of DFT calculations with the Topological method. Pd atoms in PdRh nanoparticles are found to prefer locations in the outer surface shell and to avoid mixing with Rh atoms. This results in a trend of forming core@shell Rh@Pd ordering. Similar orderings are obtained for PtAg and PtAu particles, with Ag and Au atoms occupying surface positions. In PtNi particles, Pt atoms are those preferring surface location and stabilizing Pt-Ni bonds favoring mixing, enabling the appearance of surface Ni atoms even when enough Pt atoms to complete the skin layer are present. Similarly, Pt atoms are more stable on the surface of PtCu nanoparticles, preferring terrace {111} positions. For all studied combinations of metals, the Topological equations fitted on DFT data for nanoparticles with up to *ca.* 200 atoms are used to predict the chemical ordering of particles too large be treated at DFT level. For the latter particles temperature effects on their ordering patterns were simulated, revealing, as expected, disordering of core@shell patterns stable at 0 K and appearance of inner atoms on the surface. Based on adsorption energies of molecules and atoms commonly present in the reactive environment calculated on the (111)-surface of each metal forming the binary nanoalloy modifications in

the chemical ordering were predicted due to resurfacing of the metal, which more strongly binds the species from the environment.

- The Topological method enables predicting the most energetically stable trends of chemical ordering of bimetallic nanoparticles in a simple way and rationalizing, which interactions trigger the predicted ordering. One of the simplifications is considering solely the first-neighbour interactions of atoms and not differentiating between atoms from different surface terminations. Therefore, many homotops belonging to the same topology are assigned the same energy in the Topological equations, neglecting the actual energy splitting for this group of the homotops. Also, focusing of the present formulation of the Topological method on the description of the surface as most important part of systems for catalytic applications results in that subsurface atoms are not distinguished from the more inner atoms. These limitations of the method were analysed in view of not capturing by it some exotic ordering arrangements of bimetallic nanoparticles (see Appendix H) and in order to evaluate energy inaccuracies in the description of individual homotops.
- Depending on the method used for synthesizing Cu@Pt nanoparticles, some sites featuring stronger CO binding than the homologous pure Pt sites could be exposed, resulting in enhanced CO poisoning compared to purely Pt nanoparticles. Based on DFT calculations of a series of dedicated models these sites stronger binding CO molecules are found to be: *i)* single Pt atoms surrounded by surface Cu ones, *ii)* under-coordinated Pt adatoms and *iii)* few-atom Pt vacancies in Cu@Pt nanoparticles.

LIST OF PUBLICATIONS

Published articles in refereed journals included in the Thesis:

- Vega, L., Ruvireta, J., Viñes, F. & Illas, F. Jacob's ladder as sketched by escher: Assessing the performance of broadly used density functionals on transition metal surface properties. *Journal of Chemical Theory and Computation* **14**, 395–403 (2018).
- Vega, L., Martínez, B., Viñes, F. & Illas, F. Robustness of surface activity electronic structure-based descriptors of transition metals. *Physical Chemistry Chemical Physics* **20**, 20548–20554 (2018).
- Vega, L., Aleksandrov, H. A. & Neyman, K. M. Using density functional calculations to elucidate atomic ordering of Pd-Rh nanoparticles at sizes relevant for catalytic applications. *Chinese Journal of Catalysis* **40**, 1749–1757 (2019).
- Khalakhan, I., Vega, L., Vorokhta, M., Skála, T., Viñes, F., Yakovlev, Y. V., Neyman, K. M. & Matolinova, I. Irreversible structural dynamics on the surface of bimetallic PtNi alloy catalyst under alternating oxidizing and reducing environments. *Applied Catalysis B: Environmental* **264**, 118476 (2020).
- Vega, L. & Viñes, F. Generalized gradient approximation adjusted to transition metals properties: Key roles of exchange and local spin density. *Journal of Computational Chemistry* **41**, 2598–2603 (2020).
- Vega, L., Aleksandrov, H. A., Farris, R., Bruix, A., Viñes, F. & Neyman, K. M. Chemical ordering in Pt–Au, Pt–Ag and Pt–Cu nanoparticles from density functional calculations using a topological approach. *Materials Advances* **2**, 6589–6602, (2021).
- Vega, L., Viñes, F. & Neyman, K.M, Unravelling morphological and topological key aspects of Pd nanoparticles. ***Submitted***.
- Vega, L., Garcia-Cardona, J., Viñes, F., Cabot, P.L. & Neyman, K.M, Nanostructuring determines poisoning: tailoring CO adsorption on PtCu bimetallic nanoparticles. ***Submitted.***

Other publications, to which the Thesis author contributed:

- Olobardi, S., Vega, L., Fortunelli, A., Stener, M., Viñes, F. & Neyman, K. M. Optical Properties and Chemical Ordering of Ag–Pt Nanoalloys: A Computational Study. *The Journal of Physical Chemistry C* **123**, 25482–25491 (2019).
- Danielis, N., Vega, L., Fronzoni, G., Stener, M., Bruix, A., & Neyman, K. M. AgPd, AuPd, and AuPt Nanoalloys with Ag-or Au-Rich Compositions: Modeling Chemical Ordering and Optical Properties. *The Journal of Physical Chemistry C* **125**, 17372–17384 (2021).

Journals Covers:

- Vega, L. & Viñes, F., Front Cover Image. *Journal of Computational Chemistry* **41**: C1-C1 (2020). DOI: 10.1002/jcc.26436
- Vega L., Aleksandrov, H. A., Farris, R., Bruix, A., Viñes, F. & Neyman K.M., Front Cover Image. *Materials Advances* **2**, 6457 (2021). DOI: 10.1039/D1MA90103F. This journal cover was based on the Thesis cover.

APPENDIX

A. Supplementary Information of Jacob's Ladder as Sketched by Escher: Assessing the Performance of Broadly-Used Density Functionals on Transition Metal Surface Properties

Table S1. Calculated surface energies γ^{calc} as obtained using Vosko-Wilk-Nussair (VWN), Perdew-Burke-Ernzerhof (PBE), PBE for solids (PBEsol), revised PBE (RPBE), and Tao-Perdew-Staroverov-Scuseria (TPSS) exchange-correlation (xc) functionals for each studied transition metal (TM), and each surface, alongside with the zero temperature extrapolated experimental surface energy, γ^{exp}. All values are given in J/m^2.

γ (J/m^2)	Surface	VWN	PBEsol	PBE	RPBE	TPSS	Exp.[1]
Zr	**(0001)**	1.81	1.75	1.59	1.48	1.89	2.00
	(10$\bar{1}$0)	1.85	1.79	1.63	1.52	1.93	
	(11$\bar{2}$0)	1.91	1.82	1.64	1.52	1.91	
Zn	**(0001)**	0.59	0.53	0.35	0.22	0.41	0.91
	(10$\bar{1}$0)	0.90	0.80	0.57	0.44	0.87	
	(11$\bar{2}$0)	1.35	1.21	0.91	0.73	1.12	
Y	**(0001)**	1.14	1.10	1.00	0.93	1.16	1.13
	(10$\bar{1}$0)	1.13	1.08	0.98	0.90	1.11	
	(11$\bar{2}$0)	1.17	1.11	1.02	0.94	1.15	
Ti	**(0001)**	2.07	2.16	1.97	1.84	2.14	2.10
	(10$\bar{1}$0)	2.27	2.19	2.00	1.87	2.13	
	(11$\bar{2}$0)	2.18	2.07	1.88	1.73	2.00	
Tc	**(0001)**	2.73	2.58	2.22	2.02	2.52	3.15
	(10$\bar{1}$0)	3.10	2.98	3.43	2.40	3.03	
	(11$\bar{2}$0)	3.23	3.09	2.69	2.47	3.23	
Sc	**(0001)**	1.47	1.41	1.28	1.19	1.41	1.28
	(10$\bar{1}$0)	1.40	1.32	1.21	1.11	1.31	
	(11$\bar{2}$0)	1.45	1.37	1.26	1.16	1.35	
Ru	**(0001)**	3.13	2.95	2.55	2.33	3.10	3.05
	(10$\bar{1}$0)	3.51	3.32	2.87	2.64	3.43	
	(11$\bar{2}$0)	4.03	3.81	3.32	3.05	3.97	
Re	**(0001)**	3.11	2.96	2.60	2.36	2.84	3.60
	(10$\bar{1}$0)	3.40	3.31	2.93	2.49	3.44	
	(11$\bar{2}$0)	3.62	3.53	3.12	2.69	3.14	
Os	**(0001)**	3.44	3.29	2.91	2.70	3.30	3.45
	(10$\bar{1}$0)	3.90	3.29	3.32	3.11	3.72	
	(11$\bar{2}$0)	4.67	4.35	4.02	3.77	4.48	
Hf	**(0001)**	1.95	1.89	1.71	1.61	1.80	2.15
	(10$\bar{1}$0)	2.07	2.01	1.84	1.73	2.08	
	(11$\bar{2}$0)	2.11	2.02	1.83	1.70	2.08	
Co	**(0001)**	2.79	3.21	2.10	2.75	3.14	2.55
	(10$\bar{1}$0)	2.95	2.68	2.26	2.00	3.63	

	(11$\bar{2}$0)	4.16	3.72	2.44	2.16	2.15	
Cd	**(0001)**	0.44	0.36	0.20	0.06	0.37	0.69
	(10$\bar{1}$0)	0.62	0.52	0.61	0.19	0.53	
	(11$\bar{2}$0)	0.90	0.77	0.50	0.31	0.59	
Rh	**(001)**	3.44	2.71	2.27	2.01	2.80	2.70
	(011)	3.33	2.74	2.29	2.01	2.81	
	(111)	2.88	2.10	1.72	1.49	2.16	
Pt	**(001)**	2.48	2.30	1.90	1.66	2.16	2.48
	(011)	2.57	2.38	1.95	1.70	2.27	
	(111)	2.09	1.92	1.56	1.34	1.81	
Pd	**(001)**	2.10	1.89	1.50	1.25	1.38	2.05
	(011)	2.17	1.95	1.54	1.27	1.53	
	(111)	1.68	1.48	1.14	0.91	1.38	
Ni	**(001)**	2.87	2.62	2.19	1.92	4.72	2.45
	(011)	2.96	2.70	2.27	1.99	4.14	
	(111)	2.62	2.34	1.93	1.66	4.97	
Ir	**(001)**	3.40	3.23	2.79	2.56	3.02	3.00
	(011)	3.44	3.25	2.79	2.54	3.04	
	(111)	2.55	2.40	2.05	1.83	2.32	
Cu	**(001)**	2.03	1.83	1.46	1.22	2.78	1.83
	(011)	2.08	1.90	1.51	1.27	2.30	
	(111)	1.79	1.62	1.28	1.06	2.62	
Au	**(001)**	1.37	1.19	0.86	0.64	1.19	1.50
	(011)	1.38	1.19	0.86	0.63	1.17	
	(111)	1.12	0.96	0.68	0.48	0.93	
Ag	**(001)**	1.30	1.10	0.80	0.59	1.16	1.25
	(011)	1.34	1.14	0.83	0.62	1.42	
	(111)	1.14	0.97	0.69	0.49	1.03	
W	**(001)**	4.25	4.24	3.89	3.71	4.30	3.68
	(011)	3.46	3.45	3.14	2.98	3.44	
	(111)	3.88	3.84	3.47	3.30	3.83	
V	**(001)**	2.92	2.67	2.40	2.19	2.87	2.55
	(011)	2.88	2.70	2.41	2.26	2.79	
	(111)	3.24	3.00	2.70	2.50	3.86	
Ta	**(001)**	2.92	2.79	2.51	2.34	1.22	3.15
	(011)	2.70	2.79	2.56	2.23	0.28	
	(111)	3.15	3.00	2.72	2.57	2.11	
Nb	**(001)**	2.77	2.63	2.35	2.17	1.26	2.70
	(011)	2.46	2.38	2.14	1.99	0.42	
	(111)	2.79	2.64	2.36	2.20	1.91	
Mo	**(001)**	3.43	3.34	3.01	2.81	3.45	3.00
	(011)	3.04	2.95	2.64	2.46	3.01	
	(111)	3.48	3.33	2.98	2.79	3.44	

Fe	**(001)**	4.15	3.05	2.58	2.84	7.17	2.48
	(011)	3.08	3.03	2.93	2.13	10.48	
	(111)	3.58	3.18	2.67	2.33	5.04	
Cr	**(001)**	7.15	3.83	3.42	3.20	5.30	2.30
	(011)	3.63	3.42	3.29	2.85	5.42	
	(111)	4.06	3.81	3.40	3.17	4.71	

Table S2. Proportion (in %) of each surface expressed according to Wulff construction as obtained at each density functional theory (DFT) xc level.

Wulff %	Surface	VWN	PBEsol	PBE	RPBE	TPSS
Zr	**(0001)**	34.15	34.00	33.96	33.90	33.76
	(10$\bar{1}$0)	39.27	36.31	34.71	32.15	30.45
	(11$\bar{2}$0)	26.59	29.69	31.33	33.96	35.80
Zn	**(0001)**	43.00	43.26	45.23	49.58	51.37
	(10$\bar{1}$0)	57.00	56.74	54.77	50.42	48.63
	(11$\bar{2}$0)	0.00	0.00	0.00	0.00	0.00
Y	**(0001)**	33.34	33.15	33.05	32.91	32.55
	(10$\bar{1}$0)	40.61	41.09	43.54	44.23	43.30
	(11$\bar{2}$0)	26.05	25.76	23.41	22.87	24.15
Ti	**(0001)**	34.76	32.74	32.67	32.43	32.19
	(10$\bar{1}$0)	23.02	20.00	18.56	15.49	18.24
	(11$\bar{2}$0)	42.22	47.26	48.78	52.08	49.57
Tc	**(0001)**	36.60	36.91	37.71	37.58	37.98
	(10$\bar{1}$0)	41.12	39.29	0.00	37.10	44.40
	(11$\bar{2}$0)	22.29	23.80	62.29	25.33	17.62
Sc	**(0001)**	32.47	32.31	32.34	32.16	32.01
	(10$\bar{1}$0)	41.55	42.41	43.95	44.55	40.93
	(11$\bar{2}$0)	25.99	25.28	23.71	23.29	27.06
Ru	**(0001)**	35.96	36.05	36.01	36.19	35.64
	(10$\bar{1}$0)	62.86	62.71	63.99	63.81	64.36
	(11$\bar{2}$0)	1.17	1.23	0.00	0.00	0.00
Re	**(0001)**	35.76	36.27	36.45	34.95	36.05
	(10$\bar{1}$0)	45.83	46.22	45.23	49.76	12.21
	(11$\bar{2}$0)	18.41	17.51	18.32	15.28	51.74
Os	**(0001)**	36.13	33.35	36.33	36.50	36.09
	(10$\bar{1}$0)	63.87	66.65	63.67	63.50	63.91
	(11$\bar{2}$0)	0.00	0.00	0.00	0.00	0.00
Hf	**(0001)**	34.82	34.79	34.85	34.79	36.62
	(10$\bar{1}$0)	36.72	33.51	31.58	29.03	31.58
	(11$\bar{2}$0)	28.46	31.70	33.57	36.17	31.80
Co	**(0001)**	34.54	29.39	35.41	27.03	25.52
	(10$\bar{1}$0)	65.46	70.61	49.39	55.82	0.00
	(11$\bar{2}$0)	0.00	0.00	15.19	17.15	74.48
Cd	**(0001)**	41.22	42.09	56.46	61.39	42.26
	(10$\bar{1}$0)	58.78	57.91	0.00	38.61	52.10
	(11$\bar{2}$0)	0.00	0.00	43.54	0.00	5.64
Rh	**(001)**	18.45	12.38	10.57	8.84	11.93
	(011)	13.67	0.00	0.00	0.00	0.00

	(111)	67.88	87.62	89.43	91.16	88.07
Pt	**(001)**	19.58	20.13	17.40	15.71	19.02
	(011)	0.00	0.00	0.00	0.00	0.00
	(111)	80.42	79.87	82.60	84.29	80.98
Pd	**(001)**	15.03	13.12	10.38	7.70	37.48
	(011)	0.00	0.00	0.00	0.00	14.80
	(111)	84.97	86.88	89.62	92.30	47.72
Ni	**(001)**	27.03	25.14	24.41	22.36	11.03
	(011)	16.52	11.58	8.72	5.03	88.69
	(111)	56.44	63.28	66.87	72.62	0.28
Ir	**(001)**	9.70	9.08	8.24	6.78	11.54
	(011)	0.00	0.00	0.00	0.00	0.00
	(111)	90.30	90.92	91.76	93.22	88.46
Cu	**(001)**	23.92	24.39	23.07	22.25	6.18
	(011)	10.78	8.84	7.19	2.97	90.24
	(111)	65.30	66.76	69.74	74.78	3.58
Au	**(001)**	16.36	15.64	13.72	10.03	12.82
	(011)	0.00	0.00	0.00	0.00	0.00
	(111)	83.64	84.36	86.28	89.97	87.18
Ag	**(001)**	23.40	23.54	17.39	19.59	24.79
	(011)	7.95	7.15	23.94	0.00	0.00
	(111)	68.65	69.31	58.67	80.41	75.21
W	**(001)**	5.05	4.99	3.99	4.17	3.99
	(011)	89.48	87.72	89.57	87.71	89.57
	(111)	5.47	7.29	6.45	8.12	6.45
V	**(001)**	25.60	28.88	28.36	32.72	23.36
	(011)	68.91	63.26	65.37	58.03	76.64
	(111)	5.49	7.86	6.26	9.25	0.00
Ta	**(001)**	16.95	27.47	31.20	20.22	0.00
	(011)	81.29	60.17	53.59	77.25	100.00
	(111)	1.77	12.36	15.21	2.53	0.00
Nb	**(001)**	12.76	14.60	15.39	16.08	0.00
	(011)	82.98	78.21	77.01	76.44	100.00
	(111)	4.26	7.19	7.60	7.48	0.00
Mo	**(001)**	12.26	11.99	11.20	11.06	10.57
	(011)	84.29	83.33	84.16	84.54	86.03
	(111)	3.44	4.67	4.64	4.40	3.40
Fe	**(001)**	0.59	26.68	41.93	0.87	5.75
	(011)	97.47	57.33	15.52	91.07	0.00
	(111)	1.98	15.99	42.55	8.07	94.25
Cr	**(001)**	0.00	13.05	22.25	13.12	24.52
	(011)	94.49	80.00	57.69	79.77	12.93
	(111)	5.51	6.95	20.05	7.11	62.55

Table S3. Linear regression parameters correlating most stable surface energies, γ^{calc}, or Wulff averaged values, γ^{calc}_{Wullf}, with respect experimental values, γ^{exp}, listed in Table S1. Slopes, *a*, intercepts, *b* (in J/m^2), and regression coefficients, *R*, are listed.

	γ^{calc}			γ^{calc}_{Wullf}		
	a	***b***	***R***	***a***	***b***	***R***
TPSS	0.81	0.27	0.52	0.84	0.30	0.52
RPBE	0.85	-0.34	0.88	0.95	0.18	0.56
PBE	0.89	-0.23	0.88	0.93	-0.22	0.89
PBEsol	0.97	-0.12	0.90	0.99	-0.09	0.91
VWN	0.98	-0.01	0.90	1.02	0.00	0.91

Table S4. Mean error (ME), mean absolute error (MAE), and mean absolute percentage error (MAPE) for γ^{calc} and γ^{calc}_{Wullf} with respect γ^{exp}, grouped per TMs within hexagonal close-packed (hcp), face-centered cubic (fcc), or body-centered cubic (bcc) crystallographic structures. Values of ME and MAE are given in J/m^2, whereas MAPE is given in percentage %.

				γ^{calc}		
		VWN	**PBEsol**	**PBE**	**RPBE**	**TPSS**
hcp	**ME**	-0.12	-0.22	-0.48	-0.63	-0.27
	MAE	0.19	0.25	0.48	0.63	0.29
	MAPE	11.60	14.45	25.91	33.93	16.33
fcc	**ME**	-0.17	-0.44	-0.78	-1.00	-0.15
	MAE	0.26	0.44	0.78	1.00	0.69
	MAPE	12.43	20.95	37.54	48.54	31.58
bcc	**ME**	0.20	0.12	-0.17	-0.43	-0.02
	MAE	0.46	0.39	0.48	0.59	1.52
	MAPE	17.91	15.27	17.26	20.75	57.12
				γ^{calc}_{Wullf}		
hcp	**ME**	0.02	-0.10	-0.35	1.03	-0.11
	MAE	0.18	0.19	0.35	1.19	0.18
	MAPE	9.17	10.79	19.16	66.41	10.39
fcc	**ME**	-0.09	-0.37	-0.72	-0.96	-0.10
	MAE	0.26	0.37	0.72	0.96	0.66
	MAPE	11.90	17.75	34.87	46.72	30.42
bcc	**ME**	0.24	0.17	-0.11	-0.38	0.05
	MAE	0.45	0.39	0.46	0.56	1.57
	MAPE	17.89	15.32	16.96	19.78	59.45

Table S5. Calculated work functions ϕ^{calc} as obtained using VWN, PBE, PBEsol, RPBE, and TPSS xc functionals for each studied TM and each surface, alongside with the polycrystalline experimental work function, ϕ_{PC}^{exp}, as well as single-crystal values, ϕ_{SC}^{exp} All values are given eV.

ϕ (eV)	Surface	VWN	PBEsol	PBE	RPBE	TPSS	ϕ_{PC}^{exp}[a]	ϕ_{SC}^{exp}
Zr	**(0001)**	5.32	5.09	4.95	4.83	5.37	4.05	4.33[b]
	(10$\bar{1}$0)	3.38	3.24	3.15	3.07	3.24		
	(11$\bar{2}$0)	3.60	3.49	3.38	3.19	3.63		
Zn	**(0001)**	4.61	4.33	4.12	3.99	4.46	4.33	4.90[a]
	(10$\bar{1}$0)	2.76	2.6	2.52	2.41	2.71		
	(11$\bar{2}$0)	3.25	3.06	2.62	2.77	3.43		
Y	**(0001)**	4.04	3.83	3.74	3.62	4.02	3.10	
	(10$\bar{1}$0)	2.82	2.72	2.67	2.59	2.72		
	(11$\bar{2}$0)	3.06	3.08	2.94	2.76	3.21		
Ti	**(0001)**	6.23	6.04	5.89	5.75	6.23	4.33	4.45[b]
	(10$\bar{1}$0)	3.93	3.83	3.74	3.59	2.13		
	(11$\bar{2}$0)	4.27	4.06	3.96	3.85	4.36		
Tc	**(0001)**	7.67	6.16	5.98	5.84	6.22		4.81[c]
	(10$\bar{1}$0)	5.22	4.02	3.8	3.86	3.96		4.70[c]
	(11$\bar{2}$0)	5.99	4.79	4.67	4.55	4.87		
Sc	**(0001)**	4.47	4.32	4.11	4.12	4.51	3.50	
	(10$\bar{1}$0)	3.06	2.92	2.88	2.81	3.02		
	(11$\bar{2}$0)	3.34	3.21	3.14	3.00	3.55		
Ru	**(0001)**	8.10	7.76	7.54	7.37	8.14	4.71	5.42[d]
	(10$\bar{1}$0)	5.23	5.06	4.88	4.80	3.43		
	(11$\bar{2}$0)	6.14	5.87	5.71	5.51	6.11		
Re	**(0001)**	7.28	7.2	7.08	6.76	7.28	4.96	5.75[e]
	(10$\bar{1}$0)	4.82	4.65	4.58	4.62	4.67		5.05[c]
	(11$\bar{2}$0)	5.87	5.65	5.53	5.29	5.75		
Os	**(0001)**	9.38	7.81	7.80	7.71	8.03	4.83	4.83[c]
	(10$\bar{1}$0)	6.11	5.30	5.12	5.04	5.19		6.05[c]
	(11$\bar{2}$0)	7.23	5.97	5.93	5.83	6.20		
Hf	**(0001)**	5.74	5.50	5.38	5.27	5.74	3.90	
	(10$\bar{1}$0)	3.69	3.51	3.44	3.35	3.42		
	(11$\bar{2}$0)	3.91	3.71	3.63	3.51	3.75		
Co	**(0001)**	6.30	5.87	5.73	5.55	5.73	5.00	5.26[f]
	(10$\bar{1}$0)	3.82	3.68	3.58	3.44	3.58		
	(11$\bar{2}$0)	4.54	4.25	4.12	4.01	2.15		
Cd	**(0001)**	4.41	4.20	3.89	3.73	3.89	4.22	
	(10$\bar{1}$0)	2.78	2.63	2.37	2.21	2.37		

	(11$\bar{2}$0)	3.22	2.84	2.77	2.57	2.77		
Rh	**(001)**	7.04	6.72	6.43	6.26	6.95	4.98	5.00[g]
	(011)	5.53	5.24	4.97	4.87	5.47		
	(111)	7.49	7.15	6.89	6.72	7.55		5.60[h]
Pt	**(001)**	7.35	7.15	6.89	6.72	6.92	5.65	5.82[i]
	(011)	6.02	5.75	5.54	5.39	5.70		5.35[i]
	(111)	7.87	7.61	7.34	7.20	7.38		6.08[i]
Pd	**(001)**	5.63	5.33	5.12	4.93	4.92	5.12	5.65[i]
	(011)	4.52	4.23	4.02	3.83	4.19		5.20[i]
	(111)	6.10	5.74	5.49	5.34	5.71		5.90[i]
Ni	**(001)**	5.42	5.35	5.00	4.67	5.43	5.15	5.22[a]
	(011)	4.22	3.96	3.88	3.65	4.29		5.04[a]
	(111)	5.86	5.61	5.43	5.37	6.10		5.35[a]
Ir	**(001)**	8.65	8.34	8.13	7.97	7.7	5.27	5.67[i]
	(011)	6.87	6.60	6.38	6.25	6.32		5.42[a]
	(111)	8.94	9.06	8.04	8.51	8.20		5.76[i]
Cu	**(001)**	4.51	4.27	4.08	3.94	4.87	4.65	4.59[i]
	(011)	3.71	3.51	3.35	3.25	3.99		4.48[i]
	(111)	5.04	4.74	4.53	4.01	5.8		4.94[i]
Au	**(001)**	6.02	5.67	5.41	5.28	5.25	5.10	5.47[e]
	(011)	4.99	4.61	4.43	4.28	4.56		5.40[e]
	(111)	6.45	6.18	5.89	5.69	5.87		5.31[e]
Ag	**(001)**	4.45	4.11	3.87	3.62	4.82	4.26	4.64[i]
	(011)	3.70	3.40	3.22	3.05	3.59		4.52[i]
	(111)	4.87	4.50	4.26	3.98	5.24		4.74[i]
W	**(001)**	5.57	5.53	5.41	5.35	5.70	4.55	4.63[a]
	(011)	7.17	7.21	7.11	6.94	7.11		3.90[a]
	(111)	4.06	3.84	3.97	3.30	4.23		4.47[a]
V	**(001)**	4.76	4.69	4.57	4.39	5.26	4.30	4.12[j]
	(011)	6.25	6.24	5.79	5.90	6.58		
	(111)	3.35	3.00	3.17	2.50	3.21		
Ta	**(001)**	4.78	4.57	4.43	4.32	4.57	4.25	4.15[a]
	(011)	6.17	4.56	6.25	5.71	5.80		4.95[a]
	(111)	3.42	3.00	3.15	2.57	3.22		4.55[a]
Nb	**(001)**	4.38	4.26	4.06	3.90	4.53	4.30	4.02[a]
	(011)	5.68	5.49	5.37	5.23	5.72		4.87[a]
	(111)	3.13	2.64	2.88	2.20	3.24		4.36[a]
Mo	**(001)**	5.96	5.78	5.65	5.53	5.91	4.60	4.53[a]
	(011)	7.66	7.45	7.28	7.16	8.37		4.95[a]
	(111)	4.40	3.33	4.17	2.79	4.45		4.55[a]
Fe	**(001)**	5.21	4.58	4.36	4.32	6.22	4.50	4.67[a]
	(011)	6.31	4.58	6.51	5.75	7.05		5.10[k]
	(111)	3.57	3.18	3.00	2.33	5.84		4.81[a]

Cr	**(001)**	5.20	5.24	5.08	4.94	5.94	4.50
	(011)	6.82	6.97	7.37	6.68	7.52	
	(111)	3.80	3.81	3.68	3.17	4.12	

[a] Ref. 2, [b] Ref. 3, [c] Ref. 4, [d] Ref. 5, [e] Ref. 6, [f] Ref. 7, [g] Ref. 8, [h] Ref. 9, [i] Ref. 10, [j] Ref. 11, [k] Ref. 12.

Table S6. Linear regression parameters correlating ϕ_{Wulff}^{calc} values with respect experimental polycrystalline work functions ϕ_{PC}^{exp} as well as single-crystal values, ϕ_{Single}^{calc} with respect single crystal experimental values, ϕ_{SC}^{exp}. Slopes, *a*, intercepts, *b* (in eV), and regression coefficients, *R*, are listed.

	ϕ_{SC}^{exp}			ϕ_{Wulff}^{calc}		
	a	***b***	***R***	***a***	***b***	***R***
TPSS	1.05	0.46	0.43	1.52	-1.46	0.61
RPBE	1.42	-2.02	0.51	1.75	-2.86	0.70
PBE	1.31	-1.22	0.50	1.75	-2.81	0.72
PBEsol	1.45	-1.88	0.53	1.90	-3.33	0.72
VWN	1.45	-1.46	0.53	1.89	-2.95	0.74

Table S7. ME, MAE, and MAPE for ϕ_{Wulff}^{calc} values, as well as single-crystal values, ϕ_{Single}^{calc}, with respect experiments, grouped per TMs within *hcp*, *fcc*, or *bcc* crystallographic structures. Values of ME and MAE are given in eV, whereas MAPE is given in percentage.

				ϕ_{Single}^{calc}		
		VWN	**PBEsol**	**PBE**	**RPBE**	**TPSS**
hcp	**ME**	1.41	0.79	0.64	0.52	0.89
	MAE	1.50	1.22	1.20	1.10	1.32
	MAPE	30.45	24.49	23.97	22.05	26.52
fcc	**ME**	0.63	0.37	0.10	-0.05	0.44
	MAE	0.96	0.95	0.90	0.99	0.89
	MAPE	17.90	17.82	17.05	18.68	16.93
bcc	**ME**	0.60	0.13	0.35	-0.05	0.91
	MAE	1.12	1.10	1.08	1.20	1.26
	MAPE	24.90	24.58	23.89	26.64	27.82
				ϕ_{Wulff}^{calc}		
hcp	**ME**	0.41	0.13	0.07	-0.07	0.45
	MAE	0.75	0.63	0.59	0.62	0.71
	MAPE	16.57	13.95	13.00	13.80	15.79
fcc	**ME**	1.37	1.18	0.84	0.76	0.92
	MAE	1.37	1.21	0.99	1.02	1.24
	MAPE	26.40	23.21	19.24	19.85	24.39
bcc	**ME**	1.88	1.29	1.21	1.36	1.79
	MAE	1.88	1.31	1.32	1.36	1.79
	MAPE	42.19	29.21	29.61	30.46	40.15

Table S8. Experimental interlayer distance relaxations, Δ_{ij}, given in % with respect the bulk interlayer distance. Employed reference data is highlighted in bold.

Metal	Surface	Δ_{12}	Δ_{23}	Δ_{34}	Ref.
Zr	**(0001)**	**1.6 %**			**13**
	(10$\bar{1}$0)				
	(11$\bar{2}$0)				
Zn	**(0001)**	**-1 ± 1 %**			**14**
	(10$\bar{1}$0)				
	(11$\bar{2}$0)				
Y	**(0001)**	**0 %**			**15**
	(10$\bar{1}$0)				
	(11$\bar{2}$0)				
Ti	**(0001)**	-2.1 %			16
		-4.9 ± 1 %	**1.4 ± 1 %**		**17**
	(10$\bar{1}$0)	**-6 %**			**18**
	(11$\bar{2}$0)				
Tc	**(0001)**				
	(10$\bar{1}$0)				
	(11$\bar{2}$0)				
Sc	**(0001)**	-1.7 %			19
		-6.1 ± 1.1%	**-1.1 ± 1.1 %**		**20**
	(10$\bar{1}$0)				
	(11$\bar{2}$0)				
Ru	**(0001)**	**-3.5 ± 0.9 %**			**21**
		-2.1 %			**13**
	(10$\bar{1}$0)				
	(11$\bar{2}$0)				
Re	**(0001)**	**-5 %**			**13**
	(10$\bar{1}$0)	-17 %			22
		-11 %	**1.5 %**		**23**
	(11$\bar{2}$0)				
Os	**(0001)**				
	(10$\bar{1}$0)				
	(11$\bar{2}$0)				
Hf	**(0001)**				
	(10$\bar{1}$0)				
	(11$\bar{2}$0)				
Co	**(0001)**	**0 ± 2 %**			**24**
		2.1 %	1.3 %		25
	(10$\bar{1}$0)	**-6.5 ± 2 %**	**1.0 ± 2 %**	**0.1 ± 2 %**	**26**
		-12.8 %	0.8 %	-0.3 %	27

	(11$\bar{2}$0)				
Cd	**(0001)**	**0 %**			**28**
	(10$\bar{1}$0)				
	(11$\bar{2}$0)				
	(001)	-1.16 ± 1.6 %	0 ± 1.6 %		29
		-1 ± 0.9 %			30
		0.5 ± 1.0 %	0.0 ± 1.5 %		31
		-1.14 ± 3.6 %			32
Rh		**1.0 ± 0.6 %**	**-0.7 ± 0.5 %**		**33**
		1.0 ± 0.9 %			34
		-1.3 %			35
		-1.4 ± 1.4 %	-0.6 ± 1.4 %		17
	(011)	-3 %			36
		-6.9 ± 1.2 %	**1.9 ± 1.0 %**		**37**
		-3.3 %			38
	(111)	0 %			39
		-1.37 ± 0.9 %	**-1.28 ± 1.8 %**		34
		-1.28 ± 0.9 %			**40**
		-3.0 ± 1.4 %			41
		-1.2 %	-0.7 %	0.4 %	42
	(001)	0%			43
Pt		**0.2±1.6%**			**44**
		0.2±2.6%			45
	(011)	**-18.5 ± 2.2 %**	**-24.2 ± 4.3 %**		**46**
	(111)	0.5 ± 0.9 %			47
		1.4 ± 0.9 %			**44**
		0.7 %	-0.4 %		48
		1.1 ± 4.4 %			46
		1.5 ± 0.9 %			49
		0.1 %			50
		1.1 %			51
		0.9 %			52
		0.4 %			53
		0.9 %			54
		1 %			55
		0.2 %	-1 %	0.2 %	56
	(001)	3.1 ± 1.5 %	-1 ± 1.5 %		57
		0.3 ± 2.6 %		-0.05 %	58
Pd		2.5 ± 2.5 %			59
		4.6 ± 1.5 %	0.3 ± 0.5 %		60
		0.2 ± 1.4 %	**-0.7 ± 1.3 %**		**61**

		-1.15 %			35
	(011)	-5.8 ± 2.2 %	1.0 ± 2.2 %		62
		-5.1 ± 1.5 %	**2.9 ± 1.5%**		**63**
	(111)	-0.9 ± 1.3 %			44
		1.3 ± 1.3 %	-1.3 ± 1.3 %	2.2 ± 1.3 %	64
		0 ± 4.4 %			65
		2.4 ± 0.9 %	**0.7 ± 0.9 %**	**0.7 ± 1.8 %**	**66**
	(001)	**-3.2±0.5 %**			**67**
Ni		-1±1 %	0±1%		68
		2 %			69
	(011)	**-8.7 ± 0.5 %**	**3.0 ± 0.6 %**	**-0.5 ± 0.7 %**	**70**
		-8.4 ± 0.8 %	3.1 ± 1.0 %		71
		-5 %			72
		-7.5 %			73
		-8 %			74
		0 %			75
		-4 %			76
	(111)	**-1.2 ± 1.2 %**			**77**
		-1 %			78
Ir	**(001)**	**-3.6 ± 0.5 %**			**44**
	(011)	**-7 %**			**79**
	(111)	-2 %			78
		-2.6 %			**44**
	(001)	**-1.1 ± 0.4 %**	**1.7 ± 0.6 %**		**80**
		-1.0 ± 0.4 %	2.0 ± 0.8 %		22
		-1.2 %	0.9 %		81
Cu		0 %			82
		-2 %			83
		-2.4 %	0.5 %		84
		-2 %	1 %		85
	(011)	-9 %			86
		-10 ± 2.5 %	**0 ± 2.5 %**		**87**
		-10 %	1.9 %		22
		-7.9 %	2.4 %		22
		-9.5 %	2.6 %		22
		-8.5 %	2.3 %		88
		-5.3 %	3.3 %		89
	(111)	-0.3 ± 1.0 %			89
		-0.7 ± 0.5 %			**90**
		-2 ± 1.0 %			91
Au	**(001)**	**0 ± 1.5 %**			**92**
		-20 ± 3%	2 ± 3 %		93

	(011)	**-20.1 ± 3.5 %**	**-6.2 ± 3.5 %**		**94**
	(111)	1.5 %			95
		3.3 ± 0.4 %	**-0.8 ± 0.4 %**		**96**
		0.6 %	-0.64 %	-1.1 %	97
Ag	**(001)**	**0 ± 1.5 %**			**92**
		0 %			98
	(011)	-8 %			99
		-7 %			100
		-10 %			101
		-7.8 ± 2.5 %			**102**
	(111)	0 %			103
		0 %	0 %		104
		-2.5 %	0.6 %		105
		-0.5 ± 0.3 %	**-0.4 ± 0.4 %**	**0 ± 0.4 %**	**106**
W	**(001)**	-3.13 %			107
		-5.5 ± 1.5 %			**108**
		-4.4 ± 3.0 %			109
		-7.5 %			110
		-11 ± 2 %			111
		-10 %			112
		-8 %			113
		-6.7 ± 2.0 %			114
		-7 ± 1.5 %			115
		-6.5%			116
	(011)	0 %			107
		-2.8 ± 1.2 %	0.2 ± 1.0 %	-0.7 ± 2.2 %	117
		-3 %			118
		-2.2 ± 1.1 %			119
		-3 ± 1.3 %			120
		-3.1 ± 0.6 %			**121**
		-3 ± 1.3 %	0.2 ± 1.3 %		122
		1%			116
	(111)				
V	**(001)**	-7 %	1 %		123
		-6.7 ± 1.5 %			**124**
	(011)				
	(111)				
Ta	**(001)**	**-11 ± 2 %**	**1 ± 2 %**		**124**
		-10 ± 5 %			125
	(011)				
	(111)				
Nb	**(001)**	**-13 ± 5 %**			**126**
	(011)				

	(111)				
	(001)	-11.5 %	1 ± 2 %		127
		-9.5 ± 3 %			**128**
Mo		-10 %			129
		-4 %			130
		-9%			116
	(011)	**-1.6 ± 2.0 %**			**131**
	(111)	-18.8 %	-18.9 %	6.4 %	132
		-18 ± 2 %	**4 ± 4 %**		**133**
Fe	**(001)**	**-1.4 ± 3 %**			**134**
	(011)	0.5 ± 2.0 %			135
		1 ± 2 %	**0.5 ± 2 %**		**136**
		1 %			135
	(111)	-15.4 ± 4 %			137
		-16.9 ± 3 %	**-9.8 ± 3 %**		**138**
		-29 ± 7 %	6 ± 5 %		136
Cr	**(001)**				
	(011)	**-2.2 ± 1.4 %**	**-1.3 ± 1.3 %**		**117**
	(111)				

Table S9. Calculated interlayer distance relaxations, Δ_{ij}, given in %, as obtained at different xc DFT levels.

	Surface		VWN	PBEsol	PBE	RPBE	TPSS
Zr	(0001)	Δ_{12}	-5.42	-5.81	-6.21	-6.49	-5.87
		Δ_{23}	1.77	1.91	2.18	2.53	2.32
		Δ_{34}	1.46	0.78	0.16	-0.17	-1.06
	(10$\bar{1}$0)	Δ_{12}	-3.15	-2.85	-2.78	-2.81	-5.20
		Δ_{23}	-7.48	-7.56	-7.56	-7.65	-4.00
		Δ_{34}	11.99	12.02	12.22	11.74	2.22
	(11$\bar{2}$0)	Δ_{12}	-7.98	-7.57	-7.43	-7.21	-5.83
		Δ_{23}	-0.68	-1.15	-1.38	-1.65	-1.81
		Δ_{34}	-1.56	-0.96	-0.69	-0.33	-0.09
Zn	(0001)	Δ_{12}	-0.90	-0.92	-0.04	1.75	2.82
		Δ_{23}	-3.35	-3.61	-2.63	-0.50	-1.29
		Δ_{34}	-3.89	-4.28	-3.17	-1.02	-2.66
	(10$\bar{1}$0)	Δ_{12}	-98.75	-98.86	-99.87	-98.36	-87.24
		Δ_{23}	57.42	57.51	60.57	63.28	53.14
		Δ_{34}	-98.50	-98.63	-99.55	-99.60	-74.27
	(11$\bar{2}$0)	Δ_{12}	-17.21	-14.41	-14.72	-9.93	-0.65
		Δ_{23}	19.49	17.66	20.00	17.91	7.71
		Δ_{34}	-8.93	-7.24	-8.75	-4.15	6.91
Y	(0001)	Δ_{12}	-2.61	-2.80	-3.31	-3.07	-1.75
		Δ_{23}	1.60	0.94	0.39	0.57	0.25
		Δ_{34}	-0.80	-0.72	-0.73	-0.50	-0.29
	(10$\bar{1}$0)	Δ_{12}	7.07	5.43	2.56	1.15	-0.43
		Δ_{23}	-9.18	-8.90	-8.30	-7.74	-6.64
		Δ_{34}	11.75	11.71	10.51	8.83	7.18
	(11$\bar{2}$0)	Δ_{12}	-0.98	-1.28	-2.45	-2.78	-1.46
		Δ_{23}	-4.90	-4.90	-4.40	-4.34	-4.13
		Δ_{34}	4.76	4.74	4.18	4.08	3.27
Ti	(0001)	Δ_{12}	-7.23	-7.30	-7.47	-7.62	-6.58
		Δ_{23}	2.45	2.72	3.03	3.19	2.83
		Δ_{34}	-1.06	-1.57	-1.70	-2.25	-0.68
	(10$\bar{1}$0)	Δ_{12}	4.49	1.88	0.29	0.32	1.08
		Δ_{23}	-12.18	-9.98	-8.90	-8.57	-8.12
		Δ_{34}	22.72	16.29	13.25	12.00	12.48
	(11$\bar{2}$0)	Δ_{12}	5.61	-4.94	-5.12	-5.06	-4.10
		Δ_{23}	-3.18	-3.49	-3.48	-3.75	-2.62
		Δ_{34}	0.43	0.95	1.05	1.27	1.22
Tc	(0001)	Δ_{12}	-6.45	-6.83	-7.14	-7.33	-6.65

		Δ_{23}	4.63	5.03	5.40	5.70	4.20
		Δ_{34}	-3.68	-4.03	-4.39	-4.51	-3.56
		Δ_{12}	-10.41	-10.79	-17.66	-9.31	-3.64
	(10$\bar{1}$0)	Δ_{23}	-1.56	-1.65	2.53	-2.41	-4.84
		Δ_{34}	1.84	2.03	2.40	2.70	8.32
		Δ_{12}	-15.52	-16.99	-17.45	-17.46	-13.01
	(11$\bar{2}$0)	Δ_{23}	3.97	4.40	4.67	4.62	2.99
		Δ_{34}	1.46	1.75	1.73	1.90	1.39
Sc		Δ_{12}	-4.18	-3.93	-3.90	-2.20	-3.15
	(0001)	Δ_{23}	-0.92	-0.54	-0.59	1.17	-0.20
		Δ_{34}	-1.46	-1.27	-0.93	0.22	-1.03
		Δ_{12}	6.03	4.96	4.04	3.06	4.68
	(10$\bar{1}$0)	Δ_{23}	-9.28	-9.17	-9.04	-9.04	-8.52
		Δ_{34}	13.09	12.86	12.66	12.90	12.34
		Δ_{12}	0.08	-0.24	-0.94	-1.20	0.50
	(11$\bar{2}$0)	Δ_{23}	-5.23	-4.97	-4.89	-4.85	-4.46
		Δ_{34}	5.58	5.37	5.25	4.88	5.40
Ru		Δ_{12}	-4.05	-4.05	-4.11	-4.28	-3.44
	(0001)	Δ_{23}	0.27	0.22	0.31	0.27	0.16
		Δ_{34}	1.01	0.86	0.88	0.90	0.95
		Δ_{12}	-19.40	-18.83	-19.39	-18.93	-18.99
	(10$\bar{1}$0)	Δ_{23}	1.93	1.60	2.22	1.40	2.51
		Δ_{34}	-5.63	-5.09	-4.81	-4.38	-6.73
		Δ_{12}	-6.88	-6.61	-6.70	-6.62	-6.37
	(11$\bar{2}$0)	Δ_{23}	-1.30	-1.48	-1.57	-1.69	-1.20
		Δ_{34}	3.37	3.59	3.82	4.06	2.92
Re		Δ_{12}	-8.38	-6.24	-6.49	-4.55	-7.01
	(0001)	Δ_{23}	2.17	3.97	4.14	5.36	5.29
		Δ_{34}	-5.67	-3.51	-3.64	-1.32	-3.79
		Δ_{12}	-14.65	-14.64	-15.09	-11.79	-0.61
	(10$\bar{1}$0)	Δ_{23}	-0.09	-0.05	-0.06	-7.04	-0.53
		Δ_{34}	0.18	0.03	0.07	2.54	1.98
		Δ_{12}	-18.34	-18.19	-18.73	-20.21	-18.85
	(11$\bar{2}$0)	Δ_{23}	5.58	5.49	5.81	9.90	5.33
		Δ_{34}	0.91	0.84	0.79	1.05	1.04
		Δ_{12}	-3.94	-2.81	-3.92	-3.98	-3.33
	(0001)	Δ_{23}	-0.13	1.27	-0.22	-0.25	0.01
		Δ_{34}	1.67	2.72	1.74	1.76	1.80
		Δ_{12}	-19.02	-16.42	-19.55	-19.67	-17.68
Os	**(10$\bar{1}$0)**	Δ_{23}	3.23	-1.35	3.45	3.59	3.18
		Δ_{34}	-10.00	-11.93	-10.34	-10.33	-9.70

	(11$\bar{2}$0)	Δ_{12}	-8.40	-8.77	-8.38	-8.35	-7.17
		Δ_{23}	-0.46	1.89	-0.41	-0.49	-0.71
		Δ_{34}	1.26	2.06	1.33	1.34	1.54
Hf	**(0001)**	Δ_{12}	-6.27	-6.50	-6.67	-6.83	-6.11
		Δ_{23}	2.91	3.26	3.54	3.79	2.85
		Δ_{34}	-1.03	-1.60	-2.04	-2.39	-0.56
	(10$\bar{1}$0)	Δ_{12}	-2.75	-4.59	-4.48	-4.83	-2.48
		Δ_{23}	-7.51	-6.25	-6.07	-5.64	-7.24
		Δ_{34}	12.75	8.23	7.42	6.51	10.72
	(11$\bar{2}$0)	Δ_{12}	-7.21	-6.90	-7.04	-7.03	-7.12
		Δ_{23}	-1.50	-1.88	-1.89	-2.10	-1.49
		Δ_{34}	-0.68	-0.24	0.28	0.57	-0.79
Co	**(0001)**	Δ_{12}	-2.61	-3.55	-3.23	-3.92	-3.30
		Δ_{23}	0.86	0.64	1.45	0.82	8.77
		Δ_{34}	-0.95	-2.77	-1.51	-3.40	-2.41
	(10$\bar{1}$0)	Δ_{12}	-16.89	-24.96	-17.05	-16.07	-10.98
		Δ_{23}	3.13	2.55	3.05	2.65	-5.25
		Δ_{34}	-3.33	-12.95	-2.49	-1.73	1.00
	(11$\bar{2}$0)	Δ_{12}	-9.41	-9.74	-11.42	-11.28	-0.02
		Δ_{23}	3.69	6.32	4.24	4.16	0.01
		Δ_{34}	-3.40	-5.14	0.36	0.68	0.00
Cd	**(0001)**	Δ_{12}	-0.84	0.00	0.03	1.24	0.65
		Δ_{23}	-1.91	-0.02	-0.02	0.37	-1.17
		Δ_{34}	-2.02	0.00	0.01	0.56	-2.45
	(10$\bar{1}$0)	Δ_{12}	-99.87	-99.24	-99.30	-99.16	98.98
		Δ_{23}	57.81	58.19	60.70	64.06	-49.02
		Δ_{34}	-99.82	-99.29	-98.26	-99.97	98.98
	(11$\bar{2}$0)	Δ_{12}	-11.06	-7.51	1.84	6.69	-53.00
		Δ_{23}	16.50	15.13	12.15	10.82	60.88
		Δ_{34}	-6.24	-4.62	2.51	5.02	-46.44
Rh	**(001)**	Δ_{12}	-4.13	-4.01	-4.00	-3.94	-3.80
		Δ_{23}	0.26	0.20	0.17	0.12	0.08
		Δ_{34}	0.70	0.79	0.89	0.96	0.19
	(011)	Δ_{12}	-10.14	-9.89	-10.15	-9.56	-7.68
		Δ_{23}	0.54	0.21	0.43	-0.47	-0.49
		Δ_{34}	0.59	0.96	1.56	2.17	3.24
	(111)	Δ_{12}	-1.87	-2.93	-1.88	-1.89	-1.81
		Δ_{23}	-0.29	-1.32	-0.22	-0.26	-0.24
		Δ_{34}	0.91	-0.20	0.99	1.05	0.86
	(001)	Δ_{12}	-2.89	-2.80	-2.79	-2.72	-2.18
		Δ_{23}	-0.67	-0.65	-0.70	-0.77	-0.50

		Δ_{34}	-0.26	-0.19	-0.26	-0.32	-0.21
		Δ_{12}	-14.0	-13.91	-14.25	-13.88	-11.85
Pt	**(011)**	Δ_{23}	8.88	8.54	9.07	8.90	7.08
		Δ_{34}	-4.43	-4.09	-4.08	-3.40	-2.36
		Δ_{12}	0.85	0.91	1.09	1.16	1.12
	(111)	Δ_{23}	-1.32	-1.36	-1.44	-1.48	-1.33
		Δ_{34}	-1.23	-1.35	-1.44	-1.48	-1.33
		Δ_{12}	-1.81	-1.51	-1.16	-0.67	0.12
	(001)	Δ_{23}	-0.40	-0.20	0.16	0.22	0.07
		Δ_{34}	-0.77	-0.49	-0.04	0.17	0.02
		Δ_{12}	-10.41	-9.68	-9.55	-9.28	-7.67
Pd	**(011)**	Δ_{23}	3.96	3.86	3.69	3.71	3.28
		Δ_{34}	-1.56	-1.11	-0.94	-0.48	-0.89
		Δ_{12}	0.02	0.06	0.07	0.13	0.77
	(111)	Δ_{23}	-0.44	-0.44	-0.46	-0.35	0.18
		Δ_{34}	-0.70	-0.63	-0.63	-0.53	0.19
		Δ_{12}	3.36	-3.14	-3.37	-3.03	1.77
	(001)	Δ_{23}	1.04	1.05	1.11	1.38	2.22
		Δ_{34}	0.49	0.27	0.49	0.52	-3.01
		Δ_{12}	-9.64	-9.21	-9.70	-8.85	2.64
Ni	**(011)**	Δ_{23}	2.03	2.55	1.50	2.29	-1.97
		Δ_{34}	-0.34	-0.18	0.16	0.46	4.62
		Δ_{12}	-1.01	-1.20	-1.19	-1.12	3.88
	(111)	Δ_{23}	-0.07	-0.07	-0.03	0.09	-0.24
		Δ_{34}	-0.05	0.05	0.19	0.38	-0.79
		Δ_{12}	-5.43	-5.41	-5.51	-5.51	-4.51
	(001)	Δ_{23}	0.82	0.78	0.82	0.81	0.51
		Δ_{34}	0.08	0.09	0.00	-0.01	0.11
		Δ_{12}	-11.44	-11.22	-11.47	-11.46	-10.57
Ir	**(011)**	Δ_{23}	2.38	2.14	2.22	2.14	1.12
		Δ_{34}	-2.21	-1.96	-1.91	-1.71	-0.34
		Δ_{12}	-2.17	-2.31	-2.33	-2.26	-1.89
	(111)	Δ_{23}	0.70	-0.06	-0.04	-0.04	-0.07
		Δ_{34}	0.67	0.50	0.51	0.52	0.61
		Δ_{12}	-2.83	-2.37	-2.36	-2.32	-0.21
	(001)	Δ_{23}	0.24	0.97	0.45	1.03	0.08
		Δ_{34}	-0.64	0.50	-0.33	0.55	0.25
		Δ_{12}	-10.99	-10.19	-10.21	-9.80	-10.87
Cu	**(011)**	Δ_{23}	4.70	4.72	4.48	4.64	11.63
		Δ_{34}	-2.58	-2.37	-2.22	-1.98	11.15
	(111)	Δ_{12}	-1.08	-0.93	-0.82	-1.09	7.02

		Δ_{23}	0.04	0.08	0.27	-0.21	0.47
		Δ_{34}	-0.08	0.13	0.14	-0.30	-0.06
		Δ_{12}	-1.37	-1.32	-1.07	-0.97	-5.42
	(001)	Δ_{23}	0.23	0.29	0.35	0.33	-3.93
		Δ_{34}	0.05	0.03	0.15	0.13	-3.71
		Δ_{12}	-13.81	-13.55	-13.92	-13.78	-11.06
Au	**(011)**	Δ_{23}	8.48	8.49	9.07	9.10	6.95
		Δ_{34}	-5.67	-5.38	-6.17	-5.73	-4.22
		Δ_{12}	0.07 -	0.32	0.46	0.81	-0.05
	(111)	Δ_{23}	0.50	-0.22	-0.44	-0.24	-0.54
		Δ_{34}	-0.61	-0.34	-0.81	-0.72	-0.94
		Δ_{12}	-1.87	-2.00	-1.74	-1.84	-1.69
	(001)	Δ_{23}	0.00	-0.14	-0.01	0.19	-0.44
		Δ_{34}	-0.51	-0.61	-0.46	0.11	0.41
		Δ_{12}	-9.67	-9.37	-9.25	-8.91	-6.75
Ag	**(011)**	Δ_{23}	4.33	4.03	4.18	4.31	0.98
		Δ_{34}	-2.73	-2.61	-2.59	-2.48	2.62
		Δ_{12}	-0.90	-0.70	-0.94	-0.89	-0.57
	(111)	Δ_{23}	-0.37	-0.08	-0.60	-0.68	-0.35
		Δ_{34}	-0.32	-0.10	-0.56	-0.77	-0.93
		Δ_{12}	-13.50	-13.78	-14.08	-14.01	-11.77
	(001)	Δ_{23}	3.11	3.78	4.48	4.79	5.86
		Δ_{34}	-2.78	-3.49	-4.48	-4.65	-4.28
		Δ_{12}	-3.84	-3.95	-3.83	-3.82	-3.67
W	**(011)**	Δ_{23}	0.04	0.19	0.37	0.49	0.26
		Δ_{34}	-0.13	-0.15	-0.02	-0.17	-0.23
		Δ_{12}	-26.82	-26.56	-26.70	-26.29	-27.77
	(111)	Δ_{23}	-26.67	-26.62	-26.49	-26.39	-24.10
		Δ_{34}	32.24	30.02	29.46	29.07	23.51
		Δ_{12}	-11.39	-12.33	-12.68	-12.98	-2.82
	(001)	Δ_{23}	-0.69	-0.61	-1.08	-0.78	-4.27
		Δ_{34}	3.85	2.77	3.46	2.56	2.56
		Δ_{12}	-4.85	-5.72	-11.78	-6.52	17.25
V	**(011)**	Δ_{23}	0.66	0.33	-3.25	0.49	18.56
		Δ_{34}	-0.81	-1.04	-9.64	-1.22	13.45
		Δ_{12}	-15.37	-14.20	-13.87	-13.09	0.96
	(111)	Δ_{23}	-15.46	-15.54	-15.42	-15.67	-2.40
		Δ_{34}	3.79	-0.44	-2.58	-3.95	-0.98
		Δ_{12}	-11.53	-11.41	-11.93	-12.03	-10.93
	(001)	Δ_{23}	-0.99	-0.83	-0.96	-0.89	-1.12
		Δ_{34}	3.92	4.18	4.38	4.64	-1.12

Ta	**(011)**	Δ_{12}	-4.50	-11.80	3.30	-4.80	-4.14
		Δ_{23}	0.06	-0.85	5.77	0.14	-0.12
		Δ_{34}	-0.91	4.59	6.68	-0.34	-0.93
	(111)	Δ_{12}	-21.01	-20.47	-20.40	-20.09	-20.37
		Δ_{23}	-19.43	-18.91	-19.23	-19.02	-18.98
		Δ_{34}	19.24	18.69	18.43	17.61	19.37
Nb	**(001)**	Δ_{12}	-10.56	-10.64	-11.20	-11.49	20.54
		Δ_{23}	-1.02	-1.09	-1.20	-1.14	-1.02
		Δ_{34}	5.01	4.81	4.35	4.42	4.50
	(011)	Δ_{12}	-3.93	-4.35	-4.23	-5.06	-3.18
		Δ_{23}	0.53	0.37	0.94	0.52	0.32
		Δ_{34}	-1.19	-1.47	-0.86	-1.75	-0.87
	(111)	Δ_{12}	-22.58	-21.51	-21.32	-21.08	-18.71
		Δ_{23}	-15.73	-16.08	-16.17	-16.34	-16.54
		Δ_{34}	13.18	12.29	10.74	9.93	16.08
Mo	**(001)**	Δ_{12}	-13.75	-13.66	-13.77	-13.81	-11.93
		Δ_{23}	4.31	4.38	5.21	5.49	4.02
		Δ_{34}	-4.04	-4.21	-4.98	-5.20	-3.65
	(011)	Δ_{12}	-5.04	-5.08	-5.28	-5.17	-4.88
		Δ_{23}	0.18	0.29	0.35	0.54	-0.28
		Δ_{34}	0.17	0.07	-0.11	0.10	-0.40
	(111)	Δ_{12}	-20.50	-19.93	-20.66	-20.16	-17.92
		Δ_{23}	-23.83	-23.90	-22.71	-22.10	-20.89
		Δ_{34}	24.13	23.63	21.17	19.46	20.54
Fe	**(001)**	Δ_{12}	-18.73	-2.10	-1.94	-7.14	-2.22
		Δ_{23}	2.30	2.28	2.07	4.67	-0.01
		Δ_{34}	-0.87	-1.87	-1.33	0.43	0.67
	(011)	Δ_{12}	-1.33	-0.12	6.67	-0.23	199.91
		Δ_{23}	0.20	1.75	7.54	0.52	59.78
		Δ_{34}	-0.32	3.15	6.73	-0.64	3.77
	(111)	Δ_{12}	-17.49	-9.89	-10.33	-11.06	33.09
		Δ_{23}	-51.90	-15.50	-15.22	-15.89	-6.76
		Δ_{34}	68.02	21.50	19.69	18.69	22.46
Cr	**(001)**	Δ_{12}	-13.56	-14.04	-14.98	-14.90	0.09
		Δ_{23}	6.48	7.04	7.91	8.49	0.01
		Δ_{34}	-6.26	-7.02	-7.76	-8.04	-0.16
	(011)	Δ_{12}	-4.25	-4.63	2.73	-4.80	1.72
		Δ_{23}	0.27	0.18	6.24	0.55	0.31
		Δ_{34}	0.13	-0.09	5.68	-0.13	1.40
	(111)	Δ_{12}	-18.42	-17.85	-18.20	-17.59	2.58
		Δ_{23}	-24.28	-25.21	-24.76	-25.18	-19.66

Δ_{34}	21.29	19.27	17.53	17.04	39.06

Table S10. Calculated interlayer distances, δ_{ij}, given in Å.

	Surface		VWN	PBEsol	PBE	RPBE	TPSS
Zr	(0001)	δ_{12}	2.39	2.40	2.42	2.43	2.42
		δ_{23}	2.57	2.60	2.64	2.67	2.63
		δ_{34}	2.56	2.57	2.59	2.60	2.55
	(10$\bar{1}$0)	δ_{12}	0.89	0.90	0.91	0.92	0.88
		δ_{23}	1.69	1.71	1.73	1.74	1.79
		δ_{34}	1.02	1.04	1.05	1.05	0.95
	(11$\bar{2}$0)	δ_{12}	1.46	1.48	1.50	1.52	1.52
		δ_{23}	1.57	1.58	1.60	1.61	1.59
		δ_{34}	1.56	1.59	1.61	1.63	1.61
Zn	(0001)	δ_{12}	2.36	2.40	2.47	2.55	2.45
		δ_{23}	2.30	2.33	2.40	2.49	2.35
		δ_{34}	2.29	2.32	2.39	2.48	2.32
	(10$\bar{1}$0)	δ_{12}	0.01	0.01	0.00	0.01	0.09
		δ_{23}	2.33	2.37	2.47	2.54	2.27
		δ_{34}	0.01	0.01	0.00	0.00	0.19
	(11$\bar{2}$0)	δ_{12}	1.06	1.12	1.13	1.22	1.27
		δ_{23}	1.53	1.53	1.60	1.59	1.38
		δ_{34}	1.17	1.21	1.21	1.29	1.37
Y	(0001)	δ_{12}	2.70	2.74	2.77	2.81	2.81
		δ_{23}	2.82	2.84	2.88	2.91	2.86
		δ_{34}	2.75	2.80	2.84	2.88	2.85
	(10$\bar{1}$0)	δ_{12}	1.09	1.09	1.08	1.08	1.05
		δ_{23}	1.85	1.88	1.93	1.96	1.96
		δ_{34}	1.14	1.16	1.16	1.16	1.13
	(11$\bar{2}$0)	δ_{12}	1.75	1.77	1.78	1.79	1.79
		δ_{23}	1.68	1.70	1.74	1.76	1.74
		δ_{34}	1.85	1.88	1.90	1.92	1.88
Ti	(0001)	δ_{12}	2.11	2.13	2.16	2.17	2.15
		δ_{23}	2.33	2.36	2.40	2.43	2.37
		δ_{34}	2.25	2.26	2.29	2.30	2.29
	(10$\bar{1}$0)	δ_{12}	0.86	0.85	0.85	0.86	0.85
		δ_{23}	1.45	1.51	1.54	1.56	1.54
		δ_{34}	1.01	0.97	0.96	0.96	0.94
	(11$\bar{2}$0)	δ_{12}	1.35	1.38	1.39	1.41	1.39
		δ_{23}	1.39	1.40	1.42	1.43	1.41
		δ_{34}	1.44	1.46	1.48	1.50	1.47
	(0001)	δ_{12}	2.04	2.04	2.06	2.06	2.07
		δ_{23}	2.29	2.30	2.33	2.35	2.31

		δ_{34}	2.10	2.10	2.12	2.12	2.14
		δ_{12}	0.70	0.70	0.63	0.72	0.76
Tc	**(10$\bar{1}$0)**	δ_{23}	1.54	1.54	1.56	1.55	1.51
		δ_{34}	0.80	0.80	0.78	0.82	0.86
		δ_{12}	1.15	1.13	1.14	1.14	1.20
	(11$\bar{2}$0)	δ_{23}	1.42	1.43	1.44	1.45	1.42
		δ_{34}	1.38	1.39	1.40	1.41	1.40
		δ_{12}	2.44	2.49	2.52	2.58	2.52
	(0001)	δ_{23}	2.53	2.58	2.61	2.67	2.60
		δ_{34}	2.51	2.56	2.60	2.64	2.58
		δ_{12}	0.98	0.98	0.99	0.99	0.99
Sc	**(10$\bar{1}$0)**	δ_{23}	1.68	1.70	1.73	1.75	1.72
		δ_{34}	1.04	1.06	1.07	1.09	1.06
		δ_{12}	1.60	1.62	1.63	1.65	1.64
	(11$\bar{2}$0)	δ_{23}	1.52	1.54	1.57	1.59	1.56
		δ_{34}	1.69	1.71	1.73	1.75	1.72
		δ_{12}	2.03	2.04	2.06	2.07	2.07
	(0001)	δ_{23}	2.12	2.13	2.15	2.16	2.14
		δ_{34}	2.13	2.14	2.17	2.18	2.16
		δ_{12}	0.63	0.64	0.63	0.64	0.64
Ru	**(10$\bar{1}$0)**	δ_{23}	1.59	1.59	1.61	1.61	1.61
		δ_{34}	0.74	0.74	0.75	0.76	0.73
		δ_{12}	1.24	1.25	1.27	1.27	1.27
	(11$\bar{2}$0)	δ_{23}	1.32	1.32	1.34	1.34	1.34
		δ_{34}	1.38	1.39	1.41	1.42	1.39
		δ_{12}	2.06	2.09	2.10	2.09	2.09
	(0001)	δ_{23}	2.29	2.32	2.34	2.31	2.36
		δ_{34}	2.12	2.15	2.17	2.16	2.16
		δ_{12}	0.67	0.67	0.68	0.75	0.79
Re	**(10$\bar{1}$0)**	δ_{23}	1.57	1.58	1.59	1.58	1.58
		δ_{34}	0.79	0.79	0.80	0.87	0.81
		δ_{12}	1.12	1.13	1.13	1.08	1.13
	(11$\bar{2}$0)	δ_{23}	1.45	1.46	1.47	1.49	1.47
		δ_{34}	1.39	1.39	1.40	1.37	1.41
		δ_{12}	2.06	2.05	2.09	2.09	2.10
	(0001)	δ_{23}	2.14	2.14	2.17	2.18	2.17
		δ_{34}	2.18	2.17	2.21	2.22	2.21
		δ_{12}	0.64	0.70	0.64	0.64	0.66
Os	**(10$\bar{1}$0)**	δ_{23}	1.63	1.65	1.66	1.66	1.65
		δ_{34}	0.71	0.74	0.72	0.72	0.72
	(11$\bar{2}$0)	δ_{12}	1.24	1.22	1.26	1.27	1.27

		δ_{23}	1.35	1.36	1.37	1.37	1.36
		δ_{34}	1.37	1.36	1.39	1.40	1.39
		δ_{12}	2.31	2.33	2.36	2.38	2.28
	(0001)	δ_{23}	2.54	2.58	2.62	2.65	2.50
		δ_{34}	2.44	2.46	2.48	2.49	2.42
		δ_{12}	0.88	0.87	0.88	0.89	0.87
Hf	**(10$\bar{1}$0)**	δ_{23}	1.67	1.71	1.74	1.76	1.65
		δ_{34}	1.02	0.99	0.99	0.99	0.98
		δ_{12}	1.45	1.47	1.49	1.50	1.43
	(11$\bar{2}$0)	δ_{23}	1.54	1.55	1.57	1.58	1.52
		δ_{34}	1.55	1.58	1.61	1.62	1.53
		δ_{12}	1.91	1.92	1.96	1.96	1.89
	(0001)	δ_{23}	1.98	2.00	2.05	2.06	2.13
		δ_{34}	1.94	1.93	1.99	1.97	1.91
		δ_{12}	0.58	0.53	0.60	0.61	0.67
Co	**(10$\bar{1}$0)**	δ_{23}	1.45	1.46	1.48	1.49	1.43
		δ_{34}	0.68	0.62	0.70	0.71	0.76
		δ_{12}	1.09	1.10	1.10	1.11	1.21
	(11$\bar{2}$0)	δ_{23}	1.25	1.30	1.30	1.31	1.21
		δ_{34}	1.17	1.16	1.25	1.27	1.21
		δ_{12}	2.72	2.78	2.85	2.94	2.69
	(0001)	δ_{23}	2.69	2.78	2.85	2.91	2.64
		δ_{34}	2.69	2.78	2.85	2.92	2.61
		δ_{12}	0.00	0.01	0.01	0.01	1.77
Cd	**(10$\bar{1}$0)**	δ_{23}	2.65	2.70	2.89	2.91	0.91
		δ_{34}	0.00	0.01	0.02	0.00	1.77
		δ_{12}	1.29	1.37	1.54	1.64	2.69
	(11$\bar{2}$0)	δ_{23}	1.70	1.70	1.70	1.70	2.64
		δ_{34}	1.36	1.41	1.55	1.61	2.61
		δ_{12}	1.80	1.82	1.84	1.86	1.83
	(001)	δ_{23}	1.89	1.90	1.92	1.93	1.90
		δ_{34}	1.90	1.91	1.94	1.95	1.91
		δ_{12}	1.20	1.21	1.22	1.23	1.24
Rh	**(011)**	δ_{23}	1.34	1.34	1.36	1.36	1.34
		δ_{34}	1.34	1.35	1.38	1.40	1.39
		δ_{12}	2.13	2.15	2.18	2.19	2.16
	(111)	δ_{23}	2.17	2.18	2.21	2.22	2.19
		δ_{34}	2.19	2.21	2.24	2.25	2.22
		δ_{12}	1.90	1.91	1.93	1.95	1.95
	(001)	δ_{23}	1.94	1.95	1.97	1.98	1.98
		δ_{34}	1.95	1.96	1.98	1.99	1.99

Pt	**(011)**	δ_{12}	1.18	1.19	1.21	1.22	1.24
		δ_{23}	1.50	1.51	1.53	1.54	1.51
		δ_{34}	1.32	1.33	1.35	1.37	1.38
	(111)	δ_{12}	2.28	2.29	2.32	2.34	2.33
		δ_{23}	2.23	2.24	2.26	2.28	2.27
		δ_{34}	2.23	2.24	2.26	2.28	2.27
	(001)	δ_{12}	1.89	1.91	1.95	1.98	2.00
		δ_{23}	1.92	1.94	1.98	2.00	1.97
		δ_{34}	1.91	1.93	1.97	2.00	2.00
Pd	**(011)**	δ_{12}	1.22	1.24	1.26	1.28	1.29
		δ_{23}	1.42	1.43	1.45	1.46	1.44
		δ_{34}	1.34	1.36	1.38	1.40	1.38
	(111)	δ_{12}	2.23	2.25	2.28	2.31	2.30
		δ_{23}	2.22	2.23	2.27	2.30	2.28
		δ_{34}	2.21	2.23	2.27	2.29	2.28
	(001)	δ_{12}	1.65	1.68	1.70	1.73	1.69
		δ_{23}	1.73	1.75	1.78	1.80	1.70
		δ_{34}	1.72	1.74	1.77	1.79	1.61
Ni	**(011)**	δ_{12}	1.09	1.11	1.12	1.15	1.21
		δ_{23}	1.24	1.26	1.26	1.29	1.15
		δ_{34}	1.21	1.22	1.25	1.26	1.23
	(111)	δ_{12}	1.96	1.98	2.01	2.03	1.97
		δ_{23}	1.97	2.00	2.03	2.05	1.89
		δ_{34}	1.97	2.00	2.04	2.06	1.88
	(001)	δ_{12}	1.81	1.81	1.83	1.84	1.84
		δ_{23}	1.92	1.93	1.95	1.96	1.94
		δ_{34}	1.91	1.92	1.94	1.95	1.93
Ir	**(011)**	δ_{12}	1.20	1.20	1.21	1.22	1.22
		δ_{23}	1.38	1.39	1.40	1.41	1.38
		δ_{34}	1.32	1.33	1.34	1.35	1.36
	(111)	δ_{12}	2.16	2.16	2.19	2.20	2.18
		δ_{23}	2.22	2.21	2.24	2.25	2.22
		δ_{34}	2.22	2.23	2.25	2.26	2.24
	(001)	δ_{12}	1.71	1.74	1.77	1.80	1.68
		δ_{23}	1.77	1.80	1.82	1.86	1.69
		δ_{34}	1.75	1.79	1.81	1.85	1.69
Cu	**(011)**	δ_{12}	1.11	1.13	1.15	1.17	1.06
		δ_{23}	1.30	1.32	1.34	1.36	1.33
		δ_{34}	1.21	1.23	1.26	1.27	1.33
	(111)	δ_{12}	2.01	2.04	2.08	2.10	2.04
		δ_{23}	2.03	2.06	2.10	2.12	1.91

		δ_{34}	2.03	2.06	2.10	2.12	1.90
Au	**(001)**	δ_{12}	2.00	2.02	2.06	2.09	1.97
		δ_{23}	2.04	2.05	2.09	2.11	2.00
		δ_{34}	2.03	2.05	2.09	2.11	2.01
	(011)	δ_{12}	1.24	1.25	1.27	1.28	1.29
		δ_{23}	1.56	1.57	1.61	1.62	1.55
		δ_{34}	1.35	1.37	1.38	1.40	1.39
	(111)	δ_{12}	2.35	2.37	2.42	2.45	2.37
		δ_{23}	2.33	2.36	2.40	2.43	2.36
		δ_{34}	2.33	2.36	2.39	2.41	2.35
Ag	**(001)**	δ_{12}	1.97	2.00	2.04	2.07	1.98
		δ_{23}	2.01	2.03	2.08	2.12	2.00
		δ_{34}	2.00	2.02	2.07	2.11	2.02
	(011)	δ_{12}	1.28	1.30	1.34	1.36	1.36
		δ_{23}	1.48	1.50	1.53	1.56	1.47
		δ_{34}	1.38	1.40	1.43	1.46	1.50
	(111)	δ_{12}	2.29	2.33	2.38	2.42	2.31
		δ_{23}	2.31	2.35	2.39	2.42	2.31
		δ_{34}	2.31	2.34	2.39	2.42	2.30
W	**(001)**	δ_{12}	1.36	1.36	1.36	1.37	1.40
		δ_{23}	1.62	1.63	1.66	1.67	1.68
		δ_{34}	1.53	1.52	1.52	1.52	1.52
	(011)	δ_{12}	2.14	2.14	2.16	2.17	2.16
		δ_{23}	2.23	2.23	2.25	2.26	2.25
		δ_{34}	2.22	2.22	2.24	2.25	2.24
	(111)	δ_{12}	0.66	0.67	0.67	0.68	0.66
		δ_{23}	0.67	0.67	0.67	0.68	0.70
		δ_{34}	1.20	1.18	1.19	1.19	1.13
V	**(001)**	δ_{12}	1.30	1.29	1.30	1.31	1.44
		δ_{23}	1.45	1.46	1.47	1.49	1.42
		δ_{34}	1.52	1.51	1.54	1.54	1.52
	(011)	δ_{12}	1.97	1.96	1.89	1.99	2.06
		δ_{23}	2.08	2.09	2.08	2.14	2.09
		δ_{34}	2.05	2.06	1.94	2.10	2.00
	(111)	δ_{12}	0.71	0.73	0.74	0.75	0.88
		δ_{23}	0.71	0.72	0.73	0.73	0.86
		δ_{34}	0.88	0.85	0.84	0.83	0.87
	(001)	δ_{12}	1.44	1.46	1.46	1.47	1.43
		δ_{23}	1.61	1.64	1.64	1.66	1.59
		δ_{34}	1.69	1.71	1.73	1.75	1.68
	(011)	δ_{12}	2.20	1.45	2.35	2.25	2.18

Ta		δ_{23}	2.30	1.63	2.41	2.36	2.27
		δ_{34}	2.28	1.72	2.43	2.35	2.26
		δ_{12}	0.74	0.75	0.76	0.77	0.74
	(111)	δ_{23}	0.76	0.77	0.77	0.78	0.75
		δ_{34}	1.12	1.12	1.13	1.13	1.11
		δ_{12}	1.46	1.47	1.47	1.48	1.50
	(001)	δ_{23}	1.61	1.62	1.64	1.65	1.64
		δ_{34}	1.71	1.72	1.73	1.74	1.73
		δ_{12}	2.22	2.22	2.25	2.24	2.27
Nb	**(011)**	δ_{23}	2.32	2.33	2.37	2.37	2.35
		δ_{34}	2.28	2.29	2.32	2.32	2.32
		δ_{12}	0.73	0.74	0.75	0.76	0.78
	(111)	δ_{23}	0.79	0.80	0.80	0.81	0.80
		δ_{34}	1.07	1.07	1.06	1.06	1.11
		δ_{12}	1.35	1.36	1.37	1.37	1.39
	(001)	δ_{23}	1.63	1.64	1.67	1.68	1.65
		δ_{34}	1.50	1.51	1.51	1.51	1.52
		δ_{12}	2.10	2.11	2.13	2.14	2.14
Mo	**(011)**	δ_{23}	2.22	2.23	2.25	2.26	2.24
		δ_{34}	2.22	2.22	2.24	2.26	2.24
		δ_{12}	0.72	0.73	0.73	0.73	0.75
	(111)	δ_{23}	0.69	0.69	0.71	0.72	0.72
		δ_{34}	1.12	1.12	1.11	1.10	1.10
		δ_{12}	1.12	1.36	1.39	1.33	1.33
	(001)	δ_{23}	1.41	1.42	1.44	1.49	1.36
		δ_{34}	1.36	1.37	1.39	1.43	1.37
		δ_{12}	1.92	1.39	2.05	2.02	5.77
Fe	**(011)**	δ_{23}	1.95	1.42	2.07	2.03	3.08
		δ_{34}	1.94	1.44	2.05	2.01	2.00
		δ_{12}	0.66	0.73	0.73	0.74	1.04
	(111)	δ_{23}	0.38	0.68	0.69	0.70	0.73
		δ_{34}	1.33	0.98	0.98	0.98	0.96
		δ_{12}	1.21	1.21	1.21	1.22	1.38
	(001)	δ_{23}	1.49	1.50	1.53	1.55	1.38
		δ_{34}	1.31	1.31	1.31	1.31	1.37
		δ_{12}	1.89	1.89	2.00	1.92	1.98
Cr	**(011)**	δ_{23}	1.98	1.99	2.07	2.03	1.95
		δ_{34}	1.98	1.98	2.06	2.02	1.97
		δ_{12}	0.66	0.67	0.67	0.68	0.81
	(111)	δ_{23}	0.61	0.61	0.62	0.62	0.64
		δ_{34}	0.98	0.97	0.96	0.96	1.10

Table S11. Linear regression parameters correlating δ_{ij}^{calc} values with respect experimental values δ_{ij}^{exp}. Slopes, *a*, intercepts, *b* (in Å), and regression coefficients, *R*, are listed.

	$\boldsymbol{\delta_{ij}^{exp}}$		
	a	***b***	***R***
TPSS	0.79	0.39	0.63
RPBE	0.79	0.36	0.80
PBE	0.78	0.36	0.80
PBEsol	0.76	0.36	0.79
VWN	0.77	0.33	0.80

Table S12. ME, MAE, and MAPE for δ_{ij}^{calc} values with respect experiments, grouped per TMs within *hcp*, *fcc*, or *bcc* crystallographic structures. Values of ME and MAE are given in Å, whereas MAPE is given in percentage.

		δ_{ij}^{calc}				
		VWN	**PBEsol**	**PBE**	**RPBE**	**TPSS**
hcp	**ME**	-0.11	-0.09	-0.06	-0.03	-0.06
	MAE	0.21	0.21	0.20	0.20	0.18
	MAPE	15.67	16.16	15.47	15.25	13.59
fcc	**ME**	-0.06	-0.04	-0.01	0.01	-0.03
	MAE	0.19	0.18	0.18	0.19	0.19
	MAPE	10.70	10.14	10.05	10.67	10.96
bcc	**ME**	-0.10	-0.09	-0.03	0.01	0.27
	MAE	0.11	0.10	0.06	0.05	0.35
	MAPE	9.02	6.96	4.56	4.46	20.55

Figure S1. Exchange-correlation functionals that yield the closest results to bulk and surface experimental data, extrapolated to 0 K and corrected for zero-point vibrations whenever possible, for each transition metal. Data beyond VWN, PBE, PBEsol, RPBE, and TPSS is taken from Ref. 139.

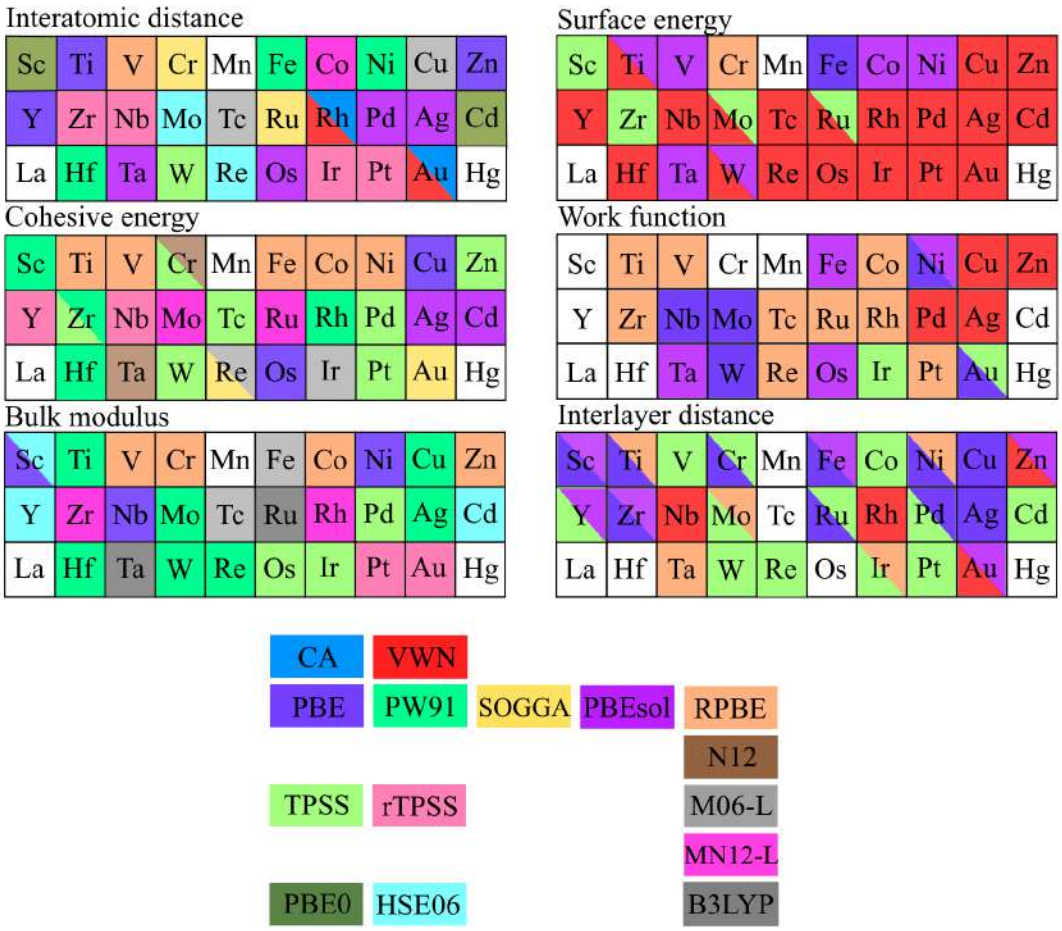

References

1. Mills, K. C.; Su, Y. C., Review of Surface Tension Data for Metallic Elements and Alloys: Part 1 – Pure Metals. *Int. Mater. Rev.* **2006**, *51*, 329.
2. Helbert B. M., The Work Function of the Elements and its Periodicity. *J. Appl. Phys.* **1977**, *48*, 4729.
3. Malamud H.; Krumbein, A., Measurement of the Effect of Chlorine Treatment on the Work Function of Titanium and Zirconium. *J. Appl. Phys.* **1954**, *25*, 591.
4. De-Peng, J.; Quanxi, Z.; Shao-Qing, W., Detailed First-Principles Studies on Surface Energy and Work Function of Hexagonal Metals. *Surf. Sci.* **2016**, *615*, 137.
5. Himpsel, F.J.; Christmann, K.; Heimann, P.; Eastman, D.E; Feibelman P., Adsorbate Band Dispersions for C on Ru(0001). *Surf. Sci.* **1982**, *115*, L159.
6. Skriver, H.L.; Rosengard, N.M., Surface Energy and Work Function of Elemental Metals. *Phys. Rev. B.* **1992**, *46*, 7157.
7. Saito, S.; Takeda, K.; Soumura, T.; Ohki, M.; Tani, T.; Maeda, T., Hysteresis of the Work Function of Co(0001) Surface Resulting from an Allotropic Transformation. *J. Appl. Phys.* **1992**, *71*, 5500.
8. *CRC Handbook of Chemistry and Physics*, 67th ed., CRC Press, Boca Raton, FL, **1987**.
9. Castro, G.R.; Busse, H.; Schneider, U.; Janssens, T.; Wandelt, K., Geometric and Electronic Structure of Potassium on Rh(111). *Physica Scripta* **1992**, *T41*, 208.
10. Wang, J.; Shao-Qing, W., Surface Energy and Work Function of *fcc* and *bcc* Crystals: Density Functional Study. *Surf. Sci.* **2014**, *630*, 216.
11. Fomenko, V.S., *Handbook of Thermionic Properties: Electronic Functions and Richardson Constants of Elements and Compounds*. Eds. Fomenko, V.S.; Samsanov, G.U., Plenum Press Data Division, New York, **1966**.
12. Himpsel, F.J., Image States at Ferromagnetic Surfaces: Fe(110), (100), (111) and Co(0001). *Phys. Rev. B.* **1991**, *43*, 13394.
13. Teeter, G.; Erskine, J.L., Surface relaxation of Ti(0001): Influence of hydrogen contamination. *Phys. Rev. B*. **2000**, *61*, 13929.
14. Unertl, W.N.; Thapliyal, H.V., Surface parameters of clean Zn(0001) determined from averaged LEED data. *J. Vac. Sci. Technol.* **1975** ,*12*, 263.
15. Barrett, S. D. ; Dhesi, S.S.; Evans, M. P.; White, R.G., Determination of the surface relaxation of Sc (0001) by video LEED analysis. *Meas. Sci. Technol*. **1993**, *4*, 114.
16. Shih, H.D.; Jona, F.; Jepsen, D.W.; Marcus, P.M., The structure of the clean Ti (0001) surface. *J. Phys. C: Solid State Phys.* **1976**, *9*, 1405.
17. Teeter, G.; Erskine, J.L., Studies of clean metal surface relaxation experiment-theory discrepancies. *Surf. Rev. Lett*. **1999**, *6(5)*, 813-817.
18. Mischenko III, J.; Watson, P.R., The termination of the titanium (100) surface. *Surf. Sci.* **1989**, *220*, L667.
19. Tougaard, S.; Ignatiev, A., Atomic structure of the scandium (0001) surface. *Surf. Sci.* **1982**, *115*, 270.
20. Dhesi, S.S.; White, R.G.; Patchett, A.J.; Evans, M.P.; Lee, M.H.; Blyth, R.I.R.; Leibsle, F.M.; Barrett, S.D., Surface-structure determination of Sc(0001) using LEED and STM. *Phys. Rev. B.* **1995**, *51*, 17946.
21. De la Figuera, J.; Puerta, J.M.; Cerda, J.I.; El Gabaly, F.; McCarty, K.F., Determining the structure of Ru(0001) from low-energy electron diffraction of a single terrace. *Surf.Sci.* **2006** , *600*, 105.

22. Davis, H.L.; Noonan, J.R., Multilayer relaxation in metallic surfaces as demonstrated by LEED analysis. *Surf. Sci*. **1983**, *126*, 245.
23. Davis, H.L.; Zehner, D.M., Structure of the clean Re(10$\bar{1}$0) surface. *J.Vac.Sci. Technol.* **1980**, *17*,190.
24. Lee, B.W.; Alsenz, R.; Ignatiev, A.; Van Hove, M.A., Surface structures of the two allotropic phases of cobalt. *Phys. Rev. B*. **1978**, *17*, 1510.
25. Lahtinen, J.; Vaari, J.; Vaara, T.; Kauraala, K.; Kaukasoina, P.; Lindroos, M., LEED investigations on Co(0001): the clean surface and the (2x2)-K overlayer. *Surf. Sci*. **1999**, *425*, 90.
26. Lindroos, M.; Barnes, C.J.; Hu, P.; King, D.A., The termination and multilayer relaxation at the Co {1010} surface. *Chem. Phys. Lett*. **1990**, *173*, 92.
27. Over, H.; Kleinle, G.; Ertl, G.; Moritz, W.; Ernst, K.-H.; Wohlgemuth, H.; Christmann, K.; Schwarz, E., A LEED structural analysis of the Co(1010) surface. *Surf. Sci*. **1991**, *254*, L469.
28. Shih, H.D.; Jona, F.; Jepsen, D.W.; Marcus, P.M., Low-energy electron-diffraction determination of the structure of successively deposited ordered layers of Cd on Ti(0001). I. The first layer. *Phys. Rev. B*. **1977**, *15*, 5550.
29. Begley, A.M.; Kim, S.K.; Jona, F.; Marcus, P.M., Surface relaxation of Rh(001). *Phys. Rev. B*. **1993**, *48*, 12326.
30. Watson, P.R.; Shepherd, F.R.; Frost, D.C.; Mitchell, K.A.R., Structural determinations of the Rh(100) and Cu(111) surfaces using the reliability factor proposed for LEED by Zanazzi and Jona. *Surf. Sci*. **1978**, *72*, 562.
31. Oed, W.; Dötsch, B.; Hammer, L.; Heinz, K.; Müller, K., A LEED investigation of clean and oxygen covered Rh(100). *Surf. Sci*. **1988**, *207*, 55.
32. Prince, K.C.; Ressel, B.; Astaldi, C.; Peloi, M.; Rosei, R.; Polcik, M.; Crotti, C.; Zacchigna, M.; Comicioli, C.; Ottaviani, C.; Quaresima, C.; Perfetti, P., Surface core level shift photoelectron diffraction of Rh(100). *Surf. Sci*. **1997**, *377*, 117.
33. Teeter, G.; Hinson, D.; Erskine, J.L.; Duke, C.B.; Paton, A., Surface structure of Rh(001) and *p*(1x1) H on Rh(001): An unresolved discrepancy between experiment and theory. *Phys. Rev. B*. **1998**, *57*, 4073.
34. Hengrasmee, S.; Mitchell, K.A.R.; Watson, P.R.; White, S.J., Some observations on the use of reliability indices in LEED crystallography. *Can. J. Phys*. **1989**, *58*, 200.
35. Batirev, I.G. Atomic forces and electronic properties of Pd(001) and Rh(001) thin films. *Philos. Mag. Lett.* **1996**, *73*, 385-394.
36. Frost, D.C.; Hengrasmee, S.; Mitchell, K.A.R.; Shepherd, F.R.; Watson, P.R., The structure of the clean (110) surface of rhodium. *Surf. Sci*. **1978**, *76*, L585.
37. Nichtl, W.; Bickel, N.; Hammer, L.; Heinz, K.; Müller, K., Surface relaxation change by hydrogen adsorption on Rh(110). *Surf. Sci*. **1987**, *188*, L729.
38. Aghemenlo, H.E.; Iyayi, S.E.; Avwiri, G.O., Surface relaxation and surface energy of face – centered Cubic metals. **2006**,*10*, 37.
39. Chan, C.M.; Thiel, P.A.; Yates, J.T.; Weinberg, W.H., The geometrical and vibrational properties of the Rh(111) surface. *Surf. Sci*. **1978**, *76*, 296.
40. Barbieri, A.; Van Hove, M.A.; Somorjai, G.A., 4th Int. Conf. on the Structure of Surfaces. *World Scientific Publ. Co*. **1994**, p.201.
41. Wander, A.; Barnes, C.J.; Mapledoram, L.D.; King, D.A., Structural transitions in ultra-thin nickel films on Rh{111}. *Surf. Sci.* **1993**, *281*, 42.

42. Fukuoka, M.; Okada, M.; Matsumoto, M.; Ogura, S.; Fukutani, K.; Kasai, T., Location of hydrogen absorbed on Rh(111) studied by low-energy electron diffraction and nuclear reaction analysis. *Phys. Rev. B*. **2007**, *75*, 235434.
43. Feder, R., Spin-polarized LEED from low-index surfaces of platinum and gold. *Surf. Sci.* **1977**, *68*, 229.
44. Watson, P.R.; Van Hove, M.A.; Hermann, K., Atlas of surface structures. *Am. Chem. Soc. 1994*.
45. Davies, J.A.; Jackman, T.E.; Jackson, D.P.; Norton, P.R. Surface relaxation of the platinum (100)−(1 × 1) surface at 175 K. *Surf. Sci.* **1981**, *199*, 20-28.
46. Adams, D.L.; Nielsen, H.B.; Van Hove, M.A., Quantitative analysis of low-energy-electron diffraction: Application to Pt(111). *Phys. Rev. B*. **1979**, *20*, 4789.
47. Feder, R.; Pleyer, H.; Bauer, P.; Müller, N., Spin polarization in low-energy electron diffraction Surface analysis of Pt(111). *Surf. Sci*. **1981**, *109*, 419.
48. Miszczuk, A.; Morawski, I.; Kucharczyk, R.; Nowicki, M., Surface relaxation of Pt(111) and Cu/Pt(111) revealed by DEPES. *Appl. Surf.Sci.* **2016**, *373*, 32.
49. Van Der Veen, J.F.; Smeenk, R.G.; Tromp, R.M.; Saris, F.W., Relaxation effects and thermal vibrations in a Pt(111) surface measured by medium energy ion scattering. *Surf. Sci.* **1979**, *79*, 219.
50. Stock, M.; Meyer-Ehmsen, G., An efficient multiple parameter evaluation of measured RHDEED rocking curves applied to Pt(111). *Surf. Sci*. **1990**, *226*, L59.
51. Materer, N.; Starke, U.; Barbieri, A.; Döll, R.; Heinz, K.; Van Hove, M.A.; Somorjai, G.A., Reliability of detailed LEED structural analyses: Pt(111) and Pt(111)-p(2x2)-O. *Surf. Sci.* **1995**, *325*, 207.
52. Gallego, S.; Ocal, C.; Soria, F., Surface and bulk reconstruction of Pt(111) 1x1. *Surf. Sci.* **1997**, *377-379*, 18.
53. Kim, C.; Höfner, C.; Rabalais, J.W., Surface structure detemination from ion scattering images. *Surf. Sci*. **1997**, *388*, L1085.
54. Karlberg, G.S.; Wahnström, G., Water desorption from an oxygen covered Pt(111) surface: Multichannel desorption. *J.Chem. Phys*. **2005**, *123*, 064711.
55. Jona, F.; Sondericker, D.; Marcus, P.M., Al(111) revisited. *J.Phys. C*. **1980**, *13*, L155.
56. Krupski, K.; Moors, M.; Józwil, P.; Kobiela, T., Structure Determination of Au and Pt(111) Surface: LEED, STM and DFT Study. *Mat.* **2015**, *8*, 2935.
57. Quinn, J.; Li, Y.S.; Tian, D.; Li, H.; Jona, F.; Marcus, P.M., Anomalous multilayer relaxation of Pd{001}. *Phys. Rev. B*. **1990**, *42*, 11348.
58. Behm, R.J.; Christmann, K.; Ertl, G., Adsorption of CO on Pd(100). *J. Chem. Phys.* **1980**, *73*, 2984.
59. Behm, R.J.; Christmann, K.; Ertl, G.; Van Hove, M.A.; Thiel, P.A.; Weinberg, W.H., The structure of CO absorbed on Pd(100):A leed and hreels analysis. *Surf. Sci.* **1979**, *88*, L59.
60. Burchhardt, J.; Lundgren, E.; Nielsen, M.M.; Andersen, J.N., Adams, D.L., The surface structures of Pd(100)-(1x1) and c(2x2)-K. *Surf. Rev.Lett.* **1996**, *3*, 1339.
61. Kim, S.H.; Meyeheim, H.L.; Barthel, J.; Kirschnner, J.; Seo, J.; Kim, J.-S., Origin of anomalous surface lattice expansion in Pd(001). *Phys. Rev. B.* **2005**, *71*, 205418.
62. Barnes, C.J.; Ding, M.Q.; Lindroos, M.; Diehl, R.D.; King, D.A., A LEED structural study of the Pd{110}-(1x1) surface and an alkali-metal-induced (1x2) surface reconstruction. *Surf. Sci*. **1985**, *162*, 59.

63. Skottke, M.; Behm, R.J.; Ertl, G.; Penka, V.; Moritz, W., LEED structure analysis of the clean and (2x1)H covered Pd(110) surface. *J. Chem. Phys*. **1987**, *87*, 6191.
64. Ohtani, H.; Van Hove, M.A.; Somorjai, G.A., Leed intensity analysis of the surface structures of Pd(111) in a $(\sqrt{3}\times\sqrt{3})$R30º arrangement. *Surf. Sci*. **1987**, *187*, 372.
65. Kuk, Y.; Feldman, L.C.; Silveman, P.J., Transition from the Pseudomorphic State to the Nonregistered State in Epitaxial Growth of Au on Pd(111). *Phys. Rev. Lett*. **1983**, *50*, 511.
66. Grillo, M.E.; Stampfl, C.; Berndt, W., Low-energy electron-diffraction analysis of the $(\sqrt{7}\times\sqrt{7})$R19.1º-S adsorbate structure on the Pd(111) surface. *Surf. Sci*. **1994**, *317*, 84.
67. Frenken, J.W.M.; Van der Veen, J.F.; Allan, G., Relation between Surface Relaxation and Surface Force Constants in Clean and Oxygen-Covered Ni(001). *Phys. Rev. Lett.* **1983**, *51*,1876.
68. Oed, W.; Lindner, H.; Starke, K.; Heinz, K.; Müller, K., Adsorbate-induced relaxation and reconstruction of c(2x2)O/Ni(100): A reinvestigation by leed structure analysis. *Surf. Sci.* **1989**, *224*, 179.
69. Demuth, J.E.; Marcus, P.M.; Jepsen, D.W., Analysis of low-energy-electron-diffraction intensity spectra for (001), (110), and (111) nickel. *Phys. Rev. B*. **1975**, *11*, 1460.
70. Adams, D.L.; Petersen, L.E.; Sørensen, C.S., Oscillatory relaxation of the Ni(110) surface: a LEED study. *J.Phys.C*. **1985**, *18*, 1753.
71. Gauthier, Y.; Baudoing, R.; Joly, Y.; Gaubert, C.; Rundgren, J., Multilayer Relaxation of Ni(110) Analysed by LEED and Metric Distances. *J. Phys. C: Solid State Phys*. **1984**, *17*, 4547.
72. Demuth, J.E.; Marcus, P.M.; Jepsen, D.W., Analysis of low-energy-electron-diffraction intensity spectra for (001), (110) and (111) nickel. *Phys. Rev. B*. **1975**, *11*, 1460.
73. Gauthier, Y.; Baudoing, R.; Clarke, L., Extensive LEED analysis of Ni(110). II. R-factor analysis of I(E) data. *J. Phys. C: Solid State Phys.* **1982**, *15*, 3231.
74. Clarke, L.J.; Baudoing, R.; Gauthier, Y., Extensive LEED analysis of Ni(110). III. Merits and drawbacks of the I(g) approach. *J. Phys. C: Solid State Phys.* **1982**, *15*, 3249.
75. Turkenburg, W.C.; Smeenk, R.G.; Saris, F.W., Investigations of surface relaxation and surface composition of Ni(110) by medium energy ion scattering spectroscopy. *Surf. Sci.* **1978**, *74*, 181.
76. Van der Veen, J.F.; Smeenk, R.G.; Tromp, R.M.; Saris, F.W., The effect of oxygen coverage on surface relaxation of Ni(110) measured by medium energy ion scattering. *Surf. Sci*. **1979**, *79*, 212.
77. Demuth, J.E.; Marcus, P.M.; Jepsen, D.W., Analysis of low-energy-electron-diffraction intensity spectra for (001), (110) and (111) nickel. *Phys. Rev. B*. **1975**, *11*, 1460.
78. Chan, C.-M., Cunningham, S.L.; Van Hove, M.A.; Weinberg, W.H.; Withrow, S.P., An analysis of the structure of the iridium (111) surface by low-energy electron diffraction. *Surf. Sci*. **1977**, *66*, 394.
79. Chan, C.-M., Cunningham, S.L.; Luke, K.L.; Weinberg, W.H.; Withrow, S.P., Determination of the atomic arrangement of the unreconstructed Ir(110) surface by low-energy electron diffraction a. *Surf. Sci*. **1978**, *78*, 15.
80. Davis, H.L.; Noonan, J.R., Cu(100) multilayer relaxation. *J.Vac.Sci.Technol.* **1982**, *20*, 842.
81. Lind, D.M.; Dunning, F.B.; Walters, G.K.; Davis, H.L., Surface-structural analysis by uses of spin-polarized low-energy electron diffraction: An investigation of the Cu(100) surface. *Phys. Rev. B*. **1987**, *35*, 9037.
82. Laramore, G.E. Analysis of low-energy-electron diffraction intensity profiles from the (100) and (111) faces of copper. *Phys. Rev. B* **1974**, *89*, 1204.

83. Fowler, D.E.; Barth, J.V.; Structure and dynamics of the Cu(001) surface investigated by medium-energy ion scattering. *Phys. Rev. B*. **1995**, *52*, 2117.
84. Tiang, Q.T.; Fenter, P.; Gustafsson, T., Geometric structure and surface vibrations of Cu(001) determined by medium-energy ion scattering. *Phys. Rev. B*. **1991**, *44*, 5773.
85. Breese, M.; Rehn, L.E.; Trautmann, C.; Vickridge, I.C. Nuclear Instruments and Methods in Physics Research Section B: Beam Interactions with Materials and Atoms. **1986**, *15*, 126.
86. Adams, D.L.; Nielsen, H.B.; Andersen, J.N., Oscillatory relaxation of the Cu(110) surface. *Surf. Sci*. **1983**, *128*, 294.
87. Davis, H.L.; Noonan, J.R.; Jenkins, L.H., Determination of a Cu(110) surface contraction by leed intensity analysis. *Surf. Sci*. **1979**, *83*, 559.
88. Adams, D.L.; Nielsen, H.B.; Andersen, J.N.; Stensgaard, I.; Feidenhasns'l, R.; Sørensen, J.E., Oscillatory Relaxation of Cu (110) Surface. Phys. Rev. Lett. 1982, 49, 669.
89. Tear, S.P.; Roll, K.; Prutton, M., A comparison of reliability (R) factors in a LEED structural analysis of the copper (111) surface. *J. Phys. C: Solid State Phys*. **1981**, *14*, 3297.
90. Lindgren, S.Å; Walldén, L.; Rundgren, J.; Westrin, P., Low-energy electron diffraction from Cu(111): Subthreshold effect energy-dependent inner potential; surface relaxation and metric distances between spectra. *Phys. Rev. B*. **1984**, *29*, 576.
91. Tear, S.P.; Röll, K., A LEED study of Cu(111) (1x1)-Ni using reliability (R) factors. *J. Phys. C: Solid State Phys*. **1982**, *15*, 5521.
92. Li, H.; Quinn, J.; Li, Y.S.; Tian, D.; Jona, F.; Marcus, P.M., Multilayer relaxation of clean Ag{001}. *Phys. Rev. B*. **1991**, *43*, 7305.
93. Ocko, B.M.; Gibbs, D.; Huang, K.G.; Zehner, D.M.; Mochrie, S.G.J., Structure and phases of the Au(001) surface: Absolute x-ray reflectivity. *Phys. Rev. B*. **1991**, *44*, 6429.
94. Bohnen, K. -P.; Ho, K.M., Surface structure of gold and silver (110)-surfaces. *Electrochimica Acta*. **1995**, *40*, 129
95. Nichols, R.J.; Nouar, T.; Lucas, C.A.; Haiss, W.; Hofer, W.A., Surface relaxation and surface stress of Au(111). *Surf. Sci.* **2002**, *513*, 263.
96. Sandy, A.R.; Mochrie, S.G.J.; Zehner, D.M.; Huang, K.G.; Gibbs, D., Structure and phases of the Au(111) surface: X-ray scattering measurements. *Phys. Rev. B* **1991**, *43*, 4667.
97. McGuirk, G.M.; Shin,H.; Caragiu, M.; Ash, S.; Bandyopadhyay, P.K.; Prince, R.H.; Diehl, R.D. Au (111) surface structures induced by adsorption: LEED I(E) analysis of (1x1) and (5x5) Au(111)-S phases. *Surf.Sci*. **2013**, 610, 42.
98. Jepsen, D.W.; Marcus, P.M.; Jona, F., Low-Energy-Electron-Diffraction Intensities from Ag{001}. II. Theory. *Phys. Rev. B*. **1973**, *8*, 5523.
99. Alff, M.; Moritz, W., Structure of the Ag(110) surface determined by using averaged leed intensities. *Surf. Sci.* **1979**, *80*, 24.
100. Zanazzi, E.; Jona, F.; Jepsen, D.W.; Marcus, P.M., Structure of Ag(110) and effect of surface roughness on LEED intensities. *J.Phys. C: Solid State Phys.* **1977**, *10*, 375.
101. Maglietta, M.; Zanazzi, E.; Jona, F.; Jepsen, D.W.; Marcus, P.M., Re-examination of the structure of the clean (110) surface of Ag. *J.Phys. C: Solid State Phys*. **1977**, *10*, 3287.
102. Kuk, Y.; Feldman, L.C., Oscillatory relaxation of the Ag(110) surface. *Phys. Rev. B*. **1984**, *30*, 5811.
103. Soria, F.; Sacedon, J.L.; Echenique, P.M.; Titterington, D., LEED study of the epitaxial growth of the thin film Au(111)/Ag(111) system. *Surf. Sci*. **1977**, *68*, 448

104. Soaresa, E.A.; Nascimentoa, V.B.; De Carvalhoa, V.E.; De Castilhob, C.M.C.; De Carvalhoa, A.V.; Toomesc, R.; Woodruffc, D.P., Structure determination of Ag(111) by low-energy electron diffraction. *Surf. Sci.* **1999**, *419*, 89.
105. Statiris, P.; Lu, H.C.; Gustafsson, T., Temperature dependent sign reserval of the surface contraction of Ag(111). *Phys. Rev. Lett.* **1994**, *72*, 3574.
106. Ontani, H.; Van Hove, M.A.; Somorjai, G.A., Leed intensity analysis of the surface structures of Pd(111) and of CO absorbed on Pd(111) in a $(\sqrt{3}\times\sqrt{3})$ R30º arrangement. *Surf. Sci*. **1987**, *187*, 372.
107. Van Hove, M.A.; Tong, S.Y., Surface structures of W(100) faces by the dynamical LEED approach. *Surf. Sci*. **1976**, *54*, 91.
108. Kirschner, J.; Feder, R., Surface structure determination by leed rotation diagrams; Application to the surface relaxation of W(001). *Surf. Sci*. **1979**, *79*, 176.
109. Debe, M.K.; King A, D.; Marsh, F.S., Further dynamical and experimental LEED results for a clean W<"001"-(1x1) surface structure determination. *Surf. Sci.* **1977**, *68*, 437
110. Feder, R.; Kirschner, J., Spin-polarized low-energy electron diffraction: Theory, experiment and analysis of results from W(001)(1x1). *Surf. Sci*. **1981**, *103*, 75.
111. Lee, B.W.; Ignatiev, A.; Tong, S.Y.; VanHove, M., Surface contraction of the clean W(001) face. *Surf. Sci*. **1977**, *14*, 291.
112. Heilmann, P.; Heinz, K.; Müller, K., Temperature dependence of W(100) leed intensities. *Surf. Sci.* **1979**, *89*, 84
113. Marsh, F.S.; Debe, M.K, King, D.A., W(001) (1x1) surface structure: pseudo-relativistic LEED calculations and R-factor analysis. *J. Phys. C: Solid State Phys.* **1980**, *13*, 2799.
114. Clarke, L.J.; Morales de la Garza, L., Surface structure of unreconstructed W(001) from alternative leed techniques. *Surf. Sci.* **1980**, *99*, 419.
115. Read, M.N.; Russell, G.J., On the contraction of the W(001)-(1x1) surface using LEED instensity analysis. *Surf. Sci.* **1979**, *88*, 95.
116. Luo, J.S; Legrand B.,Multilayer relaxation at surfaces of body-centered- cubic transition metals. *Phys. Rev. B*. **1988**, *38*, 3.
117. Santos, B.; Puerta, J.; Cerda, J.; Stumpf, R.; Von Bergmann, K.; Wiesendanger, R.; Bode, M.; McCarty, K.; de la Figuera, J., Structure and magnetism of ultra-thin chromium layers on W(110). *New. J. Phys*. **2008**, *10*, 013005.
118. Arnold, M.; Sologub, S.; Hupfauer, G.; Bayer, P.; Frie, W.; Hammer, L.; Heinz, K., Leed structure analyses of the clean and fully hydrogen-covered W(110) and Mo(110) surfaces. *Surf. Rev. Lett.* **1997**, *4*, 1291.
119. Venus, D.; Cool, S.; Plihal, M., Quantitative structural determination using spin-polarized low-energy electron diffraction rotation curves: W(110). *Surf. Sci.* **2000**, *446*, 199.
120. Teeter, G.; Erskine, J.L.; Shi, F.; Van Hove, M.A., Surface roughness and LEED crystallography: Analysis of flat and vicinal W(110). *Phys. Rev. B*. **1999**, *60*, 1975.
121. Feder, R., Relativistic Theory of Low Energy Electron Diffraction: Application to the (001) and (110) Surfaces of Tungsten. **1974**, *62*, 135.
122. Teeter, G.; Erskine, J.L., Studies of clean metal surface relaxation experiment-theory discrepancies. *Surf. Rev. Lett.* **1999**, *6*, 813.
123. Jensen, V.; Andersen, J.N.; Nielsen, H.B.; Adams, D.L., The surface structure of V(100). *Surf. Sci.* **1982**, *116*, 66.
124. Titov, A.; Moritz, W., Structure of the clean Ta(100) surface. *Surf. Sci.* **1982**, *123*, L709.

125. Bartynski, R.A.; Heskett, D.; Garrison, K.; Watson, G.M.; Zehner, D.M.; Mei, N.; Tong, S.Y.; Pan, X., Photoelectron diffraction determination of the geometry of a clean metal surface: Ta(100). **1989**, *40*, 5340.
126. Lo, W.-S.; Chien, T.-S.; Fang, B.-S.; Wei, C.M.; Nei, W.N., Photoelectron-Diffraction Studies of Nb(001). *Surf. Rev. Lett.* **1988**, *5*, 1035.
127. Ignatiev, A.; Jona, F.; Shih, H.D.; Jepsen, D.W.; Marcus, P.M., The structure of the clean Mo[001] surface. *Phys. Rev. B*. **1975**, *11*, 4787.
128. Clarke, L.J., LEED analysis of the surface structure of Mo(001). *Surf. Sci*. **1980**, *91*, 131.
129. Clarke, L.J., Structure of s adsorbed on Mo(001) by LEED analysis; Effects on CO adsorption. *Surf. Sci.* **1981**, *102*, 331.
130. Terakura, I.; Terakura, K.; Hamada, N., Electronic origin of the surface reconstruction and relaxation of the (001) surface of Mo and W. *Surf. Sci.* **1981**, *111*, 479.
131. Morales de la Garza, L.; Clarke, L.J., The surface structure of Mo(110) determined by LEED. *J.Phys.C: Solid State Phys.* **1980**, *14*, 5391.
132. Arnold, M.; Fahmi, A.; Frie, W.; Hammer, L.; Heinz, K., Unusual multilayer relaxation of the Mo(111) surface induced by hydrogen. J. Phys.: Condens. Matter. 1999, 11, 1873.
133. Overbury, S.H., Surface layer relaxation on Mo(111) measured by low energy alkali ion scattering. *Surf. Sci*. **1986**, *175*, 123.
134. Legg, KO.; Jona, F.; Jepsen, D.W.; Marcus, P.M., Low-energy electron diffraction analysis of the clean Fe(001). *J.Phys.C: Solid State Phys.* **1977**, *10*, 937.
135. Shih, H.D.; Jona, F.; Bardi, U.; Marcus, P.M., The atomic structure of Fe(110). *J.Phys.C: Solid State Phys.* **1980**, *13*, 3801.
136. Breese, M.; Rehn, L.E.; Trautmann, C.; Vickridge, I.C., Nuclear Instruments and methods in Physics Research section B: Beam interactions with materials and atoms. **1991**, *53*, 315.
137. Shih, H.D.; Jona, F.; Jepsen, D.W.; Marcus, P.M., Atomic structure of Fe {111*}*. *Surf. Sci.* **1981**, *104*, 39.
138. Sokolov, J.; Jona, F.; Marcus, P.M., Multilayer relaxation of a clean bcc Fe{111} surface. *Phys. Rev. B*. **1986**, 33, 1397.
139. Janthon, P.; Luo, S.; Kozlov, S. M.; Viñes, F.; Limtrakul, J.; Truhlar, D. G.; Illas, F., Bulk Properties of Transition Metals: A Challenge for the Design of Universal Density Functionals. *J. Chem. Theory Comput.* **2014,** *10*, 3832-3839.

B. Supplementary Information of Robustness of Surface Activity Electronic Structure-Based Descriptors of Transition Metals

Figure S1. Exemplary *d*-PDOS representation of bulk and (0001) surface of Ti obtained by PBE and the absolute difference between them. The red area belongs to the integral of this difference.

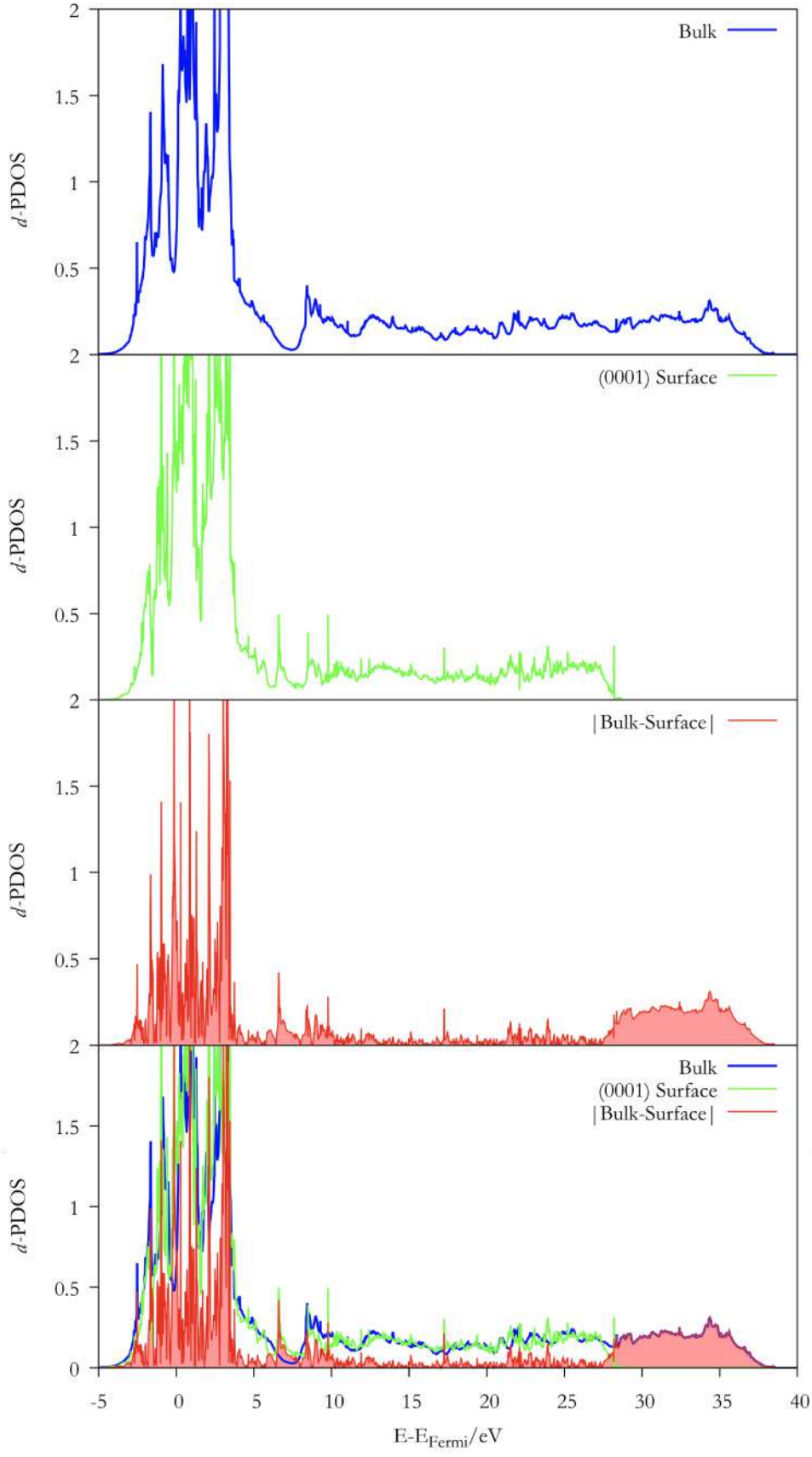

Table S1. Calculated values of ε_d (eV) for all TMs surfaces and density functionals.

ε_d	surfaces	VWN	PBE_{sol}	PBE	RPBE	TPSS
Zr	(0001)	3.52	3.23	3.00	3.01	2.73
	$(10\bar{1}0)$	3.43	3.40	3.04	2.83	2.52
	$(11\bar{2}0)$	3.19	2.93	2.41	2.55	2.19
Zn	(0001)	-7.40	-7.26	-7.21	-7.12	-7.54
	$(10\bar{1}0)$	-7.14	-7.00	-6.97	-6.92	-7.45
	$(11\bar{2}0)$	-7.34	-7.18	-7.12	-7.01	-7.47
Y	(0001)	4.83	4.26	3.80	3.42	3.17
	$(10\bar{1}0)$	4.56	3.94	3.63	3.12	3.09
	$(11\bar{2}0)$	3.82	3.34	3.08	2.76	2.65
Ti	(0001)	3.74	3.38	3.07	2.91	3.42
	$(10\bar{1}0)$	3.73	3.33	2.96	2.72	3.30
	$(11\bar{2}0)$	3.15	2.70	2.42	2.36	2.94
Tc	(0001)	-0.62	-0.52	-0.50	-0.50	-0.51
	$(10\bar{1}0)$	-0.64	-0.55	-0.68	-0.53	-0.56
	$(11\bar{2}0)$	-0.94	-0.87	-0.84	-0.86	-0.83
Sc	(0001)	5.07	4.32	3.61	3.28	3.92
	$(10\bar{1}0)$	4.33	4.08	3.71	3.15	3.72
	$(11\bar{2}0)$	3.83	3.35	3.16	2.74	2.97
Ru	(0001)	-1.53	-1.47	-1.42	-1.37	-1.45
	$(10\bar{1}0)$	-1.40	-1.38	-1.29	-1.27	-1.77
	$(11\bar{2}0)$	-1.37	-1.34	-1.27	-1.24	-1.32
Re	(0001)	1.34	1.27	1.22	1.04	1.46
	$(10\bar{1}0)$	1.22	1.09	0.99	1.11	0.64
	$(11\bar{2}0)$	1.03	0.93	0.84	0.68	1.13
Os	(0001)	-0.42	-0.42	-0.43	-0.41	-0.41
	$(10\bar{1}0)$	-0.33	-0.36	-0.35	-0.32	-0.38
	$(11\bar{2}0)$	-0.24	-0.45	-0.41	-0.35	-0.30
Hf	(0001)	3.50	3.15	2.91	2.81	3.80
	$(10\bar{1}0)$	3.34	2.98	2.71	2.56	3.50
	$(11\bar{2}0)$	2.82	2.56	2.26	2.16	3.06
Co	(0001)	-0.58	-0.58	-0.51	-0.51	-1.05
	$(10\bar{1}0)$	-0.74	-0.71	-0.60	-0.61	-1.21
	$(11\bar{2}0)$	-0.95	-0.74	-0.74	-0.74	-0.44
Cd	(0001)	-8.76	-8.71	-8.70	-8.71	-7.60
	$(10\bar{1}0)$	-8.51	-8.49	-8.63	-8.54	-7.36
	$(11\bar{2}0)$	-8.64	-8.58	-8.48	-8.48	-7.64
Rh	(001)	-1.70	-1.63	-1.52	-1.46	-1.64
	(011)	-1.73	-1.68	-1.56	-1.53	-1.90
	(111)	-1.85	-1.77	-1.64	-1.60	-1.76
Pt	(001)	-2.28	-2.19	-2.03	-1.97	-2.01
	(011)	-2.26	-2.19	-2.04	-1.97	-1.99
	(111)	-2.39	-2.31	-2.16	-2.08	-2.15
Pd	(001)	-2.00	-1.90	-1.72	-1.64	-1.70
	(011)	-1.96	-1.87	-1.72	-1.66	-1.73
	(111)	-2.10	-2.01	-1.83	-1.74	-1.90

Ni	(001)	-1.54	-1.49	-1.39	-1.34	-1.72
	(011)	-1.36	-1.33	-1.26	-1.21	-1.47
	(111)	-1.82	-1.77	-1.65	-1.59	-2.03
Ir	(001)	-0.78	-0.73	-0.63	-0.60	-0.47
	(011)	-0.77	-0.75	-0.69	-0.61	-0.45
	(111)	-0.94	-1.08	-0.99	-0.80	-0.75
Cu	(001)	-2.54	-2.41	-2.29	-2.25	-2.83
	(011)	-2.51	-2.35	-2.29	-2.20	-2.76
	(111)	-2.81	-2.69	-2.56	-2.48	-3.13
Au	(001)	-3.43	-3.36	-3.21	-3.14	-3.28
	(011)	-3.39	-3.34	-3.21	-3.15	-3.34
	(111)	-3.63	-3.55	-3.39	-3.32	-3.57
Ag	(001)	-4.03	-3.96	-3.87	-3.83	-3.51
	(011)	-4.04	-3.96	-3.91	-3.89	-3.32
	(111)	-4.21	-4.13	-4.05	-4.01	-3.73
W	(001)	1.88	2.74	2.54	2.40	2.61
	(011)	1.25	2.07	1.93	1.84	1.93
	(111)	1.88	2.95	2.63	2.44	2.92
V	(001)	2.83	3.32	3.26	3.05	3.08
	(011)	3.45	4.00	3.73	3.63	4.04
	(111)	3.51	4.05	3.97	3.97	2.81
Ta	(001)	2.20	2.12	1.99	1.78	2.41
	(011)	3.03	2.10	2.95	2.53	2.24
	(111)	3.08	2.97	2.77	2.64	3.44
Nb	(001)	0.56	0.54	0.50	0.51	0.49
	(011)	1.00	0.97	0.92	0.90	0.92
	(111)	1.05	1.01	0.98	0.96	0.90
Mo	(001)	0.16	0.21	0.14	0.12	0.13
	(011)	-0.27	-0.27	-0.27	-0.27	-0.26
	(111)	-0.09	-0.10	-0.12	-0.12	-0.14
Fe	(001)	-0.24	0.38	0.47	0.49	-0.84
	(011)	0.47	0.79	0.67	1.12	-0.25
	(111)	0.23	0.46	0.19	0.44	-1.11
Cr	(001)	-0.03	-0.01	0.01	0.01	-0.17
	(011)	-0.29	-0.26	-0.28	-0.28	-0.26
	(111)	-0.20	-0.12	-0.16	-0.16	-0.14

Table S2. Calculated values of ε_d^W (eV) for all TMs surfaces and density functionals

ε_d^W	surfaces	VWN	PBE_{sol}	PBE	RPBE	TPSS
Zr	(0001)	13.89	12.87	12.26	12.26	11.16
	$(10\bar{1}0)$	13.83	13.73	12.58	11.84	10.61
	$(11\bar{2}0)$	13.35	12.42	10.86	11.26	9.82
Zn	(0001)	-1.76	-1.79	-2.04	-2.21	-2.07
	$(10\bar{1}0)$	-2.20	-2.21	-2.43	-2.56	-1.79
	$(11\bar{2}0)$	-2.15	-2.16	-2.35	-2.44	-2.41
Y	(0001)	15.92	13.87	12.27	11.09	10.04
	$(10\bar{1}0)$	17.07	12.79	11.93	10.33	9.89
	$(11\bar{2}0)$	12.78	11.25	10.47	9.41	8.60
Ti	(0001)	16.77	15.71	14.71	14.16	16.02
	$(10\bar{1}0)$	16.90	15.71	14.51	13.68	15.83
	$(11\bar{2}0)$	15.22	13.88	12.99	12.83	14.93
Tc	(0001)	5.19	6.41	6.15	5.98	5.99
	$(10\bar{1}0)$	4.69	5.92	5.35	5.60	5.32
	$(11\bar{2}0)$	4.78	5.85	5.73	5.37	5.28
Sc	(0001)	18.08	16.30	14.22	13.01	15.11
	$(10\bar{1}0)$	18.27	15.77	14.67	12.77	15.35
	$(11\bar{2}0)$	15.20	13.73	13.07	11.61	12.36
Ru	(0001)	4.73	5.00	4.48	4.79	4.48
	$(10\bar{1}0)$	5.09	4.99	4.83	4.88	35.86
	$(11\bar{2}0)$	5.33	5.26	5.07	5.15	5.04
Re	(0001)	14.94	14.73	14.31	13.60	14.78
	$(10\bar{1}0)$	14.60	14.04	13.50	13.95	11.77
	$(11\bar{2}0)$	14.97	14.52	14.01	13.54	14.31
Os	(0001)	12.46	12.19	12.06	11.95	12.06
	$(10\bar{1}0)$	12.42	12.75	11.95	11.99	11.84
	$(11\bar{2}0)$	12.99	12.14	11.94	12.07	12.35
Hf	(0001)	14.11	12.53	11.88	11.49	15.57
	$(10\bar{1}0)$	13.74	12.27	11.33	10.69	14.81
	$(11\bar{2}0)$	12.28	11.15	10.00	9.60	13.74
Co	(0001)	8.03	7.99	7.97	7.81	7.98
	$(10\bar{1}0)$	7.35	7.94	7.34	7.22	7.66
	$(11\bar{2}0)$	6.31	7.05	6.87	6.84	7.34
Cd	(0001)	-3.64	-3.72	-3.82	-3.90	-2.76
	$(10\bar{1}0)$	-3.67	-3.74	-3.87	-3.91	-2.83
	$(11\bar{2}0)$	-3.72	-3.75	-3.81	-3.88	-3.06
Rh	(001)	4.57	4.87	4.80	4.87	4.39
	(011)	4.63	4.57	4.57	4.36	4.54
	(111)	3.81	3.87	3.84	3.68	3.86
Pt	(001)	3.87	4.11	4.08	4.05	4.04
	(011)	3.84	3.85	3.74	3.77	3.77
	(111)	3.58	3.69	3.80	3.79	3.56

Pd	(001)	1.60	1.60	1.53	1.49	1.61
	(011)	1.50	1.50	1.42	1.94	1.44
	(111)	1.54	1.53	1.47	1.43	2.01
Ni	(001)	5.09	5.87	4.97	5.77	5.00
	(011)	5.06	5.84	4.88	5.71	4.94
	(111)	4.65	4.60	4.51	4.50	5.29
Ir	(001)	12.18	12.16	12.04	11.98	11.92
	(011)	12.19	12.08	11.84	11.96	12.10
	(111)	12.50	11.30	11.22	12.11	11.34
Cu	(001)	2.24	3.11	2.14	2.92	2.26
	(011)	2.17	3.05	2.06	2.87	1.96
	(111)	2.10	2.09	2.00	1.94	2.92
Au	(001)	1.42	1.34	1.20	1.11	1.22
	(011)	1.32	1.24	1.09	0.99	1.10
	(111)	1.34	1.25	1.12	1.03	1.10
Ag	(001)	-0.08	-0.18	-0.34	-0.48	0.71
	(011)	-0.16	-0.24	-0.44	-0.57	0.45
	(111)	-0.14	-0.24	-0.41	-0.54	0.62
W	(001)	14.16	17.57	16.84	16.21	16.48
	(011)	12.65	15.93	15.27	14.92	15.27
	(111)	8.44	11.92	10.77	10.52	11.79
V	(001)	15.79	16.67	15.83	15.95	15.29
	(011)	16.99	17.89	16.66	16.98	17.80
	(111)	12.21	12.40	12.29	12.77	10.05
Ta	(001)	12.38	11.98	11.39	10.13	13.55
	(011)	14.33	11.86	13.88	12.30	14.02
	(111)	10.22	9.80	9.10	9.59	12.22
Nb	(001)	5.90	5.78	5.50	5.41	5.42
	(011)	6.81	6.62	6.32	6.18	6.24
	(111)	3.75	6.85	3.23	3.16	2.92
Mo	(001)	6.22	6.61	5.89	5.72	5.78
	(011)	5.45	5.38	5.12	4.96	5.00
	(111)	2.24	2.15	1.96	1.97	0.16
Fe	(001)	7.63	9.46	10.01	9.46	7.32
	(011)	9.94	10.79	10.22	10.63	7.22
	(111)	7.34	6.04	8.58	8.99	4.40
Cr	(001)	5.33	5.41	5.55	5.38	4.86
	(011)	5.64	5.46	5.33	4.97	6.31
	(111)	0.98	0.55	-0.09	-0.16	0.55

Table S3. Calculated values of ε_u (eV) for all TMs surfaces and density functionals.

ε_u	surfaces	VWN	PBE_{sol}	PBE	RPBE	TPSS
Zr	(0001)	4.97	12.23	4.60	4.72	5.21
	$(10\bar{1}0)$	3.15	-0.91	-0.38	5.57	1.23
	$(11\bar{2}0)$	3.29	2.91	0.08	2.69	2.93
Zn	(0001)	-7.04	-6.92	-6.92	-6.84	-7.24
	$(10\bar{1}0)$	-6.72	-6.61	-6.80	-6.83	-6.94
	$(11\bar{2}0)$	-6.89	-6.77	-6.76	-6.68	-7.12
Y	(0001)	2.29	2.44	5.51	5.16	0.42
	$(10\bar{1}0)$	3.94	2.40	4.38	3.33	5.68
	$(11\bar{2}0)$	3.36	3.14	2.98	2.89	3.19
Ti	(0001)	3.77	3.66	2.95	1.51	3.34
	$(10\bar{1}0)$	0.66	3.45	3.20	3.16	3.32
	$(11\bar{2}0)$	3.71	3.55	3.36	3.24	2.31
Tc	(0001)	3.25	-0.59	-0.59	-0.56	-0.57
	$(10\bar{1}0)$	2.13	2.12	2.13	2.57	1.94
	$(11\bar{2}0)$	3.27	-1.39	1.21	1.18	2.93
Sc	(0001)	3.59	4.07	3.27	3.19	3.36
	$(10\bar{1}0)$	3.18	2.12	2.77	2.78	3.83
	$(11\bar{2}0)$	2.63	2.48	2.36	2.32	2.50
Ru	(0001)	0.92	1.75	0.84	-1.47	0.88
	$(10\bar{1}0)$	-1.62	-1.59	0.88	0.86	-1.46
	$(11\bar{2}0)$	-0.37	1.26	1.58	-2.68	1.50
Re	(0001)	4.44	3.77	16.41	0.58	4.75
	$(10\bar{1}0)$	-2.10	2.69	3.37	-3.54	4.06
	$(11\bar{2}0)$	-4.32	-1.58	2.28	2.01	0.23
Os	(0001)	2.30	-1.68	2.18	2.15	-1.71
	$(10\bar{1}0)$	1.43	-3.01	1.34	2.66	-2.26
	$(11\bar{2}0)$	0.66	1.57	-0.10	0.60	-0.10
Hf	(0001)	11.87	11.38	5.70	-1.22	7.37
	$(10\bar{1}0)$	3.71	6.66	2.61	2.56	7.65
	$(11\bar{2}0)$	3.55	3.25	3.30	3.22	3.28
Co	(0001)	-1.10	-2.35	-3.81	-2.38	-1.75
	$(10\bar{1}0)$	-1.50	-0.41	-1.66	-1.72	-1.54
	$(11\bar{2}0)$	-2.93	-3.61	-0.73	-1.54	-0.38
Cd	(0001)	-8.32	-8.29	-8.38	-8.40	-6.99
	$(10\bar{1}0)$	-8.25	-8.35	-8.30	-8.40	-6.96
	$(11\bar{2}0)$	-8.76	-8.11	-8.09	-8.13	-7.28
Rh	(001)	0.49	0.47	0.79	0.76	0.89
	(011)	0.47	0.64	0.25	0.23	0.71
	(111)	-4.44	0.37	-3.64	0.34	-0.37
Pt	(001)	-3.31	-3.23	-0.85	0.19	0.14
	(011)	-0.26	0.09	0.09	-0.27	0.10
	(111)	0.31	0.30	-0.19	-0.19	0.30

Pd	(001)	-1.50	-0.21	-1.39	-0.08	-10.38
	(011)	0.00	0.00	0.00	0.00	0.00
	(111)	-0.22	-0.21	0.00	0.00	0.00
Ni	(001)	-2.13	-0.17	-2.03	-0.27	-4.35
	(011)	-2.56	-0.30	-0.45	-0.39	-0.49
	(111)	-1.78	-2.00	-2.27	-1.51	-12.91
Ir	(001)	-0.39	-0.37	-0.35	-0.35	0.80
	(011)	1.01	-0.10	1.69	1.66	0.86
	(111)	1.67	-2.65	-2.86	1.52	1.21
Cu	(001)	-2.52	-1.34	-1.46	-1.31	-1.69
	(011)	-1.51	-1.30	-1.44	-1.27	-1.68
	(111)	-1.85	-1.70	-1.72	-1.69	-1.85
Au	(001)	-1.43	-4.15	-3.09	-1.90	-3.13
	(011)	-1.68	-1.70	-1.75	-1.81	-1.88
	(111)	-2.10	-2.03	-2.08	-2.91	-4.09
Ag	(001)	-2.86	-2.86	-3.19	-2.93	-2.03
	(011)	-2.83	-3.49	-2.92	-2.96	-2.19
	(111)	-3.02	-3.02	-5.13	-4.98	-2.41
W	(001)	0.04	0.05	0.07	2.77	4.25
	(011)	3.99	4.03	3.89	2.79	3.89
	(111)	-3.13	-5.39	-1.34	2.54	-2.30
V	(001)	0.54	3.41	0.46	3.14	0.93
	(011)	2.66	3.62	3.01	3.35	2.87
	(111)	1.98	1.53	1.85	0.00	0.00
Ta	(001)	4.70	4.78	4.61	4.36	2.37
	(011)	13.16	0.54	5.04	4.86	5.08
	(111)	5.99	0.47	2.53	1.54	2.77
Nb	(001)	0.59	0.59	0.58	4.04	0.57
	(011)	4.44	4.71	4.29	4.42	4.56
	(111)	5.03	4.94	3.17	0.71	2.33
Mo	(001)	-0.24	-2.91	-0.21	-0.21	2.61
	(011)	2.31	-1.53	2.74	2.70	3.48
	(111)	3.66	3.59	2.49	-1.39	1.35
Fe	(001)	-1.34	-2.29	-2.15	-1.32	-13.58
	(011)	2.11	-4.16	0.07	-0.01	-12.08
	(111)	-0.93	-0.94	-2.77	-3.05	1.80
Cr	(001)	1.54	1.43	1.44	1.43	2.07
	(011)	2.88	-0.61	2.24	1.41	1.76
	(111)	1.51	-2.88	-0.84	-1.58	-0.40

Table S4. Calculated values of ε_d (eV) for all TMs surfaces by a set of density functionals optimized using PBE structure.

ε_d	surfaces	VWN	PBE_{sol}	RPBE	TPSS
Zr	(0001)	3.19	2.99	3.02	2.65
	$(10\bar{1}0)$	2.95	2.93	2.91	2.55
	$(11\bar{2}0)$	2.60	2.40	2.58	2.19
Zn	(0001)	-7.26	-7.17	-7.21	-7.40
	$(10\bar{1}0)$	-7.02	-6.93	-6.97	-7.24
	$(11\bar{2}0)$	-7.15	-7.08	-7.12	-7.36
Y	(0001)	3.93	3.81	3.76	3.20
	$(10\bar{1}0)$	3.65	3.67	3.42	3.04
	$(11\bar{2}0)$	3.10	3.14	3.00	2.60
Ti	(0001)	3.30	3.11	3.16	3.22
	$(10\bar{1}0)$	3.14	3.03	2.97	2.98
	$(11\bar{2}0)$	2.86	2.59	2.63	2.94
Tc	(0001)	-0.59	-0.51	-0.51	-0.50
	$(10\bar{1}0)$	-0.76	-0.69	-0.69	-0.73
	$(11\bar{2}0)$	-0.95	-0.87	-0.88	-0.86
Sc	(0001)	4.20	3.89	3.87	3.54
	$(10\bar{1}0)$	3.95	3.45	3.46	3.45
	$(11\bar{2}0)$	3.49	3.10	3.13	2.78
Ru	(0001)	-1.41	-1.41	-1.40	-1.43
	$(10\bar{1}0)$	-1.32	-1.28	-1.28	-1.32
	$(11\bar{2}0)$	-1.29	-1.28	-1.26	-1.30
Re	(0001)	1.25	1.23	1.20	1.41
	$(10\bar{1}0)$	1.08	1.01	0.99	0.65
	$(11\bar{2}0)$	0.94	0.85	0.90	1.19
Os	(0001)	-0.40	-0.52	-0.42	-0.40
	$(10\bar{1}0)$	-0.38	-0.35	-0.35	-0.32
	$(11\bar{2}0)$	-0.25	-0.40	-0.28	-0.49
Hf	(0001)	2.99	2.88	2.85	2.82
	$(10\bar{1}0)$	2.77	2.74	2.67	2.71
	$(11\bar{2}0)$	2.30	2.23	2.29	2.40
Co	(0001)	-0.50	-0.52	-0.59	-1.00
	$(10\bar{1}0)$	-0.62	-0.66	-0.62	-1.17
	$(11\bar{2}0)$	-0.70	-0.75	-0.75	-0.46
Cd	(0001)	-8.59	-8.62	-8.76	-7.45
	$(10\bar{1}0)$	-8.52	-8.54	-8.68	-7.25
	$(11\bar{2}0)$	-8.35	-8.41	-8.55	-7.03
Rh	(001)	-1.53	-1.55	-1.52	-1.56
	(011)	-1.58	-1.58	-1.57	-1.59
	(111)	-1.66	-1.68	-1.64	-1.69
Pt	(001)	-2.05	-2.05	-2.02	-2.05
	(011)	-2.06	-2.05	-2.04	-2.07
	(111)	-2.15	-2.14	-2.18	-2.23
Pd	(001)	-1.74	-1.74	-1.73	-1.76
	(011)	-1.73	-1.72	-1.75	*a*
	(111)	-1.84	-1.85	-1.83	-1.90
	(001)	-1.37	-1.40	-1.40	-1.45

Ni	(011)	-1.21	-1.26	-1.27	-1.32
	(111)	-1.65	-1.66	-1.67	-1.74
Ir	(001)	-0.66	-0.65	-0.63	-0.41
	(011)	-0.66	-0.66	-0.64	-0.42
	(111)	-0.84	-0.99	-0.82	-0.70
Cu	(001)	-2.33	-2.30	-2.32	-2.37
	(011)	-2.32	-2.25	-2.27	-2.29
	(111)	-2.59	-2.54	-2.57	-2.59
Au	(001)	-3.15	-3.16	-3.23	-3.22
	(011)	-3.15	-3.18	-3.23	-3.24
	(111)	-3.35	-3.37	-3.42	-3.41
Ag	(001)	-3.77	-3.81	-3.92	-3.30
	(011)	-3.82	-3.86	-3.98	-3.30
	(111)	-3.98	-3.99	-4.10	-3.46
W	(001)	1.81	2.52	2.52	2.88
	(011)	1.17	1.92	1.86	1.98
	(111)	1.75	2.59	2.59	3.12
V	(001)	2.47	3.19	3.17	3.20
	(011)	3.09	3.74	3.72	3.76
	(111)	3.31	4.02	3.87	3.99
Ta	(001)	1.98	2.03	1.98	2.01
	(011)	2.94	2.97	2.88	2.22
	(111)	2.74	2.75	2.76	2.92
Nb	(001)	0.51	0.51	0.51	0.50
	(011)	0.93	0.92	0.93	0.94
	(111)	0.97	0.96	0.92	0.96
Mo	(001)	0.12	0.14	0.16	0.17
	(011)	-0.25	-0.26	-0.26	-0.25
	(111)	-0.12	-0.12	-0.11	-0.19
Fe	(001)	0.34	0.42	0.45	-8.06
	(011)	0.53	0.64	0.76	-0.11
	(111)	0.47	0.44	0.45	-1.55
Cr	(001)	-0.01	-0.03	0.02	-0.05
	(011)	-0.29	-0.28	-0.27	-0.25
	(111)	-0.18	-0.12	-0.14	-0.15

[a] in this particular case there were strong problems of electronic convergence, while trying to force a meta-GGA solution on a GGA optimized structure.

Table S2. Calculated values of ε_d^W (eV) for all TMs surfaces by a set of density functionals optimized using PBE structure.

ε_d^W	surfaces	VWN	PBE_{sol}	RPBE	TPSS
Zr	(0001)	12.93	12.24	12.29	10.87
	$(10\bar{1}0)$	12.30	12.19	11.99	10.73
	$(11\bar{2}0)$	11.40	10.62	11.33	9.74
Zn	(0001)	-2.09	-2.00	-2.04	-2.33
	$(10\bar{1}0)$	-2.48	-2.39	-2.43	-1.94
	$(11\bar{2}0)$	-2.39	-2.31	-2.35	-2.66
Y	(0001)	12.96	12.36	12.09	10.10
	$(10\bar{1}0)$	12.10	12.06	11.20	10.26
	$(11\bar{2}0)$	10.70	10.67	10.17	8.48
Ti	(0001)	15.50	14.84	14.99	15.40
	$(10\bar{1}0)$	15.08	14.72	14.53	14.76
	$(11\bar{2}0)$	14.43	13.59	13.75	15.01
Tc	(0001)	5.01	6.12	6.10	6.69
	$(10\bar{1}0)$	4.27	5.40	5.32	5.27
	$(11\bar{2}0)$	4.47	5.57	5.34	5.72
Sc	(0001)	16.05	15.11	15.06	13.90
	$(10\bar{1}0)$	17.28	13.79	13.80	14.50
	$(11\bar{2}0)$	14.39	12.94	12.94	11.59
Ru	(0001)	4.79	4.91	4.82	4.62
	$(10\bar{1}0)$	4.58	5.02	4.83	4.61
	$(11\bar{2}0)$	5.02	5.09	5.07	5.01
Re	(0001)	14.52	14.39	14.22	14.63
	$(10\bar{1}0)$	13.90	13.61	13.50	11.48
	$(11\bar{2}0)$	14.44	14.08	14.25	14.41
Os	(0001)	12.07	11.59	12.02	12.10
	$(10\bar{1}0)$	11.75	11.99	12.01	11.37
	$(11\bar{2}0)$	12.43	12.00	12.49	11.52
Hf	(0001)	12.34	11.80	11.58	12.30
	$(10\bar{1}0)$	11.65	11.47	11.10	12.10
	$(11\bar{2}0)$	10.33	9.89	10.03	11.37
Co	(0001)	7.81	7.88	7.74	8.19
	$(10\bar{1}0)$	7.26	7.81	7.31	7.53
	$(11\bar{2}0)$	6.74	6.86	6.92	9.34
Cd	(0001)	-3.76	-3.78	-3.86	-3.02
	$(10\bar{1}0)$	-3.81	-3.83	-3.90	-2.25
	$(11\bar{2}0)$	-3.73	-3.77	-3.84	-2.98
Rh	(001)	4.95	4.56	4.89	4.36
	(011)	4.54	4.55	4.49	4.41
	(111)	3.79	3.64	3.85	3.68
Pt	(001)	4.07	4.03	4.13	3.99
	(011)	3.75	3.80	3.81	3.63
	(111)	3.76	3.87	2.89	3.50
Pd	(001)	1.56	1.56	1.50	1.67
	(011)	1.46	1.47	1.95	*a*
	(111)	1.51	1.50	1.44	2.03
Ni	(001)	4.97	5.80	5.83	4.69
	(011)	4.89	5.75	5.77	5.13

	(111)	4.46	4.54	4.50	4.70
Ir	(001)	12.03	12.01	12.05	12.02
	(011)	12.00	12.01	12.02	12.01
	(111)	12.21	11.10	12.20	11.36
Cu	(001)	2.10	3.04	3.00	4.27
	(011)	2.03	2.96	2.92	4.27
	(111)	1.96	2.03	1.98	2.39
Au	(001)	1.28	1.26	1.16	1.10
	(011)	1.18	1.14	1.05	0.99
	(111)	1.20	1.16	1.08	1.02
Ag	(001)	-0.22	-0.27	-0.41	1.12
	(011)	-0.31	-0.37	-0.51	0.45
	(111)	-0.31	-0.33	-0.46	0.46
W	(001)	13.89	16.79	16.72	17.48
	(011)	12.15	15.28	15.05	15.06
	(111)	7.99	11.21	11.20	12.49
V	(001)	14.55	16.33	16.27	15.47
	(011)	16.02	17.28	17.23	17.14
	(111)	11.65	12.33	7.95	12.27
Ta	(001)	11.40	11.58	11.29	12.45
	(011)	13.89	13.95	13.54	13.73
	(111)	9.07	9.05	9.96	10.30
Nb	(001)	5.58	5.58	5.56	5.45
	(011)	6.44	6.35	6.35	6.33
	(111)	3.27	3.22	3.02	3.10
Mo	(001)	5.82	5.88	6.07	6.02
	(011)	5.26	5.15	5.14	5.08
	(111)	2.05	1.97	2.03	0.20
Fe	(001)	9.10	9.45	9.51	33.69
	(011)	9.92	10.20	10.40	12.97
	(111)	5.85	9.02	9.07	4.70
Cr	(001)	5.27	5.11	5.56	5.04
	(011)	5.60	5.31	5.33	6.24
	(111)	1.03	0.43	0.20	1.26

[a] in this particular case there were strong problems of electronic convergence, while trying to force a meta-GGA solution on a GGA optimized structure.

Table S3. Calculated values of ε_u (eV)density for all TMs surfaces by a set of density functionals optimized using PBE structure.

ε_u	surfaces	VWN	PBESOL	RPBE	TPSS
Zr	(0001)	3.53	4.62	4.85	5.08
	$(10\bar{1}0)$	2.93	0.63	9.59	5.52
	$(11\bar{2}0)$	4.96	2.61	2.84	2.31
Zn	(0001)	-6.96	-6.86	-6.90	-7.12
	$(10\bar{1}0)$	-6.62	-6.59	-6.81	-6.88
	$(11\bar{2}0)$	-6.79	-6.71	-6.75	-7.00
Y	(0001)	5.69	2.34	2.36	2.54
	$(10\bar{1}0)$	4.35	4.39	3.44	5.58
	$(11\bar{2}0)$	2.93	2.98	3.00	3.28
Ti	(0001)	3.46	2.96	3.34	3.31
	$(10\bar{1}0)$	3.28	3.30	3.28	2.63
	$(11\bar{2}0)$	2.06	2.08	-0.33	2.05
Tc	(0001)	3.09	-0.57	-0.58	3.14
	$(10\bar{1}0)$	2.92	2.14	2.13	1.63
	$(11\bar{2}0)$	1.43	2.42	0.95	-2.00
Sc	(0001)	3.24	3.87	3.70	3.84
	$(10\bar{1}0)$	2.87	2.79	2.80	3.74
	$(11\bar{2}0)$	2.32	2.50	2.38	2.39
Ru	(0001)	1.66	-4.04	1.53	1.73
	$(10\bar{1}0)$	0.88	-1.50	0.52	1.45
	$(11\bar{2}0)$	1.87	-3.20	1.58	0.45
Re	(0001)	6.32	-1.01	3.64	4.73
	$(10\bar{1}0)$	-0.23	2.10	-3.95	2.55
	$(11\bar{2}0)$	-2.76	2.28	-1.53	2.29
Os	(0001)	-3.71	2.15	2.52	2.41
	$(10\bar{1}0)$	-4.18	1.34	1.35	13.32
	$(11\bar{2}0)$	0.31	2.10	-0.10	0.15
Hf	(0001)	6.25	6.31	0.88	10.79
	$(10\bar{1}0)$	3.33	2.60	5.55	10.18
	$(11\bar{2}0)$	0.28	3.29	3.14	2.87
Co	(0001)	-2.35	-0.58	-2.17	-1.67
	$(10\bar{1}0)$	-0.97	-0.50	-3.42	-1.71
	$(11\bar{2}0)$	-0.32	-0.70	-1.52	-0.34
Cd	(0001)	-8.24	-8.28	-8.43	-6.99
	$(10\bar{1}0)$	-8.18	-8.21	-8.42	-6.75
	$(11\bar{2}0)$	-7.95	-8.00	-8.16	-6.63
Rh	(001)	0.80	0.99	-1.51	-0.35
	(011)	0.59	0.59	0.24	0.64
	(111)	-0.91	-3.67	-3.64	0.36
Pt	(001)	-0.85	-0.85	-0.85	0.15
	(011)	-1.41	0.09	0.09	0.09
	(111)	-0.19	-0.71	0.28	-3.71
Pd	(001)	-1.48	0.00	-0.08	-0.01
	(011)	0.00	-0.27	0.00	*a*
	(111)	-0.19	0.00	0.00	0.00
Ni	(001)	-1.99	-0.22	-0.24	-3.74
	(011)	-2.06	-0.32	-0.37	-0.57

	(111)	-2.23	-2.28	-1.92	3.38
Ir	(001)	-0.42	-0.35	-0.35	-0.33
	(011)	-0.08	-0.09	-0.09	-3.18
	(111)	1.55	0.55	1.55	1.17
Cu	(001)	-1.43	-1.30	-1.33	-1.35
	(011)	-2.43	-1.27	-1.30	-1.24
	(111)	-1.76	-1.70	-1.74	-1.62
Au	(001)	-1.84	-1.89	-3.11	-1.94
	(011)	-1.64	-1.71	-1.78	-2.80
	(111)	-2.02	-3.87	-3.91	-3.88
Ag	(001)	-2.86	-3.59	-4.18	-2.07
	(011)	-2.80	-2.84	-4.67	-2.16
	(111)	-4.69	-2.99	-3.11	-2.35
W	(001)	-2.51	3.26	-2.16	-2.57
	(011)	3.87	7.95	2.83	-1.52
	(111)	-1.35	-1.33	-4.54	-3.95
V	(001)	2.63	3.27	3.25	0.52
	(011)	3.04	3.50	3.47	3.48
	(111)	1.90	11.63	0.00	0.00
Ta	(001)	4.38	4.60	4.63	4.35
	(011)	7.65	5.05	5.40	4.72
	(111)	4.44	0.46	0.47	5.12
Nb	(001)	0.57	0.58	0.59	0.57
	(011)	4.27	4.54	3.37	3.43
	(111)	2.19	-0.62	0.71	4.34
Mo	(001)	-0.21	-0.21	-2.79	-0.24
	(011)	2.70	2.31	2.70	2.79
	(111)	0.39	1.84	3.42	-2.76
Fe	(001)	-2.18	-2.35	-2.40	-71.90
	(011)	-2.67	0.22	0.23	-15.52
	(111)	-2.98	-1.02	-1.78	2.33
Cr	(001)	1.45	1.24	1.47	1.42
	(011)	2.83	1.42	1.99	1.78
	(111)	-0.82	-0.83	-1.46	-0.79

[a] in this particular case there were strong problems of electronic convergence, while trying to force a meta-GGA solution on a GGA optimized structure.

Table S4. Bulk-truncated surface and bulk calculations of ε_d at PBE level. All values are given in eV.

hcp				
ε_d	Bulk	(0001)	$(10\bar{1}0)$	$(11\bar{2}0)$
Cd	-9.16	-8.70	-8.57	-8.57
Co	-0.33	-0.45	-0.63	-0.66
Hf	3.07	2.60	2.47	2.36
Os	-0.80	-0.39	-0.37	-0.21
Re	1.02	0.85	0.96	0.75
Ru	-1.73	-1.29	-1.20	-1.19
Sc	4.18	3.24	3.58	3.19
Tc	-0.65	-0.57	-0.65	-0.65
Ti	2.96	2.82	2.65	2.64
Y	4.78	3.48	3.51	2.88
Zn	-7.69	-7.18	-7.10	-7.11
Zr	3.18	2.78	2.76	2.47
fcc				
ε_d	Bulk	(001)	(011)	(111)
Ag	-4.39	-3.84	-3.83	-4.03
Au	-3.83	-3.19	-3.04	-3.40
Cu	-2.86	-2.26	-2.20	-2.55
Ir	-1.52	-0.58	-0.47	-0.91
Ni	-0.64	-1.35	-1.14	-1.66
Pd	-2.42	-1.70	-1.56	-1.83
Pt	-2.73	-1.95	-1.77	-2.20
Rh	-2.19	-1.43	-1.38	-1.59
bcc				
ε_d	Bulk	(001)	(011)	(111)
Cr	-0.48	-0.09	-0.29	0.00
Fe	0.53	0.47	0.55	0.30
Mo	-0.41	0.06	-0.26	0.04
Nb	1.23	0.41	0.88	0.74
Ta	2.97	1.65	3.03	2.10
V	3.88	2.65	3.28	2.90
W	1.94	1.91	1.78	1.78

C. Supplementary Information of Generalized Gradient Approximation Adjusted to Transition Metals Properties: Key Roles of Exchange and Local Spin Density

Table S1. Calculated values of cohesive energies (E_{coh}), as well as experimental values corrected by ZPE and finite temperatures.

E_{coh} (eV/atom)	VV	VVsol	Exp. Corr.[a]
Cr	4.05	4.45	4.15
Fe	5.26	5.54	4.32
Mo	6.93	6.81	6.84
Nb	6.97	8.12	7.47
Ta	8.40	8.54	8.11
V	5.40	5.75	5.34
W	8.53	8.89	8.83
Ag	2.53	2.67	2.96
Au	3.04	3.25	3.83
Cu	3.53	3.76	3.51
Ir	7.63	8.05	6.96
Ni	5.09	5.39	4.48
Pd	3.77	4.00	3.93
Pt	5.57	5.87	5.87
Rh	5.98	6.34	5.76
Cd	0.78	0.82	1.18
Co	5.52	6.14	4.47
Hf	6.71	6.62	6.44
Os	8.48	8.84	8.22
Re	7.91	8.28	8.06
Ru	7.68	8.52	6.8
Sc	4.25	4.32	3.93
Tc	7.05	7.47	7.17
Ti	5.59	7.03	4.88
Y	4.24	4.31	4.42
Zn	1.15	1.27	1.38
Zr	6.34	6.58	6.32

[a] Ref. [1].

Table S3. Calculated values of bulk moduli (B_0), as well as experimental values corrected by ZPE and finite temperatures.

B_0 (Gpa)	VV	VVsol	Exp. Corr.[a]
Cr	256.7	275.1	174.5
Fe	192.5	225.1	169.8
Mo	258.2	273.0	264.7
Nb	171.7	181.4	172
Ta	191.3	200.7	193.7
V	184.6	197.5	158.9
W	310.0	323.4	312.3
Ag	86.7	109.4	103.8
Au	135.5	160.9	174.8
Cu	138.2	158.3	140.3
Ir	339.3	365.6	365.2
Ni	194.1	217.4	185.5
Pd	166.5	192.1	195.4
Pt	244.1	272.1	284.2
Rh	250.3	278.1	288.7
Cd	52.5	59.7	53.8
Co	208.0	232.0	193
Hf	110.9	111.5	109.7
Os	412.7	417.0	424.6
Re	381.9	384.9	368.8
Ru	321.3	331.7	317.7
Sc	55.8	56.1	55.6
Tc	314.6	320.8	303.1
Ti	114.8	116.3	108.3
Y	41.6	40.7	41.7
Zn	79.4	88.4	69.7
Zr	97.4	97.5	95.9

[a] Ref. [1].

Table S4. Calculated surface energies (γ) obtained either using VV or VVsol exchange-correlation functionals, along with experimental values.

γ (J/m^2)	Surface	VV	VVsol	Exp.[a]
Cr	(001)	3.49	3.73	2.30
	(011)	3.11	3.33	
	(111)	3.46	3.70	
Fe	(001)	2.53	2.95	2.48
	(011)	2.48	2.76	
	(111)	2.72	3.08	
Mo	(001)	3.04	3.24	3.00
	(011)	2.68	2.86	
	(111)	3.03	3.23	
Nb	(001)	2.38	2.56	2.70
	(011)	2.16	2.32	
	(111)	2.40	2.56	
Ta	(001)	2.54	2.72	3.15
	(011)	2.40	2.55	
	(111)	2.76	2.91	
V	(001)	2.43	2.62	2.55
	(011)	2.46	2.62	
	(111)	2.74	2.92	
W	(001)	3.94	4.13	3.68
	(011)	3.18	3.35	
	(111)	3.53	3.72	
Ag	(001)	0.82	1.04	1.25
	(011)	0.86	1.08	
	(111)	0.71	0.91	
Au	(001)	0.90	1.13	1.50
	(011)	0.89	1.13	
	(111)	0.71	0.91	
Cu	(001)	1.51	1.76	1.83
	(011)	1.55	1.80	
	(111)	1.32	1.55	
Ir	(001)	2.85	3.13	3.00
	(011)	2.85	3.14	
	(111)	2.13	2.48	
Ni	(001)	2.22	2.52	2.45
	(011)	2.31	2.61	
	(111)	1.97	2.25	
Pd	(001)	1.54	1.82	2.05
	(011)	1.58	1.87	

	(111)	1.17	1.41	
Pt	(001)	1.94	2.21	2.48
	(011)	2.00	2.29	
	(111)	1.60	1.85	
Rh	(001)	2.32	2.63	2.70
	(011)	2.34	2.65	
	(111)	1.77	2.03	
Cd	(0001)	0.21	0.32	0.69
	(10$\bar{1}$0)	0.35	0.48	
	(11$\bar{2}$0)	0.54	0.71	
Co	(0001)	2.15	2.44	2.55
	(10$\bar{1}$0)	2.31	2.59	
	(11$\bar{2}$0)	2.50	3.62	
Hf	(0001)	1.74	1.83	2.15
	(10$\bar{1}$0)	1.86	1.95	
	(11$\bar{2}$0)	1.85	1.96	
Os	(0001)	2.82	3.21	3.45
	(10$\bar{1}$0)	3.31	3.64	
	(11$\bar{2}$0)	4.00	4.38	
Re	(0001)	2.63	2.87	3.60
	(10$\bar{1}$0)	2.97	3.21	
	(11$\bar{2}$0)	3.15	3.42	
Ru	(0001)	2.60	2.86	3.05
	(10$\bar{1}$0)	2.93	3.22	
	(11$\bar{2}$0)	3.38	3.70	
Sc	(0001)	1.30	1.37	1.28
	(10$\bar{1}$0)	1.22	1.29	
	(11$\bar{2}$0)	1.27	1.34	
Tc	(0001)	2.25	2.50	3.15
	(10$\bar{1}$0)	2.64	2.89	
	(11$\bar{2}$0)	2.72	2.99	
Ti	(0001)	2.00	2.11	2.10
	(10$\bar{1}$0)	2.03	2.14	
	(11$\bar{2}$0)	1.90	2.02	
Y	(0001)	1.02	1.07	1.13
	(10$\bar{1}$0)	0.99	1.05	
	(11$\bar{2}$0)	1.03	1.09	
Zn	(0001)	0.37	0.48	0.91
	(10$\bar{1}$0)	0.60	0.74	
	(11$\bar{2}$0)	0.94	1.14	
Zr	(0001)	1.61	1.70	2.00
	(10$\bar{1}$0)	1.65	1.74	

	$(11\bar{2}0)$	1.67	1.77

[a] Ref. [2].

Table S5. Obtained proportions, in percentage, of each expressed surface, as obtained following a Wulff construction.

Wulff %	Surface	VV	VVsol
Cr	(001)	12.97	12.96
	(011)	80.34	80.50
	(111)	6.68	6.54
Fe	(001)	36.35	18.57
	(011)	58.56	75.11
	(111)	5.09	6.32
Mo	(001)	11.79	12.09
	(011)	83.57	83.06
	(111)	4.64	4.85
Nb	(001)	15.09	14.38
	(011)	77.79	77.99
	(111)	7.12	7.62
Ta	(001)	19.27	18.25
	(011)	77.71	78.06
	(111)	3.02	3.69
V	(001)	29.02	27.34
	(011)	64.17	65.96
	(111)	6.81	6.70
W	(001)	4.57	4.90
	(011)	88.50	88.31
	(111)	6.93	6.79
Ag	(001)	21.96	23.11
	(011)	1.62	5.91
	(111)	76.42	70.98
Au	(001)	14.04	15.52
	(011)	0.00	0.00
	(111)	85.96	84.48
Cu	(001)	23.40	23.73
	(011)	8.03	9.89
	(111)	68.57	66.39
Ir	(001)	9.52	14.23
	(011)	0.00	0.00
	(111)	90.48	85.77
Ni	(001)	24.44	31.58
	(011)	8.19	29.58

	(111)	67.37	38.84
Pd	(001)	10.70	12.57
	(011)	0.00	0.00
	(111)	89.30	87.43
Pt	(001)	17.55	18.66
	(011)	0.00	0.00
	(111)	82.45	81.34
Rh	(001)	10.81	10.28
	(011)	0.00	25.87
	(111)	89.19	63.85
Cd	(0001)	45.24	42.58
	$(10\bar{1}0)$	54.66	57.42
	$(11\bar{2}0)$	0.00	0.00
Co	(0001)	35.37	41.15
	$(10\bar{1}0)$	49.71	45.34
	$(11\bar{2}0)$	14.92	13.51
Hf	(0001)	34.83	34.83
	$(10\bar{1}0)$	31.61	33.97
	$(11\bar{2}0)$	33.56	31.19
Os	(0001)	37.00	36.15
	$(10\bar{1}0)$	63.00	63.85
	$(11\bar{2}0)$	0.00	0.00
Re	(0001)	36.47	36.28
	$(10\bar{1}0)$	45.21	45.79
	$(11\bar{2}0)$	18.32	17.93
Ru	(0001)	36.02	35.97
	$(10\bar{1}0)$	63.58	63.08
	$(11\bar{2}0)$	0.00	0.95
Sc	(0001)	32.34	32.34
	$(10\bar{1}0)$	43.65	42.59
	$(11\bar{2}0)$	24.01	25.08
Tc	(0001)	37.26	36.98
	$(10\bar{1}0)$	37.65	38.75
	$(11\bar{2}0)$	25.09	24.27
Ti	(0001)	32.66	32.78
	$(10\bar{1}0)$	18.50	20.42
	$(11\bar{2}0)$	48.84	46.80
Y	(0001)	33.08	33.18
	$(10\bar{1}0)$	42.46	41.47
	$(11\bar{2}0)$	24.47	25.35
Zn	(0001)	44.84	43.43
	$(10\bar{1}0)$	55.12	56.57

	$(11\bar{2}0)$	0.00	0.00
	(0001)	33.96	34.03
Zr	$(10\bar{1}0)$	34.68	36.90
	$(11\bar{2}0)$	31.36	29.07

TABLE S6. Calculated work functions (ϕ), in eV, for each studied surface, alongside with the determined experimental values.

ϕ (eV)	Surface	VV	VVsol	Exp.[a]
	(001)	5.10	5.22	
Cr	(011)	6.79	6.94	4.50
	(111)	3.71	3.79	
	(001)	4.41	4.98	
Fe	(011)	5.77	6.05	4.50
	(111)	2.99	3.14	
	(001)	5.66	5.76	
Mo	(011)	7.30	7.44	4.60
	(111)	4.18	4.25	
	(001)	4.07	4.20	
Nb	(011)	5.36	5.48	4.30
	(111)	2.90	2.97	
	(001)	4.44	4.57	
Ta	(011)	5.82	5.91	4.25
	(111)	3.16	3.24	
	(001)	4.57	4.71	
V	(011)	6.09	6.24	4.30
	(111)	3.20	3.27	
	(001)	5.46	5.56	
W	(011)	7.09	7.18	4.55
	(111)	3.99	4.04	
	(001)	3.83	4.10	
Ag	(011)	3.24	3.39	4.26
	(111)	4.27	4.50	
	(001)	5.44	5.66	
Au	(011)	4.36	4.61	5.10
	(111)	5.89	6.14	
	(001)	4.13	4.25	
Cu	(011)	3.37	3.50	4.65
	(111)	4.55	4.73	
	(001)	8.11	8.32	
Ir	(011)	6.38	6.58	5.27
	(111)	8.84	8.29	

Ni	(001)	4.85	5.36	5.15
	(011)	3.80	3.97	
	(111)	5.34	5.59	
Pd	(001)	5.13	5.34	5.12
	(011)	4.06	4.21	
	(111)	5.52	5.72	
Pt	(001)	6.88	7.12	5.65
	(011)	5.55	5.73	
	(111)	7.32	7.57	
Rh	(001)	6.45	6.71	4.98
	(011)	5.08	5.24	
	(111)	6.90	7.13	
Cd	(0001)	3.89	4.17	4.22
	$(10\bar{1}0)$	2.70	2.83	
	$(11\bar{2}0)$	2.80	2.85	
Co	(0001)	7.48	5.86	5.00
	$(10\bar{1}0)$	3.91	4.03	
	$(11\bar{2}0)$	4.15	4.24	
Hf	(0001)	5.39	5.49	3.90
	$(10\bar{1}0)$	3.76	3.81	
	$(11\bar{2}0)$	3.65	3.70	
Os	(0001)	7.82	8.00	4.83
	$(10\bar{1}0)$	5.70	5.86	
	$(11\bar{2}0)$	5.95	6.04	
Re	(0001)	7.07	7.18	4.96
	$(10\bar{1}0)$	5.11	5.19	
	$(11\bar{2}0)$	5.52	5.63	
Ru	(0001)	7.54	7.77	4.71
	$(10\bar{1}0)$	4.67	5.60	
	$(11\bar{2}0)$	5.69	5.86	
Sc	(0001)	4.20	4.31	3.50
	$(10\bar{1}0)$	3.14	3.20	
	$(11\bar{2}0)$	3.13	3.07	
Tc	(0001)	5.98	6.10	
	$(10\bar{1}0)$	4.33	4.42	
	$(11\bar{2}0)$	4.67	4.79	
Ti	(0001)	5.89	6.02	4.33
	$(10\bar{1}0)$	4.01	4.08	
	$(11\bar{2}0)$	3.98	4.06	
Y	(0001)	3.75	3.85	3.10
	$(10\bar{1}0)$	2.45	2.97	
	$(11\bar{2}0)$	2.91	3.03	

Zn	(0001)	4.11	4.30	4.33
	(10$\bar{1}$0)	2.82	2.90	
	(11$\bar{2}$0)	2.88	3.04	
Zr	(0001)	4.97	5.07	4.05
	(10$\bar{1}$0)	3.44	3.53	
	(11$\bar{2}$0)	3.39	3.48	

[a] Ref. [3]

TABLE S7. Calculated interlayer distance relaxations (Δ_{ij}), given in %. The experimental values and their references are found in the Supporting Information of Ref. [4].

Δ_{ij}	Surface	VV			VVsol		
		Δ_{12}	Δ_{23}	Δ_{34}	Δ_{12}	Δ_{23}	Δ_{34}
Cr	(001)						
	(011)	-2.51	1.64		-2.55	1.58	
	(111)						
Fe	(001)	0.25			-0.74		
	(011)	-1.26	0.09		-1.38	0.10	
	(111)	9.05	-5.80		8.09	-6.28	
Mo	(001)	-4.92			-4.76		
	(011)	-3.59			-3.60		
	(111)	-3.02	-25.77		-2.94	-26.43	
Nb	(001)	2.12			2.50		
	(011)						
	(111)						
Ta	(001)	-0.95			-0.83		
	(011)						
	(111)						
V	(001)	-6.24			-5.95		
	(011)						
	(111)						
W	(001)	-9.00			-9.10		
	(011)	-0.89			-0.92		
	(111)						
Ag	(001)	-1.70			-1.57		
	(011)	-1.15			-1.67		
	(111)	-0.43	-0.17	-0.53	-0.45	-0.12	-0.48
Au	(001)	-1.09			-1.19		
	(011)	7.71	16.30		7.78	16.08	
	(111)	-2.81	0.33		-2.99	0.29	
Cu	(001)	-1.07	-0.89		-1.62	-1.22	
	(011)	-0.12	4.41		-0.32	4.25	

	(111)	-0.38			-0.33		
	(001)	-1.91			-2.03		
Ir	(011)	-4.75			-4.77		
	(111)	-4.82			-4.78		
	(001)	-0.03			-0.19		
Ni	(011)	-0.82	-1.46	0.66	-1.01	-1.28	0.37
	(111)	-0.02			-0.03		
	(001)	-1.38	0.85		-1.78	0.48	
Pd	(011)	-4.86	0.77		-5.10	1.08	
	(111)	-2.25	-1.09	-1.27	-2.29	-1.15	-1.31
	(001)	-2.97			-3.00		
Pt	(011)	5.35	43.79		5.29	43.51	
	(111)	-0.29			-0.40		
	(001)	-4.91	0.95		-5.02	0.90	
Rh	(011)	-3.40	-1.73		-3.25	-1.68	
	(111)	-0.60	1.07		-0.64	1.04	
	(0001)	0.02			0.00		
Cd	$(10\bar{1}0)$						
	$(11\bar{2}0)$						
	(0001)	-3.21			-3.00		
Co	$(10\bar{1}0)$	-55.52	1.98	-51.22	-7.37	107.23	-8.26
	$(11\bar{2}0)$						
	(0001)						
Hf	$(10\bar{1}0)$						
	$(11\bar{2}0)$						
	(0001)						
Os	$(10\bar{1}0)$						
	$(11\bar{2}0)$						
	(0001)	-1.32			-1.39		
Re	$(10\bar{1}0)$	-52.01	-2.32		-4.10	96.74	
	$(11\bar{2}0)$						
	(0001)	-0.66			-0.63		
Ru	$(10\bar{1}0)$						
	$(11\bar{2}0)$						
	(0001)	2.50	0.78		2.43	0.64	
Sc	$(10\bar{1}0)$	-44.59			11.41		
	$(11\bar{2}0)$						
	(0001)						
Tc	$(10\bar{1}0)$						
	$(11\bar{2}0)$						
Ti	(0001)	-2.68	1.56		-2.58	1.31	
	$(10\bar{1}0)$	-46.62			8.23		

	$(11\bar{2}0)$		
	(0001)	-2.93	-2.92
Y	$(10\bar{1}0)$		
	$(11\bar{2}0)$		
	(0001)	0.81	-0.06
Zn	$(10\bar{1}0)$		
	$(11\bar{2}0)$		
	(0001)	-7.59	-7.41
Zr	$(10\bar{1}0)$		
	$(11\bar{2}0)$		

TABLE S8. Calculated interlayer distances (δ_{ij}), given in Å.

$\boldsymbol{\delta}_{ij}$	Surface	VV			VVsol		
		$\boldsymbol{\delta}_{12}$	$\boldsymbol{\delta}_{23}$	$\boldsymbol{\delta}_{34}$	$\boldsymbol{\delta}_{12}$	$\boldsymbol{\delta}_{23}$	$\boldsymbol{\delta}_{34}$
	(001)						
Cr	(011)	1.91	2.01		1.90	1.99	
	(111)						
	(001)	1.39			1.36		
Fe	(011)	1.99	2.01		1.96	1.98	
	(111)	0.74	0.69		0.72	0.68	
	(001)	1.36			1.36		
Mo	(011)	2.13			2.11		
	(111)	0.73	0.71		0.72	0.69	
	(001)	1.47			1.47		
Nb	(011)						
	(111)						
	(001)	1.46			1.45		
Ta	(011)						
	(111)						
	(001)	1.30			1.29		
V	(011)						
	(111)						
	(001)	1.36			1.35		
W	(011)	2.15			2.14		
	(111)						
	(001)	2.04			2.01		
Ag	(011)	1.34			1.31		
	(111)	2.37	2.38	2.38	2.33	2.34	2.34
	(001)	2.06			2.03		
Au	(011)	1.27	1.61		1.25	1.58	
	(111)	2.41	2.39		2.38	2.36	

	(001)	1.77	1.83		1.74	1.80	
Cu	(011)	1.15	1.34		1.13	1.32	
	(111)	2.07			2.04		
	(001)	1.83			1.82		
Ir	(011)	1.21			1.20		
	(111)	2.18			2.17		
	(001)	1.70			1.68		
Ni	(011)	1.12	1.26	1.24	1.11	1.25	1.23
	(111)	2.00			1.98		
	(001)	1.95	1.97		1.92	1.94	
Pd	(011)	1.26	1.45		1.24	1.43	
	(111)	2.28	2.27	2.26	2.25	2.24	2.24
	(001)	1.93			1.91		
Pt	(011)	1.21	1.53		1.19	1.51	
	(111)	2.32			2.30		
	(001)	1.84	1.92		1.82	1.90	
Rh	(011)	1.22	1.36		1.21	1.35	
	(111)	2.17	2.21		2.15	2.19	
	(0001)	2.84			2.79		
Cd	$(10\bar{1}0)$						
	$(11\bar{2}0)$						
	(0001)	1.95			1.94		
Co	$(10\bar{1}0)$	0.60	1.48	0.70	0.61	1.49	0.65
	$(11\bar{2}0)$						
	(0001)						
Hf	$(10\bar{1}0)$						
	$(11\bar{2}0)$						
	(0001)						
Os	$(10\bar{1}0)$						
	$(11\bar{2}0)$						
	(0001)	2.10			2.09		
Re	$(10\bar{1}0)$	0.68	1.59		0.67	1.58	
	$(11\bar{2}0)$						
	(0001)	2.06			2.04		
Ru	$(10\bar{1}0)$						
	$(11\bar{2}0)$						
	(0001)	2.52	2.61		2.49	2.58	
Sc	$(10\bar{1}0)$	0.99			0.98		
	$(11\bar{2}0)$						
	(0001)						
Tc	$(10\bar{1}0)$						
	$(11\bar{2}0)$						

Ti	(0001) (10$\bar{1}$0) (11$\bar{2}$0)	2.15 0.85	2.40	2.13 0.85	2.36
Y	(0001) (10$\bar{1}$0) (11$\bar{2}$0)	2.77		2.74	
Zn	(0001) (10$\bar{1}$0) (11$\bar{2}$0)	2.46		2.40	
Zr	(0001) (10$\bar{1}$0) (11$\bar{2}$0)	2.42		2.40	

Figure S1. Exchange and correlation functionals that yield the closest results with the experimental data of bulk and surface properties for each transition metal. Data beyond currently calculated PBE, PBEsol, VV, and VVsol is taken from Refs. [1], [4], and [5].

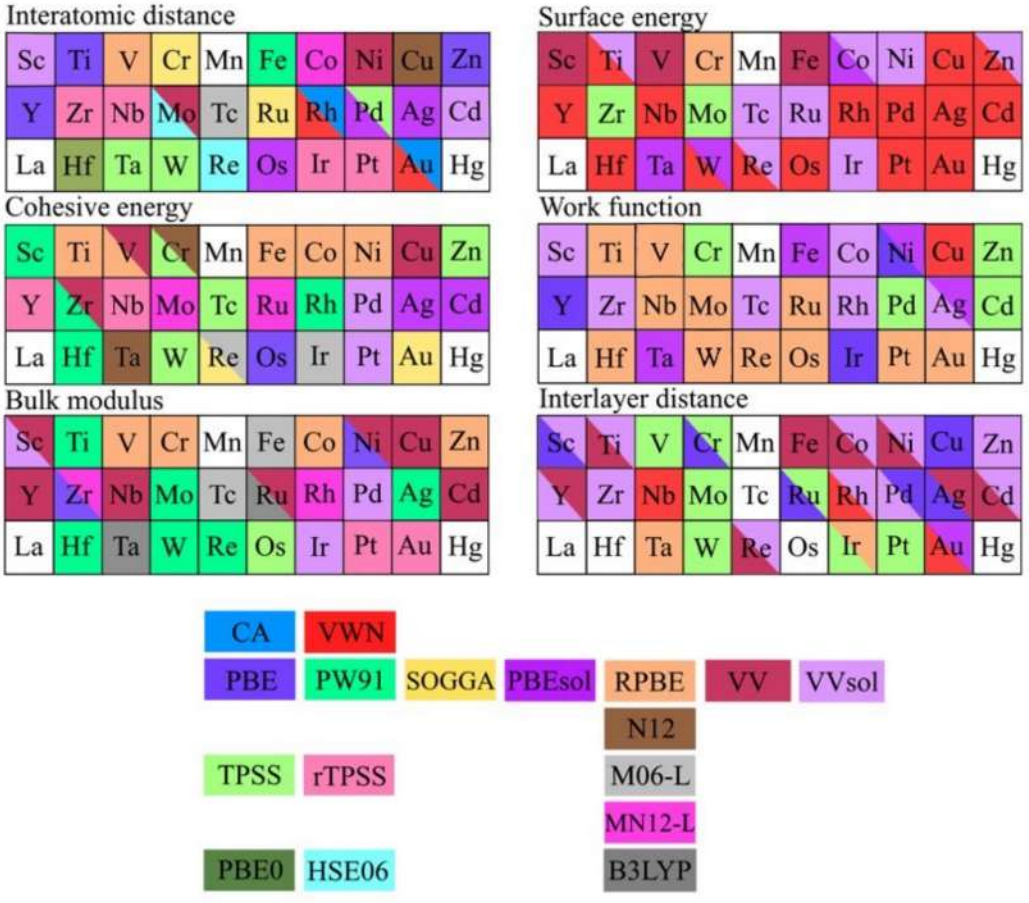

References

[1] P. Janthon, S. Luo, S. M Kozlov, F. Viñes, J. Limtrakul, D. G. Truhlar, F. Illas, *J. Chem. Theory Comput.* **2014**, *10*, 3832.

[2] K. C. Mills, Y. C. Su, *Int. Mater. Rev.* **2006**, *51*, 329.

[3] B. M. Helbert, *J. Appl. Phys.* **1997**, *48*, 4729.

[4] L. Vega, J. Ruvireta, F. Viñes, F. Illas, *J. Chem. Theory Comput.* **2018**, *14*, 395.

[5] P. Janthon, S. M. Kozlov, F. Viñes, J. Limtrakul, F. Illas, *J. Chem. Theory Comput.* **2013**, *9*, 1631.

D. Supplementary Information of Unravelling Morphological and Topological Key Aspects of Pd Nanoparticles

Table S1. Summary of Pd clusters and nanoparticles according to the number of constituent Pd atoms, n, and the adopted shape, in between Spheres (S), Truncated Octahedron (To), Octahedron (Oh), Icosahedron (Ih), Cube (C), Truncated Cube (Tc), Cuboctahedron (Ch), Tetrahedron (Th), and Decahedron (Dh).

	S	**To**	**Oh**	**Ih**	**C**	**Tc**	**Ch**	**Th**	**Dh**
n	188	38	19	55	14	32	13	10	23
	290	79	44	147	63	108	55	20	54
	370	116	85	309	172	171	147	35	105
	490	140	146	561	365	340	309	56	181
	586	201	231	923	666	357	561	84	287
	682	260	344		1099	364	923	120	
	730	314	489			500	1415		
	856	338	670			610			
	976	405	891			658			
	1264	459	1156			665			
	1408	483	1469			864			
		490				994			
		586				1074			
		640				1098			
		664							
		711							
		807							
		826							
		861							
		885							
		976							
		1072							
		1126							
		1139							
		1150							
		1288							
		1289							
		1385							
		1439							
		1504							

Table S2. Average neighboring Pd-Pd distances, δ(Pd-Pd), given in Å, for each Pd_n nanoparticle, and sorted by shape. The notation in each table item is *n*(δ(Pd-Pd))

S	To	Oh	Ih	C	Tc	Ch	Th	Dh
188(2.75)	38(2.73)	19(2.71)	55(2.76)	14(2.67)	32(2.72)	13(2.70)	10(2.66)	23(2.71)
290(2.76)	79(2.74)	44(2.73)	147(2.77)	63(2.73)	108(2.74)	55(2.73)	20(2.69)	54(2.73)
370(2.77)	116(2.75)	85(2.74)	309(2.77)	172(2.74)	171(2.75)	147(2.75)	35(2.71)	105(2.76)
490(2.77)	140(2.75)	146(2.75)	561(2.78)	365(2.76)	340(2.76)	309(2.76)	56(2.72)	181(2.77)
586(2.77)	201(2.76)	231(2.76)	923(2.78)	666(2.76)	357(2.76)	561(2.77)	83(2.73)	287(2.77)
682(2.77)	260(2.76)	344(2.76)		1099(2.77)	364(2.76)	923(2.77)	120(2.74)	
730(2.77)	314(2.76)	489(2.77)			500(2.76)	1415(2.78)		
856(2.77)	338(2.76)	670(2.77)			610(2.76)			
976(2.77)	405(2.76)	891(2.77)			658(2.76)			
1264(2.78)	459(2.77)	1156(2.77)			665(2.76)			
1408(2.78)	483(2.77)	1469(2.78)			864(2.76)			
	490(2.77)				994(2.77)			
	586(2.77)				1074(2.77)			
	640(2.77)				1098(2.77)			
	664(2.77)							
	711(2.77)							
	807(2.77)							
	826(2.77)							
	861(2.77)							
	885(2.77)							
	976(2.77)							
	1072(2.77)							
	1126(2.77)							
	1139(2.77)							
	1150(2.77)							
	1288(2.78)							
	1289(2.77)							
	1385(2.78)							
	1439(2.78)							
	1504(2.78)							

Table S3. Linear regression coefficients, R^2, as well as slopes, a, and intercepts, b, for the linear regressions of δ(Pd-Pd) *vs.* $n^{-1/3}$, according to δ(Pd-Pd) = $a \cdot n^{-1/3} + b$. Slope and intercept values are given in Å.

	a	***b***	***R²***
S	-0.24	2.80	0.988
To	-0.23	2.80	0.992
Oh	-0.23	2.80	0.997
Ih	-0.14	2.79	0.997
C	-0.30	2.80	0.988
Tc	-0.23	2.79	0.994
Ch	-0.25	2.80	0.996
Th	-0.30	2.80	0.995
Dh	-0.31	2.82	0.988

Table S4. Atomic cohesive energy, E_{coh}, given in eV·atom^{-1}, for each Pd$_n$ nanoparticle, and sorted by shape. The notation in each table item is $n(E_{coh})$.

S	To	Oh	Ih	C	Tc	Ch	Th	Dh
188(-3.15)	38(-2.78)	19(-2.51)	55(-2.91)	14(-2.33)	32(-2.65)	13(-2.22)	10(-2.12)	23(-2.60)
290(-3.26)	79(-3.00)	44(-2.83)	147(-3.16)	63(-2.88)	108(-3.03)	55(-2.88)	20(-2.46)	54(-2.88)
370(-3.29)	116(-3.09)	85(-3.01)	309(-3.29)	172(-3.13)	171(-3.13)	147(-3.12)	35(-2.67)	105(-3.06)
490(-3.34)	140(-3.13)	146(-3.13)	561(-3.37)	365(-3.26)	340(-3.28)	309(-3.26)	56(-2.83)	181(-3.18)
586(-3.35)	201(-3.21)	231(-3.22)	923(-3.43)	666(-3.35)	357(-3.27)	561(-3.34)	83(-2.94)	287(-3.26)
682(-3.38)	260(-3.24)	344(-3.29)		1099(-3.41)	364(-3.26)	923(-3.41)	120(-3.03)	
730(-3.39)	314(-3.29)	489(-3.34)			500(-3.31)	1415(-3.46)		
856(-3.41)	338(-3.29)	670(-3.38)			610(-3.36)			
976(-3.42)	405(-3.32)	891(-3.41)			658(-3.35)			
1264(-3.45)	459(-3.34)	1156(-3.44)			665(-3.35)			
1408(-3.46)	483(-3.34)	1469(-3.46)			864(-3.38)			
	490(-3.34)				994(-3.42)			
	586(-3.37)				1074(-3.42)			
	640(-3.38)				1098(-3.41)			
	664(-3.38)							
	711(-3.39)							
	807(-3.41)							
	826(-3.41)							
	861(-3.42)							
	885(-3.41)							
	976(-3.43)							
	1072(-3.44)							
	1126(-3.44)							
	1139(-3.44)							
	1150(-3.44)							
	1288(-3.45)							
	1289(-3.46)							
	1385(-3.47)							
	1439(-3.47)							
	1504(-3.48)							

Table S5. Linear regression coefficients, R^2, as well as slopes, a, and intercepts, b, for the linear regressions of E_{coh} *vs.* $n^{-1/3}$, according to $E_{coh} = a \cdot n^{-1/3} + b$. Slope and intercept values are given in eV·atom^{-1}.

	a	***b***	***R²***
S	3.53	-3.78	0.994
To	3.26	-3.76	0.999
Oh	3.30	-3.76	1.000
Ih	3.21	-3.76	0.999
C	3.40	-3.74	1.000
Tc	3.51	-3.76	0.997
Ch	3.33	-3.75	1.000
Th	3.47	-3.74	1.000
Dh	3.31	-3.76	1.000

Table S6. Linear regression coefficients, R, as well as slopes, a, and intercepts, b, for the linear regressions of E_{coh} *vs.* $n^{-1/3}$, according to $E_{coh} = a \cdot n^{-1/3} + b$, for the Truncated Octahedron (To) subfamilies. Slope and intercept values are given in eV·atom^{-1}.

	a	***b***	***R²***
To 1 level	3.25	-3.75	1.000
To 2 level	3.24	-3.76	0.999
To 3 level	3.32	-3.77	0.999
To 4 level	3.39	-3.77	0.999
To 5 level	3.70	-3.80	1.000

Figure S1. Visualization of each cross-validation (CV) iteration, corresponding to each of the m = 100 lines, applied using a shuffle split. Blue and orange represent training (75% of total data) and test (25% of total data) sets. Notice the random distribution of cases in between both sets.

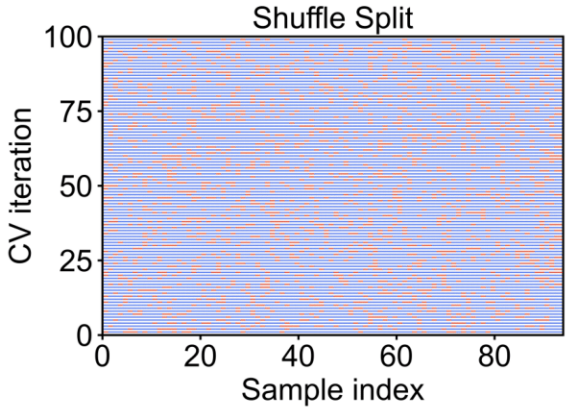

Figure S2. Comparison of most stable Cuboctahedron and Octahedron shapes and the Truncated Octahedron (To), with five levels of {001} cuts.

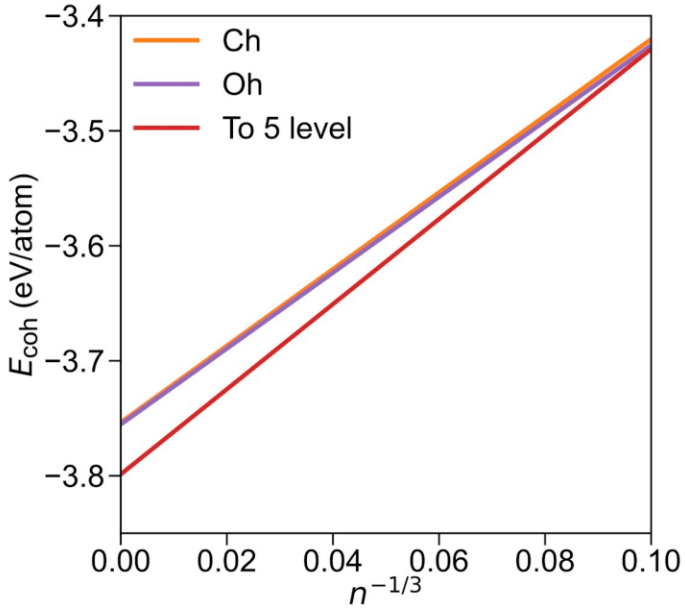

Table S7. Number of atoms for each type of CN for each studied Pd nanoparticle.

	n	**3**	**4**	**5**	**6**	**7**	**8**	**9**	**10**	**11**	**12**
S	188	—	—	24	24	24	—	24	24	—	68
	290	—	—	24	24	—	54	48	—	24	116
	370	—	—	—	72	48	6	8	48	24	164
	490	—	—	—	72	48	—	80	24	24	242
	586	—	—	24	72	—	72	48	48	24	298
	682	—	—	—	72	96	24	24	72	24	370
	730	—	—	—	72	72	72	48	—	72	394
	856	—	—	—	72	96	6	120	48	24	490
	976	—	—	24	48	120	54	48	72	48	562
	1264	—	—	—	120	96	24	144	24	96	760
	1408	—	—	—	120	24	120	192	—	72	880
To	38	—	—	—	24	—	—	8	—	—	6
	79	—	—	—	24	12	—	24	—	—	19
	116	—	—	—	24	24	6	24	—	—	38
	140	—	—	—	24	24	—	48	—	—	44
	201	—	—	—	24	36	6	56	—	—	79
	260	—	—	—	24	48	24	48	—	—	116
	314	—	—	—	24	48	6	96	—	—	140
	338	—	—	—	24	48	—	120	—	—	146
	405	—	—	—	24	60	24	96	—	—	201
	459	—	—	—	24	60	6	144	—	—	225
	483	—	—	—	24	60	—	168	—	—	231
	490	—	—	—	24	72	54	80	—	—	260
	586	—	—	—	24	72	24	152	—	—	314
	640	—	—	—	24	72	6	200	—	—	338
	664	—	—	—	24	72	—	224	—	—	344
	711	—	—	—	24	84	54	144	—	—	405
	807	—	—	—	24	84	24	216	—	—	459
	826	—	—	—	24	96	96	120	—	—	490
	861	—	—	—	24	84	6	264	—	—	483

	885	—	—	—	24	84	—	288	—	—	489
	976	—	—	—	24	96	54	216	—	—	586
	1072	—	—	—	24	96	24	288	—	—	640
	1126	—	—	—	24	96	6	336	—	—	664
	1139	—	—	—	24	108	96	200	—	—	711
	1150	—	—	—	24	96	—	360	—	—	670
	1288	—	—	—	24	120	150	168	—	—	826
	1289	—	—	—	24	108	54	296	—	—	807
	1385	—	—	—	24	108	24	368	—	—	861
	1439	—	—	—	24	108	6	416	—	—	885
	1504	—	—	—	24	120	96	288	—	—	976
Oh	19	—	6	—	—	12	—	—	—	—	1
	44	—	6	—	—	24	—	8	—	—	6
	85	—	6	—	—	36	—	24	—	—	19
	146	—	6	—	—	48	—	48	—	—	44
	231	—	6	—	—	60	—	80	—	—	85
	344	—	6	—	—	72	—	120	—	—	146
	489	—	6	—	—	84	—	168	—	—	231
	670	—	6	—	—	96	—	224	—	—	344
	891	—	6	—	—	108	—	288	—	—	489
	1156	—	6	—	—	120	—	360	—	—	670
	1469	—	6	—	—	132	—	440	—	—	891
Ih	55	—	—	—	12	—	30	—	—	—	13
	147	—	—	—	12	—	60	20	—	—	55
	309	—	—	—	12	—	90	60	—	—	147
	561	—	—	—	12	—	120	120	—	—	309
	923	—	—	—	12	—	150	200	—	—	561
C	14	8	—	—	—	—	6	—	—	—	—
	63	8	—	12	—	—	30	—	—	—	13
	172	8	—	24	—	—	78	—	—	—	62
	365	8	—	36	—	—	150	—	—	—	171
	666	8	—	48	—	—	246	—	—	—	364
	1099	8	—	60	—	—	366	—	—	—	665

Tc	32	4	—	12	—	—	12	—	—	—	4
	108	4	—	24	—	—	48	—	—	—	32
	171	—	—	36	—	—	72	—	—	—	63
	340	—	—	24	—	48	96	8	—	—	164
	357	—	—	36	—	24	126	—	—	—	171
	364	—	—	48	—	—	144	—	—	—	172
	500	4	—	48	—	—	192	—	—	—	256
	610	—	—	24	—	72	150	24	—	—	340
	658	—	—	48	—	24	222	—	—	—	364
	665	—	—	60	—	—	24	—	—	—	365
	864	4	—	60	—	—	300	—	—	—	500
	994	—	—	24	—	96	216	48	—	—	610
	1074	—	—	48	—	48	312	8	—	—	658
	1098	—	—	72	—	—	360	—	—	—	666
Ch	13	—	—	12	—	—	—	—	—	—	1
	55	—	—	12	—	24	6	—	—	—	13
	147	—	—	12	—	48	24	8	—	—	55
	309	—	—	12	—	72	54	24	—	—	147
	561	—	—	12	—	96	96	48	—	—	309
	923	—	—	12	—	120	150	80	—	—	561
	1415	—	—	12	—	216	120	120	—	—	923
Th	10	4	—	—	6	—	—	—	—	—	—
	20	4	—	—	12	—	—	4	—	—	—
	35	4	—	—	18	—	—	12	—	—	1
	56	4	—	—	24	—	—	24	—	—	4
	84	4	—	—	30	—	—	40	—	—	10
	120	4	—	—	36	—	—	60	—	—	20
Dh	23	—	5	—	7	—	10	—	—	—	1
	54	—	5	—	12	—	20	10	—	—	7
	105	—	5	—	17	—	30	30	—	—	23
	181	—	5	—	22	—	40	60	—	—	54
	287	—	5	—	27	—	50	100	—	—	105

Table S8. Topological factors for each studied Pd nanoparticle, including number of corners, *C*, total length of edges, *L*, total exposed surface area, *A*, and NP volume, *V*. L, A, and V are given in Å, Å^2, and Å^3, respectively.

	n	***C***	***L***	***A***	***V***
Oh	19	6	62.82	94.95	67.65
	44	6	94.42	214.46	229.63
	85	6	127.46	390.83	564.93
	146	6	159.93	615.27	1115.85
	231	6	192.26	889.18	1938.63
	344	6	224.73	1214.98	3096.42
	489	6	257.44	1594.33	4654.53
	670	6	290.11	2024.71	6661.19
	891	6	323.81	2522.40	9262.51
	1156	6	356.53	3057.87	12363.35
	1469	6	390.75	3673.02	16275.80
Ih	55	12	166.32	266.20	371.80
	147	12	249.01	596.65	1247.62
	309	12	332.14	1061.54	2960.75
	561	12	416.15	1666.45	5823.53
	923	12	500.35	2409.00	10121.69
C	14	8	43.64	79.36	48.10
	63	8	89.44	333.32	414.05
	172	8	135.34	763.18	1434.54
	365	8	181.38	1370.80	3453.29
	666	8	227.92	2164.57	6852.20
	1099	8	274.69	3144.05	11995.18
Ch	13	12	64.84	69.08	46.48
	55	12	129.43	275.23	369.65
	147	12	195.11	625.46	1266.31
	309	12	206.81	1117.69	3025.02
	561	12	327.15	1758.49	5969.74
	923	12	393.98	2522.40	9262.51

	1415	12	461.17	3494.44	16722.91
Th	10	4	30.58	45.00	15.61
	20	4	47.11	106.79	57.05
	35	4	63.17	192.01	137.55
	56	4	79.37	303.07	272.77
	84	4	95.56	439.33	476.07
	120	4	111.95	602.95	765.45
Dh	23	7	79.55	121.79	90.49
	54	7	120.16	277.86	309.78
	105	7	160.76	497.35	736.91
	181	7	201.80	783.71	1453.53
	287	7	242.92	1135.62	2529.00

Equation S1. Resulting model correlating atomic E_{coh} as a function of the fraction of atoms, $\boldsymbol{\chi_i}$, with i being their CN, considering all sorts of shapes, including Icosahedrons.

$$\boldsymbol{E_{coh} = -3.73 + 1.89\chi_3 + 1.83\chi_4 + 1.50\chi_5 + 1.33\chi_6 + 1.03\chi_7 + 0.75\chi_8 + 0.56\chi_9 + 0.18\chi_{10} + 0.03\chi_{11}}$$

Figure S3. Linear adjustment coefficients of ε_i *vs.* CN, when considering Icosahedrons in the E_{coh} CN breakdown. Regression coefficient, R^2, slope, a, and intercept, b, are shown.

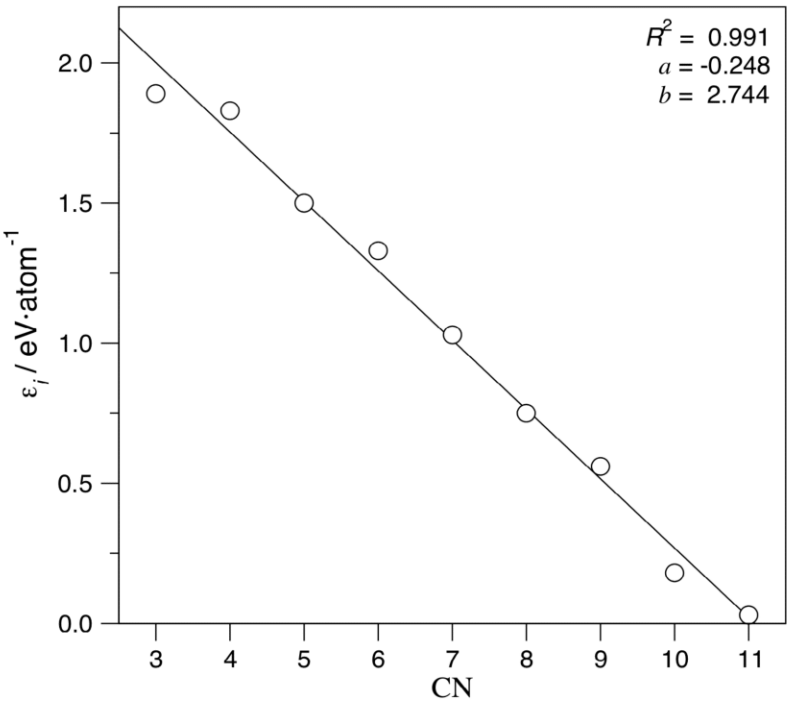

Figure S4. Comparison of calculated E_{coh} versus the predicted E_{coh}, E_{coh}^{pred}. Notice how the model overestimates the cohesion of Icosahedron shapes, with seem to follow a different linear trend.

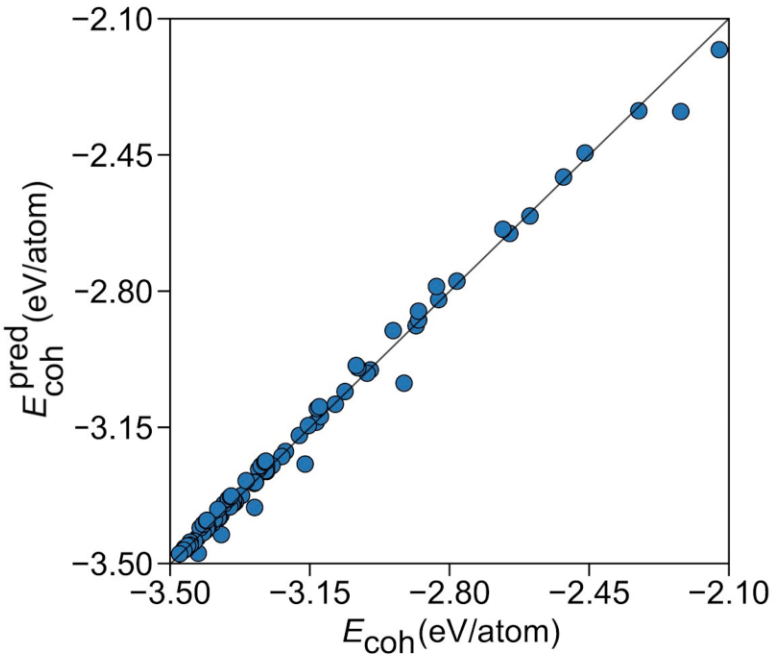

Figure S5. MAE learning curve for the training and CV scores in the E_{coh} breakdown as a matter of CN, and including Icosahedron shapes in the model. The colored areas represent the standard variation limits as a result of the 100 different fittings.

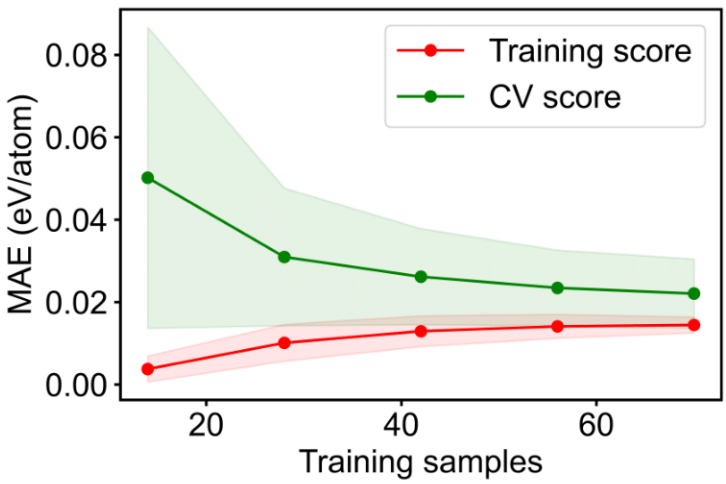

E. Supplementary Information of Irreversible Structural Dynamics on the Surface of Bimetallic PtNi Alloy Catalyst under Alternating Oxidizing and Reducing Environments

1. Characterization of as-deposited PtNi films

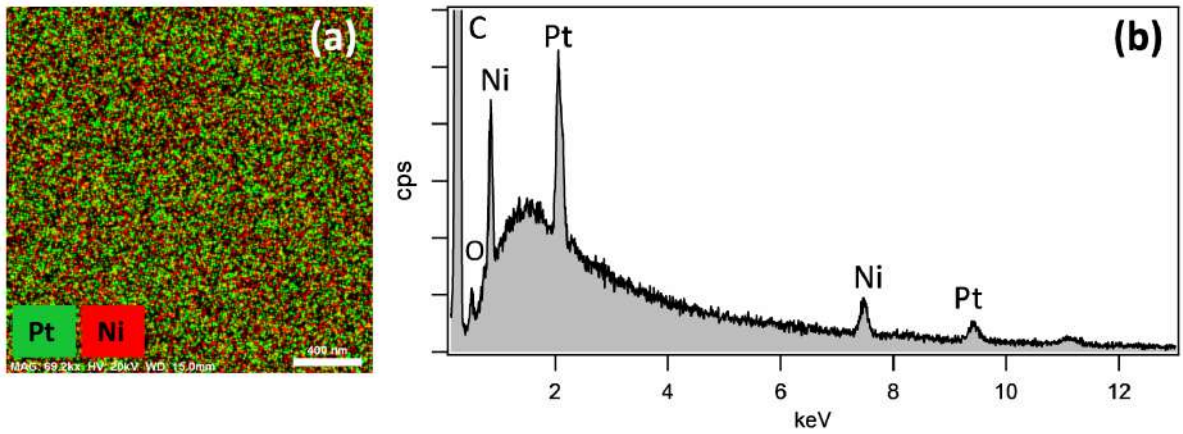

Fig. S1. EDX elemental mapping (a) and corresponding EDX spectrum (b) of as-received PtNi alloy

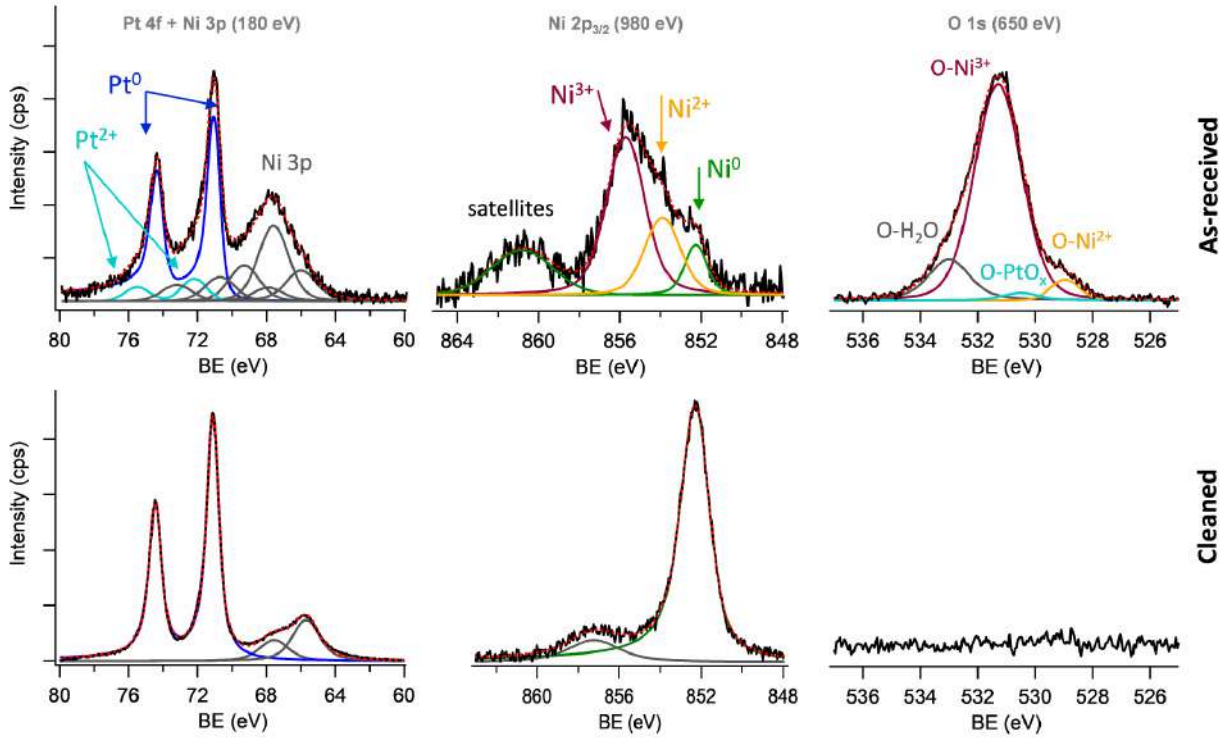

Fig. S2. SRPES spectra of the Pt 4f + Ni 3p, Ni 2p and O 1s core level regions of the PtNi catalyst before (top) and after (bottom) cleaning procedure.

2. Supplementary figures

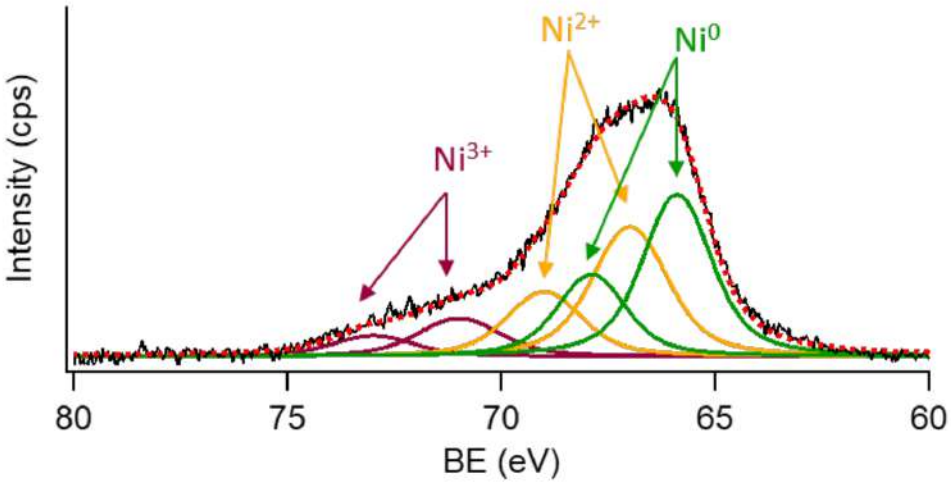

Fig. S3. The Ni 3p spectrum of pure Ni oxidized in O_2 at RT aquired at 180 eV photon energy.

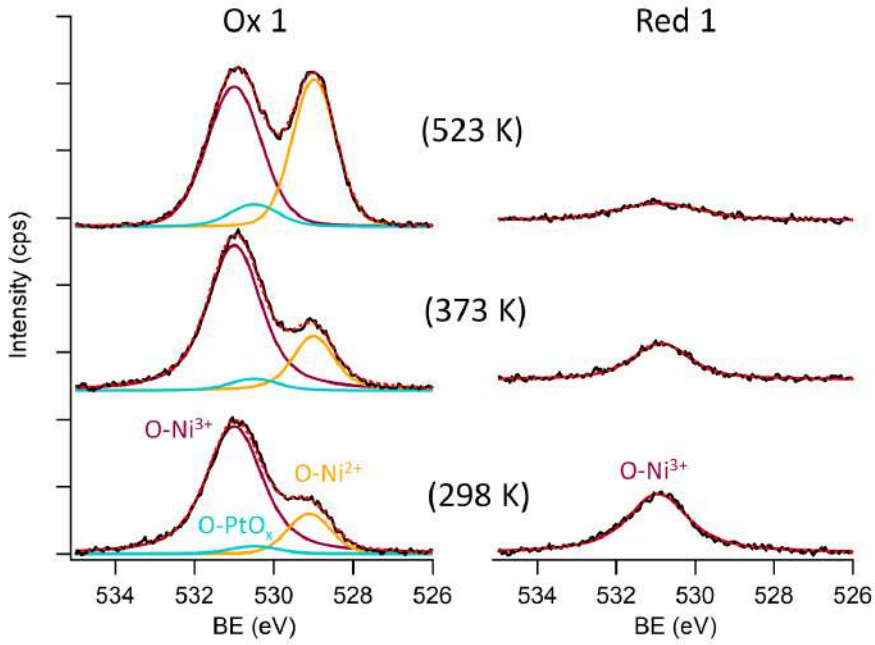

Fig. S4. SRPES spectra of the O 1s core level regions of the PtNi catalyst acquired at 650 eV photon energy after its oxidation in 5 mbar of O_2 (left) and subsequent reduction in 5 mbar of H_2 (right) at different substrate temperatures.

3. Atomic ordering in $Pt_{101}Ni_{100}$ and $Pt_{157}Ni_{157}$ nanoparticles from DFT calculations

$Pt_{101}Ni_{100}$ nanoparticle. In the most stable homotop of the $Pt_{101}Ni_{100}$ NP (Fig. S2) Pt atoms are notably favored in the surface shell with the stabilization values correlating with coordination numbers of the surface sites. The stabilization ranges from 581 meV in corner sites with the lowest coordination to 399 meV in most coordinated {111} terrace sites. Notably, these descriptors characterizing the strength of Pt-Ni bonds and the surface segregation energy of Pt atoms in the $Pt_{101}Ni_{100}$ NP agree within the statistical accuracy with the corresponding descriptors -52, -638, -504, and 432 meV calculated for a smaller truncated octahedral $Pt_{58}Ni_{58}$ NP. The lowest-energy $Pt_{101}Ni_{100}$ homotop reveals 469 Pt–Ni nearest contacts (bonds) of all 948 M–M contacts in the NP. Pt atoms occupy N_{CORNER}^{Pt} = 24 (out of a maximum of 24), N_{EDGE}^{Pt} = 30 (out of 36), $N_{TERRACE}^{Pt}$ = 37 (out of 62), N_{INNER}^{Pt} = 10 (out of 79) positions in the NP.

$Pt_{157}Ni_{157}$ nanoparticle. The interatomic interactions in the larger $Pt_{157}Ni_{157}$ NP change insignificantly compared with the $Pt_{101}Ni_{100}$ NP. Indeed, the lowest-energy homotop of the $Pt_{157}Ni_{157}$ NP (Fig. S2) also reveals notable stabilization of Pt atoms in the surface shell, from 490 meV at edge sites to 324 meV at facets terrace sites. The atomic ordering pattern of the $Pt_{157}Ni_{157}$ NP only slightly alters with the particle size increase from $Pt_{101}Ni_{100}$. As in the latter, Pt atoms tend to form a monatomic shell in the $Pt_{157}Ni_{157}$ NP, which is not complete because of the insufficient number of 157 Pt atoms to occupy all 174 exposed surface sites. More specifically, the lowest-energy $Pt_{157}Ni_{157}$ homotop reveals 676 Pt–Ni nearest contacts of 1536 M–M contacts overall in the NP and Pt atoms occupy 24 out of 24 overall available corner, 48 of 48 edge, 70 of 102 terrace, and 15 of 140 inner positions. These findings indicate that the general structure–energy relations of $Pt_{101}Ni_{100}$ and $Pt_{157}Ni_{157}$ NPs should reliably represent those of notably larger 1:1 Pt-Ni NPs.

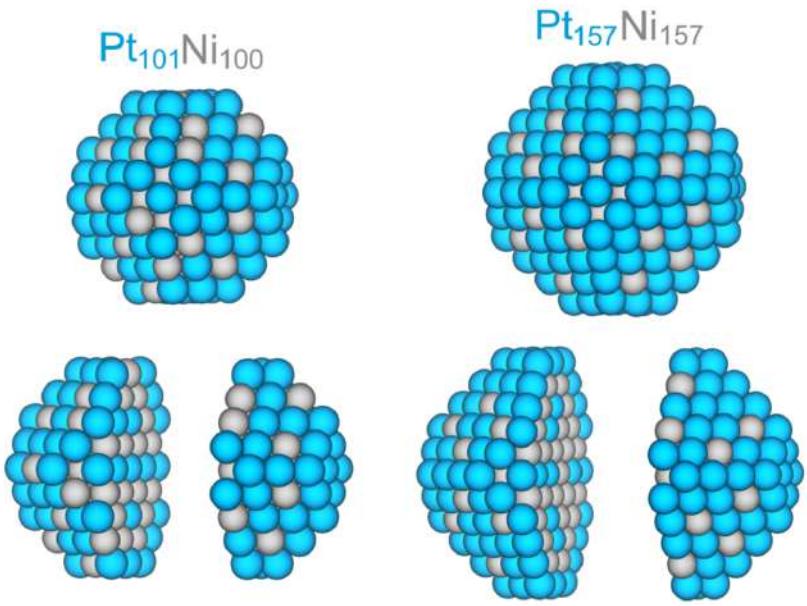

Fig. S5. Atomic ordering in the lowest-energy homotops of truncated octahedral NPs $Pt_{101}Ni_{100}$ (left column) and $Pt_{157}Ni_{157}$ (right column) according to DFT calculations. Color coding: Pt – blue, Ni – grey.

	Eq. 2				Eq. 3			
Temperature, K	rev	0	298	523	rev	0	298	523
N_{BOND}^{Pt-Ni}	4080	3911	4018	4011	4066	3575	3735	3790
N_{CORNER}^{Pt}	24	24	24	24	24	24	24	23
N_{EDGE}^{Pt}	108	108	102	98	108	108	107	107
$N_{TERRACE}^{Pt}$	0	367	352	341	0	403	372	349
N_{INNER}^{Pt}	599	232	253	268	599	196	228	252

Table S1. Temperature dependence of the atomic ordering in the representative homotop of truncated octahedral $Pt_{731}Ni_{732}$ nanoparticle (Fig. 7) obtained using TOP Eqs. 2 and 3. N_{BOND}^{Pt-Ni} – number of Pt–Ni bonds (nearest neighbours), N_{CORNER}^{Pt}, N_{EDGE}^{Pt}, $N_{TERRACE}^{Pt}$ and N_{INNER}^{Pt} – numbers of corner, edge, {111} surface terrace, and inner Pt atoms, respectively.

F. Supplementary Information of Elucidation of the Structure of PtX (X=Cu, Au, Ag) Nanoparticles of Different Sizes by Density Functional Calculations

Table S1. DFT energies of homotops with selected low- and high-energy topologies T of Pt-X (X = Au, Cu) particles, T ≡ $N^{\mathrm{Pt-X}}_{\mathrm{BOND}}.N^{\mathrm{X}}_{\mathrm{CORNER}}.N^{\mathrm{X}}_{\mathrm{EDGE}}.N^{\mathrm{X}}_{\mathrm{FACET}}$. $E^{\mathrm{DFT}}_{\mathrm{T\_min}}$ is the minimum energy and $E^{\mathrm{DFT}}_{\mathrm{T\_max}}$ is the maximum energy of 10 arbitrarily constructed homotops for a given topology, $\Delta E^{\mathrm{DFT}}_{\mathrm{T}} = E^{\mathrm{DFT}}_{\mathrm{T\_max}} - E^{\mathrm{DFT}}_{\mathrm{T\_min}}$. $E^{\mathrm{TOP}}_{\mathrm{T}}$ are the corresponding topological energies.

Particle	$N^{\mathrm{Pt-X}}_{\mathrm{BOND}}$	$N^{\mathrm{X}}_{\mathrm{CORNER}}$	$N^{\mathrm{X}}_{\mathrm{EDGE}}$	$N^{\mathrm{X}}_{\mathrm{FACET}}$	$E^{\mathrm{TOP}}_{\mathrm{T}}$ eV	$E^{\mathrm{DFT}}_{\mathrm{T\_min}}$ eV	$E^{\mathrm{DFT}}_{\mathrm{T\_max}}$ eV	$\Delta E^{\mathrm{DFT}}_{\mathrm{T}}$ meV
$Pt_{70}Au_{70}$	196	24	24	22	-586.913	-588.108	-587.081	1027
	472	13	12	25	-571.135	-574.345	-574.096	249
$Pt_{151}Au_{50}$	214	20	30	0	-978.519	-978.283	-978.258	25
	478	0	0	20	-955.212	-958.353	-958.233	120
$Pt_{101}Au_{100}$	267	24	36	40	-859.281	-859.505	-859.321	184
	594	24	0	54	-839.236	-833.665	-832.164	1501
$Pt_{51}Au_{150}$	210	24	36	62	-730.064	-729.869	-729.583	286
	312	0	36	35	-708.124	-705.958	-705.635	323
$Pt_{70}Cu_{70}$	340	24	12	0	-625.537	-626.610	-625.042	1568
	340	0	12	48	-608.392	-610.331	-609.691	640
$Pt_{151}Cu_{50}$	412	0	0	0	-1013.842	-1015.214	-1014.284	930
$Pt_{101}Cu_{100}$	560	24	8	8	-912.794	-913.767	-913.137	630
	295	13	27	60	-880.816	-891.388	-891.214	174
$Pt_{51}Cu_{150}$	418	24	36	18	-799.020	-799.627	-799.474	153

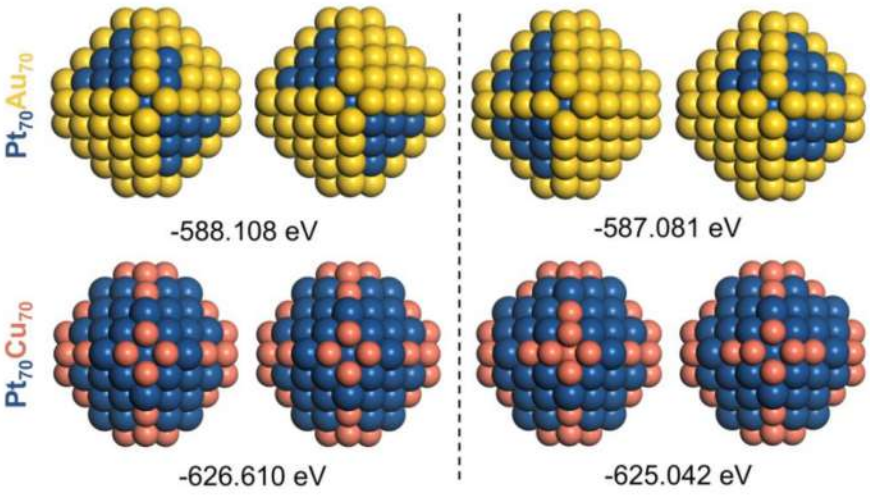

Figure S1. $E^{\mathrm{T}}{}_{\mathrm{min}}$ and $E^{\mathrm{T}}{}_{\mathrm{max}}$ homotops of the low-energy topologies 196.24.24.22 of the $Pt_{70}Au_{70}$ nanoparticle and 340.24.12.0 of the $Pt_{70}Cu_{70}$ nanoparticle. In each panel left image – front view and right image – back view. Pt – blue, Au – yellow, Cu – red-brown.

G. Supplementary Information of Nanostructuring Determines Poisoning: Tailoring CO Adsorption on PtCu Bimetallic Nanoparticles

Figure S1. Different studied CO adsorption sites exemplified on the Pt_{201} nanoparticle.

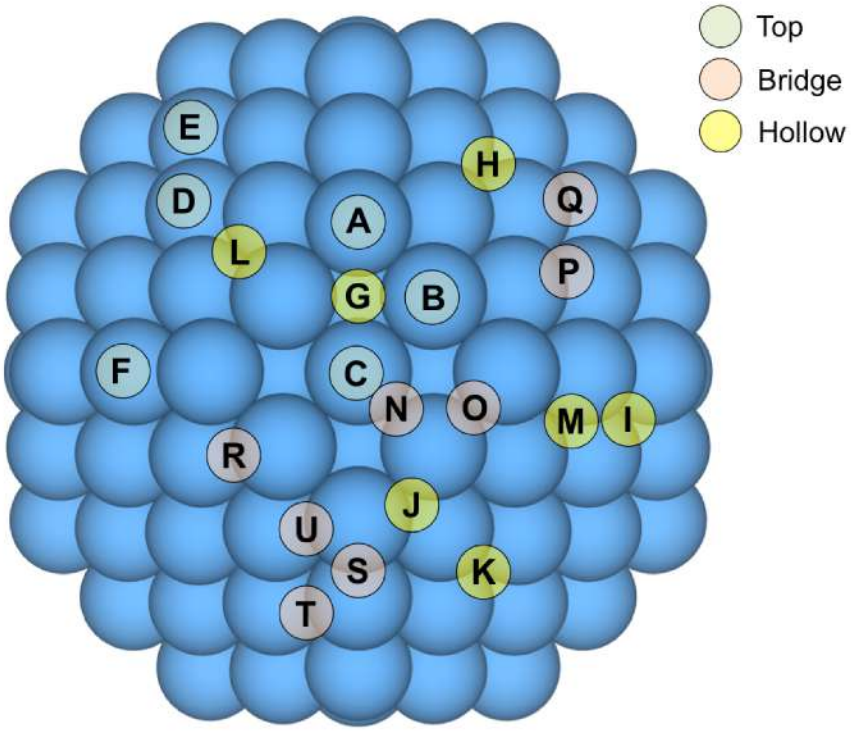

Table S1. Calculated adsorption energies, E_{ads}, given in eV, of CO molecule adsorbed through its O atom in various top positions of the nanoparticulate models **1**, **2**, **3** and **5**. The adsorption sites and models are specified in Figures S1 and Figure 2 of the main text. In model **5**, the O-end CO adsorption is explored on the exposed Cu atom.

Model / Site	A	B	C	D	F
1	~0	~0	~0	~0	~0
2	-0.01	-0.01	-0.01	~0	-0.01
3	-0.05	-0.05	-0.05	-0.04	-0.05
5	-0.03	-0.02	-0.01	-0.01	-0.02

Pt_{201}. The conjunction of under-coordination and accumulation of electron charge is thus again the main origin of a stronger back-donation, resulting as well in a larger magnitude of the adsorption energy. Finally, the most undercoordinated Pt adatom on a (111) facet bears larger positive charge on the Pt_{201} NP, 0.26 *e*, than on the Cu@Pt NP, 0.18 *e*, thus weakening the CO adsorption in the former case.

Table S4. Bader charges, Q, in *e*, on metal atoms of **A** sites, see Figure S1, of different models, see Figure 2 of the main text, prior or after to CO adsorption, as well as on the adsorbed CO molecule. Surface (Sur) and subsurface (Sub) types of atoms are indicated. A distinction is made for surface, Q_{Sur}, and subsurface, Q_{Sub}, charges. CO adsorption energies E_{ads} (in eV) are also listed for convenience.

				Prior		After		
Model	E_{ads}	M_{Sur}	M_{Sub}	Q_{Sur}	Q_{Sub}	Q_{Sur}	Q_{Sub}	Q_{CO}
1	-2.08	Pt	Pt	-0.10	0.11	0.16	0.04	-0.16
2	-0.98	Cu	Cu	-0.06	0.06	0.20	0.02	-0.17
3	-1.67	Pt	Cu	-0.14	0.30	0.14	0.28	-0.16
5	-0.95	Cu	Cu	0.29	0.29	0.47	0.28	-0.13
6	-1.87	Pt	Cu	-0.54	0.21	-0.22	0.15	-0.18
7	-2.24	Pt	Pt	-0.44	-0.43	-0.13	-0.49	-0.19
8	-2.07	Pt	Cu	-0.09	0.29	0.18	-0.31	-0.17

Table S5. Bader charges, Q, in *e*, on Pt adatoms or Pt_3 vacancy sites of Pt_{201} (model **1**) and $Cu_{79}@Pt_{119}$ (model **3**) NPs prior and after CO adsorption, as well as on the CO molecule. Surface (Sur) and subsurface (Sub) types of atoms are indicated. A distinction is made for surface, Q_{Sur}, and subsurface, Q_{Sub}, charges. CO adsorption energies E_{ads} (in eV) are also listed for convenience.

Model	E_{ads}	M_{Sur}	M_{Sub}	Q_{Sur}	Q_{Sub}	Q_{Sur}	Q_{Sub}	Q_{CO}
1: Pt_3 vacancy	-1.20	Pt	Pt	0.07	-0.06	0.20	-0.05	-0.34
1: Pt adatom	-2.25	Pt	Pt	-0.01	-0.02	0.26	~0	-0.19
3: Pt_3 vacancy	-2.43	Pt	Cu	-0.15	0.22	0.06	0.12	-0.26
3: Pt adatom	-2.53	Pt	Pt	-0.02	-0.10	0.18	-0.14	-0.21

References

(1) Bader, R. F. W. *Atoms in Molecules: a Quantum Theory*, Oxford University Press New York, 1990.

H. Inner ordered phase $L1_1$ of PtAg Nanoparticles

Using E_{TOP} method the structure of the $Ag_{158}Pt_{43}$ nanoparticle (NP) with the inner $L1_1$ ordered phase, which is the most stable homotop,[112] is not found, see Figure G.1.[113] The inner $L1_1$ layered structure is more stable than the core@shell one by 1.6 eV.

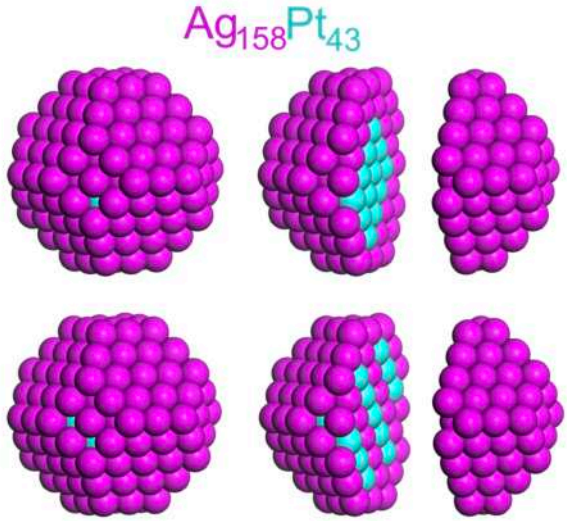

Figure G.1 Structures of core shell (obtained by E_{TOP}) and layered core $Ag_{158}Pt_{43}$. Pt and Ag atoms are shown in cyan and pink spheres respectively.

To solve this, the layer descriptor, ε_{LAYER}, was included in order to catch the inner ordered phase. It multiplies the term N_{LAYER}, which is calculated as $N_{LAYER} = \sum_{LAYERS}|n_j^A - n_j^B|$, where n_j^A and n_j^B are the numbers of atoms A and atoms B, respectively, in layer j of a NP and the sum is taken over all layers. $|n_j^A - n_j^B|$ is maximal for layers composed entirely of atoms A or B and is close to zero for layers composed of both atoms in equal proportions.[36] But, it does not work because the layer descriptor considers all the layers of the nanoparticle and not only the inner ones. Thus, we modified the MC program to count only the inner atoms for the layers descriptor. However, the inner $L1_1$ layered structure was not obtained because the negative heteroatomic bonds descriptor, $\varepsilon_{BOND}^{Pt-Ag}$, that leads to the layered inner core, is causing the presence of Pt atoms at shell. Then, the last modification to the program in

order to fix the problem was to freeze the shell of Ag atoms and let only core atoms move. A kind of inner $L1_1$ layered structure was obtained (N_{BOND}^{Pt-Ag}= 354, N_{LAYER}= 35) but not a complete one (N_{BOND}^{Pt-Ag}= 336, N_{LAYER}= 79), see Figure G.2.

$\varepsilon_{BOND}^{Pt-Ag}$	-0.032
ε_{LAYER}	-0.112

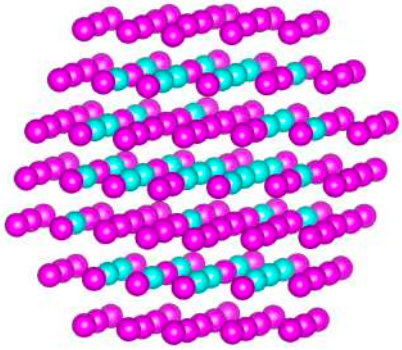

Figure G.2 Minimum structure obtained by E_{TOP} using the descriptors in top Table. Pt and Ag atoms are shown in cyan and pink spheres respectively.

REFERENCES

1. Johnston, R. L. Chapter 1 - Metal Nanoparticles and Nanoalloys. in *Frontiers of Nanoscience* (eds. Johnston, R. L. & Wilcoxon, J. P.) vol. 3 1–42 (Elsevier, 2012).
2. Ferrando, R., Jellinek, J. & Johnston, R. L. Nanoalloys: From Theory to Applications of Alloy Clusters and Nanoparticles. *Chemical Reviews* **108**, 845–910 (2008).
3. Baletto, F. & Ferrando, R. Structural properties of nanoclusters: Energetic, thermodynamic, and kinetic effects. *Reviews of Modern Physics* **77**, 371–423 (2005).
4. Bromley, S. T., Moreira, I. de P. R., Neyman, K. M. & Illas, F. Approaching nanoscale oxides: models and theoretical methods. *Chemical Society Reviews* **38**, 2657–2670 (2009).
5. Hartree, D. ~R. The Wave Mechanics of an Atom with a Non-Coulomb Central Field. Part I. Theory and Methods. *Proceedings of the Cambridge Philosophical Society* **24**, 89 (1928).
6. Fock, V. Näherungsmethode zur Lösung des quantenmechanischen Mehrkörperproblems. *Zeitschrift für Physik* **61**, 126–148 (1930).
7. Møller, Chr. & Plesset, M. S. Note on an Approximation Treatment for Many-Electron Systems. *Physical Review* **46**, 618–622 (1934).
8. Kohn, W. & Sham, L. J. Self-Consistent Equations Including Exchange and Correlation Effects. *Physical Review* **140**, A1133–A1138 (1965).
9. Perdew, J. P. & Schmidt, K. Jacob's ladder of density functional approximations for the exchange-correlation energy. *AIP Conference Proceedings* **577**, 1–20 (2001).
10. Slater, P. B. EXPLORATORY ANALYSES OF TRIP DISTRIBUTION DATA. *Journal of Regional Science* **14**, 377–388 (1974).

11. Perdew, J. P. *et al.* Atoms, molecules, solids, and surfaces: Applications of the generalized gradient approximation for exchange and correlation. *Physical Review B* **46**, 6671–6687 (1992).
12. Lee, I.-H. & Martin, R. M. Applications of the generalized-gradient approximation to atoms, clusters, and solids. *Physical Review B* **56**, 7197–7205 (1997).
13. Becke, A. D. Density-functional thermochemistry. I. The effect of the exchange-only gradient correction. *The Journal of Chemical Physics* **96**, 2155–2160 (1992).
14. Fischer, M., Evers, F. O., Formalik, F. & Olejniczak, A. Benchmarking DFT-GGA calculations for the structure optimisation of neutral-framework zeotypes. *Theoretical Chemistry Accounts* **135**, 257 (2016).
15. Ceperley, D. M. & Alder, B. J. Ground State of the Electron Gas by a Stochastic Method. *Physical Review Letters* **45**, 566–569 (1980).
16. Voski, S. H., Wilk, L. & Nusair, M. Accurate spin-dependent electron liquid correlation energies for local spin density calculations: a critical analysis. *J. Phys* **58**, 1200–1210 (1980).
17. Perdew, J. P., Burke, K. & Ernzerhof, M. Generalized Gradient Approximation Made Simple. *Physical Review Letters* **77**, 3865–3868 (1996).
18. Perdew, J. P., Burke, K. & Ernzerhof, M. Generalized Gradient Approximation Made Simple [Phys. Rev. Lett. 77, 3865 (1996)]. *Physical Review Letters* **78**, 1396–1396 (1997).
19. Perdew, J. P. & Wang, Y. Accurate and simple analytic representation of the electron-gas correlation energy. *Physical Review B* **45**, 13244–13249 (1992).
20. Zhang, Y. & Yang, W. Comment on "Generalized Gradient Approximation Made Simple." *Physical Review Letters* **80**, 890–890 (1998).

21. Perdew, J. P. *et al.* Restoring the Density-Gradient Expansion for Exchange in Solids and Surfaces. *Physical Review Letters* **100**, 136406 (2008).
22. Lieb, E. H. & Oxford, S. Improved lower bound on the indirect Coulomb energy. *International Journal of Quantum Chemistry* **19**, 427–439 (1981).
23. Hammer, B., Hansen, L. B. & Nørskov, J. K. Improved adsorption energetics within density-functional theory using revised Perdew-Burke-Ernzerhof functionals. *Physical Review B* **59**, 7413–7421 (1999).
24. Jana, S., Sharma, K. & Samal, P. Assessing the performance of the recent meta-GGA density functionals for describing the lattice constants, bulk moduli, and cohesive energies of alkali, alkaline-earth, and transition metals. *The Journal of Chemical Physics* **149**, 164703 (2018).
25. Tao, J., Perdew, J. P., Staroverov, V. N. & Scuseria, G. E. Climbing the Density Functional Ladder: Nonempirical Meta–Generalized Gradient Approximation Designed for Molecules and Solids. *Physical Review Letters* **91**, 146401 (2003).
26. Adamo, C. & Barone, V. Toward reliable density functional methods without adjustable parameters: The PBE0 model. *The Journal of Chemical Physics* **110**, 6158–6170 (1999).
27. Janthon, P. *et al.* Bulk Properties of Transition Metals: A Challenge for the Design of Universal Density Functionals. *Journal of Chemical Theory and Computation* **10**, 3832–3839 (2014).
28. Perdew, J. P., Ernzerhof, M. & Burke, K. Rationale for mixing exact exchange with density functional approximations. *The Journal of Chemical Physics* **105**, 9982–9985 (1996).
29. Vanderbilt, D. Soft self-consistent pseudopotentials in a generalized eigenvalue formalism. *Physical Review B* **41**, 7892–7895 (1990).

30. Hamann, D. R., Schlüter, M. & Chiang, C. Norm-Conserving Pseudopotentials. *Physical Review Letters* **43**, 1494–1497 (1979).
31. Blöchl, P. E. Projector augmented-wave method. *Physical Review B* **50**, 17953–17979 (1994).
32. Daga, L. E., Civalleri, B. & Maschio, L. Gaussian Basis Sets for Crystalline Solids: All-Purpose Basis Set Libraries vs System-Specific Optimizations. *Journal of Chemical Theory and Computation* **16**, 2192–2201 (2020).
33. Blum, V. *et al.* Ab initio molecular simulations with numeric atom-centered orbitals. *Computer Physics Communications* **180**, 2175–2196 (2009).
34. Frenkel, D. & Smit, B. Chapter 3 - Monte Carlo Simulations. in *Understanding Molecular Simulation (Second Edition)* (eds. Frenkel, D. & Smit, B.) 23–61 (Academic Press, 2002).
35. Metropolis, N., Rosenbluth, A. W., Rosenbluth, M. N., Teller, A. H. & Teller, E. Equation of State Calculations by Fast Computing Machines. *The Journal of Chemical Physics* **21**, 1087–1092 (1953).
36. Kozlov, S. M., Kovács, G., Ferrando, R. & Neyman, K. M. How to determine accurate chemical ordering in several nanometer large bimetallic crystallites from electronic structure calculations. *Chemical Science* **6**, 3868–3880 (2015).
37. Bader, R. F. W. *Atoms in molecules : a quantum theory*. (Clarendon Press, 1990).
38. Janthon, P., Kozlov, S. M., Viñes, F., Limtrakul, J. & Illas, F. Establishing the Accuracy of Broadly Used Density Functionals in Describing Bulk Properties of Transition Metals. *Journal of Chemical Theory and Computation* **9**, 1631–1640 (2013).
39. Janthon, P. *et al.* Bulk properties of transition metals: A challenge for the design of universal density functionals. *Journal of Chemical Theory and Computation* **10**, 3832–3839 (2014).
40. Notario-Estévez, A., Kozlov, S. M., Viñes, F. & Illas, F. Electronic-structure-based material descriptors: (in)dependence on self-

interaction and Hartree–Fock exchange. *Chem. Commun.* **51**, 5602–5605 (2015).

41. Tyson, W. R. & Miller, W. A. Surface free energies of solid metals: Estimation from liquid surface tension measurements. *Surface Science* **62**, 267–276 (1977).
42. Wulff, G. XXV. Zur Frage der Geschwindigkeit des Wachsthums und der Auflösung der Krystallflächen. in *Zeitschrift für Kristallographie - Crystalline Materials* vol. 34 449–530 (1901).
43. Tran, R. *et al.* Surface energies of elemental crystals. *Scientific Data* **3**, 160080 (2016).
44. Zhuang, H., Tkalych, A. J. & Carter, E. A. Surface Energy as a Descriptor of Catalytic Activity. *The Journal of Physical Chemistry C* **120**, 23698–23706 (2016).
45. Zhao, Y. & Truhlar, D. G. Construction of a generalized gradient approximation by restoring the density-gradient expansion and enforcing a tight Lieb–Oxford bound. *The Journal of Chemical Physics* **128**, 184109 (2008).
46. Corma, A., Boronat, M., González, S. & Illas, F. On the activation of molecular hydrogen by gold: a theoretical approximation to the nature of potential active sites. *Chemical Communications* 3371–3373 (2007).
47. Baletto, F., Ferrando, R., Fortunelli, A., Montalenti, F. & Mottet, C. Crossover among structural motifs in transition and noble-metal clusters. *The Journal of Chemical Physics* **116**, 3856–3863 (2002).
48. Schmid, G. *Clusters and colloids : from theory to applications*. (VCH, 1994).
49. Krüger, S., Vent, S. & Rösch, N. Size dependence of bond length and binding energy in palladium and gold clusters. *Berichte der Bunsengesellschaft für physikalische Chemie* **101**, 1640–1643 (1997).

50. Krüger, S., Vent, S., Nörtemann, F., Staufer, M. & Rösch, N. The average bond length in Pd clusters Pdn, n=4–309: A density-functional case study on the scaling of cluster properties. *The Journal of Chemical Physics* **115**, 2082–2087 (2001).
51. Häberlen, O. D., Chung, S.-C., Stener, M. & Rösch, N. From clusters to bulk: A relativistic density functional investigation on a series of gold clusters Aun, n=6,…,147. *The Journal of Chemical Physics* **106**, 5189–5201 (1997).
52. Barnard, A. S. & Curtiss, L. A. Predicting the Shape and Structure of Face-Centered Cubic Gold Nanocrystals Smaller than 3 nm. *ChemPhysChem* **7**, 1544–1553 (2006).
53. Che, M. & Bennett, C. O. The Influence of Particle Size on the Catalytic Properties of Supported Metals. in *Advances in Catalysis* (eds. Eley, D. D., Pines, H. & Weisz, P. B.) vol. 36 55–172 (Academic Press, 1989).
54. Kozlov, S. M. & Neyman, K. M. Catalysis from First Principles: Towards Accounting for the Effects of Nanostructuring. *Topics in Catalysis* **56**, 867–873 (2013).
55. Dietze, E. M., Plessow, P. N. & Studt, F. Modeling the Size Dependency of the Stability of Metal Nanoparticles. *The Journal of Physical Chemistry C* **123**, 25464–25469 (2019).
56. Krüger, S., Vent, S., Nörtemann, F., Staufer, M. & Rösch, N. The average bond length in Pd clusters Pdn, n=4–309: A density-functional case study on the scaling of cluster properties. *The Journal of Chemical Physics* **115**, 2082–2087 (2001).
57. Roldán, A., Viñes, F., Illas, F., Ricart, J. M. & Neyman, K. M. Density functional studies of coinage metal nanoparticles: scalability of their properties to bulk. *Theoretical Chemistry Accounts* **120**, 565–573 (2008).
58. Viñes, F., Illas, F. & Neyman, K. M. Density Functional Calculations of Pd Nanoparticles Using a Plane-Wave Method. *The Journal of Physical Chemistry A* **112**, 8911–8915 (2008).

59. Farkaš, B. & de Leeuw, N. H. Towards a morphology of cobalt nanoparticles: size and strain effects. *Nanotechnology* **31**, 195711 (2020).
60. Calle-Vallejo Federico *et al.* Finding optimal surface sites on heterogeneous catalysts by counting nearest neighbors. *Science* **350**, 185–189 (2015).
61. Rapps, T., Ahlrichs, R., Waldt, E., Kappes, M. M. & Schooss, D. On the Structures of 55-Atom Transition-Metal Clusters and Their Relationship to the Crystalline Bulk. *Angewandte Chemie International Edition* **52**, 6102–6105 (2013).
62. Piotrowski, M. J. *et al.* Theoretical Study of the Structural, Energetic, and Electronic Properties of 55-Atom Metal Nanoclusters: A DFT Investigation within van der Waals Corrections, Spin–Orbit Coupling, and PBE+U of 42 Metal Systems. *The Journal of Physical Chemistry C* **120**, 28844–28856 (2016).
63. Stone, M. Cross-Validatory Choice and Assessment of Statistical Predictions. *Journal of the Royal Statistical Society. Series B (Methodological)* **36**, 111–147 (1974).
64. Dietze, E. M., Plessow, P. N. & Studt, F. Modeling the Size Dependency of the Stability of Metal Nanoparticles. *Journal of Physical Chemistry C* **123**, 25464–25469 (2019).
65. Kozlov, S. M., Viñes, F., Nilius, N., Shaikhutdinov, S. & Neyman, K. M. Absolute Surface Step Energies: Accurate Theoretical Methods Applied to Ceria Nanoislands. *The Journal of Physical Chemistry Letters* **3**, 1956–1961 (2012).
66. Álvarez-Falcón, L., Viñes, F., Notario-Estévez, A. & Illas, F. On the hydrogen adsorption and dissociation on Cu surfaces and nanorows. *Surface Science* **646**, 221–229 (2016).
67. Ferrando, R. Chapter 6 - Stress-driven structural transitions in bimetallic nanoparticles. in *Frontiers of Nanoscience* (eds. Bromley, S. T. & Woodley, S. M.) vol. 12 189–204 (Elsevier, 2018).

68. Ferrando, R. Chapter 2 - Geometric structures and chemical ordering in nanoalloys. in *Frontiers of Nanoscience* (ed. Ferrando, R.) vol. 10 13–45 (Elsevier, 2016).
69. Mamatkulov, M. *et al.* Pd Segregation on the Surface of Bimetallic PdAu Nanoparticles Induced by Low Coverage of Adsorbed CO. *The Journal of Physical Chemistry C* **123**, 8037–8046 (2019).
70. Abdelsayed, V., Aljarash, A., El-Shall, M. S., al Othman, Z. A. & Alghamdi, A. H. Microwave Synthesis of Bimetallic Nanoalloys and CO Oxidation on Ceria-Supported Nanoalloys. *Chemistry of Materials* **21**, 2825–2834 (2009).
71. Schlatter, J. C. & Taylor, K. C. Platinum and palladium addition to supported rhodium catalysts for automotive emission control. *Journal of Catalysis* **49**, 42–50 (1977).
72. Gandhi, H. S., Graham, G. W. & McCabe, R. W. Automotive exhaust catalysis. *Journal of Catalysis* **216**, 433–442 (2003).
73. Hsieh, C.-T., Chen, Y.-F. & Yu, P.-Y. Deposition of binary Pd–Rh catalysts on nanostructured carbon supports for non-enzymatic glucose oxidation. *International Journal of Hydrogen Energy* **40**, 14857–14865 (2015).
74. Wang, S.-B., Zhu, W., Ke, J., Lin, M. & Zhang, Y.-W. Pd–Rh Nanocrystals with Tunable Morphologies and Compositions as Efficient Catalysts toward Suzuki Cross-Coupling Reactions. *ACS Catalysis* **4**, 2298–2306 (2014).
75. Pan, Y. T. & Yang, H. Rhodium-on-Palladium Nanocatalysts for Selective Methanation of Carbon Dioxide. *ChemNanoMat* **3**, 639–645 (2017).
76. Idriss, H. *et al.* A Phenomenological Study of the Metal–Oxide Interface: The Role of Catalysis in Hydrogen Production from Renewable Resources. *ChemSusChem* **1**, 905–910 (2008).
77. Hsieh, C.-T., Yu, P.-Y., Tzou, D.-Y., Hsu, J.-P. & Chiu, Y.-R. Bimetallic Pd–Rh nanoparticles onto reduced graphene oxide

nanosheets as electrocatalysts for methanol oxidation. *Journal of Electroanalytical Chemistry* **761**, 28–36 (2016).

78. Sanchez, J. M., Ducastelle, F. & Gratias, D. Generalized cluster description of multicomponent systems. *Physica A: Statistical Mechanics and its Applications* **128**, 334–350 (1984).
79. Wang, L.-L., Tan, T. L. & Johnson, D. D. Configurational Thermodynamics of Alloyed Nanoparticles with Adsorbates. *Nano Letters* **14**, 7077–7084 (2014).
80. Kovács, G., Kozlov, S. M. & Neyman, K. M. Versatile Optimization of Chemical Ordering in Bimetallic Nanoparticles. *The Journal of Physical Chemistry C* **121**, 10803–10808 (2017).
81. Kovács, G. *et al.* Revealing chemical ordering in Pt–Co nanoparticles using electronic structure calculations and X-ray photoelectron spectroscopy. *Physical Chemistry Chemical Physics* **17**, 28298–28310 (2015).
82. Wolfbeisser, A. *et al.* Surface composition changes of CuNi-ZrO2 during methane decomposition: An operando NAP-XPS and density functional study. *Catalysis Today* **283**, 134–143 (2017).
83. Son, S. U. *et al.* Designed Synthesis of Atom-Economical Pd/Ni Bimetallic Nanoparticle-Based Catalysts for Sonogashira Coupling Reactions. *Journal of the American Chemical Society* **126**, 5026–5027 (2004).
84. Liu, L. & Corma, A. Metal Catalysts for Heterogeneous Catalysis: From Single Atoms to Nanoclusters and Nanoparticles. *Chemical Reviews* **118**, 4981–5079 (2018).
85. Li, L., Chang, X., Lin, X., Zhao, Z.-J. & Gong, J. Theoretical insights into single-atom catalysts. *Chemical Society Reviews* **49**, 8156–8178 (2020).
86. Hannagan, R. T., Giannakakis, G., Flytzani-Stephanopoulos, M. & Sykes, E. C. H. Single-Atom Alloy Catalysis. *Chemical Reviews* **120**, 12044–12088 (2020).

87. Thompsett, D. Pt alloys as oxygen reduction catalysts. in *Handbook of Fuel Cells* (American Cancer Society, 2010).
88. Stamenkovic, V. R. *et al.* Trends in electrocatalysis on extended and nanoscale Pt-bimetallic alloy surfaces. *Nature Materials* **6**, 241–247 (2007).
89. Gatalo, M. *et al.* A Double-Passivation Water-Based Galvanic Displacement Method for Reproducible Gram-Scale Production of High-Performance Platinum-Alloy Electrocatalysts. *Angewandte Chemie* **131**, 13400–13404 (2019).
90. Sarkar, A. & Manthiram, A. Synthesis of Pt@Cu Core−Shell Nanoparticles by Galvanic Displacement of Cu by Pt4+ Ions and Their Application as Electrocatalysts for Oxygen Reduction Reaction in Fuel Cells. *The Journal of Physical Chemistry C* **114**, 4725–4732 (2010).
91. Baek, S., Kim, K. H., Kim, M. J. & Kim, J. J. Morphology control of noble metal catalysts from planar to dendritic shapes by galvanic displacement. *Applied Catalysis B: Environmental* **217**, 313–321 (2017).
92. Kristian, N., Yu, Y., Lee, J.-M., Liu, X. & Wang, X. Synthesis and characterization of Cocore–Ptshell electrocatalyst prepared by spontaneous replacement reaction for oxygen reduction reaction. *Electrochimica Acta* **56**, 1000–1007 (2010).
93. Li, Z. *et al.* A simple strategy to form hollow Pt3Co alloy nanosphere with ultrathin Pt shell with significant enhanced oxygen reduction reaction activity. *International Journal of Hydrogen Energy* **41**, 21394–21403 (2016).
94. Chen, Y., Yang, F., Dai, Y., Wang, W. & Chen, S. Ni@Pt Core−Shell Nanoparticles: Synthesis, Structural and Electrochemical Properties. *The Journal of Physical Chemistry C* **112**, 1645–1649 (2008).
95. Pham, V. V., Ta, V.-T. & Sunglae, C. Synthesis of NiPt alloy nanoparticles by galvanic replacement method for direct ethanol

fuel cell. *International Journal of Hydrogen Energy* **42**, 13192–13197 (2017).

96. Bokhonov, B. B. & Dudina, D. v. Preparation of porous materials by Spark Plasma Sintering: Peculiarities of alloy formation during consolidation of Fe@Pt core-shell and hollow Pt(Fe) particles. *Journal of Alloys and Compounds* **707**, 233–237 (2017).
97. Huang, Y., Tan, Z., Wu, H., Feng, C. & Ding, Y. Fe@Pt core-shell nanoparticles as electrocatalyst for oxygen reduction reaction in acidic media. *Ionics* **24**, 229–236 (2018).
98. Pupo, M. M. S. *et al.* Sn@Pt and Rh@Pt core–shell nanoparticles synthesis for glycerol oxidation. *Journal of Applied Electrochemistry* **45**, 139–150 (2015).
99. El-Khatib, K. M., Abdel Hameed, R. M., Amin, R. S. & Fetohi, A. E. Core-shell structured Pt-transition metals nanoparticles supported on activated carbon for direct methanol fuel cells. *Microchemical Journal* **145**, 566–577 (2019).
100. Wojtysiak, S., Kamiński, M., Krajczewski, J., Dłużewski, P. & Kudelski, A. Adsorption of CO on various M@Pt core–shell nanoparticles: Surface-enhanced infrared absorption and DFT studies. *Vibrational Spectroscopy* **75**, 11–18 (2014).
101. Zhang, J., Sasaki, K., Sutter, E. & Adzic, R. R. Stabilization of Platinum Oxygen-Reduction Electrocatalysts Using Gold Clusters. *Science* **315**, 220–222 (2007).
102. Zhang, J., Vukmirovic, M. B., Xu, Y., Mavrikakis, M. & Adzic, R. R. Controlling the Catalytic Activity of Platinum-Monolayer Electrocatalysts for Oxygen Reduction with Different Substrates. *Angewandte Chemie International Edition* **44**, 2132–2135 (2005).
103. Sasaki, K. *et al.* Core-Protected Platinum Monolayer Shell High-Stability Electrocatalysts for Fuel-Cell Cathodes. *Angewandte Chemie International Edition* **49**, 8602–8607 (2010).
104. Giannakakis, G., Flytzani-Stephanopoulos, M. & Sykes, E. C. H. Single-Atom Alloys as a Reductionist Approach to the Rational

Design of Heterogeneous Catalysts. *Accounts of Chemical Research* **52**, 237–247 (2019).

105. Caballero-Manrique, G. *et al.* Electrochemical synthesis and characterization of carbon-supported Pt and Pt–Ru nanoparticles with Cu cores for CO and methanol oxidation in polymer electrolyte fuel cells. *International Journal of Hydrogen Energy* **39**, 12859–12869 (2014).
106. Alekseenko, A. A. *et al.* Pt/C electrocatalysts based on the nanoparticles with the gradient structure. *International Journal of Hydrogen Energy* **43**, 3676–3687 (2018).
107. Luo, L. *et al.* Efficient CO Oxidation Using Dendrimer-Encapsulated Pt Nanoparticles Activated with <2% Cu Surface Atoms. *ACS Nano* **10**, 8760–8769 (2016).
108. Pavlets, A. *et al.* Influence of Electrochemical Pretreatment Conditions of PtCu/C Alloy Electrocatalyst on Its Activity. *Nanomaterials* **11**, 1499 (2021).
109. Garcia-Cardona, J. *et al.* Electrochemical performance of carbon-supported Pt(Cu) electrocatalysts for low-temperature fuel cells. *International Journal of Hydrogen Energy* **45**, 20582–20593 (2020).
110. Viñes, F. & Görling, A. Explaining Cu@Pt Bimetallic Nanoparticles Activity Based on NO Adsorption. *Chemistry – A European Journal* **26**, 11478–11491 (2020).
111. Zhao, Z.-J., Mu, R., Wang, X. & Gong, J. Fast Prediction of CO Binding Energy via the Local Structure Effect on PtCu Alloy Surfaces. *Langmuir* **33**, 8700–8706 (2017).
112. Pirart, J. *et al.* Reversed size-dependent stabilization of ordered nanophases. *Nature Communications* **10**, 1982 (2019).
113. Olobardi, S. *et al.* Optical Properties and Chemical Ordering of Ag–Pt Nanoalloys: A Computational Study. *The Journal of Physical Chemistry C* **123**, 25482–25491 (2019).